Transactions of the ASME®

Transactions of the ASME, Journal of Turbomachinery (ISSN 0889-504X) is published quarterly (Jan., Apr., July, Oct.) for $125.00 per year by The American Society of Mechanical Engineers, 345 East 47th Street, New York, NY 10017. Second class postage paid at New York, NY and additional mailing offices. POSTMASTER: Send address change to Transactions of the ASME, Journal of Turbomachinery, c/o THE AMERICAN SOCIETY OF MECHANICAL ENGINEERS, 22 Law Drive, Box 2300, Fairfield, NJ 07007-2300.

CHANGES OF ADDRESS must be received at Society headquarters seven weeks before they are to be effective. Please send old label and new address.

PRICES: To members, $36.00, annually; to nonmembers, $125.00.
Add $15.00 for postage to countries outside the United States and Canada.

INDEXED by Applied Mechanics Reviews and Engineering Information, Inc

Journal of Turbomachinery

Published Quarterly by The American Society of Mechanical Engineers

VOLUME 113 • NUMBER 1 • JANUARY 1991

ANNOUNCEMENTS

Experimental Study of the Three-Dimensional Flow Field in a Turbine Stator Preceded by a Full Stage

E. Boletis[1]

C. H. Sieverding

von Karman Institute for Fluid Dynamics,
B-1640 Rhode-Saint-Genèse, Belgium

The paper describes the experimental investigation of the three-dimensional flow field through a low aspect ratio, high turning turbine stator preceded by a full stage. This configuration simulates as closely as possible the flow conditions for an intermediate stator in a multistage machine, although the use of cylindrical rotor blades does not reflect typical gas turbine design practice. The inlet conditions to the stator are significantly different from those reported in previous investigations dealing with tests in isolated cascades, e.g., Sieverding (1985); Marchal and Sieverding (1977); Sieverding et al. (1984); Klein (1969); Bindon (1979, 1980); Wegel (1970); and Boletis (1985). The inlet flow field to the stator is characterized by both radial and circumferential gradients. Inlet skew occurs on both endwalls but the overall shape does not resemble those that are generated in isolated cascades by rotating the upstream endwalls. Rotor clearance effects are of predominant importance for the flow field at the tip endwall region. The flow field is explored by means of double head four-hole pressure probes in five axial planes from upstream to far downstream of the stator. The results are presented in the form of contour plots and spanwise pitch-averaged distributions.

Introduction

Modeling secondary flows in turbine blades is not an easy task. The researcher is constantly compelled to choose between (*a*) simplified models allowing more readily to establish general fundamental relationships, and (*b*) models that are closer to the complex reality of a multistage environment and therefore of more interest for the design engineer, but do not lend themselves easily to generalization.

No doubt, the secondary flow research in straight cascades contributed to a much improved understanding of basic secondary flow phenomena, as shown in a review on basic aspects of secondary flows by Sieverding (1985), but these results are only of limited value for analyzing the flow in annular cascades in which the radial pressure gradient may be of the same order of magnitude as the transverse pressure gradient. A comparison of the flow fields in straight and annular cascades using the same blade shape and very similar cascade geometries made by Sieverding and Marchal (1977) and Sieverding et al. (1984) illustrates this very clearly. However, annular cascade results with collateral inlet endwall boundary layer are representative only for first-stage guide vanes. Simple considerations show that the inlet flow to an intermediate stage guide vane is not collateral but skewed due to the transformation of the relative velocities near the endwall from a rotating to a fixed frame. Klein (1969) and Bindon (1979, 1980) attempted to simulate this effect by generating a skewed endwall boundary layer at the entrance to their cascade by means of a rotating upstream hub endwall. This method was also adopted by Boletis et al. (1983) who used the same annular cascade as Sieverding et al. (1984). The authors confirmed the significance of inlet skew for both the outlet flow angle distribution and the magnitude of secondary losses as found by Klein (1969). Wegel (1970) showed how to incorporate inlet skew in a performance prediction method. However, the deformation of the endwall boundary layer through the shearing action of a rotating upstream endwall on the otherwise collateral inlet flow oversimplifies the actual flow conditions for an intermediate stage guide vane. In this general case, both the shape and the magnitude of the inlet skewness are strongly affected by secondary and tip clearance flows in the preceding rotor. The overall flow field is also significantly influenced by radial free-stream gradients according to the rotor design and circumferential nonuniformities generated by wake and secondary motions in upstream stationary blade rows. (We note that only time-averaged flow conditions are considered in the present study.)

This paper reports results of an experimental investigation of the flow through a low aspect ratio turbine stator with inlet conditions generated by an upstream stage. For convenience

[1]Current address: Fokker BV, POB 7600, NL-1117 ZJ Schiphol, Netherlands.

Contributed by the International Gas Turbine Institute for publication in the JOURNAL OF TURBOMACHINERY. Manuscript received at ASME Headquarters March 1990.

the test stator is not followed by a second rotor. Preliminary experiments showed that for the present setup the presence of a downstream rotor would not significantly alter the stator flow conditions (Boletis and Sieverding, 1984). The results of the present investigation will be compared with those by Sieverding et al. (1984) and Boletis et al. (1983) to evaluate the merits and drawbacks of the various flow models.

Test Facility and Blade Geometry

The tests were carried out in the VKI open-loop low-speed turbine test rig. The present test arrangement of a stator preceded by a full stage is shown in Fig. 1. The stator under study is a low aspect ratio blade ($H/C = 0.6$) with constant tip and hub diameters of 0.71 m and 0.566 m, respectively. The upstream stage consists of a low aspect ratio stator ($H/C = 0.6$), with contoured tip endwall, and a rotating blade row of aspect ratio 1.2. A detailed study on the effects of tip stator contouring is reported by Boletis (1985). The meridional contour of stator I is defined by a cubic function and extends from $X/C_{ax} = 0.38$ with $D_T = 0.754$ m to $X/C_{ax} = 1.03$ with $D_T = 0.71$ m. The function has the form: $Y/H = a\cdot(X/C_{ax})^3 + b\cdot(X/C_{ax})^2 + c\cdot(X/C_{ax}) + d$ with $a = 2.2248$, $b = -4.7054$, $c = 2.6123$, and $d = 0.8702$.

The power of the rotor is absorbed by a water-brake mounted on the shaft of the turbine rotor at the exit of the conical diffuser. The test arrangement allows the turning of the first stator relative to the second.

The blade geometry is presented in Fig. 2. The most important geometric characteristics of stator II are given in Table 1. The stator blades are stacked radially about point M (Fig. 2). The blade coordinates are given in the appendix. The number of blades is equal for the two stators. In addition, both the stators and the rotor have the same untwisted blade profile, constant over the span. The only difference between rotor and stator blades is a reduced chord length: $C_R/C_S = 0.50$. The use of untwisted rotor blades (frequent in steam turbines but not in gas turbines) was dictated by manufacturing reasons. It implies unfortunately a "built-in" spanwise total pressure gradient and inlet flow angle variation for the second stator. The rotor tip clearance is $\tau/H = 0.014$. This value is typical for small gas generator turbines. The axial distance between the stator II and the preceding rotor is equal to 51 percent of

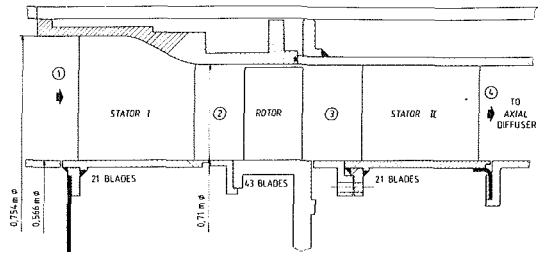

Fig. 1 Test section

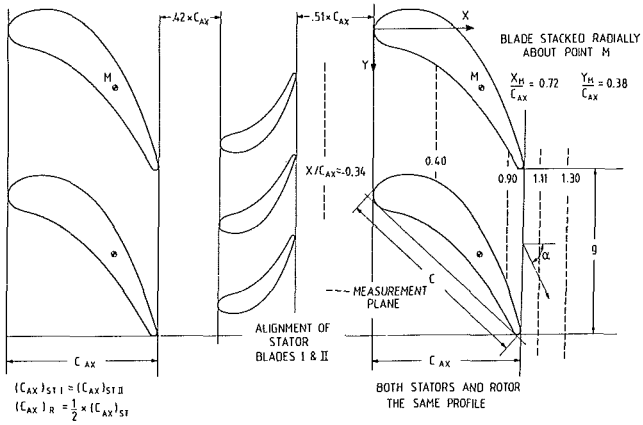

Fig. 2 Blade geometry at midspan (stators aligned)

Nomenclature

C = chord
CP_0 = local total pressure coefficient = $(P_{03,MS} - P_{0l})/(P_{03,MS} - \overline{\overline{P}}_{S4})$
CP_s = local static pressure coefficient = $(\overline{P}_{03,MS} - P_{sl})/(\overline{P}_{03,MS} - \overline{\overline{P}}_{S4})$
CP_0' = modified local total pressure coefficient = $(\overline{P}_{03}(r) - P_{0l}(r))/(\overline{P}_{03,MS} - P_{S4})$
CP_{0R}' = modified relative total pressure coefficient = $(\overline{P}_{0R,2}(r) - \overline{P}_{0R,3}(r))/(\overline{P}_{0R2,MS} - \overline{P}_{S3})$
CR = contraction ratio
D = diameter
g = pitch
H = blade height
H_{12} = boundary layer shape factor $= \delta^*/\theta$
O = throat
P = pressure
Re = Reynolds number = CV/ν
T = temperature
Tu = turbulence level = $\sqrt{\overline{v}_{ax}'^2}/V_{MS}$
U = peripheral velocity of rotating blade row or rotating hub endwall
V = velocity
v' = velocity fluctuation
X, Y = coordinates
α = absolute flow angle in blade-to-blade plane (referred to axial direction)
β = relative flow angle in blade-to-blade plane (referred to axial direction)
γ = radial flow angle = arctan(V_r/V_{ax})
δ = boundary layer thickness
δ^* = boundary layer displacement thickness
θ = boundary layer momentum thickness
ν = kinematic viscosity
ρ = density
τ = tip clearance

Subscripts

1 = upstream of stator I
2 = downstream of stator I
3 = upstream of stator II
4 = downstream of stator II
atm = atmospheric conditions
ax = axial direction
H = hub
l = local
MS = midspan
O = total conditions
p = profile
r = radial direction
R = rotating frame, rotor
s = static conditions, stator
T = tip

Superscripts

$\overline{\ }$ = pitchwise mass-averaged value
$\overline{\overline{\ }}$ = pitch- and spanwise mass-averaged value

the stator axial chord, while the distance between the two upstream rows is slightly smaller, $0.42 \times C_{ax,s}$. The rotor disk of 0.075-m total axial width extends to 0.007 m downstream of the rotor trailing edge, i.e., to $X/C_{ax} = -0.43$ from the leading edge of the stator II. The axial distances between the rotor disk and the stationary hub endwalls are kept between 0.3 mm and 0.5 mm.

The time-mean flow is measured with double-headed four-hole probes as in the previous studies. Details on the experimental procedure are given in Table 1 (Sieverding et al., 1984).

Test Program and Overall Test Conditions

Test Program. The test program consists of two series of tests. The first one, which forms the basis of this study, aims at the detailed investigation of the flow field through the stator II. The flow field is explored in five planes from upstream to downstream of the blade row (see Fig. 2). During these tests the leading edges of the two stators were placed circumferentially on a line parallel to the tunnel axis (stators aligned, see Fig. 2). The axial positions of the measurement planes inside the passage and downstream of it coincide with those used by Sieverding et al. (1984). Due to the small distance between stator II and the upstream rotor, the inlet flow field of stator II is explored at $X/C_{ax} = -0.34$ instead of $X/C_{ax} = -0.70$ as in the case of isolated stator experiments by the same authors. In each plane 12 to 18 radial traverses were made, each full traverse from tip to hub containing 35 measuring points.

The second series of tests seeks to investigate the effect of the upstream circumferential nonuniformities. To this end tests are conducted with the first stator moved circumferentially half a stator pitch (stators nonaligned). In this configuration, the flow field is explored only upstream and downstream of stator II.

Test Conditions. The test conditions are summarized in Table 2.

It should be noted that as in the previous investigations in the same facility a trip wire is placed radially on the blade suction side at $X/C_{ax} = 0.56$ ($X'/C = 0.35$ in chordwise direction). This position corresponds closely to the minimum surface pressure.

The value of the inlet skew correlating parameter, $U/V_{3,MS}$, for the present tests corresponds to that of the tests in isolated cascades with large inlet skew ($U/V_{MS} = 2.25$) (see Boletis et al., 1983). However, as will be shown later, the maximum skew angle at the hub for the present tests is close to that generated during the tests with moderate inlet skew ($U/VMS = 0.90$).

Detailed Investigation of the Flow Field Through the Stator (Stators Aligned)

Inlet Flow Conditions

Flow Quantities in the Relative Frame. Figure 3 presents the radial distribution of the pitchwise mass-averaged relative flow angle $\bar{\beta}$ and the modified relative total pressure coefficient $\overline{CP}'_{0R}$ measured at $X/C_{ax} = -0.34$ (relative to the leading edge of stator II). With respect to the rotor, the measurement plane is situated at $1.34 \times C_{ax,R}$ from the rotor leading edge. Relative quantities are obtained by transforming the measured flow field from the absolute to the rotating frame. The relative flow angle $\bar{\beta}$ is referred to the axial direction and it is indicated positive when pointing from pressure side to suction side of the rotor. The modified relative total pressure coefficient CP'_{0R} is defined as:

$$\overline{CP}'_{0R} = (\bar{P}_{0R,2}(r) - \bar{P}_{0R,3}(r))/(\bar{P}_{0R,2MS} - \bar{\bar{P}}_{S3})$$

(*a*) Relative flow angle $\bar{\beta}$: The relative flow angle shows at the lower half span the typical over- and underturning due to the rotor passage vortex. However, at the upper half span, the tip clearance effects modify the flow distribution considerably. According to Klein (1969), we distinguish three different effects influencing the β-flow angle at the vicinity of the unshrouded rotor tip: (*a*) classical secondary flow effects due to the passage vortex at the upper half of the rotor blade passage, responsible for the flow underturning at $Y/H = 0.76$; (*b*) clearance flow effects, opposite to the first, causing the ≈ 8 deg drop between $Y/H = 0.86$ and 0.96 in the region of the expected overturning for the case of zero clearance; and (*c*) effects of the rotation of the rotor blades relative to the wall, counteracting the clearance flow effect and causing the angle increase in the vicinity to the wall.

(*b*) Relative total pressure loss: The rotor total pressure loss is presented under the form of the pressure coefficient CP'_{0R}. It should be noted that in obtaining this distribution the total pressure was calculated as the difference between the inlet and exit values at a fixed radius. Hence, radial streamline shifts are not accounted for. In the vicinity of the walls the part of the curve that can be thought of as endwall layer is very thin, especially at the tip region. Two high loss concentrations are indicated between $Y/H = 0.05$ and 0.30 at the lower half span and $Y/H = 0.75$ and 0.97 at the upper half. The first one includes mainly rotor secondary flow losses, while the second is much more prominent including the strong rotor tip clear-

Table 1 Geometric characteristics of stator II

Tip diameter, D_T	0.71 m
Hub diameter, D_H	0.566 m
Chord length, C	0.12 m
Axial chord length, C_{ax}	0.087 m
Aspect ratio, H/C	0.6
Number of blades, N	21
Pitch to chord ratio, g/C, at hub, mean, tip	0.705; 0.795; 0.885
Inlet blade angle, α'_1	7 deg
Arccos (O/g) at hub, mean, tip (measured values)	69.0; 67.8; 66.8 deg

Table 2 Test conditions

Upstream of stator I, midspan	
Total pressure, P_{01}	P_{atm} + 202. mm H_2O
Flow angle, α_1	0.
Turbulence, Tu_1	0.8 percent
Rotational speed of rotor, N	940 rpm
Upstream of stator II ($X/C_{ax} = -0.34$), midspan	
Total pressure, $\bar{P}_{03,MS}$	P_{atm} + 84.5 mm H_2O
Flow angle, $\bar{\alpha}_{3,MS}$	2.5 deg
Radial flow angle, $\bar{\gamma}_{3,MS}$	2 deg
Velocity magnitude, $\bar{V}_{3,MS}$	13.7 m/s
Turbulence, $\bar{Tu}_3$	14.0 percent
Downstream of stator II ($X/C_{ax} = 1.30$), midspan	
Static pressure, $P_{S4,MS}$	P_{atm} + 2.5 mm H_2O
Reynolds number, Re_4 (based on $\bar{V}_{4,MS}$ and C)	2.7×10^5

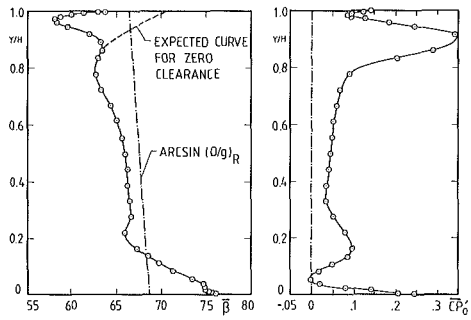

Fig. 3 Flow conditions at the inlet to stator II (absolute frame)

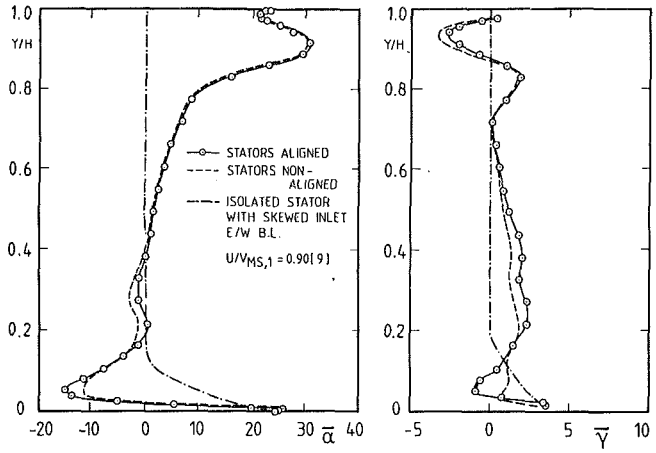

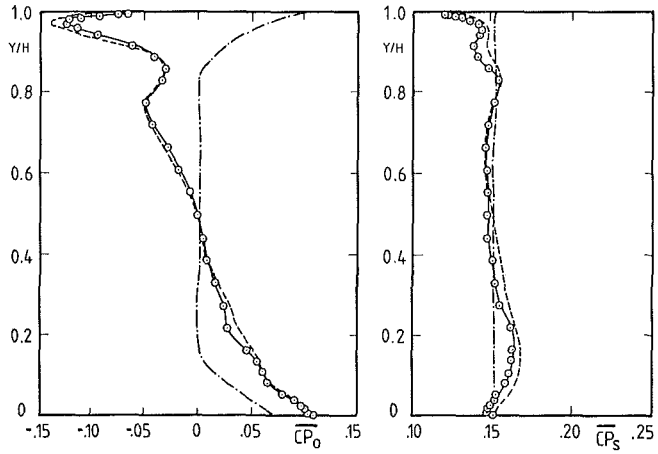

Fig. 4 Flow conditions at the inlet to stator II (absolute frame)

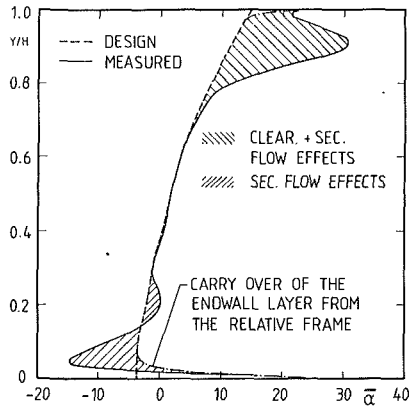

Fig. 5 Evaluation of the rotor secondary flow effect on the distribution of the inlet flow angle α

ance losses. Klein attributed the shift of the maximum tip clearance loss away from the wall to the relative movement between the rotor blades and the tip endwall.

Flow Quantities in the Absolute Frame. Figure 4 presents the pitchwise mass-averaged inlet flow quantities in the absolute frame (flow angle $\bar{\alpha}$ in blade-to-blade plane, radial flow angle $\bar{\gamma}$, total pressure and static pressure). The corresponding inlet flow distributions for the tests in an isolated cascade with moderate inlet skew (Boletis et al., 1983) are also shown. As mentioned above, the inlet measurement plane for those experiments is situated at $X/C_{ax} = -0.70$, compared to -0.34 for the present configuration. The flow angle $\bar{\alpha}$ is referred to axial direction and it is indicated positive when pointing from the pressure side to the suction side of the stator. The radial flow angle $\bar{\gamma}$ is defined as the ratio of radial to axial velocity component: $\bar{\gamma} = \arctan(V_r/V_{ax})$. It is positive when pointing from hub to tip.

(*a*) Flow angle $\bar{\alpha}$: The distribution of the absolute flow angle α shows very interesting features. At the hub the measurements show a maximum skew angle of $\approx$ 25 deg, which is close to the value measured for the isolated stator with moderate inlet skew. However, the overall shape of the α-angle distribution at the lower half span is entirely different from that of the inlet skew study. Starting from the wall the flow angle decreases rapidly, and takes negative values at $Y/H = 0.02$. After passing through a minimum of -15 deg at $Y/H = 0.05$, the angle increases and, following an S shape, reaches free-stream conditions at $Y/H = 0.3$. At the tip region the flow angle increases from 22 deg at $Y/H = 0.98$ to a maximum value of $\approx$ 32 deg at $Y/H = 0.88$ and then decreases to the free-stream value of $\approx$ 10 deg at $Y/H = 0.80$.

It is evident that the above changes of the absolute flow angle distribution are closely related to the variations of the flow quantities in the relative frame. The effects of three individual parameters can easily be distinguished: (*a*) the rotor blade design, characterized by a spanwise variation of the flow angle from -4 deg at the hub to $+14$ deg at the tip (see dotted line in Fig. 5); (*b*) the transposition of the endwall velocity profiles from the relative to the absolute frame, resulting in highly skewed flow angles in the vicinity of the walls; (*c*) the rotor secondary and clearance flows, causing in their zone of influence strong angle deviations. The individual contributions of the above parameters on the overall shape of the absolute flow angle distribution are shown in Fig. 5. It appears clearly that artificially generated inlet skew at the entrance to an isolated annular cascade by no means represents inlet conditions generated by an upstream stage.

(*b*) Total pressure: The total pressure is presented under the form of the total pressure coefficient $\overline{CP}_0$. The total pressure coefficient is defined as

$$\overline{CP}_0 = (\overline{P}_{03,MS} - \overline{P}_{0l})/(\overline{P}_{03,MS} - \overline{\overline{P}}_{S4})$$

The CP_0 distribution indicates that the free-stream flow is characterized by an important spanwise total pressure gradient ($\approx$ 20 percent of the outlet dynamic head). It is surprising that the hub secondary loss core, which is clearly defined in the relative frame, is hardly recognizable in the absolute frame.

The upstream free-stream gradients are of particular importance for the generation and evolution of the secondary flows in the blade passage as pointed out by Adkins and Smith (1982). Depending on their magnitude, upstream free-stream gradients may considerably modify the blade pressure at the front of the passage and therefore both the transverse and radial pressure gradients that are responsible for the intensity of the usual endwall vortex system. Another effect of free-stream total pressure gradients is indicated by Hawthorne (1967) and Lighthill (1956). According to Hawthorne, weakly sheared flows passing over bodies such as airfoils with blunt leading edges generate additional radial flows.

(*c*)–(*d*) Radial flow angle and static pressure: The radial flow angle $\bar{\gamma}$ is slightly positive over the largest part of the span. Near the hub endwall the value of the radial flow angle is in close agreement with that for the isolated cascade with moderate inlet skew, but the whole shape of the curve is quite different. (Note that the first recorded value of $\bar{\gamma}$ is at 2 mm wall distance. Closer to the wall the accuracy of the radial flow angle measurements diminishes considerably.) The static pressure distribution is quite uniform along the span with a small exception close to the tip endwall.

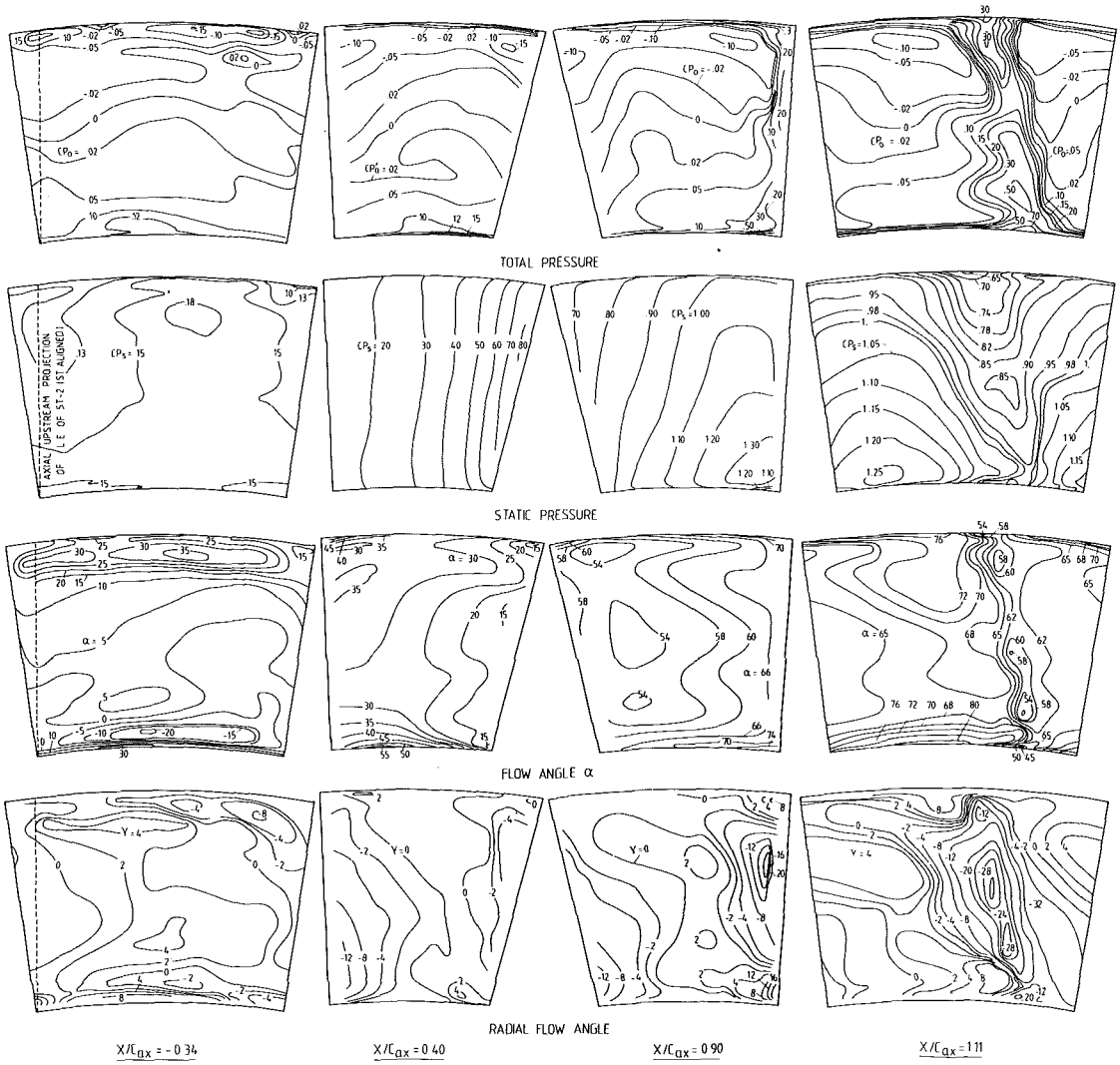

Fig. 6 Contour plots of total pressure, static pressure, flow angle α, and radial flow angle at different measurement planes (stator aligned)

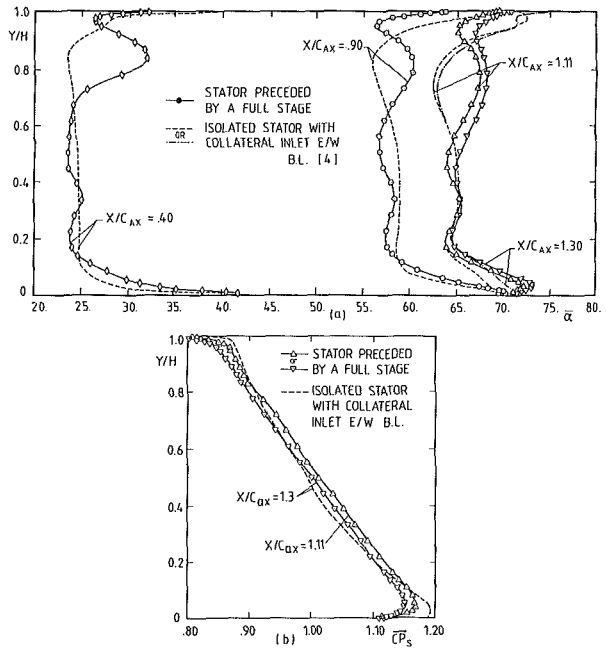

Fig. 7 Radial distribution of pitchwise averaged flow angle α and static pressure (stators aligned)

Contour Plots of Total and Static Pressure, Flow Angle, and Radial Flow Angle. Figure 6 presents for the basic test series (stators aligned) the contour plots of total pressure, static pressure, flow angles α and γ in the upstream plane ($X/C_{ax} = -0.34$), in the blade passage ($X/C_{ax} = 0.40$ and 0.90), and downstream of the blade trailing edge ($X/C_{ax} = 1.11$). The contour plots represent views of the flow looking downstream. The flow field in the last measurement plane will be presented in a following paragraph in comparison with the results of the second test series.

(*a*) Upstream flow: The upstream flow field is characterized not only by radial gradients but also by a considerable asymmetry of the flow. This is in particular the case for the total pressure and the flow angle α within 20 percent of the blade height from the walls. The fundamental reasons for these variations are to be looked for in the wake and the secondary flows of the upstream stator persisting through the rotor. The experiments show that the main features of the flow field move in line with a circumferential displacement of the upstream stator blades and the inlet asymmetries are periodic with the first stator pitch. Nonaxisymmetry of the flow downstream of a turbine stage is shown by several investigators (see, e.g., Whitney et al., 1954). We should emphasize that this is fundamentally different from the flow variations caused by the rotor itself, which are perceived by the downstream stator as unsteady flow effects.

From the tests of the isolated stator with collateral inlet endwall boundary layers we know that the upstream effect of the stator blades on the inlet flow angle extends beyond $X/C_{ax} = -0.34$. Due to the asymmetry of the incoming flow it is not possible to extract this information from the present tests.

(*b*) Flow inside the blade passage: Compared to the upstream flow field the shape of the isototal pressure lines at $X/C_{ax} = 0.40$ have undergone certain modifications. The pitchwise gradients are strengthened in the main flow but attenuated at the tip endwall. The modifications at hub are moderate. The radial gradients are more or less preserved. As far as the static pressure distribution is concerned, the isolines are quasi-radial as in the case of the isolated cascade (Sieverding et al., 1984). However, compared to those tests, the pressure difference between pressure and suction side is reduced by about 20 percent. Since the inlet angle effect at midspan ($\bar{\alpha} \cong 2.5$ deg) is negligible, it must be assumed that the static pressure is affected mainly by the free-stream total pressure gradient.

To evaluate the significance of the upstream flow field on the flow angle α distribution, let us recall that for the case of the isolated cascade with collateral inlet boundary layer, the isolines are everywhere nearly parallel to the blade pressure and suction side, except near the endwall, where the lines undergo abrupt changes due to the overturning in the boundary layer region. In the present case, the upper span is dominated by the strong inlet flow angle variations related to the rotor tip clearance flow. Two effects are particularly striking:

(*a*) a strong wiggle distribution at $Y/H = 0.85$, which gives evidence of an unusual flow motion from the pressure side to the suction side, and (*b*) a comparatively low overturning close to the tip wall due to an unloading of the front part of the blade. At the hub the situation is not very different from that for a collateral inlet boundary layer except near the pressure side. The quick change from a positive inlet angle of 25 deg at the wall to negative angles of -15 deg with 5 percent wall distance seems to have some compensating effect.

The most characteristic feature of the radial flow angle distribution is the strong inward motion along the pressure side starting from the tip and, to a lesser extent, along the upper suction side. The usual flow patterns related to the two passage vortices are hardly recognizable. The main agent for the γ distribution seems to be the total pressure gradient. Lighthill (1956), for a simple case of an inflow with a quasi-linear total pressure gradient passing over a cylindrical body, has calculated that a secondary flow motion is formed directed inward. This motion amplifies or attenuates locally the radial flows associated with the usual endwall vortex system.

Proceeding to $X/C_{ax} = 0.90$, we observe that the nonuniform distribution of the inlet free-stream total pressure in radial direction is preserved through the stator passage. We also note a considerable increase of the total pressure loss in both blade suction side corners. However, the characteristic feature of the total pressure flow field is the concentration of low-momentum material on the blade suction side at $\sim$ 35 percent of the blade height from the tip. This is underlined by highly negative radial flow angles. The loss core includes low-momentum boundary layer material fed in from the endwall–suction side corner loss core and losses due to the interference of the tip endwall crossflow with the main flow along the blade suction surface. The low-momentum material moves along the blade suction surface toward lower spanwise positions.

Compared to $X/C_{ax} = 0.40$, the position of the maximum flow overturning at the hub endwall at $X/C_{ax} = 0.90$ is closer to the suction side corner. The static pressure distribution is dominated by the radial pressure gradient due to blade design and it is very similar to that measured in isolated cascades, except at the hub.

(*c*) Flow outside the blade passage: The most characteristic feature of the outlet flow field is the radial migration of low-momentum material through the wake indicated by high negative radial flow angles (maximum values of up to -32 deg). This radial migration is first of all to be attributed to the radial static pressure gradient (see also Sieverding et al., 1984), but in the present case the radial motion is augmented by the particular inlet flow conditions, i.e., rotor tip clearance flow and spanwise total pressure gradients. Under their influence the spanwise motion of low-momentum material starts already on the suction side, resulting in a loss core at $\sim$ 35 percent of the blade height distance from the tip. These effects appear now further amplified in the downstream plane. The negative flow angle region exceeds by far the normal wake width over most of the blade height and the wake itself shows a characteristic outgrowth at about midspan.

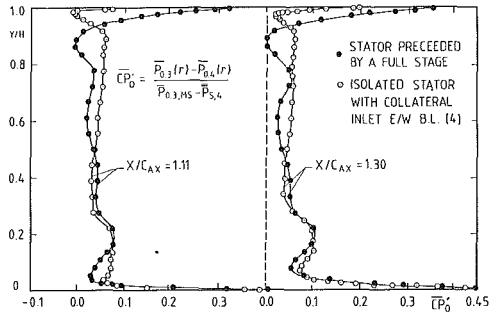

Fig. 8 Radial distribution of the exit total pressure loss (stators aligned)

It is interesting to compare the radial flow angle distribution in the downstream plane with that obtained in an isolated cascade with inlet skew generated through a rotating upstream hub endwall (Boletis et al., 1983). In the latter case the hub inlet skew caused a radial outward motion, which violently counteracted the radial inward motion due to the radial pressure gradient. However, the inlet skew generated by the rotating hub is not at all representative of that generated by an upstream rotor, as indicated before.

Spanwise Distribution of the Pitchwise-Averaged Flow Angles, Static Pressure, and Losses. Figure 7(*a*) presents the axial evolution of the spanwise distribution of the pitchwise-averaged flow angle $\bar{\alpha}$. The data are compared with those of the tests with collateral inlet endwall boundary layer (Sieverding et al., 1983). The overall inlet flow angle variation indicated by the dotted line in Fig. 5 is rapidly straightened out in the front part of the blade passage but there remain important differences at $X/C_{ax} = 0.40$ with respect to the isolated cascade with collateral inlet endwall boundary layer. The most striking difference is of course the strong local increase of $\bar{\alpha}$ between $Y/H = 0.7$ and 0.93, which is related to the rotor tip clearance flow. This overturning is conserved throughout the stator. It decreases in intensity but it gains in spanwise extension and covers at the exit more than 50 percent of the blade height.

The overturning associated with the tip endwall boundary layer is from the beginning rather small and remains always smaller than that for the reference case. The overturning at the lower endwall within the cascade is very similar to that of the reference case, which indicates that the S-type inlet skew produced by the upstream rotor influences the stator flow much less than a simple crossflow profile (see Boletis et al., 1983). However, downstream certain differences appear, notably an inversion of the overturning trend for the present case. This flow angle decrease at the wall is to be attributed to either a strong rear suction side endwall corner separation or a corner vortex.

The status of the boundary layer in this endwall region is uncertain. Of course, the trip wire on the suction side at $X/C_{ax} = 0.35$ triggers the boundary layer, thus avoiding any

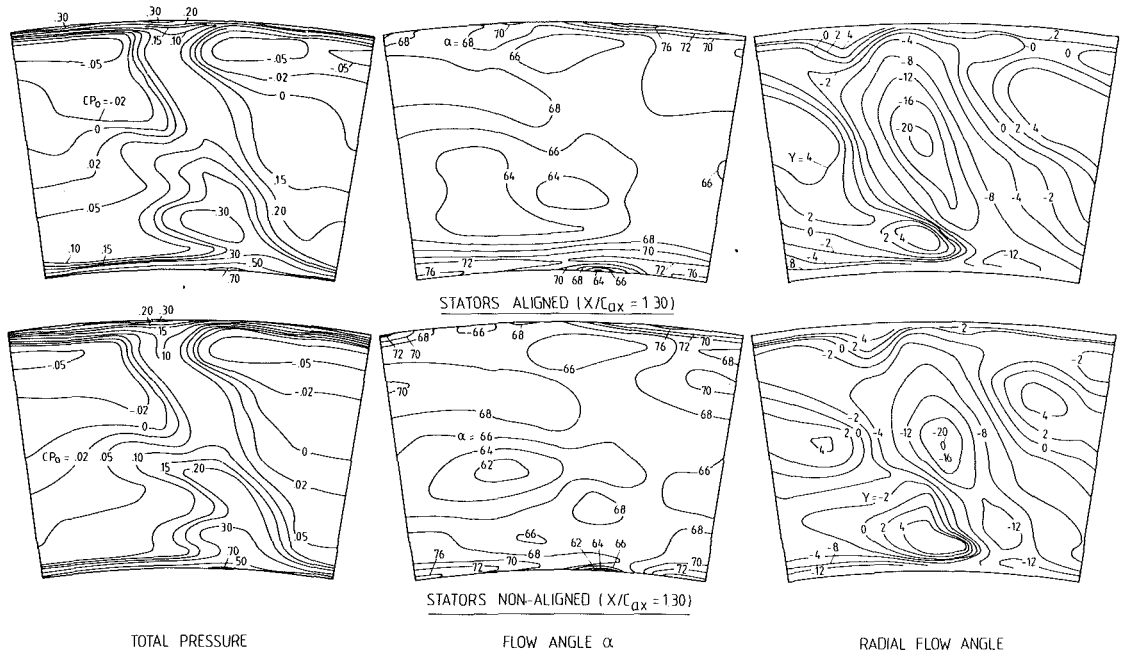

Fig. 9 Comparison of the detailed flow field at $X/C_{ax} = 1.30$ (present tests with the stators aligned and nonaligned)

major boundary layer separation, which might be expected otherwise due to the rather low Reynolds number. However, due to the downwash of the flow on the rear suction side, the flow in the rear tip region is not affected by the trip wire. Instead, this region is dominated by endwall boundary layer crossflows, the complex three-dimensional nature of which does not readily lend itself to an interpretation in terms of classical integral boundary layer values.

The exit static pressure distributions are presented in Fig. 7(*b*) in comparison with that of the tests reported by Sieverding et al. (1984) (at $X/C_{ax} = 1.30$). It is important to note that, in spite of the fact that the inlet conditions were fundamentally changed between the two tests, the exit static pressure shows only small local differences. The definite rise of the static pressure (CP_s decrease) at the hub endwall during the present tests is closely related to the local flow angle underturning.

The radial distribution of the total pressure loss in the two downstream planes is shown in Fig. 8. The presentation under the form of the modified total pressure loss coefficient CP_0' allows the comparison with the tests in isolated cascades. (The modified total pressure loss coefficient CP_0' compares the upstream and downstream total pressures at the same radial location contrary to the coefficient CP_0 used in Figs. 4 and 6, which refers all pressures to the average midspan total pressure.) Attention must be drawn to the fact that the streamlines do not move on cylindrical surfaces through the blade passage (this is more pronounced at the tip endwall region). Over significant parts of the blade height, the losses in the present tests are lower than for the reference case. The tip endwall losses are, on the contrary, considerably higher. The overall losses measured in the two exit planes are $\overline{CP}_0 = 4.6$ and 6.0 percent compared to 4.7 and 6.2 percent for the tests in an isolated cascade with a collateral inlet endwall boundary layer. These values indicate only net losses generated in the blade passage.

Effects of the Upstream Circumferential Nonuniformities

The rotor exit flow field is characterized by circumferential nonuniformities. The question arises whether variations of this

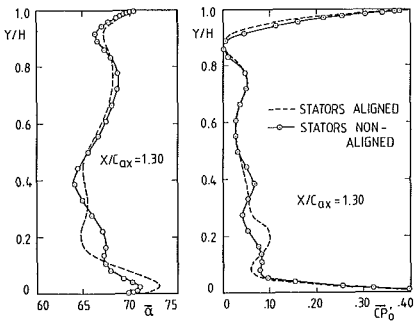

Fig. 10 Radial distribution of flow angle α and total pressure loss at $X/C_{ax} = 1.30$ (present tests with the stators aligned and nonaligned)

nature and magnitude are sufficient to affect significantly the flow field in a following stator. Apparently, nobody has yet attempted to quantify the significance of this matter for turbine blade rows. However, Okiishi (1979) in a study in a multistage compressor machine has reported that circumferential nonuniformities at the exit of a compressor stage influence considerably the flow field of a following stator. He indicated that stationary blade row wake segments exiting from the rotors were attenuated very little as they passed through the downstream blade row and had a discernible influence on that blade row exit flow. In most instances, the shape of a stator exit flow field was dependent on the position of that stator blade leading edge relative to the incoming stationary flow pattern.

Since the attenuation of stator wake flows in turbine rotors is much smaller than in compressor rotors (see Smith, 1966), the necessity of a study in turbine passage is manifest. The complementary test with the two stators nonaligned in comparison with the results of the basic study with the two stators aligned seeks to determine the effect of the upstream circumferential nonuniformities for the present case. Note that the test configuration with nonaligned stators presents a circumferential shift of the first stator with respect to the second stator by half a pitch.

The mean inlet flow distributions are presented in Fig. 4 with those of the basic tests. Since it is only the circumferential position of the upstream flow field that changes, the average

inlet flow distributions for the two tests are practically identical. The small differences of the flow angle α values between $Y/H = 0.05$ and 0.20 have probably to be attributed to the upstream effect of the stator.

Figure 9 presents the detailed flow field at $X/C_{ax} = 1.30$ for the tests with the two stators nonaligned in comparison with the basic tests. As in Fig. 6, the contour plots represent views of the flow looking downstream. Since the effect on the static pressure distribution is almost null, we restrict the comparison to the total pressure, flow angle α, and radial flow angle γ contour plots. The biggest differences occur below $Y/H = 0.60$. One observes notably at midspan a larger outgrowth of the wake and in the hub region a shift of the 30 percent loss core toward the hub, a decrease of the overturning angle, and an extension of the zone with positive α values on the left side of the wake. The stator alignment affects also the spanwise distribution of the pitch-averaged flow angle α and modified total pressure coefficient CP_0' (see Fig. 10). Of highest interest are local angle deviations between the two different stator alignments by up to 2.5 deg. The pitch- and spanwise-averaged total pressure coefficient is not affected. The overall losses remain constant ($\overline{\overline{CP}}_0 = 6.0$ percent).

Conclusions

The inlet flow conditions to a turbine stator preceded by a full stage are considerably different from those generated in isolated cascades. In particular, the shape of the inlet flow angle α and total pressure distributions are affected by radial free-stream gradients and rotor secondary and clearance flows. Artificially generated inlet skew at the entrance to an isolated cascade is not representative of inlet conditions generated by an upstream stage.

The flow field in the stator blade row is strongly influenced by the combined action of the rotor clearance flow and the free-stream total pressure gradient. They augment the effects of the radial static pressure gradient generated within the blade row causing a significant radial migration of low-momentum boundary layer material along the rear suction side. The spanwise angle variation induced by the rotor tip clearance flow persists throughout the passage. At the hub, the inlet shear is rapidly straightened out by the bend.

Downstream of the cascade the rotor tip clearance effects influence the angle distribution over the entire upper span. Compared to a cascade with collateral inlet flow the distribution has an entirely different shape and the angles differ by as much as 7 deg. At the hub, the effect of the rotor produced inlet shear on the outlet flow angle is limited to $Y/H \leq 0.15$. The spanwise static pressure distributions are hardly affected by the upstream stage and the loss distributions are similar to that found in a single stator with collateral inlet flow.

Inlet circumferential nonuniformities affect both the exit flow angle and total pressure distributions but not the overall amount of losses.

Further tests with a better rotor design to provide more uniform inlet flow conditions to the downstream stator and smaller rotor tip clearances should be of highest interest.

References

Adkins, G. G., and Smith, L. H., 1982, "Spanwise Mixing in Axial Flow Turbomachines," ASME *Journal of Engineering for Power*, Vol. 104, No. 1, pp. 97–110.

Bindon, J. P., 1979, "The Effect of Hub Inlet Boundary Layer Skewing on the Endwall Shear Flow in an Annular Turbine Cascade," ASME Paper No. 79-GT-13.

Bindon, J. P., 1980, "Exit Plane and Suction Surface Flows in an Annular Turbine Cascade With a Skewed Inlet Boundary Layer," *Int. J. Heat Fluid Flow*, Vol. 2, No. 2, pp. 57–66.

Boletis, E., Sieverding, C. H., and Van Hove, W., 1983, "Effects of a Skewed Inlet Endwall Boundary Layer on the Three Dimensional Flow Field in an Annular Turbine Cascade," in: *Viscous Effects in Turbomachines*, AGARD CP 351, Paper 16.

Boletis, E., and Sieverding, C. H., 1984, "Experimental Study of the Flow Field Behind an Annular Turbine Nozzle Guide Vane With and Without Downstream Rotor," ASME Paper No. 84-GT-15.

Boletis, E., 1985, "Effects of a Tip Endwall Contouring on the Three Dimensional Flow Field in an Annular Turbine Nozzle Guide Vane," ASME *Journal of Engineering for Gas Turbines and Power*, Vol. 107, No. 4, pp. 983–990.

Hawthorne, W. R., 1967, "The Applicability of Secondary Flow Analyses to the Solution of Internal Flow Problems," in: *Fluid Mechanics of Internal Flow*, G. Sovran, ed., Elsevier Publ. Co., Amsterdam, pp. 238–269.

Klein, A., 1969, "Investigation of the Entry Boundary Layer on the Secondary Flows in the Blading of Axial Flow Turbines," BHRA T1004.

Lighthill, M. J., 1956, "Drift," *J. Fluid Mechanics*, Vol. 1, Part 1, pp. 31–53.

Marchal, P., and Sieverding, C. H., 1977, "Secondary Flows Within Turbomachinery Bladings," in: *Secondary Flows in Turbomachines*, AGARD CP 214, Paper 1.

Okiishi, T. H., 1979, "Turbomachine Wake Transport and Interaction," in: *Unsteady Flows in Turbomachines*, VKI LS 1979-03.

Sieverding, C. H., Van Hove, W., and Boletis, E., 1984, "Experimental Study of the Three Dimensional Flow Field in an Annular Turbine Nozzle Guide Vane," ASME *Journal of Engineering for Gas Turbines and Power*, Vol. 106, No. 2, pp. 437–444.

Sieverding, C. H., 1985, "Recent Progress in the Understanding of Basic Aspects of Secondary Flows in Turbine Blade Passages," ASME *Journal of Engineering for Gas Turbines and Power*, Vol. 107, No. 2, pp. 248–257.

Smith, L. H., 1966, "Wake Dispersion in Turbomachines," ASME *Journal of Basic Engineering*, Vol. 38, No. 3, pp. 688–690.

Wegel, S., 1970, "Strömungsuntersuchungen an Beschleunigungsgittern im Windkanal und in der Axialturbine," Dissertation TH Darmstadt, Federal Republic of Germany.

Whitney, W. J., et al., 1954, "Effect of Nozzle Secondary Flows on Turbine Performance as Indicated by Exit Surveys of a Rotor," NACA RM E54B03.

APPENDIX

Blade Profile Coordinates

X	$Y_{suct.s}$	$Y_{press.s}$
0	0	0
1.08	− 4.08	4.08
2.40	− 5.76	5.76
4.20	− 7.14	7.14
6.60	− 8.40	8.04
9.00	− 9.36	8.64
11.40	−10.20	9.36
13.80	−10.80	10.08
16.20	−11.22	10.92
19.02	−11.58	11.94
21.00	−11.70	12.72
23.40	−11.64	13.80
25.80	−11.46	14.88
28.20	−11.16	16.14
30.60	−10.56	17.52
33.00	− 9.84	18.96
35.40	− 8.88	20.52
37.80	− 7.74	22.20
40.20	− 6.36	23.94
42.60	− 4.68	25.80
45.00	− 2.88	27.84
46.80	− 1.26	29.40
48.60	0.48	31.15
50.82	2.76	33.36
52.80	5.10	35.46
55.20	8.22	38.10
57.60	11.58	40.92
60.00	15.24	44.04
62.04	18.36	46.74
64.08	21.66	49.62
66.00	24.90	52.32
67.80	28.08	55.02
69.60	31.44	57.72
72.00	36.24	61.44
74.40	41.40	65.16
77.10	47.70	69.49
79.20	52.92	72.96
81.60	59.58	76.92
83.40	65.10	80.04
85.20	71.46	80.88
86.88	78.96	78.96

The table presents the coordinates of the blade section in a flat plane perpendicular to the blade stacking line (Fig. 2) at the proper stagger angle of 42.5 deg (referred to axial direction). The corresponding coordinates on cylindrical surfaces can easily be derived. Trailing and leading edges are rounded.

Simulating Boundary Layer Transition With Low-Reynolds-Number k-ϵ Turbulence Models: Part 1—An Evaluation of Prediction Characteristics

R. C. Schmidt[1]

S. V. Patankar

Department of Mechanical Engineering,
University of Minnesota,
Minneapolis, MN 55455

An analysis and evaluation of the capability of k-ϵ low-Reynolds-number turbulence models to predict transition in external boundary-layer flows subject to free-stream turbulence is presented. The similarities between the near-wall cross-stream regions in a fully turbulent boundary layer and the progressive stages through which developing boundary layers pass in the streamwise direction are used to describe the mechanisms by which the models simulate the transition process. Two representative models (Jones and Launder, 1972; Lam and Bremhorst, 1981) are employed in a series of computational tests designed to answer some specific practical questions about the ability of these models to yield accurate, reliable answers over a range of free-stream turbulence conditions.

Introduction

Of the factors hindering the accurate prediction of external heat transfer on gas turbine blades, one of the more significant is boundary-layer transition (see, for example, Graham, 1979). Transition is a complex phenomenon and is influenced by a variety of factors. The Reynolds number, free-stream turbulence, pressure gradient, surface roughness, and streamline curvature are just some of the factors that have been shown to influence this process. However, even under the simplest of flow conditions, i.e., transition occurring on a flat plate under a relatively quiescent free-stream flow, the process is complex. For this case the transition process begins with the formation of two-dimensional Tollmien–Schlichting waves moving in the direction of the flow. The flow becomes three dimensional as these waves develop spanwise variations and are amplified. From then on there is a cascade of vortex breakdowns that end in fully three-dimensional fluctuations of an almost random nature. This has been characterized experimentally as small "bursts" of turbulence occurring at random locations and spreading laterally downstream, eventually engulfing the entire boundary layer. The final stages of this process are manifested very clearly by a relatively sharp increase in the skin friction coefficient, and also, in the case of heat transfer, in a sharp increase in the Stanton number.

Of the external factors influencing boundary layer transition, one of the most dominant is the magnitude of the free-stream turbulence intensity. As a characteristic of the free stream, it provides a continuous source of energetic disturbances that are entrained into the boundary layer as it grows. This alters the nature of the boundary layer and affects the transition process, promoting a dramatic decrease in the laminar pretransition length. In addition, spanwise variations in large-scale structures, and also in the resulting time-averaged quantities such as the skin friction coefficient and the Stanton number, are suppressed. Experiments have shown that quantities such as the momentum thickness Reynolds number at the beginning of transition can be correlated to Tu_e, and a number of such correlations have been proposed. One of the most recent is that of Abu-Ghannam and Shaw (1980).

The development of transition models has naturally followed from the information gained in experiments. From an engineering perspective, the purpose of these models is generally to provide answers to the questions: (1) "Where is the effective start of transition?"; (2) "At what point is transition complete?", and (3) "In what manner do the boundary layer properties of interest vary during the process?" Since the completion of transition implies a turbulent state of the boundary layer, these models are generally developed within the framework of a turbulence model. For example, if a "mixing length" turbulence model is employed, a typical calculation might proceed as follows. The calculation begins by solving the laminar boundary layer equations from a starting location very near the leading edge or stagnation point. The computation proceeds by marching in the streamwise direction until the Reynolds number is equal to some critical value as given by a correlation. At this point, an algebraic function is introduced in the equations to vary the turbulent viscosity continuously from zero to an appropriate value as predicted by

[1] Present address: Sandia National Laboratories, Albuquerque, NM.

Contributed by the International Gas Turbine Institute for publication in the JOURNAL OF TURBOMACHINERY. Manuscript received at ASME Headquarters June 1990.

the turbulence model. The distance over which this occurs would be determined by an additional correlation.

Transition models developed within the framework of mixing length type models are relatively common and have been used in many applications. These methods are practical, relatively inexpensive, and work fairly well when within the range of the experimental data on which the correlations are based. An excellent summary and evaluation of many of these has recently been reported by Park and Simon (1987). Unfortunately, these methods have proven difficult to extend and modify such that transition is reliably predicted in the variety of interacting and complex flow conditions such as might occur on a turbine blade. Thus engineers have continued to explore other ways of solving the problem.

About eighteen years ago Jones and Launder (1972, 1973) published their work on the introduction of so-called "low Reynolds number" (hereafter referred to as LRN) functions into the framework of a k–ϵ two-equation turbulence model. Since that time a variety of other models introducing similar types of functions have been suggested by other researchers (see Patel et al., 1985, for an excellent review). These functions modify and/or add to certain terms in the k and ϵ transport equations such that near-wall damping effects are simulated. (It should be noted that these functions have almost all been formulated and applied only within the framework of boundary layer flow along a wall, where marching techniques can be applied to the resulting parabolic boundary layer equations. The generalization of these models to less restrictive conditions has not as yet been pursued, and thus these models are currently not suitable for implementation in a general purpose three-dimensional Navier–Stokes code.)

At first, LRN k–ϵ models were applied to the calculation of flow in pipes, channels, and turbulent external boundary layers. Two of the notable successes of these models were the prediction of the correct Reynolds number at which pipe flow became turbulent, and the relaminarization of a turbulent boundary layer under a large accelerating pressure gradient. Perhaps inspired by the success in these areas, it appears that Pridden (1975; also see Launder and Spalding, 1974) was the first to consider the potential of these models to simulate boundary layer transition under the influence of free-stream turbulence.

The nature of two-equation LRN turbulence models makes them attractive as potential predictive tools for transitional boundary layers. First, the LRN functions within the models are implemented such that an independent model for transition seems unnecessary (i.e., the transition model is built in). Furthermore, because these models have the capability of describing processes associated with nonequilibrium flow conditions, a broader range of problems might be modeled with less empirical input.

In the years since this potential was realized, a number of papers have been published demonstrating the use of these types of models in predicting external boundary layer transition. These include the work of Wilcox (1975, 1977, 1979), Dutoya and Mitchard (1981), Arad et al. (1982), Hylton et al. (1983), Wang et al. (1985), and especially that of Scheuerer (1983), and Rodi and Scheuerer (1985a, 1985b). However, our experience indicated that there still existed certain issues regarding the practical implementation and accuracy of methods of this type that had not been adequately addressed in previously published work. In particular, some important questions concerning initial profile specification, starting location sensitivity, and the relative accuracy of these models in predicting the correct location and length of the transition region over a range of free-stream turbulence intensities remained unanswered. It was also felt that a comparison of the predictions from two different models would be beneficial.

Motivated by these issues, the authors embarked on the task of evaluating the use of these models and considering ways in which they might be improved. Preliminary results of this work dealing only with flat-plate zero-pressure-gradient flows were previously presented (Schmidt and Patankar, 1987). However, further work has been completed, which both significantly expands upon and slightly revises these previous results. In this paper (Part 1) and its companion (Part 2), the salient results of this effort are presented.

We will begin by describing why the transition process is simulated when using two-equation k–ϵ LRN models, thereby clarifying the conditions under which we can expect these models to be useful. With this as background, the results of a series of computational tests will be presented and discussed. For conducting these computational experiments, two different but representative LRN models designed for use with a standard k–ϵ two-equation turbulence model were applied. The models chosen were those of Lam and Bremhorst (1981) and Jones and Launder (1972, 1973).

The Boundary Layer Equations

If the flow is assumed to be steady and two dimensional, and conventional time-averaging is employed, then the following equations govern the velocity within the boundary layer:

Nomenclature

C_f = skin friction coefficient
C_1, C_2, C_μ = constants in the k–ϵ turbulence model
D, E = empirical functions used in some LRN models (see Table 2)
f_1, f_2, f_μ = empirical functions introduced in LRN models (see Table 2)
k = turbulent kinetic energy
Re_x = Reynolds number based on x
Re_θ = momentum thickness Reynolds number
$\mathrm{Re}_{\theta,s}$, $\mathrm{Re}_{\theta,E}$ = values of Re_θ at the start and end of transition
Re_t = a Reynolds number defined as $k^2/\nu\tilde{\epsilon}$
Re_y = a Reynolds number defined as $\sqrt{k}y/\nu$
Tu = turbulence intensity
U, V = mean velocities in the x and y directions
$\overline{u'v'}$ = apparent turbulent stress
x = streamwise distance from the leading edge
y = cross-stream distance from the wall
δ = boundary layer thickness
ϵ = dissipation rate
μ = molecular viscosity
μ_t = eddy or turbulent viscosity
ν = kinematic viscosity $= \mu/\rho$
ρ = fluid density
σ_k, σ_ϵ = empirical constants in the k–ϵ turbulence model

Subscripts

e = denoting free-stream value
i = denoting value at the initial starting location

Continuity:

$$\frac{\partial}{\partial x}(\rho U)+\frac{\partial}{\partial y}(\rho \tilde{V})=0 \tag{1}$$

x-Momentum:

$$\rho U\left(\frac{\partial U}{\partial x}\right)+\rho \tilde{V}\left(\frac{\partial U}{\partial y}\right)=-\frac{dP}{dx}+\frac{\partial}{\partial y}\left(\mu\frac{\partial U}{\partial y}-\rho\overline{u'v'}\right) \tag{2}$$

The quantities U and V are the time-averaged mean velocities, and u' and v' are the instantaneous velocity fluctuations. The overbar implies a time-averaged quantity, the prime a fluctuating quantity, and the tilde over V indicates a mass-weighted averaging where

$$\rho \tilde{V}=\rho V+\overline{\rho' v'} \tag{3}$$

With the specification of initial starting conditions, appropriate boundary conditions, and a turbulence model for the turbulent shear stress, these equations can be solved. The numerical solution method used was the finite difference approach of Patankar and Spalding (1970) for boundary layer flows. The streamwise step size was restricted to some fraction of the calculated momentum thickness (generally about 0.5), and tests made to assure the solution was independent of this choice. A variable grid consisting of 88 grid points (refined significantly near the wall) was used for all the calculations presented. Tests showed that the grid thus specified was sufficiently refined to yield essentially grid-independent results. Greater details with respect to the numerical methods and coding can be found from Schmidt (1987).

The Low-Reynolds-Number Turbulence Models

Although many proposals have been suggested for introducing LRN functions into the k–ϵ turbulence model, it is possible to generalize these variations by writing the basic equations in a manner described by Patel et al. (1985). We begin by defining the turbulent viscosity as

$$\mu_t=\rho C_\mu f_\mu \frac{k^2}{\tilde{\epsilon}} \tag{4}$$

where C_μ is a constant, f_μ is one of the LRN functions to be described, and k and $\tilde{\epsilon}$ are the turbulent kinetic energy and dissipation rate function, respectively. The tilde has been placed over ϵ so that differences between the meaning of ϵ used in the various models can be clarified. We define

$$\tilde{\epsilon}=\epsilon-D \tag{5}$$

where in some models the quantity D is assigned to be a function of k. This change of variables is used in some models to provide a means whereby the wall boundary condition in the ϵ equation can be specified as zero. More will be explained about this later.

The transport equations for k and $\tilde{\epsilon}$ can be written as

$$\rho U\frac{\partial k}{\partial x}+\rho \tilde{V}\frac{\partial k}{\partial y}=\frac{\partial}{\partial y}\left\{\left(\mu+\frac{\mu_t}{\sigma_k}\right)\frac{\partial k}{\partial y}\right\}+\mu_t\left(\frac{\partial U}{\partial y}\right)^2-\rho(\tilde{\epsilon}+D) \tag{6}$$

$$\rho U\frac{\partial \tilde{\epsilon}}{\partial x}+\rho \tilde{V}\frac{\partial \tilde{\epsilon}}{\partial y}=\frac{\partial}{\partial y}\left\{\left(\mu+\frac{\mu_t}{\sigma_\epsilon}\right)\frac{\partial \tilde{\epsilon}}{\partial y}\right\}+\frac{\tilde{\epsilon}}{k}\left\{C_1 f_1 \mu_t\left(\frac{\partial U}{\partial y}\right)^2-\rho C_2 f_2 \tilde{\epsilon}\right\}+E \tag{7}$$

In the free-stream these equation reduce to

Table 1 The k–ϵ turbulence model constants

C_μ	C_1	C_2	σ_k	σ_ϵ
0.09	1.44	1.92	1.0	1.3

Table 2 The low-Reynolds-number functions used in the Jones–Launder and Lam–Bremhorst models

	Jones–Launder model	Lam–Bremhorst model
f_μ	$\exp\left(\frac{3.4}{1.+.02\mathrm{Re}_t)^2}\right)$	$(1\text{-}\exp(-0.0163\mathrm{Re}_y))^2(1+20\mathrm{Re}_t)$
f_1	1.0	$1.0+\left(\frac{0.055}{f_\mu}\right)^3$
f_2	$1.0-0.3\exp(-\mathrm{Re}_t^2)$	$1.0-\exp(-\mathrm{Re}_t^2)$
E	$2\nu\mu_t\left(\frac{\partial U}{\partial y}\right)^2$	0
D	$2\nu\left(\frac{\partial\sqrt{k}}{\partial y}\right)^2$	0

$$U_e\frac{dk_e}{dx}=-\epsilon_e \tag{8}$$

$$U_e\frac{d\epsilon_e}{dx}=-C_2\frac{\epsilon_e^2}{k_e} \tag{9}$$

which can be solved independently of equations (6) and (7) to provide the boundary conditions at the outer edge. Note that for the purposes of this paper, we will be assuming that the free-stream turbulence is both approximately constant and homogeneous. This implies that ϵ_e is small and that the following relationship between turbulence intensity and turbulent kinetic energy holds:

$$k_e=1.5(Tu_eU_e)^2 \tag{10}$$

Contained within equations (4)–(7) are five empirical constants: C_μ, C_1, C_2, σ_k, σ_ϵ, and five empirical functions: f_μ, f_1, f_2, D, and E. The five constants all pertain to conditions away from very near the wall (i.e., determined independently of LRN model considerations), and only small differences exist between the values recommended by most current researchers. The values used in this work, given in Table 1, are those suggested as "standard" by Launder and Spalding (1974).

Turbulent motions immediately adjacent to solid walls are significantly influenced by the presence of the wall. Here the magnitude of the effective turbulent viscosity becomes small, the effects of molecular viscosity become important, and the standard k–ϵ equations are no longer valid. One of the approaches to dealing with this is to introduce special functions into the equations, and a variety of different suggestions for the functions f_μ, f_1, f_2, D, and E have been made. These functions provide a modifying influence on the k–ϵ model in the very near wall region, thus extending the validity of the equations clear through the viscous sublayer to the wall. Various models have these functions dependent on one or more turbulent Reynolds numbers (Re_t, Re_y; see nomenclature for definitions), or the inner wall coordinate y^+. A good discussion of these functions is given by Patel et al. (1985) and the reader is referred there for a description of each of these functions individually.

The specific LRN functions of the Jones–Launder model and of the Lam–Bremhorst model as used in this work are given in Table 2. These two models were chosen for closer evaluation here for a number of reasons. First, they both have

seen application to a variety of different flows by a number of independent researchers. Furthermore, both have been applied by previous researchers to predict transitional flows on turbine blades. Second, when compared with other LRN k–ϵ models as reported by Patel et al. (1985), they were shown to be among the better models at predicting the characteristics of fully turbulent flow. Third, they represent two somewhat different approaches to introducing LRN modifications.

The major differences between these models stem from two basic choices: what dissipation rate variable to use, and how to functionalize f_μ. A brief discussion of these is of value and will now follow.

Exactly at the wall, the value of k must go to zero. However, it can be shown that the dissipation rate ϵ does not. The wall boundary condition for ϵ is

$$\epsilon\Big|_{y=0} = \nu \frac{\partial^2 k}{\partial y^2}\Big|_{y=0} \tag{11}$$

For computational reasons, some models, including that of Jones and Launder, have avoided this boundary condition by introducing a change of variables. By choosing a function D in equation (5) such that $D|_{y=\phi} = \epsilon|_{y=\phi}$, the boundary condition for the variable $\tilde{\epsilon}$ becomes zero. The function D shown for the Jones–Launder model in Table 2 is one such choice, which allows $\tilde{\epsilon}$ to be specified as zero at the wall. The Lam–Bremhorst model on the other hand introduces no such change of variables.

It should be noted that the original approach of Lam and Bremhorst was to apply the boundary condition (11) directly. However, Patel et al. (1985) found that due to the influence of the other LRN functions chosen, the computations are relatively insensitive to this boundary condition, and the simpler condition

$$\frac{\partial \epsilon}{\partial y}\Big|_{y=0} = 0 \tag{12}$$

can be applied without any change in predictions.

Another significant difference between these models is the choice of independent variables used in correlating the f_μ function. In the case of Jones and Launder, a single parameter correlation with Re_t is introduced. This implies only an indirect effect of the wall through the variables k and ϵ. In contrast, the Lam–Bremhorst formulation makes f_μ a function of both Re_t and Re_y, which introduces a direct dependence on the relative proximity of the wall. The details of how each of the other functions were chosen can be found in the original papers by Lam and Bremhorst (1981), and by Jones and Launder (1972, 1973). It is important to recognize that although some of the functional dependence chosen can be justified directly through empirical or physical arguments, other choices were in essence ad hoc.

How LRN k–ϵ Models Simulate Transition

The k and ϵ equations solved in our boundary layer calculations are simply advection diffusion equations with a particular set of nonlinear source terms. The LRN functions incorporated into the various models have each been derived after considering near-wall experimental data for fully turbulent channel and boundary layer flows. Stability or transition criteria were not factors used in formulating the LRN functions in any of these models. However, when applied to boundary layer flows with free-stream turbulence, a simulation of transition is clearly provided, and the predicted behavior does mimic some aspects of the physical behavior we generally associate with stability theory. This comes through the nature of the LRN function "near-wall" effects on the source terms in the k and ϵ equations.

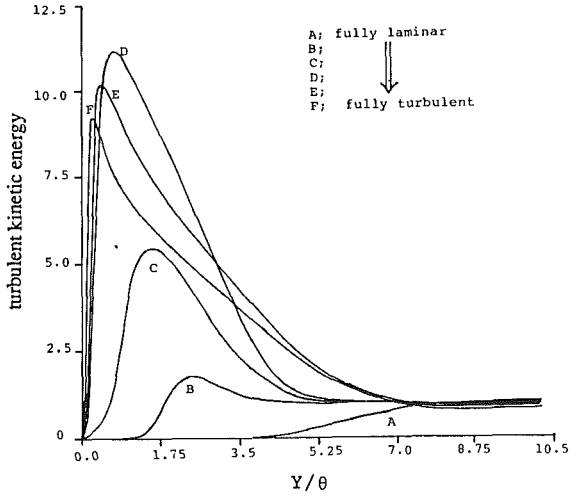

Fig. 1 Development of the turbulent kinetic energy profiles as simulated by the Lam–Bremhorst model

Consider the well-known near-wall behavior of a turbulent boundary layer. Descriptions of its structure generally refer to at least three regions: the viscous sublayer immediately adjacent to the wall, the outer turbulent "law of the wall" region, and the so-called buffer region between. Transposing in our minds the streamwise x coordinate with the cross-stream y coordinate, we see the following correspondence:

developing laminar boundary layer ↔	viscous sublayer
transitional region ↔	buffer layer
turbulent boundary layer ↔	turbulent "law of the wall" region

Now consider a boundary layer developing on a flat plate where the free-stream flow is turbulent. When the boundary layer thickness is very thin, such as is the case at low Reynolds numbers (Re_x), the edge of the boundary layer only extends out to a relatively small y^+. Thus the LRN functions, designed to simulate the proper viscous sublayer in a turbulent boundary layer, also damp out any turbulent production that would otherwise occur due to the influx of turbulent energy from the free stream. As the boundary layer grows and its edge extends to larger and larger values of y^+, the LRN functions no longer suppress the modeled turbulence production term and the computed boundary layer profiles proceed through a simulated transition. The computational process thus qualitatively mimics the functional relationship between transition and Reynolds number that we normally associate with stability theory.

The correspondence that exists between the near-wall cross-stream regions in a fully turbulent boundary layer, and the progressive stages through which developing boundary layers pass in the streamwise direction, is the basic reason why k–ϵ LRN models are able to reproduce correctly certain qualitative aspects of boundary-layer transition with free-stream turbulence.

It is useful here to illustrate this process with a calculation made with the Lam–Bremhorst model. Figure 1 shows the typical development of the turbulent kinetic energy profiles as the simulated flow proceeds from a laminar to a turbulent state. Initially, the kinetic energy profile is monotonic, increasing slowly from zero at the wall to k_e at the boundary. As the calculations march downstream, turbulent kinetic energy from the free stream is convected and diffused into the boundary layer. As this continues, the production term in the model ($P_k = \mu_t(\partial U/\partial y)^2$) starts to become significant. This in

turn increases the local value of k, and thus μ_t (see equation (6)). This process feeds on itself, causing the rapid increase in k shown. Note that a large overshoot occurs initially, then slowly decays until the parameters achieve a relatively stable state due to the LRN functions and the wall boundary conditions.

This process is initially controlled by the convection and diffusion of k into the boundary layer from the free stream. However, although the transport of k into the boundary layer is a necessary first step, it is not the whole story, for it is the interaction of this influx of k with the nonlinear source terms in the k and ϵ equations that drives the solution through a simulated transition to the turbulent state. It should also be noted that these models (in their present forms) cannot predict transition when the free stream is perfectly quiescent (i.e., there is no free-stream k to transport into the boundary layer).

Evaluating the Transition Prediction Characteristics

That k–ϵ LRN models do simulate a transition process is known, and the mechanism by which this occurs has just been described. However, their usefulness in predicting boundary layer transition can only be realized if quantitatively accurate predictions over a broad range of conditions can be made without ambiguities in the specification of starting conditions. To help evaluate this potential, a series of numerical experiments were performed to test the transition prediction characteristics of both the Lam–Bremhorst and the Jones–Launder LRN k–ϵ turbulence models. In particular, answers to the following three questions have been sought through the completion of these tests:

1 How important to the transition predictions is the specification of the initial profiles of k and ϵ?

2 How important to the transition predictions is the exact location at which the calculations are started?

3 What are the quantitative differences in the transition predictions when the free-stream turbulence varies and how do these predictions compare with experimental evidence?

Prior to transition, we expect the velocity boundary layer to behave at least approximately like a simple laminar boundary layer. Although this approximation degenerates as the free-stream turbulence becomes large, in harmony with the previous work of others we follow this practice in all of the calculations to be presented here.

Sensitivity to Starting Profiles of k and ϵ. When performing a calculation to predict transition, a marching-type solution procedure must obviously start somewhere prior to where transition will occur. Unfortunately, very few experimental data exist in the literature to guide us in specifying the initial profiles for k and ϵ prior to transition. The only applicable work of which we are aware is that of Dyban et al. (1976). They report measured $\overline{u'^2}$ values through a "pseudo-laminar" boundary layer at $\mathrm{Re}_x = 6.2 \times 10^3$, and for several different levels of free-stream turbulence. However, the limited nature of the data presented makes it difficult to justify basing one's calculations upon it. From a practical standpoint, the importance of knowing the correct initial profiles of k and ϵ depends entirely upon how sensitive the results are to these values. Thus a number of basically ad-hoc methods, based primarily on the known boundary conditions and intuition, have been implemented in previous work. One such practice is that proposed by Rodi and Scheuerer (1985a, 1985b). They chose to set

$$k = k_e \left(\frac{U}{U_e} \right)^n \quad , \quad n = 2 \tag{13}$$

$$\epsilon = a_1 k \left(\frac{\partial U}{\partial y} \right) \quad , \quad \epsilon > \epsilon_e \tag{14}$$

where the initial starting location x_i is located such that $\mathrm{Re}_\theta \leq 100$, and a_1 is an empirical function correlated to the free-stream turbulence intensity.

The nature of these equations is such that they also provide a convenient way to vary the initial profiles of k and ϵ. For example, choosing n large reduces the k profile, while setting a_1 large increases the magnitude of the ϵ profile. Since increasing ϵ tends to decrease k, the combination of specifying both n and a_1 as large yields a starting profile with essentially no turbulent kinetic energy except at the free-stream edge.

To evaluate the sensitivity of the calculations to the specification of these profiles, calculations were performed for the following conditions but with two distinctly different starting profiles and at two different starting locations:

- $Tu_e = \text{const} = 3.00$ percent (ϵ_e was set very small; see equations (8) and (9))
- $dP/dx = 0$ (constant velocity)
- Flat plate (no curvature)

The two profiles considered correspond to $n = 2$, $a_1 = 0.375$ (the recommended values of Rodi and Scheuerer at this Tu_e), and $n = 8$, $a_1 = 2.0$. The two starting locations were $\mathrm{Re}_x = 2.27 \times 10^4$ and $\mathrm{Re}_x = 1.0 \times 10^3$. Note that these values correspond to $\mathrm{Re}_\theta = 100$ and $\mathrm{Re}_\theta = 21$, respectively. When using the Jones–Launder model, which uses the modified dissipation variable $\tilde{\epsilon}$, equation (14) was slightly modified by removing the restriction $\epsilon > \epsilon_e$. This allowed $\tilde{\epsilon}$ to decrease to zero at the wall. To represent the calculated transition process, we will plot the coefficient of friction (C_f) versus Reynolds number based on x (Re_x).

Figures 2 and 3 are plots of the calculated variation in C_f versus Re_x for the four test cases described using the Jones–Launder and Lam–Bremhorst LRN models, respectively. Examination of these figures leads to the following general conclusions, which appear valid for both models:

- At any given starting location, specifying a k profile with the least amount of turbulent kinetic energy results in the onset of transition beginning at the farthest downstream location.
- The sensitivity of the transition predictions to the initial profiles of k and ϵ decreases as the starting location moves upstream, eventually becoming indepedent of these profiles.

Taken together, these observations yield another important conclusion about these tests:

- Appropriate specification of initial profiles at $\mathrm{Re}_x = 2.27 \times 10^4$ (A and B) would yield transition predictions identical to either of those that were started at $\mathrm{Re}_x = 1.0 \times 10^3$ (C and D). However, it is not possible to specify any profiles that, when starting the calculations at $\mathrm{Re}_x = 1.0 \times 10^3$, would yield transition predictions identical to either of those that were started at $\mathrm{Re}_x = 2.27 \times 10^4$.

This last conclusion is especially important in relation to choosing a starting location for the calculation. It stems from the transition process (as simulated in these models) being strongly controlled by the transport of k into the boundary layer. By moving the starting location upstream, you effectively increase the region over which k will have been diffused and convected into the boundary layer before reaching any particular downstream location. The next set of tests will further clarify this point.

Although the abovementioned conclusions can be applied to both models, obvious differences between the transition predictions also exist. Because the differences between ϵ and $\tilde{\epsilon}$ mean that the starting profiles as applied to the two models are not exactly the same, some care must be used in comparing the two results directly. However, it is quite clear that the

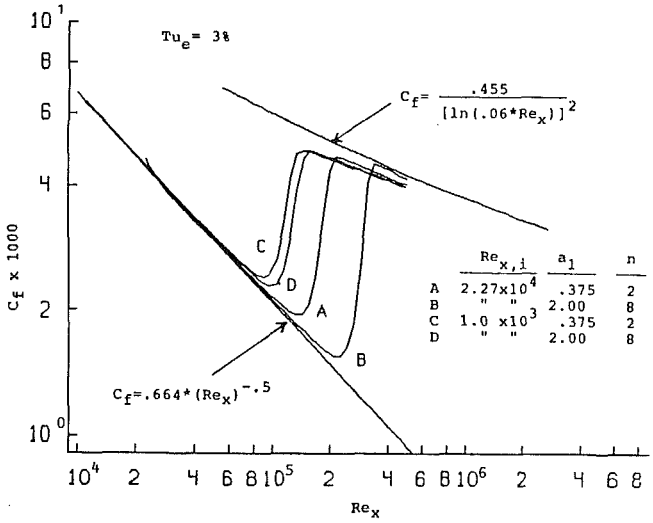

Fig. 2 Plot of C_f versus Re_x for different starting profiles of k and ϵ; Jones-Launder model

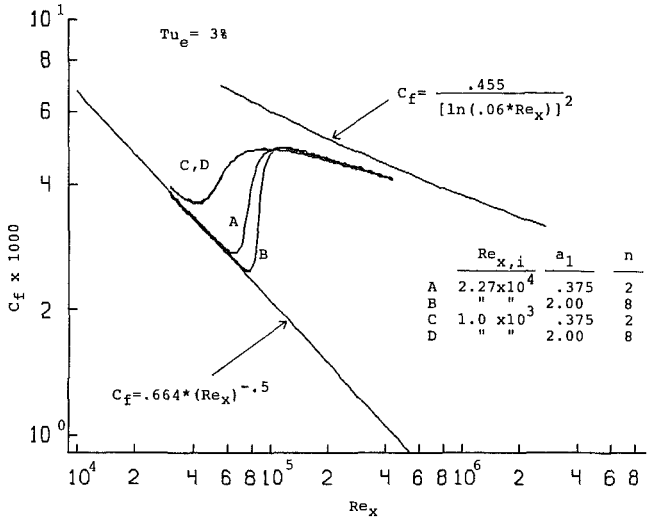

Fig. 3 Plot of C_f versus Re_x for different starting profiles of k and ϵ; Lam-Bremhorst model

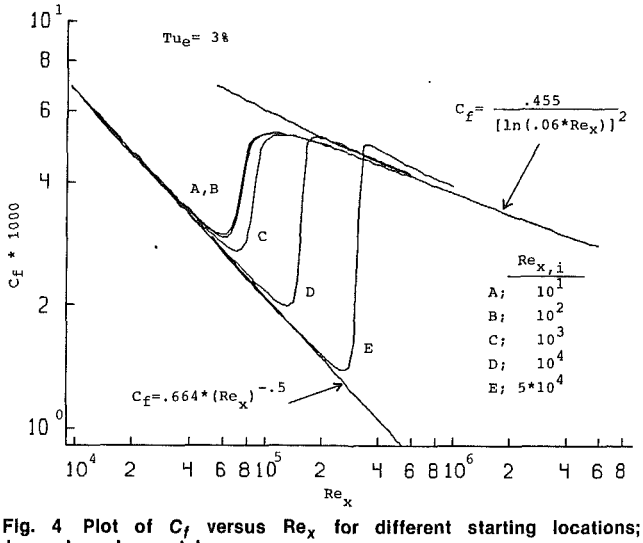

Fig. 4 Plot of C_f versus Re_x for different starting locations; Jones-Launder model

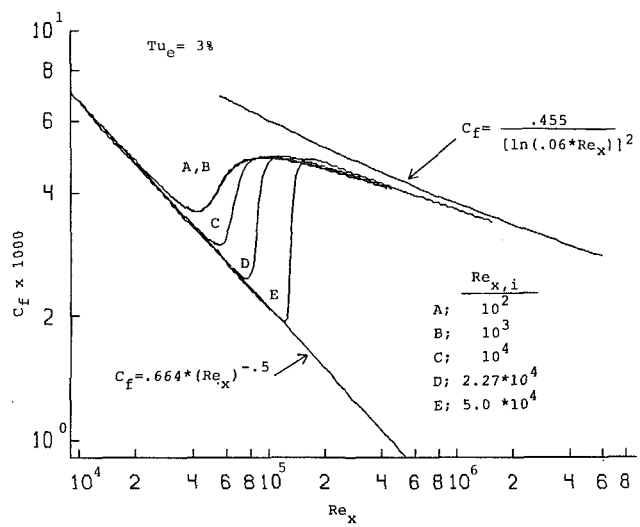

Fig. 5 Plot of C_f versus Re_x for different starting locations; Lam-Bremhorst model

Jones-Launder model tends to predict transition farther downstream than the Lam-Bremhorst model. Tests to be presented in the succeeding sections will be beneficial in clarifying these differences also.

Sensitivity to the Starting Location. To explore further the sensitivity of the predictions to the initial starting location, a set of calculations were made with identical initial profiles (scaled on δ) but at different starting locations. The basic conditions were the same as the calculations presented previously, i.e., $Tu_e = 3$ percent, $dP/dx = 0$, flat plate. The initial profiles for k and ϵ were specified using equations (13) and (14) but with $n = 8$, $a_1 = 2$. These are the same specifications used in runs B and D in Figs. 2 and 3. Recall that this will yield transition at the farthest downstream location.

Figures 4 and 5 show the results of these calculations. These results further illustrate how strongly the transition predictions are dependent on the initial starting location. For the Lam-Bremhorst model at this free-stream turbulence level, the location of transition is strongly dependent on starting location for $Re_{x,i} > 10^3$, but basically independent for $Re_{x,i} < 10^3$. In contrast, the Jones-Launder model calculations show differences until the starting location is reduced to about $Re_{x,i} = 10^2$, and even then a close inspection reveals a very slight downstream shift when compared to $Re_{x,i} = 10^1$. Since the figures are plotted using a logarithmic scale, the actual distance between these starting locations is of the same magnitude as this small shift.

The difference between the models in this respect is apparently due to the direct influence of the wall introduced in the Lam-Bremhorst model by using Re_y as well as Re_t in the f_μ function. This is more fully explored by Schmidt (1987) and will not be repeated here.

A comment is in order here concerning the implications of these results and the proposed method of predicting transition using the Lam-Bremhorst model as presented by Scheuerer (1983) and Rodi and Scheuerer (1985a, 1985b). To our knowledge, they were the first to begin explicitly to address the issues of initial profile specification and starting location and their effect on the calculations. In fact, their excellent work in part stimulated the numerical experiments presented here. As previously noted, they correlated a starting profile parameter a_1 to the free-stream turbulence in order to achieve transition at the desired location. However, the indication in their work was that the results are relatively insensitive to the starting location as long as $Re_\theta < 100$. This is at variance with the results presented here, which indicate a significant dependence on starting location down to a much smaller value of Re_θ. However, since some of the cases they calculated involved the

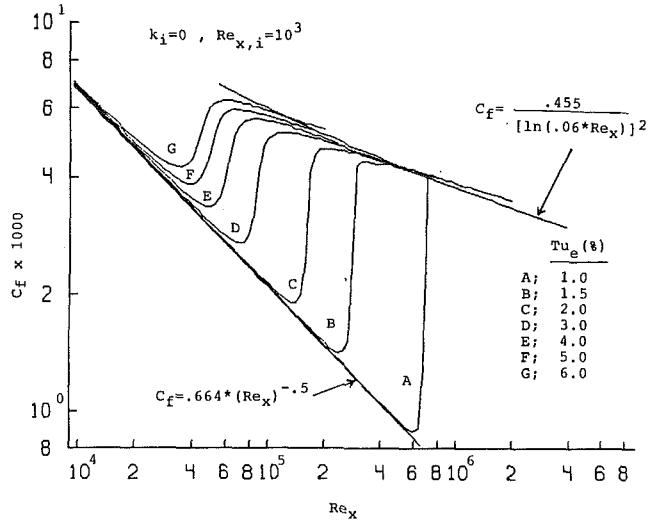

Fig. 6 Plot of C_f versus Re_x for different levels of free-stream turbulence intensity; Jones-Launder model

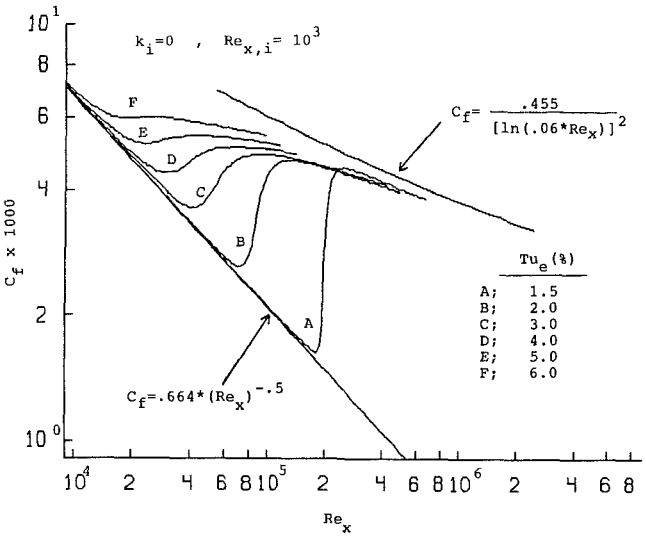

Fig. 7 Plot of C_f versus Re_x for different levels of free-stream turbulence intensity; Lam-Bremhorst model

additional effect of pressure gradient, this could have suppressed the relative importance of starting location on their results.

Response to Free-Stream Turbulence. The next set of computational tests consider the effect that different levels of Tu_e have on the transition predictions. The conditions considered are once again flat plate, zero pressure gradient flow, and the computations are all started at $Re_{x,i}=10^3$. The initial profiles are specified as per equations (13) and (14) with $n=8$ and $a_1=2.0$. Calculations were made for free-stream turbulence intensity levels ranging from 1.0 to 6.0 percent. Free-stream dissipation rates were specified low enough for the decay in Tu_e to be negligible. Figures 6 and 7 show the results of these calculations.

The first thing that might be noted is that a calculation with $Tu_e=1$ percent is not shown for the Lam-Bremhorst model. This is because transition to a turbulent state was not predicted by this model for $Tu_e=1$ percent. This failure was also mentioned by Rodi and Scheuerer (1985b), although they imply that the result seems physically plausible. This comparison exercise however would indicate that the reason is more directly related to the LRN formulation chosen by Lam and Bremhorst, since the Jones-Launder model does predict transition under these conditions. A closer analysis of this

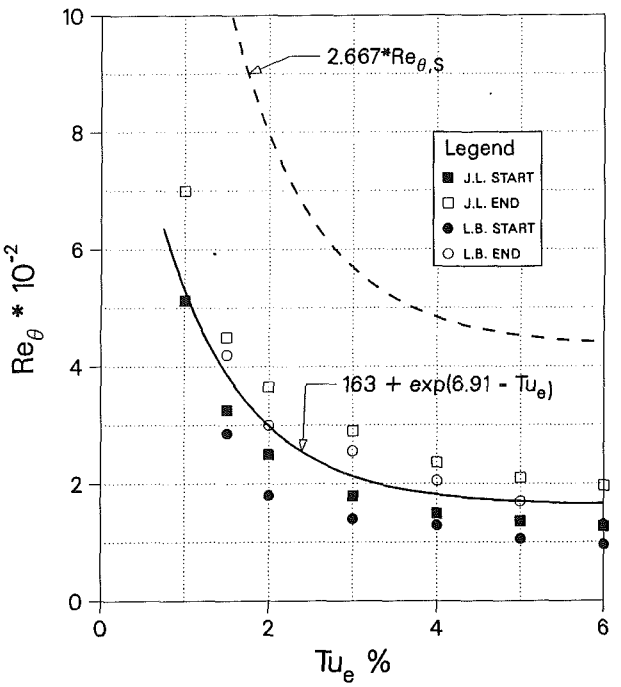

Fig. 8 Calculated momentum thickness Reynolds numbers at the start and end of transition compared to the correlation of Abu-Ghannam and Shaw (1980)

question, which supports this conclusion, is presented by Schmidt (1987) and is discussed in Part 2 of this paper, but will not be given here.

In general terms the qualitative characteristics of the variation of C_f during transition seem reasonable for both models with the onset of transition moving progressively upstream with increasing Tu_e as it should. However, significant differences between the predictions of the two models occur at higher Tu_e where the Lam-Bremhorst model shows a much smoother and more gradual transition region than the Jones-Launder model. The previously noted tendency of the Lam-Bremhorst model to predict transition earlier than the Jones-Launder model is also quite apparent.

In Fig. 8 the momentum-thickness Reynolds numbers at the start ($Re_{\theta,s}$) and the end ($Re_{\theta,E}$) of transition are plotted and compared with the correlation of Abu-Ghannam and Shaw (1980). Here, the beginning and end are defined as the point of minimum and maximum C_f, respectively. From Fig. 8 we can once again see that both models predict the correct qualitative trends, but the onset of transition is predicted too early for both models. At $Tu_e=5$ percent, both models are predicting transition occurring at $Re_{\theta,s}<150$. However, the Jones-Launder model clearly does better than the Lam-Bremhorst model. The results shown here also illustrate an important deficiency apparent in all of the tests. The region over which transition is predicted to occur is always very short. As a result, both models predict values of $Re_{\theta,E}$ that are consistently less than 50 percent of the predicted value of the correlation.

Summary and Conclusions

Boundary layer calculations using k-ϵ LRN turbulence models simulate transition through the transport of turbulent kinetic energy from the free stream into the near-wall regions and the subsequent response of the LRN functions in the equations to this process. The correspondence that exists between the near-wall cross-stream regions in a fully turbulent boundary layer, and progressive stages through which developing boundary layers pass in the streamwise direction, is the basic reason why these models are able correctly to

reproduce certain qualitative aspects of boundary-layer transition with free-stream turbulence. However, their usefulness in predicting boundary layer transition can only be realized if accurate predictions over a broad range of conditions can be made without ambiguities in the specification of initial starting conditions. To help evaluate this potential, a series of numerical experiments have been performed to test the transition prediction characteristics of both the Lam–Bremhorst and the Jones–Launder LRN k–ϵ turbulent models. The major conclusions associated with the results of these tests can be summarized as follows:

1 The predicted location of transition is moderately sensitive to the initial profiles specified for k and ϵ. Lower k and higher ϵ profiles yield transition occurring somewhat farther downstream. This sensitivity decreases with decreasing $\mathrm{Re}_{x,i}$, especially for the Lam–Bremhorst model.

2 The prediction of transition is quite sensitive to the location at which the calculations are started. The reason for this is attributed to the basic process that must occur for the models to simulate transition, i.e., the transport of k into the boundary layer. The extent to which this can occur is largely a function of the distance over which the calculations have proceeded. However, this sensitivity does appear to decrease with decreasing $\mathrm{Re}_{x,i}$, especially for the Lam–Bremhorst model.

3 Both models correctly predict the basic qualitative aspects of boundary-layer transition with free-stream turbulence, i.e., the continuous transition from laminar to turbulent flow, the onset of which moves upstream with increasing Tu_e. However, for calculations started at low $\mathrm{Re}_{x,i}$ (where the sensitivity to the initial profiles for k and ϵ is small), transition is generally predicted at unrealistically early locations.

4 Both models predict transition lengths significantly shorter than those found experimentally.

Although only two of the many currently available LRN models have been evaluated, we do not perceive any reasons why other current models would, in a qualitative sense, behave differently with respect to the issues considered here. Thus, these results would indicate that without further development or modification, current k–ϵ models have significant limitations on accuracy, at least under the conditions tested here. However, it is not our opinion that these models should be abandoned as predictive tools. A comparion article (Part 2) will discuss an approach to overcome these shortcomings.

Acknowledgments

This research was sponsored by the NASA Lewis Research Center under contract No. NAG3-579.

References

Abu-Ghannam, B. J., and Shaw, R., 1980, "Natural Transition of Boundary Layers—The Effects of Turbulence, Pressure Gradient, and Flow History," *J. Mech. Eng. Science*, Vol. 22, No. 5, pp. 213–228.

Arad, E., Berger, M., Israeli, M., and Wolfshtein, M., 1982, "Numerical Calculation of Transition Boundary Layers," *Int. J. for Numerical Methods in Fluids*, Vol. 2, pp. 1–23.

Dutoya, D., and Michard, P., 1981, "A Program for Calculating Boundary Layers Along Compressor and Turbine Blades," *Numerical Methods in Heat Transfer*, R. W. Lewis, K. Morgan, and O. C. Zienkiewicz, eds., Wiley, New York, pp. 413–428.

Dyban, Y. P., Epik, E. Y., and Suprun, T. T., 1976, "Characteristics of the Laminar Boundary Layer in the Presence of Elevated Free-Stream Turbulence," *Fluid Mechanics—Soviet Research*, Vol. 5, No. 4.

Graham, R. W., 1979, "Fundamental Mechanisms That Influence the Estimate of Heat Transfer to Gas Turbine Blades," ASME Paper No. 79-HT-43.

Hylton, L. D., Mihelc, M. S., Turner, E. R., Nealy, D. A., and York, R. E., 1983, "Analytical and Experimental Evaluation of the Heat Transfer Distribution Over the Surface of Turbine Vanes," NASA CR-168015.

Jones, W. P., and Launder, B. E., 1972, "The Prediction of Laminarization With a Two-Equation Model of Turbulence," *Int. J. Heat Mass Transfer*, Vol. 15, pp. 301–314.

Jones, W. P., and Launder, B. E., 1973, "The Calculation of Low Reynolds Number Phenomena With a Two-Equation Model of Turbulence," *Int. J. Heat Mass Transfer*, Vol. 16, pp. 1119–1130.

Lam, C. K. G., and Bremhorst, K., 1981, "A Modified Form of the k–ϵ Model for Predicting Wall Turbulence," ASME *Journal of Fluids Engineering*, Vol. 103, pp. 456–460.

Launder, B. E., and Spalding, D. B., 1974, "The Numerical Computation of Turbulent Flows," *Computer Methods in Applied Mechanics and Engineering*, Vol. 3, pp. 269–289.

Park, W., and Simon, T., 1987, "Prediction of Convex-Curved Transitional Boundary Layer Heat Transfer Behavior Using MLH Models," presented at the 2nd ASME/JSME Thermal Engineering Conference, Mar.

Patankar, S. V., and Spalding, D. B., 1970, *Heat and Mass Transfer in Boundary Layers*, 2nd ed., Intertext, London.

Patel, V. C., Rodi, W., and Scheuerer, G., 1985, "A Review and Evaluation of Turbulence Models for Near Wall and Low Reynolds Number Flows," *AIAA Journal*, Vol. 23, p. 1308.

Pridden, C. H., 1975, "The Behaviour of Turbulent Boundary Layer on Curved Porous Walls," Ph.D. Thesis, Imperial College, London.

Rodi, W., and Scheuerer, G., 1985a, "Calculation of Heat Transfer to Convection-Cooled Gas Turbine Blades," ASME *Journal of Engineering for Gas Turbines and Power*, Vol. 107, pp. 620–627.

Rodi, W., and Scheuerer, G., 1985b, "Calculation of Laminar-Turbulent Boundary Layer Transition on Turbine Blades," *AGARD Conference Proceedings No. 390*, pp. 18.1 to 18.13.

Scheuerer, G., 1983, "Entwicklung eines Verfahrens zur Berechnung zweidimensionaler Grenzschichten an Gasturbineschaufeln," Ph.D. Thesis, Universität Karlsruhe, Federal Republic of Germany.

Schmidt, R. C., 1987, "Two-Equation Low-Reynolds-Number Turbulence Modeling of Transitional Boundary Layer Flows Characteristic of Gas Turbine Blades," Ph.D. Thesis, University of Minnesota, Minneapolis, MN (also available as NASA Contract Report 4145, May 1988).

Schmidt, R. C., and Patankar, S. V., 1987, "Prediction of Transition on a Flat Plate Under the Influence of Free-Stream Turbulence Using Low-Reynolds-Number Two Equation Turbulence Models," ASME Paper No. 87-HT-32.

Wang, J. H., Jen, H. F., and Hartel, E. O., 1985, "Airfoil Heat Transfer Using Low Reynolds Number Version of a Two Equation Turbulence Model," ASME *Journal of Engineering for Gas Turbines and Power*, Vol. 107, No. 1, pp. 60–67.

Wilcox, D. C., 1975, "Turbulence Model Transition Predictions," *AIAA Journal*, Vol. 13, No. 2, pp. 241–243.

Wilcox, D. C., 1977, "A Model for Transitional Flows," AIAA Paper No. 77-126.

Wilcox, D. C., 1979, "Development of an Alternative to the e9-Procedure for Predicting Boundary-Layer Transition," Office of Naval Research, Arlington, ONR-CR-298-005-ZF.

Simulating Boundary Layer Transition With Low-Reynolds-Number k-ϵ Turbulence Models: Part 2—An Approach to Improving the Predictions

R. C. Schmidt[1]

S. V. Patankar

Department of Mechanical Engineering,
University of Minnesota,
Minneapolis, MN 55455

An approach for improving the prediction of boundary layer transition with k-ϵ *type low-Reynolds-number turbulence models is developed and tested. A modification is proposed that limits the production term in the turbulent kinetic energy equation and is based on a simple stability criterion and correlated to the free-stream turbulence level. The modification becomes inactive in the fully turbulent regime, but is shown to improve both the qualitative and quantitative characteristics of the transition predictions. Although the approach is not limited to a particular low-Reynolds-number model, it is implemented herein using the model of Lam and Bremhorst (1981).*

Introduction

Two-equation turbulence models have become a useful tool in simulating turbulent flow under a variety of conditions. A particularly popular form of these models, the "k-ϵ" model, incorporates the solution of two transport-type PDEs: one for the turbulent kinetic energy k, the other for the dissipation rate ϵ. However, in their standard form these equations are not valid in regions very close to solid boundaries. To deal with this problem, several methods have been developed, one of which is to introduce special "low-Reynolds-number" (hereafter referred to as LRN) functions into the equations for k and ϵ. These functions modify and/or add to certain terms in the equations such that near-wall damping effects are simulated. k-ϵ models that have been modified in this manner are commonly referred to as LRN k-ϵ models, and a variety of such models have been proposed and reported in the literature (see Patel et al., 1985).

LRN k-ϵ models were initially used in calculating either fully turbulent pipe flow or external turbulent boundary layer flow. Indeed, it was from knowledge of the near-wall structure that occurs in the simplest of these situations that the LRN functions introduced into the equations were developed. However, in recent years a number of articles have been published reporting the use of models of this type in predicting transition in external boundary layers with free-stream turbulence (see for example, Wang et al., 1985, Rodi and Scheuerer, 1985a, 1985b). To accomplish this simulation, a boundary layer calculation is started with a laminar velocity profile at a point prior to where transition is expected to occur. Starting profiles of k and ϵ are specified and matched at the free stream with values k and ϵ corresponding to a given turbulence intensity. As the calculation marches forward in the streamwise direction, transition is simulated through the transport of turbulent kinetic energy from the free stream into the near-wall regions and the subsequent response of the LRN functions in the equations to this process.

In a companion article (Part 1) we have described work dedicated to clarifying certain questions relative to starting profile sensitivity, starting location sensitivity, and accuracy of the transition predictions over a range of turbulence intensities. This evaluation concluded that although qualitative aspects of boundary-layer transition under the influence of free-stream turbulence were clearly predicted, without further development or modification, current k-ϵ models were not particularly accurate. The problems described included difficulties associated with the sensitivity questions mentioned, as well as the tendency to predict transition too early and over too short a distance.

The object of the work presented here was to develop an approach to overcoming the deficiencies previously described, but without abandoning the basic LRN k-ϵ framework. The idea was to seek simple modifications or empirical constraints that would provide a means of eliminating the deficiencies, without changing the basic LRN models themselves or their predictions for fully turbulent flow. Preliminary results of this work were presented earlier (Schmidt and Patankar, 1987), but only flat-plate zero-pressure-gradient flows were considered. Here we expand upon this work, extending the regime explored to include accelerating flow, and present a somewhat revised formulation.

[1]Present address: Sandia National Laboratories, Albuquerque, NM.

Contributed by the International Gas Turbine Institute for publication in the JOURNAL OF TURBOMACHINERY. Manuscript received at ASME Headquarters June 1990.

The Mathematical Equations

A LRN k–ϵ approach to simulating boundary layer transition (with heat transfer) requires the simultaneous solution of five coupled partial differential equations, two coupled ordinary differential equations (at the free-stream boundary), and a variety of other algebraic relationships. If we assume that the flow is steady and two dimensional, and apply conventional time averaging to the equations, then the equations of interest can be summarized as follows:

Continuity:

$$\frac{\partial}{\partial x}(\rho U)+\frac{\partial}{\partial y}(\rho \tilde{V})=0 \tag{1}$$

x-Momentum:

$$\rho U\left(\frac{\partial U}{\partial x}\right)+\rho \tilde{V}\left(\frac{\partial U}{\partial y}\right)=-\frac{dP}{dx}+\frac{\partial}{\partial y}\left(\mu\frac{\partial U}{\partial y}-\rho\overline{u'v'}\right) \tag{2}$$

k Equation:

$$\rho U\left(\frac{\partial k}{\partial x}\right)+\rho \tilde{V}\left(\frac{\partial k}{\partial y}\right)=\frac{\partial}{\partial y}\left\{\left(\mu+\frac{\mu_t}{\sigma_k}\right)\frac{\partial k}{\partial y}\right\}+\mu_t\left(\frac{\partial U}{\partial y}\right)^2-\rho\epsilon \tag{3}$$

ϵ Equation:

$$\rho U\left(\frac{\partial \epsilon}{\partial x}\right)+\rho \tilde{V}\left(\frac{\partial \epsilon}{\partial y}\right)=\frac{\partial}{\partial y}\left\{\left(\mu+\frac{\mu_t}{\sigma_\epsilon}\right)\frac{\partial \epsilon}{\partial y}\right\}+\frac{\epsilon}{k}\left\{C_1 f_1 \mu_t\left(\frac{\partial U}{\partial y}\right)^2-C_2 f_2 \rho\epsilon\right\} \tag{4}$$

We define the relationships between the apparent turbulent stress, turbulent viscosity, and k and ϵ such that

$$-\rho\overline{u'v'}=\mu_t\frac{\partial U}{\partial y}=\rho C_\mu f_\mu\frac{k^2}{\epsilon}\frac{\partial U}{\partial y} \tag{5}$$

In this work we adopt the concept of a turbulent Prandtl number defined such that

Table 1 The k–ϵ model constants and Lam-Bremhorst LRN functions

Constant	Value	Function	Definition
C_μ	.09		
		f_μ	$\left(1-\exp(-.0163R_y)\right)^2(1+20R_t)$
C_1	1.44		
		f_1	$1.0+\left(\frac{.055}{f_\mu}\right)^3$
C_2	1.92		
		f_2	$1.0-\exp(-R_t^2)$
σ_k	1.00		
σ_ϵ	1.30		

$$-\rho\overline{h'v'}=\frac{\mu_t}{\mathrm{Pr}_t}\left(\frac{\partial h}{\partial y}\right) \tag{6}$$

An energy equation can then be written as

$$\rho U\left(\frac{\partial H}{\partial x}\right)+\rho \tilde{V}\left(\frac{\partial H}{\partial y}\right)=\frac{\partial}{\partial y}\left\{\left(\frac{\mu}{\mathrm{Pr}}+\frac{\mu_t}{\mathrm{Pr}_t}\right)\frac{\partial H}{\partial y}\right\}+\frac{\partial}{\partial y}\left\{U\frac{\partial U}{\partial y}\left(\mu_t\left(1-\frac{1}{\mathrm{Pr}_t}\right)+\mu\left(1-\frac{1}{\mathrm{Pr}}\right)\right)\right\} \tag{7}$$

where the total enthalpy H is defined as

$$H=h+\frac{U^2}{2} \tag{8}$$

In equations (3) and (4), the constants C_1, C_2, C_μ, σ_k, and σ_ϵ are the k–ϵ model constants given in Table 1. The functions f_1, f_2, and f_μ are the LRN functions of Lam and Bremhorst (1981), also defined in Table 1. The quantities U and V are the time-averaged mean velocities, and u' and v' are the instantaneous velocity fluctuations. The overbar implies a time-averaged quantity, the prime a fluctuating quantity, and the tilde over V indicates a mass-weighted averaging where

$$\rho \tilde{V}=\rho V+\overline{\rho' v'} \tag{9}$$

Nomenclature

A, B = empirical parameters in the proposed modification
C_f = skin friction coefficient
C_1, C_2, C_μ = constants in the k–ϵ turbulence model
f_1, f_2, f_μ = empirical functions in the LRN model (see Table 1)
h = mean static enthalpy
H = total enthalpy (see equation (8))
k = turbulent kinetic energy
K = acceleration parameter $= \nu/U_e^2\ \partial U_e/\partial x$
P_k = modeled production term in the k equation
Pr, Pr_t = molecular and turbulent Prandtl numbers
Re_x = Reynolds number based on x
Re_θ = momentum thickness Reynolds number
$\mathrm{Re}_{\theta,s}$, $\mathrm{Re}_{\theta,E}$ = values of Re_θ at the start and end of transition
Re_t = Reynolds number defined as $k^2/\nu\tilde{\epsilon}$
Re_y = Reynolds number defined as $\sqrt{k}y/\nu$
St = Stanton number
$Tu_{e,T}$ = total turbulence intensity $= \sqrt{(\tilde{u}'^2+\tilde{v}'^2+\tilde{w}'^2)/3}/U_e$
$Tu_{e,u'}$ = streamwise turbulence intensity $= \sqrt{\tilde{u}'^2}/U_e$
U, V = mean velocities in the x and y directions
$\overline{u'v'}$ = apparent turbulent stress
x = streamwise distance from the leading edge
y = cross-stream distance from the wall
δ = boundary layer thickness
δ^* = displacement thickness
θ = momentum thickness
ϵ = dissipation rate
μ = molecular viscosity
μ_t = eddy or turbulent viscosity
ν = kinematic viscosity $= \mu/\rho$
ρ = fluid density
σ_k, σ_ϵ = empirical constants in the k–ϵ turbulence model

Subscripts

e = denoting free-stream value
i = denoting value at the initial starting location
w = denoting value at the wall

Boundary Conditions and Starting Profiles

If we assume that the free-stream velocity U_e is a known function of x then the variation in k_e and ϵ_e can be found by solving the following two ordinary differential equations:

$$U_e \frac{dk_e}{dx} = -\epsilon_e \tag{10}$$

$$U_e \frac{d\epsilon_e}{dx} = -C_2 \frac{\epsilon_e^2}{k_e} \tag{11}$$

Note that these are just reduced forms of equations (3) and (4).

At the wall, we set $U_w = k_w = \partial\epsilon/\partial y = 0$ (see Patel et al., 1985).

For a calculation to begin, a starting location somewhere prior to where transition can occur must be chosen and profiles for U, k, and ϵ specified. Based on the work presented in Part 1, the starting location is always chosen such that $\mathrm{Re}_\theta \leq 25$, where the sensitivity to the starting profiles of k and ϵ is insignificant. The velocity profile is approximated by a laminar profile, which in the case of zero pressure gradient flat plate flow would be the well-known Blasius profile. k and ϵ are specified using the formulas introduced by Rodi and Scheuerer (1985a), except that here the parameter a_1 is constant. These can be written as

$$k = k_e \left(\frac{U}{U_e}\right)^2 \tag{12}$$

$$\epsilon = a_1 k \left(\frac{\partial U}{\partial y}\right) \quad , \quad \epsilon > \epsilon_e \quad , \quad a_1 = 0.1 \tag{13}$$

Note however, that because of the starting location chosen, the exact form of these profiles is not significant. More will be discussed about this later.

For flat plate flows the starting enthalpy profile was derived from the approximate temperature–velocity profile relationship given below:

$$T = T_w + (T_e - T_w)\frac{U}{U_e} \tag{14}$$

The numerical solution method used in this work was the finite difference approach of Patankar–Spalding (1970) for boundary layer flows. The streamwise step size was restricted to some fraction of the calculated momentum thickness (generally about 0.5), and tests made to assure the solution was independent of this choice. A variable grid consisting of 88 grid points, and which was refined significantly near the wall, was used for all the calculations presented. Tests showed that the grid thus specified was sufficiently refined to yield essentially grid-independent results. Greater details with respect to the numerical methods and coding can be found in Schmidt (1987).

Desired Characteristics of a Model

In developing an approach for improving the transition predictions, some specific characteristics were sought. It was felt that for flat plate, zero pressure gradient flow, the following capabilities would be required, at a minimum, for the procedure to be of potential value:

1 A well-defined region where starting profiles can be specified with minimal sensitivity and without ambiguity.

2 Transition predictions starting and ending in good agreement with the correlation of Abu-Ghannam and Shaw (1981) over its entire range of validity (i.e., 1 percent $\leq Tu_e \leq 7$ percent).

After exploring a number of different alternatives to improve the model, one method was found to be fairly successful. The method is based on two ideas. The first is that some means of incorporating stability considerations into the calculational procedure should be provided. The second is that the process by which the model simulates transition, once started, must proceed at some reasonable finite rate and in accord with experiment. These two ideas are directly related to the tendency of the model to predict transition at unrealistically early locations and over too short a period.

A Modification to the Production Term

In a real, physically developing boundary layer, stability considerations control whether perturbations introduced from the free stream will be amplified or damped, and thus whether the process of transition will begin. When this occurs, energy is effectively extracted from the free stream and transferred into the near-wall turbulent kinetic energy, yielding near-wall values that greatly exceed the free-stream value (i.e., the boundary layer becomes what we call turbulent). In our k–ϵ models, the production term in the k equation (i.e., $\mu_t(\partial U/\partial y)^2$, referred to hereafter as P_k) is the only term that can drive the near-wall profile of k to values above that of the free stream. Thus, this term is a logical place for stability-related information to be applied, and also where the transition rate might be controlled.

The turbulent kinetic energy equation (equation (3)) is derived through various modeling assumptions from a more exact form. For fully turbulent flow where the boundary-layer assumptions are valid, the production term in the model corresponds to the production term in the "exact" equation as follows:

$$-\rho\overline{u'v'}\frac{\partial U}{\partial y} \simeq \mu_t \left(\frac{\partial U}{\partial y}\right)^2 = \rho C_\mu \frac{k^2}{\epsilon}\left(\frac{\partial U}{\partial y}\right)^2 \tag{15}$$

The relative success of k–ϵ modeling is evidence that this approximation is quite good in many situations of interest. However, in a "pseudo-laminar," developing, transitional boundary layer—where experiments show a complex, three-dimensional development characterized by increasingly frequent "bursts" of local turbulence production—there is no justification to assume that the "exact" term above (the term on the left) together with the dissipation ϵ, are the only source terms that are significant. Thus from a modeling standpoint, there is no compelling reason precluding us from introducing modifications in our numerically represented production term in order to improve transition predictions, as long as the fully turbulent form is not changed.

With these things in mind, a modification was introduced to limit the growth rate of the production term. Its form leaves the fully turbulent calculations undisturbed, but introduces a maximum rate at which P_k can increase in time. The time scale used is simply related to the local velocity.

Preliminary tests with a number of formulations showed that a simple but flexible representation that worked quite well was the following:

$$\frac{dP_{k_{\max}}}{dt} = A * P_k + B \tag{16}$$

where A and B are empirical parameters, and the subscript "max" denotes the maximum allowable value. The dependence of the linear term on P_k itself is arbitrary, being suggested in analogy with reaction rate theory, but was found to yield acceptable results. The need for two independent parameters, however, stems directly from the need to predict both the start and the end of transition at the correct location.

As a simple means of incorporating some stability information, we also proposed to eliminate P_k from the k equation below some critical momentum thickness Reynolds number ($\mathrm{Re}_{\theta,c}$) (i.e., the production term in the k equation is set to zero). It is important to note two things with respect to this

change. First, this modification does not preclude the transport of k through convection and diffusion. Thus high levels of free-stream turbulence will still tend to influence the calculation even when P_k is zero. Second, only the k equation is modified (i.e., the term in the ϵ equation containing $\mu_t(\partial U/\partial y)^2$ remains as is).

Numerical Implementation

At this point, a brief explanation of the numerical implementation of equation (16) may be beneficial. We first define the following;

x = streamwise location at the current point in the calculation
dx = step size in the streamwise direction
$PE(j, x)$ = computed positive source term in the ϵ equation of the jth control volume and at streamwise location x
$PK(j, x)$ = computed positive source term in the k equation for the jth control volume and at streamwise location x
U_j = local streamwise velocity at the jth control volume

To compute the value of $PK(j, x+dx)$ to be used over the next step in the solution, we implement the following (written in pseudo-Fortran):

$$PE(j, x+dx) = \frac{\epsilon}{k} C_1 f_1 \mu_t \left(\frac{\partial U}{\partial y}\right)^2$$

$$\Delta P_{k,\max} = (A * PK(j, x) + B)\frac{dx}{U_j}$$

If $\mathrm{Re}_\theta < \mathrm{Re}_{\theta,c}$ then

$$PK(j, x+dx) = 0$$

else

$$PK(j, x+dx) = PK(j, x) + \min\left[\mu_t\left(\frac{\partial U}{\partial y}\right)^2 - PK(j, x) \;,\; \Delta P_{k,\max}\right]$$

endif

For convenience, this modification will be referred to by the acronym "PTM" (for Production Term Modification).

A Simple Modification to the $f\mu$ Function

In Part 1 it was pointed out that calculations using the Lam–Bremhorst model do not predict transition when Tu_e is reduced to about 1 percent. Since experimental evidence shows that the location of transition is sensitive to free-stream turbulence levels significantly lower than 1 percent, a correction for this would be desirable.

An explanation of this problem in terms of the particular form of Lam and Bremhorst's f_μ function is given by Schmidt (1987) and will not be repeated here. Suffice it to say that during the computed transition process with low Tu_e, extremely high values of f_μ are calculated at certain locations in the boundary layer. Since the function f_μ was intended to vary from zero to one, this situation causes serious problems. Once understood, the solution to the problem was relatively straightforward: The values of f_μ simply had to be constrained to remain less than some reasonable upper bound during the transition process. The modified form of f_μ chosen, which was used in all of these calculations, was

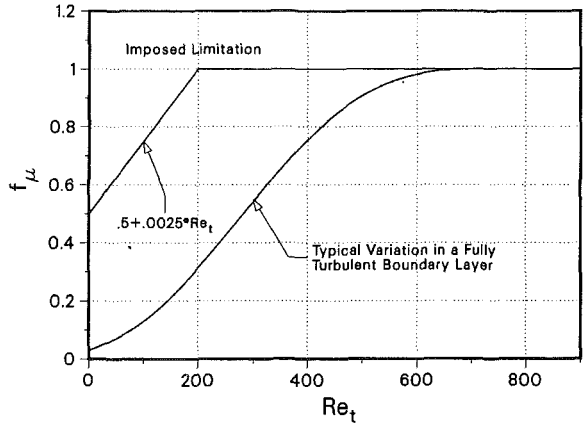

Fig. 1 The limitation placed on the Lam-Bremhorst f_μ function

$$f_\mu = \min\ [f_{\mu,LB}, 1.0, 0.5 + 0.0025\ \mathrm{Re}_t] \qquad (17)$$

where $f_{\mu,LB}$ is the Lam–Bremhorst formulation for f_μ given in Table 1. Since any restriction that remains above the fully turbulent behavior will not affect the fully turbulent calculations, the particular form chosen is somewhat arbitrary. Equation (17) was chosen because it was simple, and because it was sufficient to allow proper correlation of the transition model parameters. It must be emphasized, however, that this choice does not affect the fully turbulent predictions, and thus lies entirely within the realm of a modification to improve transition. Furthermore, this change has no effect at all on the transition predictions for $Tu_e > 2$ percent, and is only really significant for $Tu_e < 1.5$ percent.

Figure 1 illustrates how the limitation equation (17) imposes compares with a typical profile of f_μ for a fully turbulent boundary layer.

Determining the Transition Parameters A and B

A series of numerical tests were performed to determine the appropriate values of A and B. Initially it was not known if they could be held constant, or if they must become dependent on the free-stream turbulence intensity. However, preliminary tests showed that for good results, they must be made functions of Tu_e. The conditions for the tests were simple flat plate, zero pressure gradient flow but with various levels of free-stream turbulence intensity. For calibration purposes, the free-stream dissipation was kept low so that Tu_e remained essentially constant (free-stream length scale effects will be discussed later). The start and end of transition was taken to be where C_f was at its minimum and maximum, respectively.

Starting at one specific free-stream turbulence level, a series of computations were made. After an initial guess, A and B were appropriately adjusted after each run, so that each succeeding calculation agreed more closely with the correlation of Abu-Ghannam and Shaw. After a number of iterations it was then possible to find the "correct" values so as to achieve the start and end of transition exactly in accord with the correlation of Abu-Ghannam and Shaw (1980). This correlation can be expressed as follows:

$$\mathrm{Re}_{\theta,s} = 163 + \exp\ (6.91 - 100 * Tu_e) \qquad (18)$$

$$\mathrm{Re}_{\theta,E} = 2.667 * \mathrm{Re}_{\theta,s} \qquad (19)$$

Once A and B were found at one free-stream turbulence intensity, the level was changed, and the process was repeated.

In addition to the values of A and B, the critical Reynolds

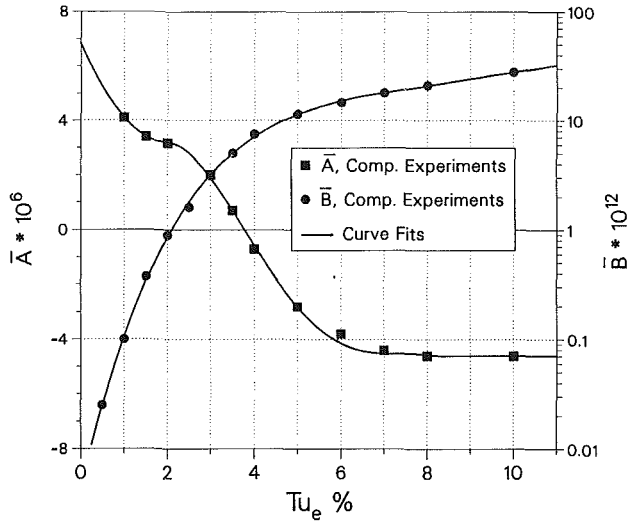

Fig. 2 Variation of $\bar{A}$ and $\bar{B}$ with free-stream turbulence intensity for the Lam-Bremhorst LRN model

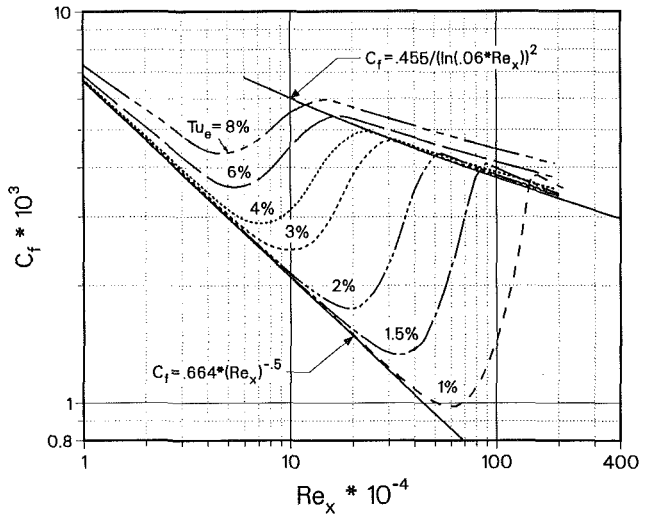

Fig. 3 Plot of C_f versus Re_x at different levels of free-stream turbulence intensity using the PTM Lam-Bremhorst model

number (below which the production of k is suppressed) must be chosen. Initially, $Re_{\theta,c} = 125$ was adopted as a constant for all of the calculations with the Lam-Bremhorst model. Although it is clear that it should be less than 163 (Blasius stability limit), the value of 125 may seem somewhat arbitrary. However, in fact it was also constrained by the following two practical considerations:

1 If $Re_{\theta,c}$ is too high, the correct start and end of transition could not be obtained through the use of equation (16) for any values of A and B.

2 The lower $Re_{\theta,c}$ becomes, the smaller the region near the leading edge within which calculations can be started without sensitivity to the starting profiles of k and ϵ.

Since insensitivity to the initial profiles of k and ϵ is a desired characteristic, there was no reason to reduce $Re_{\theta,c}$ to a value less than that which satisfied constraint (1) above. The value of 125 was thus arrived at and the calibration tests for A and B were performed with this value. Afterward, tests were made to determine just how dependent or sensitive the computations were to this value. It was found that reducing $Re_{\theta,c}$ did somewhat shorten the acceptable starting region as explained above, although it did not require the values of A and B to be changed. At high turbulence intensities, although the

Table 2 Values of A and B for the Lam-Bremhorst model

Tu_e %	$\bar{A} * 10^6$	$\bar{B} * 10^{12}$	Tu_e %	$\bar{A} * 10^6$	$\bar{B} * 10^{12}$
0.5	5.2425	0.0250	4.0	-0.5654	7.0632
1.0	4.0975	0.1056	5.0	-2.8106	11.4166
1.5	3.4125	0.3380	6.0	-4.1411	15.2813
2.0	3.1875	0.8564	7.0	-4.5192	17.9933
2.5	2.7939	1.7868	8.0	-4.5701	20.8382
3.0	1.8886	3.1812	9.0	-4.6011	24.1328

Re_θ transition relationship remained unchanged, the actual location where transition occurred was slightly shifted upstream. However, for low Tu_e, there was no significant effect at all. Greater details with respect to this issue can be found from Schmidt (1987).

Calculations to determine the transition model parameters A and B were made for a range of turbulence intensities of from 0.5 to 10.0 percent. The results of these calculations are presented in Fig. 2 and Table 2. These values cover a larger range and are somewhat different from those given by Schmidt and Patankar (1987) due to the modification to the f_μ function (equation (17)), and a more precise determination of the best values in the higher turbulence intensity range. Also note that both A and B have been nondimensionalized with respect to local free-stream conditions as follows:

$$\bar{A} = \frac{A\mu_e}{\rho_e U_e^2} \tag{20}$$

$$\bar{B} = \frac{B\mu_e^2}{\rho_e^2 U_e^6} \tag{21}$$

After these computational experiments were completed, curve fits were made to the data, which are also shown in the figures. Analytical expressions for the curve fits can be found from Schmidt (1987).

Figure 3 illustrates the predicted variation of C_f during transition for free-stream turbulence intensities of from 1.0 to 8.0 percent using the values of A and B listed in Table 2. As before, the conditions specified were simple flat plate, zero pressure gradient flows with the free-stream turbulence being the only variable parameter. In addition to the transition aspects that this figure shows, it is interesting to note the predicted effect that high free-stream turbulence has on both the pseudo-laminar region prior to transition, and on the fully turbulent conditions. This is manifested in an increase in C_f over the laminar correlation and can be easily observed far before C_f reaches its minimum. This carries through to the turbulent region where with $Tu_e = 8$ percent, C_f shows a 15–20 percent increase over the turbulent correlation. Both of these trends are consistent with experiment.

Starting Location Sensitivity of the PTM Model

To assure consistent, repeatable predictions it is important that the sensitivity of the method to the initial starting location be clearly identified. As this was done for the unmodified model in Part 1, it is now important to examine this for the PTM form of the model. To do so, tests were made for flows with $Tu_e = 3$ percent, and $Tu_e = 8$ percent. The initial starting location was then varied from $Re_{x,i} = 100$ to 22,700, and the results compared. Figure 4 shows the results of these calculations.

The important aspects of this check on sensitivity can be listed as follows:

1 As compared to the 3 percent calculations presented in Part 1 (using an unmodified Lam-Bremhorst model), the PTM Lam-Bremhorst model shows a significantly reduced sensitivity to starting location.

2 At $Tu_e = 8$ percent, the actual location in x where the

minimum in C_f occurs is not very sensitive to the starting locations chosen. However, a starting location such that $Re_{x,i} > 10^3$ did affect the magnitude of C_f prior to and during transition.

3 For both of the conditions tested, starting the calculation at $Re_{x,i} < 10^3$ reduces the starting location effects to insignificance. Note that this implies that the calculations are also insensitive to the starting profiles of k and ϵ under these conditions.

High Free-Stream Dissipation Rate and Acceleration

For the exploratory and calibration calculations presented up to this point, the flow conditions were specified such that the free-stream turbulence intensity was essentially constant. This is done computationally by simply setting the starting value of ϵ_e equal to a very small number. However, in real flow with high Tu_e, the dissipation rate is also usually high. Thus the question might arise as to how to properly account for a free-stream turbulence intensity that is changing significantly before transition occurs.

One of the advantages of using a k–ϵ approach is that the effects of this type of variation are naturally included as part of the model. As far as the transition parameters are concerned, we simply base them on the local free-stream conditions. Computationally, since the step size is usually quite small relative to the rate at which k_e and ϵ_e decay, it is usually sufficient to only update A and B after every 10 or 20 steps.

Since the relationship between k_e and Tu_e involves the free-stream velocity, acceleration can also have dramatic effects on the free-stream turbulence intensity. If the flow accelerates, Tu_e goes down, even though k_e may have remained relatively constant. Deceleration has just the opposite effect, yielding an increase in Tu_e. This does not present any additional difficulty for the model, and as before, we simply continue to base our calculations on the local free-stream conditions.

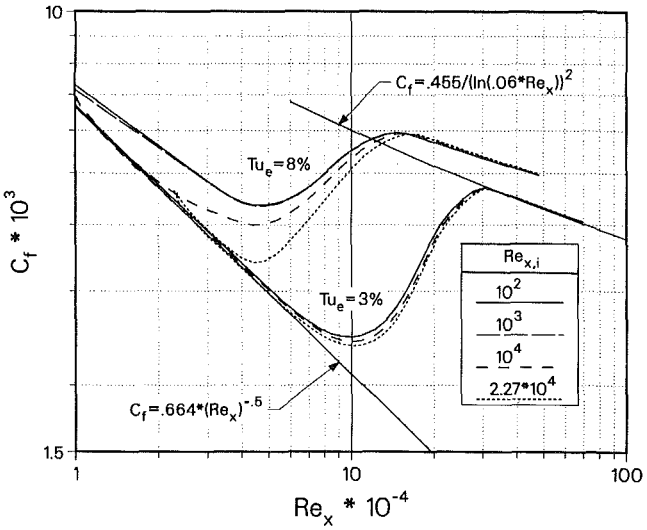

Fig. 4 Plot of C_f versus Re_x for different starting locations

Transition Calculations With the PTM Lam–Bremhorst Model

Up to this point, direct comparison with specific experimental data has been deferred, and the transition parameters were found based entirely on the empirical correlation of Abu-Ghannam and Shaw (1981). This was deliberately done to avoid the potential bias that might occur if the method were "tuned," so to speak, to one or two specific experimental data sets. However, in order truly to evaluate the effectiveness of the model, a careful comparison with a wide range of experiments is crucial.

In this section, calculations will be compared with the results of 16 separate experiments conducted by Rued (1983), Blair and Werle (1980, 1981), and Daniels (1978). These experiments investigate boundary layer transition under the influence of free-stream turbulence ranging from 1 percent to

Table 3 Some experimental data used in testing the calculational method

Reference	Identifier	At $x = x_1$ $Tu_{e,T}(Tu_{e,u})$ (%)	At $x = x_2$ $Tu_{e,T}(Tu_{e,u})$ (%)	x_1 , x_2 (m)	Thermal Boundary Condition	T_w/T_e Approx.	T_e	U_e at x_1	Acceleration
Rued(1983)	Nr 2,no grid	1.6 (1.71)	1.28 (1.37)	0., .4	T_w=302 K	0.8	378 K	47 m/s	no
"	Nr 2, grid 1	2.3 (2.8)	1.36 (1.72)	0., .4	T_w=302 K	0.8	378 K	47 m/s	no
"	Nr 2, grid 2	3.75 (4.65)	1.85 (2.68)	0., .4	T_w=302 K	0.8	378 K	47 m/s	no
"	Nr 2, grid 3	6.5 (7.4)	2.55 (3.05)	0., .4	T_w=302 K	0.8	378 K	47 m/s	no
"	Nr 2, grid 4	8.6 (10.8)	3.32 (4.13)	0., .4	T_w=302 K	0.8	378 K	47 m/s	no
Blair and Werle(1980)	grid 1	1.41 (1.12)	0.80 (0.82)	0.,1.6	Q_w=850 W/m	1.03	295 K	30.5 m/s	no
"	grid 2	2.82 (2.33)	1.6 (1.5)	0.,1.6	Q_w=850 W/m	1.03	295 K	30.5 m/s	no
"	grid 3	6.2 (5.75)	3.52 (3.44)	0.,1.6	Q_w=850 W/m	1.03	295 K	30.5 m/s	no
Blair and Werle(1981)	low K grid 1	1.03 (0.94)	0.64 (0.62)	0.,1.6	Q_w=850 W/m	1.03	297 K	15.9 m/s	$K=0.2*10^{-6}$
"	low K grid 2	2.1 (1.86)	1.1 (0.97)	0.,1.6	Q_w=850 W/m	1.03	297 K	15.9 m/s	$K=0.2*10^{-6}$
"	low K grid 3	- (4.8)	- (1.89)	0.,1:6	Q_w=850 W/m	1.03	297 K	15.9 m/s	$K=0.2*10^{-6}$
Rued(1983)	Nr 12 grid 1	2.88 (-)	0.63	0., .4	T_w=299 K	0.64	467 K	27 m/s	$K_{max}=5.7*10^{-6}$
"	Nr 12 grid 2	3.95 (-)	0.89	0., .4	T_w=299 K	0.64	467 K	27 m/s	$K_{max}=5.7*10^{-6}$
"	Nr 12 grid 3	7.73 (-)	1.70	0., .4	T_w=299 K	0.64	467 K	27 m/s	$K_{max}=5.7*10^{-6}$
"	Nr 12 grid 4	11.1 (-)	1.87	0., .4	T_w=299 K	0.64	467 K	27 m/s	$K_{max}=5.7*10^{-6}$
Daniels (1978)	Re_D	3.0-3.5	-	-	T_w=289 K	0.67	432 K	*146 m/s	-
"	Re_θ	3.0-3.5	-	-	T_w=289 K	0.67	432 K	*135 m/s	-

* Value upstream of the turbine blade

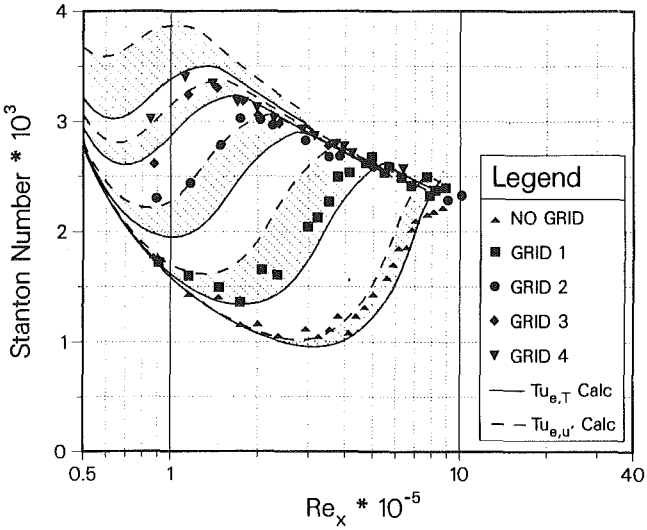

Fig. 5 Comparison of the predicted heat transfer during transition with the zero pressure gradient data of Rued (1983)

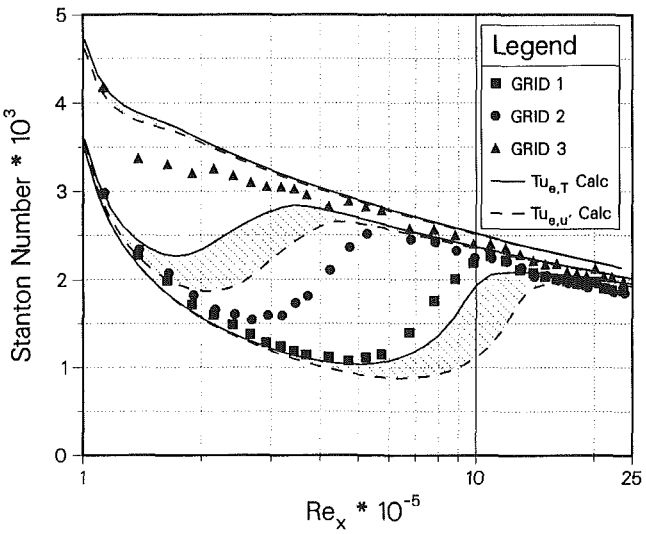

Fig. 6 Comparison of the predicted heat transfer during transition with the zero pressure gradient data of Blair and Werle (1980)

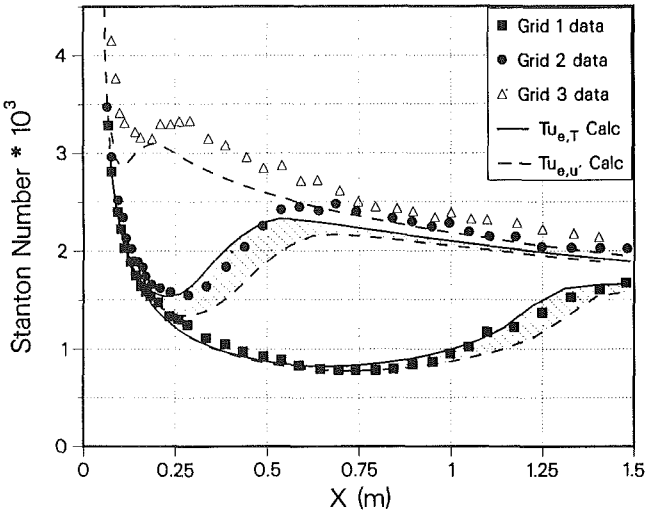

Fig. 7(a) Comparison of the predicted heat transfer during transition with the low acceleration data of Blair and Werle (1980)

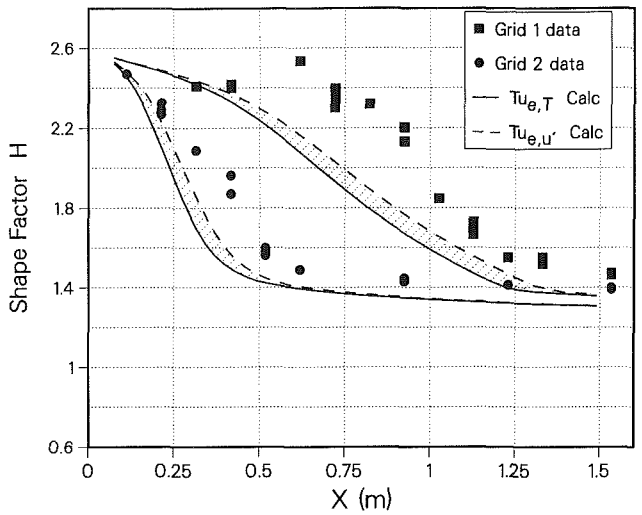

Fig. 7(b) Comparison of the predicted shape factor ($H = \delta^*/\theta$) during transition with the low acceleration data of Blair and Werle (1980)

near 10 percent, and also cover a range of pressure gradient conditions. The data of Daniels are from a turbine blade cascade rig while the other data sets are all flat plate experiments. These calculations represent roughly half of the comparison calculations of Schmidt (1987), but are felt to be sufficiently representative for the purposes of this paper. Also, due to space limitations, some of the detail associated with these calculations and the experimental data will of necessity be omitted here.

Table 3 summarizes some of the important conditions associated with each of these experiments. Note that the free-stream turbulence is in general neither constant nor homogeneous. Therefore, when possible, Table 3 lists values for both $Tu_{e,u'}$ and $Tu_{e,T}$ at two different locations in order to characterize the flow conditions better. Note also that the values listed in Table 3 are the values used in the computations. A detailed comparison of these values with the experimental data may be found in Schmidt (1987).

Flat Plate, Zero Pressure Gradient. Figures 5 and 6 compare the computational predictions with the data from two separate data sets, Rued (1983) and Blair and Werle (1980). For each experiment two calculations were made, one based on the total free-stream turbulence intensity ($Tu_{e,T}$), and the other based on the streamwise turbulence intensity ($Tu_{e,u'}$). This is intended to help quantify the relative inhomogeneity in the free-stream turbulence and thus guide our assessment of how accurate we could ideally be. Note that the experimental conditions of Rued are such $Tu_{e,u'} < Tu_{e,T}$, whereas those of Blair and Werle yielded $Tu_{e,u'} > Tu_{e,T}$.

Excellent agreement between the calculations and the data of Rued is seen in Fig. 5. Only under the highest free-stream turbulence conditions of grid 4, where the uncertainty is highest in both the experimental data and the correlation of Abu-Ghannam and Shaw, does the calculation deviate much from the data. In Fig. 6 we see fair agreement with the data of Blair and Werle, but a definite trend to predict transition somewhat early as the free-stream turbulence intensity became larger. The momentum thickness Reynolds numbers at transition associated with this experimental data also appear to be higher than predicted by the correlation of Abu-Ghannam and Shaw. Thus this result is not unexpected.

Flat Plate, Accelerating Flow. The next three figures also compare the computations with transition data occurring at different levels of free-stream turbulence, but these data include the additional effect of a favorable pressure gradient.

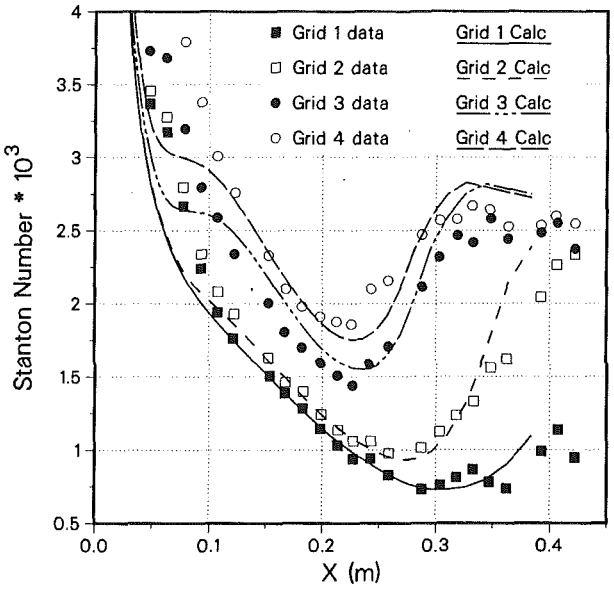

Fig. 8 Comparison of the predicted heat transfer during transition with the high acceleration data (No. 12) of Rued (1983)

Note that this has a stabilizing effect on the boundary layer, tending to delay the onset of transition. No additional modifications to the computational approach are made for these calculations.

The data of Blair and Werle shown in Figs. 7(*a*) and 7(*b*) are for flat plate flow with relatively mild constant acceleration ($K=0.2\times10^{-6}$). In Fig. 7(*a*), we compare the heat transfer results. It is interesting that better agreement is obtained for the heat transfer here than in the zero pressure gradient case shown in Fig. 6. For these experiments, Blair and Werle also measured the displacement thickness δ^*, the momentum thickness θ, and their ratio, the shape factor $H=\delta^*/\theta$. Since transition is most clearly evident by looking at the change in H, Fig. 7(*b*) compares the shape factor data with the calculation (see Schmidt (1987) for a comparison of δ^* and θ individually). Here we see that the shape factor found computationally begins to change earlier and also undergoes a more gradual change than the data. Comparison with the individual values of δ^* and θ indicate that this is primarily related to differences in the displacement thickness values. This difference is somewhat surprising considering the close agreement in the heat transfer results. Unfortunately, δ^* and θ data (during transition) are not available from the zero pressure gradient experiments of Blair and Werle, preventing comparison of this interesting result with the zero gradient case.

In contrast to the relatively low and constant acceleration seen in the experiments of Blair and Werle, the data of Rued (Fig. 8) are for a very strongly accelerated flow where the acceleration builds to a very high value and then is quickly reduced. The maximum acceleration factor experienced for this data was $K=5.7\times10^{-6}$. For these tests we find excellent agreement between the calculated transition region (as indicated by heat transfer) and the data for each level of free-stream turbulence. Note however that near the leading edge, the experimental data indicate significantly higher heat transfer in the psuedo-laminar region than the calculations.

Turbine Blade Data of Daniels. One of the major motivations for the work presented here is the need for a reliable engineering tool for predicting the effect of transition on heat transfer on gas turbine blades. Thus results of an example calculation for an actual blade under simulated operating conditions will be presented. For these conditions variable property, compressibility, and high-speed effects are accounted for through appropriate property equations, a thermodynamic state equation, and the proper formulation of the energy equation (see equations (7) and (8)). To specify the free-stream velocity, the experimental velocity data were functionally approximated by a series of polynomials to produce a smooth continuous representation of the data. However, in the calculations presented here we have neglected curvature effects and attempted to side-step the issue of a proper stagnation region flow calculation. This implies that although the calculations proceed over a streamwise distance, which corresponds to traveling around the curved surface of the blade, the equations solved do not include additional terms or corrections to otherwise account for the curvature. (Note that in regions where the ratio of the boundary-layer thickness to the radius of curvature is small, and the local free-stream velocity is accurately specified, then this approximation is fairly good.) The stagnation region flow question is avoided by starting the calculation at a point somewhat downstream from the stagnation point and accepting only approximate profiles as starting conditions. Greater detail with respect to each of these issues is reported by Schmidt (1987).

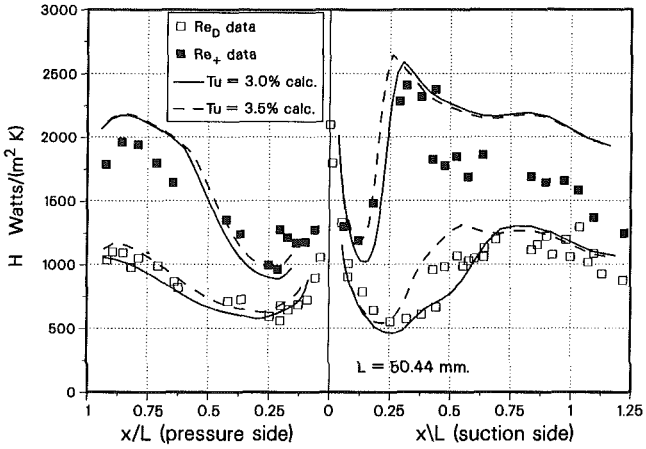

Fig. 9 Comparison of the predicted heat transfer coefficient with data from the turbine blade experiments of Daniels (1978)

In Fig. 9, a comparison of the predicted versus experimentally determined heat transfer coefficient on the turbine blade studied by Daniels (1978) is shown. Two different flow conditions were selected from the data. These are designated with respect to the design operating conditions as Re_D (design Reynolds number) and Re_+ (i.e., a higher flow rate yielding a Reynolds number greater than the design condition). The free-stream turbulence intensity measured upstream of the blade was 4.2 percent. At the actual location of the blade, Rodi and Scheuerer (1985b) estimated this to have decayed to about 3 percent based on the empirical decay rates given by Townsend (1976). However, Daniels and Browne (1981), who also presented calculations for this blade, appear to have used the value of 4 percent. Thus the calculations shown in Fig. 9 were made for both 3.0 and 3.5 percent to illustrate the sensitivity of the results to this parameter. As can be seen, the location and extent of transition (at least as represented in the heat transfer) are well predicted. The only significant variation between the data and the computation occurs at the higher Reynolds number in regions downstream of transition. Also note that the only place where the 3 percent versus 3.5 percent Tu_e makes much difference is for the design Reynolds number case, where the two calculations bracket the experimental data.

Closure

A novel approach for predicting boundary layer transition under the influence of free-stream turbulence using k-ϵ LRN

turbulence models has been developed, applied to the Lam–Bremhorst LRN model, and tested against a variety of data. The approach is based on modifying and controlling the growth rate of the production term in the k equation during the preturbulent region of the boundary layer development. This approach is shown to overcome many of the shortcomings associated with using the unmodified k–ϵ LRN models for this application. In particular, the starting location and needed starting profiles can be specified in a consistent fashion and with minimal influence on the resulting predictions. Furthermore, the predictions of this approach, unlike unmodified LRN model calculations, match the correlation of Abu-Ghannam and Shaw (1981) for flat plate, zero pressure gradient flow. Comparisons with a variety of experimental data, including accelerating flow and flow around a turbine blade, show excellent predictions of the transition region location and length.

Acknowledgments

This research was sponsored by the NASA Lewis Research Center under contract No. NAG3-579.

References

Abu-Ghannam, B. J., and Shaw, R., 1980, "Natural Transition of Boundary Layers—The Effects of Turbulence, Pressure Gradient, and Flow History," *J. Mech. Eng. Science*, Vol. 22, No. 5, pp. 213–228.

Blair, M. F., and Werle, M. J., 1980, "The Influence of Free-Stream Turbulence on the Zero Pressure Gradient Fully Turbulent Boundary Layer," UTRC Report R80-915388-12

Blair, M. F., and Werle, M. J., 1981, "Combined Influence of Free-Stream Turbulence and Favorable Pressure Gradients on Boundary Layer Transition," UTRC Report R81-914388-17.

Blair, M. F., 1982, "Influence of Free-Stream Turbulence on Boundary Layer Transition in Favorable Pressure Gradients," ASME *Journal of Engineering for Power*, Vol. 104, pp. 743–750.

Daniels, L. D., 1978, "Film Cooling of Gas Turbine Blades," Ph.D. Thesis, Dept. of Engineering Science, U. of Oxford, United Kingdom.

Daniels, L. D. and Browne, W. B., 1981, "Calculation of Heat Transfer Rates to Gas Turbine Blades," *Int. J. Heat Mass Transfer*, Vol. 24, No. 5, pp. 871–879.

Jones, W. P., and Launder, B. E., 1972, "The Prediction of Laminarization With a Two-Equation Model of Turbulence," *Int. J. Heat Mass Transfer*, Vol. 15, pp. 301–314.

Jones, W. P. and Launder, B. E., 1973, "The Calculation of Low Reynolds Number Phenomena With a Two-Equation Model of Turbulence," *Int. J. Heat Mass Transfer*, Vol. 16, pp. 1119–1130.

Lam, C. K. G., and Bremhorst, K., 1981, "A Modified Form of the k–ϵ Model for Predicting Wall Turbulence," ASME *Journal of Fluids Engineering*, Vol. 103, pp. 456–460.

Patankar, S. V., and Spalding, D. B., 1970, *Heat and Mass Transfer in Boundary Layers*, 2nd ed., Intertext, London.

Patel, V. C., Rodi, W., and Scheuerer, G., 1985, "A Review and Evaluation of Turbulence Models for Near-Wall and Low Reynolds Number Flows," *AIAA Journal*, Vol. 23, p. 1308.

Rodi, W., and Scheuerer, G., 1985a, "Calculation of Heat Transfer to Convection-Cooled Gas Turbine Blades," ASME *Journal of Engineering for Gas Turbines and Power*, Vol. 107, pp. 620–627.

Rodi, W., and Scheuerer, G., 1985b, "Calculation of Laminar-Turbulent Boundary Layer Transition on Turbine Blades," *AGARD Conference Proceedings No. 390*, pp. 18.1 to 18.13.

Rued, K., 1983, "Transitionale Grezschichten unter dem Einfluss hoher Freistromturbulenze, intensiver Wandkuehlung und starken Druckgradienten in Heissgasstroemungen," Ph.D. Thesis, University of Karlsruhe, Federal Republic of Germany (English translation, NASA Report No. TM-88524, 1987).

Rued, K., and Wittig, S., 1985, "Free-Stream Turbulence and Pressure Gradient Effects on Heat Transfer and Boundary Layer Development on Highly Cooled Surfaces," ASME *Journal of Engineering for Gas Turbines and Power*, Vol. 107, No. 1, pp. 54–59.

Rued, K., and Wittig, S., 1986, "Laminar and Transitional Boundary Layer Structures in Accelerating Flow With Heat Transfer," ASME JOURNAL OF TURBOMACHINERY, Vol. 108, pp. 116–123.

Scheuerer, G., 1983, "Entwicklung eines Verfahrens zur Berechnung zweidimensionaler Grenzschichten an Gasturbineschaufeln," Ph.D. Thesis, University of Karlsruhe, Federal Republic of Germany.

Schmidt, R. C., and Patankar, S. V., 1987, "Prediction of Transition on a Flat Plate Under the Influence of Free-Stream Turbulence Using Low-Reynolds-Number Two Equation Turbulence Models," ASME Paper No. 87-HT-32.

Schmidt, R. C., 1987, "Two-Equation Low-Reynolds-Number Turbulence Modeling of Transitional Boundary Layer Flows Characteristic of Gas Turbine Blades," Ph.D. Thesis, University of Minnesota, Minneapolis, MN (also available as NASA Contract Report 4145, May 1988).

Wang, J. H., Jen, H. F., and Hartel, E. O., 1985, "Airfoil Heat Transfer Using Low Reynolds Number Version of a Two Equation Turbulence Model," ASME *Journal of Engineering for Gas Turbines and Power*, Vol. 107, No. 1, pp. 60–67.

The Mass Transfer Analogy to Heat Transfer in Fluids With Temperature-Dependent Properties

J. N. Shadid[1]

E. R. G. Eckert

Department of Mechanical Engineering,
University of Minnesota,
Minneapolis, MN 55455

The analogy between heat transfer in a single-component fluid and isothermal mass transfer of a two-component fluid without chemical reaction is presented. The analogy is well established and frequently used for fluids with constant properties. However, in various applications such as in the cooling of hot components in gas turbines, the temperature varies widely, causing significant fluid property variations. The present paper reviews the constant-property situation and considers in detail the conditions necessary to ensure similarity of the two transport processes with temperature and concentration-dependent fluid properties. An application of the variable property analogy to mass transfer in binary mixtures is presented along with specific recommendations for the CO_2–air and Freon–air systems. It is demonstrated that the essential similarity conditions of the analogy are very well fulfilled for film cooling, total coverage film cooling, and impingement cooling when the heat (mass) flux into the wall in the transport process is zero. The heat/mass transfer analogy can, therefore, be used with confidence for these processes.

Introduction

The analogy between heat transfer in a single-component fluid and isothermal mass transfer in a two-component fluid without chemical reaction is well established and frequently used. The conditions for this analogy, which were introduced by Schmidt (1929) and Nusselt (1930), are well known for fluids with constant properties. In various applications, for instance, in the cooling of hot components in gas turbines, the temperature varies widely in the field of interest, which causes the properties to vary also. Eckert (1976) pointed out that the density variation has the strongest effect on the analogy in turbulent flow at high Reynolds number, and demonstrated that the variation of the density of an ideal gas with temperature is similar to the variation of density with mass fraction for a two-component ideal gas mixture. The present paper demonstrates this in detail and investigates to what extent the analogy still holds when the other properties are also considered. Conditions ensuring an analogy for constant property fluids are reviewed as well.

Governing Equations

The governing equations describing the transfer of thermal energy in a pure fluid system and the transfer of chemical species in an isothermal fluid are presented below. In these equations, Fourier's law of heat conduction as well as Fick's law of diffusion are assumed to hold.

Heat Transfer in a Pure Fluid. Equations (1), (2), and (3T) express the conservation laws of mass, momentum, and energy in the heat transfer system:

$$\frac{\partial \rho}{\partial t} + \nabla \cdot (\rho \mathbf{u}) = 0 \tag{1}$$

$$\rho\left(\frac{\partial \mathbf{u}}{\partial t} + \mathbf{u} \cdot \nabla \mathbf{u}\right) = -\nabla P + \nabla \cdot \left(\mu\left[\nabla \mathbf{u} + \nabla \mathbf{u}^T\right]\right) \tag{2}$$

$$\rho c_p\left(\frac{\partial T}{\partial t} + \mathbf{u} \cdot \nabla T\right) = \nabla \cdot \left(k \nabla T\right) \tag{3T}$$

The following assumptions have been made in equations (1), (2), and (3T):

(*a*) The properties including the density are temperature dependent only; the effect of pressure differences on density variation is negligible.

(*b*) Body forces (including gravity) are absent or negligible.

(*c*) Aerodynamic and viscous heating are negligible. This effect is, however, included in equation (3T) for a fluid with Pr = 1 providing the temperature T is interpreted as the total temperature (including internal and kinetic energy).

Mass Transfer in a Two-Component Fluid. The mass transfer process is stipulated isothermal and without chemical reactions. The effects of forced diffusion, pressure, and thermal diffusion have been assumed negligible. Equations (1) and (2) also describe this process with ρ interpreted as the mixture density and $\mathbf{u}$ as the mass-averaged velocity. In the mass transfer case, the fluid properties are now dependent on the mass fraction w_I of one of the two components. Equation (3T) is replaced in the mass transport system by the conservation of chemical species I equation (3w) listed below.

[1]Present address: Sandia National Labs., Albuquerque, NM 87185.

Contributed by the International Gas Turbine Institute and presented at the National Heat Transfer Conference, Houston, Texas, July 24–27, 1988. Manuscript received at ASME Headquarters November 6, 1989.

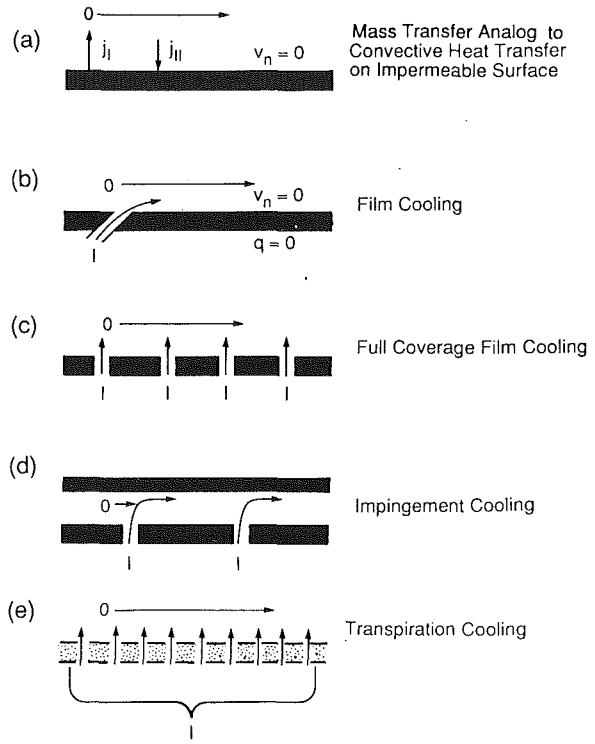

Fig. 1 Sketch of typical convective heat transfer boundary conditions (0 indicates the free-stream flow)

$$\rho\left(\frac{\partial w_I}{\partial t} + \mathbf{u}\cdot\nabla w_I\right) = \nabla\cdot\left(\rho D\nabla w_I\right) \qquad (3w)$$

The mass fraction w_{II} of the other component II is determined by the equation

$$w_I + w_{II} = 1 \qquad (4)$$

Boundary Conditions. The two systems for the heat and mass transfer processes must have similar geometries, and physical similarity must also be fulfilled in the initial and boundary conditions. This presents some restrictions on the analogy, which will be discussed in this section. In the following, the term inactive surface will be used to describe a solid surface to which no heat (mass) transfer takes place, i.e., adiabatic or impermeable surfaces. An active surface is a surface at which there is a nonzero heat (mass) flux into the wall.

Heat transfer processes with inactive (adiabatic) surfaces are of interest in a number of convection processes. For example, it is often important to determine the temperature distribution on an insulated surface exposed to a convection environment. In addition, knowledge of the adiabatic wall conditions can be used as an intermediate step to determine heat transfer coefficients to physically similar nonadiabatic walls (Goldstein, 1971). In the case of such inactive surfaces, the mass transfer system does not induce nonanalogous normal velocities due to diffusion mass transfer at the solid surface. Therefore, the velocity boundary conditions for the two systems are exactly similar. This type of heat/mass transfer analogy is commonly used to determine the adiabatic wall temperature (concentration) in film cooling, total coverage film cooling, and impingement cooling processes used for the cooling of hot components in gas turbines. Each of these processes, shown in Figs. 1(*b*, *c*, *d*), respectively, can readily be simulated by a mass transfer process in which the normal velocity on the surface downstream of the slot or row of holes is zero.

This however is not the case when active surfaces are considered, since the heat flux and analogously the mass flux at the solid surface is nonzero. This nonzero mass flux produces a nonzero normal velocity in the mass transfer process at the solid surface due to the diffusional mass transfer. This of course need not be a problem if the purpose is to simulate a heat transfer process with similar nonzero boundary velocities. Possible applications would be the transpiration cooling process (Fig. 1*e*) or an ablation cooling model (Eckert, 1976).

If it is necessary to simulate active heat transfer surfaces with zero normal velocities, then it appears that only two alternatives are available.The first method uses an analogous mass transfer process with a fluid flowing over a catalytic surface where the fluid undergoes a chemical reaction (dissociation, recombination) as shown in Fig. 1(*a*). The two diffusional mass fluxes j_I and j_{II} are equal in magnitude and opposite in sign; thus the mass-averaged velocity at the wall surface is equal to zero (Eckert and Drake, 1972). Heat generated or absorbed in the reaction has to be removed into the interior of the solid wall, if it is not negligible, to keep the mass transfer process isothermal. Experimental difficulties have probably prevented researchers from using this method. The second method is to limit mass transfer rates at active solid surfaces. For example, in processes such as condensation, sublimation, or evaporation of a fluid, the surface is impermeable to one of the fluid components. A total flow with normal velocity v_n occurs now at the surface, whereas the partial mass flow of component II by diffusion and convection is zero. The velocity at the wall surface is given by the equation

$$v_n = \frac{1}{1 - w_{I_1}} D\left[\frac{\partial w_{I_1}}{\partial n}\right]_{\text{wall}} \qquad (5)$$

Nomenclature

c_p = specific heat
D = coefficient of mass diffusion
h = heat transfer coefficient = $q/\Delta t$
h_m = mass transfer coefficient = $\dot{m}/\Delta\rho$
j = diffusional mass flux
k = thermal conductivity
L = length scale
Le = Lewis number = Pr/Sc
M = molecular weight
$\dot{m}$ = mass flux per unit area
Nu = Nusselt number = hL/k
P = pressure
Pr = Prandtl number = $\mu c_p/k$
q = heat flux per unit area
R = universal gas constant
Re = Reynolds number = $\rho VL/\mu$
s = equivalent slot width (equation (15))
Sc = Schmidt number = $\mu/\rho D$
Sh = Sherwood number = $h_m L/D$
T = absolute temperature
t = time
$\mathbf{u}$ = velocity vector
u = velocity component
V = reference velocity
v = velocity component
W^* = nondimensional mass fraction (equation (6))
w = mass fraction
x = distance from injection point (equation (15))
α = angle
Θ^* = nondimensional temperature (equation (6))
μ = viscosity
ξ = variable in equation (15)
ρ = density

Subscripts

aw = adiabatic wall condition
i = general component
n = normal component
o = reference quantity, free stream
T = heat transfer quantity
w = mass transfer quantity
I = component 1
II = component 2
1 = wall quantity, injected fluid

Superscripts

T = transpose
$*$ = dimensionless

where w_{I_1} is the mass fraction of the evaporating liquid or subliming solid (Eckert and Drake, 1972). Often these processes occur with negligibly small normal velocities in comparison to the mainstream velocity. Equation (5) indicates that the low normal velocity condition requires the concentration gradient of the fluid component I at the surface to be small, and it helps also when the mass fraction w_{I_1} at the surface is small. In such a case the variation of the mass fraction W_{I_1} throughout the region is small, and therefore this type of system cannot be used to simulate heat transfer at large temperature differences. The heat/mass transfer analogy with naphthalene sublimation is based on this system and is widely used to obtain information on convective heat transfer at small temperature differences.

Dimensionless Equations. The governing equations (1)–(3), together with the boundary conditions, are made nondimensional with prescribed reference terms taken from the boundary conditions. The analogy applies to a group of similar systems, each of which is characterized by the magnitude of a characteristic length L. Forced flow is scaled by a characteristic velocity V. No prescribed time is contained in the boundary conditions for steady flow, either for flow started impulsively or for internally generated turbulence. Therefore, a characteristic time L/V is formed with the prescribed quantities above. When the pressure variation of density is neglected, there is no available reference pressure. Therefore, a reference pressure difference $\rho_o V^2$ is used. The temperature and mass fraction are made nondimensional by evaluation relative to a reference state T_o and w_o and scaling by the reference quantities $(T_1 - T_o)$ and $(w_1 - w_o)$, respectively. All of the properties appearing in the equations are made dimensionless with the appropriately selected reference quantities, $(\rho_o, \mu_o, c_{p_o}, k_o, D_o)$. The equations are next made dimensionless by the following change of variables:

$$\left(\mathbf{x}^*, \mathbf{u}^*, t^*, P^*, \Theta^*, W^*\right) = \left(\frac{\mathbf{x}}{L}, \frac{\mathbf{u}}{V}, \frac{\mathrm{t}}{\mathrm{L/V}}, \frac{P}{\rho_o V^2}, \frac{T-T_o}{T_1-T_o}, \frac{w-w_o}{w_1-w_o}\right) \tag{6}$$

$$\left(\rho_T^*, \mu_T^*, c_p^*, k^*\right) = \left(\frac{\rho_T}{\rho_{T_o}}, \frac{\mu_T}{\mu_{T_o}}, \frac{c_p}{c_{p_o}}, \frac{k}{k_o}\right) \tag{7T}$$

$$\left(\rho_w^*, \mu_w^*, D^*\right) = \left(\frac{\rho_w}{\rho_{w_o}}, \frac{\mu_w}{w_o}, \frac{D}{D_o}\right) \tag{7w}$$

The following dimensionless parameters are defined for the heat transfer process:

$$\mathrm{Re}_{T_o} = \frac{\rho_{T_o} VL}{\mu_{T_o}}, \qquad \mathrm{Pr}_o = \frac{\mu_{T_o} c_{p_o}}{k_o} \tag{8}$$

and for the mass transfer process:

$$\mathrm{Re}_{w_o} = \frac{\rho_{w_o} VL}{\mu_{w_o}}, \qquad \mathrm{Sc}_o = \frac{\mu_{w_o}}{\rho_{w_o} \mathrm{D}_o} \tag{9}$$

The governing equations (1)–(3) and boundary conditions are now made dimensionless using the quantities introduced in the preceding section.

1 Heat Transfer:

$$\frac{\partial \rho_T^*}{\partial t^*} + \nabla \cdot (\rho_T^* \mathbf{u}^*) = 0 \tag{10}$$

$$\rho_T^* \left(\frac{\partial \mathbf{u}^*}{\partial t^*} + \mathbf{u}^* \cdot \nabla \mathbf{u}^*\right) = -\nabla P^* + \frac{1}{\mathrm{Re}_{T_o}} \nabla \cdot \left(\mu_T^* \left[\nabla \mathbf{u}^* + (\nabla \mathbf{u}^*)^T\right]\right) \tag{11}$$

$$\rho_T^* c_p^* \left(\frac{\partial \Theta^*}{\partial t^*} + \mathbf{u}^* \cdot \nabla \Theta^*\right) = \frac{1}{\mathrm{Re}_{T_o} \mathrm{Pr}_o} \nabla \cdot \left(k^* \nabla \Theta^*\right) \tag{12T}$$

2 Mass Transfer. The continuity and momentum equations, equations (10) and (11), respectively, hold for mass transfer also when the index T is replaced by the index w. In addition, the conservation of species I equation becomes

$$\rho_w^* \left(\frac{\partial W_I^*}{\partial t^*} + \mathbf{u}^* \cdot \nabla W_I^*\right) = \frac{1}{\mathrm{Re}_{w_o} \mathrm{Sc}_o} \nabla \cdot \left(\rho_w^* D^* \nabla W_I^*\right) \tag{12w}$$

3 Boundary Conditions. The nondimensional upstream boundary conditions become

$$\text{Heat transfer:} \quad u = 1, \quad \Theta^* = 0 \tag{13T}$$

$$\text{Mass transfer:} \quad u = 1, \quad W_I^* = 0 \tag{13w}$$

The boundary conditions on a solid surface with zero normal velocity in the heat transfer case are summarized in Table 1.

For active surfaces, it is apparent from Table 1 that either the heat transfer boundary condition must be prescribed with the same nonzero boundary velocity or the magnitude of the normal velocity must be made negligible in comparison to the mainstream flow, i.e., $v_n^* \ll 1$ at the wall. Clearly, this restriction limits the mass transfer process to sufficiently low mass transfer rates. The nondimensional parameter St = Sh/$(\mathrm{Re}_{w_o} \mathrm{Sc}_o)$ appearing in Table 1 is the mass transfer Stanton number. In a number of flow situations, the Stanton number can be estimated beforehand to check the normal velocity restriction.

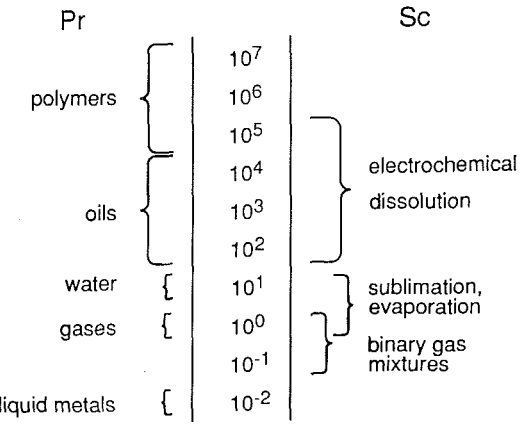

Fig. 2 Comparison of Prandtl and Schmidt numbers for various common transport processes

Table 1 Comparison of boundary conditions on a solid surface

Type	Heat transfer	Mass transfer
Active	$v_n^* = 0, \quad \Theta^* = 1$	$v_n^* = \dfrac{\mathrm{Sh}}{\mathrm{Re}_{w_o}\mathrm{Sc}_o}(w_{I_1} - w_{I_o}), \quad W_I^* = 1$
Inactive	$v_n^* = 0, \quad \dfrac{\partial \Theta^*}{\partial n} = 0$	$v_n^* = 0, \quad \dfrac{\partial W_I^*}{\partial n} = 0$

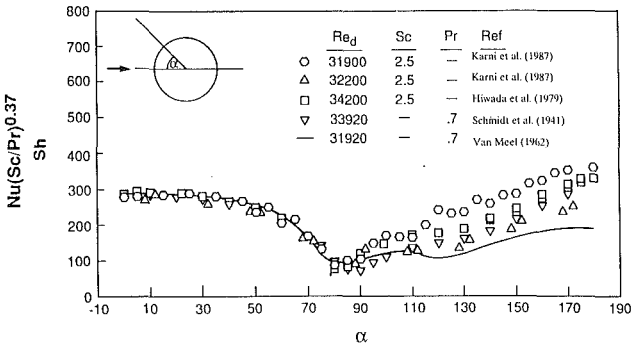

Fig. 3 Comparison of heat and mass transfer data for a cylinder in crossflow using the constant property heat and mass transfer analogy (Karni and Goldstein, 1987)

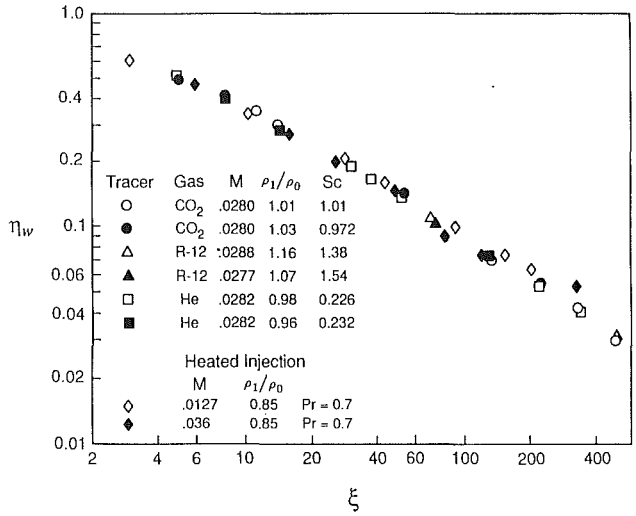

Fig. 4 Effect of Sc on mass transfer film effectiveness (Pedersen et al., 1977)

Analogy Conditions

(A) Constant-Property Fluids. In the constant fluid property situation the dimensionless property ratios in equations (6) and (7) all have the value 1 and the analogy depends only on the conditions

$$\mathrm{Re}_{T_o} = \mathrm{Re}_{w_o}, \quad \mathrm{Pr}_o = \mathrm{Sc}_o \tag{14}$$

The Reynolds numbers, therefore, have to be equal for analogous heat and mass transfer processes. Condition (14) requiring the equality of the Prandtl number and the Schmidt number can be fulfilled in various ways. Figure 2 shows that heat transfer processes can be designed for a large range of Prandtl numbers, and the same is true for mass transfer processes, which cover a considerable range of Schmidt numbers. A proper Schmidt number fluid can, therefore, in principle, be selected to match the desired Prandtl number of a heat transfer process.

Practically, this is often inconvenient, and another method is used in which previous empirical or theoretical results furnish the Pr_o (Sc_o) dependence for a specific transport process. Thus, knowing the functional relationship $\mathrm{Sh} = f(\mathrm{Re}_{w_o}, \mathrm{Sc}_o)$ or $\mathrm{Nu} = f(\mathrm{Re}_{T_o}, \mathrm{Pr}_o)$ allows experimental results for various heat (mass) transfer processes to be interpreted (by means of the analogy) for situations with $\mathrm{Pr}_o \neq \mathrm{Sc}_o$.

In a number of important transport processes, the functional relationship between Nu and Pr has been studied extensively in the past. For example, in the case of a laminar boundary layer on a flat plate, the analytic relation can be approximated with good accuracy by $\mathrm{Nu} \approx \mathrm{Pr}^{1/3}$ for Prandtl numbers larger than 0.6. Most experiments also state that for a turbulent boundary layer on a flat plate, $\mathrm{Nu} \approx \mathrm{Pr}^{1/3}$ (Eckert, 1972). For other flow situations, the relationship is found to be more involved, but equations for those flows are often available in the literature.

As an example, the results of heat and mass transfer experiments for flow normal to the axis of a circular cylinder are compared in Fig. 3 (Karni and Goldstein, 1987). It can be observed that results of all experiments agree in the region of attached flow, when $\mathrm{Nu}\,(\mathrm{Sc}/\mathrm{Pr})^{0.37}$ or Sh are plotted against the angle α measured from the forward stagnation line. The larger scatter in the separated region on the downstream side of the cylinder ($\alpha > 80$ deg) could indicate that the relation between Nu (Sh) and Pr (Sc) is different for separated flow. Results obtained by different observers at the same Pr (Sc) number also exhibit considerable scatter indicating that separated flow is sensitive to the specific test setup. Therefore, no conclusion about the usefulness of the analogy in the separated region is possible.

Another important aspect of interpreting mass transfer results in heat transfer studies, or vice versa, is that for a number of physical flow situations the influence of Pr (Sc) is known to be negligible. For example, in the case of high Reynolds number flows, it is apparent that inertia and convective mixing dominate molecular diffusion except in boundary layers near solid surfaces. It can be expected that for flow processes with inactive (adiabatic/impermeable) surfaces, the influence of molecular parameters such as Pr (Sc) will be small, since the gradients of temperature and concentration are zero at such surfaces. This expectation is confirmed by the experimental results of Pedersen et al. (1977) in their study of film cooling over an adiabatic surface by using an analogous mass transfer process. They determined the mass transfer film effectiveness $\eta_w = (w_{aw} - w_o)/(w_1 - w_o)$ over a plane, impermeable surface by foreign gas injection. Their results for a blowing ratio $\lesssim 0.4$,[2] reproduced in Fig. 4, indicate that η_w is practically independent of the Schmidt number over a fairly wide range of this parameter. The corresponding effectiveness of film cooling $\eta_T = (T_{aw} - T_o)/(T_1 - T_o)$ is then independent of Prandtl number. The semiempirical parameter ξ in this figure, given by the following equation, was found to correlate effectiveness with injection through a porous slot or through two rows of inclined holes with good accuracy.

$$\xi = \frac{x}{s}\frac{\rho_o}{\rho_1}\frac{u_o}{u_1}\left[\frac{\mu_1}{\mu_o}\mathrm{Re}_1\right]^{-0.25} \tag{15}$$

In this expression, x is distance downstream from injection, s is slot width or equivalent slot width. The subscripts o, 1 indicate free-stream and injected fluid quantities, respectively. The injection Reynolds number is $\mathrm{Re}_1 = \rho_1 u_1 s/\mu_1$. It is expected that for higher blowing rates the independence of the film effectiveness on the Schmidt number would continue for locations sufficiently far downstream of the injection hole/slot.

(B) Variable Property Fluids. The heat/mass transfer analogy for variable property fluids requires, in addition, that the following nondimensional properties in equations (10)–(12) be identical for both processes.

$$\rho_T^* = \rho_w^*, \quad \mu_T^* = \mu_w^*, \quad k^* = \rho_w^* D^*, \quad \rho_T^* c_p^* = \rho_w^* \tag{16}$$

The condition that $\rho_T^* c_p^* = \rho_w^*$ and $\rho_T^* = \rho_w^*$ be identical simultaneously is only possible when the specific heat c_p is constant, which indicates that the specific heat ratio c_p^* is equal to 1. This will be assumed in the following analysis. If the specific heat varies to such a degree that it cannot be assumed as constant, then the energy equation has to be written in terms

[2]The blowing ratio appears small because the secondary fluid was injected into the boundary layer through a 2.434-cm-wide porous strip.

of enthalpy rather than temperature. The condition $k^* = \rho_w^* D^*$ can be replaced by $\mathrm{Pr}^* = \mathrm{Sc}^*$ (or $\mathrm{Le}^* = 1$) according to

$$\mathrm{Pr}^* = \frac{\mu_T^*}{k^*} = \frac{\mu_w^*}{\rho_w^* D^*} = \mathrm{Sc}^* \tag{17}$$

The similarity conditions for a fluid with constant specific heat can, therefore, be summarized as follows:

$$\mathrm{Re}_{T_o} = \mathrm{Re}_{w_o}, \quad \mathrm{Pr}_o = \mathrm{Sc}_o \tag{18}$$

$$\rho_T^* = \rho_w^*, \quad \mu_T^* = \mu_w^*, \quad \mathrm{Pr}^* = \mathrm{Sc}^* \ (\mathrm{Le}^* = 1) \tag{19}$$

It is apparent that the conditions (18) and (19) above put a significant restriction on the fluid properties of any heat and mass transfer system that is to be used for the analogy. In general, it is expected that the variation of property ratios in isothermal mass transfer will differ from heat transfer in pure fluids since a different set of physical processes is involved. Of course the magnitude of this deviation will depend strongly on the magnitude of the concentration (temperature) variation and upon the specific mass and heat transfer systems considered. In addition, for any specific flow the relative importance of the density, the viscosity, and the Lewis number ratios cannot be established without first solving the conservation equations or performing experiments. Thus each application of the analogy must be justified in the context of the physical flow system involved and the particular heat and mass transfer systems used. This will be done in the next section for a commonly used heat and mass transfer analogy system to simulate film cooling and impingement cooling.

Even with the problems identified above, the heat and mass transfer analogy in variable property flows can prove to be a valuable experimental technique for the following reasons. First of all, the uncertainty generated by the nonmatching of fluid property ratios should be compared to the uncertainty present in the given heat transfer experiment. Heat transfer experiments with large temperature differences inherently involve many sources of uncertainty in the determination of the convective heat transfer characteristics. For example, in the presence of large temperature differences, it is difficult to eliminate unwanted conduction effects, since it is difficult to produce an effective adiabatic wall. However, an impermeable wall, which is the mass transfer equivalent of the adiabatic wall, is readily available. In addition, radiation heat transfer becomes significant at high temperatures and often cannot be accounted for accurately, thereby introducing uncertainty in the convective heat transfer measurements. This is in contrast to the mass transfer situation in which it is assured that the experiment measures convective transport, since "wall conduction" and "radiation" can be totally eliminated. In large-scale experiments it is also difficult to produce a uniform high-temperature mainstream flow or to cool the injected gases sufficiently to produce the necessary temperature differences.

Film Cooling and Impingement Cooling

An evaluation of the heat/mass transfer analogy using the similarity conditions presented above will be carried out for film cooling and impingement cooling heat transfer, and the analogous mass transfer process employing binary ideal gas mixtures. Figure 1 presents sketches of these two processes. The surface of the wall cooled by fluid 1 is postulated adiabatic and impermeable. Fluid 1 is injected through the slots or rows of holes. The fluid, which is a mixture of the two components I and II, is identified by the mass fraction w_I of component I. No component I is contained in the mainstream flow ($w_{I_o} = 0$). The heat/mass transfer analogy has been used frequently to simulate film cooling of hot components in gas turbines with air as the mainstream fluid and carbon dioxide (CO_2) or freon (F12) mixed with air as fluid 1 to increase its density. The similarity conditions (18) and (19) require the property

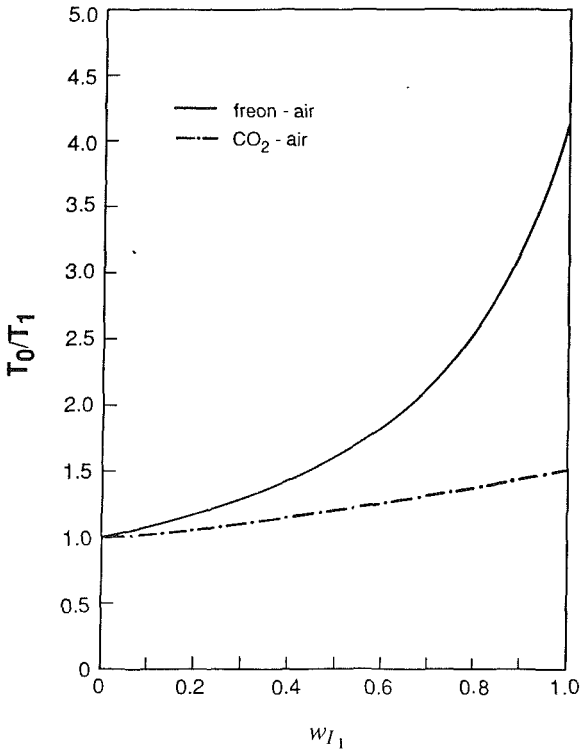

Fig. 5 Temperature ratio in the heat transfer process corresponding to mass fraction W_I^* in the injected gasses of the mass transfer process

ratios to vary in the same way over the range existing in the two systems. These conditions will be examined in the following paragraphs.

The variation of the density in the heat transfer process is assumed to be described by the ideal gas equation of state

$$\rho_T = \frac{PM}{RT} \tag{20}$$

The corresponding density variation with concentration of the mixture in the mass transfer process is obtained from the following relations valid for a multiple component mixture:

$$\sum w_i = 1, \quad \sum \rho_i = \rho_w, \quad \sum \frac{w_i}{M_i} = \frac{1}{M}, \quad \rho_i = \frac{P_i M_i}{RT}, \quad w_i = \frac{P_i M_i}{PM} \tag{21}$$

with the index i denoting any one of the components. Using these relations for a two-component mixture, one obtains the equation

$$\rho_w = \frac{M_I M_{II}/(M_{II} - M_I)}{w_I + M_I/(M_{II} - M_I)} \left[\frac{P}{RT}\right] \tag{22}$$

The dimensionless density ratio is obtained from equation (20)

$$\rho_T^* = \frac{T_o/(T_1 - T_o)}{\Theta^* + T_o/(T_1 - T_o)} \tag{23}$$

and the dimensionless density ratio of the fluid mixture is

$$\rho_w^* = \frac{M_I/[w_{I_1}(M_{II} - M_I)]}{W_I^* + M_I/[w_{I_1}(M_{II} - M_I)]} \tag{24}$$

with the stipulation $w_{I_o} = 0$. Equations (23) and (24) indicate that the density ratio of a gas with temperature difference Θ^* varies in exactly the same way as the density ratio of a two-component gas mixture with mass fraction W_I^*. Therefore, the similarity condition (19) for density will hold if the constant terms in (23) and (24) are set equal as

$$\frac{T_o}{T_1} = \left\{1 + w_{I_1}\left[\frac{M_{II} - M_I}{M_I}\right]\right\}^{-1} \tag{25}$$

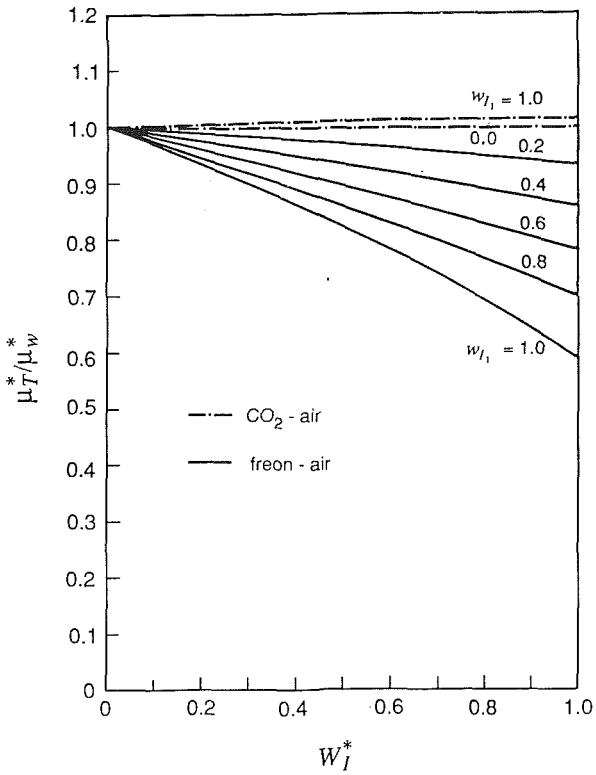

Fig. 6 Variation of heat/mass transfer viscosity ratios with nondimensional temperature (concentration)

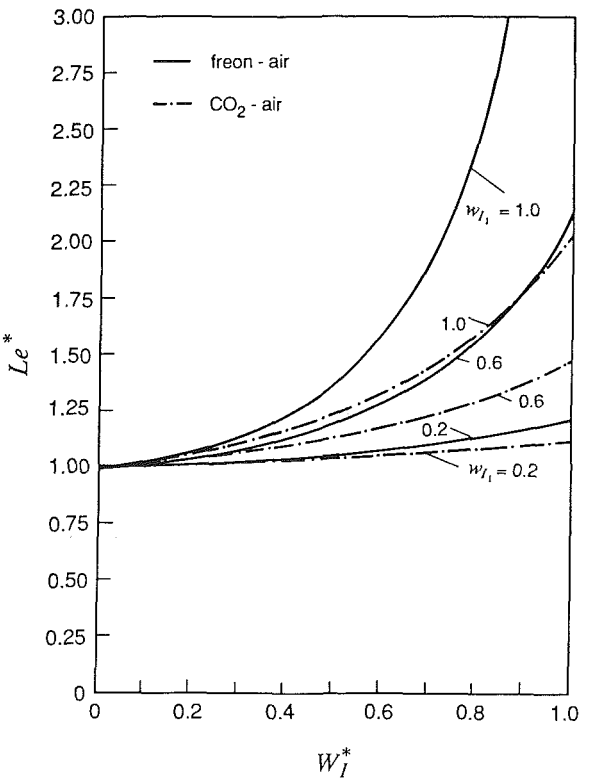

Fig. 7 Variation of Lewis number ratio with the nondimensional temperature (concentration)

This equation determines the temperature ratio corresponding to a given injection mass fraction w_{I_1} for a particular binary gas mixture. Equation (25) is illustrated by Fig. 5 for the systems freon-air and CO_2–air. It is apparent that a maximum temperature ratio of about 1.5 can be obtained in the analogy

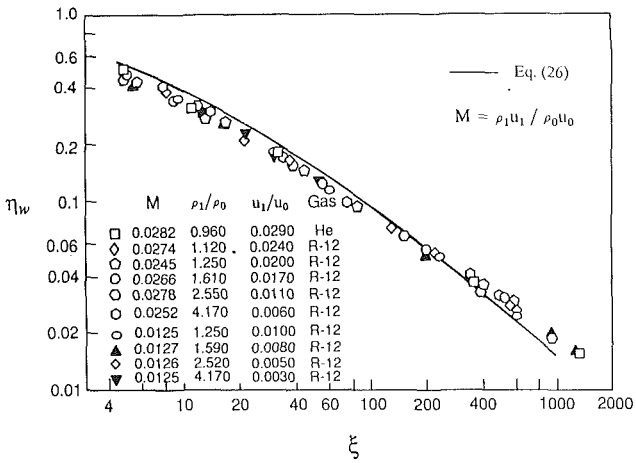

Fig. 8 Variable property effects on film effectiveness

when pure CO_2 is used as injected fluid 1, whereas a temperature ratio somewhat above 4 can be obtained by injection of pure F12.

The ratio of the dimensionless viscosities was calculated using tabulated values for $\mu(T)$ and Wilke's (1950) correlation for $\mu(w)$ and is presented in Fig. 6. These values hold for air in the range 300 K to 1800 K and for binary gas mixtures at 20°C. One recognizes that the ratio is very close to the value 1 for the system CO_2–air, whereas the system freon–air experiences larger variations. At the temperature ratio of 1.5, which is the maximum temperature ratio obtainable with the system CO^2–air, the viscosity ratio of the system freon–air varies by approximately 20 percent.

The variable property Lewis number ratio is plotted in Fig. 7. This figure indicates that for a temperature ratio of 1.5 (CO_2: w_{I_1} = 1.0, F12: w_{I_1} = 0.45) the system CO_2–air has a larger deviation of the Lewis number ratio from 1 than the corresponding freon–air system.

Conditions for the similarity of the concentration and temperature field are especially well satisfied for film cooling and impingement cooling when the system CO_2–air is used for the mass transfer experiment and when the heat (mass) flux into the solid wall is zero. The density fields are exactly similar by equations (23), (24), and (25) and the viscosity fields are similar according to Fig. 6. The similarity of the conductivity and mass diffusivity fields will again be shown to have a minor influence since the gradients of temperature (concentration) at the wall surface are zero. This was demonstrated in the constant property situation by the fact that heat and mass transfer did not depend on Pr_o (Sc_o) parameters.

Support for this claim is again obtained from the experimental work of Pedersen et al. (1977). The authors studied the effect of large density differences on film cooling effectiveness using the binary gas systems of He–air, Co_2–air, and freon–air.

Their results for blowing ratios 0.03, reproduced in Fig. 8, indicate no observable effect from the variation of Sc (w_{I_1}) as would be expected in this limiting case. The independence of the Sherwood number from Sc is expected to continue for higher blowing rates for locations sufficiently far downstream of the injection hole/slot. The effects of density ratio and variable viscosity are accounted for in the abscissa variable ξ, which was defined in equation (15). The authors also present an analytically derived equation by Kutateladze and Leont'ev describing the film effectiveness for two-dimensional film cooling. This relationship, reproduced in the following equation is plotted as a solid line in Fig. 8:

$$\eta_w = \frac{1}{1+0.249\ \xi^{0.8}} \tag{26}$$

Rearranging this equation, the following relationship for the relative influence of density and viscosity ratios can be obtained:

$$\text{Density:} \quad \frac{\eta_w}{1-\eta_w} \approx \left[\rho^*_{w_1}\right]^{0.8} \quad 1.0 \leq \rho_{w_1}^* \leq 4.17 \qquad (27)$$

$$\text{Viscosity:} \quad \frac{\eta_w}{1-\eta_w} \approx \left[\mu^*_{w_1}\right]^{0.2} \quad .68 \leq \mu_{w_1}^* \leq 1.0 \qquad (28)$$

These relationships indicate a more pronounced effect for the inertial coefficient ρ^*_w (which varies from $1.0 \leq \rho^*_{w_1} \leq 4.17$) than for the molecular diffusion coefficient term $\mu^*_{w_1}$ (which varies from $0.68 \leq \mu^*_{w_1} \leq 1.0$). These results are consistent with the argument that in such flows inertia and convective mixing dominate the molecular diffusion terms when the solid surface is inactive. It should be noted that the similarity condition $c_p^* = 1$ in this situation is not a strict constraint on the analogy. This is because unlike the density and viscosity ratios, it occurs only in the energy equation (12T). Therefore, it can be brought to the right-hand side of (12T) where it can be thought of as a modification of the thermal diffusion term. As shown above, these terms have negligible effect on the analogy in such flows.

In many applications, for instance in turbine cooling, the condition that the heat flux is zero at the wall surface is unrealistic. As pointed out before, a mass transfer analogy to heat transfer at large temperature differences with active surfaces has not been identified. However, the availability of high-speed and large storage computers should make it possible to calculate such heat transfer situations in considerable detail with some input of fine grain turbulence parameters. Therefore mass transfer experiments (even with boundary conditions that differ from the final heat transfer application) can be used as an excellent check of such numerical codes, because of the high accuracy and spatial resolution obtainable from the mass transfer experiments.

Conclusions

1 The following dimensionless parameters must have the same value for a heat transfer process, and an analogous mass transfer process, to make the dimensionless velocity and temperature fields for a fluid with temperature-dependent properties identical to the dimensionless velocity and concentration fields of a two-component isothermal fluid with concentration dependent properties:

$$\mathrm{Re}_{T_o} = \mathrm{Re}_{w_o}, \quad \mathrm{Pr}_o = \mathrm{Sc}_o$$

$$c_p^* = 1, \quad \rho_T^*, \quad \rho_w^*, \quad \mu_T^* = \mu_w^*, \quad \mathrm{Pr}^* = \mathrm{Sc}^* \ (\mathrm{Le}^* = 1)$$

Similarity of the mentioned fields also insures that the Nusselt number in heat transfer is equal to the Sherwood number in mass transfer.

2 For a number of flow situations, methods are available to calculate Nusselt numbers from measured Sherwood numbers and vice versa when the Schmidt number in the mass transfer experiment is different from the Prandtl number in the heat transfer process.

3 In high Reynolds number flows with adiabatic (impermeable) walls the importance of the Pr* (Sc*) parameters on the heat/mass transfer analogy has been shown to be negligible. In this situation, it has been demonstrated that the system CO_2–air satisfies the remaining conditions in (1) better than the freon–air system for $1.0 \leq \rho_T^* \leq 1.5$. It is therefore recommended to use the system CO_2–air rather than freon–air for the mass transfer analogy. The use of freon should also be avoided for environmental reasons as well.

4 The essential similarity conditions for the analogy to hold are very well fulfilled for film cooling, total coverage film cooling, and impingement cooling when the heat (mass) flux into the wall in the heat (mass) transfer process is zero. The heat/mass transfer analogy can, therefore, be used with confidence for these processes.

5 The similarity conditions are not as well fulfilled when the heat (mass) flux at the surface is finite. The viscosity dependencies are still similar with excellent approximation when the system CO_2–air is used. However, Pr* (Sc*) similarity is now more important. Figure 7 can be used to estimate to what temperature (concentration) ratio the analogy can be used.

References

Eckert, E. R. G., and Drake, R. M., Jr., 1972, *Analysis of Heat and Mass Transfer*, McGraw-Hill, New York, pp. 717–719.

Eckert, E. R. G., and Goldstein, R. J., 1976, *Measurements in Heat Transfer*, 2nd ed., Hemisphere Publ. Corp., Washington, DC, pp. 419–420.

Goldstein, R. J., 1971, "Film Cooling," *Advances in Heat Transfer*, Vol. 7, pp. 321–379.

Hiwada, M., Niwa, K., and Mabuci, F., 1979, "Effects of Tunnel Blockage on Local Mass Transfer From a Circular Cylinder in Cross Flow," *Heat Transfer—Japanese Research*, Vol. 8, No. 3, pp. 37–51.

Nusselt, W., 1930, "Wärmeübergang, Diffusion und Verdunstung," *Z. angen Math. Mech.*, Vol. 10, pp. 105–212.

Karni, J., and Goldstein, R. J., 1987, "Endwall Effects on Local Mass Transfer From a Cylinder in Crossflow," *Turbulence Measurements and Flow Modeling*, C. J. Chen, L. D. Chen, and F. M. Melly, eds., Hemisphere Publ. Corp., Washington, DC, pp. 3–35.

Pederson, D. R., Eckert, E. R. G., and Goldstein, R. J., 1977, "Film Cooling With Large Density Differences Between the Mainstream and the Secondary Fluid Measured by the Heat-Mass Transfer Analogy," ASME *Journal of Heat Transfer*, Vol. 99, pp. 620–627.

Schmidt, E., 1929, "Verdunstung und Wärmeübergang," *Gesundheitsingenieur*, Vol. 52, pp. 525–529.

Schmidt, E., and Wenner, K., 1941, "Wärmeaubgabe über den Umfang eines Angeblaenen Geheiztan Zylinders," *Forschung, Geb. Ingwes.*, Vol. 12, No. 2, pp. 65–73.

Van Meel, D. A., 1962, "A Method for the Determination of Local Convection Heat Transfer From a Cylinder Placed Normal to an Air Stream," *Int. J. Heat Mass Transfer*, Vol. 5, pp. 715–722.

Wilke, C. R., 1950, "A Viscosity Equation for Gas Mixtures," *J. Chem. Phys.*, Vol. 18, pp. 517–519.

G. J. Yoo

R. M. C. So

Mechanical and Aerospace Engineering,
Arizona State University,
Tempe, AZ 85287

B. C. Hwang
David Taylor Naval Ship Research
and Development Center,
Annapolis, MD 21402

Calculation of Developing Turbulent Flows in a Rotating Pipe

Internal rotating boundary-layer flows are strongly influenced by large circumferential strain and the turbulence field is anisotropic. This is especially true in the entry region of a rotating pipe where the flow is three dimensional, the centrifugal force due to fluid rotation is less important, and the circumferential strain created by surface rotation has a significant effect on the turbulence field near the wall. Consequently, viscous effects cannot be neglected in the near-wall region. Several low-Reynolds-number turbulence closures are proposed for the calculation of developing rotating pipe flows. Some are two-equation closures with and without algebraic stress correction, while others are full Reynolds-stress closures. It is found that two-equation closures with and without algebraic stress correction are totally inadequate for this three-dimensional flow, while Reynolds-stress closures give results that are in good agreement with measurements over a wide range of rotation numbers.

I Introduction

Internal rotating turbulent flows have been investigated extensively because of their intrinsic importance to turbomachinery research. Of particular interest are boundary-layer flows whose rotation is induced by a rotating surface and the axis of rotation is parallel to the flow direction. This type of flow is complicated by large circumferential strain and the role viscosity plays in decreasing fluid rotation as the fluid elements move away from the wall. The turbulence field and viscous dissipation near the surface cease to be isotropic and viscous effects become very important.

An example where all these flow features are present can be found in the flow through a rotating pipe. The fully developed characteristics of rotating pipe flow were examined by White (1964) and Murakami and Kikuyama (1980). On the other hand, the external axial boundary layer development over a rotating cylinder was studied by Bissonnette and Mellor (1974) and Lohmann (1976), and the entry flow in a rotating pipe was investigated by Kikuyama et al. (1983). All these studies reveal that turbulent energy production is greatly increased by fluid rotation. Concomitantly, turbulent diffusion and viscous dissipation rates also increase rapidly near the wall to balance the drastic rise in turbulent energy production. Furthermore, turbulent advection is significant. Therefore, production does not balance dissipation in the near-wall region and the turbulence field is not in local equilibrium as in the case of developing flow in a stationary pipe.

These flow characteristics are also a common occurrence in the flow through turbine blade passages and other rotating machines. In order to perfect the designs of gas turbines, compressors, etc., a computer code needs to be developed and validated so that the internal aerodynamics of these machines can be calculated correctly. Therefore, viscous and rotation effects have to be modeled properly and incorporated into the theoretical formulation.

Attempts to account for fluid rotation and streamline curvature in turbulence modeling have been made by numerous investigators, such as Bissonnette and Mellor (1974), So (1977, 1981), and Launder et al. (1977). These investigations accounted for the effects of fluid rotation on turbulent mixing in the form of a correction factor applied to the turbulent viscosity, which was determined from a corresponding nonrotating flow. The correction factor was expressed in terms of a Richardson number, which is defined as the ratio of the body force created by fluid rotation to a typical inertial force. However, the Richardson number correction is usually linearized and thus cannot be expected to account for the additional effects of fluid rotation completely. The anisotropic turbulence behavior of rotating flow and the shortcoming of the Richardson number correction prompted the development of a nonisotropic turbulence closure for the calculation of rotating turbulent flows.

Recently, Gibson and Younis (1986) proposed a full Reynolds-stress closure for the calculation of swirling jet flows and obtained encouraging results. In their study, they argued that fluid rotation influenced turbulence redistribution as well as turbulent energy production. They, therefore, suggested modifying the pressure redistribution model by adding mean strain effects to the return-to-isotropy term and solving the full Reynolds-stress equations to account for the additional turbulent energy production. Unfortunately, their closure assumed the flow Reynolds number to be very large and the viscous dissipation function to be isotropic. Therefore, viscous dissipation was given by Kolmogorov's (1941) model. As a result, their closure is not suitable for near-wall flow calculation in turbine blade passages.

Turbulence closures including viscous effects near a wall

Contributed by the International Gas Turbine Institute for publication in the JOURNAL OF TURBOMACHINERY. Manuscript received at ASME Headquarters May 1989.

have been proposed by numerous researchers (Patel et al., 1985). Chien (1982) suggested modifying the dissipation term in the transport equations of turbulent kinetic energy (k) and its dissipation rate (ϵ) to include viscous effects, so that the modeled equations are applicable all the way to the wall. On the other hand, Launder (1984) suggested parabolizing the governing equations in the near-wall region and then matching the solution to a fully elliptic formulation of the flow outside of the viscous layer. Thus, the outer region can be modeled assuming the flow Reynolds number to be large. For more complicated internal flows, Kebede et al. (1985) proposed incorporating the viscous dissipation model of Launder and Reynolds (1983) into the Reynolds-stress equations, while So and Yoo (1986) suggested another dissipation model for these equations. These two approaches were examined by So and Yoo (1987) and were found to give identical results in the case of fully developed pipe and channel flows. So and co-workers (1987, 1988) further applied the So and Yoo (1986) model to calculate flows with wall transpirations and with recirculation and found good agreement with measurements in both types of flow. In view of this, the model seems to be ready for further extension to more complex flows, such as the three-dimensional developing flow along a rotating surface.

In order to develop a comprehensive computational program to calculate internal flows in rotating turbomachines, the closures of Gibson and Younis (1986) and So and Yoo (1986) are used to investigate the entry flow in a rotating pipe. Verification of the closures is provided by the measurements of Kikuyama et al. (1983). Furthermore, in order to verify that turbulent convection and diffusion of Reynolds stresses are important in any turbulence closure for this type of flow, the low-Reynolds-number, two-equation k–ϵ closure of Chien (1982) coupled with an algebraic stress model is also used to calculate the flow. The results are compared with other calculations and with measurements so that the validity and suitability of the two-equation closure can be assessed.

II Governing Equations

Incompressible, turbulent flow through a circular pipe rotating about its own axis is considered. The circumferential velocity at the pipe surface is given by $W_0 = \Omega R$. If the turbulent flow is assumed to be axisymmetric and stationary and the conventional Reynolds decomposition is applied to any instantaneous flow variable $\tilde{\phi}$, such that $\tilde{\phi} = \Phi + \phi$, then the governing mean flow equations written in cylindrical coordinates (x, r, θ) become

$$\frac{\partial U}{\partial x} + \frac{1}{r}\frac{\partial}{\partial r}(rV) = 0 \tag{1}$$

$$U\frac{\partial U}{\partial x} + V\frac{\partial U}{\partial r} = -\frac{1}{\rho}\frac{\partial P}{\partial x} + \nu\nabla^2 U - \left[\frac{\partial \overline{u^2}}{\partial x} + \frac{1}{r}\frac{\partial}{\partial r}(r\overline{uv})\right] \tag{2}$$

$$U\frac{\partial V}{\partial x} + V\frac{\partial V}{\partial r} - \frac{W^2}{r} = -\frac{1}{\rho}\frac{\partial P}{\partial r} + \nu\left(\nabla^2 V - \frac{V}{r^2}\right) - \left[\frac{\partial \overline{uv}}{\partial x} + \frac{1}{r}\frac{\partial}{\partial r}(r\overline{v^2}) - \frac{\overline{w^2}}{r}\right] \tag{3}$$

$$U\frac{\partial W}{\partial x} + V\frac{\partial W}{\partial r} + \frac{VW}{r} = \nu\left(\nabla^2 W - \frac{W}{r^2}\right) - \left[\frac{\partial \overline{uw}}{\partial x} + \frac{1}{r}\frac{\partial}{\partial r}(r\overline{vw}) + \frac{\overline{vw}}{r}\right] \tag{4}$$

where

$$\nabla^2\psi = \frac{\partial^2\psi}{\partial x^2} + \frac{1}{r}\frac{\partial}{\partial r}\left(r\frac{\partial\psi}{\partial r}\right) \tag{5}$$

The complexity of developing rotating pipe flow is not just limited to solving one more mean flow equation (4). There are other complexities, however. Firstly, the boundary-layer flow is three dimensional. Secondly, the flow is affected by the introduction of the shear stresses, $\overline{uw}$ and $\overline{vw}$, associated with the rotating flow. Thirdly, these stresses are dominant only in the near-wall region of the developing flow where circumferential strain is large. Their significance decreases toward the pipe core and as the flow becomes fully developed. Consequently, the turbulence field near the wall in the developing region is most likely anisotropic. This means that developing rotating pipe flow should not be modeled by isotropic turbulence closures. The present approach is to model the flow using anisotropic low-Reynolds-number closures ranging from algebraic stress closures to full Reynolds-stress closures. This way, the flow near the wall, where viscous and rotation effects are most dominant, can be examined, and it is hoped that a closure can be identified that can replicate correctly the flow behavior in this region.

III Turbulence Closures

The incompressible Reynolds-stress transport equations can be symbolically written as (Launder et al., 1975)

$$C_{ij} = D_{ij}^{v} + D_{ij}^{t} + P_{ij} + \Phi_{ij} - \epsilon_{ij} \tag{6}$$

where C_{ij} represents the convective transport of the Reynolds stresses, and the terms on the right-hand side of equation (6) represent molecular diffusion, turbulent diffusive transport, production by mean shear, pressure redistribution, and viscous dissipation of the Reynolds stresses, respectively. If turbulence closure is to be effected at this level, then models are required for D_{ij}^{t}, Φ_{ij}, and ϵ_{ij}. The turbulence closures to be considered here are based on equation (6), or a simplified version of it, and appropriate models for D_{ij}^{t}, Φ_{ij}, and ϵ_{ij}.

So and Yoo (1986, 1987) have convincingly demonstrated that a low-Reynolds-number full Reynolds-stress closure can

Nomenclature

D = pipe diameter
k = turbulent kinetic energy
P = mean static pressure
ΔP = pressure drop along pipe
r = radial coordinate
R = pipe radius
Ro = rotation number = W_o/U_{av}
U, u = mean and fluctuating axial velocity
u' = rms of u
U_{av} = average mean axial velocity
U_o = pipe centerline mean axial velocity
u_τ = friction velocity = $(\tau_w/\rho)^{1/2}$
u_i = ith component of fluctuating velocity
V, v = mean and fluctuating radial velocity
v' = rms of v
W, w = mean and fluctuating circumferential velocity
w' = rms of w
W_o = circumferential velocity of pipe surface = ΩR
$\overline{u_i u_j}$ = Reynolds stress tensor
x = axial coordinate
x_2 = normal coordinate measured from the wall
ϵ = modified dissipation rate of k
η = normalized wall coordinate = $u_\tau(R-r)/\nu$
ν = fluid kinematic viscosity
ρ = fluid density
τ_w = wall shear stress
Ω = angular velocity of pipe

Table 1 The different turbulence closures considered

Closure	Modeled equations solved	Models			Additional equations		Wall Function
		D_{ij}^t	Φ_{ij}	ϵ_{ij}	ϵ	k	
$A-1$	Equation (6)	Hanjalic and Launder (1972)	and (1951)	Equation (7)	Chien (1982)	—	No
$A-4$	Equation (6)	Hanjalic and Launder (1972)	Gibson and Younis (1986)	Equation (7)	Chien (1982)	—	No
$(L-k-\epsilon)_{RC}$	Equation (8)	—	Rotta (1951)	Kolmogorov (1941)	Chien (1982)	Chien (1982)	No
$L-k-\epsilon$	—	—	—	—	Chien (1982)	Chien (1982)	No
$H-A-1$	Equation (6)	Hanjalic and Launder (1972)	Rotta (1951)	Kolmogorov (1941)	Chien (1982)	—	Yes

be formulated based on equation (6) with conventional high-Reynolds-number models proposed for D_{ij}^t and Φ_{ij} but with an anisotropic viscous dissipation model for ϵ_{ij}. Their closure is based on Hanjalic and Launder's (1972) model for D_{ij}^t and Rotta's (1951) return-to-isotropy model for Φ_{ij}, and the model for ϵ_{ij} is given by

$$\epsilon_{ij}=\frac{2}{3}\delta_{ij}\epsilon+\frac{2\nu\delta_{il}\delta_{jm}\overline{u_l u_m}}{x_2^2} \tag{7}$$

They closed equation (6) by adopting the ϵ transport equation of Chien (1982) and designated their closure A-1. Their results showed that the closure not only reproduced the near-wall region of fully developed pipe and channel flows correctly but also developing pipe flow with uniform suction applied through the pipe wall. In fact, A-1 is the only closure that can correctly predict the axial pressure drop in the uniform suction case. Other high-Reynolds-number closures and Chien's (1982) low-Reynolds-number k-ϵ closure fail to predict the axial pressure drop in the uniform suction case correctly. Later, So et al. (1988) applied A-1 to calculate flows over a backward-facing step where flow recirculation and reattachment occur and again found good agreement with measurements. In order to establish the validity of A-1 for more complicated turbulent flows, it is proposed to use A-1 to close the set of governing equations (1)-(4), and further establish that A-1 is also applicable to three-dimensional flows with large circumferential strain effects.

Gibson and Younis (1986) argued that mean strain effects in Φ_{ij} modeling are important for complex turbulent flows, especially for flows with a strong swirl component. Since the rotating pipe flow is also dominated by a strong circumferential velocity, the arguments of Gibson and Younis should be equally applicable to this flow. Therefore, if their Φ_{ij} model is used instead of the return-to-isotropy model, then improvement in the calculated results should be realized. If not, their arguments are not quite appropriate for wall-bounded flows. In order to demonstrate this point, another closure, based on equation (7) for ϵ_{ij}, Hanjalic and Launder's (1972) model for D_{ij}^t, and Gibson and Younis' (1986) model for Φ_{ij}, is also used to calculate the developing rotating pipe flow. This closure is designated A-4.

The importance of convective and diffusive transport on the turbulence field near the wall will be examined by considering a closure where the equilibrium assumption is invoked (So, 1977). Under such an assumption, equation (6) reduces to

$$0\simeq P_{ij}+\Phi_{ij}-\epsilon_{ij} \tag{8}$$

Again, closure of equation (8) depends on the modeling of Φ_{ij} and ϵ_{ij}. For the present, the algebraic stress closure proposed by So (1977) for swirling flows is adopted. Since the modeling of Φ_{ij} and ϵ_{ij} introduces two more unknowns, k and ϵ, transport equations for k and ϵ are required. Here, the equations proposed by Chien (1982) are adopted. Therefore, the proposed closure is a low-Reynolds-number closure with anisotropic stress correction applied. This closure is designated $(L$-k-$\epsilon)_{RC}$.

For convenience, the different closures are summarized in Table 1. The L-k-ϵ closure is essentially Chien's k-ϵ model and is included in this study to demonstrate the inadequacy of an isotropic turbulence closure for complex turbulent flows. On the other hand, H-A-1 is a high-Reynolds-number closure and requires the assumption of wall functions. Its difference with A-1 is in the near-wall modeling of turbulence. Therefore, a comparison of the H-A-1 and A-1 results will illustrate the importance of near-wall flow modeling. In each case, the modeling constants proposed by the various researchers are adopted without change.

IV Method of Solution

The no-slip boundary condition is specified at the wall. As a result, all velocity components except W are set to zero. As for W, it is specified as $W=W_o$. In addition, the modified dissipation rate ϵ and $\overline{u_i u_j}$ are also set to zero at the wall. At the symmetry plane, the radial gradients of all flow properties, except pressure and the turbulent shear stresses, are specified as zero. The shear stresses, on the other hand, are assumed zero at $r=0$, the symmetry axis. Inlet conditions are determined from measurements and the equilibrium assumption, while $\partial/\partial x$ of all flow properties, except pressure, is specified as zero at the pipe exit.

The coupled equations (1)-(4) and boundary conditions are solved numerically using either a hybrid or a quadratic upwind finite differencing scheme, staggered grids, and the SIMPLE algorithm of Patankar and Spalding (1972). The transport equations for all turbulent quantities are solved based on an intermediate calculated velocity field. These calculations are updated as the velocity field is improved until a convergent solution is obtained. The convergency criterion is specified as < 1 percent of the relative mass and momentum residuals.

A nonuniform grid system is used to resolve the flow in the domain of interest ($0\le x/2R<100$). In the axial direction, 51 grid points are specified. As for the grid spacing in the radial direction, So and Yoo (1986) have previously found that a minimum of 10 grid points is required between the wall ($r=R$) and the grid point just outside the viscous sublayer. Although this spacing works well for So and Yoo (1987), the present radial grid spacings are specified as follows: 5 grid points between $0\le\eta<5$, 15 grid points between $5\le\eta<65$, and 36 grid points from $\eta=65$ to pipe centerline. This grid spacing allows the flow near a wall to be resolved correctly, especially

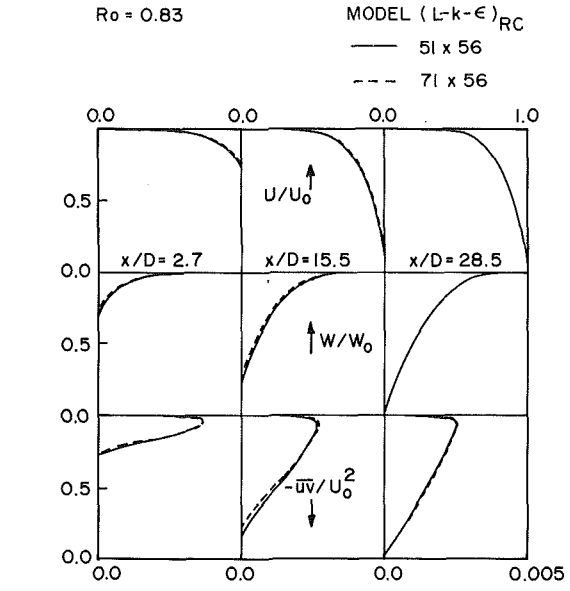

Fig. 1 A comparison to show grid independence of the calculations

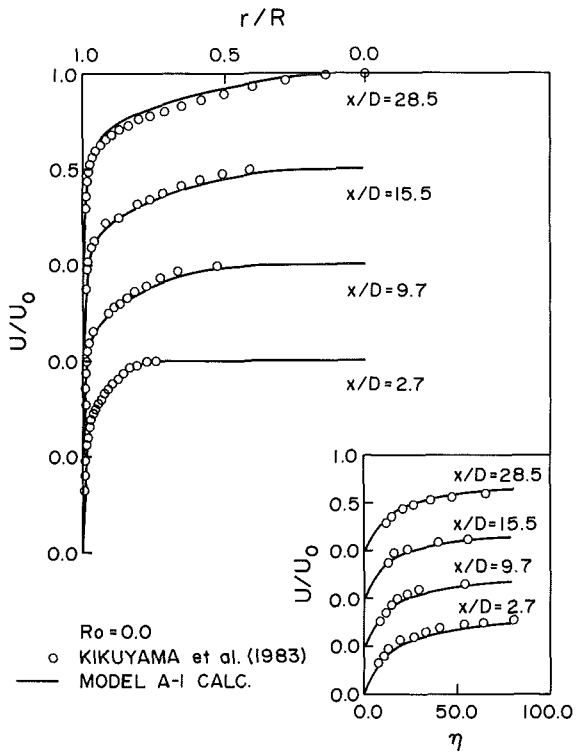

Fig. 2 Comparison of calculated and measured U for $Ro = 0$

the rapid change of W in this region. As a result, all calculations were carried out with a 51×56 grid.

V Discussion of Results

The primary objective of the present study is to develop an anisotropic turbulence closure for flows with large circumferential strain. In particular, the circumferential strain is created by a rotating surface and, as a result, viscosity plays an important role in the near-wall flow. Therefore, the turbulence closure should be able to account for viscous effects near a wall and avoid the assumption of wall functions. Furthermore, the closure should be able to account for the effects of fluid rotation. Here, conventional wisdom dictates that the pressure redistribution model should include mean strain effects. A second objective of the present study is to make an attempt

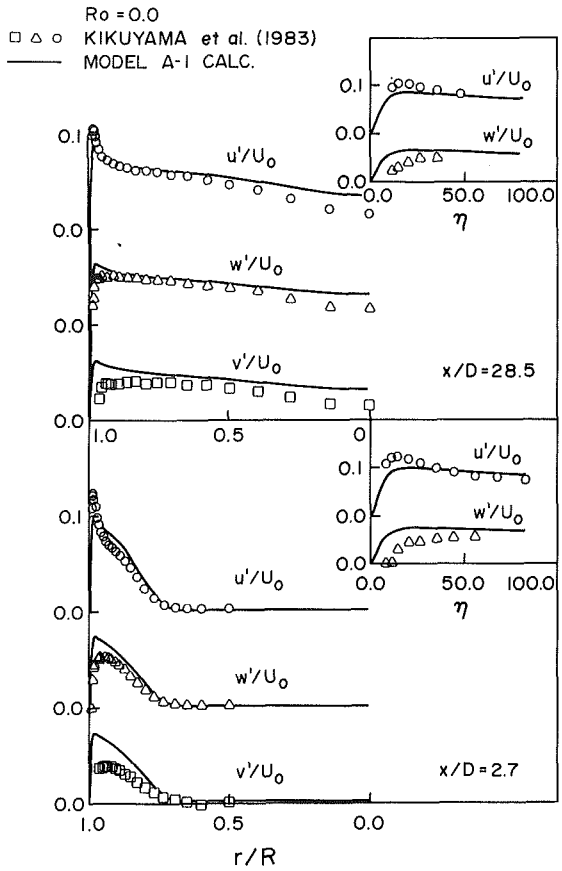

Fig. 3 Comparison of calculated and measured normal stresses for $Ro = 0$

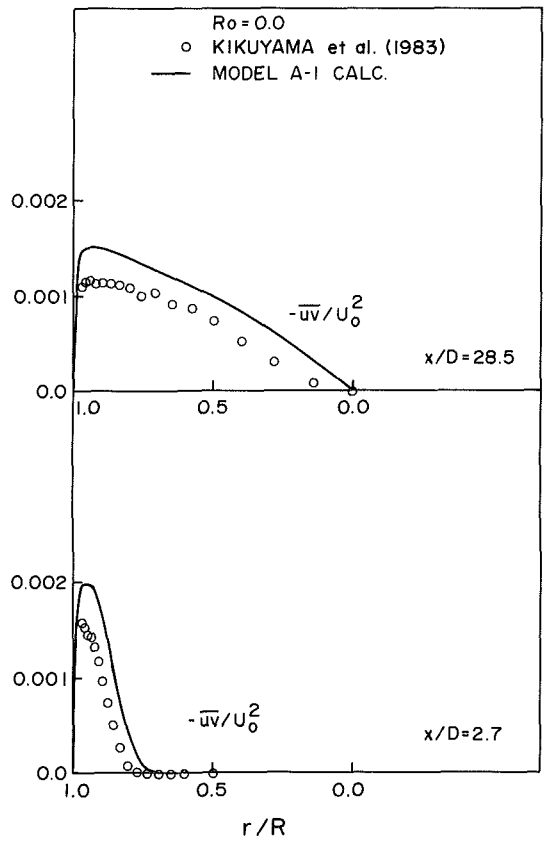

Fig. 4 Comparison of calculated and measured $\overline{uv}$ for $Ro = 0$

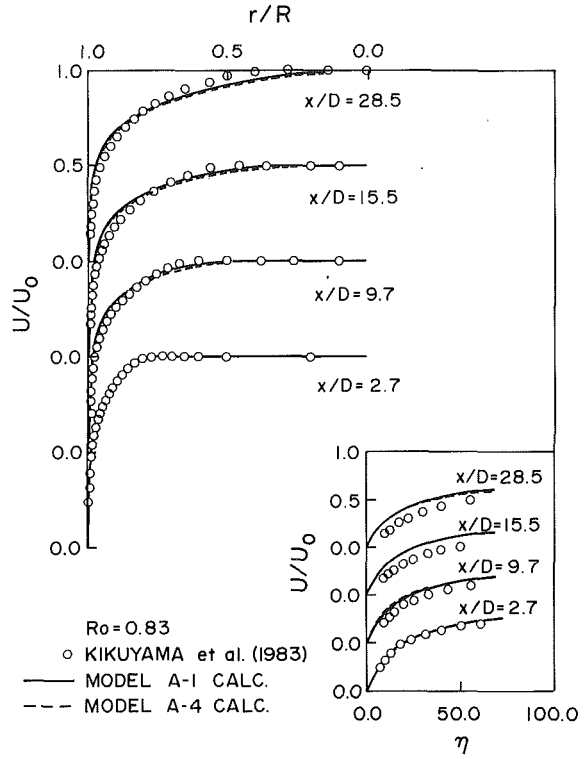

Fig. 5 Comparison of calculated and measured U for $Ro = 0.83$

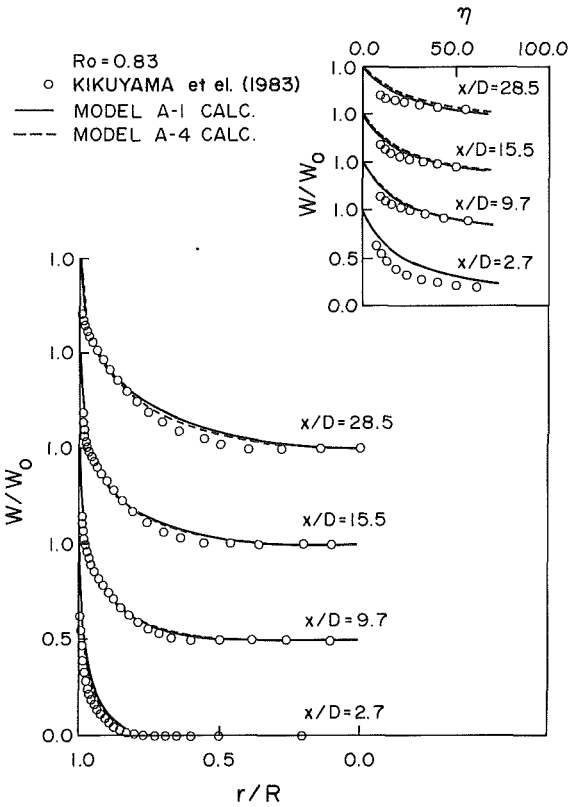

Fig. 6 Comparison of calculated and measured W for $Ro = 0.83$

to resolve this question, particularly for wall-bounded flow. Consequently, two similar closures with different pressure redistribution models are examined for their suitability. Since experimental measurements of rotating boundary-layer flows reveal that turbulent convection and diffusion of the Reynolds stresses are quite significant near the wall, a third objective of the present study is to examine the necessity of incorporating these effects into the turbulence closure. As a result, a low-Reynolds-number algebraic stress closure is also used to calculate the developing rotating pipe flow and the results compared to the other closure calculations. Finally, the suitability of wall function assumptions and the applicability of an isotropic turbulence closure for this kind of complex turbulent flow are also examined.

The developing pipe flow experiments of Kikuyama et al. (1983) are used to compare the performance of different closures. Whenever possible, the comparisons are made with U, W, u', v', w', $-\overline{uv}$, $-\overline{vw}$, $-\overline{uw}$, and $k=(u'^2+v'^2+w'^2)/2$. Three sets of experiments are available, each with a different rotation number. Kikuyama et al. (1983) defined the rotation number as $Ro = W_o/U_{av}$. The three cases are: $Ro = 0$, 0.5, and 0.83. Therefore, they cover a wide range of Ro and provide a severe test for any proposed turbulence closure.

The 51×56 grid has been used by So and Yoo (1987) to calculate developing flow in a pipe with and without uniform suction. They found the calculated results to be grid independent. Since the same has not been demonstrated for rotating developing pipe flow, experimental runs with A-1 and $(L$-k-$\epsilon)_{RC}$ were carried out for the $Ro = 0.83$ case using 51×56 and 71×56 grids. Some sample results of the $(L$-k-$\epsilon)_{RC}$ calculations are shown in Fig. 1. As expected, the calculations of the rotating pipe flow are also grid independent as long as the grid size is 51×56 or finer. The same is also true of the A-1 calculations. Consequently, all calculations were carried out using a 51×56 grid.

The boundary-layer flow in the entry region of a rotating pipe is three dimensional and very complex. Since the boundary layer in this region is very thin, fluid rotation is confined to within this thin layer. As a result, the boundary-layer flow is dominated by a destabilizing effect created by the large circumferential strain. Outside the boundary layer, the flow is irrotational. As the boundary layer becomes thicker and thicker, the intensity of the destabilizing effect decreases. When the flow becomes fully developed, the fluid inside the rotating pipe rotates as a solid body. Since the solid-body rotation curve has a zero slope, turbulence production due to circumferential strain is also zero, and rotation gives rise to a stabilizing effect. It follows that, as the flow develops through the pipe, the destabilizing effect will give way to the stabilizing centrifugal force effect and the turbulence field will pass through a region where both effects are of equal importance. Therefore, the flow is very complicated and provides a severe test for any turbulence closure. The low-Reynolds-number full Reynolds-stress closure of So and Yoo (1986) has been validated against a variety of complex turbulent flows. If it also performs well for developing rotating pipe flow, the closure can also be claimed to work for three-dimensional complex turbulent flows.

The baseline case ($Ro = 0$) is first examined and the A-1 results are compared with measurements in Figs. 2–4. This is a simple developing pipe flow and, as expected, all four closures (A-1, A-4, L-k-ϵ, and $(L$-k-$\epsilon)_{RC}$) give essentially the same results. Therefore, the other three closure results are not shown in Figs. 2–4. As expected, the boundary-layer development is predicted correctly and so is the flow near the wall, shown as insets in Figs. 2–4 with the flow properties plotted versus η. Since measurements are not available beyond $x/D = 28.5$, the present comparison cannot be made with the approach to fully developed flow. However, this last point has already been examined by So and Yoo (1987) and good agreement with measurements was obtained.

A second comparison is carried out with the most severe case, namely, $Ro = 0.83$. The results are shown in Figs. 5–8 with the comparisons of the near-wall flow given in the insets. In all of these plots, the comparison is made with A-1 and A-4, while in some of these plots the comparison is also made with H-A-1. The results obtained from $(L$-k-$\epsilon)_{RC}$ and L-k-ϵ

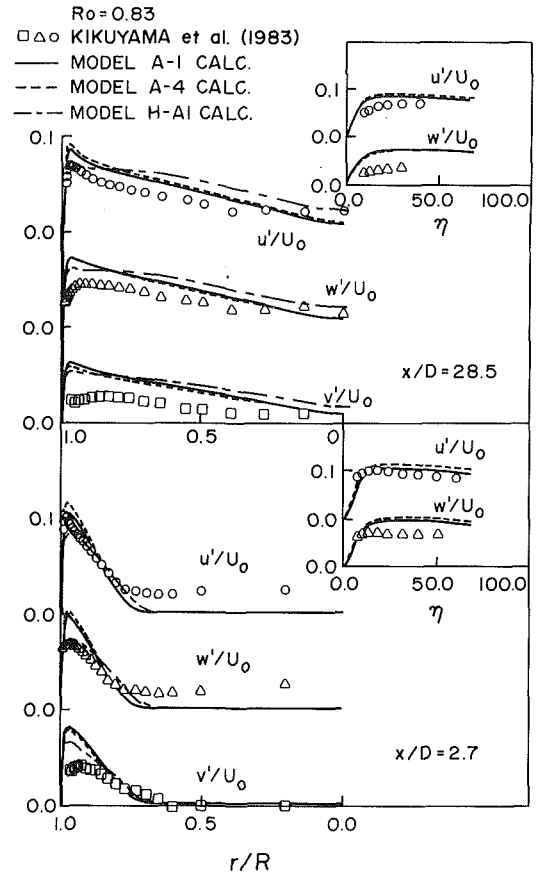

Fig. 7 Comparison of calculated and measured normal stresses for $Ro = 0.83$

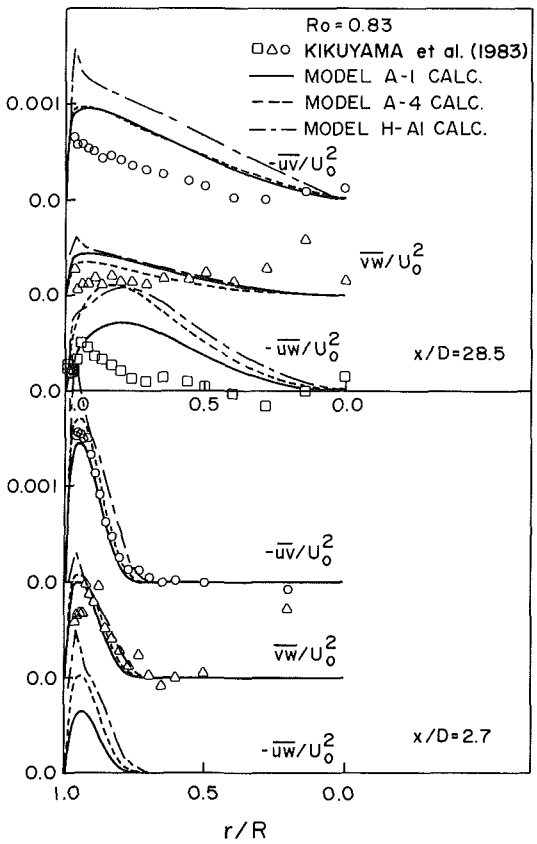

Fig. 8 Comparison of calculated and measured Reynolds shear stresses for $Ro = 0.83$

are not shown. Therefore, this comparison answers the following important questions: (1) the ability of A-1 to replicate the near-wall flow, (2) A-1's capability to mimic the flow development from being dominated by the large circumferential strain to being controlled by the centrifugal force, (3) the necessity of accounting for mean strain effects in the modeling of pressure redistribution, (4) the suitability of wall functions, and (5) the correctness of the calculated results.

In general, both A-1 and A-4 give excellent comparison with the mean flow measurements (Figs. 5 and 6). The only difference between the two calculations occurs in the prediction of u' and the shear stresses (Figs. 7 and 8). Furthermore, the calculated Reynolds stresses are not in as good an agreement with data as the mean flow calculations. Model A-4 tends to overpredict the maximum reached by u' compared to A-1. Initially, model predictions of u', v', and w' are in good agreement with measurements, but farther downstream, the disagreement increases. This trend could be due to the inability of the models to mimic the combined stabilizing and destabilizing effects correctly. Near the pipe entrance, A-4 gives larger shear stresses than A-1. Even then, both results compare favorably with measurements. Farther downstream at $x/D = 28.5$, A-4 give a larger $-\overline{uw}$ but a smaller $-\overline{vw}$ compared to A-1. However, their prediction of $-\overline{uv}$ is essentially identical. Therefore, it can be concluded that, for this particular flow, mean strain effects are not important in the modeling of pressure redistribution. The reason is simple, because in the pipe entry region, a great portion of the flow is not affected by rotation effects. In the region where rotation effects are present, viscous effects are dominant. Hence, it is more important to account for viscous effects in this region.

Both A-1 and A-4 have the ability to predict the near-wall flow correctly. They can also mimic the effects of circumferential strain in the entry region very well. However, their ability to reproduce the interaction between the destabilizing and stabilizing effects is not as good. This is evident in the comparison of the normal and shear stresses at $x/D = 28.5$, where the correlation with measurements is deteriorating.

The applicability of the wall function assumption is examined next. Therefore, the results of H-A-1 are compared with those of A-1 or A-4. In general, there is very little difference in the U and W profiles obtained for the flow away from the wall. Consequently, the H-A-1 results are not shown in Figs. 5 and 6. On the other hand, there are significant differences between the Reynolds stresses obtained from H-A-1 and A-1 closures, especially in the near-wall region. These differences impact on the calculations of wall shear and hence the axial pressure drop. The H-A-1 results are also shown in Figs. 7 and 8 for comparison. It can be seen that failure to account for viscous effects near the wall leads to incorrect prediction of the Reynolds stresses not only in the near-wall region but also in the region away from the wall. This points to the inadequacy of the wall function assumption. The effect of this assumption on wall pressure drop prediction is discussed in the next paragraph.

A third comparison is made to illustrate the inadequacy of an isotropic closure and the incorrectness of an equilibrium turbulence assumption. The comparison is again made with the $Ro = 0.83$ case. Only results for W, k, and $-\overline{uv}$ are shown in Fig. 9. It is clear that L-k-ϵ and $(L$-k-$\epsilon)_{RC}$ give essentially the same results for W and k. However, $(L$-k-$\epsilon)_{RC}$ is far better than L-k-ϵ in the prediction of $-\overline{uv}$. In general, their results are substantially different from those obtained from A-1 and A-4 and show significant disagreement with measurements. Further evidence that L-k-ϵ and $(L$-k-$\epsilon)_{RC}$ are not suitable closures for this kind of flow is provided by a comparison of the different calculated axial pressure drop $(\Delta P/\rho U_{av}^2)$ for the case $Ro = 0.83$ (Fig. 10). In this comparison, a fifth calculation is also performed. Closure H-A-1 is used for this calculation. Therefore, its comparison with $(L$-k-$\epsilon)_{RC}$ tends to illustrate

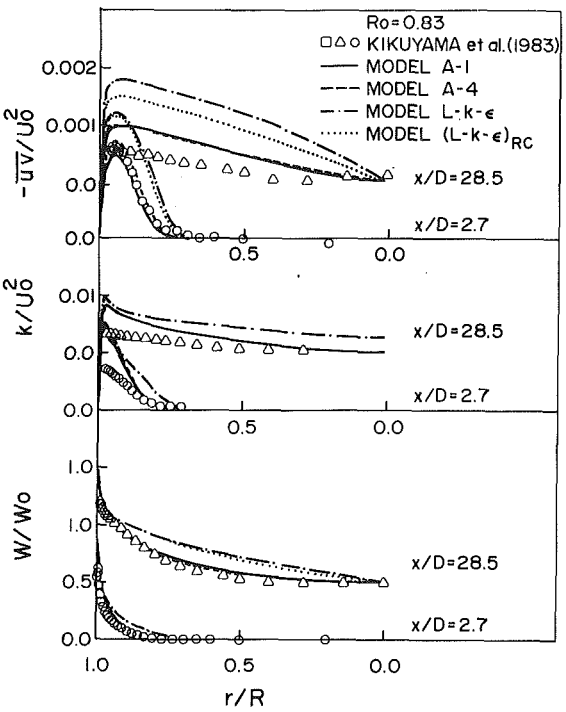

Fig. 9 Comparison of calculated and measured W, K, and $\overline{uv}$ for $Ro = 0.83$

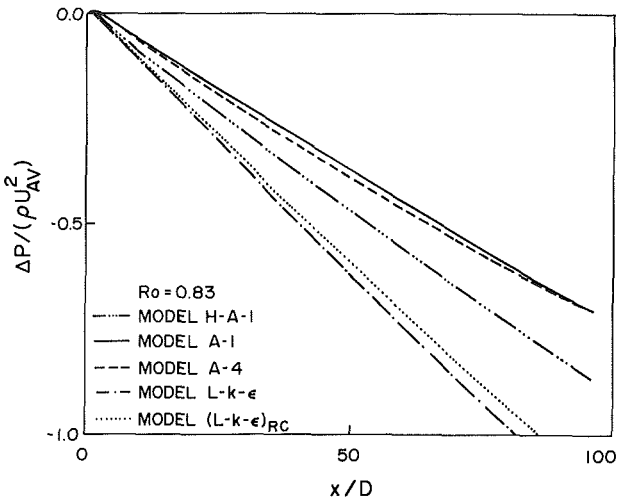

Fig. 10 Comparison of calculated axial pressure drop along the pipe for $Ro = 0.83$ using different closures

the relative importance of accounting for viscous effects compared to transport effects in the near-wall region. It can be seen that the $(L\text{-}k\text{-}\epsilon)$ and $(L\text{-}k\text{-}\epsilon)_{RC}$ models give the steepest pressure drop while the model calculations of A-1 and A-4 are essentially the same and the calculated pressure drop is the mildest. The H-A-1 result is between these two limits. These results are consistent with the predictions obtained by So and Yoo (1987) in their analysis of turbulent pipe flow with uniform wall transpiration. They found that model A-1 results are in good agreement with measurements. In view of this, the $(L\text{-}k\text{-}\epsilon)$, $(L\text{-}k\text{-}\epsilon)_{RC}$, and H-A-1 model results are not likely to be correct. The result, therefore, shows that the turbulence field is greatly affected by convection and diffusion near the wall and hence is not in local equilibrium. Furthermore, it is far more important to account for the nonequilibrium turbulence effects than viscous effects.

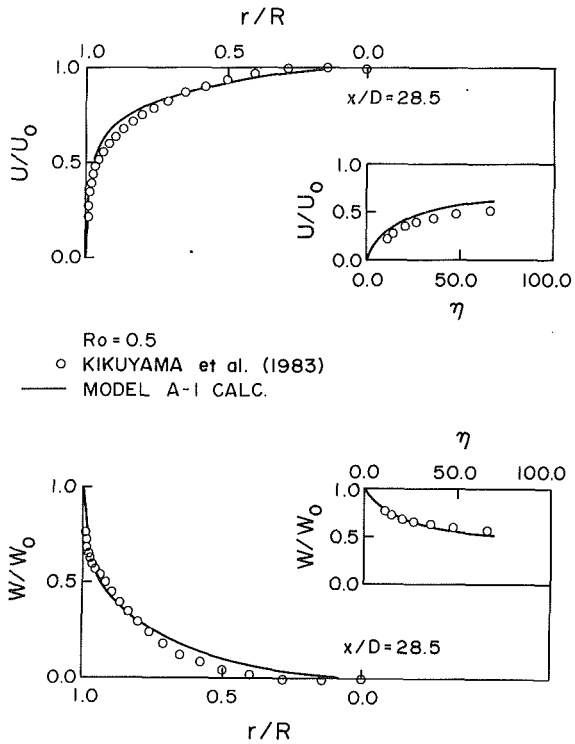

Fig. 11 Comparison of calculated and measured U and W for $Ro = 0.5$

Based on the above analysis, it can be concluded that models A-1 and A-4 are equally valid for this type of three-dimensional complex turbulent flow. However, the results seem to indicate that the added complexity of the Φ_{ij} model of Gibson and Younis (1986) does not contribute to any significant improvement of the predictions.

Finally, the comparison with measurements for the case $Ro = 0.5$ is given in Figs. 11-13. Only A-1 results are shown. As expected, the mean flow calculations agree with measurements very well. The discrepancy noted in the u' comparison for the $Ro = 0.83$ case has disappeared, while the discrepancy noted in the comparison of the shear stresses, though much decreased, still remains, especially at $x/D = 28.5$. This means that model A-1 could better account for the weakened combined stabilizing and destabilizing effects when $Ro = 0.5$. In other words, for low to moderate Ro, A-1 could replicate the interaction between the destabilizing and stabilizing effects more accurately.

VI Conclusions

The present study on developing rotating pipe flow reveals the following:

1 An anisotropic turbulence closure is required for the calculation of this complex three-dimensional flow.

2 It is also important to account for viscous effects near the wall because of the dominance of the large circumferential strain.

3 It is not sufficient to take into account the anisotropic behavior of the turbulence field by invoking the local equilibrium assumption. The turbulence field near the wall is not in equilibrium. Therefore, it is just as important to have this characteristic modeled in the closure.

4 Mean strain effects in pressure redistribution modeling have little influence on the calculated flow. Consequently, their inclusion in the pressure redistribution model is unnecessary for this kind of complex turbulent flow.

5 The resultant A—1 closure takes all these points into account and gives results that are in good agreement with measurements.

6 A—1 can mimic the destabilizing circumferential strain

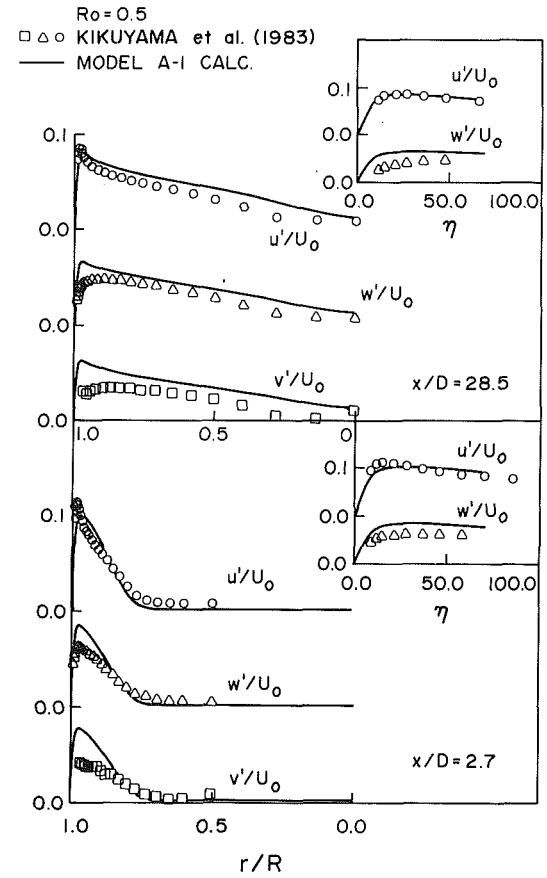

Fig. 12 Comparison of calculated and measured normal stresses for $Ro = 0.5$

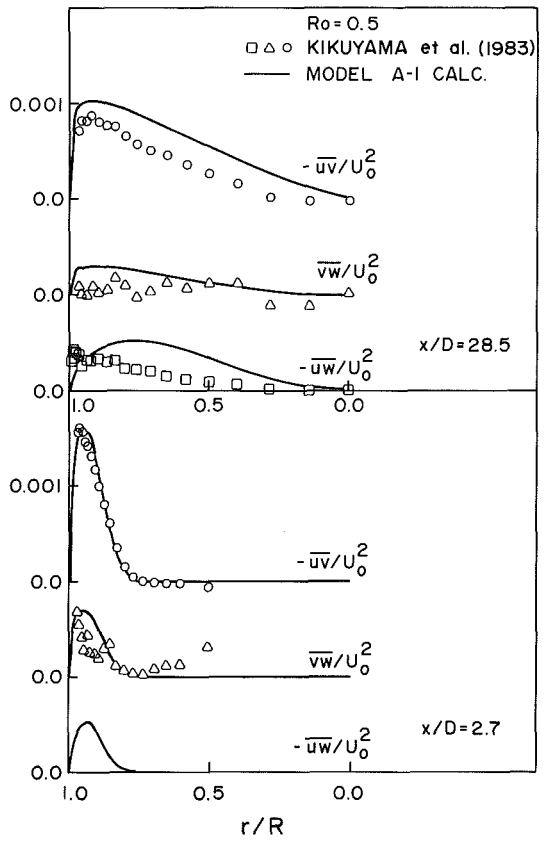

Fig. 13 Comparison of calculated and measured Reynolds shear stresses for $Ro = 0.5$

effect in the flow development correctly and also the interaction between this effect and the stabilizing centrifugal force effect that becomes more and more dominant downstream of the pipe entrance.

7 In view of the fact that A—1 also performs well for a wide variety of internal, two-dimensional complex turbulent flows, it can be concluded that A—1 is a valid closure for two- and three-dimensional, wall-bounded, complex turbulent shear flows.

Acknowledgments

This research was supported by the Naval Weapons Center, China Lake, CA under Contract N60530-85-C-0191, monitored by F. Zarlingo. Additional support was also provided by DTNSRDC, Annapolis, MD, 21402, under Contract No. N00167-86-K-0075. The authors would also like to express their appreciation to Dr. K. Nishibori for providing them with the data reported by Kikuyama et al. (1983).

References

Bissonnette, L. R., and Mellor, G. L., 1974, "Experiments on the Behavior of an Axisymmetric Turbulent Boundary Layer With a Sudden Circumferential Strain," *Journal of Fluid Mechanics*, Vol. 63, pp. 369–413.

Chien, K. Y., 1982, "Predictions of Channel and Boundary Layer Flows With a Low-Reynolds-Number Two-Equation Model of Turbulence," *AIAA Journal*, Vol. 20, pp. 33–38.

Gibson, M. M., and Younis, B. A., 1986, "Calculation of Swirling Jets With a Reynolds Stress Closure," *Physics of Fluids*, Vol. 29, pp. 38–48.

Hanjalic, K., and Launder, B. E., 1972, "A Reynolds-Stress Model of Turbulence and Its Application to Thin Shear Flows," *Journal of Fluid Mechanics*, Vol. 52, pp. 609–638.

Kebede, W., Launder, B. E., and Younis, B. A., 1985, "Large Amplitude Periodic Pip Flow: A Second-Moment Closure Study," *Proceedings, 5th Turbulent Shear Flows Symposium*, pp. 16.23–16.29.

Kikuyama, K., Murakami, M., and Nishibori, K., 1983, "Development of Three-Dimensional Turbulent Boundary Layer in Auxially Rotating Pipe," ASME *Journal of Fluids Engineering*, Vol. 105, pp. 154–160.

Kolmogorov, A. N., 1941, "The Local Structure of Turbulence in Incompressible Viscous Fluid for Very Large Reynolds Numbers," *Comp. rend., Acad. Sci. URSS*, Vol. 30, pp. 301–305.

Launder, B. E., Reece, G. J., and Rodi, W., 1975, "Progress in the Development of a Reynolds-Stress Turbulence Closure," *Journal of Fluid Mechanics*, Vol. 68, pp. 537–566.

Launder, B. E., Priddin, C. H., and Sharma, B. S., 1977, "The Calculation of Turbulent Boundary Layers on Spinning and Curved Surfaces," ASME *Journal of Fluids Engineering*, Vol. 99, pp. 231–239.

Launder, B. E., and Reynolds, W. C., 1983, "Asymptotic Near-Wall Stress Dissipation Rates in a Turbulent Flow," *Physics and Fluids*, Vol. 26, pp. 1157–1158.

Launder, B. E., 1984, "Numerical Computation of Convective Heat Transfer in Complex Turbulent Flows: Time to Abandon Wall Functions?" *International Journal of Heat and Mass Transfer*, Vol. 27, pp. 1485–1531.

Lohmann, R. P., 1976, "The Response of a Developed Turbulent Boundary Layer to Local Transverse Surface Motion," ASME *Journal of Fluids Engineering*, Vol. 98, pp. 354–363.

Murikami, M., and Kikuyama, K., 1980, "Turbulent Flow in Axially Rotating Pipes," ASME *Journal of Fluids Engineering*, Vol. 102, pp. 97–103.

Patankar, S. V., and Spalding, D. B., 1972, "A Calculation Procedure for Heat, Mass and Momentum Transfer in Three-Dimensional Parabolic Flows," *International Journal of Heat and Mass Transfer*, Vol. 15, pp. 1787–1806.

Patel, V. C., Rodi, W., and Schuerer, G., 1985, "Turbulence Models for Near-Wall and Low Reynolds Number Flows: A Review," *AIAA Journal*, Vol. 23, pp. 1308–1319.

Rotta, J. C., 1951, "Statische Theorie Nichthomogener Turbulenz," *Zeitschrift fur Physik*, Vol. 129, pp. 547–572.

So, R. M. C., 1977, "Turbulence Velocity Scales for Swirling Flows," *Turbulence in Internal Flows*, S. N. B. Murthy, ed., Hemisphere Publishing Corp., Washington, DC, pp. 347–367.

So, R. M. C., 1981, "Heat Transfer Modeling for Turbulent Shear Flows on Curved Surfaces," *Zeitshrift fur angewandte Mathematik and Physik*, Vol. 32, pp. 514–532.

So, R. M. C., and Yoo, G. J., 1986, "On the Modelling of Low-Reynolds-Number Turbulence," NASA CR-3994.

So, R. M. C., and Yoo, G. J., 1987, "Low-Reynolds-Number Modelling of Turbulent Flows With and Without Wall Transpiration," *AIAA Journal*, Vol. 25, pp. 1556–1564.

So, R. M. C., Lai, Y. G., Hwang, B. C., and Yoo, G. J., 1988, "Low-Reynolds-Number Modelling of Flows Over a Backward-Facing Step," *Zeitschrift fur angewandte Mathematik und Physik*, Vol. 39, pp. 13–27.

White, A., 1964, "Flow of a Fluid in an Axially Rotating Pipe," *Journal of Mechanical Engineering Science*, Vol. 6, pp. 47–52.

Heat Transfer in Rotating Passages With Smooth Walls and Radial Outward Flow

J. H. Wagner

B. V. Johnson

United Technologies Research Center,
East Hartford, CT 06108

T. J. Hajek
Commercial Engine Business,
Pratt & Whitney Division,
East Hartford, CT 06108

Experiments were conducted to determine the effects of rotation on heat transfer in turbine blade internal coolant passages. The experiments were conducted with a smooth wall, large-scale heat transfer model. The objective was to obtain the heat transfer data base required to develop heat transfer correlations and to assess computational fluid dynamic techniques for rotating coolant passages. An analysis of the governing equations showed that four parameters influence the heat transfer in rotating passages (coolant density ratio, Rossby number, Reynolds number, and radius ratio). These four parameters were varied over ranges that exceed the ranges of current open literature results, but that are typical of current and advanced gas turbine engine operating conditions. Rotation affected the heat transfer coefficients differently for different locations in the coolant passage. For example, heat transfer at some locations increased with rotation, but decreased and then increased again at other locations. Heat transfer coefficients varied by as much as a factor of five between the leading and trailing surfaces for the same test condition and streamwise location. Comparisons with previous results are presented.

Introduction

In advanced gas turbine engines, increased speeds, pressures, and temperatures are used to increase thrust/weight ratios and reduce the specific fuel consumption. As a result, the turbine blades are subjected to increased gas path temperatures in addition to increased levels of stress. Internal convection cooling is usually required to maintain acceptable airfoil metal temperatures and to obtain an acceptable blade life. Knowledge of the local heat transfer in the cooling passages and around the external blade surface is essential to predict blade metal temperatures. It has been demonstrated that rotation can significantly alter the local heat transfer in the internal coolant passages. Therefore, the turbine blade designer needs accurate local heat transfer predictions for blade coolant passages under conditions of rotation to estimate blade life effectively.

Predictions of heat transfer and pressure loss in airfoil coolant passages currently rely on correlations derived from the results of stationary experiments. Adjustment factors are usually applied to these correlations to bring them into nominal correspondence with engine experience. This practice is unsatisfactory when blade cooling conditions for new designs lie outside the range of previous experience.

Heat transfer and pressure loss data are difficult and costly to obtain under conditions of rotation. As a consequence, there are limited amounts of data in the open literature that a turbine designer can use to account for the effects of rotation in typical turbine blade designs. The data available are far from comprehensive and are limited in scope.

Rotation of turbine blade cooling passages gives rise to Coriolis and buoyancy forces. Both of these forces can substantially affect coolant flow patterns, which influence the heat transfer inside turbine blade cooling passages. The complex coupling of the Coriolis and buoyancy forces has prompted many investigators to study the secondary flows generated in unheated, rotating circular and rectangular passages without the added complexity of heat transfer and buoyancy. Much of the earlier work was conducted for laminar flow, because rig limitations (i.e., unpressurized passages) allowed only low Reynolds number flows with corresponding low rotation numbers (i.e., high Rossby numbers). The effects of rotation on secondary flow and stability have been investigated by Hart (1971), Wagner and Velkoff (1972), Moore (1967), and Johnson et al. (1972). These investigators have documented strong secondary flows and have identified aspects of flow stability in near-wall flow in rotating radial passages.

Buoyancy forces in gas turbine blades are substantial because of the high rotational speeds and large blade-wall-to-coolant temperature differences. The effects of buoyancy on heat transfer without the complicating effects of Coriolis-generated secondary flow have been studied in vertical stationary passages. Early experiments in this area were reported by Eckert et al. (1953), Metais and Eckert (1964), and Brundrett and Burroughs (1967). Flow criteria for forced, mixed, and free-

Contributed by the International Gas Turbine Institute and presented at the 34th International Gas Turbine and Aeroengine Congress and Exhibition, Toronto, Ontario, Canada, June 4–8, 1989. Manuscript received at ASME Headquarters February 14, 1989. Paper No. 89-GT-272.

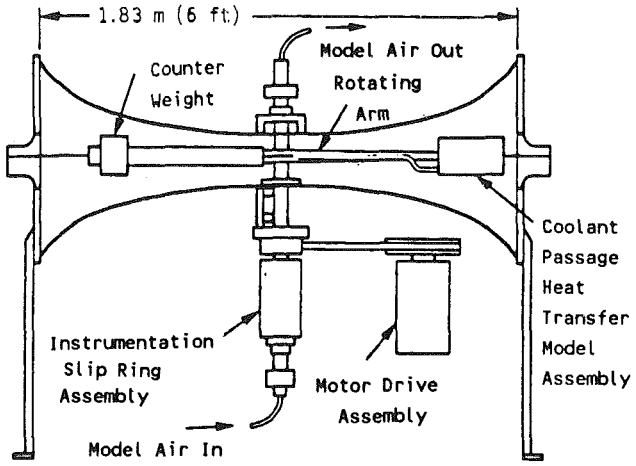

Fig. 1 Rotating heat transfer facility

convection heat transfer was developed for parallel flow and counterflow configurations by Eckert et al. (1953) and Metais and Eckert (1964). Based on previous stationary combined, free, and forced-convection experimental results and turbine blade operating conditions, buoyancy forces are expected to cause significant changes in the heat transfer in the rotating coolant passages.

The combined effects of Coriolis and buoyancy forces on heat transfer have been studied by a number of investigators. Heat transfer in rotating, smooth wall models has been investigated by Mori et al. (1971), Johnson (1978), Morris and Ayhan (1979), Lokai and Gunchenko (1979), Morris (1981), Iskakov and Trushin (1983) and, more recently, Guidez (1988). Large increases and decreases in local heat transfer were found by some investigators to occur under certain conditions of rotation while others showed lesser effects. Analysis of these results does not produce consistent trends in the effects of rotation on heat transfer. The disparity of the results is indicative of differences in the measurement techniques and models used in the experiments as well as the nonuniformity of the test conditions.

A comprehensive experimental program was formulated to identify the separate effects of Coriolis and buoyancy for the range of dimensionless heat transfer and flow parameters encountered in large aircraft gas turbines. The overall objective of the program was to acquire and correlate benchmark-quality local heat transfer and pressure loss data for multipass, rotating coolant passages under conditions similar to those expected in the first stages of advanced aircraft gas turbines. Heat transfer data were obtained under varying conditions of flow rate, rotation, model radius, and wall-to-coolant temperature difference. The experiments were conducted by varying each parameter while holding the remaining parameters constant. The data were analyzed to separate the effects of Reynolds number, Coriolis forces, buoyancy, streamwise location, and the geometric location in the coolant passage (i.e., leading or trailing surfaces).

The results presented in this paper are from the first phase of a three-phase program, which studied the effects of rotation on a multipass model with smooth and rough wall configurations. The first phase utilized the smooth wall configuration. Subsequent phases will include normal and skewed trip geometries. This paper presents heat transfer results obtained in the first, radially outward flowing passage of a four-pass, smooth wall, square passage model. The results will show (1) agreement with previous investigators for stationary conditions, (2) effects of Coriolis forces, which cause the leading and trailing side heat transfer to vary by factors as large as five, and (3) effects of buoyancy, which cause heat transfer to increase by as much as a factor of two.

Description of Experimental Equipment

Rotating Heat Transfer Facility. The experimental facility consists of the containment vessel with rotating arm assembly and a motor with controller (Fig. 1). The containment vessel is 6 ft (1.83 m) in diameter. The vessel was designed for operation at pressures as low as 5 mm Hg absolute to reduce the power required to rotate the arm. The rotating arm assembly was turned by a 15 HP DC motor via a toothed belt. Shaft rpm was controlled by an adjustable feedback electronic controller. For this series of experiments, shaft speed was varied from 0 to 1100 rpm producing maximum gravitational forces on the model of approximately 1100g at the tip of the model and approximately 800g at the root.

The shaft assembly is comprised of a main outer shaft with two shorter inner shafts. This shaft arrangement was designed for dual fluid paths from each rotary union mounted on the ends of the shaft to the rotating assembly. The rotary unions had carbon faced seals and were tested at assembly to be "bubble tight" to 150 psia (1034 kPa). The total leakage rate through all the components in stationary tests was less than 0.2 percent of the baseline flow rate. Grooves located on the exterior surface of the outer shaft allow instrumentation and power leads to extend from the rotating arm to the rotating portion of the instrumentation slipring. Two slipring assemblies (a 40-channel unit located on the upper end of the shaft and a 200-channel unit located on the lower end of the shaft) were used to transfer heater power and instrumentation leads between the stationary and rotating frames of references.

Heat Transfer Model. The heat transfer model was designed to simulate the multipassage geometry of an internally cooled turbine blade (Fig. 2). The model consists of three heated straight sections, three heated turn sections, and one

Nomenclature

A = cross-sectional area of coolant passage
C_p = specific heat of coolant
D = hydraulic diameter
Gr = rotational Grashof number
h = heat transfer coefficient
k = thermal conductivity
$\dot{m}$ = mass flow rate
Nu = Nusselt number = hD/k
Pr = Prandtl number
Q = heat flux
R = radius
Re = Reynolds number = $\dot{m}D/\mu/A$
Ro = Rotation number = $\Omega D/V$
T = temperature
V = mean coolant velocity
x = streamwise distance from inlet
$\Delta\rho/\rho$ = density ratio = $(\rho_b-\rho_w)/\rho_b$
μ = absolute viscosity
ρ = coolant density
Ω = rotational speed

Subscripts

b = local bulk condition
d = outlet of system of heated surfaces
H = constant heat flux
i = inlet to coolant passage
u = inlet to system of heated surface
w = heated surface location
∞ = fully developed, smooth tube

Superscripts

$\bar{}$ = average

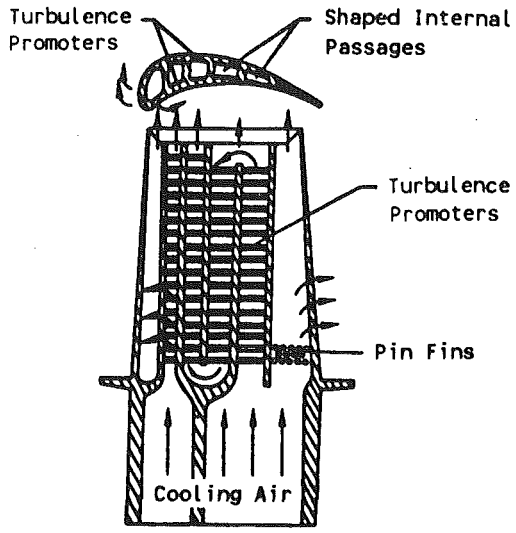

Fig. 2 Typical turbine blade internal convection cooling configuration (from Han et al., 1984)

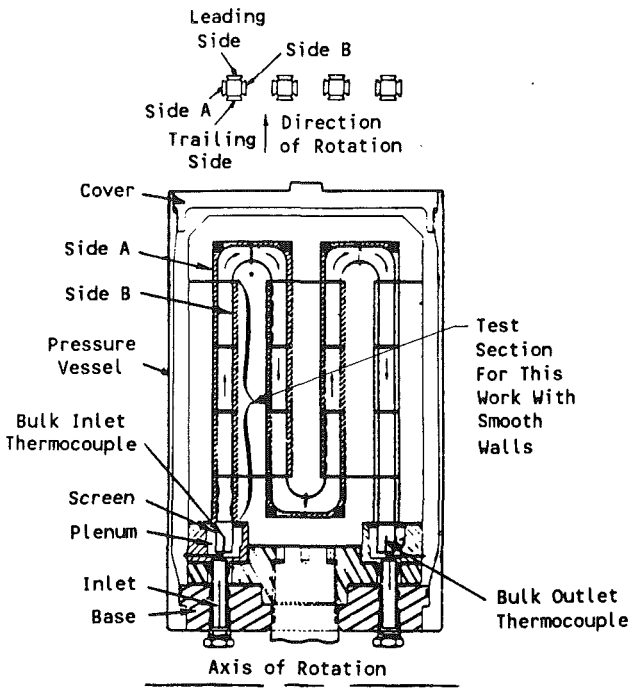

Fig. 3 Cross-sectional views of coolant passage heat transfer model assembly

unheated straight section, as shown in Fig. 3. All data presented herein were obtained in the first heated passage with radially outward flow. The model passages are square with a sidewall dimension of 0.5 in. (12.7 mm). The heated length of the first passage is 14 hydraulic diameters and is comprised of 16 heated copper elements at four streamwise locations. Four elements form the walls of the square coolant passage at each streamwise location. The two cross-sectional views shown in the figure show the orientation of the leading, trailing, and side wall surfaces. Each copper element is heated on the side opposite the test surface with a thin-film, 0.003 in. (0.1 mm) resistance heater. Each element is 0.150 in. (3.8 mm) thick and is thermally isolated from surrounding elements by 0.060 in. (1.5 mm) thick fiberglass insulators. The power to each element was adjusted to obtain an isothermal wall boundary condition. The heat flux between elements with a 2°F (1°C) temperature difference was estimated to be less than 2 percent of a typical stationary heat flux from a test element. The combination of distributed heating on the back of the copper element and the thickness of the element produced an almost uniform (<2°F) temperature element.

The heat transfer model was operated at dimensionless flow conditions typical of current and advanced gas turbine designs. The required dimensionless rotation numbers were obtained with rotation rates of 1100 rpm or less by operating the model at a pressure of approximately 10 atm. The inlet coolant temperature was typically 80°F (27°C) and the copper test surface elements were 120°F, 160°F, 200°F, and 240°F (49°C, 71°C, 93°C, and 116°C) for coolant-to-wall temperature differences of 40°F, 80°F, 120°F and 160°F (22°C, 44°C, 67°C, and 89°C). Temperatures of the copper elements were measured with two chromel-alumel thermocouples inserted in holes drilled in each copper element. Heat transfer coefficients were obtained for each heated surface location by the method described below.

Data Reduction. Data acquisition/analysis consisted of two tasks: determination of the conduction back-loss of the model and determination of the heat transfer coefficients. Model back-loss measurements were obtained with no coolant flow and uniform wall temperature under steady-state conditions with rotation, identical to the heat transfer experiments, but without coolant flow. The model back-losses in the first passage ranged from 10 to 20 percent of the total heat generated for stationary heat transfer levels. Heat transfer coefficients were determined for each wall section by applying an energy balance on each heated surface. The net heat added to the coolant by convection was determined from the electrical power used to heat each surface less the heat conducted from the element to the model support structure.

The coolant temperature was determined with a thermodynamic energy balance through each set of heated surfaces. The mean bulk temperature was determined by marching along the test section and calculating the temperature rise due to the net heat addition to the coolant. The calculation was started at the inlet of the coolant passage where the coolant temperature was measured. The average coolant temperature for each heated surface was determined by averaging the inlet and exit calculated bulk temperatures for each set of four heated surfaces

$$T_d = \Sigma Q_{\text{net}}/(\dot{m}C_p) + T_u \tag{1}$$

where Q_{net} is the convective heat flux from each of the four test surfaces at the specific streamwise location.

Variations of coolant bulk temperature relative to the typical inlet coolant temperature of 80°F are shown in Fig. 4 for rotation numbers of 0.0 and 0.48. The shaded symbols are the calculated coolant temperatures from equation (1). The open symbols are the average coolant and wall temperatures for each element. The uncertainty of the measurement of temperature is estimated to be ±2.5°F (±1.4°C).

The average heat transfer coefficient for each element was determined by dividing the net heat input to the coolant by the projected heated surface area and the temperature difference between the average heated surface temperature and the calculated average coolant bulk temperature:

$$h = \frac{Q_{\text{net}}}{\text{Surface Area} * (\overline{T}_w - \overline{T}_b)} \tag{2}$$

Dimensionless heat transfer and flow parameters were calculated for each element (e.g., Nu and Re). The properties in the Nusselt and Reynolds numbers were evaluated at the film temperature, i.e., $T_f = (\overline{T}_w + \overline{T}_b)/2$. All the heat transfer results presented herein have been normalized with a smooth tube correlation for fully developed, turbulent flow. The constant heat flux Colburn equation adjusted for constant wall temperature was used to obtain the Nusselt number for fully de-

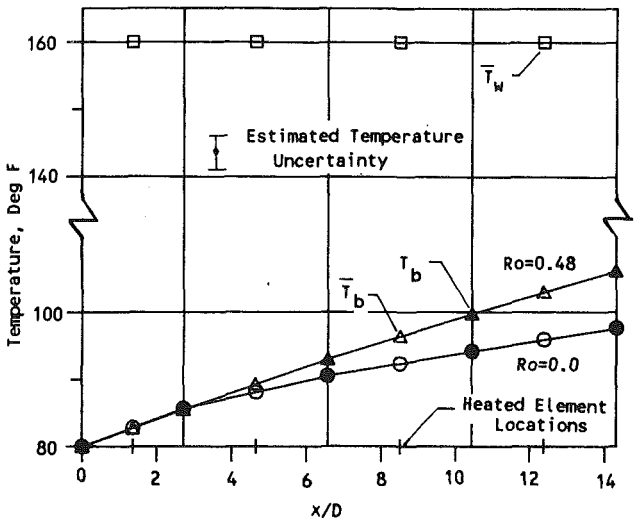

Fig. 4 Variation of coolant bulk temperature with streamwise location; Re = 25,000, $(\Delta\rho/\rho)_i = 0.13$

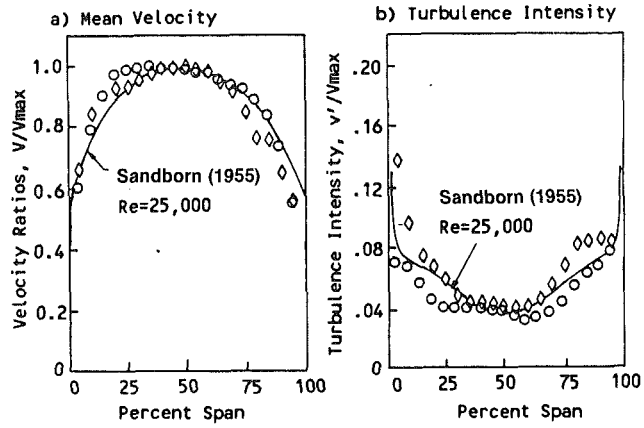

Fig. 5 Mean axial velocity and turbulence intensity profiles at heat transfer passage inlet plane; Re = 15,000, Ω = 0, ○ — plane through axis of rotation, ◇ — plane perpendicular to axis of rotation

veloped, turbulent flow in a smooth tube (Kays and Perkins, 1973)

$$Nu_H = 0.022 * Re_d^{0.8} * Pr^{0.6} \text{ (Colburn equation)} \quad (3)$$

$$\text{with } Pr = 0.72$$

$$Nu_\infty = 0.0176 * Re_d^{0.8} \quad (4)$$

An uncertainty analysis of the data reduction equations showed that approximately 3/4 of the estimated uncertainty in calculating heat transfer coefficient was due to the temperature measurement. Estimates of the uncertainty in calculating heat transfer coefficient typically varied from approximately ±6 percent at the inlet of ±8 percent at the exit of the first passage of the heat transfer model for the baseline test condition. The uncertainty of the heat transfer coefficient is influenced mainly by the wall-to-coolant temperature difference and the net heat flux from each element. Uncertainty in the heat transfer coefficient increases when either the temperature difference or the net heat flux decreases. For increasing x/D, the uncertainty increases because the wall-to-coolant temperature difference decreases (see Fig. 4). For low heat fluxes (e.g., for low Reynolds numbers and on the leading surfaces with rotation) the uncertainty in the heat transfer coefficient increased. The uncertainty in the lowest heat transfer coefficient on the leading side of the passage with rotation was estimated to be 20 percent.

Coolant Passage Inlet Documentation. Velocity and turbulence measurements were obtained at the exit of the screen assembly (inlet of coolant passage; see Fig. 3) for a Reynolds number of 15,000 with no rotation. For these measurements, the four-legged duct was removed from the model. The measurements were obtained by traversing a hot-film probe across the 0.5 by 0.5 in. (12.7 by 12.7 mm) opening downstream of the coolant inlet assembly. Average and rms voltages from the linearized hot-film signal were used to determine the local mean velocity and local turbulence intensity. The mean velocity and turbulence intensity results for the flow from the exit of the screen assembly (entrance to the coolant passage) are shown in Fig. 5. The inlet screen system was designed to produce an inlet velocity profile similar to that for a fully developed turbulent pipe flow. The mean velocity profiles have an approximately parabolic shape but are slightly skewed toward the outside (side A) and trailing side of the passage. Turbulence profiles at the exit of the screen assembly show increases in local turbulence intensity near the edges of the flow with a centerline turbulence level of approximately four percent. The mean velocity and turbulence profiles are in good agreement with those of Sandborn (1955) for fully developed pipe flow. The effects of rotation on the inlet velocity distribution are not known. However, an analytical study is being initiated to determine the effects of rotation on the inlet velocity distribution and results will be reported at a future date.

Results

Heat transfer in stationary experiments with smooth passages is primarily a function of the Reynolds number (a flow parameter) and the streamwise distance from the inlet, x/D (a geometric parameter). However, when rotation is applied, the heat transfer is also strongly influenced by the coupled effects of Coriolis and buoyancy and becomes asymmetric around the passage. An unpublished analysis of the equations of motion by Suo (1980), similar to that of Guidez (1988), showed that the basic dimensionless fluid dynamic parameters governing the flow in a radial coolant passage were the Reynolds number, the rotation number $\Omega D/V$, fluid density ratio $\Delta\rho/\rho$, and the geometric parameter R/D. (Note that the rotation parameter is the reciprocal of the Rossby number, $V/\Omega D$.) The rotation number $\Omega D/V$, the fluid density ratio $\Delta\rho/\rho$, and the geometric parameter R/D can be combined to form a buoyancy parameter $(\Delta\rho/\rho)(R/D)(\Omega D/V)^2$. This combined parameter influences the formation of both cross-stream and buoyancy-driven secondary flow and, consequently, also influences the heat transfer. Thus, with rotation, the heat transfer is primarily a function of two geometric parameters (x/D and surface orientation relative to the direction of rotation) and three flow parameters (Reynolds number, rotation number and buoyancy parameter).

The effect of each of the five parameters on the heat transfer is difficult to determine when most of the parameters influence the heat transfer by similar amounts. Our approach to developing understanding of the cause/effect relationships is, first, to show the effects of each primary variable about a baseline flow condition and then, second, to examine our entire body of experimental results to determine regimes where each of the three flow parameters dominates the heat transfer.

Baseline Experiments. Two baseline experiments, one stationary and one rotating, were conducted to obtain data for comparison with all other data generated in this program. The stationary and rotating baseline experiments had dimensionless flow conditions, which consisted of a Reynolds number of 25,000 and an inlet density ratio, $(\Delta\rho/\rho)_i = (T_w - T_b)/T_w$, of 0.13. The rotating baseline experiment had a rotation number $\Omega D/V$ of 0.24 and a radius ratio at the average model radius

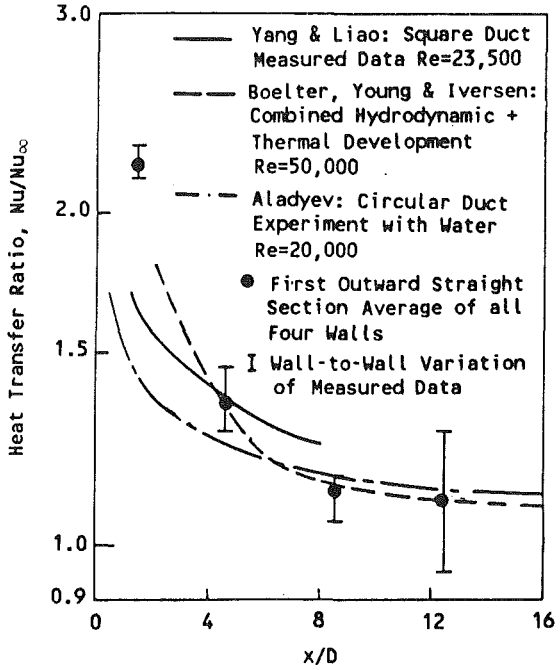

Fig. 6 Variation of heat transfer with streamwise location for "nonrotating" baseline flow conditions; Re = 25,000, $(\Delta\rho/\rho)_i = 0.13$, average of $\Omega = -15, 0, +15$ rpm, Ro = 0.006

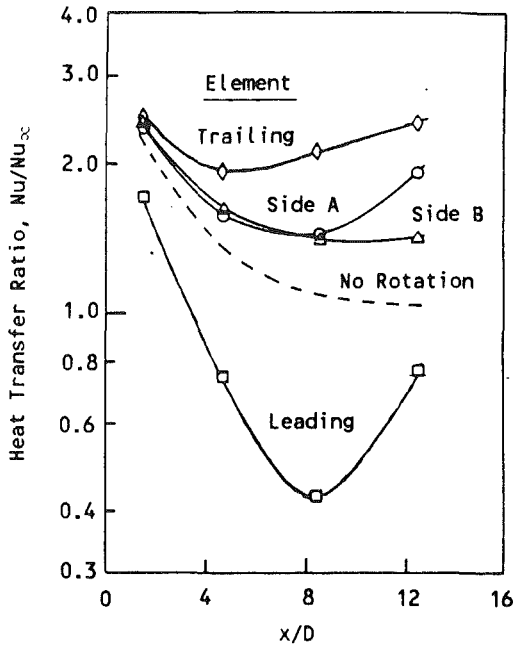

Fig. 7 Variation of heat transfer ratio with streamwise location for "rotating" baseline flow conditions; Re = 25,000, Ro = 0.24, $(\Delta\rho/\rho)_i = 0.13$

$\overline{R}/D$ of 49. These parameters were selected because they are in the central region of the operating ranges of current large aircraft gas turbine engines.

Stationary. The streamwise distribution of the average heat transfer ratio for the stationary (and very low rotation rate) baseline experiments are shown in Fig. 6. The wall-to-wall variation of the heat transfer results from the four surfaces around the circumference of the coolant passage are also shown. Results from other investigators (Boelter et al., 1948; Aladyev, 1954; Yang and Liao, 1973) are shown for comparison.

The streamwise variations in average heat transfer ratio are indicative of developing flow in the entrance region of a passage. Note that the heat transfer ratio decreases from over 2.0 near the inlet of the first passage to about 1.0 near the exit. A heat transfer ratio of 1.0 is that expected for fully developed, turbulent flow with a constant wall temperature. Although the mean inlet velocity profiles were conditioned to be hydrodynamically "fully developed" for a circular passage, the heat transfer results indicate that an additional development process occurs along the passage length. This development is attributed to thermal and near-wall flow development as well as the hydrodynamic development of flow in a square cross-sectional passage. The wall-to-wall variation in heat transfer ratio for each streamwise location is less than 15 percent, indicating good passage symmetry. The wall-to-wall variation was random in nature except at $\overline{x}/D = 12.4$, where the wall-to-wall variation was judged to be systematic. The greatest wall-to-wall difference in heat transfer ratio occurred at $\overline{x}/D = 12.4$ and was attributed to upstream effects of the turn. In general, consistent wall-to-wall heat transfer results were obtained.

Rotating. The streamwise distributions of heat transfer ratio for the rotating baseline condition for the four surface locations around the coolant passage are shown in Fig. 7. The streamwise distribution of the average heat transfer ratio from all four surfaces from the stationary baseline test is also shown.

With rotation, heat transfer increases and decreases by factors of more than two from the trailing and leading surfaces, respectively, compared to the heat transfer from the stationary model. The heat transfer from the sidewall surfaces increases by factors of 1.2 to 1.5. Note that the local heat transfer ratio on the leading side of the coolant passage decreases rapidly with increasing streamwise distance to about 40 percent of the stationary value at $\overline{x}/D = 8.5$ and then increases at the larger x/D location. The heat transfer ratio on the trailing side increases with increasing streamwise distance to almost 2.5 times that of a fully developed, smooth tube. This results in a 6-to-1 ratio of the heat transfer coefficients between the trailing and leading surfaces.

The difference in heat transfer between the rotating and nonrotating flow conditions on the trailing and sidewall surfaces is attributed to both the increasing strength of the secondary flow cells associated with the Coriolis force and the buoyancy. The decrease in heat transfer near the inlet of the passage on the leading surfaces is attributed to the stabilizing of the near-wall flow, as observed by Johnston (1972). The subsequent increase in heat transfer near the end of the passage is postulated to occur when the secondary flow cells become more developed and interact with the buoyant, stabilized near-wall flow on the leading side of the passage. Further discussion of this interaction will be presented in subsequent sections. The heat transfer effects described above are characteristic of radially outward flow in rotating passages and are attributed to the combined Coriolis and buoyancy forces.

As noted above in the discussion of the baseline results, rotation significantly changes the heat transfer from the leading and trailing surfaces but causes smaller changes on the sidewall surfaces. Therefore, the following discussion will focus on the heat transfer results from only the leading and trailing surfaces.

Varying Rotation Number. The rotation number $\Omega D/V$ was varied from 0 to 0.48 for this series of flow conditions. The Reynolds number, inlet density ratio, and radius ratio were held constant at the nominal values of 25,000, 0.13, and 49, respectively.

Trailing Surfaces. Increasing the rotation rate causes significant increases in heat transfer on the trailing surfaces (Fig. 8*a*). As the rotation parameter is increased from 0 to 0.12, the heat transfer ratio increases more than 50 percent above the stationary values in the latter half of the coolant passage and only slightly in the first half. As rotation is further increased,

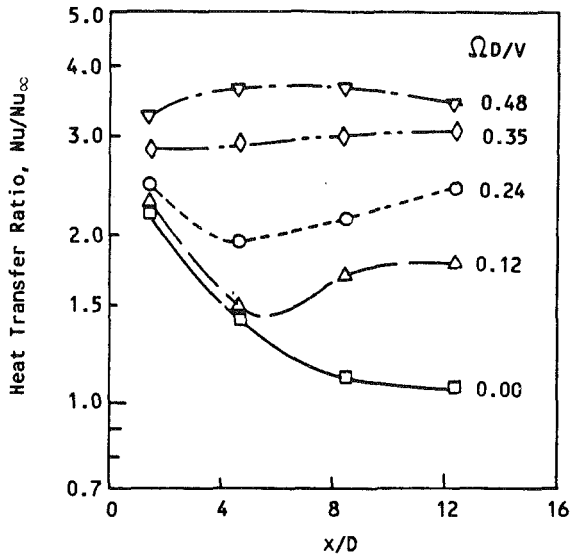

Fig. 8(*a*) Effect of Rotation number on heat transfer ratio for trailing surfaces; Re = 25,000, $(\Delta\rho/\rho)_i = 0.13$, $\bar{R}/D = 49$

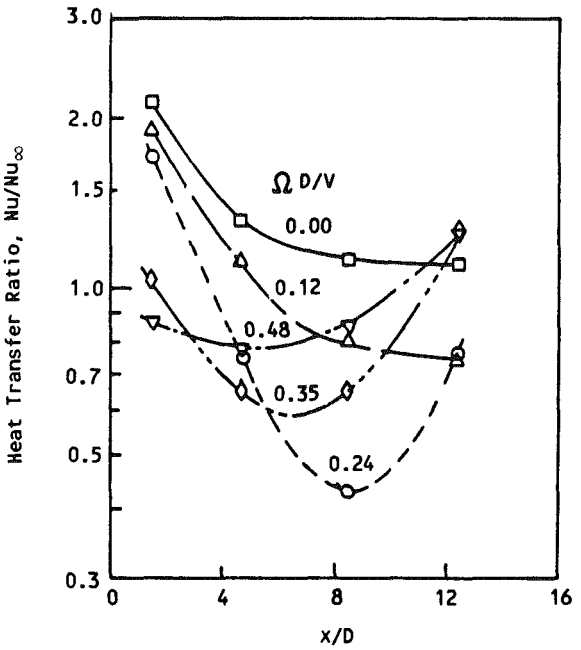

Fig. 8(*b*) Effect of Rotation number on heat transfer ratio for leading surfaces; Re = 25,000, $(\Delta\rho/\rho)_i = 0.13$, $\bar{R}/D = 49$

the heat transfer ratio increases over the whole passage length to values of almost 4 for the rotation number of 0.48.

The large increases in the heat transfer ratio in the latter half of the passage for low rotation numbers are attributed to the development of Coriolis generated secondary flow cells. The general increase in heat transfer ratio on the entire trailing side of the passage for larger rotation numbers is attributed to the upstream movement of the onset and the increasing strength of these secondary flow cells. The coolant near the trailing side of the passage (high pressure side for radially outward flow) is also believed to be influenced by the destabilization of the wall shear layers due to rotation. Additionally, cooler mainstream fluid is accelerated towards this side of the passage by the Coriolis forces. The large increases in the heat transfer from the trailing surfaces are attributed to a combination of these effects.

Leading Surfaces. Heat transfer from the leading surfaces

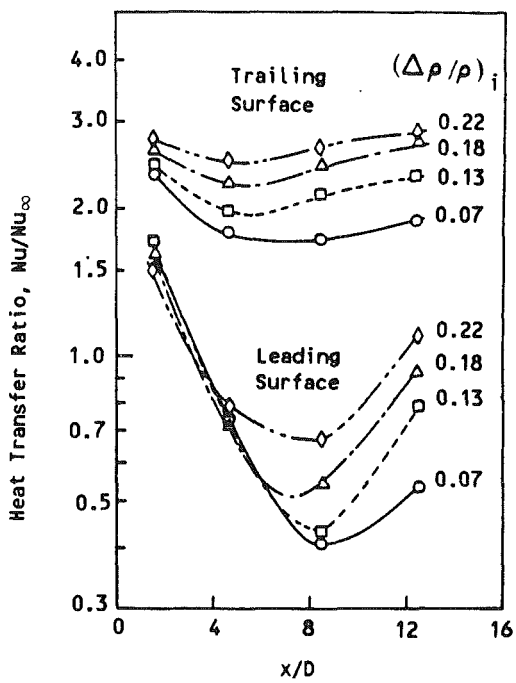

Fig. 9 Effect of wall-to-coolant density difference on heat transfer ratio; Re = 25,000, $R_o = 0.24$, $\bar{R}/D = 49$

is also strongly influenced by rotation (Fig. 8*b*). However, the effect of rotation is markedly different from that observed on the trailing surfaces. In contrast to the continual increase in heat transfer with increasing rotation number on the trailing side, the heat transfer ratio decreases with increasing rotation number on the leading side of the passage near the inlet. For all of the remaining locations on the leading side of the passage, the heat transfer ratio decreases and then increases again with increasing rotation number. Examination of the leading side results shows that the location of the local minimum in the heat transfer ratio for each rotation number moves toward the inlet of the passage as the rotation number is increased.

Significantly lower heat transfer rates were measured along the leading side of the coolant passages for even low values of rotation numer. The decreases in the heat transfer ratio are attributed, for the most part, to the cross-stream flow patterns in the passage as well as the stabilization of the flow near the leading side of the passage (discussed in the previous section). The cross-section flows cause already heated, relatively quiescent fluid from the trailing and sidewall surfaces to accumulate near the leading side of the coolant passage. In addition, the rotation stabilizes the shear layers along this wall and further reduces the potential for heat transfer from turbulent transport. The increase in the heat transfer ratio in the latter half of the coolant passage for the larger rotation numbers is attributed to the large-scale development of the Coriolis-generated secondary flow cells.

Varying Density Ratio. The inlet density ratio $(\Delta\rho/\rho)_i$ was varied from 0.07 to 0.22 for this series of flow conditions. The Reynolds number, rotation number, and radius ratio were held constant at the nominal values of 25,000, 0.24, and 49, respectively.

Increasing the inlet density ratio (i.e., the wall-to-coolant temperature difference) from 0.07 to 0.22 causes the heat transfer ratio to increase on all trailing surfaces by as much as 50 percent and on the two downstream leading surfaces by as much as 100 percent (Fig. 9). The largest increases in heat transfer with increasing density ratio are in areas of the passage where the effects of Coriolis are also strong. The exception to

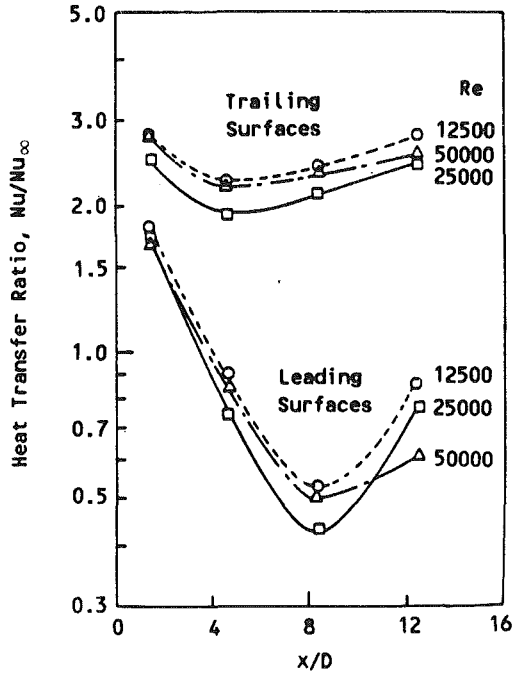

Fig. 10 Effect of Reynolds number on heat transfer ratio; Ro = 0.24, $(\Delta\rho/\rho)_i = 0.13$, $\overline{R}/D = 49$

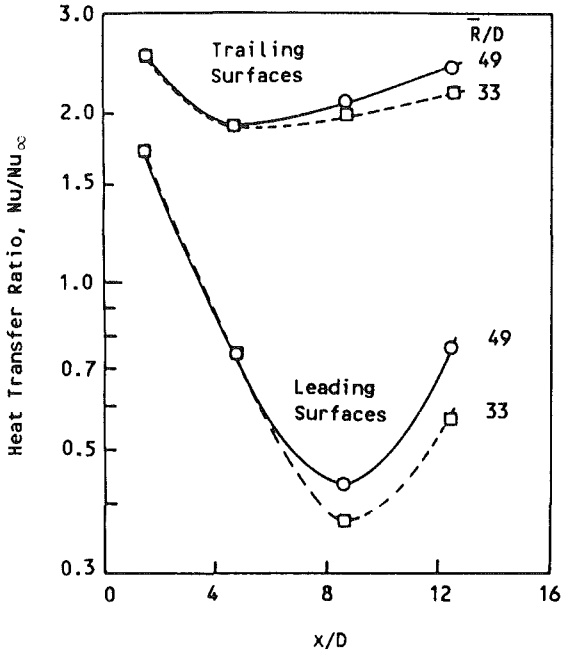

Fig. 11 Effect of model radius on heat transfer ratio distribution; Re = 25,000, Ro = 0.24, $(\Delta\rho/\rho)_i = 0.13$

the general increase in heat transfer with increasing density ratio occurred near the inlet on the leading side of the passage, where the heat transfer ratio is observed to decrease slightly. The heat transfer for this particular location, as noted above, is relatively unaffected by the Coriolis-generated secondary flow for this rotation number and is believed to be dominated by near-wall flow stabilization. Increasing the density ratio in this region adds an additional stabilizing effect due to the opposing signs of the buoyancy force and the direction of the mainstream flow. This localized decrease in heat transfer ratio is also consistent with the results of Morris and Ayhan (1979) and Morris (1981), who found a decrease in heat transfer on leading surfaces with increasing Grashof number (i.e., either increasing density ratio and/or increasing rotation number). This decrease was observed by Morris at values of rotation number of approximately 0.05.

Varying Reynolds Number. The Reynolds number was varied from 12,500 to 50,000 for this series of flow conditions. The rotation number, inlet density ratio, and radius ratio were held constant at the rotating baseline values of 0.24, 0.13, and 49, respectively.

The streamwise distributions of heat transfer ratio for three Reynolds numbers are shown in Fig. 10. For these tests, the coolant mass flow rate, $\dot{m}$, and rotation rate, Ω, were varied to maintain a constant rotation number of 0.24. Changing the Reynolds number about the rotating baseline condition yielded a variation of heat transfer ratios with streamwise location similar to those for the rotating baseline flow condition. There is no consistent trend in the heat transfer results with variations in the Reynolds number for this rotation number. However, there is a significant decrease in heat transfer ratio with increasing Reynolds number on the leading side of the passage at the most downstream location, $\overline{x}/D = 12.4$.

Varying Model Radius. In order to isolate the effect of the radius ratio $\overline{R}/D$, the mean model radius was decreased to about two-thirds of its baseline value (from $\overline{R}/D = 49$ to 33). The Reynolds number, rotation number, and inlet density ratio were held constant at the baseline values of 25,000, 0.24, and 0.13, respectively.

The effects of decreasing the model radius on the heat transfer ratio are shown in Fig. 11. Heat transfer ratios near the inlet of the passage on both the leading and the trailing surfaces are relatively unaffected by the radius change. However, the heat transfer ratio did decrease with a decrease in model radius in the latter half of the passage. These results are similar to those discussed above where density ratio was decreased from the baseline value of 0.13 to 0.07. Because the effects of buoyancy are coupled as the product of two flow parameters and one geometric parameter into a combined buoyancy parameter; $(\Delta\rho/\rho)\ (R/D)(\Omega D/V)^2$, varying the density ratio or the radius ratio by similar amounts should cause similar variations in the heat transfer distributions.

Varying Rotation Number and Density Ratio. Additional data from parametric variations of density ratio and rotation parameter were necessary to isolate the effects of rotation and buoyancy. The inlet density ratio was varied from 0.07 to 0.22 for selected rotation numbers. Heat transfer results from these experiments were plotted versus inlet density ratio with rotation number as a secondary variable. The distributions of heat transfer ratio with density ratio (not shown) were extrapolated for each value of the rotation number to obtain a value of the heat transfer ratio for a density ratio of 0.0 (i.e., limit as ΔT approaches 0). The heat transfer results obtained from the experiments plus the extrapolated values for a density ratio of 0.0 are presented in Fig. 12 as the variation of heat transfer ratio with the rotation number with the density ratio as the secondary variable for three streamwise locations.

Trailing Surface. The heat transfer ratios for the trailing surfaces increase with increases in either the density ratio or the rotation number. The heat transfer from the two downstream surfaces on the trailing side increases by a factor of almost two as density ratio increases from 0 to 0.22 at values of rotation number from 0.18 and 0.35. Note that there is no effect of density ratio on the heat transfer ratio for a rotation number of 0 when film properties are used for the dimensionless heat transfer and flow parameters. Increasing the rotation number causes local increases in the heat transfer by factors as much as 3.5 compared to the heat transfer for a rotation number of 0. The trend (but not the magnitude) for

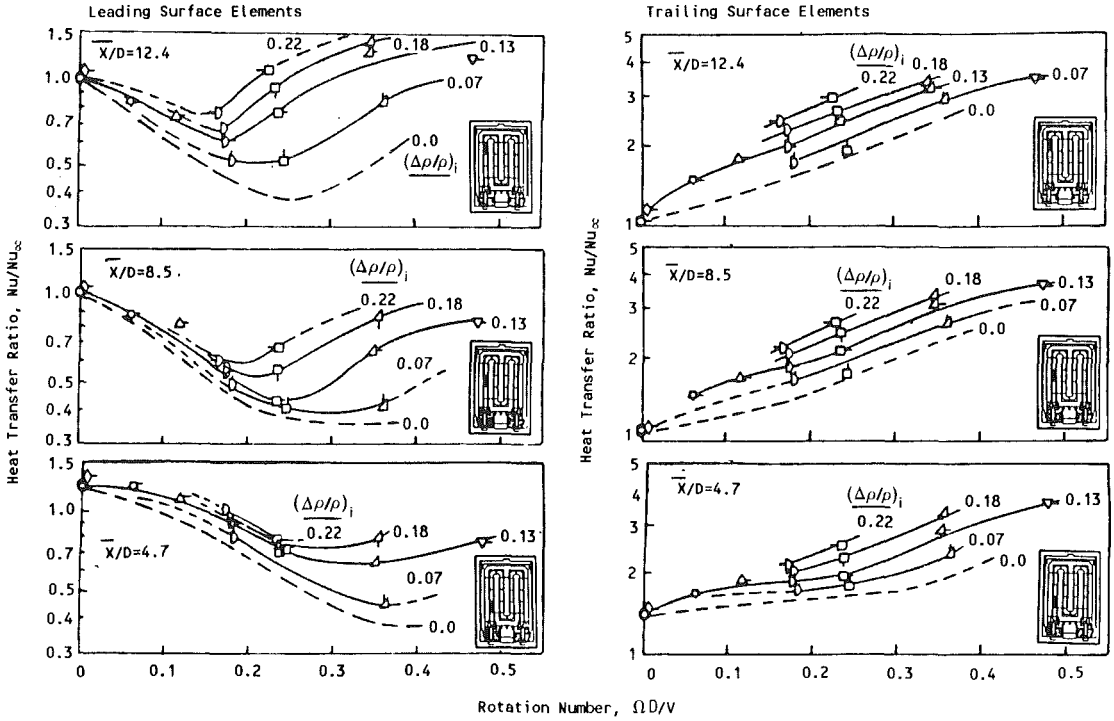

Fig. 12 Variation of heat transfer ratio with Rotation number at selected density ratios and streamwise locations; Re = 25,000, $\overline{R}/D = 49$

continuously increasing heat transfer coefficients with increasing density ratio and rotation number is consistent with the combined free and forced convection results of Eckert et al. (1953) and Metais and Eckert (1964) where the buoyancy force direction is opposite to the mean flow direction as it is for radially outward flowing rotating passages. However, the flow in the present experiment with rotation is more complicated than the flow in stationary experiments because all surfaces do not behave in a similar manner.

Leading Surfaces. The heat transfer from the leading surfaces is more complex than that from the trailing surfaces. Heat transfer decreases with increasing rotation number for low values of rotation number (i.e., $\Omega D/V < 0.2$ at the downstream location) and then subsequently increases again with increases in rotation for larger values of rotation number. Additionally, as with the trailing surfaces, heat transfer increases with increases in the density ratio. The more complicated heat transfer distributions on the leading side of the coolant passage are attributed to (1) the combination of buoyancy forces and the stabilization of the near-wall flow for low values of the rotation number and (2) the developing, Coriolis-driven secondary flow cells for the larger values of the rotation number.

Variations in the absolute and relative changes of the heat transfer coefficients on the leading and trailing surfaces can be deduced from the results shown in Fig. 12. The relative increase in heat transfer ratio for the downstream location on the leading side is greater than 3 as the inlet density ratio is increased from 0 to 0.22 for a rotation number of 0.25. However, note that the absolute increase in the heat transfer ratio is 0.8. This absolute increase is substantially less than the absolute increase in the heat transfer ratio from the trailing side for this rotation number and same increase in inlet density ratio (approximately 1.3). The difference in the increase in heat transfer ratio for the same increase in inlet density ratio suggests that the interaction of the Coriolis and buoyancy effects is different for the leading and trailing surfaces, even where the effects of Coriolis-driven secondary flows are strong.

Correlating Parameters

The analysis of the equations of motion for flow in a rotating radial passage by Suo (1980), discussed above, showed that (1) the variations in the momentum of the flow in the plane perpendicular to the passage centerline (cross-stream flow) will be proportional to the rotation number, $\Omega D/V$, and (2) the variations in the momentum of the flow parallel to the passage centerline (buoyant flows) will be proportional to the buoyancy parameter, $(\Delta\rho/\rho)(R/D)(\Omega D/V)^2$. The buoyancy parameter defined above is equivalent to the ratio of the Grashof number (with a rotational gravitation term, $R\Omega^2$) to the square of the Reynolds number and has previously been used to characterize the relative importance of free and forced convection in the analysis of stationary mixed-convection heat transfer. Guidez (1988) used a similar analysis to establish appropriate flow parameters for the presentation of his results. These parameters, $\Omega D/V$ and $(\Delta\rho/\rho)(R/D)(\Omega D/V)^2$, will also be used in the present discussion of the effects of Coriolis and buoyancy forces on the heat transfer.

The data and extrapolated results presented in Fig. 12 show that the effect of Coriolis and buoyancy forces are coupled through the entire operating range investigated. The results from Fig. 12, combined with those for $\overline{R}/D = 33$, are presented in Fig. 13 as the variation of the heat transfer ratio with the buoyancy parameter. The local density ratio and radius, R, are used in the buoyancy parameter. Thus, the range of the buoyancy parameter decreases with increasing values of x/D. Results for the same value of the rotation number are connected with dashed lines where the results are not well correlated by the buoyancy parameter. The lines at constant rotation number are extrapolated to the value of the heat transfer ratio estimated for a density ratio (and also buoyancy parameter) of 0 as described in the discussion of Fig. 12.

The heat transfer ratios for the trailing side of the passage increase with the buoyancy parameter. The rate of increase in the heat transfer ratio with increasing buoyancy parameter is greatest at the $\overline{x}/D = 12.4$ location for values of buoyancy parameter less than 0.4. For values of the buoyancy parameter

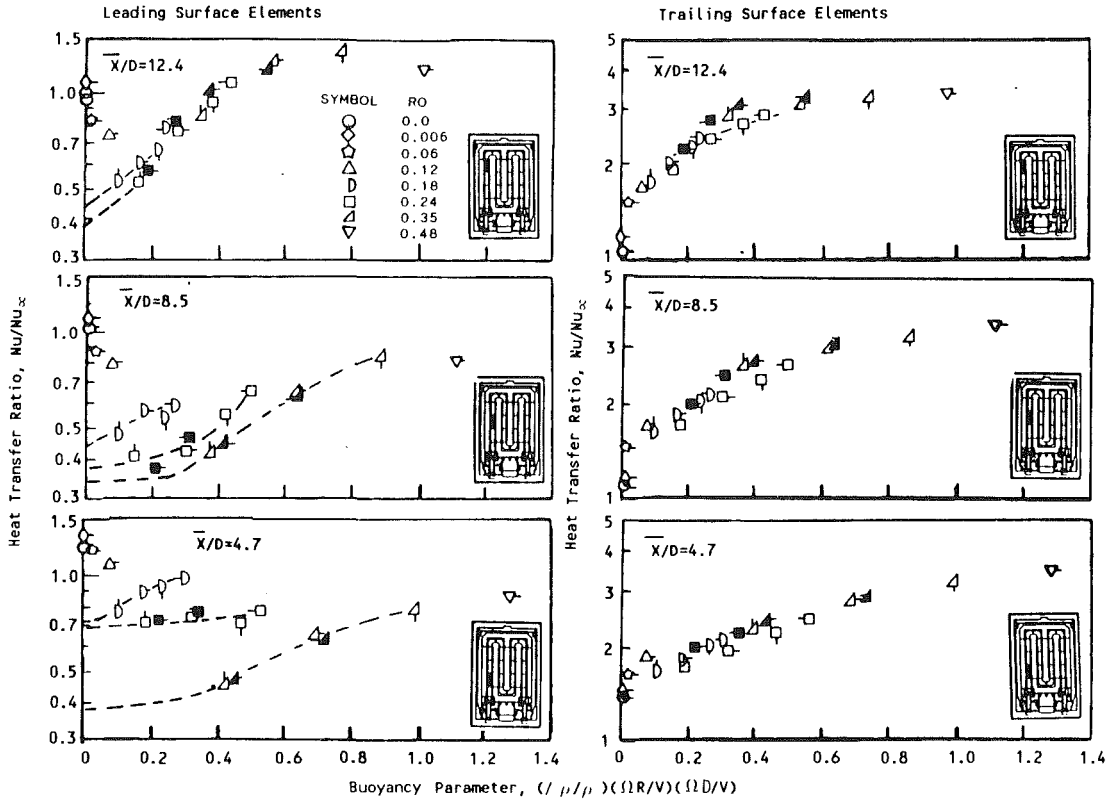

Fig. 13 Variation of heat transfer ratio with buoyancy parameter; Re = 25,000, $\bar{R}/D = 49$: open symbols, $R/D = 33$: shaded symbols

greater than 0.4, the rate of increase is less. Thus, two ranges of buoyancy parameter appear to exist with different heat transfer characteristics. Generally, the heat transfer variations from the trailing side form a one-to-one correspondence with the buoyancy parameter (i.e., singled valued function) and are well correlated by the buoyancy parameter for all values of $\bar{x}/D$ shown.

Examination of the heat transfer results from the leading side suggests that at least three ranges of buoyancy parameter exist where the heat transfer is dominated by different fluid dynamic mechanisms (i.e., Coriolis, buoyancy, etc.). Comparing the results at $\bar{x}/D = 12.4$ from the leading side with those from the trailing side, note that there is a range of buoyancy parameter for values less than 0.1 where the heat transfer ratios decrease sharply with increasing values of the buoyancy parameter. Within the second range from 0.1 to approximately 0.5, the heat transfer ratios increase sharply with increasing values of the buoyancy parameter. For the third range, with values of the buoyancy parameter greater than 0.5., the heat transfer ratio increases at a lower rate, with increasing values of buoyancy parameter. For lower values of $\bar{x}/D$, the values of buoyancy parameter that define the limits of the three ranges increase in magnitude. The heat transfer on the leading surface at values of $\bar{x}/D = 4.7$ and 8.5 is governed by a more complex relationship of streamwise distance, rotation number, and buoyancy parameter. However, the results from the leading side for $\bar{x}/D = 12.4$ are well correlated by the buoyancy parameter for values of the buoyancy parameter greater than 0.2.

The analyses of these heat transfer results show that (1) the buoyancy parameter correlates the heat transfer ratio data from the trailing side of the coolant passage and from the leading side at the downstream location, (2) the data were not correlated by the buoyancy parameter near the inlet on the leading surface due to a complex interaction of stabilization, buoyancy forces, and Coriolis effects, and (3) the heat transfer

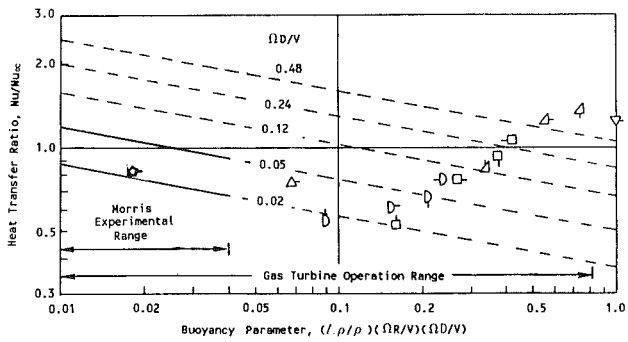

Fig. 14 Comparisons of leading surface rotating heat transfer results for $\bar{x}/D = 12.4$ with Morris correlation: $Nu = 0.022\,(Ra/Re^2)^{-0.186}Ro^{0.33}Re^{0.8}$ or $Nu/Nu_\infty = 1.35\,[(\Delta\rho/\rho) * (R/D) * (\Omega D/\nu)^2]^{-0.186}(\Omega D/\nu)^{0.33}$

in rotating, smooth passages is governed by complex interactions of the viscous, Coriolis, and buoyancy forces on the fluid.

Comparison With Previous Experimental Results

The heat transfer results from the leading surface at $\bar{x}/D = 12.4$ are compared in Fig. 14 with the correlation from Morris (1981). Morris' experiment consisted of a rotating circular tube with radially outward flow with constant wall heat flux. The solid lines on the figure indicate the range of Morris' data, while the dashed lines represent extrapolations of his correlation. The heat transfer results (and symbols) shown in the figure are identical to those in Figs. 12 and 13 for the leading surface elements with $\bar{x}/D = 12.4$. The heat transfer results obtained on the leading surface at the low rotation number of 0.06 are within 20 percent of Morris' correlation. This agreement occurs within Morris' experimental range, which is indicated in the figure. For values of the buoyancy

parameter and rotation number that fall outside the Morris data range, the present data show increases with rotation number that are in general agreement with the Morris correlation. However, the present data show increases in heat transfer with increasing density ratio or buoyancy centripetal parameter, whereas the Morris correlation would predict a decrease in heat transfer with increasing density ratio.

The more recent results of Guidez (1988) for a smooth rectangular passage (aspect ratio 2:1) were obtained at rotation numbers up to 0.2 and values of the buoyancy parameter up to 0.1. The present results from the trailing side of the coolant passage are compatible with those of Guidez (1988), who showed heat transfer ratios of 1.7 for a Reynolds number of 24,000 and a rotation number of 0.2. However, the decrease in heat transfer ratio on the leading side of the passage shown by Guidez (i.e., $Nu/Nu_\infty = 0.7$ at $\bar{x}/D = 11.5$) was considerably less than that obtained in the present experiment (i.e., $Nu/Nu_\infty = 0.5$) for similar conditions. These differences are attributed to differences in the aspect ratios of the passages (i.e., 2:1 for Guidez's experiment compared to 1:1 for the present experiment).

Concluding Comments

This paper has presented an extensive body of experimental data from heat transfer experiments in a rotating square passage with smooth walls. It is believed that the large range of test parameters makes this data set unique. The extensive data base aided greatly in the data analysis and correlation and in developing physical models for the complex heat transfer characteristics.

The analysis of these experimental results to determine the separate effects of forced convection, Coriolis, and buoyancy on the heat transfer in a rotating, smooth-wall, square passage has produced the following observations and conclusions:

1 The streamwise distribution of heat transfer in the first passage from the stationary baseline experiment is similar to that from developing flow in the entrance region of a passage and is in good agreement with previous investigator's results.

2 Heat transfer is strongly affected by rotation, causing increases in heat transfer up to 3.5 times fully developed, smooth tube levels on the trailing surfaces and decreases to 40 percent of fully developed, smooth tube levels on the leading surfaces.

3 The decreases in heat transfer on the leading surfaces with increases in rotation number are attributed to the combined effects of stabilization of the near-wall flow and cross-stream flows.

4 The increases in heat transfer at the downstream locations on the leading side and the increases on the trailing side are attributed to the effects of the large-scale development of Coriolis-generated secondary flows.

5 Local heat transfer increases with increases in density ratio over most of the passage surface area.

6 Heat transfer decreases with increases in density ratio on the leading side of the passage near the inlet. These decreases are believed to be governed by both the interaction of the near-wall flow stability and the buoyancy effects.

7 The effects of varying Reynolds number on heat transfer ratio are reasonably well correlated by normalizing the heat transfer results with a correlation for fully developed, turbulent flow in a stationary environment.

8 Similar changes in the distributions of heat transfer occurred when either density ratio or model radius ratio were varied.

9 Increases in heat transfer ratio on the trailing surfaces were 60 percent greater than increases on the leading surfaces for the same increases in density ratio and for the same rotation number. This difference in heat transfer increase suggests that the interaction of the Coriolis and buoyancy effects is different for the flow near leading and trailing surfaces.

10 The buoyancy parameter correlates the heat transfer ratio results from the trailing side and from the most downstream location of the leading side. The results were not correlated by the buoyancy parameter near the inlet on the leading surface. The lack of correlation was attributed to a complex interaction of stabilization, buoyancy, and Coriolis effects.

Acknowledgments

The work published in this paper was supported by the NASA/Lewis Research Center under the HOST Program, Contract No. NAS3-23691 to the Pratt & Whitney Commercial Engine Business/Engineering Division, and by UTRC's independent research program. The heat transfer models used in this program were furnished by Pratt & Whitney. The experimental portion of the program was conducted at the United Technologies Research Center. The authors are appreciative of the support and guidance by the contract monitor team at NASA/Lewis Research Center, especially Dr. Frederick C. Yeh, and by their colleagues at P&W and UTRC.

References

Aladyev, I. T., 1954, "Experimental Determination of Local and Mean Coefficients of Heat Transfer for Turbulent Flow in Pipes," NACA TN 1356 (translation from Russian).

Boelter, L. M. K., Young, G., and Iverson, H. W., 1948, NACA TN 1451, Washington.

Brundrett, E., and Burroughs, P. R., 1967, "The Temperature Inner-Law and Heat Transfer for Turbulent Air Flow in a Vertical Square Duct," *Int. J. Heat Mass Transfer*, Vol. 10, pp. 1133–1142.

Eckert, E. R. G., Diaguila, A. J., and Curren, A. N., 1953, "Experiments on Mixed-Free- and Forced-Convective Heat Transfer Connected With Turbulent Flow Through a Short Tube," NACA Technical Note 2974.

Guidez, J., 1988, "Study of the Convective Heat Transfer in Rotating Coolant Channel," ASME Paper 88-GT-33.

Han, J. C., Park, J. S., and Lei, C. K., 1984, "Heat Transfer and Pressure Drop in Blade Cooling Channels With Turbulence Promoters," NASA Contractor Report 3837.

Hart, J. E., 1971, "Instability and Secondary Motion in a Rotating Channel Flow," *J. Fluid Mech.*, Vol. 45, Part 2, pp. 341–351.

Iskakov, K. M., and Trushin, V. A., 1983, "Influence of Rotation on Heat Transfer in a Turbine-Blade Radial Slot Channel," *Izvestiya VUZ. Aviatsionnaya Tekhnika*, Vol. 26, No. 1, pp. 97–99.

Johnson, B. V., 1978, "Heat Transfer Experiments in Rotating Radial Passages With Supercritical Water," *ASME Heat Transfer 1978*, proceedings from the ASME Winter Annual Meeting.

Johnston, J. P., Halleen, R. M., and Lezius, D. K., 1972, "Effects of Spanwise Rotation on the Structure of Two-Dimensional Fully Developed Turbulent Channel Flow," *J. Fluid Mech.*, Vol. 56, Part 3, pp. 533–557.

Kays, W. M., and Perkins, H. C., 1973, "Forced Convection, Internal Flow in Ducts," in: *Handbook of Heat Transfer*, W. M. Rohsenow and J. P. Hartnett, eds., McGraw-Hill, pp. 7-28 and 7-33.

Lokai, V. I., and Gunchenko, E. I., 1979, "Heat Transfer Over the Initial Section of Turbine Blade Cooling Channels Under Conditions of Rotation," *Therm. Engineering*, Vol. 26, pp. 93–95.

Metais, B., and Eckert, E. R. G., 1964, "Forced, Mixed, and Free Convection Regimes," ASME *Journal of Heat Transfer*, Vol. 64, pp. 295–296.

Moore, J., 1967, "Effects of Coriolis on Turbulent Flow in Rotating Rectangular Channels," M.I.T. Gas Turbine Laboratory Report No. 89.

Mori, Y., Fukada, T., and Nakayama, W., 1971, "Convective Heat Transfer in a Rotating Radial Circular Pipe (2nd Report)," *Int. J. Heat Mass Transfer*, Vol. 14, pp. 1807–1824.

Morris, W. D., and Ayhan, T., 1979, "Observations on the Influence of Rotation on Heat Transfer in the Coolant Channels of Gas Turbine Rotor Blades," *Proc. Inst. Mech. Engrs.*, Vol. 193, pp. 303–311.

Morris, W., 1981, *Heat Transfer and Fluid Flow in Rotating Coolant Channels*, Research Studies Press.

Rothe, P. H., and Johnston, J. P., 1979, "Free Shear Layer Behavior in Rotating Systems," ASME *Journal of Fluids Engineering*, Vol. 101, pp. 117–120.

Sandborn, V. A., 1955, "Experimental Evaluation of Momentum Terms in Turbulent Pipe Flow," NACA TN 3266.

Suo, M., 1980, Unpublished Notes, United Technologies Research Center.

Wagner, R. E., and Velkoff, H. R., 1972, "Measurements of Secondary Flows in a Rotating Duct," ASME *Journal of Engineering for Power*, Vol. 94, pp. 261–270.

Yang, J. W., and Liao, N., 1973, "An Experimental Study of Turbulent Heat Transfer in Converging Rectangular Ducts," ASME *Journal of Heat Transfer*, Vol. 95, pp. xx-oo.

Transient Liquid Crystal Measurement of Local Heat Transfer on a Rotating Disk With Jet Impingement

D. E. Metzger

R. S. Bunker

G. Bosch

Mechanical and Aerospace Engineering Department,
Arizona State University,
Tempe, AZ 85253

An experimental technique has been developed for measurement of local convection heat transfer characteristics on rotating surfaces, utilizing thin liquid crystal surface coatings in a thermal transient test procedure. The encapsulated liquid crystal coatings used are sprayed directly on the test surface and their response is observed and processed during the transient with automated computer vision and data acquisition systems. Heat transfer coefficients are calculated from the thermal transient response of the test surface, as determined from the color indication from the thin coating. A significant advantage of the method, especially for convection in disk/shroud cavities that may contain recirculating fluid regions, is that appropriate thermal boundary conditions are naturally imposed on all of the boundary surfaces. The method is also relatively fast and inexpensive, and allows the geometry of the disk and stator surfaces to be changed easily, without the expenses of mounting discrete heat flux and temperature sensors and equipment to transfer information to a stationary frame of reference. Application of the experimental technique is demonstrated with detailed radially local surface Nusselt number distributions acquired for cases involving jet impingement onto a smooth disk, rotating in close proximity to a parallel plane stator disk. A single circular jet, with nozzle exit flush mounted in the stator, is oriented normal to the disk surface at various radii and flow rates. Local Nusselt numbers are presented nondimensionally as functions of both disk and flow Reynolds numbers. The results indicate that the local radial heat transfer distribution can be controlled by varying the impingement radius, but maximum radially averaged heat transfer is obtained with impingement at the disk center.

Introduction

Heat transfer on rotating disks is a commonly occurring topic in convection heat transfer, especially in rotating machinery. Rotating disks are also found in various manufacturing processes where materials are dropped onto and spun off of the rotating disk face or in applications where the edge of the disk is used in rolling operations.

In most of these applications, it is important to have knowledge of the disk temperature and the ability to control it. In gas turbine engines, for example, knowledge of the temperature distribution on turbine disks is needed in order to predict stresses and durability, and is also important from the standpoint of dimensional control. The temperature distribution throughout the entire disk plays a major role in determining the radial position of the turbine blade tips and thus in establishing the clearance space between blade tip and stationary outer seal.

On all rotating disks, whether smooth or roughened, there is an inherent, unavoidable pumping of fluid radially outward along the disk surface. If not counteracted in some way, this pumping action will also act to induce a radially inward flow of fluid from the disk rim region to replenish the flow pumped from the radially in-board regions. In a gas turbine engine this radially inward flow will often consist of hot combustion gases, causing elevated disk temperatures, temperature differences, and shortened disk life. In the gas turbine application, cooling air is generally bled from the compressor section and routed to the wheel space where it is used both for cooling the rotating and stationary components and for sealing the wheel space against ingress of hot combustion gases. Since the bleeding of compressor gas imposes a performance penalty on the engine cycle, the designers of cooling and sealing systems want to accomplish these tasks with the minimum possible amount of bleed air. For this to be accomplished, the designer must have accurate and detailed knowledge of the convection heat transfer and flow characteristics associated with the wheel-space flows. Moreover, detailed local knowledge of the convection heat transfer on the disks themselves is a necessary prerequisite

Contributed by the International Gas Turbine Institute and presented at the 34th International Gas Turbine and Aeroengine Congress and Exhibition, Toronto, Ontario, Canada, June 4–8, 1989. Manuscript received at ASME Headquarters February 14, 1989. Paper No. 89-GT-287.

to the calculation of disk temperature distribution and the corresponding disk stresses, radial growth, and predicted durability.

Despite the recognized need for detailed heat transfer information on rotating surfaces, such information has been acquired slowly starting with, among others, the analysis of von Karman (1921) and the experiments of Cobb and Saunders (1956) and Kreith et al. (1959). A concise review of literature addressing both the fluid mechanics and heat transfer aspects of the subject through 1982 is provided by Owen (1984).

The majority of published work deals with the flow aspects of the problem rather than with the heat transfer, e.g., Daily and Nece (1960) and Bayley and Owen (1970). The acquisition of heat transfer information has been slowed and is still incomplete because of the expense and complexity involved with making local heat transfer measurements on rotating surfaces. Conventionally such measurements involve mounting expensive heat flux gages, or spot heaters and thermocouples, on the disk surface, and transmitting electrical power and measurement signals from and to the rotating apparatus through slip rings. The expense and time factors involved usually result in testing of only limited geometric arrangements of the disk and stator system, and in most previous work both the disk and shroud surfaces used in tests have been plane and smooth. In contrast, in gas turbine applications both the disk and adjacent stator are generally not plane and often not smooth. Moreover, the flow in the wheel space between rotor and stator often contains recirculating regions where the flow exchanges heat with both the stator and the rotor. In conventional testing, the disk is usually the only active heat transfer surface and heat transfer to or from the stationary surfaces is not properly modeled or accounted for in the experiments.

The main objective of the present work has been to develop a method capable of making local convection heat transfer measurements on rotating surfaces without the difficulty and expense of conventional techniques. The technique developed utilizes thin crystal surface coatings in a thermal transient test procedure.

Thermochromic liquid crystals have been utilized in heat transfer experimentation for several years. Early experimental applications in convective heat transfer problems were made by den Ouden and Hoogendoorn (1974), Cooper et al. (1975), and Butefisch (1976) using conventional steady-state test methods. More recent applications of liquid crystals include the work of Hippensteele et al. (1983) using a composite heater element and liquid crystal sheet, and studies of Ireland and Jones (1985) using a semi-infinite transient experimental technique.

In the present study, encapsulated liquid crystal coatings are sprayed directly on the test surface and their response is observed and processed during an imposed thermal transient with automated computer vision and data acquisition systems. Heat transfer coefficients are calculated from the transient response of the test surface, as indicated by the color reflected from the thin coating. A significant advantage of the method, especially for convection in disk/shroud cavities that may contain recirculating fluid regions, is that appropriate thermal boundary conditions are naturally imposed on all of the boundary surfaces. The method is also relatively fast and inexpensive, and allows the geometry of the disk and stator surfaces to be changed easily, without the expenses of mounting discrete heat flux and temperature and equipment to transfer information to a stationary frame of reference.

A second objective of the present work was to apply the experimental method developed to the acquisition of local data for heat transfer between a rotating disk and impinging jet. This situation, for which there is only sparse local heat transfer information available, has been investigated only for the case of free, unenclosed disks in studies by Popiel et al. (1974), Metzger and Grochowsky (1977), Metzger et al. (1979), Bogdan (1982), and Popiel and Boguslawski (1986). Jet impingement has been used, most recently on the space shuttle main engine, as a method for cooling turbine disks, particularly for localized cooling of the blade attachment regions. In gas turbine engines, the disks invariably rotate in the presence of some type of nearby stator arrangement, and if the axial spacing between disk and stator is small, both the disk windage and the tendency to ingest hot gases can be reduced. The present study uses the experimental method developed to investigate jet impingement heat transfer in such a confined disk/stator wheel space.

Experimental Apparatus and Procedures

A schematic of the test apparatus is shown in Fig. 1. The disk is rotated at speeds up to 10,000 rpm by a 3/4 hp motor connected by flat belt to a high-speed quill, consisting of precision sealed shaft and bearings. The disk is composed of two pieces as shown in the detailed test section schematic of Fig. 2. The disk test surface is made of black, cell-cast acrylic plastic of 0.635 cm thickness and 10.16 cm radius. The plastic disk is tightly fit into an aluminum retaining disk, and the two-piece disk assembly is fastened to the quill shaft.

The rotating disk is faced by a plane stationary shroud, or stator disk, at a spacing of z. The stator surface is maintained parallel to the disk surface and positioned laterally with a shroud support assembly attached to the quill housing. The shroud includes an attached rim at the stator disk edge to discourage entrainment of air into the disk-shroud cavity from the rim region. The shroud rim is positioned and angled to direct jet supplied air out of the disk-shroud cavity and away from the apparatus. The stator disk contains an insert piece along one radial location for the purpose of positioning the jet nozzle. By means of various inner pieces the radial location of jet impingement may be varied in a continuous fashion from the disk hub to the disk rim. The jet nozzle, which affixes perpendicularly to the insert piece at a desired position, uses a circular jet of 0.476 cm diameter and is fitted with a thermocouple to indicate the jet transient temperature. The shroud,

Nomenclature

A = heat transfer surface area
c_p = fluid specific heat
h = convection coefficient = $q/A(t_m - t)$
k = test surface thermal conductivity
k_f = fluid thermal conductivity
Nu_{ro} = local Nusselt number = hr_o/k_f
Pr = Prandtl number = $\mu c_p/k_f$
q = surface heat transfer rate
Q = volume flow rate
Q_p = disk pumping flow, equation (5)
r = radial coordinate
r_i = impingement radius
r_o = disk outer radius
Re_m = flow Reynolds number = $Q/(2\pi z\nu)$
Re_{ro} = rotational Reynolds number = $\omega r_o^2/\nu$
t = local test surface temperature
t_i = test surface initial temperature
t_m = fluid mixed mean temperature
t_p = plenum temperature
z = disk-to-shroud axial spacing
α = test surface thermal diffusivity
θ = time
μ = fluid dynamic viscosity
ν = fluid kinematic viscosity
τ = time step

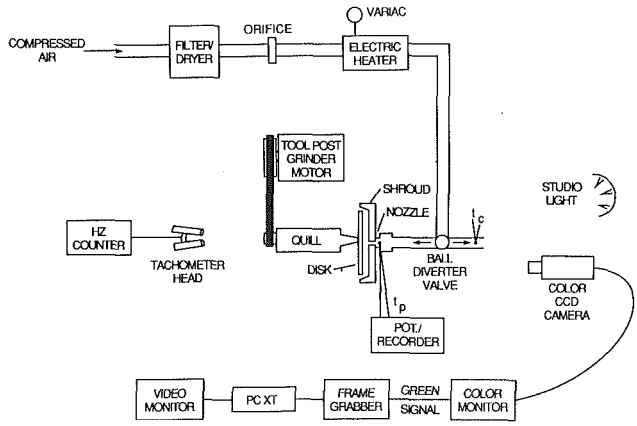

Fig. 1 Schematic of the experimental apparatus

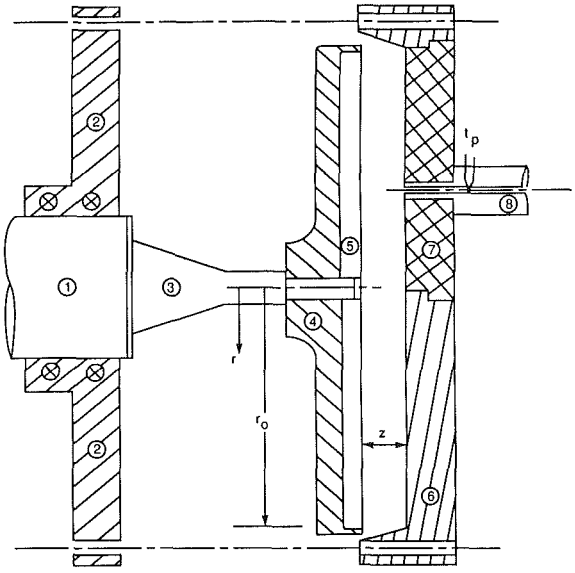

1. QUILL
2. SHROUD SUPPORT
3. SHAFT
4. DISK RETAINER
5. ACRYLIC DISK
6. SHROUD WITH SHROUD RIM
7. NOZZLE RETAINING INSERT
8. JET NOZZLE

Fig. 2 Disk and shroud details

nozzle positioning insert, and jet nozzle are all made of clear acrylic plastic.

The present experiments utilized a fixed shroud spacing of $z/r_o = 0.1$ together with discrete jet nozzle radial locations of $r/r_o = 0$, 0.2, 0.4, 0.6, and 0.8. The rotational Reynolds number Re_{ro} is determined using angular speed ω detected by a photoelectric tachometer head and electronic counter. The flow Reynolds number Re_m is determined by metering the jet supply air through an ASME standard orifice. Both Re_{ro} and Re_m are varied in this study. Additional details of the experimental apparatus are given by Bosch (1988).

Laboratory compressed air, filtered, dried, and accurately metered, is supplied to a heating section followed by a diverter ball valve. Local surface heat transfer is determined from the color response pattern of a thermochromic liquid crystal (TLC) coating sprayed onto the acrylic plastic disk surface. Each test run is a thermal transient, initiated by the sudden introduction of heated air to the test section, resulting in the sequential color change display of the surface coating. The experimental method and procedures used are similar in most respects to those described previously by Metzger and Larson (1986) using a melting point surface coating, so only a brief description will be given here with specific attention given to the TLC coatings.

A test run begins with heated air first diverted away from the test section so that the test section and upstream duct remain uniformly at the laboratory ambient temperature. The valve remains in the diverted position until steady flow and a steady-state temperature (above the selected color indicating temperature of the TLC coating) have been achieved in the diversion channel. At that time the valve is used suddenly to route the heated air flow through the test section. A data acquisition program in the IBM PC is initiated simultaneously with the change of valve position.

A thin layer of the TLC coating (less than 5×10^{-3} cm) is sprayed evenly on the test surface. The coating material used in the present study is a commercially available, chiral nematic TLC (Hallcrest, Type B-M/R38C5W/C17-10, Glenview, IL). This very sensitive encapsulated TLC is essentially clear when sprayed onto the surface in a very thin layer. The strongest intensity (near primary) colors displayed are red, green, and blue, in that order. For this TLC, the nominal temperatures at which red, green, and blue are initiated in the display are 38.4°C, 39.8°C, and 43.5°C, respectively, as viewed under room lighting conditions without filters or other modifying factors. After proceeding through the full display of colors, this TLC returns to a clear coating again. The color display of the TLC is a result of a re-orientation (rotation) of the crystal's lattice such that different wavelengths of light are reflected more or less strongly depending upon the temperature. While all TLC types experience a finite time response for the lattice rotations, Ireland and Jones (1987) have shown that micro-encapsulated chiral nematic coatings on the order of 10^{-3} cm thick require only a few milliseconds for this action. This time lag is negligible in comparison with the thermal transients of the present study.

A particular surface temperature is determined by detecting a desired color in a monochromatic manner. The system utilizes a color CCD camera with an analytic line filter covering the lens (peak wavelength of 535 nm and bandwidth of 10 nm). The camera signal is sent to a color monitor from which only the green color gun signal is used. The determination of the desired color by the frame grabber is based on the intensity level of the test surface display as shown by the green signal. When a small region of the surface covered by a single pixel has reached a preset threshold intensity level, the surface temperature at this point is known. The desired color and preset threshold are determined by calibrating the data acquisition system with a TLC-coated copper bar. The response of the copper bar to a heat rate input is monitored through a thermocouple in the bar. The visual response of the system is monitored with the color and video monitors. By varying the intensity threshold level set in the computer, an appropriate threshold and surface temperature are determined for reliable data acquisition.

The use of of studio lighting and a black acrylic plastic surface both serve to improve the TLC color display intensity and clarity. Variable intensity studio lighting is used to obtain the appropriate illumination level at the desired disk radial locations for each experiment. Since the radial disk surface illumination is typically nonuniform due to camera and lighting arrangement restrictions, the lighting intensity is varied along with jet driving temperature to obtain local color change information at various disk radial segments. While the studio lighting represents a high-temperature radiant heat source, its contribution of energy to the disk surface was negligible due to a small view factor and the shielding effect of the disk shroud. This method of data acquisition is not limited to the green signal used in the present study, which results in an indicated surface temperature of 39°C, but may be used with

any color of the TLC display of sufficient intensity and duration.

For the acrylic plastic test surface material used, the depth of heating into the disk over the time duration needed to complete the test is less than the disk thickness. In addition, lateral conduction in the disk is not expected to have a significant effect on the local surface temperature response for the surface heat transfer gradients anticipated, as shown by Vedula et al. (1988) and Metzger and Larson (1986). At any surface point, the disk temperature is thus represented by the classical one-dimensional response of a semi-infinite medium to the sudden step application of a convecting fluid at temperature t_p:

$$(t-t_i)/(t_p-t_i)=1-\exp(h^2\alpha\theta/k^2)\cdot\mathrm{erfc}(h\sqrt{\alpha\theta/k}) \quad (1)$$

If each surface point of interest were subjected to a true step increase in t_p, then measurement of the required times to reach the known color indicating temperature allows solution of equation (1) for the heat transfer coefficients. This is the essence of the method, with the thin coating of TLC material providing a means of acquiring an array of temperature–time pairs covering the surface region of interest.

However, in the actual experiments, the wall surfaces will not experience a pure step change in the driving air temperature because of the transient heating of the upstream nozzle piece and duct walls. Nevertheless, equation (1) is a fundamental solution that can be used to represent the response to a superposed set of elemental steps in t_p, arranged to represent the actual air temperature rise:

$$t-\sum_{i=1}^{N} t_i = U(\theta-\tau_i)\Delta t_p \quad (2)$$

where

$$U(\theta-\tau_i)=1-\exp\left[\frac{h^2\alpha(\theta-\tau_i)}{k^2}\right]\cdot\mathrm{erfc}\left[\frac{h\sqrt{\alpha(\theta-\tau_i)}}{k}\right) \quad (3)$$

In the present experiments, air temperature t_p is determined from thermocouple measurement in the nozzle just prior to jet issue. The t_p variation with time is recorded and approximated by steps, and the resulting superposed solution, equations (2) and (3), is solved for the local surface heat transfer coefficients, using the observed array of local color indication times. The experimental uncertainty for the present study (including possible lighting intensity variations) is estimated to be ± 10 percent, using the methods of Kline and McClintock (1953) for single-sample experiments.

Results and Discussion

Impingement at r = 0. Figure 3 shows local Nusselt numbers for a case with injection at the disk center of rotation, $r_i = 0$. Local Nusselt number in the figure is based on r_o, rather than on local radius, so that the numbers directly indicate the radial variation in local heat transfer coefficient, h. Because of the large variation in h, apparent in the figure, the results were obtained with four different test runs, each employing a different jet temperature driving the transient, and a slightly different lighting source intensity (but essentially the same disk surface illumination over the desired radial locations of each test). In addition to extending the results over a wider radial range, the good agreement between the separate test runs obtained in regions where they overlap provides confidence in the test and data reduction techniques. The results from the three separate tests all agree well within the estimated experimental uncertainty, and this remains the case for subsequent tests, as will be seen in subsequent similar figures.

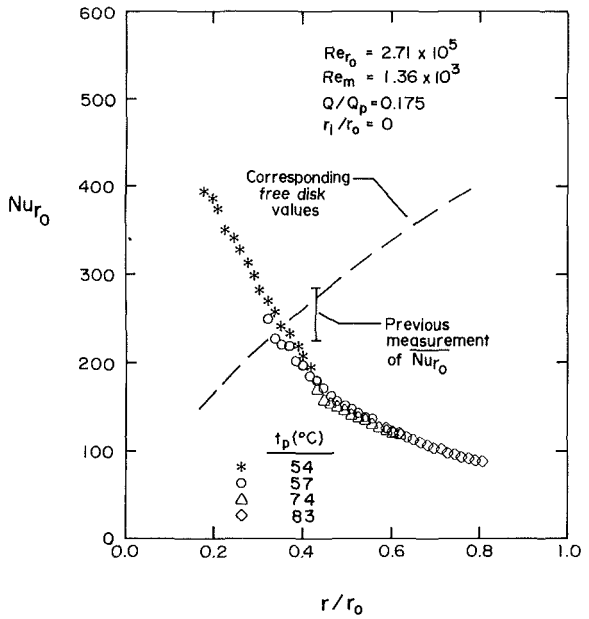

Fig. 3 Radial variation of local Nusselt number, r_i/r_o = 0, Re_{ro} = 2.71 × 10^5, Re_m = 1.36 × 10^3

No similar local heat transfer results are available for comparison with those of Fig. 3, but some additional confidence in the general level of the present results is provided by comparison with the experimental results of Metzger (1970) where radially averaged Nusselt numbers were measured for a configuration geometrically similar to the present case. The average value is shown as a band to account for the possible effect of differences in z/r_o, as shown by both Kreith (1959) and Metzger (1970). The present results are for $z/r_o = 0.1$, where significant lowering of the heat transfer occurs because of the proximity of the shroud, whereas the average results with which they are compared were acquired at $z/r_o = 0.167$.

One immediate observation regarding the character of the results of Fig. 3 is that the radial heat transfer distribution is dominated by the impingement character of the flow and the fact that the total flow rate is provided at the disk center and forced outward through the relatively narrow gap between disk and stator. As a result, the heat transfer coefficients are very high on the center region of the disk, where the forced velocities are large, and then decrease markedly in the radial direction. This is in sharp contrast to the behavior expected for heat transfer in the rotationally induced turbulent boundary layer on a disk without a stator where the heat transfer coefficient is expected to increase with radius. Kreith (1968) and Dorfman (1963) give the usual recommended expression for local turbulent Nusselt number on an isothermal disk, which in terms of Nu_{ro} and Re_{ro} is

$$Nu_{ro}=0.0257Re_{ro}^{0.8}Pr^{0.6}(r/r_o)^{0.6} \quad (4)$$

For the rotational Reynolds number corresponding to that of Fig. 3, equation (4) is shown as the dashed line.

It should also be noted that the supplied flow rate in the present case is significantly less than the amount that would be induced by disk pumping on an unenclosed disk. For the rotationally induced turbulent boundary layer on a full-faced free disk, von Karman (1946) derives the expression

$$Q_p=0.0697\pi r_o Re_{ro}^{0.8} \quad (5)$$

In comparison, the flow rate provided by the jet in Fig. 3 is only 17.5 percent of the amount given by equation (5). This reduced flow rate, in comparison with the freely pumped flow, undoubtedly also contributes to the present low values of h measured on the radially outward portion of the disk.

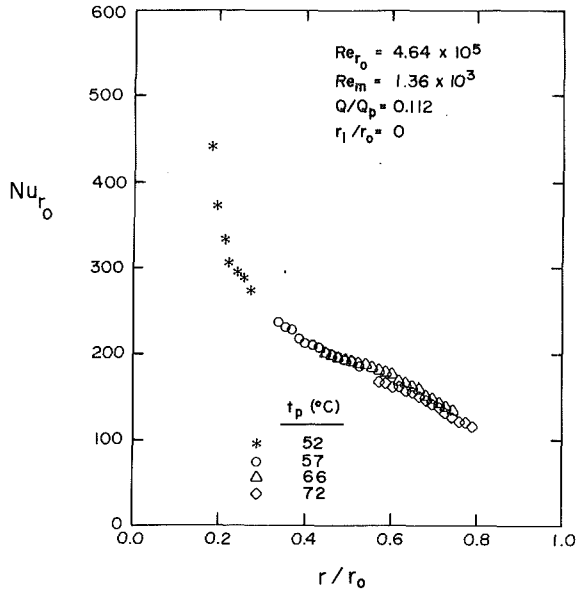

Fig. 4 Radial variation of local Nusselt number, $r_i/r_o = 0$, $Re_{ro} = 4.64 \times 10^5$, $Re_m = 1.36 \times 10^3$

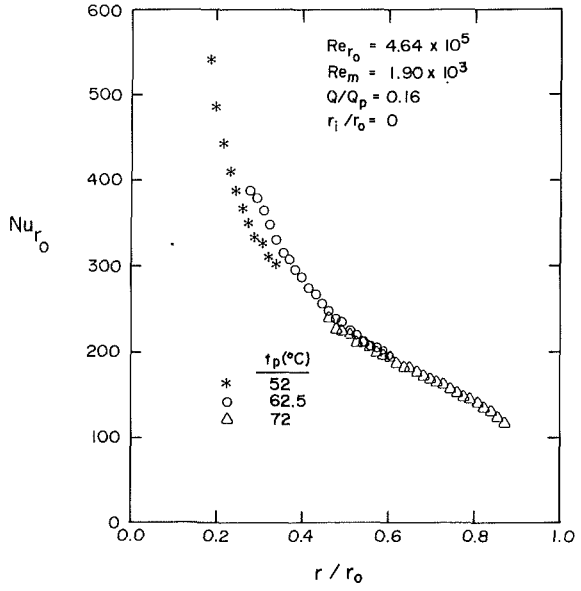

Fig. 6 Radial variation of local Nusselt number, $r_i/r_o = 0$, $Re_{ro} = 4.64 \times 10^5$, $Re_m = 1.90 \times 10^3$

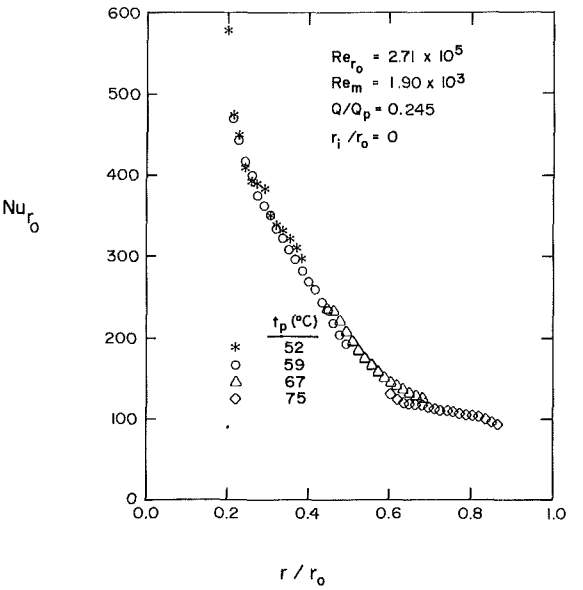

Fig. 5 Radial variation of local Nusselt number, $r_i/r_o = 0$, $Re_{ro} = 2.71 \times 10^5$, $Re_m = 1.90 \times 10^3$

In should be noted that even though the laminar-to-turbulent transition for a free disk has been measured at the order of $Re_r = 2 \times 10^5$ for smooth unenclosed disks, the turbulent expression is used here to estimate the pumping flow at all values of Re_{ro} tested, because the stator and the forced flow have both been shown to hasten transition. Kreith et al. (1963) observed that the presence of a close stator tends to hasten transition, and additionally that a forced source flow is turbulent over the entire surface of the disk for flow Reynolds numbers Re_m greater than 5×10^3. Metzger (1970) measured pumping flows for Re_r down to 5×10^4 that agree quite well with the turbulent expression, equation (5).

Figure 4 shows results similar to those of Fig. 3, obtained with all conditions remaining the same except for an increase in disk rotational speed, increasing Re_{ro} by approximately 70 percent. A slight radial redistribution of the local Nusselt numbers is apparent, but overall the heat transfer level remains essentially the same. This dominance of Re_m over Re_{ro} on Nusselt number is also consistent with the radial average results of Metzger (1970) in the present range of forced flows, but the local details of the radial distributions were not observable in that study because of the physical averaging that took place in the high thermal conductivity disk used.

Figures 5 and 6 show results obtained for test conditions identical to those of Figs. 3 and 4, except for an increase in supplied flow rate, raising Re_m 40 percent. Assuming a reasonable extrapolation of the results from $r/r_o = 0.8$ to $r/r_o = 1.0$, this amount of flow increase raises the observed disk average Nusselt numbers approximately 20 percent for $Re_{ro} = 2.71 \times 10^5$ (compare Figs. 3 and 5), which is in excellent agreement with the average results from Metzger (1970) for a similar value of rotational Reynolds number, $Re_{ro} = 2.06 \times 10^5$. A like comparison of Figs. 4 and 6 for the higher rotational Reynolds number shows an average Nusselt number increase of about 17 percent for the same 40 percent increase in flow rate. The lowering of flow Reynolds number influence as rotational Reynolds number is increased is consistent with what would be expected from the previous average data, although the previous results did not extend to such a high rotational Reynolds number.

Impingement at r>0. Figure 7 shows local Nusselt numbers obtained with impingement at $r_i/r_o = 0.4$. In all aspects except impingement location, conditions are virtually identical to those of Fig. 5. Again, the radial range of the results acquired has been extended by making three separate tests. As evident, little additional information was acquired with the additional test runs beyond what could be reasonably extrapolated from the central set of results, although the good agreement between the separate tests in overlapping regions reinforces confidence in the results. Although not all of the disk radius is covered by the three tests in terms of indicated Nusselt numbers, the nature of the tests does establish that the local Nusselt numbers in the regions not covered are less than the lowest values indicated. Thus reasonable extrapolations from the central set of results are possible, and only a single test run was conducted for each of the remaining off-center impingement cases.

The results of Fig. 7 are typical of all the testing done for radially outward impingement location, as will be seen in subsequent figures. Comparing Figs. 5 and 7 shows that impingement at $r \geq 0$ moves the peak heat transfer to the impingement location but severely reduces the magnitude of the peak heat transfer coefficients. Plausibly, this reduction could be caused

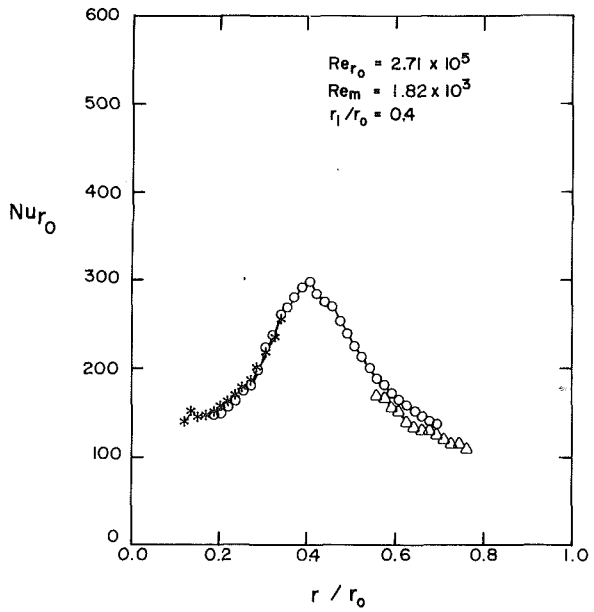

Fig. 7 Radial variation of local Nusselt number, r_i/r_o = 0.4, Re_{ro} = 2.71 × 10^5, Re_m = 1.82 × 10^3

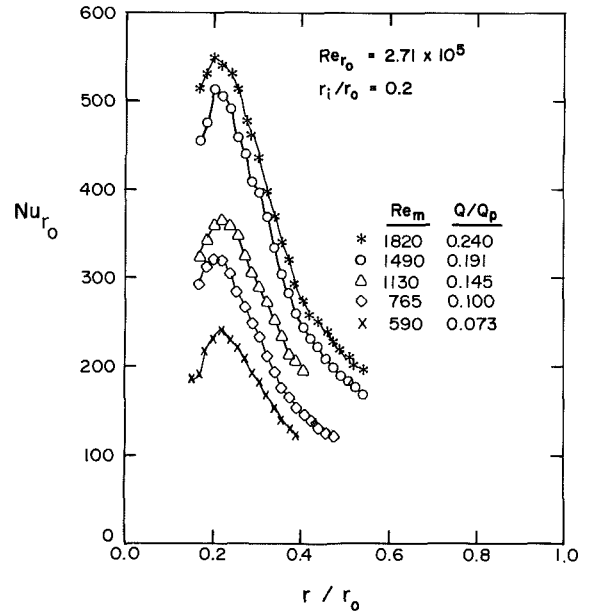

Fig. 8 Effect of Re_m on Nu_{ro}, r_i/r_o = 0.2, Re_{ro} = 2.71 × 10^5

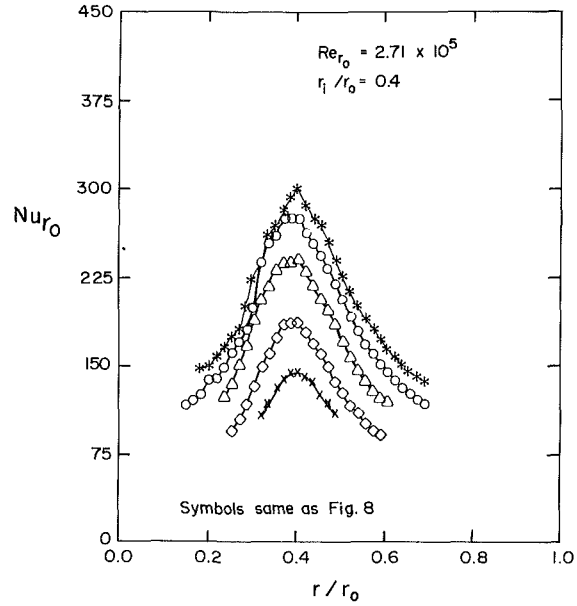

Fig. 9 Effect of Re_m on Nu_{ro} r_i/r_o = 0.4, Re_{ro} = 2.71 × 10^5

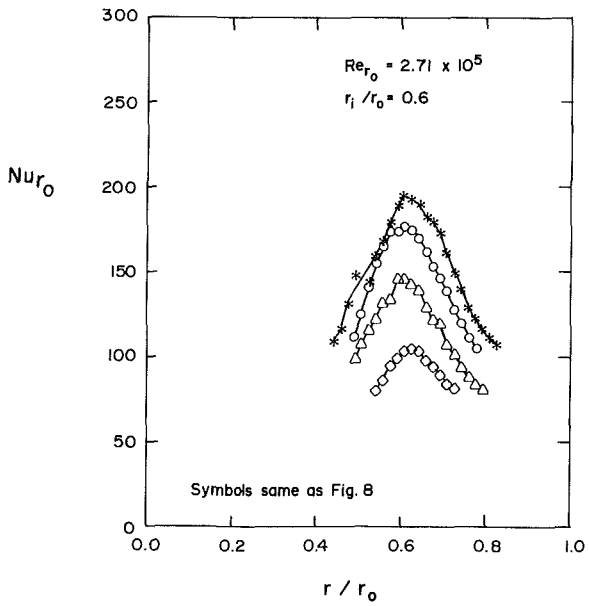

Fig. 10 Effect of Re_m on Nu_{ro} r_i/r_o = 0.6, Re_{ro} = 2.71 × 10^5

by either or both of two factors. First, impingement radially outboard of the disk centerline spreads the heat transfer effect of the jet over a growing (proportional to r) disk area; and, the second, the jet could be deflected by the boundary layer flow pumped between the disk center and the impinging location. However, the near symmetric distribution of heat transfer radially inward and outward from the impingement location strongly suggests that the interaction of the jet with the pumped boundary layer has little effect on the heat transfer near the impingement location. This is reasonable since the jet flow used in the tests of Fig. 7 is nearly four times the local disk pumping flow. The nominal threefold augmentation of local heat transfer at the impingement point indicated in Fig. 7, relative to the surrounding values, is consistent with the "impingement-dominated" regime results of Metzger et al. (1979).

Figures 8–11 present similar results over a range of flow Reynolds numbers for impingement locations r_i/r_o of 0.2, 0.4, 0.6, and 0.8, respectively. The preceeding discussion of Fig. 7 applies equally well to all of the curves shown in Figs. 8–11. Comparison of the results of Fig. 9, for r_i/r_o = 0.4, with those of Fig. 11, for r_i/r_o = 0.8, shows that for the same jet flow rate and disk speed, the heat transfer coefficients for r_i/r_o = 0.8 are slightly greater than one-half of their level for r_i/r_o = 0.4. The heat transfer area swept out by the disk rotation at r/r_o = 0.8 is twice that swept out at r/r_o = 0.4, so these results confirm that the interaction of the jet with the disk pumping flow is not significantly affecting the heat transfer. The rise in heat transfer at r/r_o = 0.8 beyond the one-half value is probably attributable to the heat transfer to the pumped boundary layer, which would be expected to be greater at r/r_o = 0.8 than it is at r/r_o = 0.4.

Finally, Fig. 12 shows a composite plot of the measured local Nusselt numbers for the highest jet flow rate (nominal flow Reynolds number of 1860) at all four nonzero values of

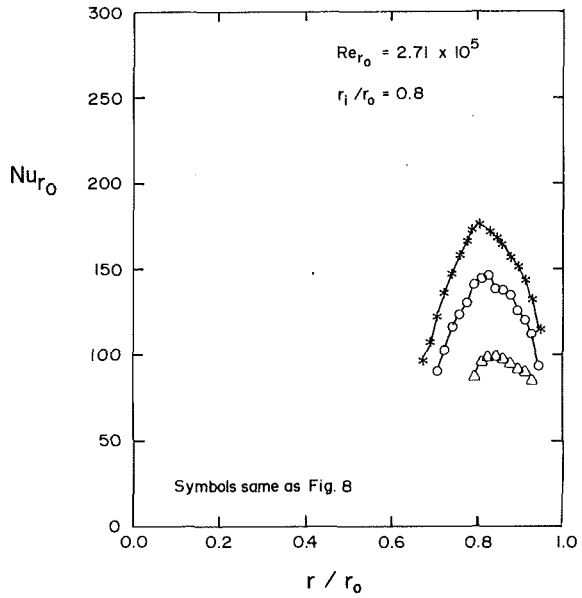

Fig. 11 Effect of Re_m on Nu_{ro} r_i/r_o = 0.8, Re_{ro} = 2.71 × 10^5

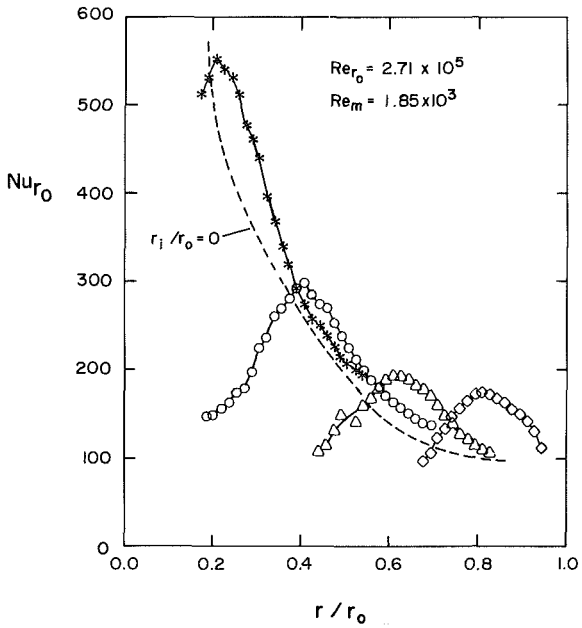

Fig. 12 Effect of r_i/r_o on Nu_{ro}

the impingement radii. Composite plots of local Nusselt number for the lower values of jet flow rate are not shown, but appear very similar to Fig. 12, except for the reduced range of Nusselt number consistent with the smaller flow rates. Superimposed on Fig. 12, for nearly the same conditions as the plotted results, is a dashed line representing a smooth curve through the plotted results in Fig. 3, for impingement onto the disk center at $r_i/r_o = 0$. For a given impingement flow and disk speed, the local radial heat transfer coefficients attained with impingement onto the disk center at $r_i = 0$ appear to establish the general level of the maximum heat transfer possible at the various radii, regardless of the impingement radius. Impingement at radial outboard locations does, however, somewhat increase the local heat transfer in the vicinity of impingement over what would be the case with center-supplied flow, with the increase ranging from a very small amount of $r_i/r_o = 0.2$ to about 80 percent at $r_i/r_o = 0.8$. The distributions indicate that the radial average heat transfer decreases with increasing impingement radius, so that the most efficient use of disk cooling fluid is attained with center impingement. However, in a given application, it may be desirable to tailor the radial heat transfer coefficient distribution, and the results indicate that off-center impingement can be an effective means of doing so.

Summary and Conclusions

The principal conclusions of the present work can be summarized as follows:

- An experimental method has been developed that enables measurements of local convection heat transfer coefficients on rotating surfaces with minimal expense and difficulty. The technique utilizes encapsulated liquid crystals, sprayed in a thin coat onto the test surface to be rotated. The test surface temperature response, indicated by the coating color, is observed and analyzed with a color CCD camera and automated computer analysis.
- The experimental method developed was applied to the measurement of local heat transfer on a rotating disk, with flow between the disk and a closely spaced stationary stator disk provided by jet impingement onto the disk from a single jet nozzle in the stator. The radial location of the jet was varied in discrete steps from the disk center to near the disk edge, and for each location the local Nusselt number variation over the disk face is given for various combinations of jet flow rate and disk rotational speed.
- For a given impingement flow and disk speed, the local radial heat transfer coefficients attained with impingement onto the disk center at $r_i = 0$ establish the general level of the maximum heat transfer possible at the various radii, regardless of the impingement radius.
- Impingement at $r_i \geq 0$ increases the local heat transfer in the vicinity of impingement over what would be the case with center-supplied flow, with the increase ranging from a very small amount with $r_i/r_o = 0.2$ to about 80 percent with $r_i/r_o = 0.8$.
- For a given jet flow rate and disk speed, radial average heat transfer decreases with increasing impingement radius, and the most efficient use of disk cooling fluid is attained with center impingement.

References

Bayley, F. J., and Owen, J. M., 1970, "The Fluid Dynamics of a Shrouded Disk System With a Radial Outflow of Coolant," ASME *Journal of Engineering for Power*, Vol. 92, p. 335.

Bogdan, Z., 1982, "Cooling of a Rotating Disk by Means of an Impinging Jet," *Proceedings, 7th International Heat Transfer Conference*, U. Grigull et al., eds., Hemisphere Publishing Corp., Washington, DC, Vol. 3, pp. 333-336.

Bosch, G., 1988, "Measurement of Local Heat Transfer on Shrouded Rotating Disks With Jet Impingement," MS Thesis, Arizona State University, Tempe AZ.

Butefisch, K. A., 1976, "The Liquid Crystal Method for the Visualization and Measurement of Heat Transfer Distributions," *Methods for Heat Transfer Measurement*, DLR-Mitt 75-11, European Space Agency, Paris, pp. 48-68.

Cobb, E. C., and Saunders, O. A., 1956, "Heat Transfer From a Rotating Disk," *Proceedings of the Royal Society*, Vol. A236, p. 343.

Cooper, T. E., Field, R. J., and Meyer, J. F., 1975, "Liquid Crystal Thermography and Its Application to the Study of Convective Heat Transfer," ASME *Journal of Heat Transfer*, Vol. 97, pp. 442-450.

Daily, J. W., and Nece, R. E., 1960, "Chamber Dimension Effects on Induced Flow and Frictional Resistance of Enclosed Rotating Disks," ASME *Journal of Basic Engineering*, Vol. 82, pp. 217-232.

Den Ouden, C., and Hoogendoorn, C. J., 1974, "Local Convective Heat Transfer Coefficients for Jet Impinging on a Plate—Experiments Using a Liquid Crystal Technique," *Proceedings of the Fifth International Heat Transfer Conference*, Vol. V, AIChE, New York, pp. 293-297.

Dorfman, L. A., 1963, *Hydrodynamic Resistance and the Heat Loss of Rotating Solids*, Oliver and Boyd, London.

Hippensteele, S. A., Russell, L. M., and Stepka, F. S., 1983, "Evaluation of a Method for Heat Transfer Measurements and Thermal Visualization Using a Composite of a Heater Element and Liquid Crystals," ASME *Journal of Heat Transfer*, Vol. 105, pp. 184-189.

Ireland, P. T., and Jones, T. V., 1985, "The Measurement of Local Heat Transfer Coefficient in Blade Cooling Geometries," *AGARD Conference on*

Heat Transfer and Cooling in Gas Turbines, CP 390, Paper No. 28, Bergen.

Ireland, P. T., and Jones, T. V., 1987, "The Response Time of a Surface Thermometer Employing Encapsulated Thermochromic Liquid Crystals," *Journal of Physics E*, Vol. 20, pp. 1195–1199.

Kline, S. J., and McClintock, F. A., 1953, "Describing Uncertainties in Single Sample Experiments," *Mechanical Engineering*, Vol. 75, p. 3.

Kreith, F., Taylor, J. H., and Chong, J. P., 1959, "Heat and Mass Transfer From a Rotating Disk," ASME *Journal of Heat Transfer*, Vol. 81, pp. 95–105.

Kreith, F., Doughman, E., and Kozlowski, H., 1963, "Mass and Heat Transfer From an Enclosed Rotating Disk With and Without Source Flow," ASME *Journal of Heat Transfer*, Vol. 85, pp. 153–163.

Kreith, F., 1968, "Convection Heat Transfer in Rotating Systems," *Advances in Heat Transfer*, Vol. 5, T. F. Irvine and J. P. Hartnett, eds., Academic Press, New York, pp. 129–251.

Metzger, D. E., 1970, "Heat Transfer and Pumping on a Rotating Disk With Freely Induced and Forced Cooling," ASME *Journal of Engineering for Power*, Vol. 92, pp. 342–347.

Metzger, D. E., and Grochowsky, L. D., 1977, "Heat Transfer Between an Impinging Jet and a Rotating Disk," ASME *Journal of Heat Transfer*, Vol. 99, pp. 553–667.

Metzger, D. E., Mathis, W. J, and Grochowsky, L. D., 1979, "Jet Cooling at the Rim of a Rotating Disk," ASME *Journal of Engineering for Power*, Vol. 101, pp. 68–72.

Metzger, D. E., and Larson, D. E., 1986, "Use of Fusion Point Coatings for Local Convection Heat Transfer Measurements in Rectangular Channel Flows With 90 Deg Turns," ASME *Journal of Heat Transfer*, Vol. 108, pp. 48–54.

Owen, J. M., 1984, "Fluid Flow and Heat Transfer in Rotating Disc Systems," *Heat and Mass Transfer in Rotating Machinery*, D. E. Metzger and N. H. Afgan, eds., Hemisphere Publishing Corporation, Washington, DC, pp. 81–103.

Popiel, C. O., Boguslawski, L., and Tuliska, E., 1974, "Heat Transfer From a Rotating Disk in an Impinging Round Air Jet," *Proceedings of the 5th International Heat Transfer Conference*, Vol. 3, pp. 212–216.

Popiel, C. O., and Boguslawski, L., 1986, "Local Heat Transfer From a Rotating Disk in an Impinging Round Jet," ASME *Journal of Heat Transfer*, Vol. 108, pp. 357–364.

von Karman, T., 1921, "Uber Laminare und Turbulente Reibung," *Z. Angew. Math. Mech.*, Vol. 1, p. 233.

von Karman, T., 1946, "On Laminar and Turbulent Friction," NACA Report No. 1092.

Pressure Loss and Heat Transfer in Channels Roughened on Two Opposed Walls

R. E. Mayle
Department of Mechanical Engineering,
Rensselaer Polytechnic Institute,
Troy, NY 12180-3590

Consultant to Pratt & Whitney
East Hartford, CT

In order to increase cooling effectiveness selectively, coolant channels in gas turbine components are often only roughened on one or two walls of the channel. A model is presented for flow in rectangular channels having two opposed roughened walls and a theory is developed for both the pressure loss and heat transfer. The theory allows one to calculate the heat transfer coefficient on each wall separately in addition to the overall friction factor and heat transfer coefficient. Comparisons are made to data for similarly configured channels, tubes, and surfaces roughened by regularly spaced transverse ribs placed normal to the flow direction. Correlations for the displacement velocity in the logarithmic law and the roughness Stanton number in terms of the rib pitch-to-height ratio and roughness Reynolds number are also presented.

Introduction

In most cooling situations, the designer of gas turbine components is faced with cooling a component selectively in order to increase the component's life while using coolant efficiently. For example, the pressure side of a turbine airfoil is cooled differently from, and sometimes separately from, the leading edge or suction side of the airfoil. In these situations, both the cooling schemes and the coolant mass flow may be completely different. Another example is where different walls of a single cooling channel are separately roughened in order to tailor the heat transfer coefficient around the perimeter of the channel. This situation is shown in Fig. 1. Here high heat transfer coefficients (maybe different) are required on the channel walls forming the airfoil's surface in order to cool the surface, while lower heat transfer coefficients are required on the side walls to reduce thermal strains. These channels are often designed with two artificially roughened and two smooth walls, and the designer must know the heat transfer coefficient on each of the walls in order to predict the airfoil's life correctly. Of course, it is also necessary to know the pressure loss for such a channel.

Work on fully developed turbulent flow in rough tubes was conducted by Nikuradse (1933). Nikuradse measured friction factors and velocity profiles in pipes artificially roughened with sand grains and found that the effect of roughness on the fully turbulent velocity distribution when plotted in the law-of-the-wall format was simply to displace it downward by an amount $\Delta u/u_\tau^*$. For fully rough flow in pipes, that is where the roughness Reynolds number $\mathrm{Re}_k = ku_\tau^*/\nu \geq 70$, Schlichting (1979) provides the following correlation for this displacement.

$$\frac{\Delta u}{u_\tau^*} = 2.5 \ln \mathrm{Re}_k - 3.0 \text{ (sand grain)} \qquad (1)$$

where u_τ^* is the shear velocity at the rough wall.

Nunner (1958), Webb et al. (1971), Lewis (1975), Kadar and Yaglom (1977), Han et al. (1978), Gee and Webb (1980), and Sethumadhavan and Raja Rao (1983) investigated the pressure loss and heat transfer in tubes or between roughened parallel plates with repeated roughness elements, while Dvorak (1969), Simpson (1973), and Furuya et al. (1976) examined the development of a turbulent boundary layer on plates roughened by repeated roughness elements. In general, they all found that the constant (=3) in equation (1) depends on the roughness

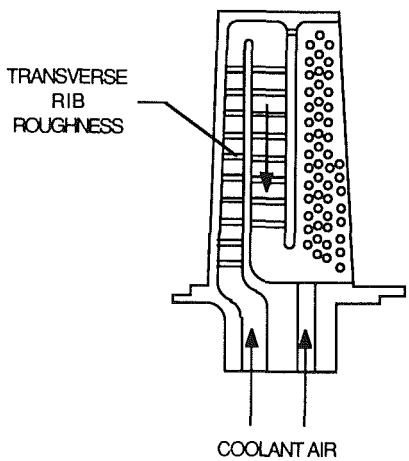

Fig. 1 Cooled turbine airfoil with a multipass, rib-roughened channel

Contributed by the International Gas Turbine Institute and presented at the 34th International Gas Turbine and Aeroengine Congress and Exhibition, Toronto, Ontario, Canada, June 4–8, 1989. Manuscript received at ASME Headquarters January 17, 1989. Paper No. 89-GT-86.

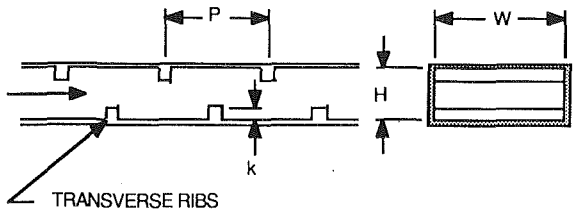

Fig. 2 Rectangular channel with two opposed rib-roughened walls

type being considered. For roughness elements of height k placed across the flow at a pitch P in a tube having a hydraulic diameter of D_H, the above expression may be generalized to the form

$$\frac{\Delta u}{u_r^*} = 2.5 \ln \mathrm{Re}_k + C(P/k, k/D_H) \tag{2}$$

For flow in ribbed tubes with $\mathrm{Re}_k \geq 35$, $P/k \geq 10$, and $0.01 \leq k/D_H \leq 0.04$, Webb et al. obtained

$$C = 5.5 - 0.95(P/k)^{0.53} \tag{3}$$

For $\mathrm{Re}_k \geq 25$, they also obtained an expression for the corresponding displacement in the temperature distribution. The latter may be expressed in the form of a roughness Stanton number St_k (to be defined in the next section) as

$$\mathrm{St}_k = 0.222\, \mathrm{Re}_k^{-0.28}\, \mathrm{Pr}^{-0.57} \tag{4}$$

where Pr is the Prandtl number.

Experiments with flow in straight channels having two opposed roughened walls and two smooth walls were conducted by Burggraf (1970) and more recently by Han (1984), Han et al. (1985), Han and Park (1988), and Han (1988). Work on multipass channels similar to that shown in Fig. 1 has been conducted by Boyle (1984), Han et al. (1988), and Chandra et al. (1988). In each case, channels roughened on two opposite walls were considered with roughness elements in the form of transverse ribs similar to that shown in Fig. 2. This collection of work contains measurements of pressure loss and heat or mass transfer (including very local measurements) for different rib heights, rib pitches, rib angles, channel aspect ratio H/W, and flow Reynolds number Re. In general, it is found that the heat/mass transfer on the rough wall can be 3–4 times greater than the smooth channel result, while the friction factor can be eight times greater. Also, the heat transfer and pressure drop in multipass channels beyond the turn are found to be higher than those in an equivalent straight channel. This effect is attributed to a large separated region and vortical motion in the flow caused by the turning.

In addition, Han (1984) provides a prediction method for determining the pressure drop and heat transfer in rectangular channels with two-opposed roughened walls and two smooth walls. This consists of using a weighted average of both the four-sided smooth and rough friction factors and Stanton numbers to determine the overall values. The friction factor and Stanton number for a four-sided, rib-roughened channel were obtained by using equations (3) and (4) above, after integrating the velocity and temperature profiles across the channel. In reality, however, Han only obtained expressions appropriate to flow between two infinite parallel roughened walls rather than those for a four-sided roughened channel.

The present paper describes a simple model for flow in channels having two opposed rough walls and two smooth walls (as shown in Fig. 2) and presents a theory for calculating the pressure loss and heat transfer in the channel. In particular, the theory is developed for a rectangular channel having identical roughness on the rough walls and for a channel aspect ratio, $H/W \leq 1$. The theory is not, however, limited to this situation and can be just as easily developed for channels having walls of different roughness and $H/W \geq 1$. Similar to that for uniformly roughened tubes, the theory requires that the velocity displacement $\Delta u/u_r^*$ and a roughness Stanton number St_k be known as a function of the roughness. These are shown to be, for the most part, already available in the literature.

Theory

Consider incompressible, fully developed turbulent flow in a straight, rectangular channel as shown in Fig. 2. Consider the upper and lower walls of the channel roughened with either uniformly distributed roughness, three-dimensional turbulators, or by transverse-rib type elements such as shown. In addition, consider the two remaining walls to be smooth. Nikuradse (1926) found that the iso-velocity contours for flow in a smooth-wall rectangular channel are approximately rectangular, as shown in Fig. 3(*a*), such that each wall affects the flow in a region immediately adjacent to it and outward toward the center of the duct in a nearly two-dimensional manner. Assuming a similar distribution of contours in channels with two opposed rough walls and two smooth, the flow above each wall can be considered two dimensional within its own region of influence. Consider the two rough walls to have identical

Nomenclature

A = channel flow area
c = specific heat
D_H = hydraulic diameter
f = friction factor
H = channel height
k = roughness height
L = length of channel
p = pressure
P = pitch of roughness element
Pr = Prandtl number
Pr_t = turbulent Prandtl number
q = heat flow per unit area
r = channel aspect ratio = H/W
Re = Reynolds number based on hydraulic diameter and average flow velocity
Re_k = roughness Reynolds number
St = Stanton number
St_k = roughness Stanton number
T = temperature
T_b = bulk temperature
T_m = maximum temperature
T_w = wall temperature
u = local velocity = $u(y)$
u^+ = dimensionless velocity = u/u^*
u^* = friction velocity
U = average flow velocity
U_m = maximum flow velocity
W = channel width
x = distance in flow direction
y = distance normal to wall
y^+ = dimensionless distance = yu^*/ν
α = thermal diffusivity
ϵ_h = eddy diffusivity
ϵ_m = eddy viscosity
ν = kinematic viscosity
ρ = density
τ = shear stress

Subscripts

r = quantity associated with rough wall
s = quantity associated with smooth wall

Figure 3a

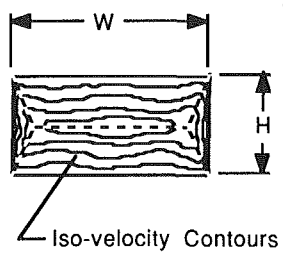

Figure 3b

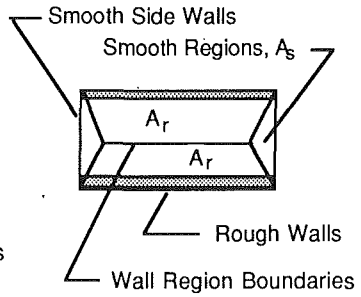

Figure 3c

Final Geometric Description

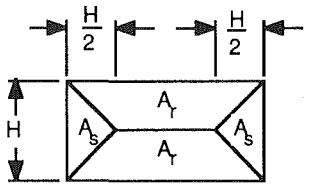

Fig. 3 Rough and smooth wall regions of influence

roughness. Then the regions of influence from each wall will be geometrically symmetric about the horizontal and vertical planes passing through the center of the channel and the "boundaries" of these regions will look as shown in Fig. 3(*b*). In reality these boundaries are more likely curved and could be determined by matching the velocity in each region at them, but this is too complicated for a simple model. For simplicity, further assume that the boundary between adjacent regions in the corners simply bisects the corner as shown in Fig. 3(*c*). This is somewhat more difficult to accept since the secondary flow near the corner and shear stress distribution on the two meeting walls determine this angle. Nevertheless, the assumption is a reasonable approximation, as will be indicated, and allows one to define the regions of influence solely on a geometric basis. With only these assumptions the analysis becomes rather straightforward in that it uses two-dimensional methods (similar to those described by Kays and Crawford, 1980) to determine both the overall and individual-wall friction factors and Stanton numbers. Here, it should be noted that once regions of influence are defined, the same analysis can be applied with little alteration to flow in channels of any shape and with different roughness on each wall.

Pressure Loss. For fully developed channel flow, the net change in inertia forces vanishes and the momentum equation becomes

$$\Delta p\, HW = 2(H\tau_s + W\tau_r)L \tag{5}$$

where Δp is the pressure loss in a length L of the channel, H is the channel height, W is the channel width, and τ_s and τ_r are the shear stresses on the smooth and rough walls, respectively. The overall friction factor f is defined by

$$f = \frac{D_H}{4L}\frac{\Delta p}{(\rho U^2/2)} \tag{6}$$

where $D_H = 2HW/(W+H)$ is the hydraulic diameter of the channel, ρ is the fluid density, and U is the average velocity. Define the friction factors on the smooth and rough walls as

$$f_s = \frac{\tau_s}{(\rho U^2/2)} \text{ and } f_r = \frac{\tau_r}{(\rho U^2/2)} \tag{7}$$

Equations (5)–(7) may be combined to yield

$$f = \frac{1}{1+r}(rf_s + f_r) \tag{8}$$

where r is the channel aspect ratio H/W. This states that the overall friction factor is the area-weighted average of the smooth- and rough-wall friction factors but, in this case, f_s and f_r are not equal to the four-sided values defined by Han (1984). The velocity distributions in the separate regions of influence, using law of the wall notation, are

$$u_s^+ = A_1 \ln y_s^+ + B \quad \text{(smooth)}$$
$$u_r^+ = A_1 \ln y_r^+ + B - \frac{\Delta u}{u_r^*} \quad \text{(rough)} \tag{9}$$

where u_i^+ ($i = s$ or r) is the local velocity u divided by the friction velocity $u_i^* = \sqrt{\tau_i/\rho} = \sqrt{f_i/2}\,U$, A_1 and B are constants, y_i^+ is yu_i^*/ν where y is the distance normal to the wall, ν is the kinematic viscosity, and Δu is the shift in the logarithmic profile caused by roughness. The maximum velocity in the channel is found along the central line in the channel. According to Fig. 3(*c*), this corresponds to the position $y = H/2$ in each region, which, from equation (9), provides

$$\sqrt{2/f_s}\left(\frac{U_m}{U}\right) = A_1 \ln (H_s^+/2) + B \quad \text{(smooth)}$$
$$\sqrt{2/f_r}\left(\frac{U_m}{U}\right) = A_1 \ln (H_r^+/2) + B - \frac{\Delta u}{u_r^*} \quad \text{(rough)} \tag{10}$$

where

$$H_i^+ \equiv \frac{Hu_i^*}{\nu} = \frac{1+r}{2}\,\mathrm{Re}\sqrt{f_i/2}; \qquad (i = s \text{ or } r) \tag{11}$$

and where Re is the Reynolds number based on the channel's average velocity U and hydraulic diameter D_H. If one prefers, the regions of influence as shown in Fig. 3(*b*) can be accommodated here by introducing a factor (less than unity) that changes (reduces) the height of the region of influence for the smooth walls. This factor, however, must be determined by some other means, presumably from a statement involving the shear stresses on each wall. Some calculations were carried out including such a factor, but its effect was found to be small and not worth the additional complexity.

Integrating the velocity distribution over the whole flow area to obtain the total flow through the channel provides another expression relating the average and maximum velocities in the channel, namely

$$U = \frac{1}{HW}\left[2\int_{A_s} u\,dA + 2\int_{A_r} u\,dA\right]$$
$$= U_m\left[1 + \frac{3}{4}rA_1\sqrt{f_s/2} + \left(1 - \frac{1}{4}r\right)A_1\sqrt{f_r/2}\right]^{-1} \tag{12}$$

In the above integrals, dA is the infinitesimal area perpendicular to the flow direction, u is the appropriate velocity distribution given in equation (9), and A_s and A_r are the areas of the smooth and rough regions of influence.

Equations (8), (10), and (12) can be simplified by eliminating U_m/U and H_i^+. This provides the following set of equations:

$$f = \frac{1}{1+r}(rf_s + f_r)$$

$$\sqrt{f_s/2} = \frac{1 + \left(1 - \frac{1}{4}r\right)A_1\sqrt{f_r/2}}{A_1 \ln\left(\frac{1+r}{4}\mathrm{Re}\sqrt{f_s/2}\right) + B - \frac{3}{4}rA_1} \tag{13}$$

$$\sqrt{f_r/2} = \frac{1 + \frac{3}{4}rA_1\sqrt{f_s/2}}{A_1 \ln\left(\frac{1+r}{4}\mathrm{Re}\sqrt{f_r/2}\right) + B - \Delta u/u_r^* - \left(1 - \frac{1}{4}r\right)A_1}$$

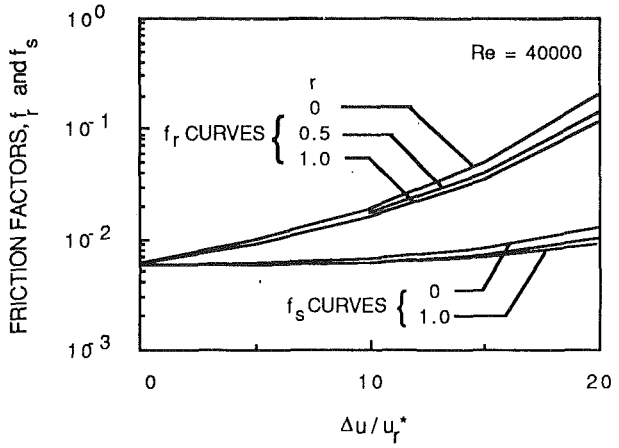

Fig. 4 Effect of aspect ratio on rough and smooth wall friction factors

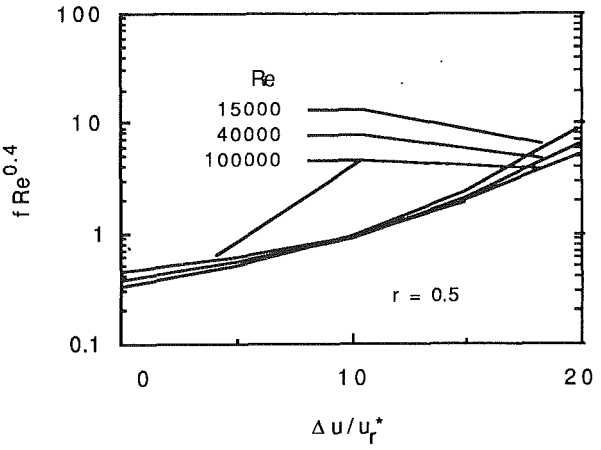

Fig. 6 Overall friction factor variation with Reynolds number

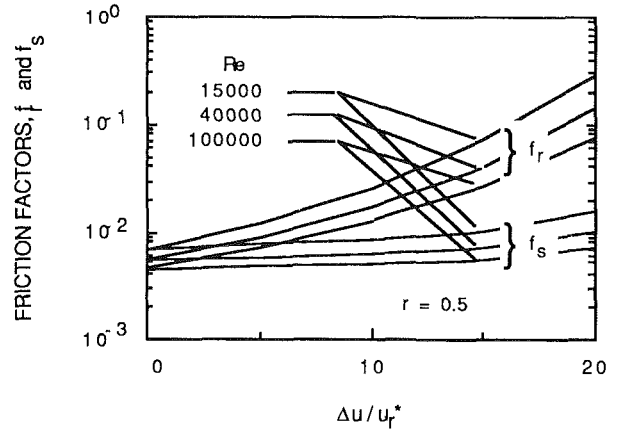

Fig. 5 Effect of Reynolds number on rough and smooth wall friction factors

Once $\Delta u/u_r^*$ is known, this set of equations may be solved for the friction factor f using an iterative method of solution. It should be noted here that the individual-wall friction factors f_s and f_r are obtained as well. For rib-type roughness, a correlation for $\Delta u/u_r^*$ will be provided below. For sand grain roughness, however, one may use equation (1).

For $r \to 0$, it is easy to see that $f \to f_r$ with f_r determined through the last equation in the above set. This is identical to that obtained for flow between two infinite, parallel, rough walls and is equivalent to Han's (1984) equation (16).

For $\Delta u = 0$ (all walls smooth) and $r = 1$ (square channel), $f_r = f_s = f$ is to be expected. Comparing either one of the last two equations in (13) with $\Delta u = 0$ to the expression for a smooth wall friction factor as given by Schlichting (1979, equation 20.30) yields $A_1 = 2.46$ and $B = 5.68$. These values will be used from now on.

Calculations were carried out using equation (13) for various values of r, $\Delta u/u_r^*$, and Re. The variation of the rough- and smooth-wall friction factors with $\Delta u/u_r^*$ for different channel aspect ratios is shown in Fig. 4. In this figure, Re = 40,000. Increasing $\Delta u/u_r^*$ implies increasing roughness. As can be seen, the rough-wall friction factor rises quickly to values 5–10 times greater than the smooth-wall values. The latter, in turn, are 1–2 times greater than the four-sided, smooth-wall value found at $\Delta u/u_r^* = 0$. Notice also, in agreement with the concept of using a hydraulic diameter as the characteristic channel dimension, that the four-sided, smooth-wall friction factor is independent of the channel aspect ratio. This is, however, not true for a channel with walls of different roughness. For a channel with two opposed rough walls, the difference in the rough friction factor can be as much as 50 percent between the $r = 0$ and $r = 1$ results, while that for the smooth friction factor is somewhat less.

The variation of the rough and smooth friction factors with $\Delta u/u_r^*$ for various Reynolds numbers is shown in Fig. 5. These calculations were done for $r = 0.5$. The variation with Reynolds number is very nearly given by $\mathrm{Re}^{-0.4}$. Using this, a relation between the overall friction factor and $\Delta u/u_r^*$ for $r = 0.5$ is shown in Fig. 6. Although this figure may be used to obtain a quick idea of the friction factor once $\Delta u/u_r^*$ is known, it is recommended that equation (13) be used.

Heat Transfer. Consider heat transfer from a channel as shown in Fig. 2 with all walls having a uniform, constant wall temperature T_w. If q is the total heat transferred from the walls per unit area to the fluid, then a heat balance on an element of fluid of length dx yields

$$2q(H+W) = 2(Hq_s + Wq_r) = \rho cUA \frac{dT_b}{dx} \tag{14}$$

where q_s and q_r correspond to the heat transferred from the smooth and rough walls, respectively, c is the specific heat, A is the channel's cross-sectional area, T_b is the bulk temperature, and x is the distance along the length of the channel. Define an overall Stanton number St, and Stanton numbers for the smooth and rough walls, St_s and St_r, as

$$\mathrm{St}_i \equiv \frac{q_i}{\rho cU(T_w - T_b)}; \qquad i = \text{nothing, } s, \text{ or } r \tag{15}$$

Then the first equality in equation (14) may be written as

$$\mathrm{St} = \frac{1}{1+r}(r\mathrm{St}_s + \mathrm{St}_r) \tag{16}$$

Note the similarity between equation (16) and equation (8). Once the overall Stanton number is known, the fluid's bulk temperature distribution can be determined from the second equality in equation (14), i.e.,

$$T_w - T_b = (\text{const}) \times \exp\left(-\frac{4\mathrm{St}}{D_H} x\right)$$

The temperature distribution in each region of influence is determined by using Reynolds analogy in each region. This may be written as

$$\frac{dT_i}{(q_i/\rho c)} = -\frac{(\nu + \epsilon_m)_i}{(\alpha + \epsilon_h)_i} \frac{du_i}{(\tau_i/\rho)}; \qquad i = r \text{ or } s \tag{17}$$

where ν is the kinematic viscosity, ϵ_m is the eddy viscosity, α is the thermal diffusivity, and ϵ_h is the eddy diffusivity. Integrating equation (17) between the limits $y = 0$ and $H/2$, and

introducing the definitions for the Stanton number, equation (15), and friction factors, equation (7), one obtains

$$\frac{1}{\mathrm{St}_i}\frac{T_w-T_m}{T_w-T_b}=\sqrt{\frac{2}{f_i}}\int_0^{H_i^+/2}\mathrm{Pr}_t\frac{(1+\epsilon_m/\nu)_i}{(\mathrm{Pr}_t/\mathrm{Pr}+\epsilon_h/\nu)_i}\frac{du_i^+}{dy_i^+}\,dy_i^+ \tag{18}$$

where T_m is the maximum temperature (temperature at $y=H/2$), Pr_t is the turbulent Prandtl number ϵ_m/ϵ_h (≈ 0.9), and Pr is the molecular Prandtl number ν/α (air; ≈ 0.7). Away from the walls, since $\mathrm{Pr}_t/\mathrm{Pr}\approx 1$ and $\epsilon_m/\nu \gg 1$, the integrand in equation (18) simplifies to $\mathrm{Pr}_t\,du_r^+$ and may be evaluated using equation (9). Near the walls, however the integration in the rough- and smooth-wall regions must be treated differently. The integral for the rough-wall region will now be evaluated, then that for the smooth-wall region.

Near the rough wall, the velocity distribution is unknown. Therefore, the integral for the rough-wall region is evaluated in two parts: (1) from the wall to the top of the roughness elements, and (2) from the roughness elements to half the channel height. This provides

$$\frac{1}{\mathrm{St}_r}\frac{T_w-T_m}{T_w-T_b}=\sqrt{\frac{2}{f_r}}\left[\frac{1}{\mathrm{St}_k}+\mathrm{Pr}_t\int_{k_r^+}^{H_r^+/2}\frac{du_r^+}{dy_r^+}\,dy_r^+\right] \tag{19}$$

where the turbulent Prandtl number has been assumed constant, and where a roughness Stanton number St_k has been defined as

$$\mathrm{St}_k\equiv\left[\mathrm{Pr}_t\int_0^{k_r^+}\frac{(1+\epsilon_m/\nu)_r}{(\mathrm{Pr}_t/\mathrm{Pr}+\epsilon_h/\nu)_r}\frac{du_r^+}{dy_r^+}\,dy_r^+\right]^{-1} \tag{20}$$

The quantity St_k must be determined experimentally as will be discussed below. From equation (9) one obtains $du_r^+/dy_r^+ = 2.46/y_r^+$ ($A_1 = 2.46$). Substituting this into equation (19) and integrating provides an expression for the Stanton number on the rough walls:

$$\mathrm{St}_r=\frac{\sqrt{f_r/2}}{[1/\mathrm{St}_k+2.46\mathrm{Pr}_t\ln(H/2k)]}\frac{T_w-T_m}{T_w-T_b} \tag{21}$$

An expression for the Stanton number on the smooth walls can be obtained by setting $i = s$ in equation (18) and using the law of the wall for u_s^+. Similar to Kays and Crawford, use

$$\begin{aligned}
&u_s^+ = y_s^+, \quad \epsilon_m/\nu=0; && 0<y_s^+<5\\
&u_s^+ = 5.0\ln y_s^+ - 3.05, \ \epsilon_m/\nu=y_s^+/5-1; && 5<y_s^+<30\\
&u_s^+ = 2.46\ln y_s^+ + 5.68, \ \epsilon_m/\nu \gg 1; && y_s^+>30
\end{aligned} \tag{22}$$

The last equation in the above set is identical to that in equation (9) with $A_1 = 2.46$ and $B = 5.68$. The expressions for ϵ_m have been obtained using $\tau_s = (\nu+\epsilon_m)(du_s/dy) = \text{const}$. Substituting these expressions for u_s^+ and ϵ_m into equation (18), integrating, and solving for St_s provides

$$\mathrm{St}_s=\frac{\sqrt{f_s/2}}{5\mathrm{Pr}+\mathrm{Pr}_t\ln[5(\mathrm{Pr}/\mathrm{Pr}_t)+1]+\mathrm{Pr}_t\ln(H_s^+/60)}\frac{T_w-T_m}{T_w-T_b} \tag{23}$$

The bulk temperature is defined as

$$T_b=\int_A uTdA\Big/\int_A udA \tag{24}$$

This may be evaluated using either the exact velocity and temperature profile distributions or reasonable approximations to them. In the interest of simplicity, a 1/7th power law profile will be used for each distribution in both the smooth and rough regions, namely

$$\frac{u}{U_m}=\frac{T-T_w}{T_m-T_w}=\left(\frac{2y}{H}\right)^{\frac{1}{7}} \tag{25}$$

Substituting these expressions into equation 24 and evaluating yields

$$\frac{T_b-T_w}{T_m-T_w}=\frac{8}{9}\frac{(1-0.125r)}{(1-0.067r)}\approx 0.85 \tag{26}$$

to within 3 percent for $0 < r < 1$.

The overall Stanton number is then obtained by substituting equations (21), (23), and (26) into equation (16). For Pr = 0.72, $\mathrm{Pr}_t = 0.9$, this yields

$$\mathrm{St}=\frac{1.17}{1+r}\left(\frac{r\sqrt{f_s/2}}{1.78+2.21\ln H_s^+}+\frac{\sqrt{f_r/2}}{1/\mathrm{St}_k+2.21\ln(H/2k)}\right) \tag{27}$$

where H_s^+ has been defined in equation (11).

For $r\to 0$, the resulting Stanton number approaches that for flow between two infinite, parallel walls as it should. The limit when the roughness is reduced to zero, however, is not that found for flow in a completely smooth channel since St_k combines the resistances to heat flow from both the sublayer and roughness. This can be seen by rearranging the last term in equation (27) to

$$\frac{\sqrt{f_r/2}}{[1/\mathrm{St}_k-3.31-2.21\ln k_r^+]+1.78+2.21\ln H_r^+}$$

and comparing with the first term. For $k_r^+ = 0$ (no roughness), the term in brackets in the denominator should vanish in order that the resistance to heat flow from all the walls be identical. Using the present definition for St_k (equation (20)) the term becomes -3.31, and suggests that a new roughness Stanton number, say $(1/\mathrm{St}_k)_{\text{new}} = 1/\mathrm{St}_k - 3.31$, should be used. Since values of St_k are near 0.04, this would represent about a 12 percent correction to the present definition. In the following, however, St_k as defined originally is used.

A simpler expression for the overall Stanton number can be realized by rewriting the equation for St_s. Eliminating H_s^+ in equation (23) by using equation (10), realizing that $\mathrm{St}_s \ll 1$, and substituting the numerical values for Pr and Pr_t, one obtains the relatively simple result

$$\mathrm{St}_s = 0.65\left(\frac{U}{U_m}\right)f_s = 0.50(1-0.125r)f_s$$

or simply

$$\mathrm{St}_s \approx 0.47\,f_s \text{ (within 6 percent)};\ \mathrm{Pr} = 0.7,\ \mathrm{Pr}_t = 0.9 \tag{28}$$

A similar simple expression relating St_r and f_r cannot be obtained. Hence, the overall Stanton number, equation (27), is well represented by

$$\mathrm{St}=\frac{1}{1+r}\left(0.47rf_s+\frac{1.17\sqrt{f_r/2}}{1/\mathrm{St}_k+2.21\ln(H/2k)}\right) \tag{29}$$

since the contribution from the smooth wall to the overall Stanton number in most instances is usually small compared to that from the rough wall. Once the channel geometry, Reynolds number, friction factors f_s and f_r, and roughness Stanton number are known, the overall Stanton number can be obtained from the above expression. The rough- and smooth-wall Stanton numbers are then provided by equations (21) (using $\mathrm{Pr}_t = 0.9$ and a temperature ratio of 1.17) and (28), respectively. The latter is a simple relation. The rough-wall Stanton number divided by the square root of the rough wall friction factor, $\mathrm{St}_r\sqrt{f_r}$, is plotted as a function of the roughness Stanton number, St_k, and relative roughness, k/H, in Fig. 7. As either the roughness Stanton number or the relative roughness increases, the normalized Stanton number increases. This curve may be used directly to obtain the rough-wall Stan-

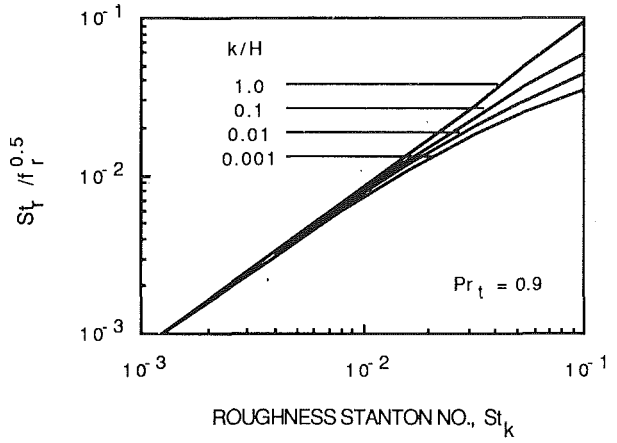

Fig. 7 Effect of roughness height and Stanton number on the rough-wall Stanton number

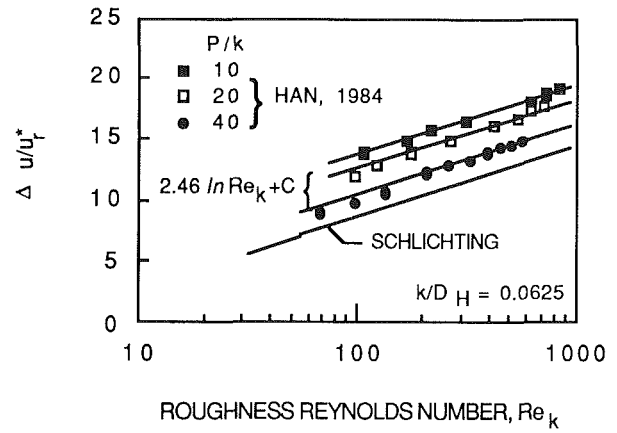

Fig. 8 Effect of roughness Reynolds number and pitch-to-height ratio on the velocity profile

ton number once f_r and the roughness Stanton number are known. Notice that St_r and St_s are affected by the channel aspect ratio only through its influence on f_r and f_s.

Comparisons With Experiments

The main comparisons are made using Han's (1984) results for a square channel with traverse, square-shaped ribs placed normal to the flow at pitch-to-height ratios of 10, 20, and 40. Values of $\Delta u/u_r^*$ were obtained by solving equation (13) using his measurements of overall friction factor. The results are shown in Fig. 8 for $k/D_H = 0.0625$ where $\Delta u/u_r^*$ is plotted against the roughness Reynolds number. The result for sand roughened channels, equation (1), is also shown. All of the data may be expressed in the generalized format given in equation (2) where the best fit yields $C = 2.3$, 1.1, and -1.0 for $P/k = 10$, 20, and 40, respectively. A plot of C as a function of the roughness pitch-to-height ratio is shown in Fig. 9. This figure also includes the results of Furuya et al. for boundary layer flow over a plate with circular rods and the correlation of Webb et al. for rib-roughened tubes, i.e., equation (3). The agreement of all the results in this format is remarkable. A somewhat better correlation

$$C = 5.62 - P/k^{0.5} \qquad (P/k \geq 10) \tag{30}$$

includes the boundary layer results as well.

Han's rough wall Stanton numbers, St_r, were used to determine the roughness Stanton number from equation (21) with $Pr_t = 0.9$. As above, the rough-wall friction factor was determined from equation (13) and his corresponding values of

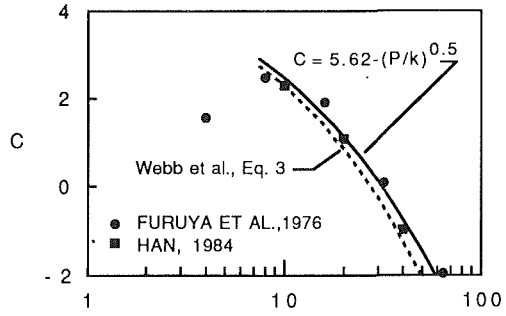

Fig. 9 Parameter C variation with roughness pitch-to-height ratio

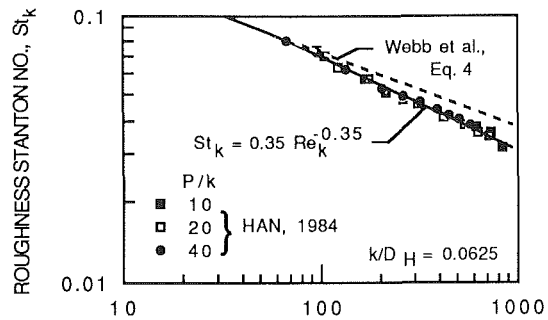

Fig. 10 Roughness Stanton number variation with roughness Reynolds number

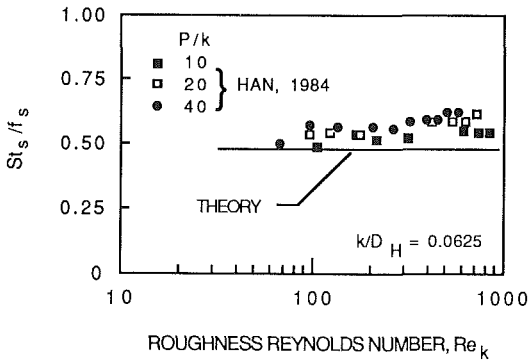

Fig. 11 Smooth-wall Stanton number results

f. The result is shown in Fig. 10 where the roughness Stanton number is plotted against the roughness Reynolds number. Within the accuracy of the experiments, it is seen that the roughness Stanton number is independent of the pitch-to-height ratio. The correlation of Webb et al., equation (4), is also shown. A better correlation to the data is given by

$$St_k = 0.35\ Re_k^{-0.35} \text{ (air)} \tag{31}$$

Han's smooth-wall Stanton number results were divided by the smooth-wall friction factor determined from equation (13) and plotted in Fig. 11. Although the ratio St_s/f_s is nearly independent of the roughness pitch-to-height ratio and constant as predicted by the theory, the average lies about 15 percent above the theoretical value of 0.47. The reason for this discrepancy is not yet known.

Conclusions

A relatively simple model has been presented that allows one to calculate the overall and individual-wall friction factors and Stanton numbers. An analysis, which was completed for two opposed rough walls in a rectangular channel, showed that

the rough-wall friction factor rises quickly to values 5–10 times greater than the smooth-wall values as the roughness is increased. In addition, it was found that the effect of aspect ratio becomes quite significant at large roughness and that errors up to 40–50 percent are possible if it is not taken into account properly. The theory also predicts that the ratio of the smooth-wall Stanton number to friction factor, St_s/f_s, is nearly constant.

The theory was also used to evaluate overall friction factor and individual-wall Stanton number data for a two opposed wall, rib-roughened channel. The friction factor results were found to compare quite well to available information for flow in rib-roughened tubes and over rib-roughened surfaces. In order to include the boundary layer results, a new correlation, i.e.,

$$C = 5.62 - P/k^{0.5},\ P/k \geq 10,$$

is proposed. The comparison of the Stanton number results showed that the roughness Stanton number for two opposed wall, rib-roughened channels is independent of the roughness pitch-to-height ratio and is better correlated using

$$St_k = 0.35\ Re_k^{-0.35}\ \text{(air)}$$

It was also shown that the ratio of the smooth-wall Stanton number to friction factor is nearly independent of the roughness pitch-to-height ratio and roughness Reynolds number as predicted by theory.

Acknowledgments

The author is truly indebted both to Pratt & Whitney and Alexander von Humboldt Stiftung, Federal Republic of Germany. The theory presented in this paper was first developed for P & W. The comparisons with experiments and paper composition were completed during the author's tenure at the Institute für Thermische Strömungsmaschinen, Universität Karlsruhe as a recipient of the Alexander von Humboldt Award for Senior Scientist.

References

Boyle, R. J., 1984, "Heat Transfer in Serpentine Passages With Turbulence Promoters," ASME Paper No. 84-HT-24.

Burggraf, F., 1970, "Experimental Heat Transfer and Pressure Drop With Two-Dimensional Turbulence Promoter Applied to Two Opposite Walls of a Square Tube," *Augmentation of Convective Heat and Mass Transfer*, A. E. Bergles and R. L. Webb, eds., ASME, New York, pp. 70–79.

Chandra, P. R., Han, J. C., and Lau, S. C., 1988, "Effect of Rib Angle on Local Heat/Mass Transfer Distribution in a Two-Pass Rib-Roughened Channel," ASME JOURNAL OF TURBOMACHINERY, Vol. 110, pp. 233–241.

Dvorak, F. A., 1969, "Calculation of Turbulent Boundary Layers on Rough Surfaces in Pressure Gradient," *AIAA Journal*, Vol. 7, pp. 1752–1759.

Furuya, Y., Miyata, M., and Fujita, H., 1976, "Turbulent Boundary Layer and Flow Resistance on Plates Roughened by Wires," ASME Paper No. 76-FE-6.

Gee, D. L., and Webb, R. L., 1980, "Force Convection Heat Transfer in Helically Rib-Roughened Tubes," *International Journal of Heat and Mass Transfer*, Vol. 23, pp. 1127–1136.

Han, J. C., Glicksman, L. R., and Rohsenow, W. M., 1978, "An Investigation of Heat Transfer and Friction for Rib-Roughened Surfaces," *International Journal of Heat and Mass Transfer*, Vol. 21, pp. 1143–1156.

Han, J. C., 1984, "Heat Transfer and Friction in Channels With Two Opposite Rib-Roughened Walls," ASME *Journal of Heat Transfer*, Vol. 106, pp. 774–781.

Han, J. C., Park, J. S., and Lei, C. K., 1985, "Heat Transfer Enhancement in Channels With Turbulence Promoters," ASME *Journal of Engineering for Gas Turbines and Power*, Vol. 107, pp. 628–635.

Han, J. C., 1988, "Heat Transfer and Friction Characteristics in Rectangular Channels With Rib Turbulators," ASME *Journal of Heat Transfer*, Vol. 110, pp. 321–328.

Han, J. C., Chandra, P. R., and Lau, S. C., 1988, "Local Heat/Mass Transfer Distributions Around Sharp 180° Turns in Two-Pass Smooth and Rib-Roughened Channels," ASME *Journal of Heat Transfer*, Vol. 110, pp. 91–98.

Han, J. C., and Park, J. S., 1988, "Developing Heat Transfer in Rectangular Channels With Rib Turbulators," *International Journal of Heat and Mass Transfer*, Vol. 31, pp. 183–195.

Kader, B. A., and Yaglom, A. M., 1977, "Turbulent Heat Transfer From a Wall With Parallel Roughness Ridges," *International Journal of Heat and Mass Transfer*, Vol. 20, pp. 354–357.

Kays, W., and Crawford, M., 1980, *Convective Heat and Mass Transfer*, McGraw-Hill, New York.

Lewis, M. J., 1975, "An Elementary Analysis for Predicting the Momentum and Heat Transfer Characteristics of a Hydraulically Rough Surface," ASME *Journal of Heat Transfer*, Vol. 97, pp. 249–254.

Nikuradse, J., 1926, "Untersuchungen über die Geschwindigkeitsverteilung in turbulenten Strömungen," Diss. Göttingen, or see Schlichting, 1979, Fig. 20.13.

Nikuradse, J., 1933, "Strömungsgesetze in rauhen Rohren," *Forsch. Arb. Ing.-Wes. Heft* 361, or 1950, "Laws of Flow in Rough Pipes," NACA TM 1292.

Nunner, W., 1958, "Heat Transfer and Pressure Drop in Rough Tubes," AERE lib/Trans. 786.

Schlichting, H., 1979, *Boundary Layer Theory*, McGraw-Hill, New York.

Sethumadhavan, R., and Raja Rao, M., 1983, "Turbulent Flow Heat Transfer and Fluid Friction in Helical-Wire-Coil-Inserted Tubes," *International Journal of Heat and Mass Transfer*, Vol. 26, pp. 1833–1844.

Simpson, R. L., 1973, "A Generalized Correlation of Roughness Density Effects on the Turbulent Boundary Layer," *AIAA Journal*, Vol. 11, pp. 242–244.

Webb, R. L., Eckert, E. R. G., and Goldstein, R. J., 1971, "Heat Transfer and Friction in Tubes With Repeated-Rib Roughness," *International Journal of Heat and Mass Transfer*, Vol. 14, pp. 601–617.

Aerodynamic and Torque Characteristics of Enclosed Co/Counterrotating Disks

W. A. Daniels
Research Engineer.

B. V. Johnson
Supervisor,
Heat Transfer Technology.

United Technologies Research Center,
East Hartford, CT 06108

D. J. Graber
Project Engineer,
Pratt and Whitney Engineering Division,
West Palm Beach, FL 33410

Experiments were conducted to determine the aerodynamic and torque characteristics of adjacent rotating disks enclosed in a shroud. These experiments were performed to obtain an extended data base for advanced turbine designs such as the counterrotating turbine. Torque measurements were obtained on both disks in the rotating frame of reference for corotating, counterrotating, and one-rotating/one-static disk conditions. The disk models used in the experiments included disks with typical smooth turbine geometry, disks with bolts, disks with bolts and partial bolt covers, and flat disks. A windage diaphragm was installed at midcavity for some experiments. The experiments were conducted with various amounts of coolant throughflow injected into the disk cavity from the disk hub or from the disk o.d. with swirl. The experiments were conducted at disk tangential Reynolds number up to 1.6 $\times$ 10^7 with air as the working fluid. The results of this investigation indicated that the static shroud contributes a significant amount to the total friction within the disk system, the torque on counterrotating disks is essentially independent of coolant flow total rate, flow direction, and tangential Reynolds number over the range of conditions tested, and a static windage diaphragm reduces disk friction in counterrotating disk systems.

Introduction

In advanced gas turbine engines, air is supplied to the turbine to cool the disks and to seal the disk area from the hot primary gas path. The amount of air supplied to the turbine is generally less than the amount of flow that is pumped in the rotating disk boundary layers (also denoted Ekman layers, Owen et al., 1985). As a result, recirculating flow fields are generated in the cavity adjacent to the disks. The work done on the fluid in the boundary layer in generating these flows results in a rise in the total temperature of the fluid, which reduces the capability of the fluid to cool the disk. Thus, disk friction plays an important role in the heat transfer process within the turbine and "windage losses" must be accurately predicted during the design process.

Disk friction is dependent on a number of factors, chief of which are the disk/cavity geometry and the disk rotation. Farthing and Owen (1988) showed that the geometry of the disks and disk cavity influences the cavity recirculation patterns and the disk heat transfer. Szeri et al. (1983) showed that the flow field in a cavity between a rotating disk and a stationary wall is quite different from that between two corotating (or two counterrotating) disks. Picha and Eckert (1958) were among the first to show the importance and the effects that the shroud can have on the flow in a rotating disk system. Other factors influencing disk friction and disk recirculation characteristics include coolant flow rate, coolant injection location, disk speed, and hardware such as bolt-heads. The present state of the art concerning rotating disk systems has evolved primarily from studies done with single, plane disk/static shroud systems at relatively low Reynolds numbers, compared with those found in large aircraft gas turbines. Disk friction and windage loss data for advanced turbine disk designs, such as those in counterrotating turbines, are not available in the open literature.

The purpose of this paper is to present disk friction and aerodynamic results obtained for adjacent disk systems typically found in large aircraft gas turbines. The disk systems investigated include corotating disks enclosed in a static shroud, counterrotating disks enclosed in a static shroud, and the one-rotating/one-static disk system. The disk models investigated were plane (flat) disks, disks with typical turbine disk geometry (nonplane disks), turbine disk models with bolts, turbine disk models with bolts and partial bolt covers at two disk spacings, and turbine disk models with a static windage diaphragm installed at midcavity. Aerodynamic and torque measurements were obtained on both disks for outward and inward throughflow at various flow rates. The flow injected inward from the disk cavity outer diameter was injected with a simulated gas path swirl of approximately one-half the disk tip velocity. The data were obtained at disk tangential Reynolds numbers from 0.4 to 1.6 $\times$ 10^7 with air as the working fluid.

Contributed by the International Gas Turbine Institute and presented at the 34th International Gas Turbine and Aeroengine Congress and Exhibition, Toronto, Ontario, Canada, June 4–8, 1989. Manuscript received at ASME Headquarters January 27, 1989. Paper No. 89-GT-177.

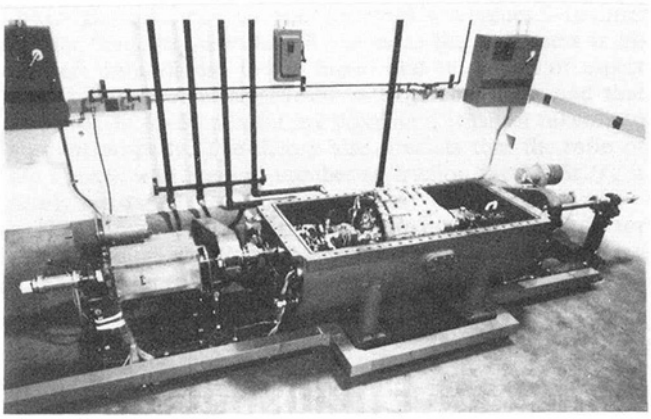

Fig. 1 Photograph of the UTRC internal flow systems and heat transfer facility

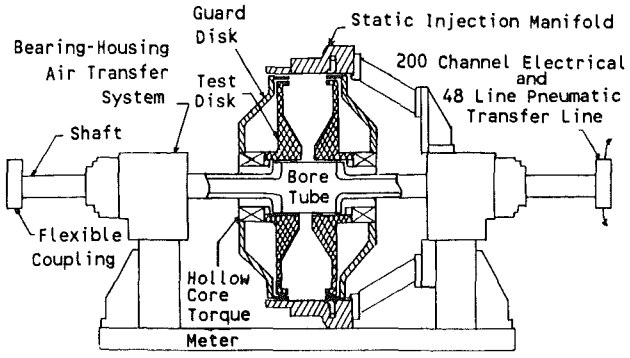

Fig. 2 Sketch of adjacent disk test assembly

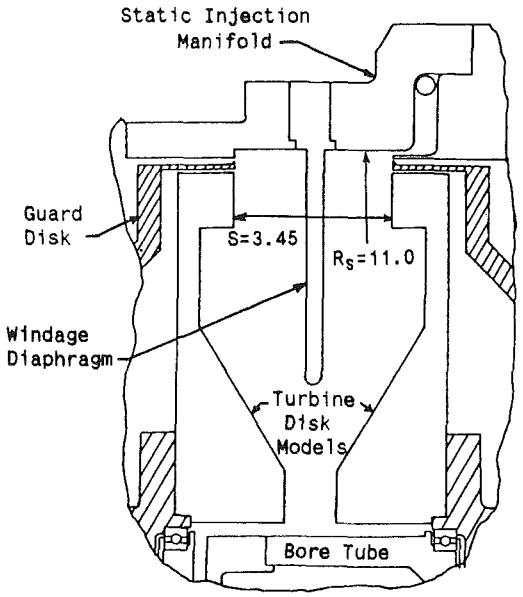

Fig. 3 Sketch of the test assembly with turbine disk models and windage diaphragm installed

Experimental Apparatus

The experiments were conducted in the Internal Air Systems and Heat Transfer Facility at the United Technologies Research Center. The facility has two independently operated drive systems for experiments with co- or counterrotating components and is capable of providing test conditions with nondimensional parameters (Reynolds number, flow parameter, etc.) typical of those found in current and proposed aircraft gas turbines. This is accomplished at modest disk speeds by conducting the experiments with large disk models at pressures up to 10 atm. A photograph of the pressure vessel and drive-motor assemblies is presented in Fig. 1.

A sketch of the adjacent disk model test assembly used in this investigation is shown in Fig. 2. The assembly consists of two disk assemblies, which are rotated independently in either direction at speeds to 3500 rpm. The principal components of each disk assembly are the test disk, the torque meter, the guard disk, the bearing and support housing, and the stationary-to-rotating frame air transfer system. The disk assemblies can be separated from the main assembly support to facilitate changing test disk models, changing disk spacing, and adding test hardware such as windage diaphragm and bolts.

Flow was injected into the cavity between the test disks at the disk bore through 24 injection holes located in the bore tube (Fig. 3) or from the cavity outer diameter (o.d.) through a static injection manifold incorporated in the shroud. The nozzles in the static injection manifold were arranged in three sets of six equally spaced (circumferentially) nozzles. Each set of nozzles was sized to produce a swirl velocity of approximately one-half the disk tip velocity with a specific flow rate. The swirl was produced by orienting the nozzles of each set to discharge air in a direction tangential to the disk tip. Each nozzle set received air from an individually controlled supply manifold. The total flow capability of the assembly is approximately 1 lb/sec (0.45 kg/s).

Sketches of the cross sections of the disk geometries used in this investigation are shown in Fig. 4. The disk rim radius for each disk configuration was 10.51 in. (26.7 cm) and the disk bore radius was 2.61 in. (6.6 cm). The test disk configuration with bolts (Fig. 4(*c*)) contained 40 equally spaced 10–24 NC socket had cap screws located on a bolt-circle radius of 9.25 in. (23.5 cm). The partial bolt covers used were "full ring" covers, which extended to the length of the bolt heads as shown in Fig. 4(*d*). Figure 3 shows a cross section of the disk test assembly with the windage diaphragm installed. The diaphragm was located at midcavity and extended from the

Nomenclature

C_m = torque coefficient = $\tau/\left(\frac{1}{2}\rho\Omega^2 R_o^5\right)$
k = core rotation factor = $V/(\Omega r)$
$\dot{m}$ = mass flow rate, lb/sec
$\Delta p/q_o$ = pressure drop coefficient = $(P-P_o)/q_o$
P = pressure at radius r, lb/ft^2
P_o = pressure at the cavity o.d., lb/ft^2
q_o = dynamic pressure = $\frac{1}{2}\rho V_o^2$, lb/ft^2
Re_r = radial Reynolds number = $\dot{m}/(2\pi\mu R_o)$
Re_t = tangential Reynolds number = $\rho\Omega R_o^2/\mu$
R_i = disk inner radius, ft
R_o = disk outer radius, ft
R_s = shroud outer radius, ft
r = radius, ft
r/R_o = radius ratio
S = axial spacing between disks, ft
S/R_o = disk spacing ratio
V = core flow tangential velocity, ft/sec
V_o = disk tip velocity = $R_o\Omega$, ft/sec
V/V_o = velocity ratio
μ = viscosity, lb/(ft sec)
ρ = density, lb/ft^3
τ = torque, ft lb
Ω = disk angular rotation rate, sec^{-1}

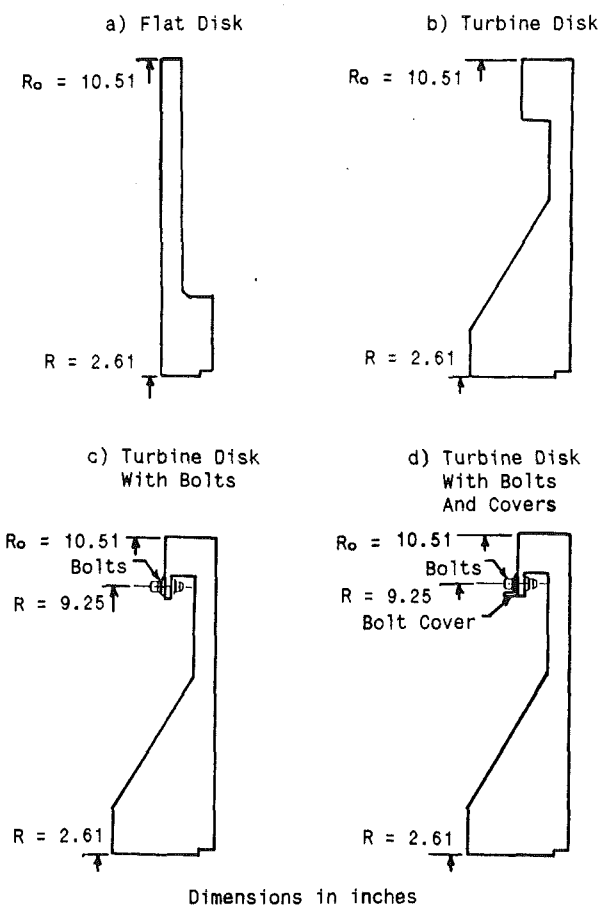

Fig. 4 Schematic of the disk model geometries investigated

cavity o.d. to a radius of 5.65 in. (14.4 cm). The outer diameter of the shroud was 11.00 in. (27.9 cm).

Each disk model was instrumented with 24 static pressure taps located at different radial and azimuthal positions on the disks. All pressure taps were installed flush with the disk test surface. A Model 48J4-1 Scanivalve assembly was utilized with each disk unit to measure the static pressure in the rotating frame of reference. Centrifugal force was taken into account for all pressures measured in the rotating frame of reference. The torque on each disk model was measured in the rotating frame of reference by a LeBow Model 2404-128 torque meter. Each disk test assembly was designed such that the torque meters measured only the torque exerted on the test surface of the disk. This was achieved by creating a "buffer" cavity between the test disk and the guard disk. The fluid in the buffer cavity rotated as a "solid body" during the experiment and no aerodynamic torque was exerted on the back surface of the test disk. Carbon seals adjacent to the bore tube were used to prevent radial flow between the guard disk and the test disk.

The torque meters were statically and dynamically calibrated. The static calibration was performed with weights and a "calibration arm" supplied with each of the torque sensors. The dynamic calibration procedure used the flat disk models with classical "free disk" flow conditions (e.g., von Karman, 1946). A typical dynamic calibration curve is shown in Fig. 5. The results of the torque meter dynamic calibration runs indicated that the measured torque on the flat disks agreed to within 10 percent of the value predicted by classical free disk theory. This result was found to be repeatable for each calibration run performed between test disk configuration changes. A more detailed description of the test facility is presented by Graber et al. (1987).

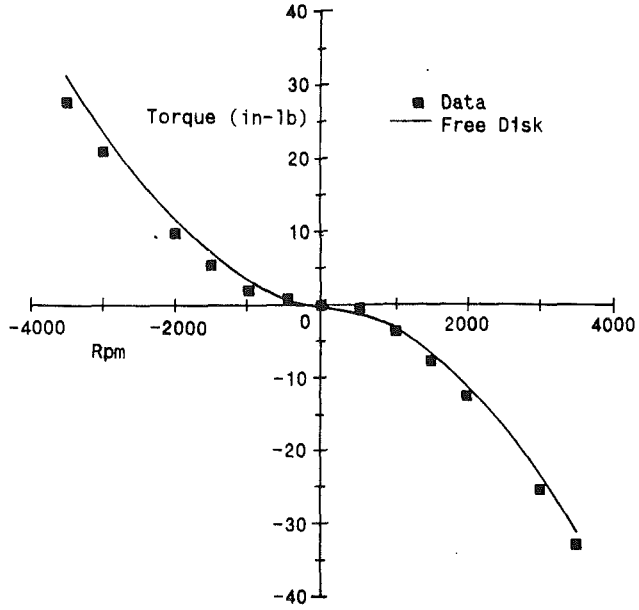

Fig. 5 Torque meter dynamic calibration curve

Experimental Results and Discussion

Torque and aerodynamic experiments for the six disk configurations investigated were conducted with various amounts of throughflow, either inward from the cavity o.d. or outward from the disk hub. The flow conditions for the experiment can be formulated in nondimensional form with the throughflow written as $\mathrm{Re}_r = \dot{m}/2\pi\mu R_o$ where Re_r is denoted the radial Reynolds number. A positive Re_r indicates outward flow and a negative Re_r indicates inward flow. Dibelius et al. (1984) have conducted single plane-disk/static housing torque experiments with throughflow in both directions and have denoted the flow direction as "centrifugal" for outward flow and "centripetal" for inward flow. Unless otherwise specified, the results presented below were obtained from measurements taken on the disk model directly under the o.d. injection manifold (the right-hand disk in Fig. 3). Therefore, for all tests with inward flow, swirl was used only on one disk.

Torque Measurements

Flat Disk Model. The results of the torque measurements obtained for the flat disk models are presented in Fig. 6. The torque coefficient, C_m, is shown as a function of the radial Reynolds number, Re_r. The data were obtained at a disk tangential Reynolds number of 1.6×10^7 (Ω = 3500 rpm) and a nondimensional disk spacing of $S/R_o = 0.328$. The results shown in Fig. 6 are for one disk only. The results indicate that for these test conditions:

(*a*) C_m is highest for counterrotating disks and lowest for corotating disks for both inward and outward flow;

(*b*) C_m is dependent on flow rate and flow direction for corotating and one-static-disk conditions and increases with increasing flow rate for outward flow and decreases with increasing flow rate for inward flow; and

(*c*) C_m is independent of flow rate and flow direction for counterrotating disks.

These results are discussed in the following paragraphs.

Single rotating disk. Results obtained for the one-static-disk condition with outward flow are similar to those obtained by Zimmermann et al. (1986) who have conducted rotating disk experiments with an enclosed single plane disk and a radial outflow of air. Zimmermann et al. (1986) found that the torque coefficient for this disk condition increased with increasing outward flow rate. Using the same facility that Zimmermann

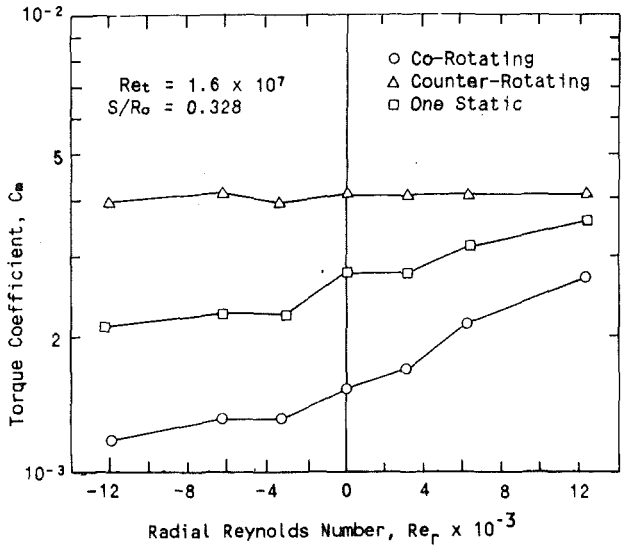

Fig. 6 Torque coefficients obtained for flat disk models

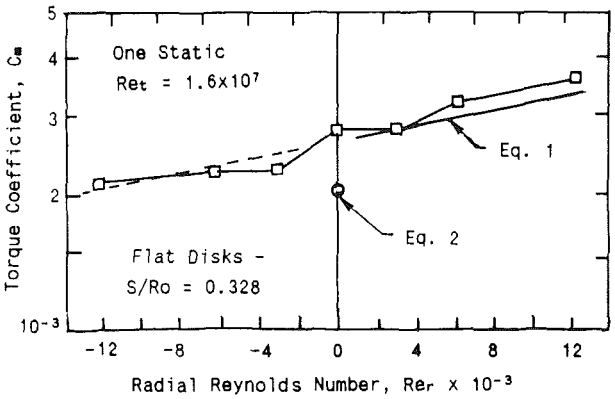

Fig. 7 Comparison of measured torque coefficient for single rotating disk with throughflow and correlation of Zimmermann et al. (1986), equation (1)

et al. (1986) used, Dibelius et al. (1984) conducted single enclosed plane-disk friction experiments for both inward and outward flow. For outward flow, Dibelius et al. (1984) concluded that the torque coefficient increased with increasing flow rate. For inward flow, Dibelius et al. (1984) found that the torque coefficient decreased with increasing flow rate and that for a given flow rate, the torque coefficient for outward flow was larger than that for inward flow.

For the single rotating disk with a radial outflow of air, Zimmermann et al. (1986) present an empirical correlation for the torque coefficient. Using the nomenclature in this paper, their correlation is given by

$$C_m = 0.073\mathrm{Re}_t^{-0.2}\,[1 - 2\pi(\mathrm{Re}_r \times 10^{-4})(4.1\mathrm{Re}_t^{-0.16} - 0.32)][1 - (R_i/R_o)^{5.7}]^{0.8} \quad (1)$$

Values of C_m given by equation (1) are presented in Fig. 7 as a solid line. The measured values of C_m for the single rotating disk obtained in this investigation are shown in Fig. 7 for comparison. Note in Fig. 7 that the torque coefficients given by equation (1) have been extrapolated to the conditions of radial inflow and are shown as a dashed line.

Note that the curve given by equation (1) and the extrapolated curve do not include low flow rates or the zero flow rate condition. For the zero flow rate condition, Zimmermann et al. (1986) present the correlation

$$C_m = 0.073\mathrm{Re}_t^{-0.2}\,[1 - 0.39\mathrm{Re}_t^{-0.11\ (S/R_o)}][1 - (R_i/R_o)^{5.7}]^{0.8} \quad (2)$$

which appears to agree well with their zero flow rate torque

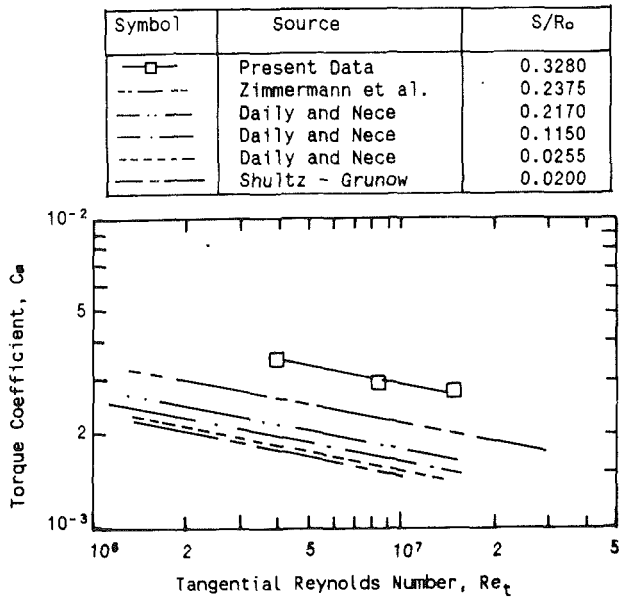

Fig. 8 Comparison of measured torque coefficients for single rotating disk and $\dot{m} = 0$ with results from previous experiments with various values of S/R_o

measurements. Because equation (1) does not reduce to equation 2 for $\mathrm{Re}_r = 0$, equation (1) was applicable for a limited range of flow rates, which were not specified by Zimmermann et al. (1986).

The value of the torque coefficient predicted by equation (2) for the zero flow rate condition is shown in Fig. 7. The value of C_m measured in this investigation is larger than that given by equation (2) and more compatible with equation (1). This may be due to large disk spacing used in the present investigation and/or to the difference in the disk cavity shroud geometry between the present test apparatus and that used by Zimmermann et al. (1986).

The results from the present study employing flat disks are compared in Fig. 8 with results from previous experiments. For this range of tangential Reynolds numbers, Daily and Nece (1958, 1960) found that the torque coefficient increased with increasing disk spacing. Results obtained by Schultz-Grunow (1935), Zimmermann et al. (1986), Daily and Nece (1958), and results obtained in the present investigation are compatible in that the torque coefficient increases with increasing distance between disks. The cases or shrouds surrounding the disks in each of the experiments are not identical. The difference between the results for $S/R_o = 0.217$ (Daily and Nece), $S/R_o = 0.2375$ (Zimmermann et al.), and the present data with $S/R_o = 0.328$ may be due to the difference in the shroud geometry for each of these investigations. Note that the slope of the C_m versus Re_t curve for all data is the same ($C_m \propto \mathrm{Re}_t^{-0.2}$).

The torque coefficients, measured at $\mathrm{Re}_t = 10^7$ by these investigators, are presented as a function of nondimensional disk spacing, S/R_o, in Fig. 9. The measured values are also compared with the correlation for C_m with disk spacing (Daily and Nece, 1960). Note that the measured values of C_m tend to be higher than the values predicted by the Daily and Nece correlation for disk spacing greater than 0.21.

Corotating disks. The torque coefficients for the corotating disk system (Fig. 6) also increase with increasing outward flow rate and decrease with increasing inward flow rate. As expected, the torque coefficients for both inward and outward flow with the corotating disks are considerably less than those with the single rotating disk. For inward flow, the torque coefficients for the corotating system are approximately one-half those of the single rotating disk.

Counterrotating disks. The torque coefficients for the coun-

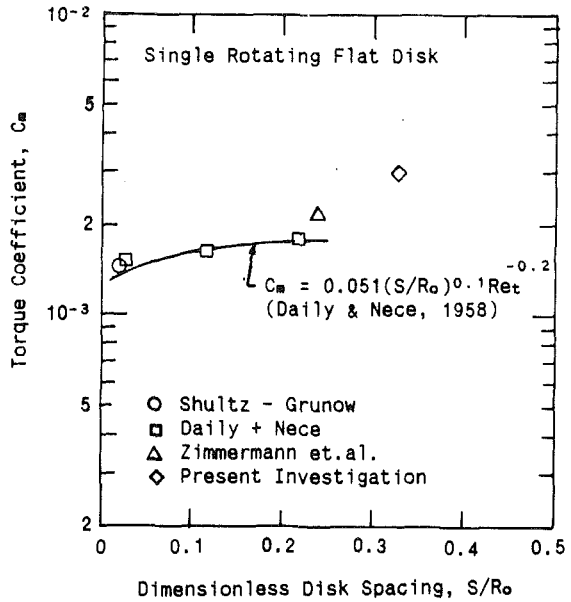

Fig. 9 Comparison of torque coefficients obtained by several investigators for flat disk at various disk spacing; $Re_r = 0$, $Re_t = 10^7$

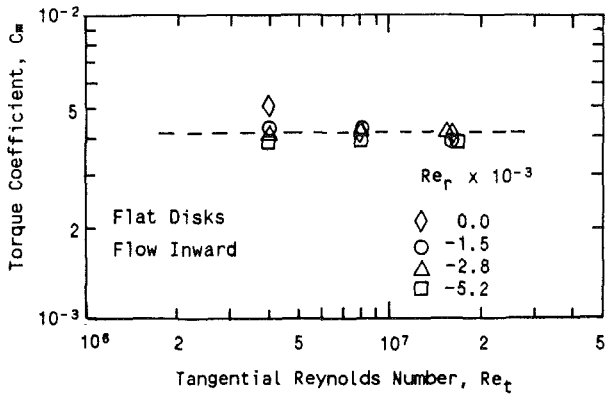

Fig. 10 The effects of flow rate and Reynolds number on torque coefficients for counterrotating disks

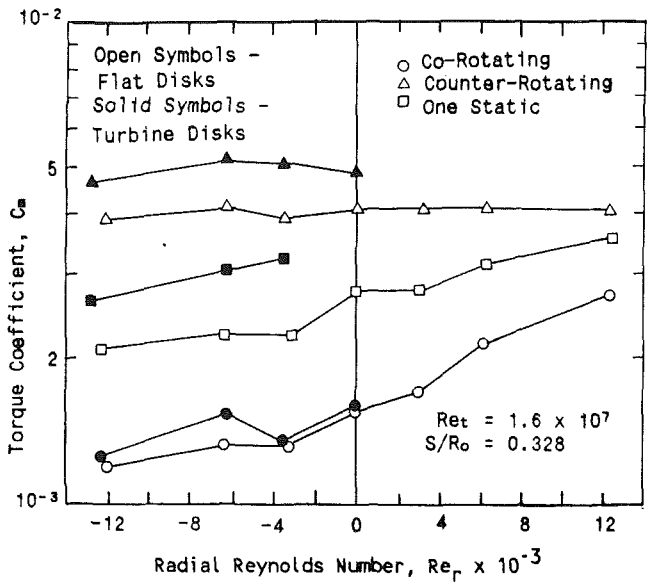

Fig. 11 Comparison of torque coefficients obtained for flat disk models and turbine disk models

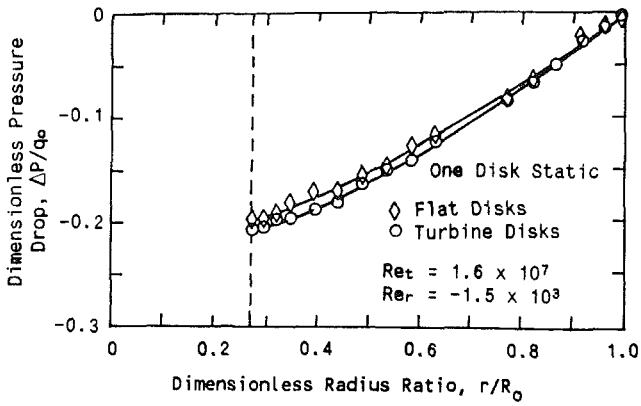

Fig. 12 Comparison of radial pressure distribution for flat disk models and turbine disk models

terrotating disks (Fig. 6) are insensitive to flow rate and flow direction. The measured torque coefficients for counterrotating disks were also insensitive to changes in disk tangential Reynolds number. The torque coefficients for counterrotating flat disks at three values of disk tangential Reynolds number and several flow rates (inward) are presented in Fig. 10. This apparent insensitivity of the torque coefficient with changes in flow rate, flow direction, and tangential Reynolds number is not understood. However, insight to the phenomena can be obtained from studies conducted in the 1950s by Picha (1957), Picha and Eckert (1958), Stewartson (1953), and more recently by Dijkstra and van Heijst (1983). In these studies, the laminar flow between enclosed counterrotating disks without throughflow was investigated theoretically and experimentally. The most pertinent result to this investigation is that the main body of fluid outside of the disk boundary layer was found to be virtually at rest for counterrotating disks rotating at the same speed. This result was independent of disk speed and disk spacing. The level of turbulence generated by the merging of the boundary layers from the two disks is expected to be high. Ingestion of highly turbulent flow into the boundary layers on the disks could account for the apparent insensitivity of C_m to flow rate flow direction and Reynolds number displayed by the counterrotating disks. Hot wire, LV, or flow visualization studies will be required further to clarify and define the characteristics in the flow field.

Turbine Disk Model. Results obtained for the turbine disk models (Fig. 4(*b*)) are presented in Fig. 11. Data were obtained for inward flow only. The results from the flat disk experiments are presented for comparison. The results indicate that the magnitudes of the torque coefficients for the turbine disk models are greater for all disk rotation conditions than those of the flat disks. This increase was attributed to the increase in the total wetted area of the turbine disk models (approximately 15 percent more area) compared to that of the flat disk models and not to a change in cavity aerodynamics. Farthing and Owen (1988) conducted flow visualization studies in rotating cavities having plane disks and disks with hubs ("cobs") typical of turbine disks and have concluded that there is no appreciable difference in the cavity flow regimes produced by the two disk types. Pressure measurements obtained in this study (Fig. 12) also indicate no significant difference in cavity aerodynamics between the flat disk and the turbine disk models, except at the lower radii, where the effects on disk torque are small.

Torque coefficients obtained for both disks with one disk static are presented in Fig. 13. Note that the torque coefficient for the rotating disk is approximately 2 to 3 times greater than that of the stationary disk. The difference between the torque on the rotating disk and that on the stationary disk is attributed to the static shroud at the cavity o.d. This indicates that the shroud contributes a substantial amount to the total frictional losses within the system.

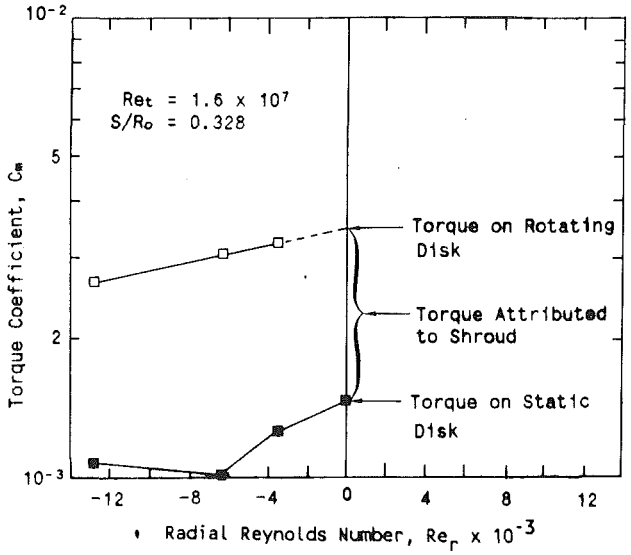

Fig. 13 Comparison of torque coefficients obtained on both disks for one-static/one-rotating turbine disk models

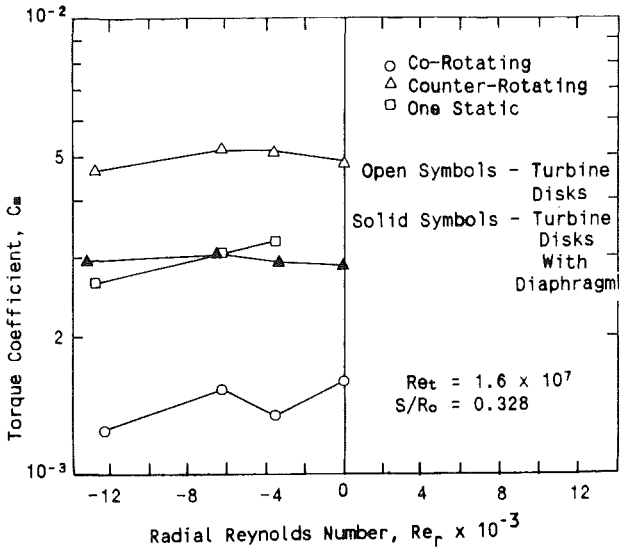

Fig. 14 Effects of windage diaphragm on disk torque measurements for counterrotating disk models

Turbine Disk Model With Windage Diaphragm. A windage diaphragm can be used in counterrotating disk systems to transform the counterrotating cavity into two one-rotating/one-stationary cavities. The desired effect of the windage diaphragm is to reduce the high torque levels experienced by the counterrotating cavity to the lower levels experienced by the one-static disk system. The results of torque measurements obtained for the turbine disk models with windage diaphragm are compared with results obtained for the same disks without a windage diaphragm (Fig. 14). The results indicate that the torque coefficients for counterrotating disks with windage diaphragm are approximately the same as those for the one-rotating/one-stationary turbine disk models without the diaphragm. The measurements shown are for one disk only. The conclusion is that a windage diaphragm can reduce disk torque by as much as 50 percent and hence reduce windage losses in counterrotating disk systems.

Turbine Disk Model With Bolts and Partial Bolt Covers. Torque coefficients obtained for the turbine disk models with bolts are shown in Fig. 15. These measurements are compared with the results obtained for the turbine disk models without bolts. The torque coefficients for disks with bolts are greater

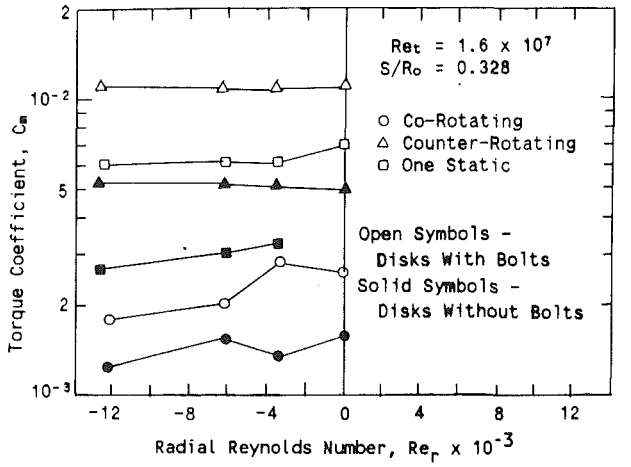

Fig. 15 Comparison of torque coefficients for turbine disk models with and without bolts

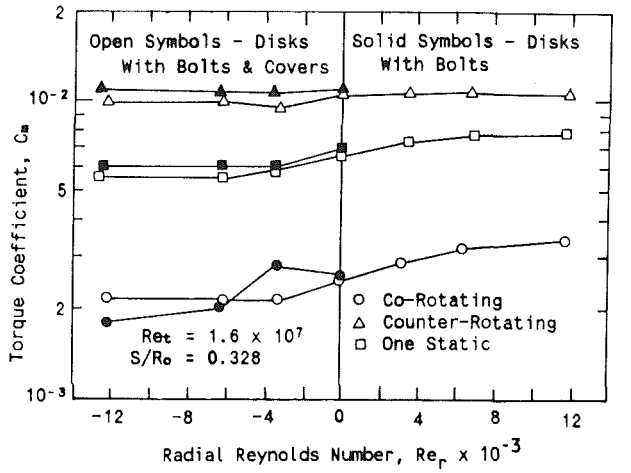

Fig. 16 Comparison of torque coefficients for turbine disk models with bolts and with bolts and covers

by a factor of two than the torque coefficients obtained for disks without bolts. In general the net increase in the friction of disks with bolts compared to disks without bolts will depend on the number of bolts, the bolt circle radius, and the shape of the bolt heads (Zimmermann et al., 1986).

An exploratory experiment was conducted to determine whether a partial bolt cover would reduce the increase in torque due to the bolts. An effective bolt cover would reduce the increase in torque due to the bolts by preventing pumping of fluid by the bolt heads and by reducing the form drag due to the interaction of the bolt heads with the core flow. The torque coefficients obtained with the covers installed were compared with the torque coefficients obtained for disks with bolts only. The comparison of results is shown in Fig. 16. Unfortunately, the torque coefficients obtained for the partially covered bolts were only 5 to 10 percent less than those obtained for the uncovered bolts for the counterrotating and one rotating disk configurations. This modest decrease in torque coefficient is compatible with results obtained by Zimmermann et al. (1986) who conducted experiments with disks having bolts, partial bolt covers, and full bolt covers and concluded that only full bolt covers were effective in reducing the torque due to bolts.

Torque measurements were also obtained for the turbine disk models with bolts and partial covers at a second disk spacing (Fig. 17). The nondimensional disk spacing was decreased from $S/R_o = 0.328$ to $S/R_o = 0.233$ for these measurements. Two observations can be made that are incompatible with previous results of studies using plane disks (Fig. 8). The first is that no measurable differences in torque coefficients

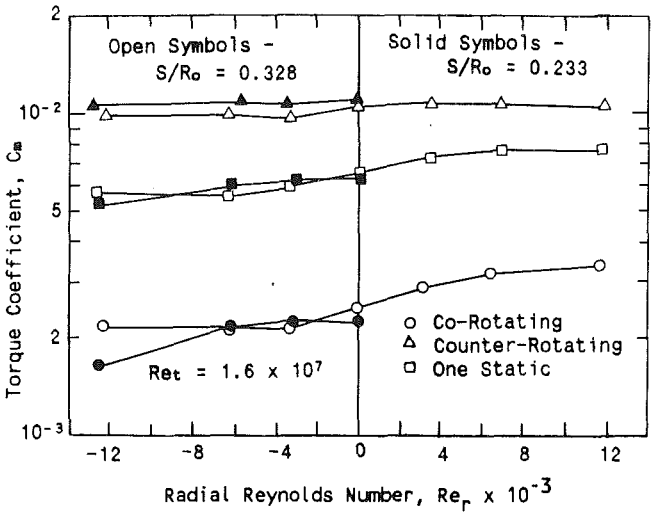

Fig. 17 Comparison of torque coefficients for turbine disk models with bolts and partial covers at two disk spacings

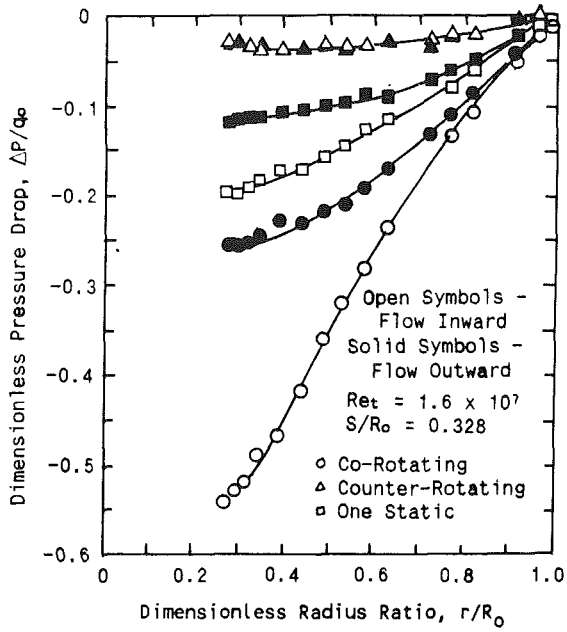

Fig. 18 Comparison of radial pressure drop for flat disk models with inward and outward flow; $|Re_r| = 1.5 \times 10^3$

were obtained for the two spacings for the corotating and the one-static-disk conditions at the flow rates investigated. The second observation is that the torque coefficients for the counterrotating disks appear to increase slightly with decreasing disk spacing. No results are available in the open literature for comparison at the high torque levels (due to the bolts) of the present investigations. The apparent anomalies in the torque coefficient with disk spacing for the case with bolts and partial covers may be due to high turbulence levels generated by the bolts.

Aerodynamic Measurements

Flat Disk Models. Radial pressure measurements as well as torque measurements were obtained in each experiment presented above. The pressure measurements were used to determine the rotation of the core flow induced by disk pumping. Dimensionless radial pressure distributions obtained for the flat disk models are presented in Fig. 18. The absolute value (same flow rate for inward and outward flow directions) of the radial Reynolds number for the data shown was $|Re_r| = 1.5 \times 10^3$. As expected, (*a*) the pressure drop from the disk o.d. to the disk hub was largest for the corotating disks and smallest for the counterrotating disks, and (*b*) the pressure drop from the disk o.d. to the disk hub was found to be larger for inward flow than for outward flow for the corotating and the one-static-disk conditions. An unexpected result was that the pressure drop from the disk o.d. to the disk hub was independent of flow direction for the counterrotating disks. The expected results can be attributed to the convection of the angular momentum of the fluid injected into the disk cavity and to the nature of the disk cavity flow fields generated by the different disk rotation conditions. As the angular momentum of the injected fluid is convected inward from larger radii, the cavity core rotational rate increases as the flow moves radially inward. Thus, the relative rotation between the fluid and the disk is reduced thereby reducing disk friction. Conversely, the rotational rate of fluid injected at the disk hub will decrease as the fluid is convected outward. This increases the relative rotation between the fluid and the disk thereby increasing disk friction.

Turbine Disk Models. The dimensionless pressure drop obtained for turbine disk models with one disk static and one flow rate (inward) was presented in Fig. 12 and was compared with the pressure drop obtained with flat disk models at the same flow conditions. The results indicated that there was no measurable difference in the pressure drops between the disk models at this flow rate and flow direction except at the lower radii. For the corotating and the counterrotating disk conditions, the measured pressure distributions for the turbine disk models with both inward and outward throughflow were found to be similar to the measured pressure distributions for the co- and counterrotating flat disk models, respectively. The conclusion from these results for smooth disks is that disk geometry had little effect on the cavity flow field induced by disk pumping.

The rotation rate of the induced core flow may be estimated from the measured pressure distributions by integrating an approximate form of the radial momentum equation. Assuming small axial and radial velocities within the cavity and an inviscid, incompressible fluid, the radial momentum equation (in cylindrical coordinates) is reduced to $dp/dr = \rho k^2 \Omega s 2r$. Here, $V = kr\Omega$ is the core tangential velocity, k is the dimensionless core rotation factor, and dp/dr is the radial pressure gradient. These approximations are considered valid for the corotating and the one-rotating-disk flow conditions where the tangential velocities are much greater than the radial velocities. However, the approximations may not be valid for the counterrotating flow condition where the tangential velocities are very small (Stewartson, 1953). The cavity core tangential velocity profiles in this study were obtained for the corotating and the one-rotating-disk condition from the measured pressure distributions by assuming the core rotation factor $k(r)$ was constant over a small radial interval and integrating this equation over the disk radius in increments containing three pressure taps (one at each endpoint). The average length of each interval was approximately 0.9 in. (2.3 cm). With the pressure drop over the interval known, the value of the core rotation factor was determined and the core flow tangential velocity was calculated.

Tangential velocity profiles obtained for the turbine disk models are presented in Fig. 19(*a*, *b*) for these disk rotation conditions with radial flow inward. For the corotating (Fig. 19(*a*)) and the one-static-disk conditions (Fig. 19(*b*)), the core tangential velocity increases with increasing flow rate. For the low flow rates (i.e., $Re_r = -1.5$ and -2.8×10^3) the relative difference between the rotation rate of the disk and that of the core flow is decreased resulting in decreased disk friction. For the high flow rate ($Re_r = -5.2 \times 10^3$) with corotating disks (Fig. 19(*a*)), the rotation rate of the fluid over part of the disk between the disk hub and a nondimensional radius of $r/$

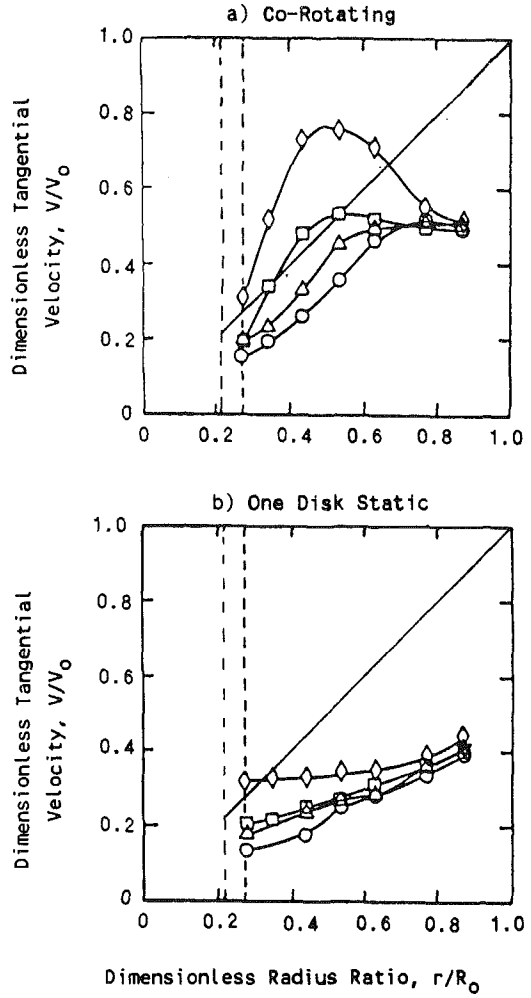

Fig. 19 Comparison of cavity core tangential velocity profiles for turbine disk models at $Re_f = 1.6 \times 10^7$, $S/R_o = 0.328$ and inward flow rates of $Re_r \times 10^{-3} = 0.0$ ○; -1.5 △; -2.8 □; -5.2 ◇

$R_o = 0.625$ is greater than that of the disk. Therefore, the flow accelerates the disk in this region. Dibelius et al. (1984) reported that at high flow rates the disk "... might be accelerated to such an extent that the torque changes its direction" but gave no evidence of this effect.

The final comments in this section concern the realization of the desired inlet swirl velocity for the inward flow condition. Note that the core rotational rate for the corotating (Fig. 19(*a*)) and the one-static-disk (Fig. 19(*b*)) conditions approach the value of one-half the disk speed at the outer radius of the disk. This indicates that the objective of injecting the inward throughflow at a simulated gas path swirl level of approximately one-half the disk speed was achieved. This boundary condition is believed to be representative of the tangential velocity at which ingested flow enters a turbine disk cavity between rotating and stationary rims. Note also in Fig. 19(*a*) that V/V_o approaches the value of one-half the disk speed for the case $Re_r = 0$. This is probably due to the shroud, which has been shown above to contribute a significant amount of friction to the system.

Conclusions

This investigation was conducted to determine disk torque and aerodynamic characteristics for adjacent rotating disk system typical of advanced gas turbine designs such as the counterrotating turbine. The experiments were conducted with a unique experimental facility capable of operating at nondimensional parameters typical of current and advanced large aircraft gas turbine levels.

The most significant results of this investigation have shown that:

(*a*) The shroud contributes a significant amount to the torque required to drive adjacent rotating disk systems;

(*b*) the high torque associated with counterrotating disk systems can be reduced by adding a windage diaphragm between the disks;

(*c*) the class of partial bolt covers tested is ineffective in reducing the increase in torque due to bolts; and

(*d*) the disk torque in a counterrotating disk system is essentially independent of coolant flow rate and flow direction.

Acknowledgments

This work was supported by the Aero Propulsion Laboratory, Air Force Wright Aeronautical Laboratories with Mr. R. J. Martin as technical project manager. The work was conducted under contract F33615-83-C-2331 with the Government Products Division of Pratt & Whitney, United Technologies Corporation. The experiments and the data analysis were conducted at the United Technologies Research Center. The authors also gratefully acknowledge the contributions of Dr. E. J. Kawecki (P&W) for initiating and initially directing the project.

References

Daily, J. W., and Nece, R. E., 1958, "Roughness and Chamber Effects on Induced Flow and Frictional Resistance of Enclosed Rotating Disks," Technical Report No. 27, Massachusetts Institute of Technology, Cambridge, MA, pp. 1-162.

Daily, J. W., and Nece, R. E., 1960, "Roughness and Chamber Effects on Induced Flow and Frictional Resistance of Enclosed Rotating Disks," ASME *Journal of Basic Engineeering*, Vol. 82, pp. 217-232.

Dibelius, G., Radtke, F., and Ziemann, M., 1984, "Experiments on Friction, Velocity and Pressure Distribution of Rotating Disks," *Heat and Mass Transfer in Rotating Machinery*, D. E. Metzger and N. H. Afgan, eds., Hemisphere Publishing Company, Washington, pp. 117-130.

Dijkstra, D., and van Heijst, G. J. F., 1983, "The Flow Between Two Finite Rotating Disks Enclosed by a Cylinder," *Journal of Fluid Mechanics*, Vol. 128, pp. 123-154.

Farthing, P. R., and Owen, J. M., 1988, "The Effect of Disk Geometry on Heat Transfer in a Rotating Cavity With a Radial Outflow of Fluid," ASME *Journal of Engineering for Gas Turbines and Power*, Vol. 110, pp. 70-77.

Graber, D. J., Daniels, W. A., and Johnson, B. V., 1987, "Disk Pumping Test," Air Force Wright Aeronautical Laboratories Report AFWAL-TR-87-2050.

Owen, J. M., 1984, "Fluid Flow and Heat Transfer in Rotating Disk Systems," *Heat and Mass Transfer in Rotating Machinery*, D. E. Metzger and N. H. Afgan, eds., Hemisphere Publishing Company, Washington, pp. 81-103.

Owen, J. M., Pincombe, J. R., and Rogers, R. H., 1985, "Source-Sink Flow Inside a Rotating Cylindrical Cavity," *Journal of Fluid Mechanics*, Vol. 155, pp. 233-265.

Picha, G. K., 1957, "An Experimental Study of the Flow Between Two Rotating Coaxial Disks," Doctoral Dissertation Series, Pub. No. 23,947, University Microfilms, Ann Arbor, MI, pp. 193-199.

Picha, G. K., and Eckert, E. R. G., 1958, "Study of the Air Flow Between Coaxial Disks Rotating With Arbitrary Velocities in an Open or Enclosed Space," *Proc. 3rd U.S. Nat'l Cong. App. Mech.*, pp. 791-798.

Schultz-Grunow, F., 1935, "Der Reibungswiderstand rotierender Scheiben in Gehausen," *Z. Angew Math. Mech.*, Vol. 15, pp. 191-204.

Stewartson, K., 1953, "On the Flow Between Two Rotating Coaxial Disks," *Proc. Camb. Phil. Soc.*, Vol. 49, pp. 333-341.

Szeri, A. Z., Schneider, S. J., Labbe, F., and Kaufman, H. N., 1983, "Flow Between Rotating Disks. Part 1. Basic Flow," *Journal of Fluid Mechanics*, Vol. 134, pp. 103-131.

von Karman, T., 1946, "On Laminar and Turbulent Friction," NACA TM 1092.

Zimmermann, H., Firsching, A., Dibelius, G. H., and Ziemann, M., 1986, "Friction Losses and Flow Distributions for Rotating Disks With Shielded and Protruding Bolts," ASME *Journal of Engineering for Gas Turbines and Power*, Vol. 108, No. 3, pp. 547-552.

An Experimental Investigation of Heat Transfer Coefficients in a Spanwise Rotating Channel With Two Opposite Rib-Roughened Walls

M. E. Taslim

A. Rahman

Mechanical Engineering Department,
Northeastern University,
Boston, MA 02115

S. D. Spring

Aircraft Engine Business Group,
General Electric Company,
Lynn, MA 01910

Liquid crystals are used in this experimental investigation to measure the heat transfer coefficient in a spanwise rotating channel with two opposite rib-roughened walls. The ribs (also called turbulence promoters or turbulators) are configured in a staggered arrangement with an angle of attack to the mainstream flow, α, of 90 deg for all cases. Results are presented for the three values of turbulator blockage ratio e/D_h (0.1333, 0.25, 0.333) and for a range of Reynolds numbers from 15,000 to 50,000 while the test section is rotated at different speeds to give rotational Reynolds numbers between 450 and 1800. The Rossby number range is 10 to 100 (rotation number of 0.1 to 0.01). The effect of turbulator blockage ratios on heat transfer enhancement is also investigated. Comparisons are made between the results of geometrically identical stationary and rotating passage of otherwise similar operating conditions. The results indicate that a significant enhancement in heat transfer is achieved in both the stationary and rotating cases, when the surfaces are roughened with turbulators. For the rotating case, a maximum increase over that of the stationary case of about 45 percent in the heat transfer coefficient is seen for a blockage ratio of 0.133 on the trailing surface in the direction of rotation and the minimum is a decrease of about 6 percent for a blockage ratio of 0.333 on the leading surface, for the range of rotation numbers tested. The technique of using liquid crystals to determine heat transfer coefficients in this investigation proved to be an effective and accurate method especially for nonstationary test sections.

Introduction

In modern gas turbine airfoil designs, operating in the presence of high turbine inlet temperatures, effective blade cooling is a necessity. As the need increases for these airfoils to operate in a higher temperature environment, the need for more effective blade cooling becomes critical. The heat transfer from the blade surface to the internal cooling air is considerably enhanced when the internal passages are roughened with turbulence promoters (ribs or turbulators) located at discrete positions along the passage wall. Geometric parameters such as passage aspect ratio (AR), turbulator height to passage hydraulic diameter or blockage ratio (e/D_h), turbulator pitch-to-height ratio (S/e), turbulator angle of attack (α), and the manner in which the turbulators are positioned with respect to each other have pronounced effects on both local and overall heat transfer coefficients. Turbulators of different blockage ratios positioned at different angles of attack are presently used in advanced aircraft engines.

Experimental results for the stationary case have been widely reported for a variety of geometric variations. The interested reader is referred to work done by Burgraff (1970), Metzger et al. (1983), Han (1984), Han et al. (1978, 1985), and Taslim and Spring (1987, 1988). However, in actual operating conditions, the blade is rotated at high speeds. Hence, the coolant air experiences Coriolis and centripetal forces, which affect the heat transfer to a considerable extent. Results of several investigations have been reported for rotating passages with smooth walls. Mori et al. (1971) presented a theoretical as well as experimental analysis for both laminar and turbulent flows in a rotating circular pipe. Johnston et al. (1972) showed that the effect of rotation on fully developed flow in a rectangular channel was to change the structure of turbulence near the leading and trailing walls. They used water as the working fluid, with dye for visualization, and tested a Reynolds number range of 2500 to 36,000 while the rotation number was varied

Contributed by the International Gas Turbine Institute and presented at the 34th International Gas Turbine and Aeroengine Congress and Exhibition, Toronto, Ontario, Canada, June 4–8, 1989. Manuscript received at ASME Headquarters January 25, 1989. Paper No. 89-GT-150.

from 0.01 to 0.25. Lokai and Limanski (1975) conducted a series of experiments with radially outward flow for a heated circular tube with turbulent conditions. These authors noted improved heat transfer and proposed a correlation. Zysina-Molozhen et al. (1977) undertook a program of experiments with a radially outward flow and suggested that the flow tends to exhibit a more laminar-like behavior when rotation is present; at the higher end of their Reynolds number range (Re $\geq$ 2.5×10^4), rotation has no serious effect. Mityakov et al. (1978) measured local and average effects of rotation on turbulent heat transfer in a circular tube rotating in an orthogonal mode. While maintaining a constant heat flux boundary condition, they reported results for a Reynolds number range of 5500 to 50,000 while Rossby number was varied from 14 to 50. Morris and Ayhan (1979) presented results of an experimental investigation of rotational effects showing changes in the average Nusselt numbers to be of the order ± 30 percent due to rotation. In their case, Reynolds number was varied from 5000 to 15,000 and three rotational speeds of 0, 1000, and 2000 revolutions per minute were tested. In a later paper (1981) they examined radially inward flows and centripetal buoyancy effects, and concluded that centripetal buoyancy adversely affects heat transfer relative to a stationary case when the flow is radially outward. Data were presented showing the converse for radially inward flow. They suggested that Coriolis acceleration improves heat transfer for radially outward flow with converse conditions for inward flow. Wagner et al. (1986) performed experiments with typical airfoil internal cooling passages. They tested two models, a two-pass model (one radially outward flow channel connected with a 180 deg bend to a radially inward channel) and an actual engine scale model. In the two-pass model, the aspect ratio of the channels was 0.25. Experiments were conducted at rotational speeds up to 700 rpm for Reynolds numbers of 15,000 and 30,000. The model pressure was 10 atm. The scaled engine model coolant passages were tested over a rotation number range of 0 to 0.09. They concluded that the average heat transfer coefficients on the leading and trailing surfaces can be significantly increased or decreased depending upon flow direction and magnitude of Rossby number. Further, they suggested that the shape and orientation of the coolant passage can be expected to affect the heat transfer. Harasgama and Morris (1988) reported on the influence of Coriolis induced secondary flow within typical cooling passages. They experimented with square, triangular, and circular sectioned passages over a Reynolds number range of 7000 to 25,000 and rotational Reynolds number (defined as $\Omega D^2/\nu$) ranging from 100 to 1000. They concluded that for a radially inward flow, mean Nusselt numbers with rotation generally tend to be higher that the corresponding zero speed case and as rotational Reynolds number increases, heat transfer on the leading side decreases. For radially outward flow, rotation caused a reduction in mean Nusselt number on the leading side with respect to zero speed comparisons. The heat transfer coefficient was higher on the trailing side than on the leading side, which they attributed to secondary flow effects, and as rotational speeds increased, mean Nusselt number increased.

The objective of the experimental investigation reported upon in this paper is to measure the heat transfer coefficient in a spanwise rotating cooling passage roughened with turbulators of different geometries. Two opposite walls are turbulated in a staggered arrangement. Emphasis is put on the influence of Coriolis forces on internal heat transfer. Results are reported for three blockage ratios, 0.133, 0.250, and 0.333. The rotation number varies between 0.01 and 0.1 and the Reynolds number is in the range of 15,000 to 50,000. The rotational Reynolds number varies from 450 to 1800. The liquid crystal technique is used for temperature measurement.

Experimental Apparatus

A schematic representation of the rotating test rig is shown in Fig. 1. The plenum, test section, and camera assembly are mounted on a light-weight circular disk 2.44 m in diameter. A 3.6-kW d-c motor rotates the disk. Air is supplied to the test rig through two filters and measured via a custom-made critical flow venturi, then enters the plenum and test section

Nomenclature

a = test section width (see Fig. 2)
A_h = heat transfer area
AR = aspect ratio of passage = a/b
b = test section height
d = distance of camera lens from the beginning of the heater on which h_t is measured in the direction of flow
D = diameter of a circular passage
D_h = hydraulic diameter of passage = $2ab/(a+b)$
e = turbulator (rib) height
h_t = heat transfer coefficient on turbulated wall
Gr = Grashof number = Ra/Pr = $\left(\frac{r}{D_h}\right) J_{D_h}\mathrm{RoRe}\beta\Delta T$
i_k = current drawn by kth heater
J_D = rotational Reynolds number based on circular tube diameter = $\Omega D^2/\nu$
J_{D_h} = rotational Reynolds number based on hydraulic diameter = $\Omega D_h^2/\nu$
k = thermal conductivity of air
L = length of each heater in flow direction = 27.95 cm
$\dot{m}$ = mass flow rate of air
Nu_s = Nusselt number on the turbulated wall of the test section when the passage is stationary
Nu_r = Nusselt number on the turbulated wall of the test section when the passage is rotating
P = perimeter
Pr = Prandtl number
$\dot{q}''$ = heat flux generated by electric heater
$\dot{q}_b''$ = heat flux lost through back of test section
$\dot{q}_r''$ = heat flux lost by radiation
$\dot{Q}$ = total heat added to air
r = radial distance from the camera lens to the axis of rotation
Ra = rotational Rayleigh number = $r\Omega^2(T_w - T_m)\beta D_h^3\mathrm{Pr}/\nu^2 = \left(\frac{r}{D_h}\right) J_{D_h}\mathrm{RoRePr}\beta\Delta T$
Re = Reynolds number based on test section hydraulic diameter
Ro = Rotation number = $\Omega D_h/U_m$
Ross = Rossby number = 1/Ro
S = turbulator (rib) pitch
T = temperature
T_f = film temperature
T_m = air mixed mean temperature
T_w = wall surface temperature
ΔT = $(T_w - T_m)$
U_m = mean velocity of air
V_k = voltage across kth heater
X' = nondimensional distance between two turbulators
α = angle of attack
β = volumetric coefficient of thermal expansion
ν = kinematic viscosity of air
ρ = density
Ω = angular velocity

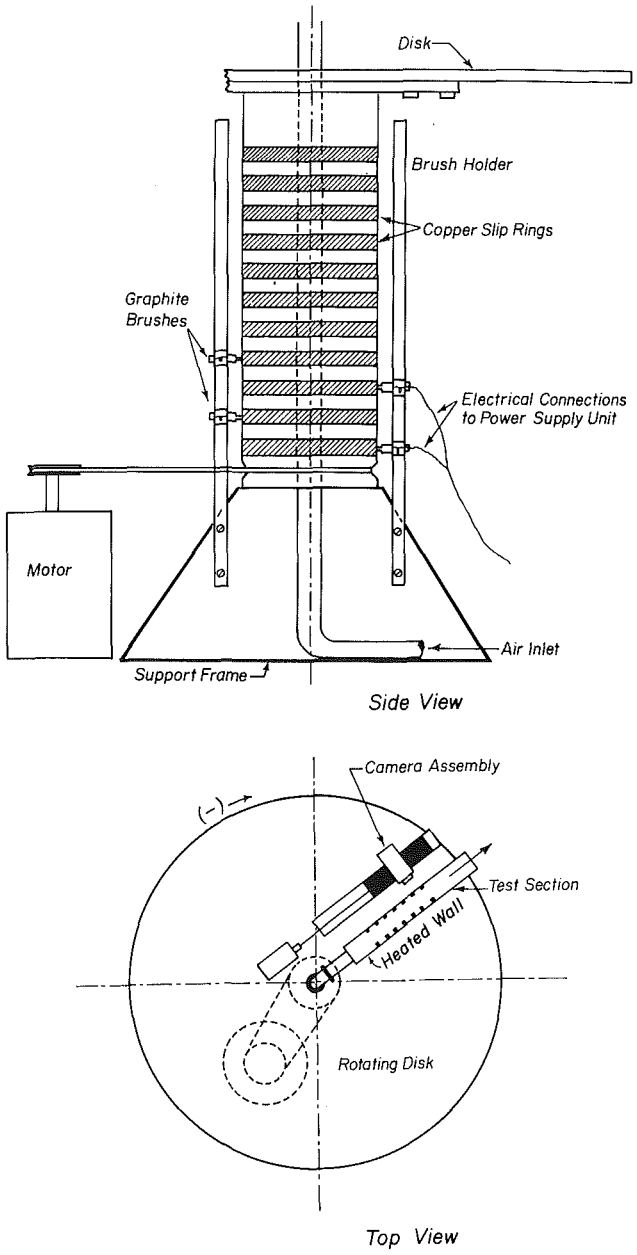

Fig. 1 Experimental apparatus

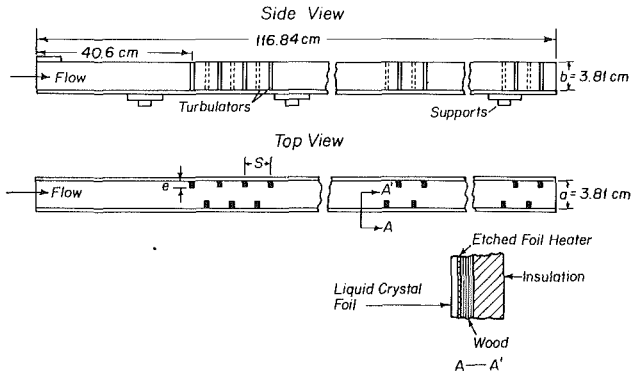

Fig. 2 Layout of a typical test section

through a rotary joint. The air, which is now at about ambient pressure and temperature, flows through a honeycomb-type flow straightener located in the plenum and enters the test section through a bellmouth opening.

Three test sections are used, one for each size of turbulator. The test section length in the direction of flow is 116.84 cm and has a cross-sectional area of 3.81 × 3.81 cm. Thus, the aspect ratio in each case is 1 and the hydraulic diameter is 3.81 cm. Figure 2 shows the layout of a typical test section. Three walls are made of 1.27-cm-thick clear plexiglass and the fourth is made of 1.06-cm-thick white pinewood. Turbulators are placed in a staggered arrangement on two opposite sides, one of which forms the heated wall on which measurements are taken. For the three test sections, the location of the first turbulator from the test section inlet is 40.6, 43.8, or 40.6 cm depending on the turbulator height. Others are placed consistent with keeping $S/e = 10$, constant for all three sizes of turbulators (e = 5.08, 9.53, and 12.7 mm). The turbulators are glued into grooves machined in the plexiglass sides. They are also made of clear plexiglass with a square cross section equal to e and of length equal to passage side, 3.81 cm. The plexiglass walls and turbulators are glued and bolted together as one piece and then bolted onto the wooden wall, on which the liquid crystal sheet is attached and all measurements are taken. The wooden wall is 7.6 cm wide and has the same length as the passage. It sits snugly against the plexiglass sides and turbulators to complete the passage.

Four custom-made etched foil heaters are placed on the wooden wall using a special double-stick 0.05-mm-thick tape with minimal temperature deformation. The heaters are each 27.95 cm long and 3.81 cm wide and cover the entire test section length including the nonturbulated entry length. However, they do not extend over the actual turbulator surface. Details of heater materials and arrangement are found in Rahman (1988). The liquid crystal sheet is placed on the heaters. The thickness of the liquid crystal layer is 0.15 mm.

The test section is covered on all sides, except for a small window at the location where the pictures are taken, by 5-cm-thick styrofoam sheets to minimize heat losses to the environment. A 35-mm, programmable camera is mounted on a platform that can travel along the length of the test section. The camera location is altered by activating a 50-W geared d-c motor through a lead screw running the length of the camera assembly. The camera, which is activated remotely using an infrared transmitter and receiver set, takes pictures of isochrome patterns formed on the liquid crystal sheet.

The disk is fastened to a hollow nylon cylinder having an outside diameter of 19 cm with a wall thickness of 1.27 cm. Power to the heaters and small d-c motor on the rotating disk is provided through a slip-ring-graphite-brush assembly. Copper slip rings are mounted on the nylon cylinder and graphite brushes are held in vertical brush holders. They are spring loaded to ensure constant contact with the slip rings. The nylon cylinder is housed on a steel shaft with double packed bearings for smooth operation. The complete setup is supported on a steel platform bolted to the laboratory floor to minimize vibrational effects.

Heat is transferred to the air in the test section via the heaters through a custom-designed power supply unit. Each heater is individually controlled by a variable transformer.

Procedure

At the beginning of the set of test runs the liquid crystal was calibrated. A water bath was used to attain uniform isochromes on a small piece of the liquid crystal sheet used throughout this investigation. The temperature corresponding to each color was measured using a precision thermocouple and photographs were taken at laboratory conditions simultaneously so as to simulate closely the actual testing environment. The color green, corresponding to a temperature of 37°C, was chosen as the prime indicator for the temperature

field. This color was easily identifiable and fluctuations in shades of green were of the order of 0.2°C.

For verification of liquid crystal accuracy, a smooth duct having an aspect ratio of 1 and a hydraulic diameter of 3.81 cm was tested in a stationary state and compared with the well-known Dittus-Boelter correlation. Reynolds numbers were varied by changing the air mass flow rate. For each Reynolds number the heat flux was varied by changing the input voltage across the heaters. All four heaters were kept at the same power level so as to simulate a constant heat flux boundary condition. A detailed description of the data reduction process is presented by Rahman (1988). For this investigation, there existed good agreement between Nusselt numbers obtained using the liquid crystal and the Nusselt numbers predicted by the Dittus-Boelter correlation.

Each geometric configuration was first tested in a stationary state. With the turbulators in place and fully turbulent flow conditions, the flow was hydrodynamically and thermally fully developed at the location of interest, as was seen in the periodic repetition of the isochromes on the liquid crystal sheet between each pair of turbulators at steady-state conditions. For all three test sections the photographs were taken at approximately the same location, well downstream of the inlet. The area of interest was between a pair of turbulators on the heated wall. The strategy was as follows. First the Reynolds number was set by precisely fixing the mass flow rate. Heat flux was induced by switching on the power supply to the heaters. A small band of the calibrated reference color was seen immediately downstream of the left turbulator. A photograph was taken. The heater power supply was then increased so that the reference color line moved in the flow direction and another photograph was taken. This was continued until eventually the whole area between the turbulators on the heated wall was covered by the reference color at one time or another. It was observed that an average of 16 photographs were required to cover the complete area satisfactorily for a given mass flow rate. A smaller number of pictures was taken for the test section with the smaller turbulator heights and more for the test section with the largest turbulator heights. The next Reynolds number was set by changing the flow rate and the whole process was repeated, until all flow rates were tested. The same procedure was used for the other test sections.

The next step was to conduct experiments on the rotating test rig. The disk was rotated to the desired rpm and the system was allowed to come to steady state. A picture was taken and the heat flux was increased in a manner similar to the stationary case, until a sufficient number of pictures was taken to cover the whole field. The number of pictures to be taken and the increase of heat supplied per picture was arrived at empirically. The mass flow rate was increased and another set of pictures was taken. The process was repeated for four different rpm's: 50, 100, 150, and 200. Then the direction of rotation was reversed and the whole procedure was repeated for the complete range of mass flow rate. Data acquisition was through specially written programs run on a VAX 11/785 through a dedicated IBM PC.

Data Reduction

The total heat added to the air by the heaters from the inlet of the test section to the point of camera location is calculated using the formula

$$\dot{Q} = \sum_{n=1}^{k-1} i_n V_n + \left(\frac{d}{L}\right) i_k V_k - \dot{Q}_{\text{loss}} \tag{1}$$

where the camera is in front of the kth heater, d is the distance of the camera from the beginning of that heater in the flow direction, and L is the length of the heater. i_n and V_n are the current and voltage of the nth heater and $\dot{Q}_{\text{loss}}$ is the heat loss to the ambient air. The total heat is used in an energy balance equation from the test section inlet to the camera location to calculate the air mixed mean temperature at the camera location given by the following equation:

$$T_m = \frac{\dot{Q}}{\dot{m}C_p} + T_i \tag{2}$$

With T_i at about ambient temperature, T_m ranged from 24 to 28°C. The heat flux, $\dot{q}''$, for the kth heater is calculated as

$$\dot{q}'' = \frac{i_k V_k}{A_h} \tag{3}$$

where A_h is the heat transfer area. The losses to the environment from the back of the heaters as well as the radiational losses from the heated surface to the unheated walls were calculated. Iterations had to be performed since the unheated wall temperature was not known a priori. The heat transfer coefficient on the turbulated side was then calculated from

$$h_t = \frac{\dot{q}'' - \dot{q}_b'' - \dot{q}_r''}{(T_w - T_m)} \tag{4}$$

where T_w is the wall surface temperature and T_m is the air mixed mean temperature calculated from the energy balance mentioned above. $\dot{q}_b''$ is the heat loss through the back of the test section and $\dot{q}_r''$ is the radiational loss from the heated wall to the three unheated walls of the test section. Substituting for the air mixed mean temperature, the expression for the heat transfer coefficient is reduced to

$$h_t = \frac{\dot{q}'' - \dot{q}_b'' - \dot{q}_r''}{T_w - T_i - \dot{Q}/(\dot{m}C_p)} \tag{5}$$

The specific heat at constant pressure, C_p, and other air properties are evaluated at the film temperature T_f, which is the average of the wall surface temperature and the air mixed mean temperature.

The local Nusselt number is calculated from the formula

$$\text{Nu} = \frac{h_t D_h}{k} \tag{6}$$

where k is the air conductivity. The above calculations were repeated for all pictures taken. The resulting data were organized into files for the appropriate test sections and runs. These results were further processed through a program to integrate these local quantities to get area-weighted averages.

From observations of the liquid crystal display, under steady-state conditions, it was found that the temperature patterns exhibit regular periodic behavior. For this reason only one such period, between two turbulators on the heated wall, was examined in detail, and the local quantities were area-weighted over such a region. For verification, tests were repeated at two different locations from the inlet, for otherwise identical conditions, and the same results were obtained.

For all the cases, using equation (5), error analysis was done based on the method of Kline and McClintock (1953). Experimental uncertainties on the heat transfer coefficients are estimated to be ±6 percent.

Results and Discussion

The following results present data reduced for the turbulated wall. The results are reported in terms of dimensionless numbers such as Nu_r, which is average Nusselt number on the turbulated wall, Re, which is Reynolds number based on hydraulic diameter D_h, rotation number, defined as $\Omega D_h/U_m$, and rotational Reynolds number, J_{D_h}, defined as $\Omega D_h^2/\nu$. Reynolds number, rotational Reynolds number, and rotation number are related as

$$\text{Ro} = J_{D_h}/\text{Re}$$

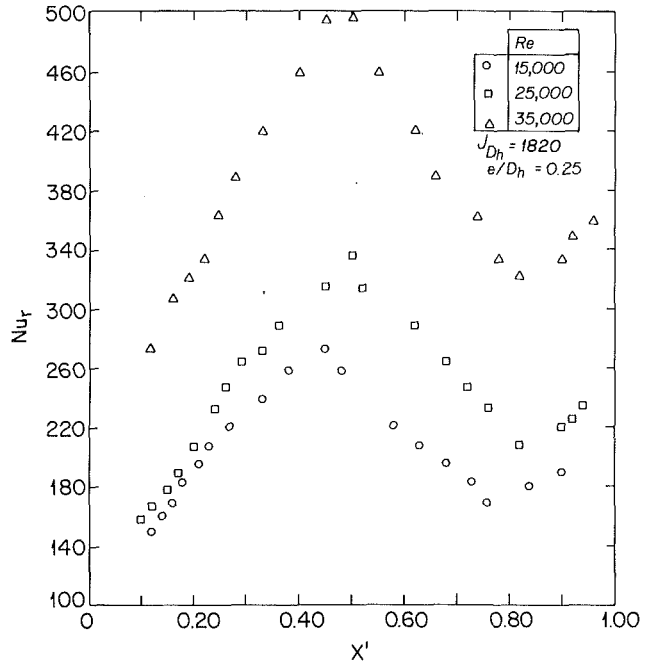

Fig. 3 Typical variation of Nusselt number between a pair of turbulators

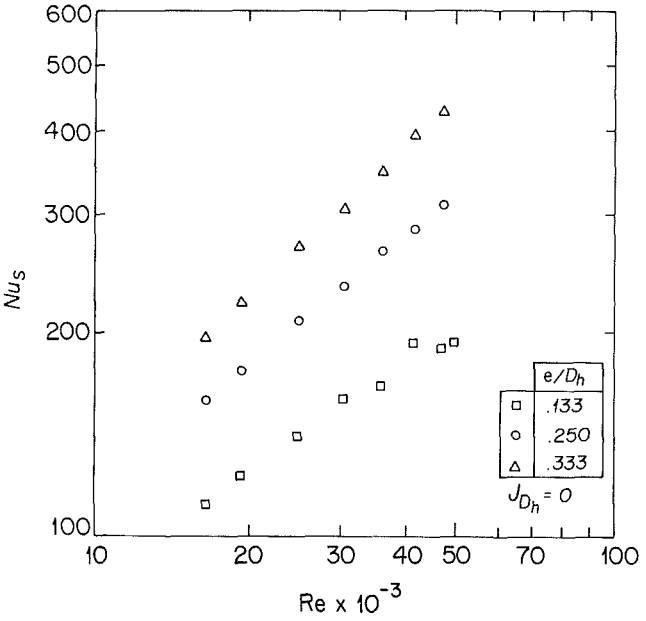

Fig. 4 Nusselt versus Reynolds number, stationary case

$\mathrm{Gr/Re^2} = \left(\frac{r}{D_h}\right)\mathrm{Ro^2}\beta\Delta T$ ranged from 0.016 to 0.064 and the effect of centripetal buoyancy on Nusselt number was not investigated. Geometric variations are in terms of turbulator height-to-passage hydraulic diameter ratio (blockage ratio), e/D_h. The direction of rotation is taken care of by specifying the leading or trailing side of the test section. To an observer looking at the disk from the top (see Fig. 1), with the disk rotating clockwise and the heated wall on his right, then measurement is for the leading side. The wall to his left is the trailing side. If the direction of rotation is reversed, then measurements are for the trailing side. It should be noted that heat transfer coefficient is measured on the turbulated wall, but the turbulators themselves are not covered by the heaters, and hence fin type effects are not reported.

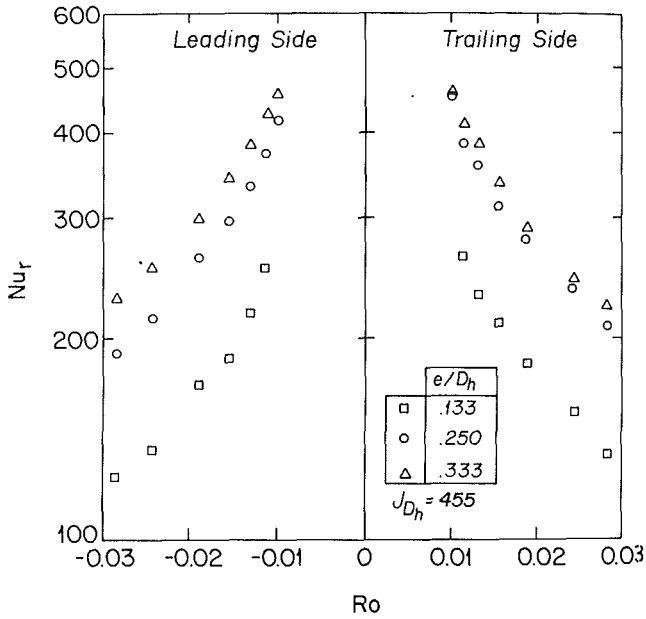

Fig. 5 Variation of Nusselt number with rotation number for three blockage ratios at a rotational Reynolds number of 455

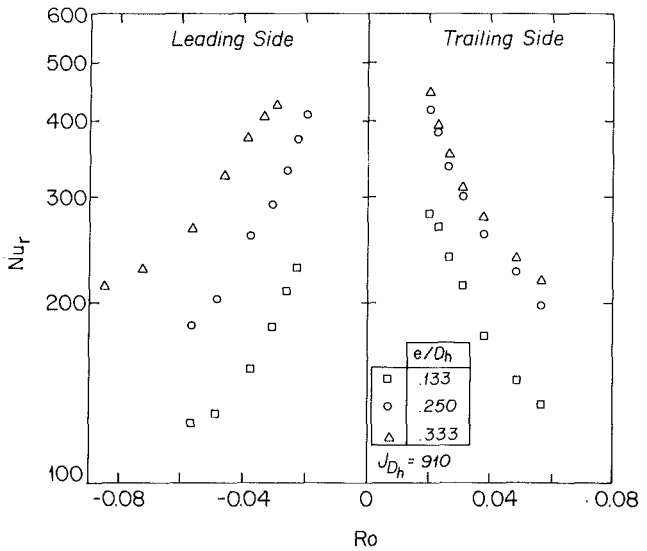

Fig. 6 Variation of Nusselt number with rotation number for three blockage ratios at a rotational Reynolds number of 910

Figure 3 shows the typical variation of local Nusselt numbers in the region between two turbulators. It is seen that the heat transfer coefficient reaches a maximum where flow reattachment occurs and then decreases until the air flow approaches the next turbulator where the heat transfer coefficient increases again. This behavior is explained by the fact that after passing over the left turbulator the air flow touches the heated surface near the middle of the region thereby increasing h_t dramatically. Then as the air approaches the right turbulator a stagnation point type of situation arises with a resulting increase in heat transfer coefficient.

Figure 4 shows the variation of Nusselt number for the turbulated wall with Reynolds number when the test section is stationary. These results, which are presented for the three turbulator geometries tested, are used in ensuing figures to compare the rotating versus stationary cases of otherwise identical conditions. As expected, a large increase in Nu_s is seen for test sections with higher blockage ratios over those with lower blockage ratios, due to higher level of mixing of air inside the test section.

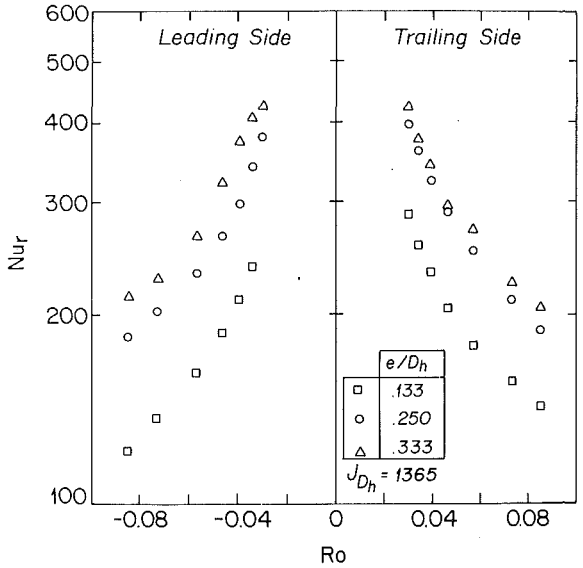

Fig. 7 Variation of Nusselt number with rotation number for three blockage ratios at a rotational Reynolds number of 1365

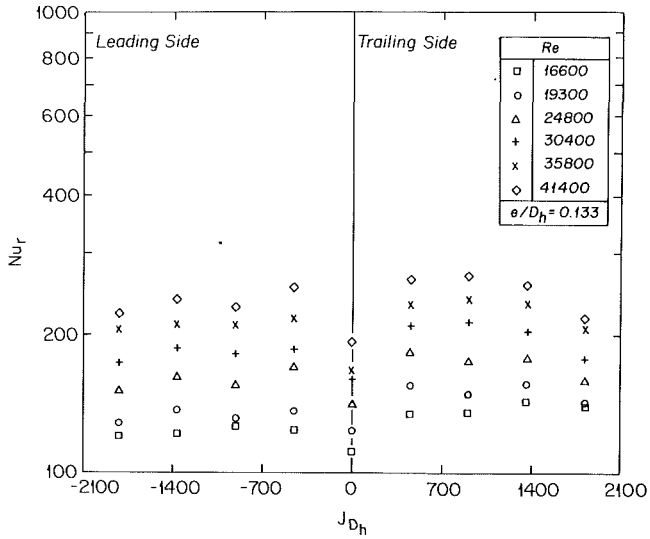

Fig. 9 Nu, versus rotational Reynolds number for the smallest blockage ratio

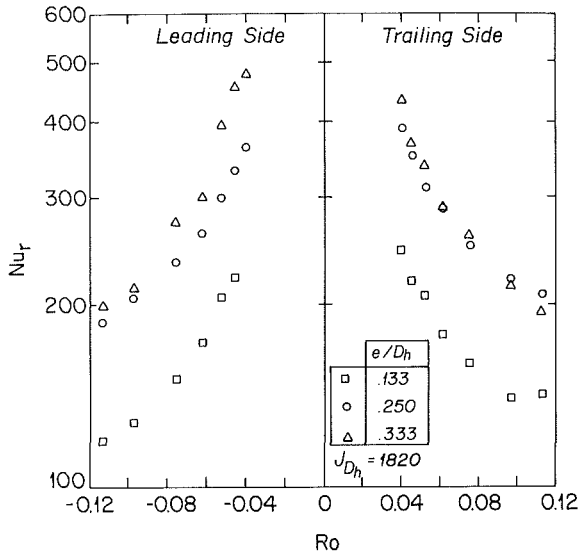

Fig. 8 Variation of Nusselt number with rotation number for three blockage ratios at a rotational Reynolds number of 1820

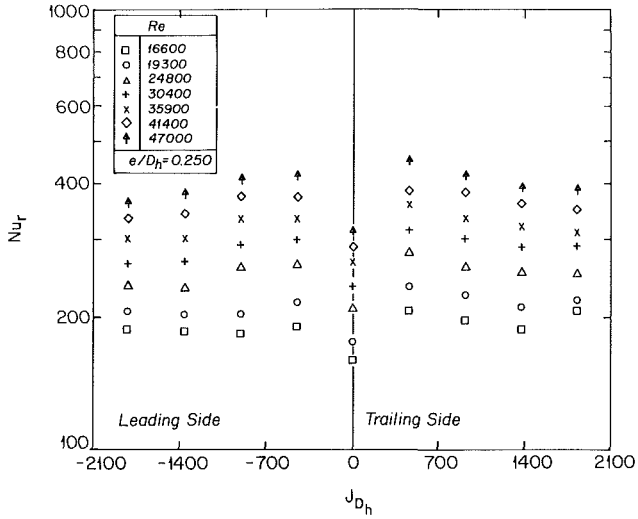

Fig. 10 Nu, versus rotational Reynolds number for the medium blockage ratio

Figures 5–8 show the variation of Nu_r versus rotation number. Each figure is for a specific rotational Reynolds number ($\Omega D_h^2/\nu$), i.e., a fixed value of Ω. Negative rotation numbers imply measurements on the leading side. It is seen that Nusselt number decreases with increasing rotation number ($\Omega D_h/U_m$) for all turbulator heights. The reason for this behavior is that, with the angular velocity Ω being fixed on each case, higher rotation numbers correspond to lower values of U_m, which in turn correspond to lower Nusselt numbers, as is seen for stationary cases (see Fig. 3).

Figures 9–11 show the variation of Nusselt number with the rotational Reynolds number for the three turbulator geometries at several Reynolds numbers. Nusselt numbers for the stationary case are shown on the $J_{D_h} = 0$ axes. It can be observed that the Nusselt number first increases as the rotational Reynolds number (i.e., the angular velocity Ω) increases until it reaches a maximum and then, with the exception of the lowest Reynolds number on the trailing side, the Nusselt number decreases with J_{D_h}. This decrease is more pronounced for the smallest turbulator size. It is speculated that this behavior is due to the increase of centripetal forces with J_{D_h}, which adversely affect the heat transfer coefficient in a radially outward flow. Nevertheless, compared with the stationary case, for the range of rotation numbers tested, the heat transfer coefficient is enhanced on both leading and trailing sides for the smallest and medium height turbulators. This, however, is not the case for bigger turbulators.

A comparison between the Nusselt numbers in the stationary and rotating cases is made by plotting the ratio Nu_r/Nu_s versus rotation number for various rotational Reynolds numbers, as shown in Figs. 12–14. As can be observed, rotation has a significant effect on this ratio. Large percentage increases are seen for the test sections with blockage ratios, (e/D_h), of 0.133 and 0.250. The least effect is for the largest size turbulators with a blockage ratio of 0.333. The maximum increase due to rotation occurs for the case of $e/D_h = 0.1333$. A 45 percent increase on the trailing side is seen for this blockage ratio when the rotation number is 0.03 and J_{D_h} is 1365. The minimum occurs when the ratio Nu_r/Nu_s falls about 6 percent below the stationary value on the leading side for $e/D_h = 0.333$ at a rotation number of 0.0617 and J_{D_h} of 1820. The increase for $e/D_h = 0.133$ ranges from 3 to 45 percent. The middle sized

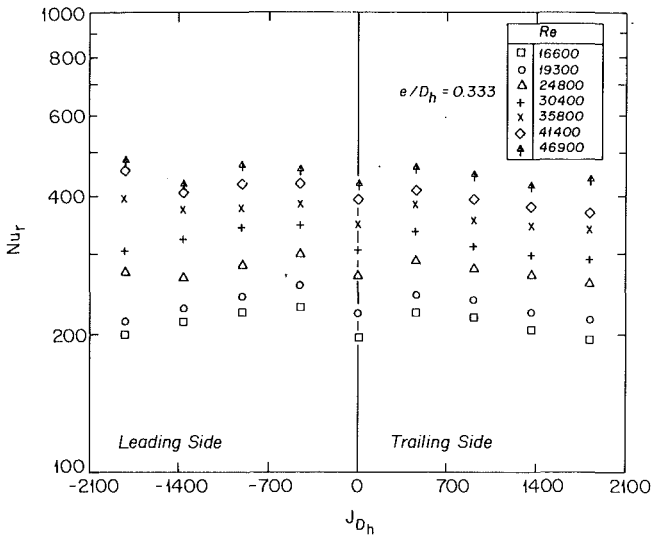

Fig. 11 Nu_r versus rotational Reynolds number for the highest blockage ratio

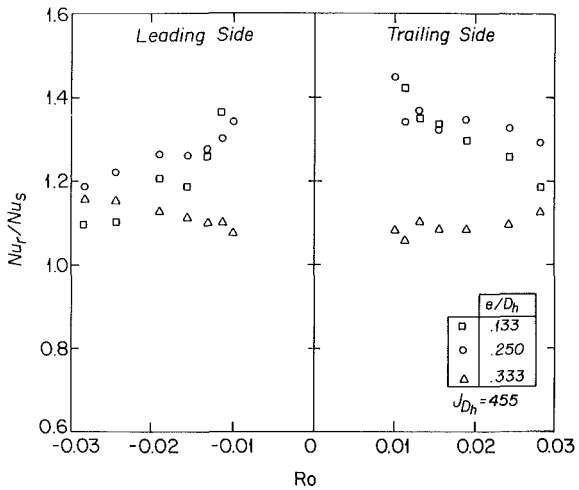

Fig. 12 Nu_r/Nu_s versus rotation number for three blockage ratios at a rotational Reynolds number of 455

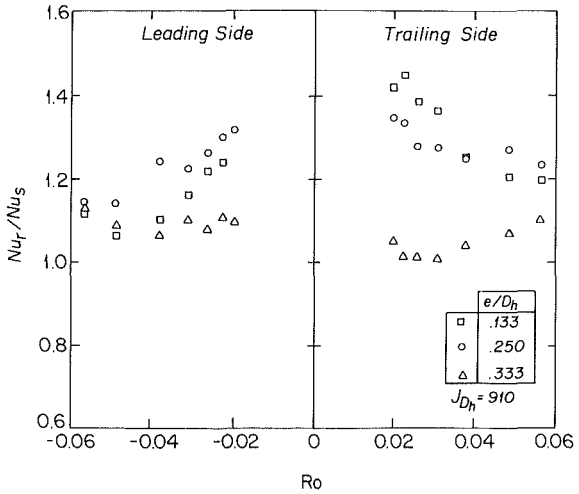

Fig. 13 Nu_r/Nu_s versus rotation number for three blockage ratios at a rotational Reynolds number of 910

turbulators, with a blockage ratio of 0.250, experience an increase in the range of 11 to 40 percent.

The case with highest blockage ratio does not show as appreciable a change as the lowest one. Again the trend is that the ratio Nu_r/Nu_s decreases with increasing rotational Reynolds number for the range tested.

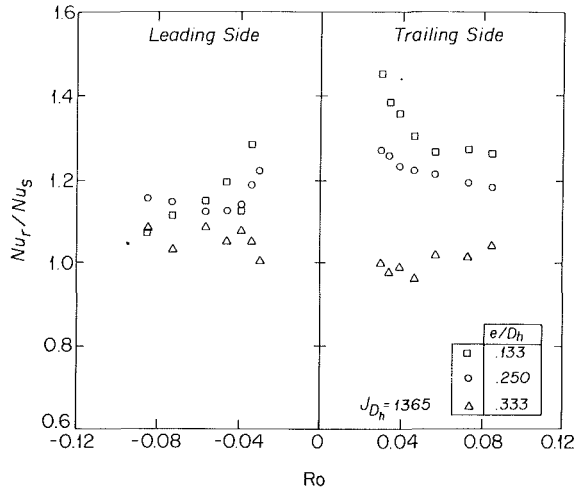

Fig. 14 Nu_r/Nu_s versus rotation number for three blockage ratios at a rotational Reynolds number of 1365

Conclusions

Based on the experimental program described in this paper it can be concluded that: (*a*) A significant enhancement in heat transfer is achieved both in stationary and rotating cases when the surfaces are roughened with ribs. (*b*) For the rotating case as compared to the stationary case, a maximum increase of about 45 percent in the heat transfer coefficient is observed for a blockage ratio of 0.1333 and the minimum is a decrease of about 6 percent for a blockage ratio of 0.333, for the range of rotation numbers tested. (*c*) The technique of using liquid crystals to determine heat transfer coefficients in this investigation proved to be an effective and accurate method, especially for rotating test sections.

Acknowledgments

Financial support of The General Electric Company, Aircraft Engine Business Group, Lynn, Massachusetts is hereby gratefully acknowledged. The authors would also like to thank Mr. R. E. Gladden for his valuable suggestions during the course of this investigation.

References

Burgraff, F., 1970, "Experimental Heat Transfer and Pressure Drop With Two Dimensional Turbulence Promoters Applied to Two Opposite Walls of a Square Tube," *Augmentation of Convective Heat and Mass Transfer*, A. E. Bergles and R. L. Webb, eds., ASME, New York, pp. 70–79.

Han, J. C., Glicksman, L. R., and Rohsenow, W. M., 1978, "An Investigation of Heat-Transfer and Friction for Rib Roughened Surfaces," *Int. J. Heat Mass Transfer*, Vol. 21, pp. 1143–1156.

Han, J. C., 1984, "Heat Transfer and Friction in Channels With Two Opposite Rib-Roughened Walls," ASME *Journal of Heat Transfer*, Vol. 106, No. 4, pp. 774–781.

Han, J. C., Park, J. S., and Lei, C. K., 1985, "Heat Transfer Enhancement in Channels With Turbulence Promoters," ASME *Journal of Engineering for Gas Turbines and Power*, Vol. 107, pp. 628–635.

Harasgama, S. P., and Morris, W. D., 1988, "The Influence of Rotation on the Heat Transfer Characteristics of Circular, Triangular, and Square-Sectioned Coolant Passages of Gas Turbine Rotor Blades," ASME JOURNAL OF TURBOMACHINERY, Vol. 110, pp. 44–50.

Johnston, J. P., Halleen, R. M., and Lezius, D. K., 1972, "Effects of Spanwise Rotation on the Structure of Two-Dimensional Fully Developed Turbulent Channel Flow," *J. Fluid Mech.*, Vol. 56, Part 3, pp. 533–557.

Kline, S. J., and McClintock, F. A., 1953, "Describing Uncertainty in Single-Sample Experiments," *Mechanical Engineering*, Vol. 75, pp. 3–8.

Lokai, V. I., and Limanski, A. S., 1975, "Influence of Rotation on Heat and Mass Transfer in Radial Cooling Channels of Turbine Blades," *Izvestiya VUZ, Aviatsionnaya Tekhnika*, Vol. 18, No. 3, p. 69.

Metzger, D. E., Pennington, J. W., and Fan, C. S., 1983, "Heat Transfer and Flow Friction Characteristics of Very Rough Transverse Ribbed Surfaces With and Without Pin Fins," *Proc. ASME-JSME Thermal Engineering Joint Conference*, Vol. 1, pp. 429–436.

Mityakov, V. Y., et al., 1978, "Turbulent Flow and Heat Transfer in Rotating Channels and Tubes," Leningrad Polytechnic Institute.

Mori, Y., Fukada, T., and Nakayama, W., 1971, "Convective Heat Transfer in a Rotating Radial Circular Pipe (2nd Report)," *Int. J. Heat Mass Transfer*, Vol. 14, pp. 1807–1824.

Morris, W. D., and Ayhan, T., 1979, "Observations on the Influence of Rotation on Heat Transfer in the Coolant Channels of Gas Turbine Rotor Blades," *Proc. IMechE*, Vol. 193, No. 21, p. 303.

Morris, W. D., and Ayhan, T., 1981, "Heat Transfer in a Rotating Tube With Radially Inward Flow," University of Hull, Department of Engineering Design and Manufacture, Report No. EDM/4/81.

Rahman, A., 1988, "An Experimental Investigation of Heat Transfer in a Spanwise Rotating Turbulated Passage Using Liquid Crystal Technique," M. S. Thesis, Mechanical Engineering Department, Northeastern University, Boston, MA 02115.

Taslim, M. E., and Spring, S. D., 1987, "Friction Factors and Heat Transfer Coefficients in Turbulated Cooling Passages of Different Aspect Ratios, Part I: Experimental Results," presented at the 23rd AIAA/ASME/SAE/ASEE Joint Propulsion Conference, San Diego, CA, Paper No. AIAA-87-2009.

Taslim, M. E., and Spring, S. D., 1988, "An Experimental Investigation of Heat Transfer Coefficients and Friction Factors in Passages of Different Aspect Ratios Roughened With 45° Turbulators," presented at the ASME 25th National Heat Conference, Houston, TX.

Taslim, M. E., and Spring, S. D., 1988, "Experimental Heat Transfer and Friction Factors in Turbulated Cooling Passages of Different Aspect Ratios, Where Turbulators Are Staggered," presented at the 24th AIAA/ASME/SAE/ASEE Joint Propulsion Conference, Boston, MA, Paper No. AIAA-88-3014.

Wagner, J. H., Kim, J. C., and Johnson, B. V., 1986, "Rotating Heat Transfer Experiments With Turbine Airfoil Internal Flow Passages," ASME Paper No. 86-GT-133.

Zysina-Molozhen, L. M., Dergach, A. A., and Kogan, G. A., 1977, "Experimental Investigation of Heat Transfer in a Radially Rotating Pipe," *HGEEE High Temp.*, Vol. 14, p. 988.

An Analysis Methodology for Internal Swirling Flow Systems With a Rotating Wall

M. Williams
Rotating Machinery
Aerothermodynamics/CFD Group.

W. C. Chen

G. Baché[1]

A. Eastland
Hydrodynamics Group.

Rockwell International,
Rocketdyne Division,
Canoga Park, CA 91304

This paper presents an analysis methodology for the calculation of the flow through internal flow components with a rotating wall such as annular seals, impeller cavities, and enclosed rotating disks. These flow systems are standard components in gas turbines and cryogenic engines and are characterized by subsonic viscous flow and elliptic pressure effects. The Reynolds-averaged Navier-Stokes equations for turbulent flow are used to model swirling axisymmetric flow. Bulk-flow or velocity profile assumptions aren't required. Turbulence transport is assumed to be governed by the standard two-equation high Reynolds number turbulence model. A low Reynolds number turbulence model is also used for comparison purposes. The high Reynolds number turbulence model is found to be more practical. A novel treatment of the radial/swirl equation source terms is developed and used to provide enhanced convergence. Homogeneous wall roughness effects are accounted for. To verify the analysis methodology, the flow through Yamada seals, an enclosed rotating disk, and a rotating disk in a housing with throughflow are calculated. The calculation results are compared to experimental data. The calculated results show good agreement with the experimental results.

Introduction

The traditional analysis and design of turbomachinery flow components with a rotating wall, such as seals and cooling cavities, rely on one-dimensional analysis, multidimensional analysis based on drastic simplifying assumptions, or correlation functions derived from experimental studies of simple geometries. These methods have been extremely successful but require a significant amount of experience when applying them to nonstandard configurations. They are also limited in the amount of information they provide. For example, to estimate the flow losses through a constant gap annular seal, Yamada's (1962) friction factor expression for smooth annular seals is used to predict the overall friction factor (Chen and Jackson, 1985). However, for an annular seal with varying gap, Yamada's expression must be applied in an ad-hoc fashion and supplemented with other correlations.

To be able to calculate the general flow properties of most axisymmetric geometries with a rotating wall, a computational approach is essential. By solving the Navier-Stokes equations without relying on perturbations or velocity profile assumptions, a consistent and detailed analysis of rotating wall turbomachinery components can be performed, and the interdependence of various flow phenomena can be accounted for.

The solution of Navier-Stokes models for internal turbomachinery components has been treated by several researchers. Launder and Leschziner (1978) presented a Navier-Stokes procedure for the calculation of flow in two-dimensional finite-width thrust bearings. Their results included inertial effects but required assumptions about the velocity distribution within the bearing film.

Wittig et al. (1987) and Demko et al. (1988) have presented Navier-Stokes calculations for labyrinth seals. The Wittig calculation did not account for wall rotation but achieved good agreement with experimental results. The Demko calculation accounted for wall rotation and swirl and provided realistic results for straight through labyrinths. The standard high Reynolds number turbulence model was used to provide turbulence closure.

Morse (1988) calculated the turbulent flow in rotating cavities. The Launder and Sharma (1974) low Reynolds number turbulence model was used to account for turbulence transport. The solutions were a slight but definite improvement over corresponding mixing length calculations (Chew, 1984).

Computational fluid dynamics (CFD) technology is well developed, but has yet to be applied to the analysis and design of nontrivial internal fluid machine components in a routine fashion. To accomplish this, an analysis code based on the full Navier-Stokes equations must be robust, economical, and reasonably accurate. It is hoped that this paper presents a CFD methodology, that meets, or has the potential to meet, these goals. This methodology shares some of the numerical features found in Launder and Leschziner (1978), Wittig et al. (1987), and Demko et al. (1988). Primitive variables are used and a two-step predictor-corrector methodology is used to

[1] Currently at Aerojet Propulsion Systems, Sacramento, CA.

Contributed by the International Gas Turbine Institute and presented at the 34th International Gas Turbine and Aeroengine Congress and Exhibition, Toronto, Ontario, Canada, June 4-8, 1989. Manuscript received at ASME Headquarters January 27, 1989. Paper No. 89-GT-185.

solve the Navier-Stokes equations. However, the current methodology uses a nonstaggered finite volume scheme developed by Peric (1985) and is based on his two-dimensional computer code. Also, a novel treatment of the swirl equation source terms is developed and used to provide enhanced convergence.

The role of the turbulence model and wall functions in predicting, within engineering accuracy, parameters of interest is clarified by comparing high Reynolds number model results with the Lam-Bremhorst (1981) low Reynolds number turbulence model results for the enclosed rotating disk.

The physical assumptions and numerics of the calculation procedure are discussed. The CFD analysis is then applied to the Yamada (1962) seal, the Daily and Nece (1960) enclosed rotating disk, and the Dibelius et al. (1982) disk in a housing with throughflow. These cases feature axial, zero, and axial/radial throughflow, respectively, and provide a test of the generality of the methodology.

Physical Model and Calculation Numerics

The flow situation for the current analysis consists of axisymmetric swirling flow. All flow processes are assumed to be steady. The governing equations are the Navier-Stokes equations written in cylindrical coordinates. The concept of an isotropic turbulent viscosity is employed so the governing equations are (Ramos, 1986)

Continuity

$$r^{-1}\partial_r(r\rho V)+\partial_x(\rho U)=0 \tag{1}$$

Axial Momentum

$$r^{-1}\partial_r\, r(\rho UV-\mu\,\partial_r U)+\partial_x(\rho UU-\mu\,\partial_x U)= -\partial_x P+r^{-1}\partial_r r(\mu\,\partial_x V)+\partial_x(\mu\,\partial_x U) \tag{2}$$

Radial Momentum

$$r^{-1}\partial_r\, r(\rho VV-\mu\,\partial_r V)+\partial_x(\rho UV-\mu\,\partial_x V)= -\partial_r p+\rho r^{-1}W^2-2\mu r^{-2}V+r^{-1}\partial_r r(\mu\,\partial_r V)+\partial_x(\mu\,\partial_r U) \tag{3}$$

Swirl Momentum

$$r^{-1}\partial_r r(\rho VW-\mu\,\partial_r W)+\partial_x(\rho UW-\mu\,\partial_x W)= -\rho r^{-1}VW-r^{-2}W\,\partial_r(r\mu) \tag{4}$$

These equations are supplemented by a turbulence model, which is described in the next section. For laminar flow, $\mu=\mu_l$, and $2\mu r^{-1}V$ becomes $\mu r^{-1}V$ in the radial momentum equation.

The governing equations are discretized using a nonstaggered, body-fitted finite-volume formulation described by Peric (1985). The basic Navier-Stokes algorithm used is a predictor-corrector scheme, which uses a Poisson pressure correction equation. The flow algorithm is primarily for incompressible or slightly compressible viscous flow. The governing equations are the steady-state Navier-Stokes equations, written as

$$L\rho\mathbf{u}=\nabla p;\quad \nabla\cdot\rho\mathbf{u}=0 \tag{5}$$

where L is a Navier-Stokes operator, ∇ is the spatial gradient operator, ρ is the density, $\mathbf{u}$ is the velocity field, and a boldface letter denotes a vector quantity. The predictor-corrector algorithm proceeds by predicting a velocity field $\mathbf{u}^*$ based on a guessed pressure field; p^n,

$$\rho\mathbf{u}^*=L^{-1}\nabla p^n \tag{6}$$

The predicted velocities carry the correct amount of vorticity but do not satisfy mass continuity. The velocities are corrected to satisfy continuity

$$\rho\mathbf{u}^{n+1}=\rho\mathbf{u}^*-L^{-1}\nabla\phi \tag{7}$$

where ϕ is the pressure correction. The scalar function ϕ is determined by the equation

$$\nabla\cdot L^{-1}\nabla\phi=\nabla\cdot\rho\mathbf{u}^* \tag{8}$$

and the updated pressure is

$$p^{n+1}=p^n+\omega_p\phi \tag{9}$$

ω_p is an underrelaxation factor that is required since ϕ is not the physical pressure. Equations (6) and (8) are solved in a segregated fashion (one equation at a time) using standard SOR and conjugate gradient technology. A first-order upwind treatment was used for the convection terms. The special interpolation of the predicted velocities at the cell interfaces required for a nonstaggered grid arrangement is described in detail by Peric (1985).

The Turbulence Model. The standard high Reynolds number k-ϵ turbulence model is used to provide Navier-Stokes equation closure. A single update is performed for the turbulence transport equations for each global relaxation step. Wall functions are used to supply boundary conditions for the k-ϵ equations. To provide boundary conditions for the k-ϵ equations, the relations

$$k=C_\mu^{-1/2}U_*^2$$
$$\epsilon=U_*^3/\kappa y$$
$$U^+=U_{\text{res}}/U_*=\kappa^{-1}\ln(y^+)+5.5-\ln(1+.3\,\epsilon_r^+) \tag{10}$$

are used, where $y^+=\rho y U_*/\mu$, $\epsilon_r^+=\rho\epsilon_r U_*/\mu_l$, C_μ (0.09) and κ(0.4197) are turbulence model constants, y is the normal distance from the wall, ϵ is the average roughness height, and U_* the friction velocity. These relations assume that the turbulence local equilibrium hypothesis is valid. A law of the wall is required to relate the friction velocity and the velocity profile near the wall. However, swirling flows are three dimensional and a rigorous three-dimensional law of the wall has not

Nomenclature

a = disk radius
C_M = disk moment coefficient
C_p = pressure number
f = friction factor
k = turbulent kinetic energy
K = ratio of core swirl velocity to disk rotation velocity
P = static pressure
r = radial coordinate
r_1, r_0 = inner, outer pipe radius
Re_a = $\rho Us/\mu_l$ = axial Reynolds number
Re_ω = $\rho\omega a^2/\mu_l$ for enclosed rotating disk, $\rho\omega r_1 s/\mu_l$ for Yamada seal; rotational Reynolds number
Re_t = $k^2/\epsilon\nu$ = turbulence Reynolds number
Re_y = $k^{0.5}y/\nu$ = wall distance Reynolds number
s = gap spacing
U, V, W = axial, radial, and swirl velocities
U_* = friction velocity
x = axial coordinate
y = distance from no-slip wall
ϵ_r = average roughness height
ϵ = dissipation rate of turbulent kinetic energy
μ = effective viscosity
μ_l = molecular viscosity
μ_t = turbulent eddy viscosity
ν = kinematic viscosity
ρ = fluid densitiy
ω = angular velocity

Table 1 Damping functions for the k-ϵ models

Model	f_μ	f_1	f_2
High Re	1.0	1.0	1.0
Low Re	$(1-e^{-.0165R_y})^2 \cdot(1+20.5/R_t)$	$1+(0.05/f_\mu)^3$	$1-e^{-R^2_t}$

$C_\mu = 0.09$, $C_1 = 1.44$, $C_2 = 1.92$, $\sigma = 1/1.3$.

been formulated. There are several suggestions for defining a resultant velocity that correlates the velocity profile into a two-dimensional form. Of these it has been concluded that Johnston's secant approximation is the best (White, 1974). Johnston's secant approximation is given by

$$U_{\text{res}} = q\{(\partial_n q)^2 + (\partial_n W)^2\}^{1/2}/\partial_n q \tag{11}$$

where $q = \{U^2 + V^2\}^{1/2}$ and ∂_n is the wall normal derivative. This formulation was used in all the subsequent calculations and performed satisfactorily.

The high Reynolds number turbulence model is only valid for high turbulence Reynolds numbers Re_t ($= k^2/\nu\epsilon$) and consequently requires a wall function approach to provide boundary conditions for the k and ϵ equations. This wall function assumes a logarithmic velocity distribution. If y^+ is too small for the log law to be valid, the relation $u^+ = y^+$ is used but its use can result in the overprediction of viscous effects for channel type flows. Use of clustered grid points near a wall often requires a low Reynolds number formulation. The Lam-Bremhorst model is simple and theoretically self consistent, that is, the model allows k and ϵ to approach the correct limiting near wall values (Patel et al., 1985) and can be used to predict relaminarization due to rapidly accelerating boundary layers. The model is given as

$$r^{-1}\partial_r\, r(\rho Vk - \mu\,\partial_r k) + \partial_x(\rho Uk - \mu\,\partial_x k) = \Pi - \rho\epsilon \tag{12}$$

$$r^{-1}\partial_r\, r(\rho V\epsilon - \sigma\mu\,\partial_r\epsilon) + \partial_x(\rho U\epsilon - \sigma\mu\,\partial_x\epsilon) = f_1 C_1 \epsilon k^{-1}\Pi - f_2 C_2 \rho\epsilon^2 k^{-1} \tag{13}$$

where

$$\Pi = \mu_t\{2(\partial_x U)^2 + 2(\partial_r V)^2 + 2(r^{-1}V)^2 + (r\partial_r r^{-1}W)^2 + (\partial_x V + \partial_r U)^2 + (\partial_x W)^2\}$$

is the rate of production of turbulent kinetic energy, and the effective eddy viscosity is $\mu = \mu_l + \mu_t$, where $\mu_t = f_\mu C_\mu \rho k^2/\epsilon$.

These equations, with different damping functions (f_1, f_2, f_μ), also apply to high Reynolds number turbulence flow. The values of the turbulence model constants and damping functions for both the low and high turbulence models are given in Table 1. These equations are discretized in a manner similar to the Navier-Stokes momentum equations and are solved using standard SOR technology.

The normal practice is to integrate equations (12) and (13) to the wall with $k = 0$ and $\epsilon = \nu\partial_{nn}k$ (or $\partial_n\epsilon = 0$) at the wall. The condition $\partial_n\epsilon = 0$ is inappropriate for a totally enclosed cavity because the ϵ solution may not be unique since Neumann type boundary conditions are used everywhere. The use of the conditions $k = 0$ and $\epsilon = \nu\partial_{nn}k$ proved to be very sensitive to initial conditions and grid clustering near the wall, and therefore, was not very robust. To avoid convergence problems, the turbulent kinetic energy and dissipation were specified at the first grid point away from the wall. However, these values are not derived from the local equilibrium assumption but from the continuity equation and the no-slip condition (Patel et al., 1985). They are given as

$$k = 0.028\rho^2 y^2 U_*^4/\mu^2$$
$$\epsilon = 2\mu k/\rho y^2 \tag{14}$$

These expressions are valid in the viscous sublayer ($y^+ \sim 1$). The use of a turbulence model that is valid in the viscous sublayer (the current formulation or even the $k = 0$ system) does not imply a laminar flow solution, since the large-scale core turbulence still exists for high Reynolds numbers.

Treatment of Swirl Source Terms. The discretized radial (V) and swirl (W) momentum equations can be written as

$$a_p V_i^* + a_e V_{i+1}^* + a_w V_{i-1}^* = S_v^n + \mathbf{A}W^2,$$
$$i = 2,\ i\text{max} - 1 \text{ (node locations)} \tag{15}$$

$$a_p W_i^* + a_e W_{i+1}^* + a_w W_{i-1}^* = S_w^n + \mathbf{BVW} \tag{16}$$

where the a's are the discretization coefficients and are not necessarily the same for the swirl and radial equations, S_v^n and S_w^n are the radial and swirl equation source terms at the old iteration level, respectively, and AW^2 and BVW are the swirl coupling terms. The j dependence ($a_s V_{j-1}^*$, etc.) is omitted for the sake of brevity. Equations (15) and (16) form an implicit system for the predicted velocities V^* and W^*. The usual practice is to treat the coupling terms explicitly. Because segregated solutions of these equations do not account for the source interdependence, convergence can be hampered. To make the equations more implicit, and therefore improve convergence, the source terms in equations (15) and (16) are written as

$$2AW^2 = AW^2 V^{-1}(1 - e_1)V^* + AW^2 V^{-1}(1 + e_1)V^n \tag{17}$$

$$2BVW = BV(1 - e_2)W^* + BV(1 + e_2)W^n \tag{18}$$

where $e_1 = \text{sign}\,(AV^{-1})$ and $e_2 = \text{sign}\,(BV)$. So when $BV < 0$ and $AV^{-1} < 0$, the source terms are treated implicitly and the numerical solution convergence can be improved.

Boundary Conditions. At no-slip boundaries the velocity components were set equal to zero. For rotating boundaries, the swirl velocity is prescribed. For inflow boundaries, the velocity profiles were prescribed and the turbulence properties were set from boundary layer considerations. At outflow boundaries, mass conservation was required. Neumann type boundary conditions were used for the pressure at all boundaries. The pressure level was set at a single interior cell.

Numerical Results

The preceding computational methodology is validated by examining three different internal flow systems with a rotating wall.

With a first-order treatment of the convection terms, artificial diffusion caused by truncation errors can be a problem. The truncation error varies like $q\partial_{ss}\phi$ where q is a velocity and ϕ is a convected quantity. For axisymmetric swirling flows, $\partial_{\theta\theta}\phi = 0$ in the swirl direction (θ) so the first-order truncation error in this direction is negligible. For the fully developed Yamada seal flow, $\partial_{xx}\phi \sim 0$ and $v \sim 0$ so the first-order truncation errors in the axial and radial directions are small. Use of a refined grid for the Yamada seal configuration confirmed this conclusion. For the laminar flow in the enclosed rotating disk, the truncation error can be significant and a fine grid was necessary to minimize truncation errors. For turbulent flow in the enclosed disk and the disk with throughflow, $W > U$, V and the truncation error is confined to the weak secondary flow. The computational results were calculated on grids selected by a grid refinement study unless otherwise indicated.

All turbulent flow calculations were performed using the high Reynolds number turbulence model formulation for smooth walls. For the enclosed rotating disk, the low Reynolds number model was also used. The flow solutions were considered to be converged after the equation residuals decreased by about a factor of 200 from their maximum value. A typical moment coefficient convergence history is shown in Fig. 1. This history is for the turbulent flow in the enclosed rotating disk. The high Reynolds number turbulence model was used. The moment coefficient is converged to its steady-

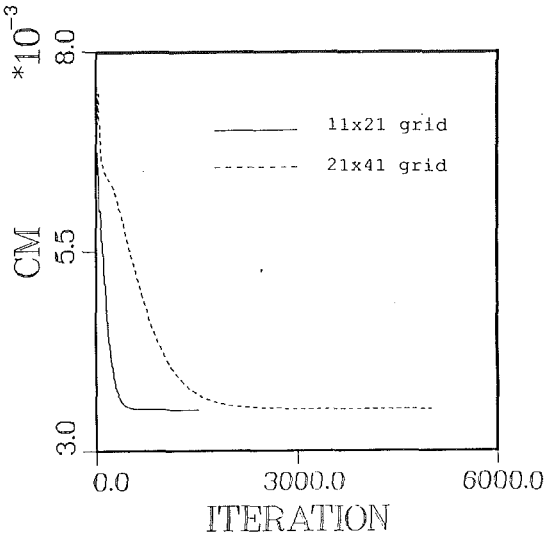

Fig. 1 Typical convergence history

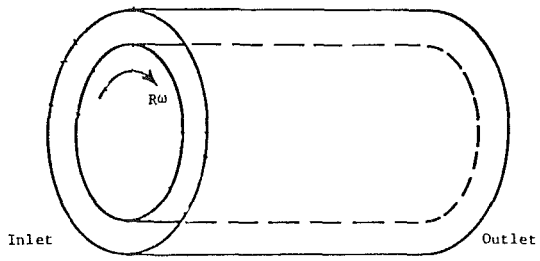

Fig. 2 Annular seal geometry

state value when the equation residuals decrease by a factor of 200 from their maximum values. More iterations are required to get a converged solution on the mesh with more grid points (smaller mesh size).

Annular Seal Friction Factor. An experiment to measure the friction losses through a smooth constant gap annular seal has been carried out by Yamada (1962). The experiment was performed for a range of axial and rotational (inner cylinder rotating) Reynolds numbers. The annular seal consists of coaxial cylinders (Fig. 2). The flow calculation procedure was applied to this geometry and the computed friction factor was compared to the experimentally measured and theoretically predicted friction factors.

The seal geometry was discretized using a 51×11 grid. The grid points were uniformly distributed in the axial and radial directions. The working fluid is water.

At the seal entrance the axial velocity profile is uniform. At the seal exit, the axial and radial velocities are extrapolated from the interior and updated to conserve mass. The swirl velocity is extrapolated from the interior.

The friction factor f is calculated by the following relationship

$$f = 4\Delta P\, s/L\rho U^2_{\text{ave}} \tag{19}$$

where s is the seal gap size, ρ is the density, U_{ave} is the average axial velocity, and ΔP is the average pressure difference over the distance L. The calculation is carried out near the discharge where fully developed flow is reached.

Calculations were performed for two different seal gap to inner radius ratios and for a variety of axial and rotation Reynolds number combinations. The numerical results for the concentric seal are compared to Yamada's test results and correlation equation in Tables 2 and 3. The agreement is very good. This indicates that the pressure calculation methodology is accurate and the three-dimensional wall function formulation is appropriate for swirling flows.

Table 2 Friction factor for Yamada seal ($s = 3.315$ mm, $r_1 = 28.836$ mm)

R_a	R_ω	Yamada's Eq.	Yamada's exp.	Present method	% error from test
2×10^4	27470	0.0272	0.029	0.0275	5.1
2×10^4	18880	0.0256	0.027	0.0257	4.8
2×10^4	9438	0.0245	0.026	0.0247	5.0
2×10^4	0	0.0241	0.025	0.0239	4.4
5000	27470	0.0708	0.072	0.0724	0.6
5000	18880	0.0341	0.060	0.0587	2.1
5000	9438	0.0339	0.048	0.044	8.3
5000	0	0.0338	0.0345	0.0347	0.6

Table 3 Friction factor for Yamada seal ($s = 1.456$ mm, $r_1 = 30.695$ mm)

R_a	R_ω	Yamada's Eq.	Yamada's exp.	Present method	% error from test
9956	14930	0.0327	0.034	0.0341	0.3
9956	4978	0.0290	0.029	0.0290	0.0
9956	995	0.0285	0.028	0.0285	1.8
9956	0	0.0285	0.028	0.0285	1.8

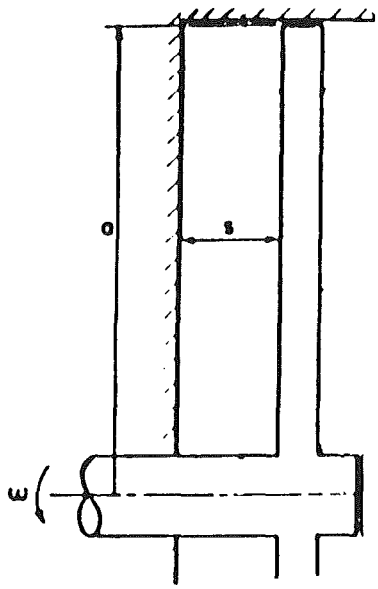

Fig. 3 Enclosed rotating disk geometry

Enclosed Rotating Disk. The enclosed rotating disk consists of a smooth circular disk placed in a cylindrical chamber. An experimental study of this flow system has been performed by Daily and Nece (1960). The flow geometry is indicated in Fig. 3. The rotor radius ($=a$) is 0.25 m and the shaft radius is 0.0254 m. Calculations were performed for several gap widths and rotational Reynolds numbers. The working fluid is water.

Laminar Flow. For the laminar flow case the rotational Reynolds number ($=\rho\omega a^2/\mu_l$) is equal to 4.2×10^4. The rotor and shaft are rotating at 0.6840 rad/s. For this Reynolds number, the secondary flow is about the same magnitude as the swirling velocity and fine grids are required to obtain accurate results. Gap-to-disk radius ratios ($=s/a$) of 0.051, 0.102, and 0.217 were examined.

The secondary flow streamlines are indicated in Fig. 4. The

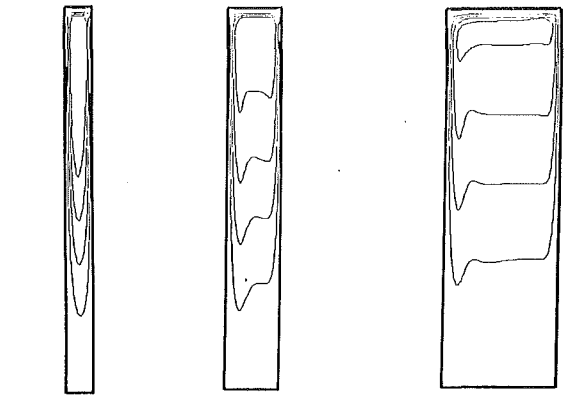

Fig. 4 Secondary flow for $Re_\omega = 4.2 \times 10^4$

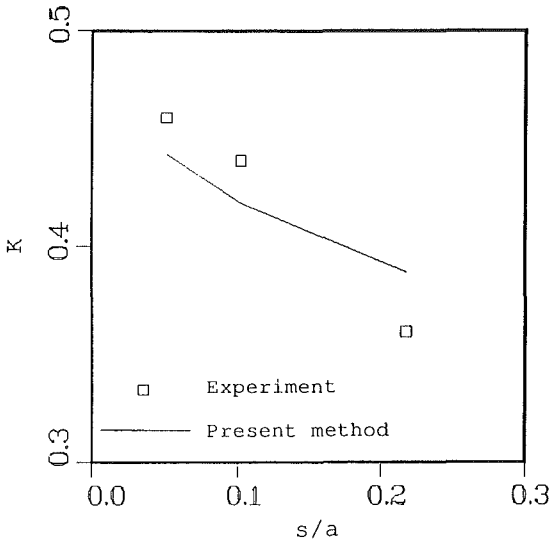

Fig. 5 Core swirl velocity at $r/a = 0.765$ for $Re_\omega = 4.2 \times 10^4$

asymmetry of the flow pattern increases as the gap width increases.

The gap core rotation velocity is an indication of disk pumping and was measured by Daily and Nece (1960). The calculated results at $r/a = 0.765$ are compared to the experimental data in Fig. 5. The agreement is good. The semi-empirical torque coefficient correlation developed by Daily and Nece (1960) and the Navier-Stokes results are in agreement with the experimental results as shown in Fig. 6.

Turbulent Results. For the turbulent flow cases, the rotor and shaft rotation speed is 71.3 rad/s and the rotational Reynolds number is 4.4×10^6. These cases were calculated with both the high and low Reynolds number turbulence models.

Figure 7 compares the computed tangential velocity with experimental data at $r/a = 0.765$ for the case $s/a = 0.0255$. The high Reynolds number turbulence calculation was performed with an 11×21 grid and a 21×41 grid. The calculated profile depends upon the y^+ of the first grid point away from the rotor wall. Several grids were examined and it was concluded that keeping the maximum rotor y^+ in the range of applicability of the logarithm law of the wall provided the best results. Figure 1 indicates that the 11×21 and 21×41 grids give similar rsults. The 21×41 result is used for comparison with experimental and theoretical data. The low Reynolds number turbulence model was used on a 41×71 grid with y^+ on the order of 1. The swirl velocity profile near the stator wall

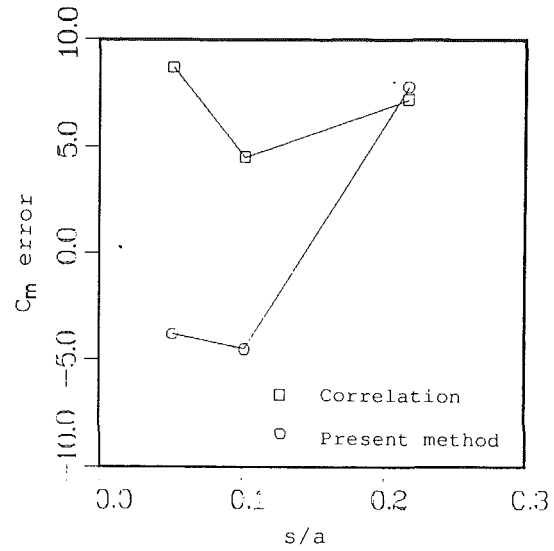

Fig. 6 C_M percent difference from experimental results for $Re_\omega = 4.2 \times 10^4$

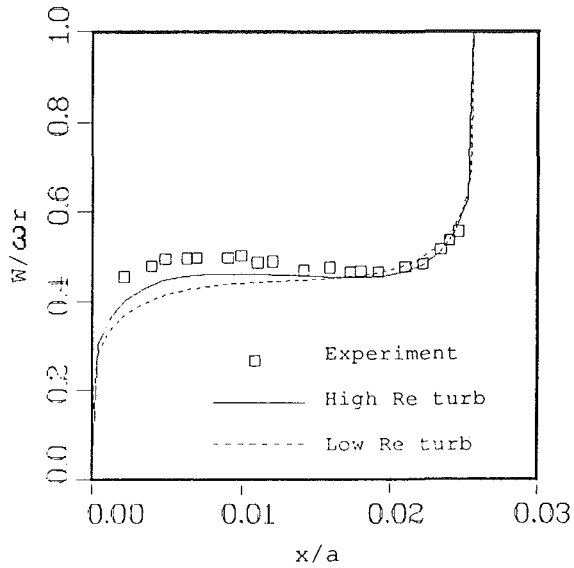

Fig. 7 Swirl velocity at $r/a = 0.765$ for $s/a = 0.0255$ and $Re_\omega = 4.4 \times 10^6$

is not predicted as well with the low Reynolds number model compared to the high Reynolds number model.

The secondary flow boundary layers are quite distinct in Fig. 8. The computed radial velocity is in general agreement with the experimental results. The pumping velocities are predicted accurately.

The next case computed is for $s/a = 0.0637$. The swirl velocity at $r/a = 0.765$ is shown in Fig. 9. The calculated results follow the experimental data closely except near the stator wall. The experimental results show a hump near the stator wall that is not completely captured by the calculation results. The high and low Reynolds number turbulence model were used on 21×41 and 41×71 grids, respectively. Both models performed equally well in predicting the swirl velocity profile.

The radial velocity profile (Fig. 10) is flat near the disk core and the stator/rotor radial boundary layers are more distinct than the radial layers for the $s/a = 0.0255$ case. The peak radial velocities are overpredicted.

To determine the ability of the current methodology to predict the pump axial load, the theoretical pressure head gradient on the rotor wall (the pressure gradient across the gap is

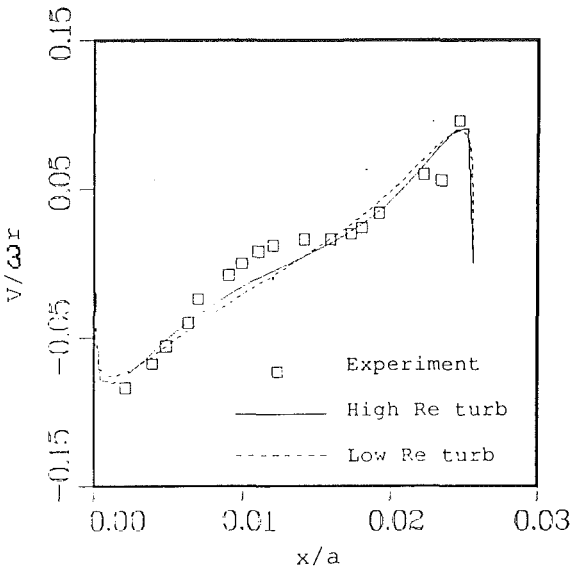

Fig. 8 Radial velocity at $r/a = 0.765$ for $s/a = 0.0255$ and $Re_\omega = 4.4 \times 10^6$

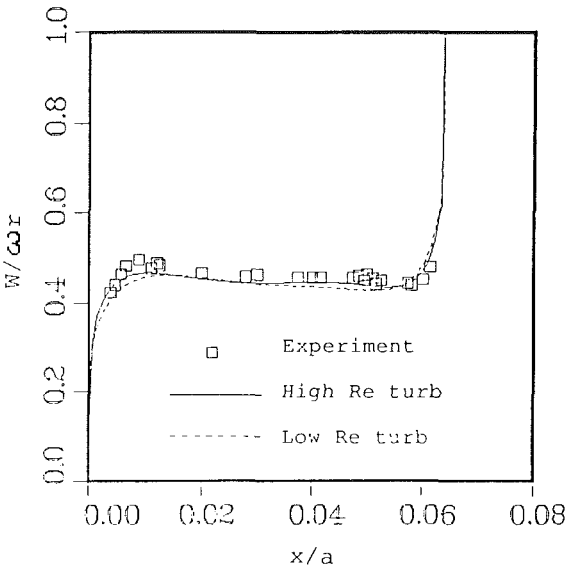

Fig. 9 Swirl velocity at $r/a = 0.765$ for $s/a = 0.0637$ and $Re_\omega = 4.4 \times 10^6$

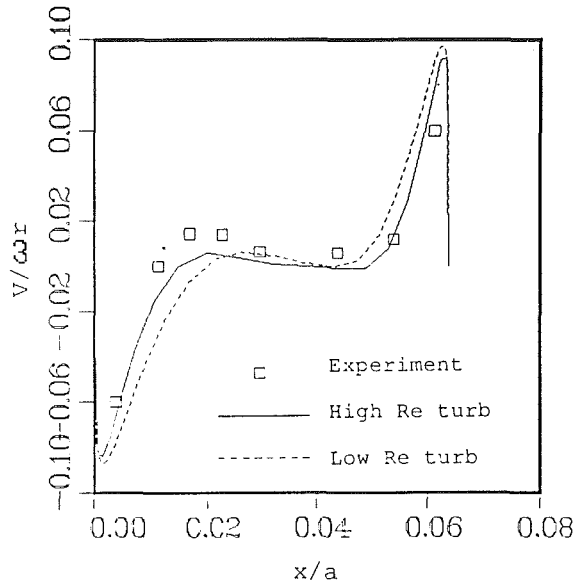

Fig. 10 Radial velocity at $r/a = 0.765$ for $s/a = 0.0637$ and $Re_\omega = 4.4 \times 10^6$

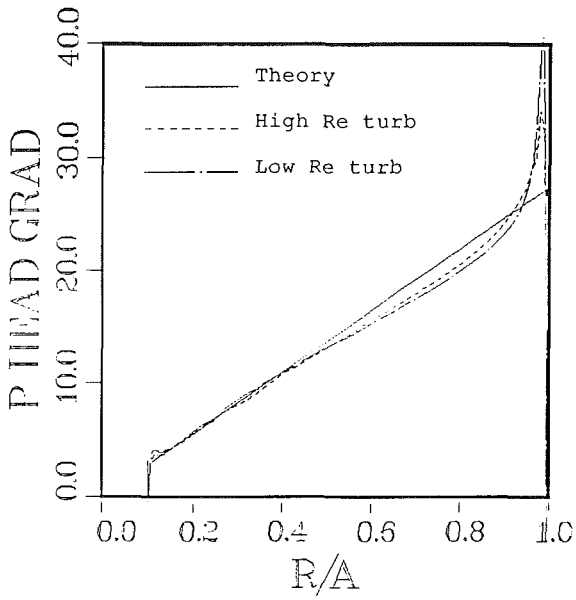

Fig. 11 Radial pressure head gradient for $s/a = 0.0637$ and $Re_\omega = 4.4 \times 10^6$

very small) is compared to the corresponding calculation result for $s/a = 0.0637$ (Fig. 11). The computed pressure head gradient agrees with theory. Daily and Nece (1960) indicate that the agreement between theory and their experimental pressure data was good.

The computed torque coefficients are compared to experiment and theory in Fig. 12. The low Reynolds turbulence model results overpredict the torque coefficient by as much as 30 percent.

Rotating Disk With Throughflow. The effect of throughflow on frictional effects and related flow mechanisms in a gap between a housing and a rotating disk has been investigated experimentally (Dibelius et al., 1982). The throughflow can have a significant effect on disk pumping. Impeller cavities and turbine wheel cavities are represented by a rotating disk in a housing with throughflow. The test configuration is indicated in Fig. 13. The calculation methodology was applied to this geometry using a 68×16 computational grid. This grid was generated using the previous calculation results as a guideline and a complete grid refinement study was not performed.

The working fluid is air. The throughflow number $(= \dot{m}/a\mu_l)$ is 1.4×10^5, the flow is directed centripetally, and the Reynolds number is 4.2×10^6. The disk radius is 0.4 m. The disk gap is 0.025 m and the shaft radius is 0.08 m. The exit angle of the swirl vanes is 12 deg. The shaft and disk are rotating at 400 rad/s.

The computed swirl velocity profiles are compared to the experimental data in Fig. 14. The agreement is good but gets worse near the flow discharge. The maximum error is about 14 percent.

The pressure number $(C_p = 1 - (P(a) - P(r))/a^2\rho\omega^2)$ as a function of the radius is shown in Fig. 15. The computed results agree with experiment and theory of Dibelius et al. (1982).

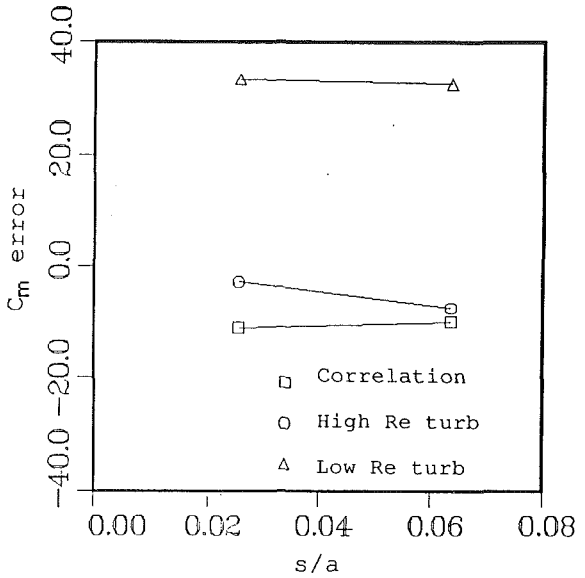

Fig. 12 C_M percent difference from experimental results for $Re_\omega = 4.4 \times 10^6$

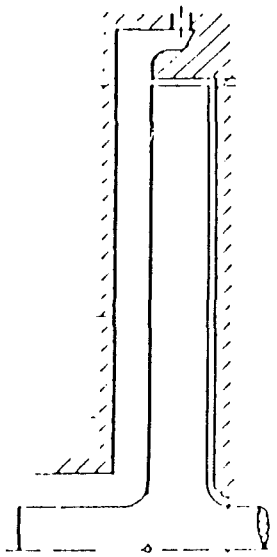

Fig. 13 Rotating disk with throughflow

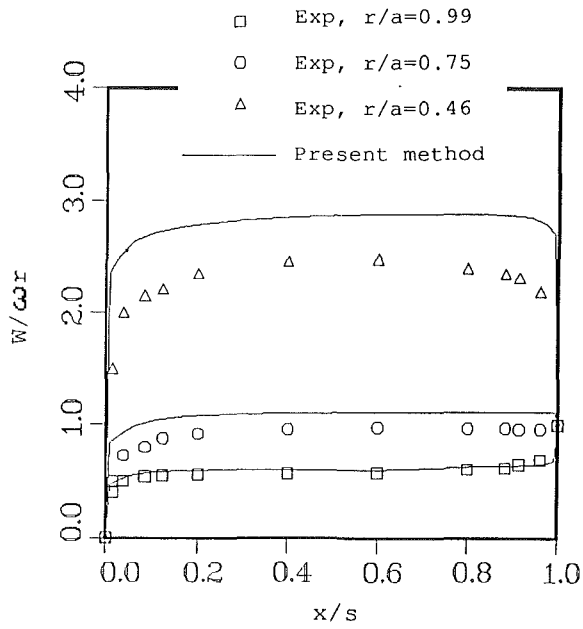

Fig. 14 Swirl velocity profiles for the disk with throughflow

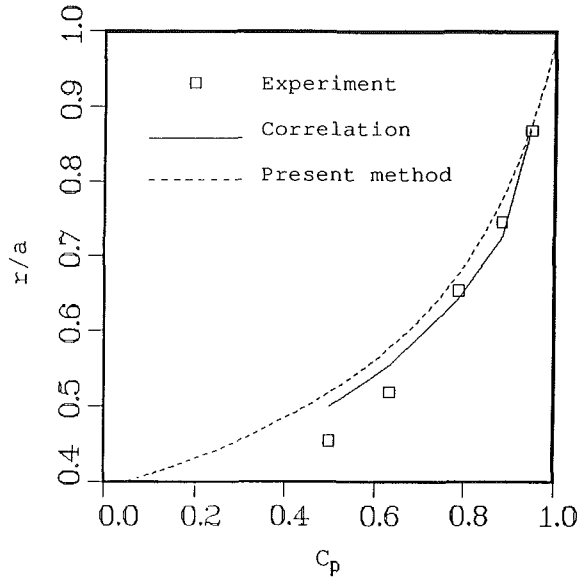

Fig. 15 Pressure number

Discussion

The Navier–Stokes methodology performed well for the internal flow systems considered. The friction factors for the Yamada seal were calculated correctly. The turbulent flow torque coefficients for the enclosed rotating disk tend to be overpredicted by about 30 percent when the low Reynolds number turbulence model is used. Patel et al. (1985) indicate that some low Reynolds number turbulence models tend to overpredict the flat plate friction coefficient by as much as 20 percent, even when 50 grid points are placed in the viscous sublayer. Also, the effect of the end-wall and shaft layers on the overall torque may be significant and tip leakage was not modeled. The swirl velocity profiles and axial force on the disk with throughflow was calculated correctly. The high Reynolds number turbulence model performed well for all the flow cases considered and was more economical than the low Reynolds number turbulence model computations.

The preceding Navier–Stokes methodology can be used to analyze flow systems for which experimental data do not exist.

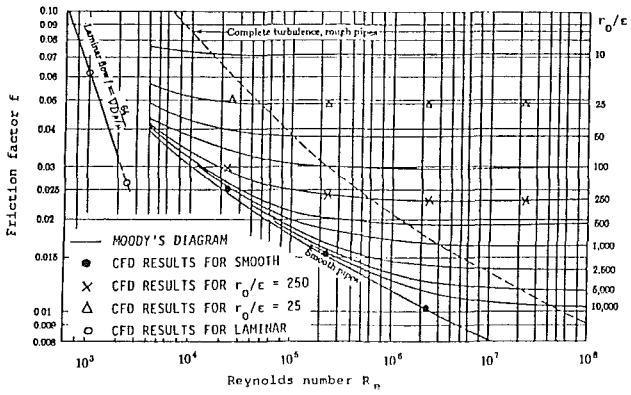

Fig. 16 Moody's diagram and present CFD results

For example, the three-stage Rocketdyne Mark-49 turbopump design assumed that the pumping factors for the forward and rear impeller cavities were 0.5 for all three stages. However, a calculation using the current methodology indicated that the pumping factors were different for the different stages. This computational methodology was also used in the multizone calculation of turbopump cooling cavities (Williams, 1988).

To tailor seal leakage or cavity pumping factors, it is common practice to use roughness on the rotor or stator. The Navier–Stokes methodology presented here can handle rough surfaces. The Moody diagram results for smooth and rough pipe flow can be reproduced using the current procedure with the high Reynolds number turbulence model (see Fig. 16). It would be quite a challenge to simulate rough wall flows with a low Reynolds number k–ϵ turbulence model since the actual roughness contour would have to be resolved and grid points would have to be maintained in the viscous sublayer.

Conclusions

A Navier–Stokes analysis methodology for the calculation of the flow through internal flow components with a rotating wall has been developed. A novel treatment for the swirl coupling source terms was developed to improve equation convergence. Johnston's secant approximation was used to formulate a three-dimensional law of the wall. The methodology was applied to three swirling flow systems and the calculation results were compared to experiment. Good agreement with experiment was obtained in all the cases. A low Reynolds number formulation based on the Lam–Bremhorst turbulence model and specified near wall distributions of k and ϵ was used. The low Reynolds number turbulence model calculation results were in general agreement with the high Reynolds number turbulence model results. The high Reynolds number turbulence model was more efficient in terms of computing and grid point costs.

References

Chen, W. C., and Jackson, E. D., 1985, "Eccentricity and Misalignment Effects on the Performance of High-Pressure Annular Seals," *ASLE Trans.*, Vol. 28, No. 1, 1984, pp. 104–110.

Chew, J. W., 1984, "Prediction of Flow in a Rotating Cavity With Radial Outflow Using a Mixing Length Turbulence Model," *Proc. 4th Int. Conf. on Numerical Methods in Laminar and Turbulent Flow*, Swansea, United Kingdom.

Daily, J. W., and Nece, R. E., 1960, "Chamber Dimension Effects on Induced Flow and Frictional Resistance of Enclosed Rotating Disks," ASME *Journal of Basic Engineering*, Vol. 82, p. 217

Demko, J. A., Morrison, G. L., and Rhode, D. L., 1988, "The Prediction and Measurement of Incompressible Flow in a Labyrinth Seal," AIAA Paper No. 88-0190.

Dibelius, G., Radtke, E., and Ziemann, M., 1982, "Experiments on Friction, Velocity and Pressure Distribution of Rotating Disks," *Heat and Mass Transfer in Rotating Machinery*, D. E. Metzger and N. H. Afgan, eds., Hemishere Publishing Co., New York, pp. 117–130.

Lam, C. K. G., and Bremhorst, K. A., 1981, "Modified Form of the k–ϵ Model for Predicting Wall Turbulence," ASME *Journal of Fluids Engineering*, Vol. 103, p. 456

Launder, B. E., and Leschziner, M. A., 1978, "Flow in Finite-Width Thrust Bearings Including Inertial Effects: I—Laminar Flow; II—Turbulent Flow," ASME *Journal of Lubrication Technology*, Vol. 100, pp. 330–345.

Launder, B. E., and Sharma, B. I., 1974, "Application of the Energy-Dissipation Model of Turbulence to the Calculation of Flow Near a Spinning Disc," *Letters in Heat and Mass Transfer*, Vol. 96, p. 204.

Morse, A. P., 1988, "Numerical Prediction of Turbulent Flow in Rotating Cavities," ASME JOURNAL OF TURBOMACHINERY, Vol. 110, pp. 202–212.

Patel, V. C., Rodi, W., and Scheuerer, G., 1985, "Turbulence Models for Near-Wall and Low Reynolds Number Flow: A Review," *AIAA J.*, Vol. 23, p. 1308.

Peric, M., 1985, "A Finite Volume Method for the Prediction of 3-D Fluid Flow in Complex Ducts," Ph.D. Thesis, Imperial College, London, United Kingdom.

Ramos, J. I., 1986, "Incompressible Swirling Flows," *Eng. Comput.*, Vol. 3, pp. 53–63.

White, F. M., 1974, *Viscous Fluid Flow*, McGraw-Hill, New York.

Williams, M., 1988, "The Multi-Zone Calculation of Turbomachinery Flows: Part I—Iterative Domain Coupling for Incompressible Navier–Stokes Flow Calculations," AIAA Paper No. 88-3096.

Wittig, S., Schelling, U., Kim, S., and Jacobsen, K., 1987, "Numerical Predictions and Measurements of Discharge Coefficients in Labyrinth Seals," ASME Paper No. 87-GT-188.

Yamada, Y., 1962, "Resistance of Flow Through an Annulus With an Inner Rotating Cylinder," *Bulletin of JSME*, Vol. 5, No. 18, pp. 302–310.

A Theoretical Study of Ingress for Shrouded Rotating Disk Systems With Radial Outflow

J. W. Chew
Rolls-Royce plc,
Derby, United Kingdom

Sealing of the cavity formed between a stationary disk and a rotating disk under axisymmetric conditions is considered. A mathematical model of the flow in the cavity based on momentum integral methods is described and this is coupled to a simple model of the seal for the case when no ingress occurs. Predictions of the minimum imposed flow required to prevent ingress are obtained and shown to be in reasonable agreement with the data of Bayley and Owen (1970), Owen and Phadke (1980), Phadke (1982), and Phadke and Owen (1983a, 1983b, 1988). With an empirical constant in the model chosen to match these data, predictions for the minimum sealing flow are shown to be in good agreement with the measurements of Graber et al. (1987). The analysis of Phadke's data also indicates the measurements for small seal clearances must be viewed with caution due to errors in setting the seal clearance. These errors are estimated to be twice the minimum clearance considered. Seal behavior when ingress occurs is also considered and estimates of the amount of ingress are made from the available data.

Introduction

In a gas turbine engine, ingress of the the hot mainstream gas into the space between a rotating turbine disk and a stator can lead to overheating and reduced life of the disk. To prevent or limit this effect, cooler air may be channeled radially outward through the cavity and ejected into the mainstream flow. In order to gain insight into such flows in the engine, Bayley and Owen (1970), Owen and Phadke (1980), Phadke (1982), and Phadke and Owen (1983a, 1983b, 1988) have studied the flow in the cavity between two plane disks, one rotating and the other stationary. In these tests various shroud designs have been assessed by comparing the minimum throughflow rate that is required to prevent ingress of air from the quiescent environment into the cavity. In the present paper a theoretical study of such flows will be reported. Although these idealized conditions are not truly representative of conditions in the engine, they provide a convenient starting point and testing ground for theoretical methods.

Bayley and Owen's experimental rig incorporated a stationary shroud with a simple axial seal, denoted seal A in Fig. 1. These workers obtained the following correlation for the minimum value of the mass flow parameter $C_{w,\min}$ required to seal the cavity:

$$C_{w,\min} = 0.61\, G_c\, \mathrm{Re}_\phi \qquad (1)$$

Here $C_w = \dot{m}/\mu b$, $\mathrm{Re}_\phi = \rho\Omega b^2/\mu$, and $G_c = s_c/b$, $\dot{m}$ being the mass flow rate, Ω the angular velocity of the disk, s_c the seal clearance, b the disk outer radius, ρ density, and μ viscosity. A simple theoretical argument supporting the form of equation (1) was also proposed. However, this argument rests on a different interpretation of the flow from that put forward below. Phadke and Owen have also considered this seal geometry and found that their results, covering a wider parameter range, suggested a nonlinear relationship between $C_{w,\min}$ and G_c. Results for the various seals have been presented in the form of correlations but, without a sound understanding of the flow, it is not clear how these are best extrapolated to engine conditions.

Prediction of ingress and its effects does not appear to have received much attention in the open literature. Some work using finite difference methods to solve the axisymmetric partial differential equations modeling laminar flow was reported by Sambo (1985). This was extended to three-dimensional laminar flow and axisymmetric turbulent flow using a mixing-

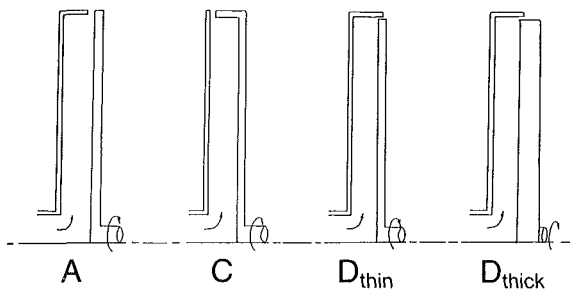

Fig. 1 Seal classification

Contributed by the International Gas Turbine Institute and presented at the 34th International Gas Turbine and Aeroengine Congress and Exhibition, Toronto, Ontario, Canada, June 4–8, 1989. Manuscript received at ASME Headquarters January 27, 1989. Paper No. 89-GT-178.

length model of turbulence by Vaughan and Turner (1987) and Vaughan (1987). The turbulent flow results showed qualitative agreement with data and the three-dimensional computations also showed promise. Vaughan's results also indicate that Sambo's computations are unreliable. The extent of these studies was severely limited by the high computing cost of the calculations.

Less sophisticated modeling techniques have been used by some workers. Haaser et al. (1988) characterized the flow through a rim seal by an empirically determined discharge coefficient and coupled this to a very basic model of the cavity flow. Graber et al. (1987) formulated a seal model that incorporated a turbulent transport coefficient and agreement with experiment was claimed if different transport coefficients were used for each seal configuration. These models provide a good indication of the state of the art for predicting ingress and its effects in design calculations.

The approach adopted here is to couple a solution for the flow in the cavity between the two disks to a model for the seal flow. An integral solution technique is used to predict the flow behavior in the cavity and this is presented in the next section. Seal behavior will then be discussed and a simple model of seal behavior is proposed for conditions in which ingress does not occur. Some of the available data are re-examined and used to deduce ingress levels when there is no imposed throughflow. The proposed model is tested by comparing predictions for the minimum sealing flow with the available experimental data. Incompressible flow has been assumed in the analysis as this is a good approximation to the experimental conditions.

Cavity Flow

A schematic of the flow in a rotor-stator cavity is shown in Fig. 2. This is deduced from experimental work (e.g., Daily and Nece, 1960) and numerical solutions (e.g., Chew and Vaughan, 1988). The cavity width s is assumed to be sufficiently large for distinct boundary layers to develop on the two disks. Fluid is centrifuged out near the rotor and, outside the source region, which is influenced by inlet conditions, fluid next to the stationary disk travels radially inward. Between the disk boundary layers a rotating core develops in which there is a

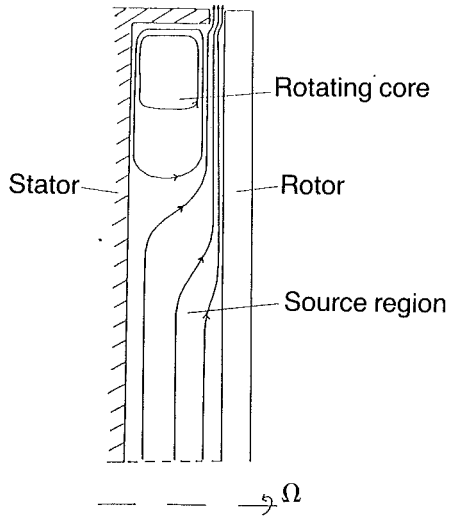

Fig. 2 Schematic of flow

weak axial flow, but, to a good approximation, no radial motion and no axial variation in the tangential velocity. For a sealed system the core is known from experiments to rotate roughly as a solid body at 40 to 50 percent of disk speed. With radial outflow the angular velocity of the core depends on inlet conditions and varies with radial position.

Several workers have previously applied variations of von Karman's (1921) integral method to the rotor-stator system (see, e.g., Daily and Nece, 1960; Owen, 1989). However, previous treatments have involved some approximations that are considered questionable and so a different approach has been used here. Some guidance for the development of this method was obtained from Chew and Vaughan's (1988) finite difference solutions of the Reynolds-averaged Navier–Stokes equations with a mixing length model of turbulent. A von Karman type treatment is retained for the boundary layer on the rotating disk, but a modified integral method is applied on the stationary disk. A simple treatment of the shroud boundary layer is also included.

Nomenclature

a = inlet radius
b = disk outer radius
C_D, C_D' = discharge coefficients, equations (17) and (18)
C_w = mass flow parameter = $\dot{m}/\mu$b
f = function defining radial velocity profile, equation (11)
F = friction factor
G_c = seal clearance ratio = s_c/b
H = overlap ratio, i.e., axial overlap of seal divided by b
I = coefficients in momentum integral equations
k = empirical constant in seal model
$\dot{m}$ = mass flow rate; when not subscripted = imposed throughflow rate
N = number of grid points in numerical solution
p = static pressure
r = radial coordinate
Re_ϕ = rotational Reynolds number = $\rho\Omega b^2/\mu$
s = cavity width
s_c = seal clearance
u = radial velocity component
u_{dm} = mixed-out radial velocity for near-wall flow on the rotating disk at $r=b$
u_m = mean velocity through seal in r–z plane
u_1 = function of r in radial velocity profile
v = tangential velocity component
w = axial velocity component
z = axial coordinate
δ = boundary layer thickness
Δp = pressure difference across seal
Δp_r = radial pressure difference across cavity
η = z/δ
λ = throughflow parameter = $C_w/\mathrm{Re}_\phi^{0.8}$
μ = dynamic viscosity
ρ = density
τ_r, τ_ϕ = radial and tangential shear stress components
ϕ = angular coordinate
Φ = cooling effectiveness, equation (19)
Ω = angular velocity of disk

Subscripts

b = refers to $r=b$ or shroud
ex = external flow
in = ingress
min = minimum sealing flow
s = stationary disk
0 = surface $z=0$

Superscripts

$\bar{}$ = denotes values at the boundary layer edge $z=\delta$

Treatment of the Rotating Disk. Generalizations of von Karman's assumptions are used for the velocity profiles across the boundary layer and the shear stress at the disk. Employing a cylindrical coordinate system (r, ϕ, z) with the disk at $z = 0$, these assumptions may be written:

$$v - \Omega r = (\bar{v} - \Omega r)\ (z/\delta)^{1/7} \tag{2}$$

$$u = u_1(r)\ (z/\delta)^{1/7}\ (1 - z/\delta) \tag{3}$$

$$\tau_{\phi,0} = 0.0225\rho\left(\frac{\mu}{\rho\delta}\right)^{1/4}(\bar{v} - \Omega r)[u_1^2 + (\bar{v} - \Omega r)^2]^{3/8} \tag{4}$$

$$\tau_{r,0} = \tau_{\phi,0} u_1/(\bar{v} - \Omega r) \tag{5}$$

Here u and v are the radial and tangential velocity components, $\tau_{r,0}$ and $\tau_{\phi,0}$ are the radial and tangential components of the shear stress at the wall, Ω is the disk angular velocity, δ is the boundary layer thickness, ρ denotes density, u_1 is a function of r only, and the overbar denotes a value at the boundary layer edge $z = \delta$. Note that equation (3) gives $u = 0$ at $z = \delta$. Although this condition may not strictly apply in the source region, it is a valid approximation provided the disk speed is much larger than the radial velocity in the inviscid flow region.

Assuming rotationally dominated flow outside the boundary layers, the radial momentum equation in this region reduces to

$$\frac{dp}{dr} = \frac{\rho \bar{v}^2}{r} \tag{6}$$

where p denotes static pressure. Using this result, equations (2) and (3), and the usual boundary layer assumptions, the mass and momentum conservation equations for the boundary layer may be integrated from $z = 0$ to δ to give

$$\rho \bar{w} = -\frac{I_1}{r}\frac{d}{dr}(r\rho u_1 \delta) \tag{7}$$

$$\frac{I_2}{r}\frac{d}{dr}(\rho r u_1^2 \delta) + \frac{\rho}{r}\delta I_5(\Omega r - \bar{v})^2 - 2\rho\delta I_4 \Omega(\Omega r - \bar{v}) = -\tau_{r,0} \tag{8}$$

$$-I_3\frac{1}{r^2}\frac{d}{dr}[\rho r^2 u_1(\Omega r - \bar{v})\delta] - \rho\bar{w}(\Omega r - \bar{v}) + 2I_1\rho u_1 \delta\Omega = -\tau_{\phi,0} \tag{9}$$

where w is the axial velocity component and the coefficients I, which arise from integration of the power law velocity profiles, are given by

$$I_1 = 49/120,\ I_2 = 343/1656,\quad I_3 = 49/144,$$
$$I_4 = 1/8,\quad I_5 = 2/9 \tag{10}$$

Further details of the derivation of these equations can be found elsewhere (e.g., Chew, 1987; Chew and Rogers, 1988).

Treatment of the Stationary Disk. From earlier work it seems that the assumed velocity profiles and shear stress relations in equations (2)–(5) are unsuitable for the boundary layer on a stationary disk. The treatment of this layer has therefore been modified, although the approach is very similar to that for the rotating disk.

Equation (2) for the tangential velocity profile (with Ω set to zero) is retained. The following form is assumed for the radial velocity profile:

$$u = u_{1,s}(r) f(\eta),\ \eta = z/\delta \tag{11}$$

where $f(0)$ and $f(\infty)$ must be zero and $f(\eta) \to \eta^{1/7}$ as $\eta \to 0$. With these velocity profiles equations (4) and (5) for the shear stress may still be assumed to hold. Contrasting with the treatment of the rotor, some variation of u and v for z greater than the nominal boundary layer thickness δ is assumed. This accounts for the oscillatory behavior of the velocity profiles that has been observed in both experiments and computations. For $\eta > 2$ the variation in u and v is expected to be negligible. The integral equations (7) and (9) are valid for the stator boundary layer provided Ω is set to zero and the following definitions are used for the coefficients I:

$$I_1 = \int_0^\infty f\, d\eta,\quad I_2 = \int_0^\infty f^2 d\eta,\quad I_3 = \int_0^\infty v/\bar{v} f\, d\eta,$$

$$I_5 = 1 - \int_0^\infty (v/\bar{v})^2 d\eta \tag{12}$$

From finite difference results over a range of different conditions it appeared reasonable to require that the velocity vector of the flow close to the disk should be at an angle of about 20 deg to the tangential direction. This implies

$$u_{1,s} = -0.364\ \bar{v} \tag{13}$$

It was also found that the following choices of I_1 and I_3 gave reasonable agreement of the integral and finite difference results for a sealed rotor-stator system:

$$I_1 = 49/120,\quad I_3 = 539/1440 \tag{14}$$

No use of the radial momentum integral equation is made for this boundary layer and so I_2 and I_5 need not be specified. In effect this equation has been discarded and replaced by equation (13). This approach was considered adequate for present purposes as it gave reasonable agreement with the available data. Should further improvements become available in the future they can easily be incorporated into the numerical solution scheme described below.

Treatment of the Shroud. A simple model has been developed to account for the influence of the shroud. The principal assumptions made are that the mass flow in this boundary layer is constant, the boundary layer thickness is negligibly small relative to the radius b, and the tangential shear stress on the shroud can be estimated using a constant friction factor.

The shroud boundary layer mass flow ($\dot{m}_b$) must equal that in the rotating disk boundary layer at $r = b$ less any flow that leaves the cavity at this point. Defining $v_b(z)$ to be the average tangential velocity of the fluid in the boundary layer and F to be a friction factor, the tangential shear stress on the shroud $\tau_{\phi,b}$ is given by

$$\tau_{\phi,b} = -\frac{F}{2}\rho\,|\Omega_b - v_b(z)|\ (\Omega_b b - v_b(z)) \tag{15}$$

where Ω_b is the angular velocity of the shroud. Supposing the rotating and stationary disks to be at $z = s$ and $z = 0$, respectively, an angular momentum balance for the flow in the boundary layer gives

$$\dot{m}_b \frac{dv}{dz} b = 2\pi b \tau_{\phi,b} \tag{16}$$

With equation (15), this equation may be integrated directly to give $v_b(0)$ as a function of $v_b(s)$.

The boundary layer solutions for the shroud and two disks are patched so that mass and angular momentum are conserved. The mass flow in the boundary layer on the stationary disk at $r = b$ thus equals $\dot{m}_b$ minus any flow leaving the cavity at this point. Similarly angular momentum conservation gives relationships between $v_b(0)$, $v_b(s)$, and the disk boundary layer solutions at $r = b$. The friction factor F was assumed to equal the value obtained from the integral solution for the rotating disk at the outer radius.

Solution Method. The boundary layer solutions for the two disks are coupled through the shroud boundary layer, as described above, and the inviscid flow regions. In the source region of the flow $\bar{v}$ is calculated from inlet conditions assuming free vortex behavior outside the boundary layers. In the inviscid rotating core the radial velocity and axial gradient of tangential velocity are assumed to be zero.

Numerical solution of the integral momentum equations for the disks is achieved through use of standard library routines

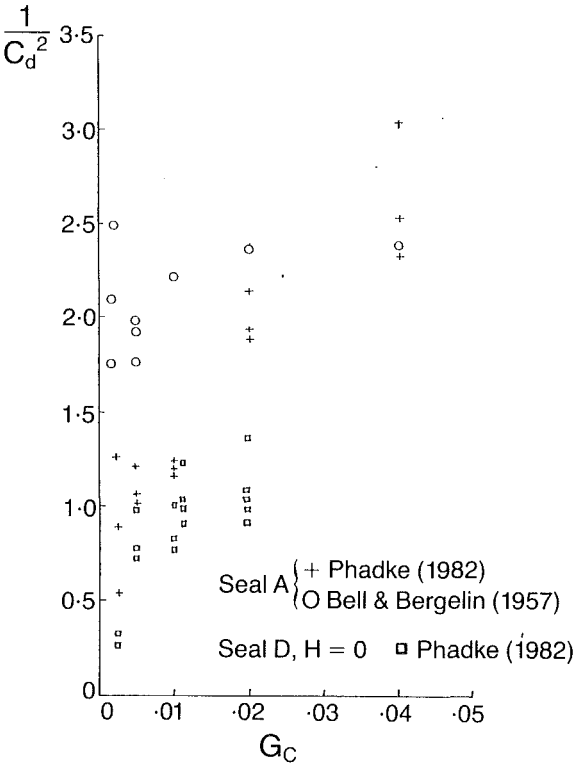

Fig. 3 Effect of seal type and clearance on discharge coefficient for $Re_\phi = 0$ (variation of C_w causes scatter)

for solution of ordinary differential equations. In the source region the solution for the rotor is straightforward. With $\bar{v}$ known, equations (8) and (9) are solved to find u_1 and δ. The nondimensional form of the equations used in the computations, and the specification of starting conditions, follows the methods developed in earlier studies. Effectively the mass flow in the boundary layer and the boundary layer thickness are set to zero at inlet radius $r = a$. The edge of the source region is defined as the point at which all the supplied flow has been entrained into the rotor boundary layer. Any boundary layer flow on the stator in the source region is neglected.

Outside the source region an iterative solution scheme was employed. The problem is discretized by specifying N radial locations covering the solution domain and assuming a linear variation of $\bar{v}$ between these points. For any specified distribution of $\bar{v}$ boundary layer solutions can then be obtained. Starting conditions for the rotor layer are obtained from the solutions in the source region. From the solution for the rotor starting conditions can be obtained for the stator layer. Of course, the resulting solution does not generally satisfy the patching conditions. These require the net mass flow at each radial location to equal the throughflow rate and conservation of angular momentum at the interface of the shroud and stator boundary layers. If there is no flow from the shroud layer to the stator the latter condition is replaced by the condition that the flow on the shroud must be at least sufficient to supply any seal flow at $z = 0$. Equations are defined at each radial location based on these patching conditions and a standard library routine for the solution of simultaneous nonlinear equations was used to find the distribution of $\bar{v}$ satisfying these equations. Comparing results for various values of N it was found that $N = 40$ gave essentially grid-independent solutions.

The integral solution, when suitably nondimensionalized, is a function of the three independent variables, radius ratio a/b, aspect ratio s/b, and throughflow parameter $\lambda = C_w/Re_\phi^{0.8}$. Details of the dimensional analysis will not be given here; similar results have been deduced for other disk flows (e.g., Chew and Snell, 1988). The position of the outlet will also affect the solution, but the seal clearance ratio $G_c = s_c/b$ is assumed small so that the cavity flow is independent of G_c. However, as will be shown below, G_c will enter the problem when flow through the outlet is considered.

Validation of the Model. Some confirmation of the validity of this model has been obtained through comparison with experiment. Predictions for the moment coefficient were found to be in excellent agreement with Daily and Nece's (1960) correlation of measurements for a sealed cavity and in reasonable agreement with Daily et al.'s (1964) correlation for a cavity with throughflow. Note also that the finite difference results used to guide the development of this model were in reasonable agreement with experiment.

Seal Flow

Seal Behavior With No Rotation. Before introducing the complication of rotation, it is useful to consider the case when both disks are stationary and $Re_\phi = 0$. In this case the velocity of the fluid approaching the seal is expected to be small compared to the velocity through the seal.

A discharge coefficient C_d is defined by the relationship

$$\frac{1}{C_d^2} = \frac{2\Delta p}{\rho u_m^2} \tag{17}$$

where Δp is the pressure drop across the seal and u_m is the mean velocity in the r–z plane through the seal.

Figure 3 shows $1/C_d^2$ for seals A and D in Fig. 1 as calculated from Phadke's (1982) data. In these experiments the radius ratio a/b and the aspect ratio s/b were both 0.1. For each value of G_c the different data points correspond to different throughflow rates. Values of the discharge coefficient for seal A were also estimated from Bell and Bergelin's (1957) results and these data are also shown on the figure. Bell and Bergelin measured discharge coefficients for the annular orifice between a circular disk and a cylindrical tube for a range of length-to-width ratios and Reynolds number. Their results give an indication of the values of C_d that might be expected from Phadke's data. Clearly the values of C_d obtained from Phadke's data are generally higher than those of Bell and Bergelin and many of the results give $C_d > 1$. Only for $G_c = 0.02$ and 0.04 for seal A are Phadke's results of similar magnitude to those of Bell and Bergelin. The most likely explanation for this is that errors have occurred in setting the seal spacing G_c. Errors of order 1 mm (i.e., $G_c \sim 0.005$) would account for the discrepancies with Bell and Bergelin's data. This interpretation is supported by the more recent experimental work of Dadkhah and Turner (1987).

Seal Behavior for $C_w > C_{w,min}$. Rotation may change both the flow within the cavity and the behavior of the seal. The pressure drop through the seal may be divided into two components: one associated with the centripetal force term and the other associated with the change in the radial and axial velocity components. In Phadke's experiments the shroud thickness and seal gap were of order $0.01b$. Assuming the radial pressure gradient balancing the centrifugal force is similar to that in a sealed rotor-stator system, the pressure difference across this distance is of order $0.003\ \rho\Omega^2 b^2/2$. The second component of Δp is related to $\rho u_m^2/2$. Using equation (1) to estimate $C_{w,min}$ and the results in Fig. 3 it follows that this term is of order $0.02\ \rho\Omega^2 b^2/2$ or greater for $C_w > C_{w,min}$. Thus, as a first approximation, it is reasonable to assume that the effect of rotation on the pressure drop across the seal will be principally through changes induced in the radial and axial velocity distribution.

The fluid flowing out of the seal will have first been entrained into the boundary layer on the rotating disk and will have picked up a radial velocity. To quantify this effect a "mixed-

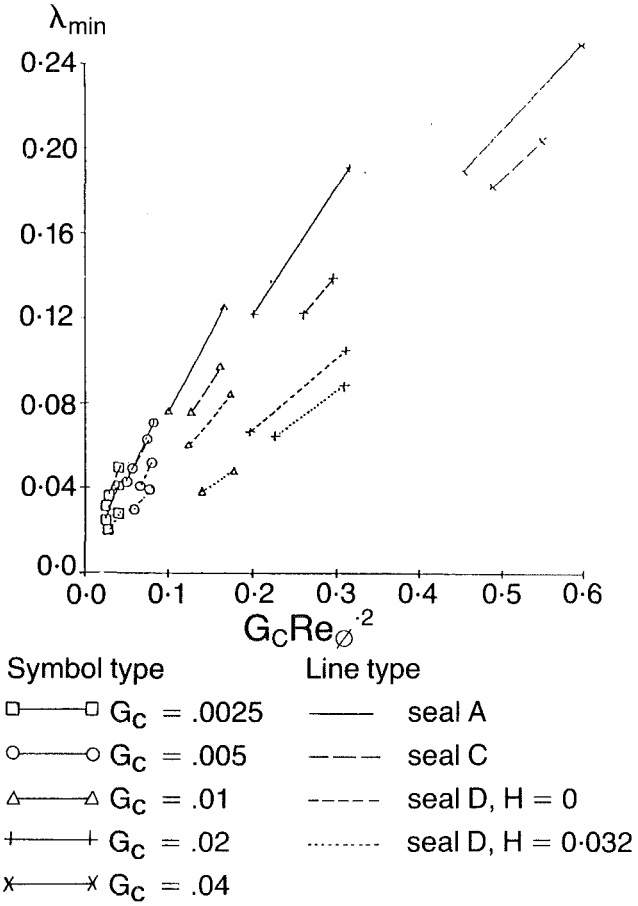

Fig. 4 Minimum sealing flows according to Phadke (1982)

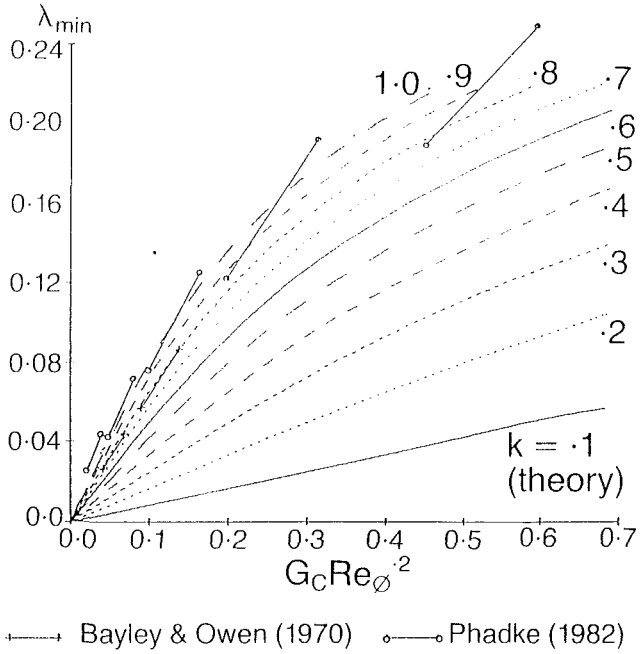

Fig. 5 Calculated and measured minimum sealing flows for seal A

out'' velocity u_{dm} is defined. This is calculated from the integral solution for the boundary layer at $r = b$ in such a way as to conserve radial momentum. It is assumed that the seal flow is supplied from the near-wall region of the layer and averaging is carried out over only that portion of the boundary layer supplying the seal. A discharge coefficient C_d' is introduced as follows:

$$\frac{1}{C_d'^2} = \frac{2\Delta p}{\rho(u_m^2 - k^2 u_{dm}^2)} \tag{18}$$

where k is an empirical constant, which will be different for each seal. Note that for $k = 1$ equation (18) is of the same form as the equivalent relation for a pipe-orifice.

From Phadke's experimental work it is known that for $C_w = C_{w,\min}$ the pressure difference across the seal is approximately zero. Thus, assuming C_d' remains finite, the cavity will be just sealed when $u_m = ku_{dm}$. For a given cavity and seal geometry $u_{dm}/\Omega b$ is a function of λ only and it may be deduced that $\lambda_{\min}$ will be function of $G_c\mathrm{Re}_\phi^{0.2}$ only. Use of the throughflow parameter λ is equivalent to nondimensionalizing the flow rate by dividing by the flow entrained by a free disk as given by von Karman's (1921) solution. Use of the group $G_c\mathrm{Re}_\phi^{0.2}$ is equivalent to scaling the seal gap with von Karman's solution for the boundary layer thickness.

Seal Behavior for $C_w < C_{w,\min}$. For $C_w < C_{w,\min}$ the flow through the seal will involve both inflow and outflow. The nondimensional ingress flow λ_{in} will be a function of the imposed throughflow λ, the seal geometry, and the cavity geometry. It is reasonable to hypothesize that the dependency on seal and cavity geometry may be carried through the minimum sealing flow $\lambda_{\min}$, so that λ_{in} is a function of λ and $\lambda_{\min}$ only. This hypothesis and the relationship between λ_{in}, λ, and $\lambda_{\min}$ will be discussed further in the next section where theory and experiment are compared.

Predictions will be presented below for the flow in the cavity for specified values of λ_{in}. In these calculations it has been assumed that the flow that enters the cavity through the seal has no angular momentum. The flow out of the cavity through the seal is assumed to be supplied by the rotor boundary layer, as before. The patching conditions between the shroud and disk boundary layers are adjusted accordingly, so that angular momentum is conserved.

Results

Minimum Sealing Flows. Phadke's (1982) correlations for the minimum sealing flow are shown in Fig. 4, where $\lambda_{\min}$ is plotted against $G_c\mathrm{Re}_\phi^{0.2}$. According to the above theory the results for each seal should collapse onto a single line when plotted on this basis. For seals A and C Phadke's results do shown some sign of this. Some scatter is to be expected due to approximations in the theory and errors in the gap setting as discussed above. Two sets of results for seal D are shown: one for which the shroud does not overlap the rotor and one for which the axial overlap was fixed giving $H = 0.032$. Here H is the axial overlap divided by the disk radius b. The results for seal D with $H = 0$ perhaps show the least sign of correlating on this basis; this case is further examined later.

Phadke's and Bayley and Owen's (1970) correlations for $\lambda_{\min}$ for seal A are compared with theory in Fig. 5. Theoretical curves were obtained as described above and are given for $k = 0.1$–1.0, although for this seal k is expected to be of order unity. The theoretical points do not go above $\lambda_{\min} = 0.22$ as at this point the supplied flow equals the free disk entrainment and the cavity is assumed to be effectively sealed. Each separate line for the measurements represents results at different values of G_c. Phadke's results are reasonably well correlated by the theory for $k = 1$, but Bayley and Owen's results lie almost on the curve $k = 0.8$. This discrepancy can be explained by the errors in G_c in Phadke's work. The present theory with $k = 0.8$ can be considered an improvement on Bayley and Owen's correlation as it shows a similar nonlinear behavior to Phadke's data at the higher values of $G_c\mathrm{Re}_\phi^{0.2}$. Note that the Reynolds number range for Phadke's experiments was

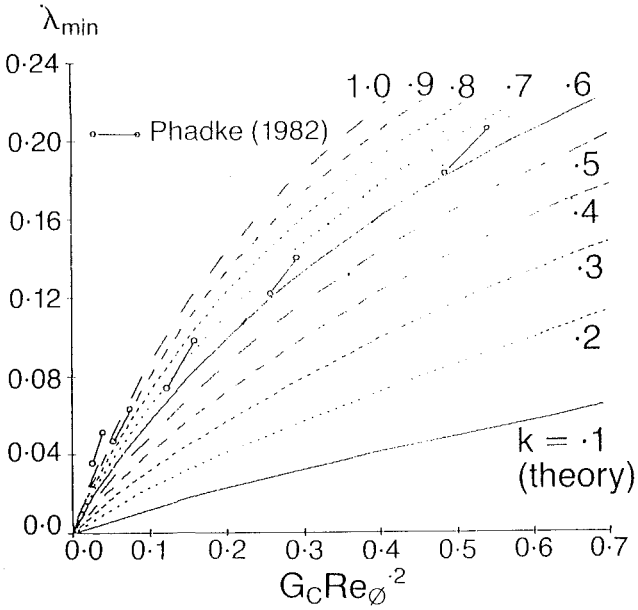

Fig. 6 Calculated and measured minimum sealing flow for seal C

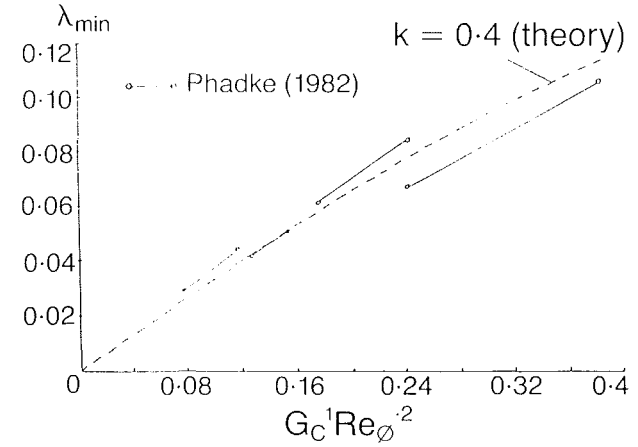

Fig. 7 Calculated and measured minimum sealing flow for seal C, $H = 0.G_c' = G_c = +0.0048$

$10^5 < \mathrm{Re}_\phi < 1.2 \times 10^6$, whereas von Karman's solution for free disk entrainment agrees with measurements for $\mathrm{Re}_\phi > 8 \times 10^5$ (Newman, 1983). Thus Reynolds number effects could account for some of the differences between measurements and theory. It should also be noted that the measurement of the minimum sealing flow was subject to some uncertainty.

Figure 6 shows a comparison between calculated and measured minimum sealing flows for seal C. The theoretical curves differ slightly from those in Fig. 5 owing to the rotating shroud giving different values of u_{dm} in the integral solution. At higher values of $G_c\mathrm{Re}_\phi^{0.2}$ Phadke's results are reasonably well correlated by the theory for $k \sim 0.65$. The departure from this curve at lower gap ratios is within the level of uncertainty due to errors in G_c.

Phadke's results for seal D with $H = 0$ do not appear to fit in with the proposed model. However, it may be shown that, given the level of errors deduced for G_c, these results are not inconsistent with the present theory. Figure 7 shows the effect of increasing Phadke's nominal value of G_c by 0.0048. This increase is within the error band for G_c indicated by the measurements for $\mathrm{Re}_\phi = 0$. The measurements with G_c increased are reasonably well correlated by the theory for $k = 0.4$, showing that within the (large) degree of experimental uncertainty, theory and measurements agree.

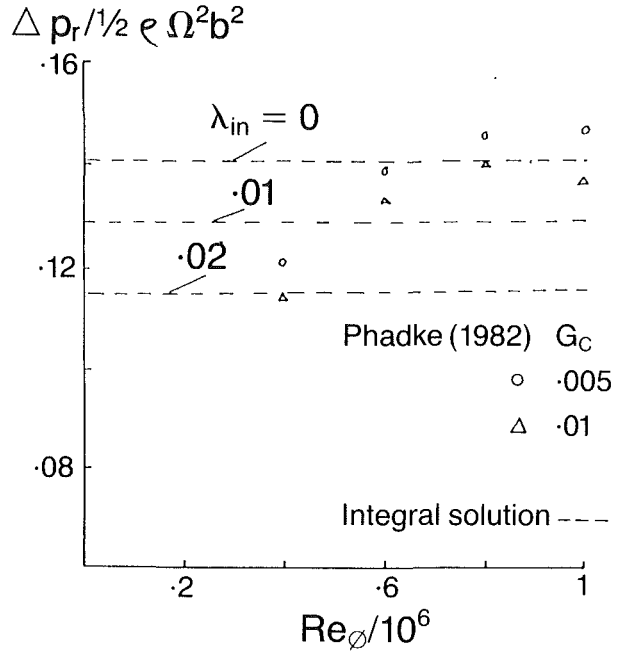

Fig. 8 Pressure rise across the cavity with a simple axial-clearance seal, $C_w = 0$

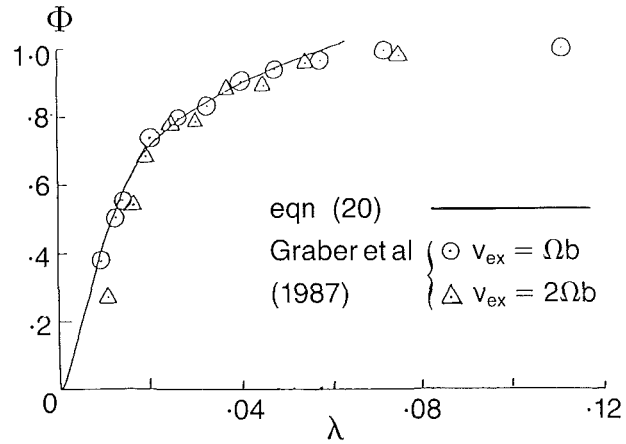

Fig. 9 Cooling effectiveness parameter for seal C

Ingress Flow. For seal A with $G_c = 0.005$ and 0.01 Phadke measured pressure distributions in the cavity for the case of no imposed throughflow. The radial pressure difference across the cavity between $r/b = 0.4$ and 0.97, denoted Δp_r, obtained from these measurements is shown in Fig. 8. Also shown on this figure are predictions from the integral solution with assumed ingress flow rates of $\lambda_{in} = 0$, 0.01, and 0.02. While the theory cannot be expected to agree exactly with experiment on the level of Δp_r, it does give a guide to the sensitivity of the pressure distribution to ingress. Note that at the lower values of Re_ϕ the flow may not be fully turbulent in the experiments. Comparing theory and measurements at $\mathrm{Re}_\phi = 10^6$ suggests that the difference in λ_{in} in the experiments for $G_c = 0.005$ and 0.01 is of order 0.01. This compares with a difference in the minimum sealing flows $\lambda_{\min}$ given by Phadke's correlations for these conditions of 0.052. Thus it appears that the ingress flow is of order 20 percent of the minimum sealing flow.

The recently published measurements of Graber et al. (1987) give further information regarding ingress. These workers use a gas concentration technique to estimate a cooling effectiveness parameter, defined as

$$\Phi = \dot{m}/(\dot{m} + \dot{m}_{in}) \quad (19)$$

In these experiments an axial flow outside the cavity was imposed to simulate the main gas path. However, varying the swirl of the gas path flow (v_{ex}) did not greatly affect Φ. For individual seals the measurements for Φ correlated well against the parameter λ. Figure 9 shows the results of Graber et al. for a seal of type C with $G_c = 0.0048$, $\mathrm{Re}_\phi = 5.1 \times 10^6$. The cavity in this case has radius ratio $a/b \sim 0.8$ and aspect ratio $s/b = 0.1$. The minimum sealing flow given by the present theory for these conditions is $\lambda_{\min} = 0.064$, where k has been set to 0.65 as indicated by Phadke's results. Assuming that the ingress flow λ_{in} varies linearly with λ, such that $\lambda_{in} = 0.2\,\lambda_{\min}$ when $\lambda = 0$ and $\lambda_{in} = 0$ when $\lambda = \lambda_{\min}$, equation (19) gives the following equation for Φ:

$$\Phi = \lambda/(0.8\lambda + 0.2\lambda_{\min}) \quad (20)$$

This relation is shown in Fig. 9 and is remarkably close to the measurements, indicating some agreement with the minimum sealing flow and level of ingress deduced from Phadke's data. Note that direct application of Phadke's correlations for seal C to Graber et al.'s conditions gives a minimum sealing flow 35 to 50 percent higher than that calculated here.

Conclusions

The problem of ingress of fluid through the peripheral seal between a rotor and a stator has been studied theoretically and previously published experimental data have been re-examined. This work has given fresh insight into the behavior of such flows and the mathematical model developed provides a means of extrapolating from the available data to engine conditions.

Analysis of Phadke's (1982) data indicates that there are errors in the experimental work. The recorded pressure differences across the seal when there is no rotation imply discharge coefficients greater than unity in some cases. It is concluded that errors of order 0.005 must have occurred in the gap setting G_c. This error is twice the minimum gap setting studied. These errors could account for the differences between Owen and Phadke's (1980) measurements of $C_{w,\min}$ and the earlier work of Bayley and Owen (1970). Owen and Phadke previously attributed these differences to different shroud shapes on the two rigs, different pressure tapping locations, and errors in correlating the data. Given this level of experimental error some of Phadke and Owen's (1982) conclusions regarding the performance of different seals are also questionable.

To model the flow in the space between the two disks, an integral momentum solution technique has been developed. Unlike some previously published integral models, the present method does not make ad hoc simplifications to the equations that enable a solution to be found but are not justified mathematically. This model provides a rational basis upon which more elaborate models, which might account for compressibility, heat transfer, and surface roughness, can be based.

A simple seal model involving an empirical constant and a discharge coefficient has been proposed for conditions in which ingress does not occur. Predictions for the minimum sealing flow $C_{w,\min}$ are obtained by coupling of the seal and cavity flow models. These predictions are in reasonable agreement with the available experimental data. With empirical constants determined from Phadke's data the theory shows agreement with the measurements of Graber et al. (1987).

Matching Phadke's pressure measurements for seal A with the mathematical model, it is deduced that the ingress flow, when there is no imposed throughflow, is of order 20 percent of the minimum sealing flow for this seal. Graber et al.'s (1987) concentration measurements for seal C show a similar level of ingress and are consistent with a linear variation of the rate of ingress, from zero when $C_w = C_{w,\min}$ to 0.2 $C_{w,\min}$ when $C_w = 0$.

There is clearly scope for further investigations of this problem. The methods presented here may form a useful basis for future modeling and data analysis. Published work by Abe et al. (1979) and Phadke and Owen (1988) indicates that pressure asymmetries in the external flow increase the level of ingress and may dominate over the effects of rotation on $C_{w,\min}$. Future investigations should therefore give consideration to nonaxisymmetric effects.

Acknowledgments

I would like to thank Mr. L. Harvey for his assistance in analyzing the experimental data and Mr. D. A. Campbell and Dr. A. B. Turner for their helpful comments.

References

Abe, T., Kikuchi, J., and Takeuchi, H., 1979, "An Investigation of Turbine Disk and Cooling," *13th CIMAC Congress*, Vienna.

Bayley, F. J., and Owen, J. M., 1970, "The Fluid Dynamics of a Shrouded Disk System With a Radial Outflow of Coolant," ASME *Journal of Engineering for Power*, Vol. 92, pp. 335–341.

Bell, K. J., and Bergelin, O. P., 1957, "Flow Through Annular Orifices," *Trans ASME*, Vol. 79, pp. 593–601.

Chew, J. W., 1987, "Computation of Flow and Heat Transfer in Rotating Disk Systems," *Proc. 2nd ASME–JSME Thermal Engineering Conference*, Hawaii, pp. 361–367.

Chew, J. W., and Rogers, R. H., 1988, "An Integral Method for the Calculation of Turbulent Forced Convection in a Rotating Cavity With Radial Outflow," *Int. J. Heat Fluid Flow*, Vol. 9, pp. 37–48.

Chew, J. W., and Snell, R. J., 1988, "Prediction of the Pressure Distribution for Radial-Inflow Between Co-Rotating Disks," ASME Paper No. 88-GT-61.

Chew, J. W., and Vaughan, C. M.,1988, "Numerical Predictions for the Flow Induced by an Enclosed Rotating Disk," ASME Paper No. 88-GT-127.

Dadkhah, S., and Turner, A. B., 1987, "External Flow Rig Progress Report. Simple Axial Gap Rim Seal," Report TFMRC/TN57, University of Sussex, United Kingdom.

Daily, J. W., and Nece, R. E., 1960, "Chamber Dimension Effects on Induced Flow and Frictional Resistance of Enclosed Rotating Disks," ASME *Journal of Basic Engineering*, Vol. 82, pp. 217–232.

Daily, J. W., Ernst, W. D., and Asbedian, V. V., 1964, "Enclosed Rotating Disks With Superposed Throughflow: Mean Steady and Periodic Unsteady Characteristics of Induced Flow," Report No. 64, Hydrodynamics Lab., Massachussetts Institute of Technology, Cambridge, MA.

Graber, D. J., Daniels, W. A., and Johnson, B. V., 1987, "Disk Pumping Test," Report No. AFWAL-TR-87-2050, Wright-Patterson Air Force Base, OH.

Haaser, F., Jack, J., and McGreehan, W., 1988, "Windage Rise and Flowpath Gas Ingestion in Turbine Rim Cavities," ASME *Journal of Engineering For Gas Turbines and Power*, Vol. 110, pp. 78–85.

Karman, T., von, 1921, "Uber laminare and turbulent reibung," *Z. Angew. Math. Mech.*, Vol. 1, pp. 204–209.

Newman, B. G., 1983, "Flow and Heat Transfer on a Disk Rotating Beneath a Forced Vortex," *AIAA J.*, Vol. 21, pp. 1066–1070.

Owen, J. M., 1989, "An Approximate Solution for the Flow Between a Rotating and a Stationary Disk," ASME JOURNAL OF TURBOMACHINERY, Vol. 111, pp. 323–332.

Owen, J. M., and Phadke, U. P., 1980, "An Investigation of Ingress for a Simple Shrouded Rotating Disk System With a Radial Outflow of Coolant," ASME Paper No. 80-GT-49.

Phadke, U. P., 1982, "Aerodynamic Aspects of the Sealing of Rotor-Stator Systems in Gas Turbines," D. Phil. thesis, University of Sussex, United Kingdom.

Phadke, U. P., and Owen, J. M., 1983a, "An Investigation of Ingress for an 'Air-Cooled,' Shrouded Rotating Disk System With Radial-Clearance Seals," ASME *Journal of Engineering for Power*, Vol. 105, pp. 178–183.

Phadke, U. P., and Owen, J. M., 1983b, "The Effect of Geometry on the Performance of 'Air-Cooled' Rotor Stator Seals," 15th CIMAC Congress, Paris.

Phadke, U. P., and Owen, J. M., 1988, "Aerodynamics Aspects of the Sealing of Gas-Turbine Rotor-Stator Systems," Parts 1 to 2," *Int. J. Heat Fluid Flow*, Vol. 9, pp. 98–117.

Sambo, A. S., 1985, "Numerical Computation of Laminar Flows in Rotor-Stator Cavities," *Proc. 4th Int. Conf. on Num. Methods in Laminar and Turbulent Flow*, Pineridge Press, pp. 274–286.

Vaughan, C. M., 1987, "A Numerical Investigation Into the Effect of an External Flow Field on the Sealing of a Rotor-Stator Cavity," D. Phil. thesis, University of Sussex, United Kingdom.

Vaughan, C. M., and Turner, A. B., 1987, "Numerical Predictions of Axisymmetric Flow in a Rotor-Stator System with an External Mainstream Flow," *Proc. 5th Int. Conf. on Num. Methods in Laminar and Turbulent Flow*, Pineridge Press, pp. 1640–1651.

Application of a Low Reynolds Number k-ϵ Turbulence Model to High-Speed Rotating Cavity Flows

A. P. Morse
Thermo-Fluid Mechanics Research Centre,
School of Engineering & Applied Sciences,
University of Sussex,
Falmer, Brighton, United Kingdom

A low turbulence Reynolds number k-ϵ model has been used in conjunction with an elliptic flow calculation procedure to obtain finite-difference solutions for radial outflow in the cavity formed between two plane corotating disks and an outer peripheral shroud. Air enters the cavity axially through a central hole in one of the disks and is assumed to leave via a uniform sink layer adjacent to the shroud. The main emphasis of the paper is the extension of the solution procedure to cover high rotational speeds, with rotational Reynolds numbers up to 10^7. As a necessary prerequisite to this exercise, the turbulence model is validated by its good predictive accuracy of existing experimental data up to a maximum rotational Reynolds number of 1.1×10^6.

1 Introduction

The cylindrical cavity formed between two corotating plane disks and a peripheral shroud provides a convenient model geometry for understanding the flow structure in the more complex passages found in practical gas turbine engines. The rotating cavity with a superimposed flow of air has particular relevance to the cooling of turbine and compressor disks, where the objective is to maintain the surface temperatures and temperature gradients within safe working limits, using the minimum amount of coolant. In addition to the more complex geometries involved, flows in real engine systems are subject to the effects of turbulence, high rotational speeds, three dimensionality, compressibility, heat transfer, buoyancy, and also transient conditions, experienced during periods of engine acceleration and deceleration. The present work is restricted to steady, axisymmetric, isothermal, and incompressible flow, but, in dealing with the first two topics in this list, demonstrates the feasibility of obtaining meaningful design calculations for conditions a step nearer those found in practical gas turbine geometries.

Figure 1 shows details of the flow geometry of interest, the coordinate system used, and predicted streamline contours for two test cases typical of those investigated experimentally (Pincombe, 1983; Owen et al., 1985). Air enters the cavity axially through a central hole in the upstream disk and is deflected, impinging on the downstream disk and flowing radially outward. The source region acts to distribute the flow equally to the two disks and is characterized by divergence of the incoming streamlines and the presence of a recirculating toroidal vortex, around which a small percentage of the flow is passed before being entrained into a boundary layer on the upstream disk.

Beyond the source region, the flow develops into two closely symmetric nonentraining boundary layers (Ekman layers) on the disks, and subsequently leaves the cavity through a thin sink layer adjacent to the outer shroud. Bounded by the source

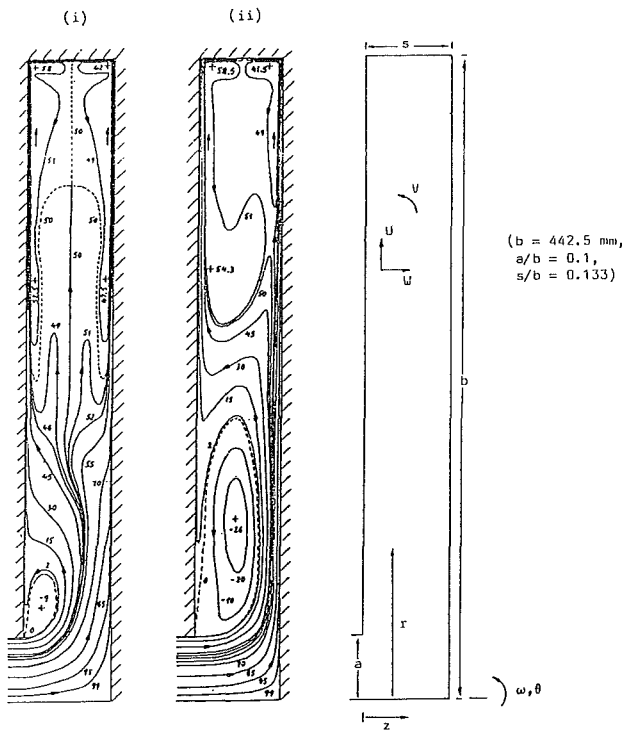

Fig. 1 Predicted streamline contours and details of coordinate systems: (*i*) $Re_\theta = 4 \times 10^5$, $C_w = 772$; (*ii*) $Re_\theta = 4 \times 10^5$, $C_w = 2184$

Contributed by the International Gas Turbine Institute and presented at the 34th International Gas Turbine and Aeroengine Congress and Exhibition, Toronto, Ontario, Canada, June 4–8, 1989. Manuscript received at ASME Headquarters January 27, 1989. Paper No. 89-GT-180.

and sink regions and the boundary layers is an interior core of rotating fluid in which, for true Ekman layer flow on the disks, the axial and radial velocity components are zero. Although the flow in the Ekman layers is predominantly outward, regions of weak inflow exist alongside the inviscid core, which appear to originate from the zones of recirculation in the sink layer.

The flow conditions may be characterized by a rotational Reynolds number, $\mathrm{Re}_\theta = \omega b^2/\nu$, where ω is the common angular velocity of the disk and the shroud, and a flow rate parameter, $c_w = Q/\nu b$, where Q denotes the volumetric flow rate through the cavity. The relative sizes of the individual flow regions vary in a systematic way with both Re_θ and C_w (Owen et al., 1985). As can be seen from Fig. 1, reducing the value of C_w (at constant Re_θ) has the effect of compressing the source region, leading to the earlier establishment of flow symmetry. More importantly, the reduction of C_w brings about an appreciable thinning of the Ekman layers, which is qualitatively the same effect as that produced by increasing the rotational Reynolds number at a constant value of C_w. The paper will illustrate the influences on the flow structure of varying Re_θ between limits of 10^5 and 10^7 at a fixed flow rate corresponding to $C_w = 2500$.

Source-sink flows in rotating cavities have been treated analytically using integral momentum techniques by, e.g., Owen et al. (1985), and parabolic (boundary-layer) procedures by Ong and Owen (1988). In each case, solutions of the linear and nonlinear forms of the Ekman layer equations were obtained, which portray many aspects of the flows near the disks satisfactorily at modest computational expense. More detailed investigation of the flow in the whole cavity space requires the use of an elliptic solver. Using a computer program based on the familiar TEACH code, Chew (1984, 1985) solved the full elliptic equations for turbulent flow with respectively, the low Reynolds number k–ϵ model of Launder and Sharma (1974) and a mixing length approach to estimate the turbulent fluxes.

The k–ϵ model was re-examined by Morse (1988) on the bases of both radial outflow and radial inflow in rotating cavities, with a view to removing the inconclusive findings reported by Chew. With the inclusion of an additional sink term in the ϵ equation, the model was found largely to avoid the premature laminarization effect manifest in Chew's results. However, some predictive errors remained and, considering the extra complexity and cost of using the model, the calculations did not represent a significant improvement over those obtained with the mixing length approach. In the present work, a different correlation is employed in the near-wall damping function of the "turbulent viscosity" expression, which leads to much improved predictive accuracy. Furthermore, improvements in the elliptic solution procedure have removed the difficulties, often alluded to by Chew, in obtaining converged solutions at high rotational Reynolds numbers.

Whereas the previous investigations adopted the assumption of a uniform source-sink flow with a radial inlet (which enabled attention to be restricted to a half-cavity solution with symmetry about the midaxial plane), the current work employs a solution for the whole cavity with the axial inlet geometry of the experiments. In the experimental rig, the flow left the cavity through a series of holes located centrally in the peripheral shroud. For reasons of computational convenience, this exit condition has here been modeled as a simple uniform sink; hence symmetry has been imposed at the external flow boundary.

2 Numerical Solution

2.1 Generalized Transport Equation. For steady, axisymmetric, incompressible flows, the momentum equations and the transport equations for the turbulent kinetic energy and dissipation rate can be written in the conveniently common form

$$\frac{\partial}{\partial z}(\rho W\phi) + \frac{1}{r}\frac{\partial}{\partial r}(\rho r U\phi) = \underbrace{\quad}_{\text{(convection)}}$$

$$\underbrace{\frac{\partial}{\partial z}\left(\Gamma_{\phi,z}\frac{\partial\phi}{\partial z}\right) + \frac{1}{r}\frac{\partial}{\partial r}\left(r\Gamma_{\phi,r}\frac{\partial\phi}{\partial r}\right)}_{\text{(diffusion)}} + \underbrace{S_\phi}_{\text{(source)}} \tag{1}$$

where ϕ represents the generalized transport variable. For the momentum equations, the particular expressions comprising the effective axial and radial diffusivities, $\Gamma_{\phi,z}$ and $\Gamma_{\phi,r}$, and the net source terms S_ϕ are given by Morse (1988) and are not repeated here. One important difference from the earlier work is that the circumferential equation is solved for the angular velocity, V/r, rather than the angular momentum, rV, as the former has less associated truncation error for use near the axis of symmetry; the two equations are easily transposed.

Nomenclature

a = inlet flow radius
A^+ = coefficient in near-wall damping function
b = outer radius of cavity
C_m = moment coefficient = $M/\frac{1}{2}\rho\omega^2 b^5$
C_w = flow rate parameter = $Q/\nu b$
D = source term in k equation
E = source term in ϵ equation
F = source term in ϵ equation
f_μ = near-wall damping function
G = production rate of turbulent kinetic energy
k = turbulent kinetic energy
M = frictional moment = $2\pi\int_0^b r^2\tau_{\theta,z}dr$
Q = volumetric flow rate through cavity
r = radial coordinate
Re_y = wall-distance Reynolds number = $yk^{1/2}/\nu$
Re_T = turbulence Reynolds number = $k^2/\epsilon\nu$
Re_θ = rotational Reynolds number = $\omega b^2/\nu$
Re^* = local rotational Reynolds number = $\omega r^2/\nu$
s = disk spacing
U = time-averaged *radial* velocity component
U_τ = friction velocity = $\sqrt{\tau_w/\rho}$
$\overline{u_i u_j}$ = Reynolds stress tensor
$\overline{uw}$ = turbulent shear stress (r–z plane)
V = time-averaged *circumferential* velocity component
$\overline{vw}$ = turbulent shear stress (θ–z plane)
W = time-averaged *axial* velocity component
y = generalized wall distance
y^+ = wall-distance Reynolds number = yU_τ/ν
z = axial coordinate
ϵ = dissipation rate of turbulent kinetic energy
θ = circumferential coordinate
Γ = diffusivity
μ = viscosity (without subscript = molecular viscosity)
ν = kinematic viscosity = μ/ρ
ρ = fluid density
σ = turbulent Prandtl/Schmidt number
τ = total shear stress
ϕ = generalized transport variable
ω = angular velocity

Subscripts

i, j = Cartesian tensor coordinates
in = value at cavity inlet
T = turbulent
w = wall value

2.2 The Turbulence Model. In the generalized form of equation (1), the diffusivities and source terms for the kinetic energy and dissipation rate equations of the low Reynolds number k–ϵ model are expressed as

$\phi = k$ (*turbulent kinetic energy*):

$$\Gamma_{\phi,z} = \Gamma_{\phi,r} = \mu + \mu_T/\sigma_k; \qquad (2)$$

$$S_\phi = G - \rho\epsilon - D: \quad D = 2\mu\left(\frac{\partial\sqrt{k}}{\partial x_j}\right)^2$$

$\phi = \epsilon$ (*dissipation rate*):

$$\Gamma_{\phi,z} = \Gamma_{\phi,r} = \mu + \mu_T/\sigma_\epsilon;$$

$$S_\phi = C_{\epsilon 1}\frac{\epsilon}{k}G - c_{\epsilon 2}\rho\frac{\epsilon^2}{k} + E - F: \qquad (3)$$

$$E = \frac{2\mu\mu_T}{\rho}\left(\frac{\partial^2 U_i}{\partial x_j^2}\right)^2; \quad F = 2\mu\left(\frac{\partial\sqrt{\epsilon}}{\partial x_j^2}\right)^2,$$

in which μ and μ_T are the laminar and turbulent components of the effective viscosity and G denotes the rate of production of turbulent kinetic energy from the mean flow ($= -\overline{u_i u_j}\partial U_i/\partial x_j$). The forms of the D, E, F, and G terms appropriate to axisymmetric flow in cylindrical-polar coordinates may be found from Morse (1988). Values of the numerical coefficients appearing in equations (2) and (3) are here taken as

$$\sigma_k = 1.0,\ \sigma_\epsilon = 1.3,\ c_{\epsilon 1} = 1.44,$$
$$c_{\epsilon 2} = 1.92 - 0.42\exp(\mathrm{Re}_T^2/36),$$

where Re_T denotes the turbulence Reynolds number.

With the exception of the sink term, F, in the ϵ-equation, the modeled equations are identical to those first used by Jones and Launder (1972) and subsequently used for the prediction of rotating flows by Launder and Sharma (1974). (The numerical constants and functions, however, show some variation.) The F term is included to give the correct value for the dissipation rate at the wall in fully developed pipe flow (note that the true dissipation rate is here represented as the sum of the dissipation variable, ϵ, used in the transport equation, and the quantity D/ρ). Also, without the F term, the transition from laminar to turbulent flow is not always easy to accomplish. Inclusion of the E term is essential to predict the well-documented peak in the energy level near a solid surface; without this term, flows such as the flat-plate boundary layer undergo transition much too rapidly.

Values of k and ϵ from the transport equations furnish a turbulent viscosity according to

$$\mu_T = C_\mu \rho k^2/\epsilon \qquad (4)$$

where the coefficient C_μ incorporates a near-wall damping function, viz.

$$C_\mu = 0.09\, f_\mu \qquad (5)$$

The turbulent viscosity from equation (4) is usually held to be isotropic, i.e., the same for all six Reynolds stresses. These latter are obtained from the constitutive relationship

$$\rho\overline{u_i u_j} = \frac{2}{3}\delta_{ij}\rho k - \mu_T\left(\frac{\partial U_i}{\partial x_j} + \frac{\partial U_j}{\partial x_i}\right) \qquad (6)$$

As noted by Patel et al., (1985) in a review of the various proposals made for low Reynolds number k–ϵ models, the particular form chosen for the damping function f_μ has a crucial bearing on model performance, irrespective of any deficiencies in the equations adopted for k and ϵ. Correlations for f_μ have been proposed in terms of three parameters, which are suitable to express these effects, viz., the turbulence Reynolds number, Re_T, and the wall-distance Reynolds numbers, Re_y and y^+. Of the three, Re_T is the most preferable, since it is composed of scaler quantities and hence is invariant to rotations of the coordinate system. In contrast, the other two parameters explicitly contain the normal wall distance, y, the use of which detracts from ease of application of the model in complex flow geometries.

However, in a recent paper, Nagano and Hishida (1987) have demonstrated that a correlation in terms of y^+ is the most effective, particularly for flows in adverse pressure gradients, where models containing a correlation in terms of Re_T or Re_y [e.g., the model of Lam and Bremhorst (1981), which uses both parameters] consistently overpredict the skin-friction coefficients (Rodi and Scheuerer, 1986). A similar conclusion, regarding the greater suitability of y^+, was reached in the present work. Examination of the predictions shown by Morse (1988), which incorporated a correlation in terms of Re_T, indicated that the turbulence Reynolds number often did not increase monotonically with distance from the wall, but rather exhibited a plateau region beyond the location of the peak energy level. This resulted in excessive damping beyond the viscous sublayer and buffer zone, underestimated turbulent transport in the outer Ekman layers, and retarded boundary layer growth. In contrast, y^+ can be recognized as a parameter that is guaranteed to increase monotonically with distance from the wall.

The damping function suggested by Nagano and Hishida takes the form

$$f_\mu = [1 - \exp(-y^+/A^+)]^2 \qquad (7)$$

with A^+ ascribed a value of 26.5. There are some differences between their model and that described in Equations (2) and (3), most notably in the coefficient of the E term and the omission of the F- term in the ϵ equation. Within the format of the present model, the optimum value of A^+ has been set at 24.5. It is emphasized that this optimization is not specific to the case of rotating flows but has been carried out on the basis of application of the model to a range of boundary layer flows in zero, positive, and negative pressure gradients, including cases where significant departures from the usual log-law velocity profile occur.

While it is inappropriate to discuss the results fully here, these are, not surprisingly, of similar accuracy to those presented by Nagano and Hishida. For the simplest boundary-layer flow of all, that over a flat plate in zero pressure gradient, the model predicts very accurately the logarithmic region of the velocity profile and the dependence of the skin-friction coefficient on the momentum thickness Reynolds number. Additionally, the predicted peak energy level ($k/U_\tau^2 = 4.35$) and the magnitude of the dissipation rate at the wall ($\nu\epsilon/U_\tau^4 = 0.095$) are close to the values recommended by Patel et al. (1985).

2.3 Application to Flow Over a Free Disk. The flow over a free disk (i.e., a disk rotating in an infinite, quiescent environment) serves as a useful test case to assess the performance of the turbulence model in a flow subject to strong rotation. For rotational Reynolds numbers up to approximately 7×10^6, the moment coefficient is known to follow closely the equation of Dorfman (1963), which, for one side of the disk, is

$$C_m = 0.491(\log_{10}\mathrm{Re}_\theta)^{-2.58} \qquad (8)$$

Computations of the flow were made using the parabolic (marching) procedure of Patankar and Spalding (1970) with a finite-difference mesh of 120 nodes, heavily concentrated in the viscous sublayer. The radial step length was fixed at 0.05 times the local boundary thickness. An ad hoc procedure, discussed by Morse (1989), was employed to effect transition to turbulent flow at a radius corresponding to a local rotational Reynolds number, Re^* [$= (r/b)^2\mathrm{Re}_\theta$], of 3×10^5, in accordance with the experimental evidence of Theodorsen and Regier (1944).

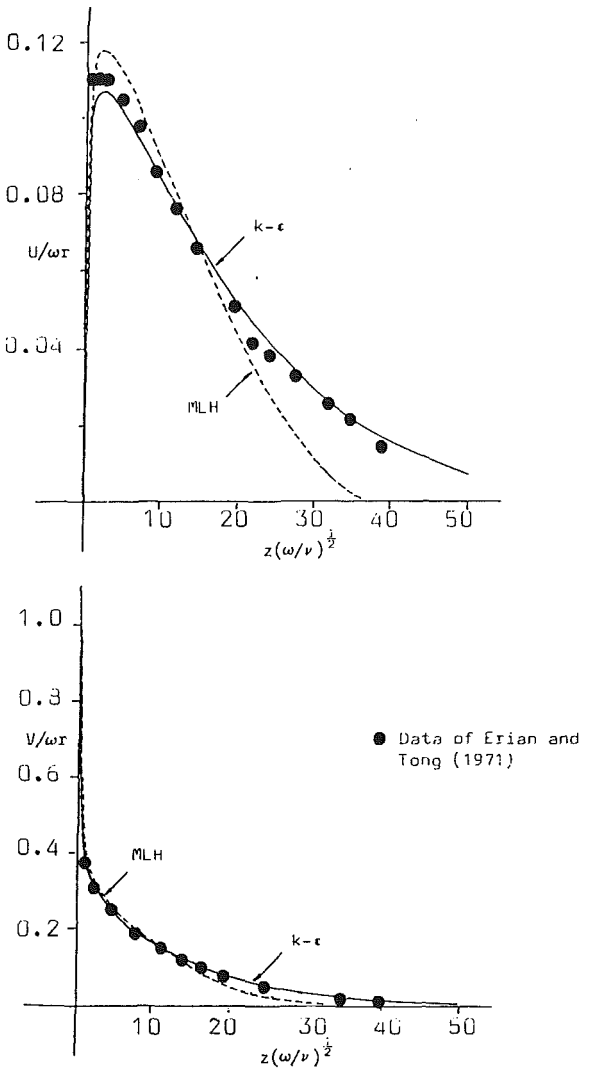

Fig. 2 Predicted profiles of radial and circumferential velocity components for flow over a free disk ($Re^* = 9.95 \times 10^5$)

Figure 2 shows a comparison of predicted profiles of the radial and circumferential velocity components with the measurements of Erian and Tong (1971) for a value of $Re^* = 9.95 \times 10^5$. Also shown are the results of computations obtained from a simple mixing length hypothesis (MLH). Although there is a slight underestimate in the magnitude of the peak radial velocity near the disk, the k-ϵ model clearly performs well for this flow. In contrast, the mixing length hypothesis considerably underestimates the spreading rate of the boundary layer and, to a lesser degree, the flow entrained by the disk.

Ironically, the mixing length model gives moment coefficients, which agree with the Dorfman equations to within ± 1 percent for $Re_\theta > 10^6$, whereas the k-ϵ model results in a consistent underprediction of about 6 percent. Similar findings are reported by Morse (1989) for the flows in rotor-stator systems. Furthermore, discrepancies of the same order result from the k-ϵ models of Launder and Sharma (1974) and Lam and Bremhorst (1981). It would appear that changes in the model constants to improve the calculated moment coefficients cannot be made without adversely affecting the predictions for nonrotating flows, and hence no attempt at rectifying this situation has been made in the present work.

2.4 The Computational Procedure. A modified version of the TEACH elliptic solver was used for the rotating cavity predictions, with a finite-difference mesh varying from 65 × 115 to 97 × 115 (axial-radial) nodes. A combination of geometrically expanding/contracting and uniform grid spacings was employed, with the nodes being increasingly clustered near the disks to obtain the required resolution of flow detail at high values of the rotational Reynolds number and the axial nodes placed symmetrically with respect to the midaxial plane in order to assist in the establishment of flow symmetry. Geometric expansion factors were varied as thought necessary (up to a maximum value of 1.15) to provide a closest off-wall node spacing of $y^+ < 0.5$ under all the test conditions. Fluid properties were taken as those appropriate to air at a pressure of 1 bar and a temperature of 20°C, viz, $\rho = 1.19$ kg/m^3 and $\mu = 1.81 \times 10^{-5}$ kg/ms. For the geometry shown in Fig. 1, the first internal grid node was situated within 3 μm of the surfaces of both the disks and the shroud at $Re_\theta = 10^7$.

The computer code used the hybrid power-law discretization scheme of Patankar (1980) and the SIMPLEC algorithm of Van Doormaan and Raithby (1984), in conjunction with a block-correlation procedure, to satisfy mass continuity and to update the pressure field. As a test for grid independence, the converged solution for $Re_\theta = 1.1 \times 10^6$ and $C_w = 2500$ was expanded (using quadratic interpolation) from a 65 × 115 grid onto grids of 97 × 115 and 145 × 172 nodes. No material differences resulted for the velocity profiles in the regions near the disks and the calculated moment coefficients fell within a spread of 0.6 percent, indicating a sensible degree of grid independence. Some slight differences were, however, detectable in the central core of the flow, where the node density is necessarily lower than the disks and numerical diffusion and truncation error are thus likely to be significant. For this reason, the weak vortex structures that are shown filling the core region in Figs. 1 and 6 should be treated with caution.

Solutions were considered converged when the residuals of all the dependent variables, normalized with the product of the mass flow rate through the cavity and the value of the variable at entry, were less than 10^{-6}. Each iteration of the solution takes approximately 1.5 ms per grid node on a VAX VMS/8530 computer. For $Re_\theta < 10^6$, convergence on a 65 × 115 grid could generally be accomplished within 1 h CPU time. The largest CPU time requirement for any computation was for $Re_\theta = 10^7$, $C_w = 2500$, which was 3.4 h (740 iterations) on a 97 × 115 grid.

Boundary conditions were based on a uniform axial velocity at the cavity inlet and a uniform radial velocity at outlet. The flow was also assumed to enter the cavity with an angular velocity equal to that of the disks. The turbulent kinetic energy at entry was taken as 10^{-4} times the square of the inlet axial velocity (1 percent turbulence intensity) and the dissipation rate then obtained by inversion of the definition of the turbulence Reynolds number, using a value of $Re_T = 100$. At solid boundaries, $k = \epsilon = 0$.

Values of y^+ for use in the viscosity damping function were based on the distance to the nearest solid surface and the resultant shear stress on that surface.

3 Numerical Results

3.1 Validation of the Turbulence Model. Figure 3 shows computed profiles of the radial velocity component in the Ekman layer on the upstream disk at $r/b = 0.833$ for the flow conditions $Re_\theta = 10^5$, $C_w = 1092$. Comparison is drawn between predictions with the current turbulence model (designated $k\epsilon3$) and that used by Morse (1988), essentially the model of Launder and Sharma (1974) and designated $k\epsilon2$. Also shown, for reference, are the laminar-flow solution and the prediction of the high Reynolds number k-ϵ model ($k\epsilon1$). The profiles are normalized with the (uniform) axial velocity at the cavity inlet. It is clear from the figure that the flow is only weakly turbulent under these conditions. The $k\epsilon2$ predictions do display a slight reduction in the peak velocity compared to the laminar-flow

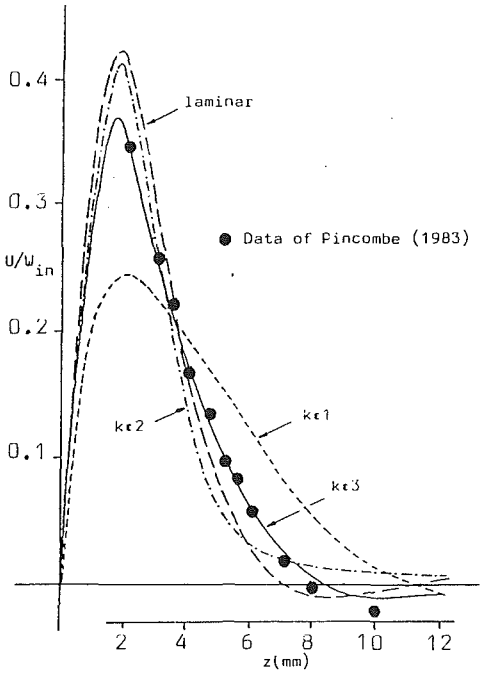

Fig. 3 Comparison of predicted profiles of radial velocity component at r/b = 0.833 (Re_θ = 10^5, C_w = 1092; upstream disk)

solution, but also a retarded spreading rate in the outer Ekman layer, where there is additionally no predicted occurrence of reverse flow. As mentioned earlier, these effects are largely due to the leveling out of the turbulence Reynolds number (between approximately $z = 3$ mm and 6 mm), with the result that the turbulence is excessively damped in this region. In contrast, with the $k\epsilon3$ model, the f_μ function increases monotonically with distance from the disk surface and these defects are removed. As expected, the high Reynolds number form of the model considerably overestimates turbulent transport for these flow conditions.

Figures 4 and 5 show predictions with the $k\epsilon3$ model for $Re_\theta = 4 \times 10^5$ and values of C_w varying between 772 and 2184. It is evident from Fig. 4 that the model faithfully reproduces the experimental measurements for the radial velocity component, which, for all four cases, indicate a slight reduction in the thickness of the Ekman layer between $r/b = 0.633$ and 0.833. Agreement between prediction and experiment is excellent, especially considering the uncertainty in positional measurement, estimated by Pincombe (1983) as ± 0.45 mm.

Corresponding predictions of the circumferential velocity at the midaxial plane (Fig. 5) are also in close agreement with the data, although there are only two measurements for each test case. Note that the flow near the axis of symmetry rotates at an angular velocity less than that of the cavity, the rotational level increasing as C_w is raised. This effect is reversed in the cavity space beyond the source region ($r/b \gtrsim 0.4$).

Associated streamline contours for the limiting values of C_w have already been introduced as Fig. 1. The values indicated for the streamlines denote mass flow rates normalized with the total mass flow rate through the cavity, with a datum of ψ = 0 at the surface of the upstream disk; thus ψ = 100 for the downstream disk and at the axis of rotation, and varies quadratically at the inlet and linearly at the outlet plane.

The flow pattern for $C_w = 772$ indicates greater streamline divergence in the initial source region, which accounts for the lower angular velocity evident in Fig. 4. Also, compared to the predictions for C_w = 2184, there is a more rapid entrainment of fluid into the upstream disk boundary layer, a much less pronounced wall-jet effect on the downstream disk and an appreciable reduction in both the size and the strength of

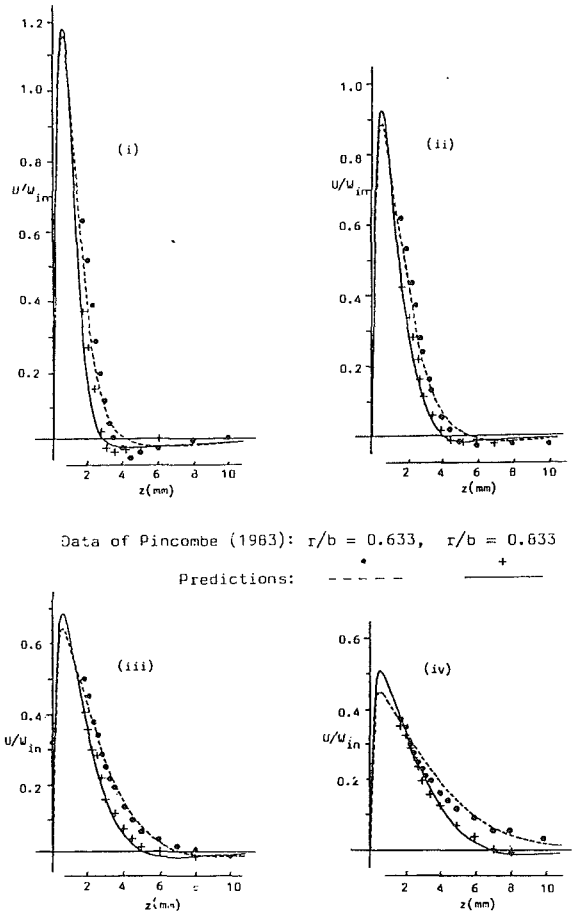

Fig. 4 Predicted profiles of radial velocity component at r/b = 0.633 and 0.833 (upstream disk); $Re_\theta = 4 \times 10^5$: (*i*) C_w = 772, (*ii*) C_w = 1092, (*iii*) C_w = 1544, (*iv*) C_w = 2184

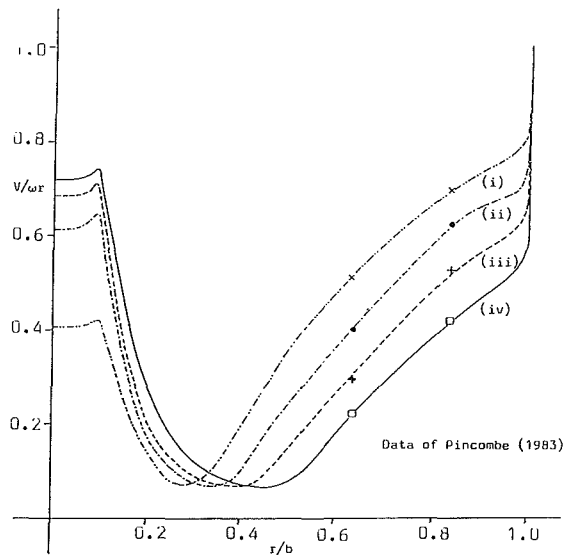

Fig. 5 Predicted profiles of circumferential velocity component at midaxial plane; $Re_\theta = 4 \times 10^5$: (*i*) C_w = 772, (*ii*) C_w = 1092, (*iii*) C_w = 1544, (*iv*) C_w = 2184

the source vortex, which recirculates only about a third as much of the total flow rate. As evidenced by the streamline ψ = 50, which eventually indicates the division of the flow into close symmetry about the midaxial plane, bifurcation is essentially complete at r/b = 0.4, although weak filaments of

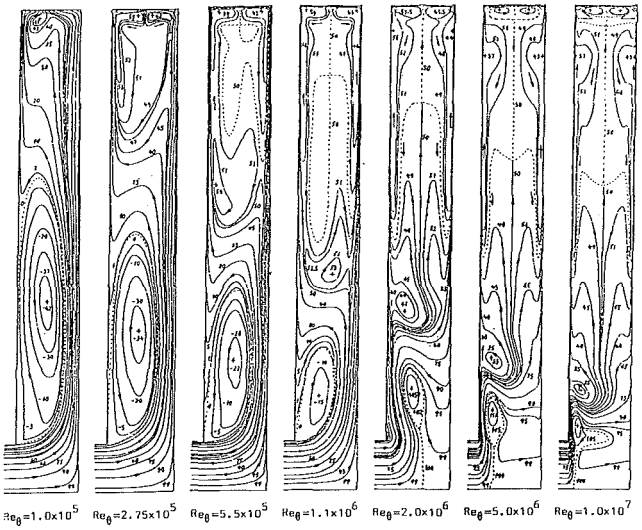

Fig. 6 Predicted streamline contours illustrating effect of rotational Reynolds number (C_w = 2500)

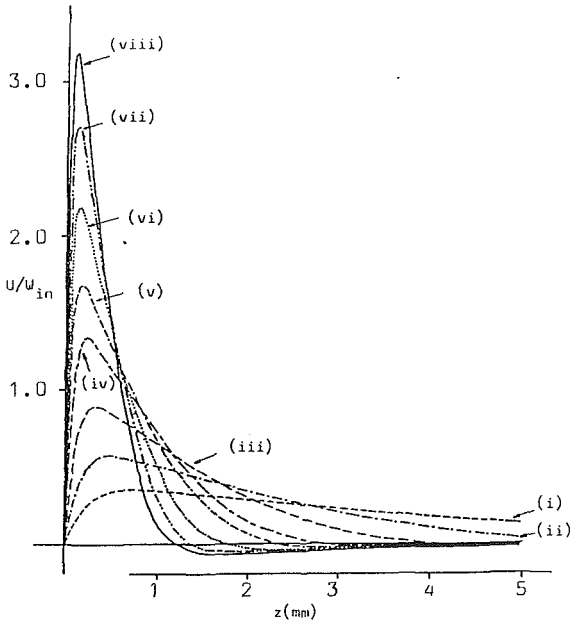

Fig. 7 Predicted profiles of radial velocity component at r/b = 0.833 (upstream disk); C_w = 2500: (*i*) Re$_\theta$ = 2.75 × 10^5, (*ii*) Re$_\theta$ = 5.5 × 10^5, (*iii*) Re$_\theta$ = 1.1 × 10^6, (*iv*) Re$_\theta$ = 2 × 10^6, (*v*) Re$_\theta$ = 3 × 10^6, (*vi*) Re$_\theta$ = 5 × 10^6, (*vii*) Re$_\theta$ = 7.5 × 10^6, (*viii*) Re$_\theta$ = 10^7

flow apparently protrude into the central core. In contrast, at $C_w = 2184$, disgorging of fluid from the downstream to the upstream disk persists as far as $r/b \sim 0.7$ and a flow structure that is truly symmetric on a fine scale does not evolve. For both values of C_w, the sink layer is characterized by the appearance of a fairly strong vortex, recirculating about 17 percent of the mass flow rate associated with each Ekman layer, although the bulk of this recirculation is confined to the immediate vicinity of the sink. A small proportion does, however, provide the weak inflow characteristic of the outer regions of the Ekman layers.

3.2 Extension to Flows at High Rotational Reynolds Number. Figure 6 shows streamline plots illustrating the changes in the flow structure that are predicted to occur as the rotational Reynolds number is increased from 10^5 to 10^7 at a constant value of $C_w = 2500$. In each case, dividing streamlines (shown as broken curves) and definitive vortex centers (+) have been identified.

At $Re_\theta = 10^5$, the wall-jet effect on the downstream disk is very pronounced and Ekman layer flow does not arise; such symmetry as exists is largely brought about by that imposed at the exit plane. Increase of Re_θ reduces the wall-jet effect and the size and strength of the vortex in the source region, but it is not until Re_θ attains a value of 1.1×10^6 that the dividing streamline appears at the midaxial plane, indicating fine-scale symmetry of the flow. At lower rotational Reynolds numbers, the core region appears to contain a complicated system of nested vortices, which transfer small amounts of flow between the disk in an attempt to establish symmetry. Increase of Re_θ brings about a progressively earlier entrainment of the flow into the boundary layer on the upstream disk.

Beyond $Re_\theta = 1.1 \times 10^6$, there is an abrupt change in the flow in the source region, the incoming jet no longer impinging on the downstream disk, but suffering a sharp deflection toward the upstream disk, where it is directly entrained. As a result, the vortex formerly appearing in the source region is almost completely suppressed at $Re_\theta = 2 \times 10^6$, although a vortex rotating in the opposite sense is formed, around which all the flow is driven before dividing equally between the disks. It can be anticipated that, in practice, the flow would be unstable for Re_θ of this order. Some of the flow associated with the upstream disk apparently rolls up into a further vortex within the source region, but separation does not occur. As the rotational Reynolds number is increased toward 10^7, the deflection of the incoming jet becomes more abrupt and the source region more compact, leading to a progressively earlier

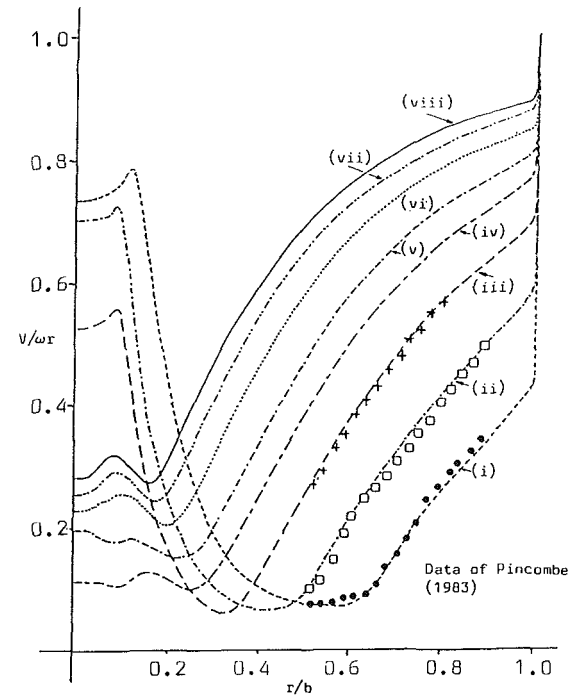

Fig. 8 Predicted profiles of circumferential velocity component at midaxial plane; C_w = 2500: (*i*) Re$_\theta$ = 2.75 × 10^5, (*ii*) Re$_\theta$ = 5.5 × 10^5, (*iii*) Re$_\theta$ = 1.1 × 10^6, (*iv*) Re$_\theta$ = 2 × 10^6, (*v*) Re$_\theta$ = 3 × 10^6, (*vi*) Re$_\theta$ = 5 × 10^6, (*vii*) Re$_\theta$ = 7.5 × 10^6, (*viii*) Re$_\theta$ = 10^7

establishment of flow symmetry. Apart from a small change in the nature of the sink layer, however, the basic flow structure remains the same.

It should be noted that the simplifying assumption of incompressible flow becomes increasingly less valid for $Re_\theta \geq 4 \times 10^6$, at which point the pressure differential across the cavity exceeds 5 percent for air entering at atmospheric pressure.

As is evident from the merging of the streamlines and the loss of detail near the disks in Fig. 6, there is a continuous decrease in Ekman layer thickness with increasing rotational

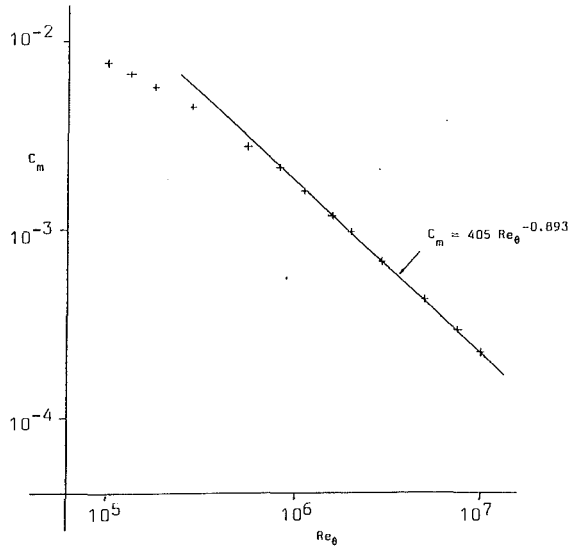

Fig. 9 Predicted variation of moment coefficient with rotational Reynolds number (C_w = 2500; upstream disk)

Reynolds number. This effect is exemplified in Fig. 7, which shows predicted profiles of the radial velocity component at $r/b = 0.833$ over the range $2.75 \times 10^5 \leq \mathrm{Re}_\theta \leq 10^7$. The predictions are restricted to the 5 mm of the flow space adjacent to the upstream disk; unfortunately, no experimental data are available for comparison. The reduction in Ekman layer thickness, from approximately 10 mm at $\mathrm{Re}_\theta = 2.75 \times 10^5$ to 1.1 mm at $\mathrm{Re}_\theta = 10^7$, is accompanied by a steady increase in the peak velocity and also a gradual shift in the location of this peak toward the disk.

Corresponding predictions of the circumferential velocity at midaxis are shown in Fig. 8. Experimental measurements are available for the three lowest rotational Reynolds numbers and can be seen to be reproduced fairly accurately. Away form the source region, the calculations indicate a continuous rise in the rotation level relative to that of the cavity, but this trend toward solid-body rotation is far from complete at $\mathrm{Re}_\theta = 10^7$. Within the source region, the predicted profiles show more erratic behavior. Initially, as Re_θ is increased, the angular velocity near the axis of rotation drops steadily, but there is an abrupt fall at $\mathrm{Re}_\theta = 2 \times 10^6$ as the flow structure in the source region changes and the incoming jet is deflected toward the upstream disk (see Fig. 6). As a result, the central regions of the flow become starved of the influx of angular momentum from the jet. With further increase of Re_θ, the vortex in the source region moves away from the midaxial plane and the rotation level recovers slightly. Note also that there is a very strong shear layer adjacent to the outer shroud, although the relative degree of shear falls as the rotational Reynolds number is increased.

Finally, Fig. 9 shows predicted moment coefficients for the upstream disk. For $\mathrm{Re}_\theta = 10^5$, the moment coefficient for the upstream disk is approximately 14 percent less than for the downstream disk, due to the lack of flow symmetry. However, this difference decreases steadily, and, for $\mathrm{Re}_\theta \geq 1.1 \times 10^6$, is never greater than 0.2 percent. At low values of the rotational Reynolds number, the flow is essentially laminar in a significant proportion of the cavity, but beyond $\mathrm{Re}_\theta \sim 8 \times 10^5$, the influence of these laminar regions becomes minimal (in the frictional torque, the shear stress is weighted with r^2) and the moment coefficients conform, to within ± 0.5 percent, to the correlation

$$C_m = 405\ \mathrm{Re}_\theta^{-0.893} \tag{9}$$

Bearing in mind the results of similar calculations for the flows over a free disk (see Section 2.3) and in rotor–stator systems (Morse, 1989), it is however anticipated that the moment coefficients shown in Fig. 9 have an accuracy of no better than 6 percent. Note that the linear theory of Owen et al. (1985), which becomes increasingly valid as the core rotation increases relative to the disk speed, predicts the moment coefficient to be inversely proportional to Re_θ. Presumably, an exponent closer to -1 would be obtained in the predictions for lower values of C_w.

4 Discussion

The modification to the near-wall damping function in the turbulent viscosity expression has considerably improved the performance of the low turbulence Reynolds number k–ϵ model in comparison to the work published earlier (Morse, 1980). Over the full range of the flow parameters, Re_θ and C_w investigated by Pincombe (1983), the current model gives superior predictions, there being no inability to produce turbulent flow from quasi-laminar inlet conditions, nor any tendency to premature laminarization once turbulent flow has been established. Morse (1988) suggested that the main reason for the indifferent performance of the model was the inclusion of the E term [see equation (3)], which often dominates the ϵ equation at low turbulence Reynolds numbers. This now appears not to be the case. Put rather simply, the dominance of the E term is more a consequence of the low turbulent Reynolds number than a cause; if Re_T is high enough, the term becomes small compared to the other positive source of ϵ.

In view of the good all-round accuracy of prediction, it is indeed disappointing that the model appears to underestimate the disk movement coefficients in rotating flows, particularly as the simpler mixing length hypothesis generally performs rather better in this respect. One possibility for removing the 6 percent discrepancy between calculated frictional coefficients for rotating and nonrotating flows is the introduction of anisotropic effects into the model. Although the concept of an isotropic turbulent viscosity is severely restricted in use, examination of the (exact) production terms in the Reynolds stress equations (e.g., Launder and Morse, 1977), suggests that the degree of anisotropy can only be small in the present application for the most important of the shear stresses, viz., $\overline{uw}$ and $\overline{vw}$ (which govern axial diffusion of momentum).

The modeled ϵ equation is highly idealized and its construction largely mimics effects in the equation for the turbulent kinetic energy. Deficiencies in the ϵ equation have long been held responsible for disparities in the prediction of free shear flows with the high Reynolds number k–ϵ model (e.g., Morse, 1980). Most notably, the spreading rate of the round jet is overestimated by about 40 percent with the model constants appropriate to the plane jet and most wall-bounded shear layers. The free disk is a flow that has something in common with the round jet, in that the turbulence quantities change rapidly in the streamwise direction. It may well be the case that the failure of the model to predict these flows accurately has a common cause in the neglect of historical effects in the ϵ equation.

Regarding the computational procedure, convergence has not proved a problem, although there is clearly a penalty as regards CPU time for converged solutions at high rotational Reynolds numbers. Single-grid methods like that employed here have notoriously poor convergence properties toward the end of the solution and it is unusual for the residuals to decrease by a factor of more than 1 percent between successive iterations. Chew and Vaughan (1988) have recently used multigrid methods for the computations of flows in rotor–stator systems. A direct comparison between their work and that reported by Morse (1989) is difficult on account of the different turbulence models, finite-difference grids, and convergence criteria that were used, but it seems likely that such methods could result

in a reduction of at least 50 percent in the CPU time requirements quoted here.

5 Conclusions

A modified form of the low turbulence Reynolds number k–ϵ model of Jones and Launder (1972) has been used to predict, with good accuracy, the flows in rotating cavities with a radial outflow of air. The improved performance of the model has been brought about by a change in the nature of the damping function, which represents the influence of wall proximity on the turbulent shear stresses. However, this modification does, unfortunately, make the model more difficult to apply in complex flow situations. A deficiency of the model is still apparent in its underestimation of disk moment coefficients. This topic is currently receiving attention.

The computational procedure has been extended to high rotational Reynolds numbers, although a comparison with experimental data has not been possible. The assumption of incompressible flow has been retained, but it is acknowledged that the large pressure differences across the cavity, which occur at high rotational speeds (there is a 38 percent pressure differential at $Re_\theta = 10^7$), will profoundly affect the flow structure via changes in the fluid density. However, the extension to compressible flow has since proved possible, and will be presented, alongside heat transfer results, in future work.

Acknowledgments

The author is glad to acknowledge the interest shown in this work by Dr. J. M. Owen and Dr. C. Ong, colleagues at the Thermo-Fluid Mechanics Research Centre, University of Sussex; and the continuing collaboration with Rolls-Royce plc.

References

Chew, J. W., 1984, "Prediction of Flow in Rotating Disc Systems Using the k–ϵ Turbulence Model," ASME Paper No. 84-GT-229.

Chew, J. W., 1985, "Prediction of Flow in a Rotating Cavity With Radial Outflow Using a Mixing Length Turbulence Model," *Proc. 4th Int. Conf. on Numerical Methods in Laminar and Turbulent Flow*, Pineridge Press, Swansea, United Kingdom.

Chew, J. W., and Vaughan, C. M., 1988, "Numerical Predictions for the Flow Induced by an Enclosed Rotating Disc," ASME Paper No. 88-GT-127.

Dorfman, L. A., 1963, *Hydrodynamic Resistance and Heat Loss of Rotating Solids*, Oliver and Boyd, Edinburgh, United Kingdom.

Erian, F. F., and Tong, Y. H., 1971, "Turbulent Flow Due to a Rotating Disk," *Phys. Fluids*, Vol. 14, p. 2588.

Jones, W. P., and Launder, B. E., 1972, "The Prediction of Laminarization With a Two-Equation Model of Turbulence," *Int. J. Heat and Mass Transfer*, Vol. 15, p. 301.

Lam, C. K. G., and Bremhorst, K. A., 1981, "Modified Form of the k–ϵ Model for Predicting Wall Turbulence," *J. Fluids Eng.*, Vol. 103, p. 456.

Launder, B. E., and Sharma, B. I., 1974, "Application of the Energy-Dissipation Model of Turbulence to the Calculation of Flow Near a Spinning Disc," *Letters in Heat and Mass Transfer*, Vol. 1, p 131.

Launder, B. E, and Morse, A. P., 1979, "Numerical Prediction of Axisymmetric Free Shear Flows With a Second-Order Reynolds Stress Closure," in: *Turbulent Shear Flows I*, Springer-Verlag, New York.

Morse, A. P., 1980, "Axisymmetric Free Shear Flows With and Without Swirl," Ph.D. Thesis, University of London, United Kingdom.

Morse, A. P., 1988, "Numerical Prediction of Turbulent Flow in Rotating Cavities," ASME JOURNAL OF TURBOMACHINERY, Vol. 110, p. 202.

Morse, A. P., 1989, "Assessment of Laminar–Turbulent Transition in Closed Disk Geometries," 89-GT-179.

Nagano, Y., and Hishida, M., 1987, "Improved Form of the k–ϵ Model for Wall Turbulent Shear Flows," *J. Fluids Eng.*, Vol. 109, p. 156.

Ong, C. L., and Owen, J. M., 1988, "Boundary Layer Flows in Rotating Cavities," ASME Paper No. 88-GT-292.

Owen, J. M., Pincombe, J. R., and Rogers, R. H., 1985, "Source-Sink Flow Inside a Rotating Cylindrical Cavity," *J. Fluid Mech.*, Vol. 155, p. 233.

Patankar, S. V., and Spalding, D. B., 1970, *Heat and Mass Transfer in Boundary Layers*, Intertext Books, London, United Kingdom.

Patankar, S. V., 1980, *Numerical Heat Transfer and Fluid Flow*, Hemisphere, Washington, DC.

Patel, V. C., Rodi, W., and Scheuerer, G., 1985, "Turbulence Models for Near-Wall and Low Reynolds Number Flows: A Review," *AIAA J.*, Vol. 23, p. 1308.

Pincombe, J. R., 1983, "Optical Measurements of the Flow Inside a Rotating Cylinder," D. Phil. Thesis, University of Sussex, United Kingdom.

Rodi, W., and Scheuerer, G., 1986, "Scrutinizing the k–ϵ Turbulence Model Under Adverse Pressure Gradient Conditions," *J. Fluids Eng.*, Vol. 108, p. 174.

Theodorsen, T., and Regier, A., 1944, "Experiments on Drag of Revolving Disks, Cylinders and Streamline Rods at High Speeds," NACA Rept. 793.

Van Doormal, J. P., and Raithby, G. D., 1984, "Enhancements of the SIMPLE Method for Predicting Incompressible Fluid Flows," *Num. Heat Transfer*, Vol. 7, p. 147.

The Use of Deswirl Nozzles to Reduce the Pressure Drop in a Rotating Cavity With a Radial Inflow

P. R. Farthing
Thermo-Fluid Mechanics Research Centre,
School of Engineering and Applied Sciences,
University of Sussex,
Brighton, BN1 9QT, United Kingdom

J. W. Chew
Rolls Royce plc,
Derby, DE2 8BJ, United Kingdom

J. M. Owen
Thermo-Fluid Mechanics Research Centre,
School of Engineering and Applied Sciences,
University of Sussex,
Brighton, BN1 9QT, United Kingdom

A combined theoretical and experimental study is described in which deswirl nozzles were used to reduce the radial pressure drop in a rotating cavity with a radial inflow of air. The nozzles, which were attached to the outer part of the cavity, were angled such that the angular speed of the air at inlet could be in the opposite direction to that of the cavity. Solutions of the momentum-integral equations were used to predict the resulting radial distributions of pressure throughout the cavity. Flow visualization was used to confirm the flow structure, and transducers attached to one of the rotating disks in the cavity were used to measure the radial pressure distributions. Results are presented for "swirl fractions" (that is, the ratio of the angular speed of the air leaving the nozzles to that of the cavity) in the range -0.4 to $+0.9$, and for $0.01 < |C_w| Re_\phi^{-0.8} < 0.5$, where C_w and Re_ϕ are the nondimensional flow rate and rotational Reynolds number, respectively. The measured pressures are in good agreement with the predicted values, and the pressure drop across the cavity can be significantly less than that associated with solid-body rotation. The flow rate produced by the pressure drop across the cavity is not unique: There are up to three possible values of flow rate for any given value of pressure drop.

1 Introduction

In a gas turbine engine, cooling air for the turbine has to be bled from the compressor, and it is sometimes required that the air should flow radially inward through the cavity between two corotating compressor disks. Various devices may be used to reduce the pressure drop across the cavity, and an investigation of the effect of fins attached to one of the disks was reported recently (Chew et al., 1989). In this paper, the use of deswirl nozzles to control the pressure drop is considered. Although deswirler devices have been considered previously for application in gas turbine engines (see, for example, Scheper, 1962; Brown and Manente, 1977; Kraftwerk Union Aktiengesellschaft, 1977), a literature search has failed to reveal any detailed study of their operation.

The deswirl nozzles may be fitted to the peripheral shroud, which rotates with the disks, and the nozzles are angled so as to produce a tangential component of velocity of the air in the opposite direction to the rotation of the disks. Thus the air will enter the cavity with a lower angular velocity than the disks themselves, and may even be rotating in the opposite direction to the disks. In the present study the performance of such a system has been investigated both theoretically and experimentally.

Contributed by the International Gas Turbine Institute and presented at the 34th International Gas Turbine and Aeroengine Congress and Exhibition, Toronto, Ontario, Canada, June 4–8, 1989. Manuscript received at ASME Headquarters January 27, 1989. Paper No. 89-GT-184.

The flow structure in a rotating cavity with radial inflow has been established from experimental and theoretical studies by a number of research workers (Firouzian et al., 1985; Owen et al., 1985; Chew, 1987; Morse, 1988). Referring to Fig. 1, the flow comprises a source region, Ekman-type boundary layers on the disks, an interior core of rotating fluid, and a sink layer near the outlet (which in this case is assumed to be a uniform cylindrical sink). On entering the cavity, the air mixes with the recirculating flow in the outer part of the source region and then flows radially inward. Inside the source region, the flow is similar to that of a free vortex, and the associated pressure drop can be very large.

In Fig. 1 the mixing is assumed to occur rapidly, close to the inlet; this assumption will be discussed further below. As the fluid travels radially inward, its angular momentum is conserved and its tangential velocity increases. At some radius r_s, say, the fluid velocity reaches that of the disk, and downstream of this point the air will rotate faster than the disks and the flow will gradually be entrained into the disk boundary layers. When all the supplied flow has been entrained, these boundary layers become nonentraining, and a rotating core develops in which there is little radial or axial motion.

Pressure and velocity measurements for radial inflow through a rotating cavity have previously been presented by Owen et al. (1985), Firouzian et al. (1986), Alberga et al. (1987), and Graber et al. (1987). In these experiments either the flow entered the cavity at the same tangential velocity as the disk or

the inlet conditions were such that the tangential velocity of the flow at inlet was uncertain. The measurements are generally consistent with the flow structure described above, but Alberga et al. and Graber et al. give a different interpretation of the flow outside the boundary layers. These workers put forward a mathematical model in which turbulent exchange is significant in the core region, whereas Owen et al. and Firouzian et al. proposed a model that neglects any such effect. In both cases the models included solutions of the momentum-integral equations for the boundary layers and agreement with experiment was claimed. It should be noted, however, that the model of Alberga et al. includes an empirical constant, and it is not entirely clear how much tuning of this constant was required.

The application of integral methods to this problem was also discussed by Chew and Snell (1988). In their paper a model is described for radial inflow through a rotating cavity with the inlet angular velocity of the air equal of that of the disk. The model is similar to that of Owen et al., but incorporates a more satisfactory treatment of the entraining boundary layer in the source region. Predictions from the model were shown to be in good agreement with the measurements of Firouzian et al. and in fair agreement with the data of Alberga et al. Comparison of Chew and Snell's predictions with Graber et al.'s measurements of the pressure drop across the cavity also shows good agreement.

In this paper, the integral method is extended to include the effects of deswirl as described in the next section. The experimental apparatus and comparison between measurements and theory are presented in Sections 3, 4 and 5.

2 Theory

2.1 Outline of the Model. The flow is treated as steady and axisymmetric with the flow structure as shown in Fig. 1 and described above. It is also assumed that the flow is rotationally dominated so that the radial and axial components of velocity are generally small compared with a representative tangential velocity. Outside the boundary layers and the mixing region, viscous effects are neglected and approximate analytical solutions are used to describe the flow. These are the free vortex relationship in the source region and the equations of the rotating core, which imply zero axial and radial velocities

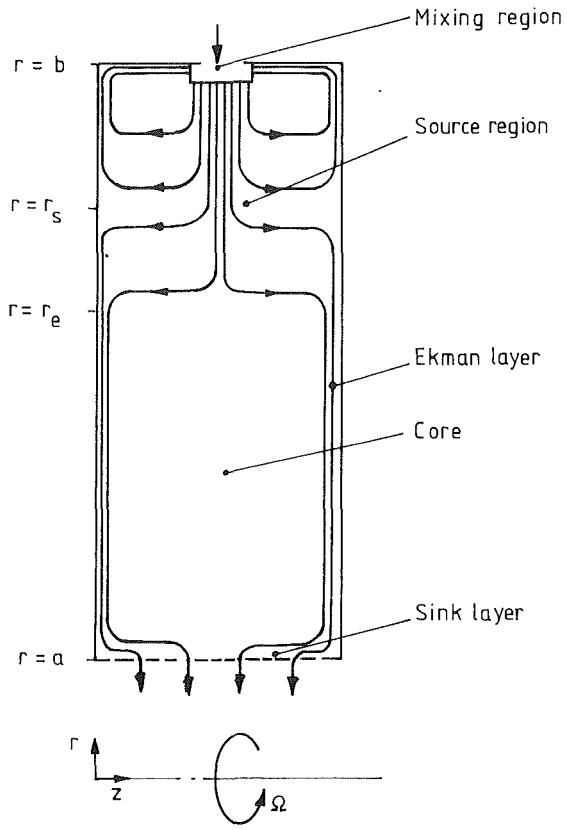

Fig. 1 Schematic of radial inflow in a rotating cavity

Nomenclature

a = inner radius of cavity
b = outer radius of cavity (inner radius of nozzle ring)
c = inlet swirl fraction
c_{eff} = effective inlet swirl fraction
C_p = nondimensional pressure difference = $(p_b - p)/\frac{1}{2}\rho\Omega^2 b^2$
$C_{p,c}$ = pressure coefficient = $(p_b - p_{\text{ref}})/\frac{1}{2}\rho\Omega^2 b^2$
C_w = mass flow coefficient = $\dot{m}/\mu b$
d = outlet diameter of deswirl nozzles
F = friction factor
I = constant in momentum-integral equations, equation (7)
$\dot{m}$ = inlet mass flow rate (negative for radial inflow)
$\dot{m}_s$ = mass flow rate for the shroud boundary layer
N = number of deswirl nozzles
p = static pressure
q = speed, relative to disk, of fluid leaving deswirl nozzles
Q_L = leakage flow rate
r = radial coordinate
r_e = radius of inner boundary of source region
r_s = radius of stagnation point on disk
Re_r = radial Reynolds number = $C_w/2\pi x$
Re_ϕ = rotational Reynolds number = $\Omega b^2/\nu$
s = axial spacing between disks
u = radial component of velocity
u_o = function of r in equation (1)
v = tangential component of velocity relative to disk
$\bar{v}$ = tangential component of velocity, relative to disk, outside the boundary layer
v_m = mean tangential velocity, relative to disk, of fluid in the shroud boundary layer
x = nondimensional radius = r/b
z = axial coordinate
δ = boundary-layer thickness
ΔP_s = pressure drop across experimental rig
θ = angle of deswirl nozzle to tangential direction
λ_L = laminar flow parameter = $C_w/\text{Re}_\phi^{0.5}$
λ_T = turbulent flow parameter = $C_w/\text{Re}_\phi^{0.8}$
μ = absolute viscosity
ν = kinematic viscosity = μ/ρ
ρ = density
$\tau_{r,o}, \tau_{\phi,o}$ = radial and tangential shear-stress components on disk
ϕ = angular coordinate
Ω = angular velocity of cavity

Subscripts

a = value at inner radius of cavity
b = value at outer radius of cavity
ref = reference value

and an axially uniform tangential velocity. These solutions are coupled directly to solutions of the momentum integral equations for the disk boundary layers. A simple treatment of the shroud boundary layer is also incorporated, and this is coupled to the core solution through mixing of the recirculating and inlet flows. Outlet effects are assumed to be confined to a small region and are neglected in this analysis.

Some justification for the assumption of rapid mixing of the nozzle flow and the recirculating flow is given by finite-difference solutions of the Reynolds-averaged Navier–Stokes equations (Chew, 1987; Morse, 1988). In these studies the inlet was modeled by a narrow axisymmetric slot and the solutions showed a rapid change of tangential velocity near the inlet followed by a region in which the flow is similar to that of a free vortex. This aspect of the model is also consistent with the assumption of rotationally dominated flow in which the pressure gradient in inviscid regions must balance the centrifugal force. Thus any axial variation in angular velocity will produce an axial variation in pressure, which, in turn, will produce an axial motion tending to eliminate the axial variation of velocity.

The details of the mathematical model are described below. Incompressible flow is assumed as this is adequate to model the experimental conditions considered later. Extension to compressible flow requires inclusion of an energy equation, but this is reasonably straightforward (see Chew and Rogers, 1988; Chew and Snell, 1988).

2.2 The Momentum-Integral Equations. A cylindrical coordinate system (r, ϕ, z) rotating with the disks is employed. The disks are located at $z = 0$ and $z = s$ but, assuming symmetry, only the half cavity $0 \le z \le s/2$ need be considered. The momentum-integral equations for the disk boundary layer may be derived by integrating the full equations of motion, or by considering a control volume of vanishing radial thickness across the width of the boundary layer. Assumptions must be made regarding the boundary-layer velocity profiles and the wall shear stress. The assumptions used here are generalizations of those of von Karman (1921) for free-disk flow and may be written as follows:

$$u = u_o\,(1 - z/\delta)(z/\delta)^{1/7} \tag{1}$$

$$v = \bar{v}(z/\delta)^{1/7} \tag{2}$$

$$\tau_{\phi,o} = 0.0225\,\rho\left(\frac{\nu}{\delta}\right)^{1/4}\bar{v}(u_0^2 + \bar{v}^2)^{3/8} \tag{3}$$

$$\tau_{r,o} = \frac{u_o}{\bar{v}}\,\tau_{\phi,o} \tag{4}$$

Here u and v are the radial and tangential velocity components in the rotating coordinate system, δ is the boundary-layer thickness, u_o is a function of r only, $\bar{v}$ is the tangential velocity at the boundary-layer edge, $\tau_{\phi,o}$ and $\tau_{r,o}$ are the tangential and radial components of shear stress at the disk, and ρ and ν denote fluid density and kinematic viscosity.

With the usual boundary-layer assumptions, using equations (1) and (2), and using the radial momentum equation for the inviscid flow region to eliminate the pressure, the following momentum-integral equations may be derived:

$$\frac{I_2}{r}\frac{d}{dr}(r\rho u_o^2\delta) + \frac{\rho}{r}\,\delta\bar{v}^2 I_5 + 2\rho\delta\bar{v}\Omega I_4 = -\tau_{r,o} \tag{5}$$

$$\frac{I_3}{r^2}\frac{d}{dr}(r^2\rho u_o\bar{v}\delta) - \frac{I_1}{r}\bar{v}\frac{d}{dr}(r\rho u_o\delta) + 2I_1\rho u_o\Omega\delta = -\tau_{\phi,o} \tag{6}$$

where Ω is the angular velocity of the disk. The coefficients I are given by

$$I_1 = \frac{49}{120},\quad I_2 = \frac{343}{1656},\quad I_3 = \frac{49}{144},\quad I_4 = \frac{1}{8},\quad I_5 = \frac{2}{9} \tag{7}$$

Equations (5) and (6) express the conservation laws for radial and angular momentum; for further details of the derivation the reader is referred to Chew and Rogers (1988). Substituting equations (3), (4), and (7) into equations (5) and (6) gives two first-order differential equations in the unknowns u_o, $\bar{v}$, and δ, all of which are functions of r. To close the problem a further equation is required and appropriate boundary conditions must be specified.

An additional equation giving $\bar{v}$ in the source region is provided by the solution for the flow outside the boundary layer. This is the free-vortex relation

$$r(\bar{v} + \Omega r) = c_{\text{eff}}\,\Omega b^2 \tag{8}$$

where c_{eff} is an effective inlet swirl fraction (to be defined below) and b is the outer radius of the cavity. In the rotating core, there is no radial flow and the flow in the two nonentraining Ekman-type layers must equal the net flow through the cavity, $\dot{m}$, so that

$$4\pi\, I_1\rho\delta u_o = \dot{m} \tag{9}$$

The boundary layer on the disk can be divided into three distinct regions: the outflow region $b > r > r_s$, the entraining inflow region $r_s > r > r_e$, and the nonentraining inflow region $r_e > r > a$. The stagnation point on the disk occurs when the fluid velocity given by equation (8) equals the disk speed, which, in the rotating frame, is zero. Thus

$$r_s^2 = c_{\text{eff}}\,b^2 \tag{10}$$

At this point there is no flow in the boundary layer, and starting conditions for both the inflow and outflow regions must be chosen to give zero or very small δ and δu_o at this point. The position $r = r_e$ is defined as the point at which all the flow has been entrained into the inflow layer and is determined from the solution. Starting conditions for the nonentraining layer are provided by the solution for the entraining layer at $r = r_e$.

The pressure drop across the cavity may be obtained from the radial-momentum equation in the inviscid region, which reduces to

$$\frac{dp}{dr} = \frac{\rho}{r}(\bar{v} + \Omega r)^2 \tag{11}$$

where p denotes static pressure.

2.3 Treatment of the Shroud and Mixing Regions. The mass flow in the boundary layer along the shroud is assumed to be constant and equal to that in the outflow boundary layer on the disk at $r = b$. It is also assumed that the boundary-layer thickness is small compared with b. A friction factor F is defined such that the tangential shear at the surface is $-\frac{1}{2}F\rho v_m^2$ where v_m is the mean angular velocity of the fluid relative to the shroud. The angular-momentum balance for the flow in the shroud boundary layer then gives the following equation:

$$\dot{m}_s\frac{dv_m}{dz} = \pi b\,F\rho v_m^2 \tag{12}$$

If F is assumed constant this equation may be integrated between $z = 0$ and $z = s/2$ to give

$$(v_m)_{z=s/2} = \frac{-2\dot{m}_s\,(v_m)_{z=0}}{\pi bs\rho F\,(v_m)_{z=0} - 2\dot{m}_s} \tag{13}$$

Equation (13) was used to estimate the increase in angular momentum due to friction at the shroud, and F and $(v_m)_{z=0}$ were then estimated from the disk-boundary-layer solution at $r = b$.

The inlet swirl fraction c of the fluid leaving the nozzles is defined as the tangential velocity of the fluid in a stationary coordinate system divided by the disk speed. The effective inlet swirl fraction c_{eff} is defined as the tangential velocity of the mixed recirculation and inlet flows divided by the disk speed.

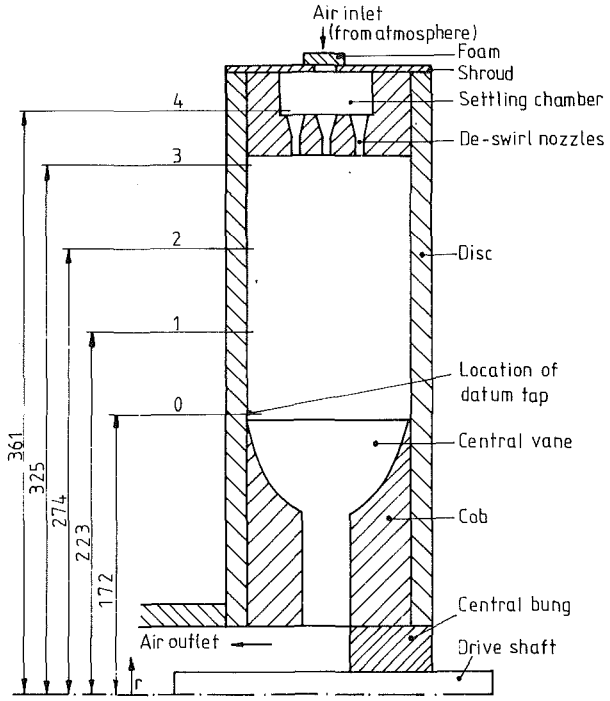

Fig. 2 Rotating cavity and location of pressure taps (numbered 0 to 4); dimensions in mm

If c is less than unity, radial outflow occurs in the boundary layer on the disk, and this results in the recirculation shown in Fig. 1. For a given flow rate, c may be estimated from the nozzle geometry, as discussed in Section 3.1. A simple mixing sum then gives the following relationship for c_{eff}:

$$(2\dot{m}_s + \dot{m})\, c_{\text{eff}} = 2\dot{m}_s \left[\frac{(v_m)_{z=s/2}}{\Omega b} + 1 \right] + \dot{m}c \qquad (14)$$

Note that the treatment of the boundary layers described above would not be expected to be valid for $c_{\text{eff}} < 0$.

2.4 Dimensional Analysis. A pressure coefficient $C_{p,c}$, rotational Reynolds number Re_ϕ, mass flow coefficient C_w, and throughflow parameter λ_T are defined as follows:

$$C_{p,c} = \frac{2}{\rho \Omega^2 b^2}(p_b - p_{\text{ref}}), \quad \text{Re}_\phi = \frac{\Omega b^2}{\nu},$$

$$C_w = \frac{\dot{m}}{\mu b}, \quad \lambda_T = \frac{C_w}{\text{Re}_\phi^{0.8}} \qquad (15)$$

where the subscript b refers to the outer radius and "ref" refers to a suitable reference location.

For the special case where the inlet swirl fraction, c, is unity, Chew and Snell (1988) have shown that $C_{p,c}$, calculated from the above equations, is a function of only λ_T and the radius ratio a/b. When $c \neq 1$, a similar analysis (details of which are not given here) shows that $C_{p,c}$ is a function of λ_T, a/b, c, and s/b. Thus, for any particular geometry, $C_{p,c}$ depends only on λ_T and c.

2.5 Numerical Solution of the Equations. As in earlier studies, solutions of the integral equations (5) and (6) with the auxiliary relations (3), (4), and (7)–(11) were obtained using a standard mathematical library routine for ordinary differential equations. The computer program used was developed from that of Chew and Rogers (1988) and works with a nondimensional representation of the equations. The solutions for both the outflow and inflow regions of the layer were started at the stagnation point $r = r_s$ and proceed in the direction of the boundary-layer flow. Some iteration is required to find the effective inlet swirl fraction c_{eff}. Initially, a guessed value is used to obtain a solution for the outflow region of the disk boundary layer, and an improved estimate of c_{eff} is then obtained using equations (13) and (14). This process is repeated until satisfactory convergence is obtained. For any particular example, only a few seconds of CPU time on an IBM 3081 were required to obtain a solution.

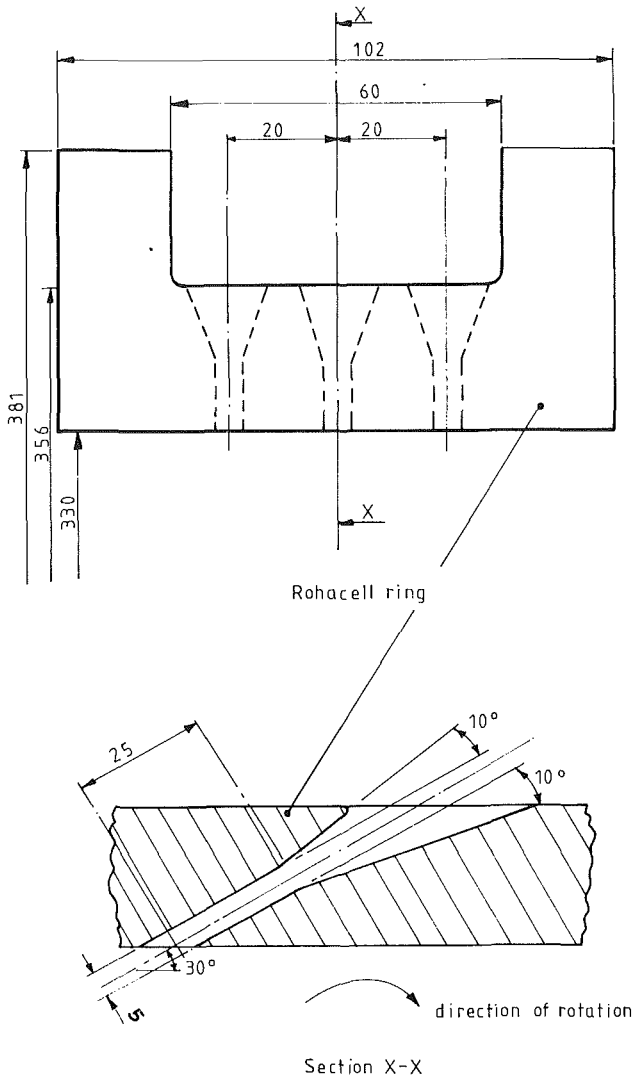

Fig. 3 Deswirl nozzles used in experiments; dimensions in mm

3 Experimental Apparatus

3.1 The Rotating-Cavity Rig. Simplified diagrams of the rotating cavity and the deswirl nozzles are shown in Figs. 2 and 3. The cavity comprised two steel disks, of outer radius 381 mm and thickness 12.7 mm, and a 1.5-mm-thick Paxolin peripheral shroud. The latter contained 30 equispaced holes, of 28.6 mm diameter, in its midaxial plane. To obtain an initial swirl fraction of unity, and to generate a settling chamber for the air upstream of the deswirl nozzles, the shroud was covered by a layer of porous rubber foam.

Each disk was mounted on a hollow tube with an inner radius of 38.1 mm. One tube was blanked off and the other was connected, via stationary piping, to the inlet of a centrifugal compressor, which could produce flow rates up to 0.1 kg/s. The disks could be rotated up to 2000 rpm by means of a variable-speed electric motor.

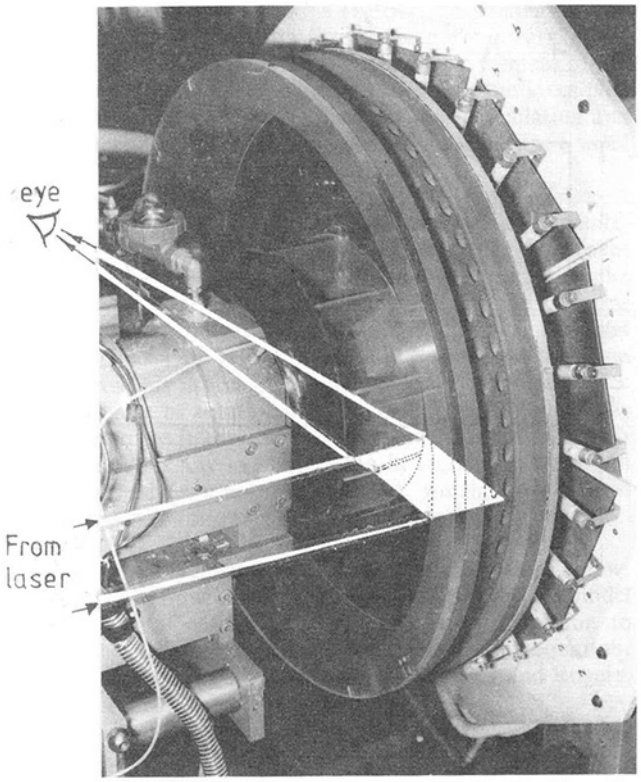

Fig. 4 Photograph of the rotating-cavity rig showing the deswirl nozzles and the plane of illumination

The deswirl nozzles were machined from a ring of Rohacell, a lightweight, high-strength, plastic foam. Sixty equispaced holes were drilled at an angle of $\theta = 30$ deg to the tangential direction at each of three axial locations, as shown in Fig. 3. Convergent nozzles were formed by machining a conical inlet section, with a 10 deg half-angle, and a parallel outlet section of diameter $d = 5$ mm. The outer radius of the cavity was taken to be the inner radius of the nozzle ring where $r = b = 330$ mm. The complete nozzle assembly was bonded to the disks, as shown in Fig. 4.

The inlet-swirl fraction is given by

$$c = \frac{\Omega b - q \cos \theta}{\Omega b} \tag{16}$$

where q is the magnitude of the velocity, relative to the disk, of the air leaving the nozzles at $r = b$. If N nozzles are used then

$$q = \frac{4|\dot{m}|}{\pi d^2 \rho N} \tag{17}$$

Hence, using the definition of C_w, Re_ϕ, and λ_T given in equation (15), it follows that

$$c = 1 - \frac{4 \cos \theta}{\pi N} \left(\frac{b}{d}\right)^2 \frac{|C_w|}{\mathrm{Re}_\phi} = 1 - \frac{4 \cos \theta}{\pi N} \left(\frac{b}{d}\right)^2 \frac{|\lambda_T|}{\mathrm{Re}_\phi^{0.2}} \tag{18}$$

For given values of C_w and Re_ϕ, c can be varied by altering N, and this was done in practice by placing rubber plugs in some of the 180 nozzles.

Cobs (bulbous hubs) also made from Rohacell, and identical to those used by Farthing and Owen (1988), were attached to the center of the disks. The shape was chosen to be representative of that used in gas turbine design, and the inner and outer radii of the cobs were 38.1 and 168 mm. The minimum axial spacing between the cobs was 33 mm and the parallel section extended to a radius of 107 mm. To reduce the overall pressure drop, ten Rohacell central vanes, as described by Chew et al. (1989), were positioned between the cobs.

3.2 Instrumentation. Holes of 5 mm diameter were drilled axially through one of the disks (the left-hand disk shown in Fig. 2) at radial locations of $r = 172$, 223, 274, 325, and 361 mm. These holes were used as static-pressure taps, and a Kulite XT-190 series miniature differential-pressure transducer was flush-mounted to each of the four outermost taps (numbers 1–4). The innermost tap (number 0) was used as a datum from which the outer four pressures were measured. The reference tubes from each of the four transducers were connected, via a common tube, to this datum tap. To minimize imbalance, the transducers were located on a diametral line, with two on one radius and two on the other. Thus, two datum taps and two common tubes were used. The electrical signals from, and the power supply to, the transducers were brought out through a silver slip-ring assembly, and the voltages were measured by a Solartron IMS 3510 data-logger controlled by a PDP 11/44 minicomputer.

Solid-body rotation occurred inside the common tube, whereas inside the cavity the pressure difference could be less or greater than that associated with solid body rotation. As a consequence, the transducers were individually calibrated, off the rig, over the entire operating range of $\pm$ 6 kN/m^2. The largest source of error was caused by "zero drift": The sensitivity (volts/unit pressure) of the transducers remained constant but, depending on the rotational speed, the voltage level varied with time. The results were corrected for this zero drift, which was determined immediately before each test. The maximum correction was 15 percent of the reading.

The flow rate was measured, by Annubar differential-pressure devices, to an accuracy of $\pm$ 3 percent. However, a relatively small amount of air leaked into the system (which was at subatmospheric pressure) through the seals between rotating and stationary components. A series of calibrations revealed that the leakage flow rate, Q_L, was independent of rotational speed but was proportional to $\Delta P_s^{1/2}$, where ΔP_s was the pressure drop across the system measured by a static pressure tap downstream of the cavity. The measured flow rate was corrected to account for the leakage, which was less than 15 percent of the measured value.

For flow visualization, the left-hand steel disk in the cavity was replaced by one made from transparent polycarbonate. A 4 W argon-ion laser was used to provide slit illumination through the polycarbonate disk (see Fig. 4), and the air entering the cavity was "seeded" with micron-sized oil particles produced by a Concept smoke generator. Video recordings and photographs were used to study the flow structure in the cavity.

4 Flow Visualization

4.1 Flow Structure. Using the flow visualization apparatus described in the preceding section, photographs, as shown in Fig. 5, were taken of the smoke patterns in the r–z plane of the cavity. The top and bottom of each photograph correspond to the exit of the deswirl nozzles and the edge of the central vanes, respectively. (The vanes prevented optical access below $x = 0.5$.) The opaque deswirl nozzles prevented the illumination of the r–z plane through the shroud, and so visualization was via the transparent (left-hand) disk shown in Fig. 4 (which appears as the right-hand disk of Fig. 5). The field-of-view was at an angle of approximately 50 deg to the plane of illumination, and so the edges of the nozzle ring and the central vanes appear as oblique lines at $x = 1$ and 0.5. For these photographs, all 180 deswirl nozzles were used.

Figure 5 shows smoke patterns photographed at different times for $C_w = -480$, $\mathrm{Re}_\phi = 3.8 \times 10^4$, and $c \approx 0.66$; for this value of C_w, the flow is expected to be laminar, and interpretation of the flow structure is aided by reference to Fig. 1.

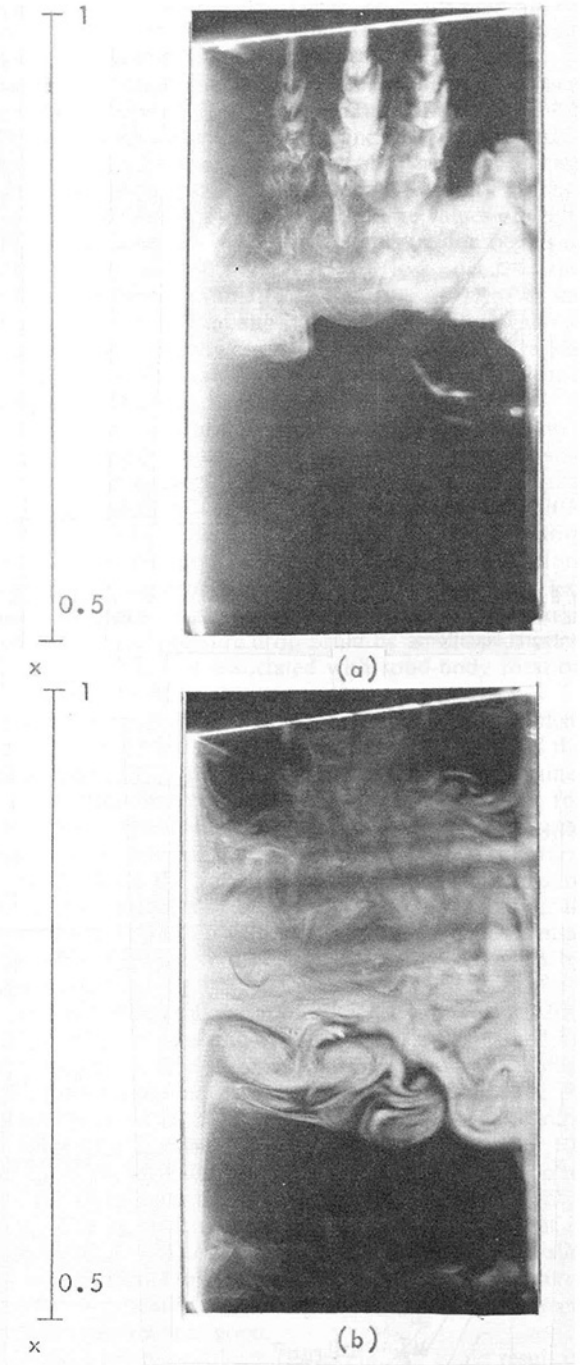

Fig. 5 Smoke patterns in the r-z plane for $|C_w| = 480$, $Re_\phi = 3.8 \times 10^4$, and $c = 0.66$

Figure 5(a) shows that the smoke, after entering the cavity in three jets, is beginning to fill the source region. The smoke pattern on the right-hand disk provides evidence that there is radial outflow as well as inflow inside the source region. Figure 5(b) was taken a few seconds later when smoke had penetrated through the source region, Ekman layers, and sink layer, and the interior core appears as a black region for $x \leq 0.7$. The other black region, for $x \geq 0.9$, is caused by recirculation in the source region; as discussed in Section 2.3, this recirculation occurs when $c_{\text{eff}} < 1$.

The photographs shown in Fig. 5 provide evidence that the usual source-sink flow patterns still occur even when the fluid enters the cavity through deswirl nozzles. Other photographs showed that, as expected, the size of the source region increased with increasing flow rate and with decreasing rotational speed.

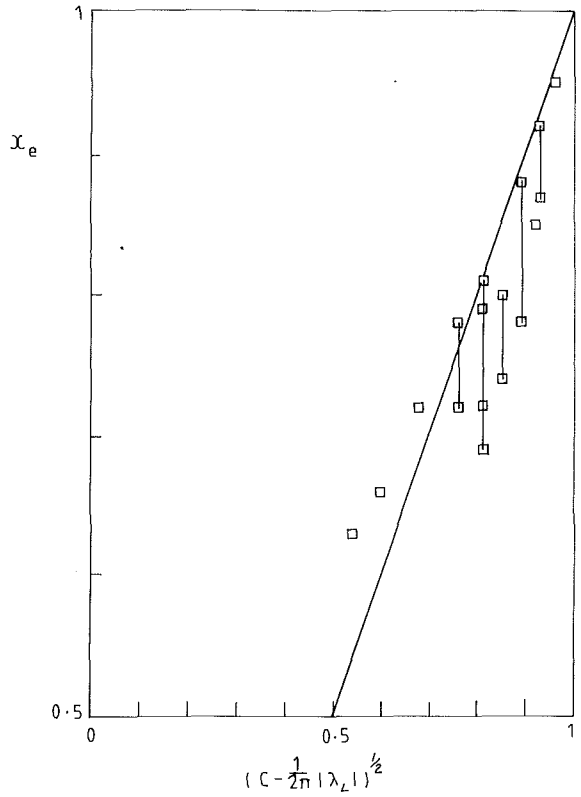

Fig. 6 Size of source region for laminar flow; □ experimental measurements; | difference between maximum and minimum values; —— equation (19)

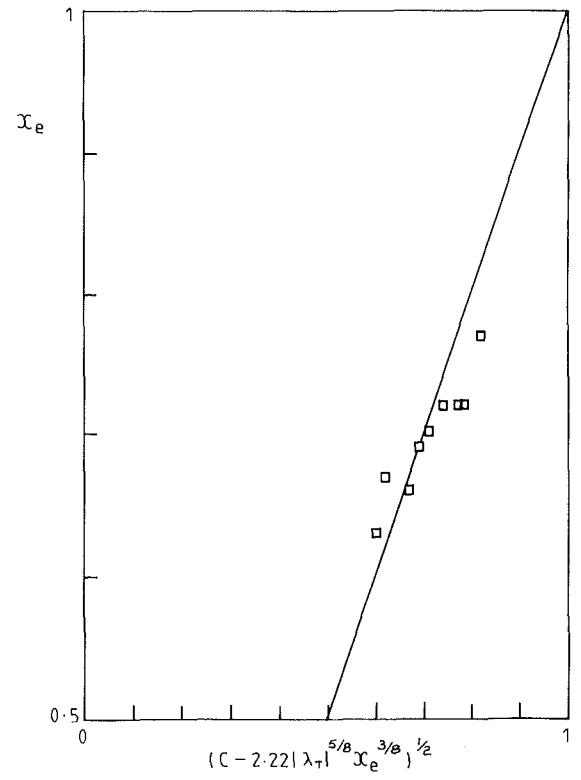

Fig. 7 Size of source region for turbulent flow; □ experimental measurements; —— equation (20)

4.2 Size of the Source Region. A series of tests was conducted for $200 \leq |C_w| \leq 2300$ and $0.17 \leq Re_\phi/10^5 \leq 4.6$ with all 180 nozzles. The radius of the edge of source region,

r_e, was measured, to an estimated accuracy of ± 10 mm, from video recordings of the flow structure. These measurements were compared with the theoretical values of Firouzian et al. (1985) where $x_e = r_e/b$ and

$$x_e = \left(c - \frac{1}{2\pi}|\lambda_L|\right)^{1/2} \tag{19}$$

for laminar flow, and

$$x_e = (c - 2.22|\lambda_T|^{5/8}x_e^{3/8})^{1/2} \tag{20}$$

for turbulent flow.

These equations were derived from the so-called linear momentum-integral equations: When $\bar{v}/\Omega r \ll 1$, the Coriolis forces dominate over the nonlinear inertial terms, and the latter can be neglected. The radius r_e, is taken to be the point where all the fluid flowing radially inward has been entrained into the boundary layers on the disks. For the experimental measurements shown in Figs. 6 and 7, $c \doteq 1$ and consequently equations (19) and (20) are expected to give similar results to the numerical solution of the full nonlinear equations described in Section 2.

Transition from laminar to turbulent flow is assumed to occur when $\mathrm{Re}_r = 180$, and the results for laminar and turbulent flow are shown in Figs. 6 and 7, respectively. For some cases of laminar flow, the source region appeared to oscillate, and this is indicated by the bar lines in Fig. 6, which join the maximum and minimum values of x_e. Similar instabilities in the flow structure were observed by Firouzian et al., who noted that the size of the source region could increase or decrease periodically in a nonaxisymmetric fashion. From Fig. 6 it is evident that, where no instabilities occur, there is reasonable agreement between the theoretical predictions and the measured values. For the cases where the size of the source region fluctuated, reasonable agreement is obtained with the maximum value of x_e (i.e., the smaller size of the source region). For turbulent flow no oscillations were observed, and Fig. 7 shows reasonable agreement between the experimental and theoretical results.

5 Pressure Drop in the Rotating Cavity

Pressure transducers 1, 2, and 3, at the locations shown in Fig. 2, were used to determine the static pressure relative to the datum pressure tap. The nondimensional pressure difference, C_p, was defined as

$$C_p = \frac{p_b - p}{\frac{1}{2}\rho\Omega^2 b^2} \tag{21}$$

where, for convenience, p_b was taken to be the pressure recorded by transducer number 3 (this was actually located at r = 325 mm where $x = 0.985$). Tests were conducted for $550 \le |C_w| \le 2.1 \times 10^4$ and $0.15 \le \mathrm{Re}_\phi/10^6 \le 1.4$; by using N = 40, 80, or 160 (see equation (18)) it was possible to vary the swirl fraction in the range $-0.4 \le c \le +0.9$ for a relatively large range of the flow parameter λ_T.

Figure 8 shows a comparison between the variation of C_p with x obtained from the momentum-integral equations, as discussed in Section 2, and the measured values at x = 0.52, 0.68, and 0.83. The measurements were made at $\mathrm{Re}_\phi = 0.61 \times 10^6$ with N = 40, and it can be seen that the agreement between the theoretical and experimental results is good. The agreement was also good for most of the other results obtained, and this gave confidence in both the theoretical model and the experimental procedures.

Figure 9 shows the variation of the pressure coefficient for the cavity, $C_{p,c}$ (based on the pressure difference between transducer 3 and the reference tap), with $|\lambda_T|$ for a range of different inlet swirl fractions. For solid-body rotation, the value of $C_{p,c}$ for the cavity is approximately 0.75. For each value of c, up to three clusters of experimental data can be seen: These cor-

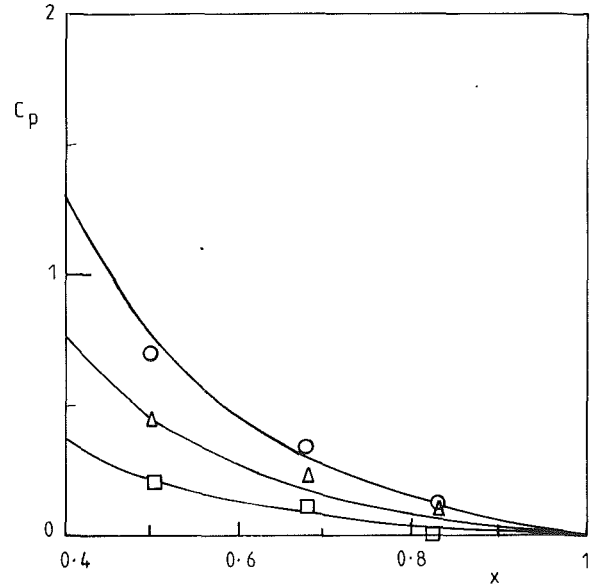

Fig. 8 Variation of C_p with x for $\mathrm{Re}_\phi = 0.61 \times 10^6$; □ $c = -0.2$, $|\lambda_T| = 0.144$; △ $c = 0$, $|\lambda_T| = 0.120$; ○ $c = +0.2$, $|\lambda_T| = 0.096$; —— solutions of integral equations

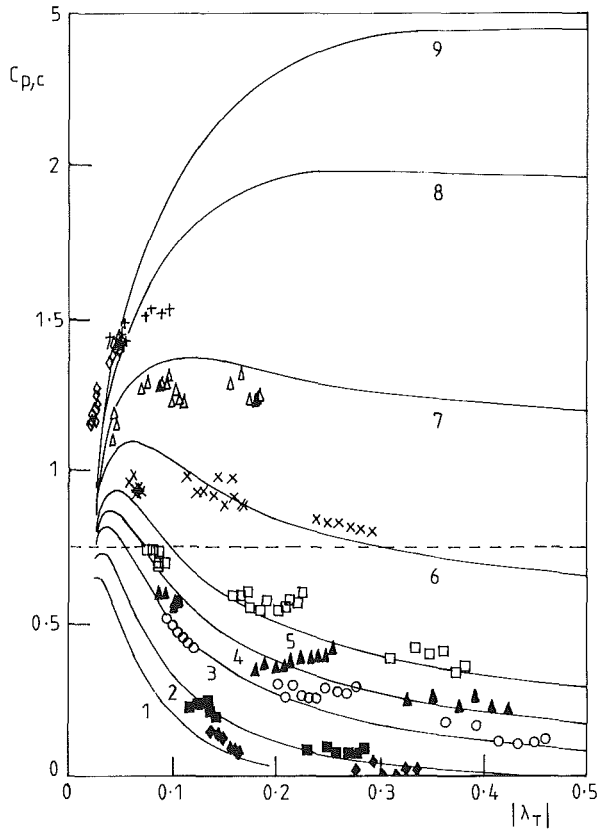

Fig. 9 Effect of c on variation of $C_{p,c}$ with $|\lambda_T|$:

Curve	Measurements	c	
1	◆	−0.4	——Solutions of integral equations
2	■	−0.2	
3	○	0	
4	▲	+0.1	
5	□	+0.2	- - - Solid-body rotation
6	×	+0.4	
7	△	+0.6	
8	+	+0.8	
9	◇	+0.9	

respond to $N = 40$, 80, and 160. The experiments were carried out by fixing N then varying C_w and Re_ϕ to keep c constant for as large a range of λ_T as possible.

It can be seen from Fig. 9 that, for most values of c, there is a maximum value of $C_{p,c}$: The magnitude of this maximum and the value of $|\lambda_T|$ at which it occurs increase with increasing c. These effects can be explained by considering the mixing process discussed in Section 2.3; c_{eff} tends to unity as $|\lambda_T|$ approaches zero, and c_{eff} tends to c for large values of $|\lambda_T|$. Also for large values of $|\lambda_T|$, as the source region begins to fill the entire cavity, free-vortex flow occurs and $C_{p,c}$ tends to a limiting value ($C_{p,c} = c^2(x_{\mathrm{ref}}^{-2} - 1)$). For the larger values of c where mixing is weak, this limiting value is approached monotonically as $|\lambda_T|$ is increased (see curve 9 in Fig. 9); for the smaller values of c where mixing is significant, a turning point is apparent (for example, see curve 6).

The minimum value of $C_{p,c}$ occurs when the positive swirl in the outflowing boundary layer on the disks in the source region neutralizes the negative swirl created by the nozzles such that $c_{\mathrm{eff}} = 0$; the fluid then moves radially inward with little or no residual swirl, thereby minimizing the pressure drop across the cavity. For large ranges of $|\lambda_T|$ and c, it is therefore possible to reduce the pressure drop across the cavity to less than that associated with solid-body rotation. Without the deswirl nozzles, the pressure drop could be an order of magnitude greater than that associated with solid-body rotation (see Chew et al., 1989).

In the experiments, the pressure drop was the dependent variable; λ_T and c were varied in a controlled fashion and the resulting value of $C_{p,c}$ was measured. In a gas turbine engine, the pressure drop between the compressor bleed-off and, for example, the turbine-blade-cooling air is fixed: The flow rate of cooling air is determined by the available pressure difference. To illustrate the variation of flow rate with pressure difference, the variation of $|C_w|$ with $C_{p,c}$ is shown in Fig. 10 for $N = 80$ and for various values of Re_ϕ. For the experimental data, as $|C_w|$ increases c decreases in the manner given by equation (18).

Figure 10(a) shows the variation of $|C_w|$ with $C_{p,c}$ for $\mathrm{Re}_\phi = 0.23 \times 10^6$; the resulting "$s$-curve" can be explained by referring to Fig. 9. The turning point at $|C_w| \simeq 10^3$ corresponds to the approximate maximum value of $C_{p,c}$ in Fig. 9; the turning point at $|C_w| \simeq 5 \times 10^3$ corresponds to the minimum value of $C_{p,c}$ (where $c_{\mathrm{eff}} = 0$). For $|C_w| > 5 \times 10^3$ (where $c_{\mathrm{eff}} < 0$), the fluid rotates in the opposite direction to that of the disks, and the pressure drop increases as $|C_w|$ increases. The agreement between theory and experiment is good up to $|C_w| = 5 \times 10^3$; the theoretical model is invalid for $c_{\mathrm{eff}} < 0$. Similar results are shown in Figs. 10(b) and 10(c) for $\mathrm{Re}_\phi/10^6 = 0.38$ and 0.61, and again the agreement between theory and experiment is good.

The s-curve behavior, illustrated in Fig. 10, could result in unstable conditions inside an engine. As $C_{p,c}$ is increased in the engine, $|C_w|$ might jump from a low to a high branch of the curve; conversely, a jump from a high to a low branch could occur as $C_{p,c}$ is reduced. In the experiments (where $|C_w|$ rather than $C_{p,c}$ was controlled), no such jump phenomena were observed.

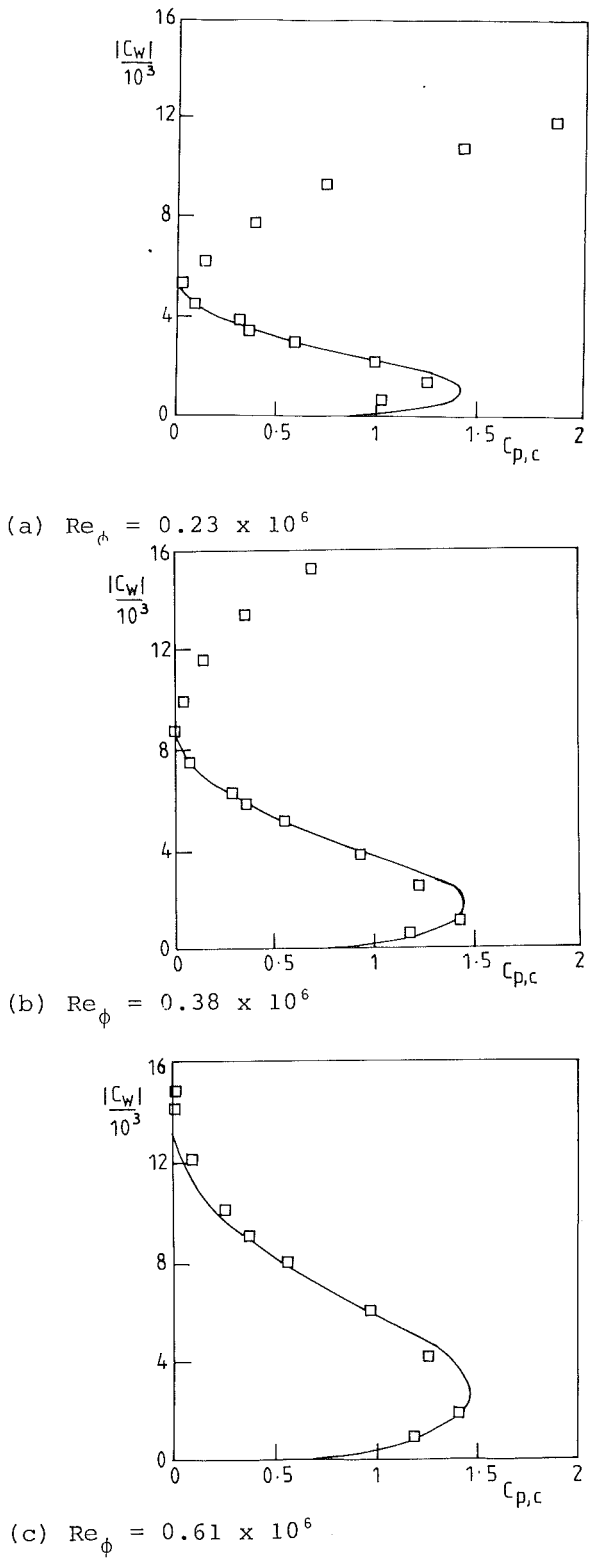

Fig. 10 Variation of $|C_w|$ with $C_{p,c}$; □ experimental measurements; — solutions of integral equations

6 Conclusions

Solutions of the momentum-integral equations have been used to calculate the effect of inlet swirl on the pressure drop in a rotating cavity with a radial inflow of fluid. The theoretical values were compared with measurements made inside a rig in which deswirl nozzles were used to reduce the swirl fraction of the incoming air. Flow visualization confirmed that "conventional" source-sink flow structure still occurred when the deswirl nozzles were fitted, and pressure transducers attached to one of the disks were used to measured the static pressure inside the rotating cavity.

In the main, there is good agreement between the theoretical and experimental values of pressure distribution. The mixing that occurs between the radially outward flow in the boundary layers on the disks and the radially inward flow through the deswirl nozzles modifies the inlet swirl fraction. However, if

these two flows are suitably matched, the effective swirl fraction can be reduced to zero, and the resulting pressure drop across the cavity is then negligibly small. For a constant value of rotational speed, the variation of flow rate with pressure drop exhibits an "*s*-curve" behavior in which there are up to three different values of flow rate for each value of pressure drop. In a gas turbine engine, this behavior may well result in flow rates that jump between different branches of the *s*-curve.

It should be pointed out that the pressure measurements described above were all made inside the rotating cavity itself; the pressure drop across the deswirl nozzles is also important. This pressure drop, and the matching of the nozzles and the cavity, will be the subject of a future paper.

Acknowledgments

We wish to thank the Science and Engineering Research Council, Rolls Royce plc, and Ruston Gas Turbines Ltd. for funding the research described in this paper.

References

Alberga, D. G., Stephens, G. E., and Johnson, B. V., 1987, "Comparison of Predicted and Measured Velocities in a Compressor Disc Drum Model," ASME Paper No. 87-GT-208.

Brown, W. M., and Manente, J. C., 1977, "Compressor Bleed System," US Patent No. 4,008,977.

Chew, J. W., 1987, "Computation of Flow and Heat Transfer in Rotating Disc Systems," *Proc. of the 2nd ASME-JSME Thermal Engineering Joint Conference*, Vol. 3, pp. 361-367.

Chew, J. W., and Rogers, R. H., 1988, "An Integral Method for the Calculation of Turbulent Forced Convection in a Rotating Cavity With Radial Outflow," *Int. J. Heat Fluid Flow*, Vol. 9, pp. 37-48.

Chew, J. W., and Snell, R. J., 1988, "Predictions of the Pressure Distribution for Radial Inflow Between Co-rotating Discs," ASME Paper No. 88-GT-61.

Chew, J. W., Farthing , P. R., Owen, J. M., and Stratford, B., 1989, "The Use of Fins to Reduce the Pressure Drop in a Rotating Cavity With a Radial Inflow," ASME JOURNAL OF TURBOMACHINERY, Vol. 111, pp. 349-356.

Farthing, P. R., and Owen, J. M., 1988, "The Effect of Disc Geometry on Heat Transfer in a Rotating Cavity With a Radial Outflow of Fluid," ASME *Journal of Engineering for Gas Turbines and Power*, Vol. 110, pp. 70-77.

Firouzian, M., Owen, J. M., Pincombe, J. R., and Rogers, R. H., 1985, "Flow and Heat Transfer in a Rotating Cavity With a Radial Inflow of Fluid. Part 1: The Flow Structure," *Int. J. Heat Fluid Flow*, Vol. 6, pp. 228-234.

Firouzian, M., Owen, J. M., Pincombe, J. R., and Rogers, R. H., 1986, "Flow and Heat Transfer in a Rotating Cavity With a Radial Inflow of Fluid. Part 2: Velocity, Pressure and Heat Transfer Measurements," *Int. J. Heat Fluid Flow*, Vol. 7, pp. 21-27.

Graber, D. J., Daniels, W. A., and Johnson, B. V., 1987, "Disc Pumping Test," Report No. AFWAL-TR-87-2050, Wright-Patterson Air Force Base, OH.

Karman, T. von, 1921, "Uber Laminare und Turbulente Reibung," *Z. angew. Math. Mech.*, Vol. 1, pp. 233-252.

Kraftwerk Union Aktiengesellschaft, 1977, "Improvements in or Relating to Gas Turbine Assemblies," UK Patent No. 1,541,533.

Morse, A. P., 1988, "Numerical Prediction of Turbulent Flow in Rotating Cavities," ASME JOURNAL OF TURBOMACHINERY, Vol. 110, pp. 202-212.

Owen, J. M., Pincombe, J. R., and Rogers, R. H., 1985, "Source-Sink Flow Inside a Rotating Cylindrical Cavity," *J. Fluid Mech.*, Vol. 155, pp. 233-265.

Scheper, G. W., 1962, "Turbine Rotor Ventilation System," US Patent No. 3,043,561.

Prediction of Heat Transfer in a Rotating Cavity With a Radial Outflow

C. L. Ong[1]

J. M. Owen[2]

Thermo-Fluid Mechanics Research Centre,
School of Engineering & Applied Sciences,
University of Sussex,
Falmer, Brighton, BN1 9QT,
United Kingdom

Solutions of the differential boundary-layer equations, using the Keller-box scheme and the Cebeci–Smith eddy-viscosity model for turbulent flow, have been used to predict the Nusselt numbers on the disks of a heated rotating cavity with a radial outflow of cooling air. Computed Nusselt numbers were in satisfactory agreement with analytical solutions of the elliptic equations for laminar flow and with solutions of the integral equations for turbulent flow. For a wide range of flow rates, rotational speeds, and disk-temperature profiles, the computed Nusselt numbers were in mainly good agreement with measurements obtained from an air-cooled rotating cavity. It is concluded that the boundary-layer equations should provide solutions accurate enough for application to air-cooled gas turbine disks.

1 Introduction

A rotating cavity with a radial outflow of fluid (see Fig. 1) provides a simplified model of the flow that occurs between two corotating air-cooled gas turbine disks. To predict the stress, fatigue life, and radial growth of the disks, the designer needs to be able to calculate their temperature distribution. This requires the calculation of the convective heat transfer coefficients, and it is the object of this paper to show that the boundary-layer equations can be used for this purpose.

The flow structure in a rotating cavity with a radial outflow of air has been studied theoretically and experimentally by many research workers (see, for example, Chew, 1982; Morse, 1988; Owen et al., 1985; Pincombe, 1983). Referring to Fig. 1, the flow structure comprises a source region near the inlet, Ekman-type boundary layers on the disks, and a sink layer near the outlet, all of which surround an interior inviscid core of rotating fluid.

Although it is necessary to solve the elliptic equations of motion if quantification of the entire flow is required, the flow near the disks can be determined from the boundary-layer equations. The latter equations were solved by Shirazi and Truman (1988) and by Ong and Owen (1989). As the former authors considered only the "narrow-gap case," where the boundary layers merge, their solutions are not relevant to the geometries found inside gas turbines.

The isothermal solutions of Ong and Owen are applicable to the source-sink flows described above. Two particular problems occur in such flows: (*i*) The boundary layer entrains fluid in the source region but is nonentraining outside; (*ii*) reverse flow can occur in the nonentraining Ekman-type layers outside the source region. The authors outlined methods of overcoming these problems and, using a modified form of the Cebeci and Smith (1974) eddy-viscosity model, they computed velocity distributions that were in good agreement with the measurements of Pincombe.

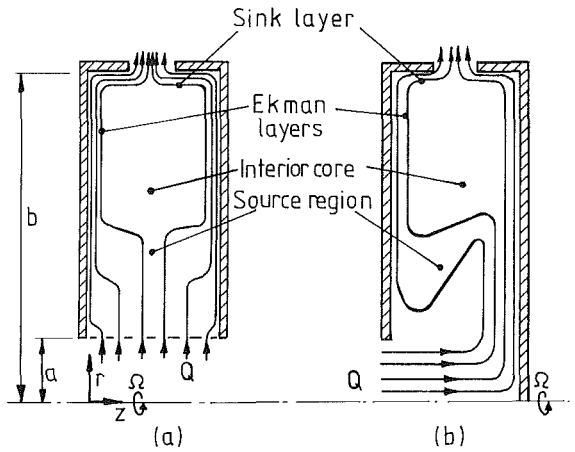

Fig. 1 Simplified flow structure in a rotating cavity with a radial outflow of fluid

The method is extended below to include the effects of property variations and the solution of the energy equation. The boundary-layer equations, the eddy-viscosity model, and the numerical solutions are described in Sections 2, 3, and 4, and the predicted Nusselt numbers are compared with other theoretical values and with experimental measurements in Sections 5 and 6.

2 The Boundary-Layer Equations

For the axisymmetric boundary layer on each disk, the time-averaged conservation equations for mass, momentum, and

[1]Present address: The National Grid Company plc, Research and Development Centre, Kelvin Ave., Leatherhead, United Kingdom.

[2]Present address: School of Mechanical Engineering, University of Bath, Bath, United Kingdom.

Contributed by the International Gas Turbine Institute and presented at the 34th International Gas Turbine and Aeroengine Congress and Exhibition, Toronto, Ontario, Canada, June 4–8, 1989. Manuscript received at ASME Headquarters February 14, 1989. Paper No. 89-GT-286.

energy can be expressed in a stationary cylindrical coordinate (r, ϕ, z) system as:

$$\frac{1}{r}\frac{\partial}{\partial r}(\rho r u)+\frac{\partial}{\partial z}(\rho w)=0 \tag{2.1}$$

$$u\frac{\partial u}{\partial r}+w\frac{\partial u}{\partial z}-\frac{v_\phi^2}{r}=-\frac{1}{\rho}\frac{\partial p}{\partial r}+\frac{1}{\rho}\frac{\partial \tau_r}{\partial z} \tag{2.2}$$

$$u\frac{\partial v_\phi}{\partial r}+w\frac{\partial v_\phi}{\partial z}+\frac{uv_\phi}{r}=\frac{1}{\rho}\frac{\partial \tau_\phi}{\partial z} \tag{2.3}$$

$$u\frac{\partial h}{\partial r}+w\frac{\partial h}{\partial z}=\frac{1}{\rho}\frac{\partial}{\partial z}(-q+u\tau_r+v_\phi\tau_\phi) \tag{2.4}$$

where the total enthalpy, h, for incompressible flow is given by

$$h=C_pT+\frac{1}{2}(u^2+v_\phi^2)+\frac{p}{\rho} \tag{2.5}$$

and for compressible flow by

$$h=C_pT+\frac{1}{2}(u^2+v_\phi^2) \tag{2.6}$$

Here, u, v_ϕ, and w are the radial, tangential, and axial components of velocity, T is the temperature, p is the static pressure, and ρ and C_p denote density and specific heat at constant pressure. For turbulent flow, employing the concepts of effective exchange coefficients, the radial and tangential shear-stress components, τ_r and τ_ϕ, and the heat flux, q, are defined by

$$\frac{1}{\rho}\tau_r=\nu_{\text{eff}}\frac{\partial u}{\partial z} \tag{2.7}$$

$$\frac{1}{\rho}\tau_\phi=\nu_{\text{eff}}\frac{\partial v_\phi}{\partial z} \tag{2.8}$$

and

$$q=-\rho c_p\left(\frac{\nu}{\text{Pr}}\right)_{\text{eff}}\frac{\partial T}{\partial z} \tag{2.9}$$

The effective viscosity, ν_{eff}, is the sum of the molecular and turbulent contributions, such that

$$\nu_{\text{eff}}=\nu+\nu_t \tag{2.10}$$

and the effective Prandtl number, Pr_{eff}, is related to the molecular and turbulent values by

$$\left(\frac{\nu}{\text{Pr}}\right)_{\text{eff}}=\frac{\nu}{\text{Pr}}+\frac{\nu_t}{\text{Pr}_t} \tag{2.11}$$

For the results presented below, the turbulent Prandtl number, Pr_t, is taken to be constant with a value of 0.9. For laminar flow, the eddy viscosity, ν_t, is zero; the formulation for turbulent flow is given in Section 3.

If disk-surface temperatures, T_w, are prescribed, the appropriate boundary conditions to be satisfied are

$$\left.\begin{aligned} &z=0:\ u=w=0,\ v_\phi=\Omega r,\ T=T_w(r)\\ &z\to\infty:\ u=0,\ \partial v_\phi/\partial z=0,\ \partial T/\partial z=0\end{aligned}\right\} \tag{2.12}$$

In general, the pressure gradient in equation (2.2) is unknown but can be determined by considering the flow outside the boundary layer (in the "inviscid core," where values are denoted by overbars). In the limit as $z\to\infty$ and $\bar{u}$ and $\partial\bar{u}/\partial z$ are negligible, equation (2.2) reduces to

$$\frac{1}{\rho}\frac{dp}{dr}=\frac{\bar{v}_\phi^2}{r} \tag{2.13}$$

In the source region, free-vortex flow is assumed to occur such that

$$\frac{\bar{v}_\phi}{\Omega r}=cx^{-2} \tag{2.14}$$

Nomenclature

a = inner radius of cavity
$A+$ = Van Driest's damping constant
b = outer radius of cavity
c = swirl fraction
C_p = specific heat at constant pressure
C_w = mass flow parameter $\equiv Q/\nu b$
Ec = Eckert number $\equiv \Omega^2r^2/C_p(T_w-T_I)$
f = nondimensional stream function $\equiv \psi/r^2\rho_I(\nu_I\Omega)^{1/2}$
f' = nondimensional radial component of velocity $\equiv u/\Omega r$
g' = nondimensional tangential component of velocity $\equiv v_\phi/\Omega r$
h = total enthalpy
k = thermal conductivity
l = mixing length
n = exponent
Nu = local Nusselt number $\equiv rq_w/k_I(T_w-T_I)$
p = static pressure
p^* = nondimensional static pressure $\equiv p/\rho_I\Omega^2r^2$
Pr = Prandtl number $\equiv \mu C_p/k$
q = heat flux
Q = volumetric flow rate
Q_l = local volumetric flow rate
r = radial distance
Re_ϕ = rotational Reynolds number $\equiv \Omega b^2/\nu$
s = axial distance between disks
T = temperature
(u, v_ϕ, w) = time-averaged velocity components relative to stationary (r, ϕ, z) coordinate system
u_τ = friction velocity $\equiv (\tau_w/\rho)^{1/2}$
v_{rel} = resultant velocity relative to disk
x = nondimensional radius $\equiv r/b$
z = axial distance
z^+ = nondimensional axial distance $\equiv z(\tau_w\rho)^{1/2}N/\mu$
δ = boundary-layer thickness
η = transformed z coordinate
θ = nondimensional total enthalpy ratio $\equiv (h-h_I)/(h_w-h_I)$
κ = mixing-length constant
μ = dynamic viscosity
ν = kinematic viscosity $\equiv \mu/\rho$
ν_t^+ = nondimensional eddy viscosity $\equiv \nu_t/\nu$
ρ = density
τ = resultant shear stress $\equiv (\tau_r^2+\tau_\phi^2)^{1/2}$
τ_r, τ_ϕ = radial and tangential shear-stress components
τ^+ = nondimensional resultant shear stress $\equiv \tau/\tau_w$
ϕ = angular coordinate
ψ = stream function
Ω = angular velocity of the cavity

Subscripts

eff = effective value
i = inner region of boundary layer
I = value at inlet of cavity
o = outer region of boundary layer
t = turbulent value
w = value at disk surface

where $x = r/b$ and c is related to the initial swirl of the fluid entering the cavity. In the present case, the flow is assumed to enter without swirl ($c = 0$) so that the pressure gradient is zero in the source region; this is referred to below as the "free-disk case."

Outside the source region, where nonentraining Ekman-type layers are formed on the disks, the local volumetric flow rate, Q_l, in each layer is half the total superimposed flow rate, Q, entering the cavity, such that

$$Q_l = \frac{1}{2} Q = 2\pi r \int_0^\infty u dz \tag{2.15}$$

This, therefore, provides the additional condition from which the pressure gradient can be determined outside the source region. Three different methods were used to determine the pressure gradient (see Ong, 1988); for the results presented below, the so-called Mechul-function method was used.

3 Eddy-Viscosity Model

The eddy-viscosity model, which was previously demonstrated by Ong and Owen (1989) to be effective in the prediction of the incompressible flow in a rotating cavity, has been adapted to allow the calculations of compressible flow. For the flow considered here, this model can be used provided that local values of density and viscosity are substituted in the formulation, since it may be assumed that the turbulence processes are little affected by density fluctuations. The basic model follows that proposed by Cebeci and Smith (1974) in which the boundary layer is assumed to comprise an inner and outer region, denoted here by the subscripts i and o, respectively.

For the inner region, close to the disk surface, ν_t is based on Prandtl's mixing-length hypothesis. Using the resultant velocity gradient, $\nu_{t,i}$, is given by

$$\nu_{t,i} = l^2 \left[\left(\frac{\partial u}{\partial z} \right)^2 + \left(\frac{\partial v_\phi}{\partial z} \right)^2 \right]^{1/2} \qquad 0 \le z \le z_c \tag{3.1}$$

where z_c is the axial location at which $\nu_{t,i} = \nu_{t,o}$. The mixing length, l, is modified by Van Driest's damping factor, which is further extended following Koosinlin et al. (1974) such that

$$l = \kappa z \, [1 - \exp \{ -z^+ (\tau^+)^n / A^+ \}] \tag{3.2}$$

where $\kappa = 0.4$ and $A^+ = 26$. The nondimensional axial distance and local shear stress, z^+ and τ^+, respectively, are given by

$$z^+ = z(\tau_w \rho)^{1/2} N/\mu \text{ and } \tau^+ = \tau/\tau_w \tag{3.3}$$

where τ_w is the resultant wall shear stress and, following Cebeci and Smith, the effects of pressure gradient are accounted for by the parameter N, which is given by

$$N^2 = 1 - 11.8 \frac{\mu_w}{\mu_I} \left(\frac{\rho_I}{\rho_w} \right)^2 p^+ \tag{3.4}$$

$$p^+ = -\frac{\nu_I}{u_\tau^3} \frac{1}{\rho} \frac{\partial p}{\partial r} \tag{3.5}$$

In the above expression, u_τ is the friction velocity defined by

$$u_\tau = \left(\frac{\tau_w}{\rho} \right)^{1/2} \tag{3.6}$$

Here and in the subsequent discussion, the subscript I denotes values appropriate to the incoming air at the inlet of the cavity.

The effects of different values of the exponent $n = 0$, 0.5, and 1.5 in the damping factor in equation (3.2) have previously been reported by Ong and Owen. The value of $n = 0$ was found appropriate for fully turbulent conditions occurring at high values of Re_ϕ, and it is this value that is used here.

For the outer region of the boundary layer

$$\nu_{t,o} = 0.0168 \left| \int_0^\infty \{ v_{\mathrm{rel}} - (u^2 + v_{\mathrm{rel}}^2)^{1/2} \} \, dz \right| \quad z_c \le z \le \delta \tag{3.7}$$

where v_{rel} is the resultant velocity, relative to the disk, given by

$$v_{\mathrm{rel}} = \Omega r - (\bar{u}^2 + \bar{v}_\phi^2)^{1/2} \tag{3.8}$$

Klebanoff's intermittency factor (see Cebeci and Smith), used to account for the effect of the unsteady turbulent front at the edge of the boundary layer, appeared to have little influence on the wall shear stress, and for simplicity it was omitted from equation (3.7).

4 Numerical Solutions

4.1 Transformation of the Boundary-Layer Equations. For the numerical solution of equations (2.1)–(2.4), it is convenient to introduce a similarity variable η, which for compressible flow is defined by

$$\eta = \left(\frac{\Omega}{\nu_I} \right)^{1/2} \int_0^z \frac{\rho}{\rho_I} dz \tag{4.1}$$

and a nondimensional stream function $f(r, \eta)$ given by

$$f(r, \eta) = \psi(r, z)/r^2 \rho_I (\nu_I \Omega)^{1/2} \tag{4.2}$$

The stream function $\psi(r, z)$ is defined by

$$\rho u = \frac{1}{r} \frac{\partial \psi}{\partial z} \text{ and } \rho w = -\frac{1}{r} \frac{\partial \psi}{\partial r} \tag{4.3}$$

such that the continuity equation (2.1) is satisfied.

With the introduction of the following additional nondimensional quantities:

$$\left.\begin{aligned} g'(r, \eta) &= v_\phi/\Omega r \\ p^*(r) &= p/\rho_I \Omega^2 r^2 \\ \text{and} \\ \theta(r, \eta) &= (h - h_I)/(h_w - h_I) \end{aligned}\right\} \tag{4.4}$$

equations (2.2)–(2.4) can be expressed as

$$(\alpha f'')' + 2ff'' - (f')^2 + (g')^2 = r\left(f' \frac{\partial f'}{\partial r} - f'' \frac{\partial f}{\partial r} \right) + \beta \left(2p^* + r \frac{\partial p^*}{\partial r} \right) \tag{4.5}$$

$$(\alpha g'')' + 2fg'' - 2f'g' = r\left(f' \frac{\partial g'}{\partial r} - g'' \frac{\partial f}{\partial r} \right) \tag{4.6}$$

$$[\lambda \theta' + \gamma (f'f'' + g'g'')]' - \sigma f' \theta + 2f'\theta' = r\left(f' \frac{\partial \theta}{\partial r} - \theta' \frac{\partial f'}{\partial r} \right) \tag{4.7}$$

where

$$\left.\begin{aligned} \alpha &= \zeta(1 + \nu_t^+) \\ \beta &= \frac{\rho_I}{\rho} \\ \gamma &= \frac{\zeta \Omega^2 r^2}{h_w - h_I} \left[1 - \frac{1}{\mathrm{Pr}} + \nu_t^+ \left(1 - \frac{1}{\mathrm{Pr}_t} \right) \right] \\ \lambda &= \frac{\zeta}{\mathrm{Pr}} \left(1 + \frac{\mathrm{Pr}}{\mathrm{Pr}_t} \nu_t^+ \right) \\ \sigma &= \frac{r}{h_w - h_I} \frac{d}{dr} (h_w - h_I) \end{aligned}\right\} \tag{4.8}$$

$$\left.\begin{aligned} \zeta &= \frac{\mu \rho}{\mu_I \rho_I} \\ \nu_t^+ &= \frac{\nu_t}{\nu} \end{aligned}\right\} \tag{4.9}$$

Here, the primes indicate differentiation with respect to η. Note that when β and ζ are unity, equations (4.5)–(4.7) reduce to the constant-property form.

In terms of the transformed variables, the appropriate boundary conditions, corresponding to equations (2.12) and (2.15), become

$$\eta=0:\quad f=f'=g=0,\qquad g'=1,\quad \theta=1$$

$$\eta\to\infty:\ f'=g''=\theta'=0,\quad f(r,\infty)\ =\frac{1}{4\pi}\,C_w\mathrm{Re}_\phi^{-1/2}\,x^{-2} \tag{4.10}$$

where x is the nondimensional radius, C_w is the nondimensional flow rate, and Re_ϕ is the rotational Reynolds number.

4.2 Solution of the Equations. The momentum and energy equations (4.5)–(4.7) were supplemented by the axial momentum equation, $(p^*(r,\eta))' = 0$. (The latter equation was required since the Mechul-function method treats p^* in equation (4.5) as a function of r and η.) These equations were transformed to a system of nine first-order equations, and the complete system was then discretized by use of the semi-implicit Keller-box scheme.

For the constant-property case, the seven momentum and the two energy equations were uncoupled, and the solution procedure was sequential. First the momentum equations were solved for values of the velocity components, then the linear energy equation was solved. For the variable-property case, the direct coupling of the momentum equations and the (now) nonlinear energy equation required that all nine equations be solved simultaneously. For either case, solution of the system of equations was obtained by Newton's method.

The computation was started at the inlet radius, $r = a$, with initial conditions for the dependent variables provided by the laminar local-similarity approximations to the governing equations. (For the laminar free-disk case, the similarity solution is, in fact, the exact solution.) For turbulent flow calculations, fully turbulent conditions were assumed to prevail for $r > a$.

The variable-property computations required increased storage and CPU time due to the handling of larger matrices and to the slower rate of convergence caused by the increased nonlinearity. With these complications in mind, the reverse-flow region that occurs in the Ekman-type layers was ignored (see Ong and Owen, 1989); this was accomplished by setting any negative radial component of velocity to zero. The resulting solutions, while suffering some loss of accuracy near the edge of the boundary layer, yielded good approximations near the disk. In particular, the shear stresses and heat fluxes could be calculated accurately enough for all practical purposes.

Using the above method, computations presented in this paper were performed with a geometrically increasing grid system in the axial direction. This gave a fine mesh near the wall, where gradients were large, and a coarse mesh near the outer part of the boundary layer. However, in order to reduce the errors incurred by the removal of the reverse-flow region, it was necessary to maintain some control on the size of the grid spacing near the outside of the boundary layer. A satisfactory compromise between accuracy at the wall and at the edge of the layer was achieved by setting the first nondimensional grid spacing to 0.02 and the expansion factor to 1.05. This produced typically 150 to 200 axial nodes in the computation domain; for incompressible flow, fewer nodes were required to achieve acceptable accuracy. A distribution of approximately 110 nodes in the radial direction was found satisfactory for most cases. With this grid resolution, typical run times were less than 12 minutes on a VAX 8530.

The evaluation of the variable fluid properties could, very occasionally, result in instabilities; these were controlled by further grid refinement in both the radial and axial directions. The fluid properties used at each iteration were based on pressures and temperatures calculated in the preceding iteration. The density was calculated using the perfect gas law (that is, $\rho = \rho_I\, pT_I/p_I T$). The dynamic viscosity μ was computed from Sutherland's formula for air ($\mu = 1.46 \times 10^{-6}\, T^{3/2}/(110 + T)$ kg/m s) where T is the absolute temperature (Kelvin) computed from the total-enthalpy ratio, θ. The specific heat of air at constant pressure, C_p, was assumed to be constant and equal to 1005 J/kg K.

Further details of the numerical method are given by Ong (1988).

5 Testing the Boundary-Layer Method

Before making comparisons with experimental data, it is useful to see how the boundary-layer solutions compare with other theoretical work, for both laminar and turbulent flow, and to examine the effects of variable properties and viscous dissipation on the computed Nusselt numbers.

5.1 Incompressible Laminar Flow. Chew (1982) used an elliptic solver to obtain numerical solutions of the Navier–Stokes equations and the energy equation, neglecting dissipation, for laminar flow and heat transfer in a rotating cavity with a radial outflow of fluid. He also obtained analytical solutions for the Ekman layers and used Dorfman's (1963) solution for the free-disk flow that occurs in the boundary layers in the source region.

For convenience, a "power-law" temperature profile is assumed for which

$$T_w - T_I \propto x^n \tag{5.1}$$

where the subscripts w and I refer to conditions on the surface of the disk and in the fluid at inlet to the system, and n is a constant. Chew's Ekman-layer solution for a rotating cavity of radius b and axial width s is

$$\mathrm{Nu}=\frac{n}{4\pi x}\,\mathrm{Pr}C_w\left\{1-\frac{3}{16\pi}\,(n-2)\,\frac{\mathrm{Pr}C_w}{x^2\mathrm{Re}_\phi^{1/2}}\right\}-\frac{n^2 s}{2xb} \tag{5.2}$$

Figure 2 shows the radial variation of Nu for $C_w = 79$, $\mathrm{Re}_\phi = 2.5 \times 10^4$, $s/b = 0.267$, $a/b = 0.1$, Pr = 0.72, and $n = 1$, 2, and 3. Except near $x = 0.1$, 0.3, and 1, the boundary-layer solutions are in reasonable agreement with the numerical solutions of the elliptic equations. The boundary-layer approximations are invalid at the inlet ($x = 0.1$) and at the outlet ($x = 1$); and the differences near $x = 0.3$ are associated with the "switch" from an entraining to a nonentraining layer that occurs, in the boundary-layer model, at the edge of the source region.

In the source region ($0.1 < x < 0.3$), the elliptic and boundary-layer solutions are in good agreement with Dorfman's free-disk solution. Outside the source region ($0.3 < x < 1$), there is good agreement between the elliptic, boundary-layer and Ekman-layer (equation (5.2)) solutions; as x increases, the flow becomes more like an Ekman-layer flow. It can also be seen that the distribution of surface temperature on the disk has a significant effect on the magnitude of the Nusselt number, particularly in the Ekman-type layers.

5.2 Turbulent Flow. Figure 3 shows the effects of dissipation and of variable properties on the radial variation of Nu, for turbulent flow with Pr = 1, $C_w = 1.4 \times 10^4$, and $\mathrm{Re}_\phi = 3 \times 10^6$ for three different distributions of temperature. The variable-property case used the perfect gas law for the density and Sutherland's formula for the viscosity (see Section 4); the constant-property case used constant values for these quantities. While the effect of the variation of properties is very small, that of dissipation can be significant. The importance of the dissipation term depends on the Eckert number, Ec, and the largest value (Ec = 0.9) occurs for curves 3 at $x = 1$ where dissipation has its greatest effect.

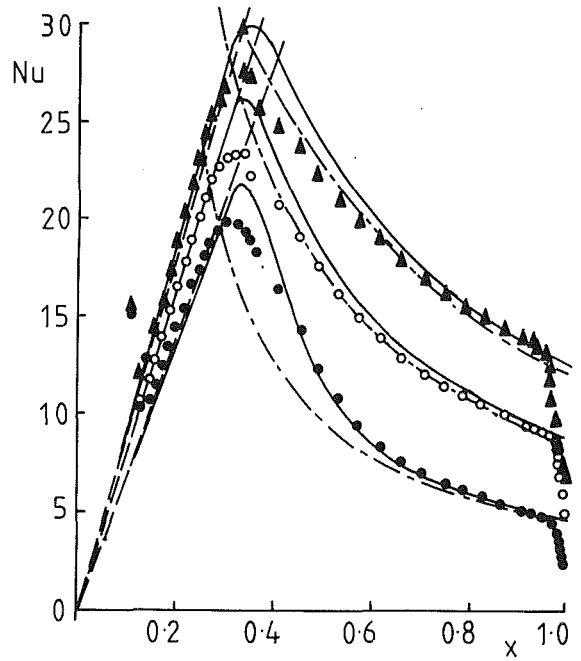

Fig. 2 Effect of temperature distribution ($T_w - T_I \propto x^n$) on the computed radial variation of local Nusselt number: $C_w = 79$, $Re_\phi = 2.5 \times 10^4$, Pr = 0.72.

n	1	2	3
Chew's (1982) computations	●	○	▲
Free-disk solution	— —		
Equation (5.2)	— —		
Current boundary-layer solutions	———		

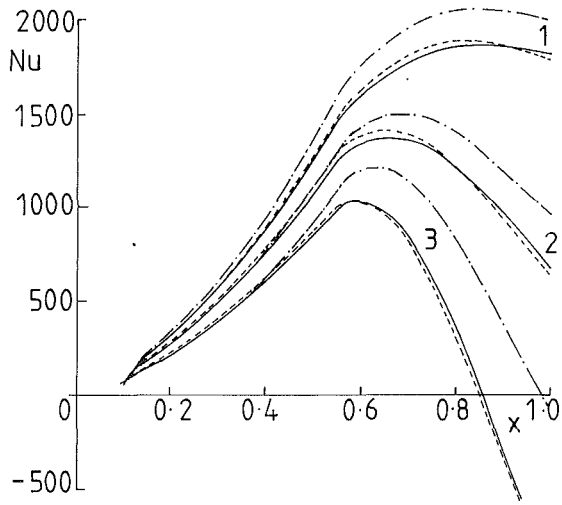

Fig. 3 Effects of dissipation and of variable properties on the computed radial variation of the local Nusselt number: $C_w = 1.4 \times 10^4$, $Re_\phi = 3 \times 10^6$, Pr = 1; curves: (1) $T_w - T_I = 70\ x^2$ °C; (2) $T_w - T_I = 45$°C; (3) $T_w - T_I = 14x^{-1}$°C; ------ variable property, dissipation included; —·— variable property, dissipation neglected; ___ constant property, dissipation included

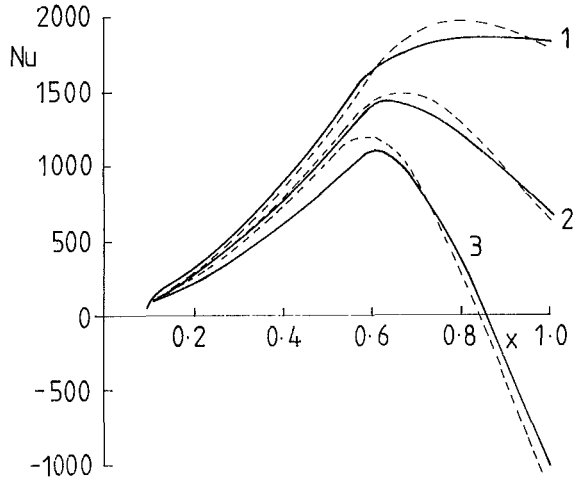

Fig. 4 Comparison between computed local Nusselt numbers: $C_w = 1.4 \times 10^4$, $Re_\phi = 3 \times 10^6$, Pr = 1; curves: (1) $T_w - T_I = 70\ x^2$ °C; (2) $T_w - T_I = 45$°C; (3) $T_w - T_I = 14x^{-1}$ °C; ___ current boundary-layer solutions; ------ integral solutions (Chew and Rogers, 1988)

It is interesting to note that for curves 3 in Fig. 3, Nu becomes negative at the larger values of x. Under these conditions, the temperature of the disk decreases with x at a faster rate than that of the adjacent fluid: Heat flows from the fluid into the disk despite the fact that $T_w > T_I$. Dissipation exacerbates this effect.

Figure 4 shows a comparison between solutions of the boundary-layer equations and the integral equations for the conditions considered above. The integral equations were solved by Chew and Rogers (1988) whose used 1/7th power-law profiles and Blasius relationships for the shear stresses on the disk. Their computed values for the local Nusselt numbers were in good agreement with the data of Northrop and Owen (1988) (whose work is discussed below). It can be seen from Fig. 4 that, apart from differences between the two solutions in the entraining layers inside the source region ($0.1 < x < 0.6$), the two sets of Nusselt numbers agree reasonably well.

6 Comparison With Experimental Data

For this comparison, the experimental data of Northrop and Owen (1988) were chosen. The measurements were made on a rotating-cavity rig with an outer radius of $b = 428$ mm and an axial spacing of $s = 59$ mm. Air entered the cavity through a central hole, of radius $a = 42.8$ mm, in one of the disks (the "upstream disk"), and left through a series of holes in the peripheral shroud. The disks of the cavity were heated by built-in electric heaters, and thermocouples and fluxmeters were used to determine the temperatures and heat fluxes on the disk surfaces. Local Nusselt numbers were presented for $1400 \le C_w \le 14{,}000$ and $6.08 \times 10^5 \le Re_\phi \le 3.29 \times 10^6$.

Various temperature distributions could be generated on the disks, and three typical distributions are shown in Fig. 5. These are referred to below as "T_w increasing" (with radius), "T_w

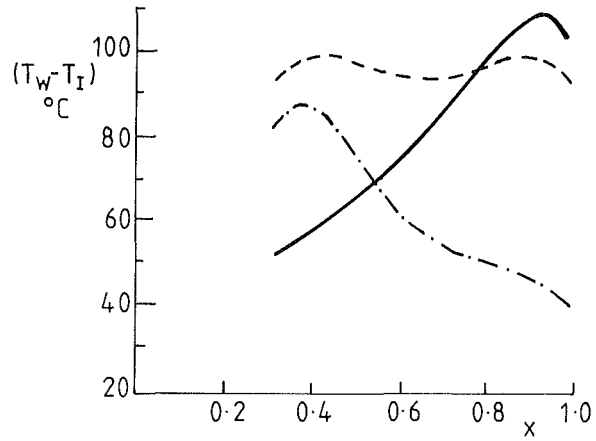

Fig. 5 Typical disk-temperature distributions used by Northrop and Owen (1988): $C_w = 7 \times 10^3$, $Re_\phi = 2 \times 10^6$, Pr = 0.71; ___ T_w increasing with radius; ------ T_w approximately constant; —·— T_w decreasing with radius

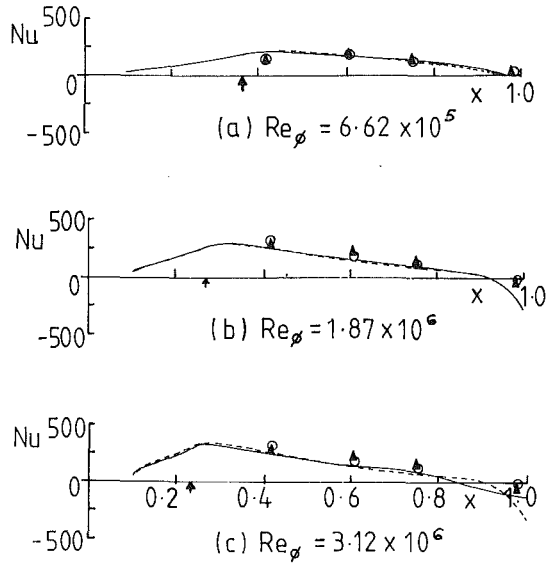

Fig. 6 Effect of Re_ϕ on the radial variation of the local Nusselt numbers: $C_w = 1.4 \times 10^3$, Pr = 0.71, T_w increasing; ↑ denotes edge of source region

	Downstream disk	Upstream disk
Data of Northrop and Owen (1988)	○	▲
Boundary-layer solutions	———	------

constant," and "T_w decreasing," and broadly similar distributions were produced on both disks.

For the computations discussed below, the measured disk temperatures were fitted by a cubic-spline smoothing curve, which was used to provide the thermal boundary conditions for the boundary-layer equations. As measurements were not made for $x < 0.2$, and computations were started at $x = 0.1$, a quadratic extrapolation curve was fitted to the cubic spline for $0 < x < 0.2$. Other extrapolation procedures were also tested, and it was found that the solutions became independent of the starting values for $x > 0.15$. For these computations, the Prandtl number was taken to be Pr = 0.71.

Figure 6 shows the effect of Re_ϕ on the radial variation of the local Nusselt numbers for $C_w = 1400$ with T_w increasing. Computed and measured Nusselt numbers for both the upstream and downstream disks are presented. Although the assumption of flow symmetry should make the computed values identical, the differences evident are attributable to small variations in the temperatures produced on the disk surfaces.

The agreement between the numerical solutions and the experimental measurements shown in Fig. 6 is generally good except near $x = 1$ at the higher values of Re_ϕ where negative values of Nu occur. (Negative Nusselt numbers occur when heat flows from the "cooling" air into the disk even though $T_w > T_I$.) The maximum value of Nu occurs near the edge of the source region (the computed position of which is indicated on the figure). In the entraining boundary layers inside the source region, Nu increases as x increases; in the nonentraining Ekman-type layers, the core temperature increases and Nu consequently decreases as x increases.

Figures 7, 8, and 9 show the effect of Re_ϕ on the radial variation of Nu for $C_w = 7000$ with T_w increasing, constant, and decreasing, respectively. From these three figures, it can be seen that the boundary-layer solutions predict, with good accuracy, the effects of Re_ϕ and of temperature distribution on the radial variation of Nu.

Figure 10 shows the results for $C_w = 14{,}000$ with T_w increasing. The agreement between the boundary-layer solutions

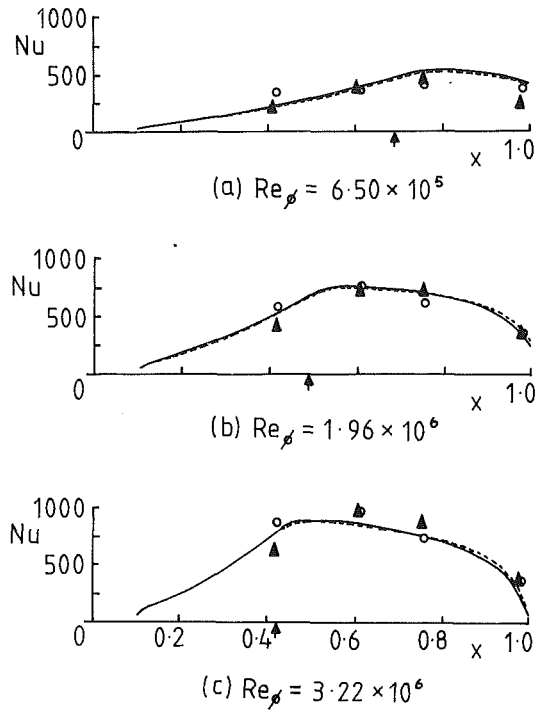

Fig. 7 Effect of Re_ϕ on the radial variation of the local Nusselt numbers: $C_w = 7 \times 10^3$, Pr = 0.71, T_w increasing; ↑ denotes edge of source region

	Downstream disk	Upstream disk
Data of Northrop and Owen (1988)	○	▲
Boundary-layer solutions	———	------

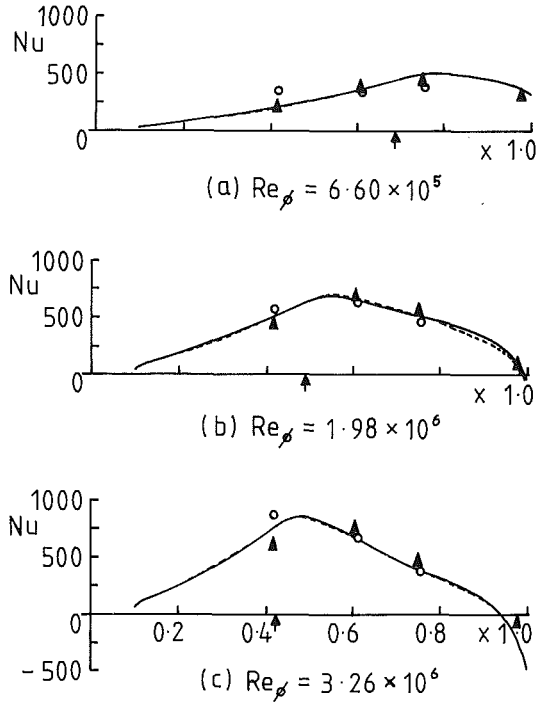

Fig. 8 Effect of Re_ϕ on the radial variation of the local Nusselt numbers: $C_w = 7 \times 10^3$, Pr = 0.71, T_w constant; ↑ denotes edge of source region

	Downstream disk	Upstream disk
Data of Northrop and Owen (1988)	○	▲
Boundary-layer solutions	———	------

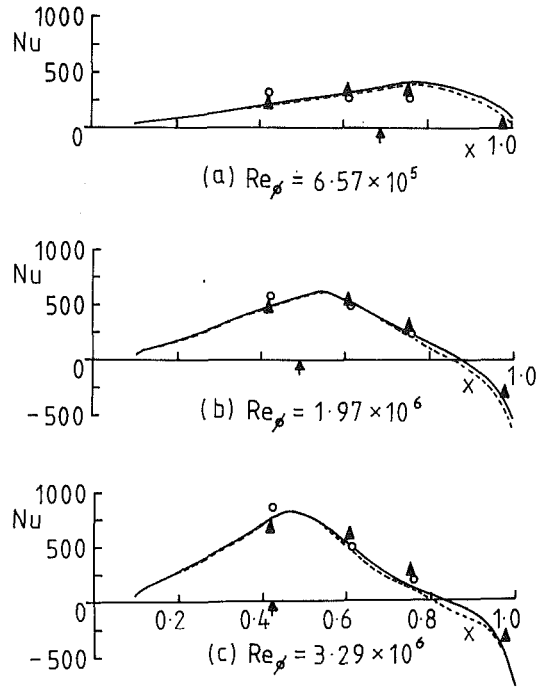

Fig. 9 Effect of Re_ϕ on the radial variation of the local Nusselt numbers: $C_w = 7 \times 10^3$, Pr = 0.71, T_w decreasing; ↑ denotes edge of source region

	Downstream disk	Upstream disk
Data of Northrop and Owen (1988)	○	▲
Boundary-layer solutions	———	------

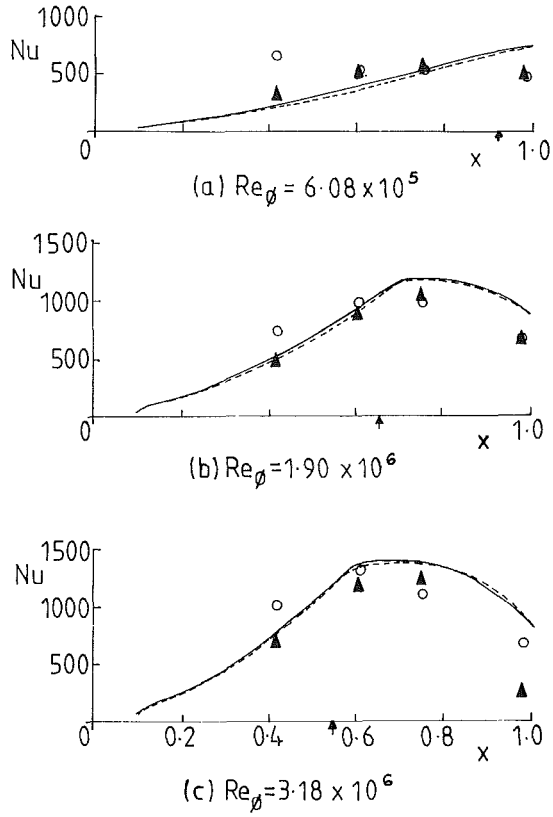

Fig. 10 Effect of Re_ϕ on the radial variation of the local Nusselt numbers: $C_w = 1.4 \times 10^4$, Pr = 0.71, T_w increasing; ↑ denotes edge of source region

	Downstream disk	Upstream disk
Data of Northrop and Owen (1988)	○	▲
Boundary-layer solutions	———	------

and the experimental data is not as good as for the lower values of C_w. In practice, for high flow rates, the cooling air impinges on the downstream disk and flows outward in a wall jet. The resulting increase in the heat transfer rates near the center of the downstream disk cannot be predicted by the boundary-layer equations. For the upstream disk, the boundary-layer solutions are in good agreement with the measured Nusselt numbers except near the outer part of the cavity. Comparing Fig. 10 with Fig. 6 shows that C_w has a significant effect on the magnitude of the Nusselt numbers.

Comparison between the numerical solutions and the measured data for a wide range of conditions produced satisfactory results provided that the source region did not fill the entire cavity. For high flow rates and low rotational speeds, where the source region was large enough to ensure that Ekman-type layers never formed, the predicted values of Nu were significantly smaller than the measurements. Under the conditions that occur inside gas turbine rotors, the source region is unlikely to be too extensive, and the boundary-layer solutions should be sufficiently accurate for practical purposes.

7 Conclusions

The boundary-layer method used by Ong and Owen (1989) to compute the incompressible flow of fluid in a rotating cavity with a radial outflow has been extended to the case of heat transfer in compressible flow. For turbulent flow, the Cebeci and Smith (1974) eddy-viscosity model was modified, and a turbulent Prandtl number of $Pr_t = 0.9$ was used in the energy equation. For simplicity, the reverse-flow region was disregarded in the Ekman-type layers.

The computed local Nusselt numbers were in satisfactory agreement with Chew's (1982) solutions of the laminar elliptic equations and with the Chew and Rogers (1988) solutions of the turbulent integral equations. For the range of temperatures and flows considered, property variation had a negligible influence on the computed Nusselt numbers. However, for turbulent flow at large Eckert numbers, viscous dissipation could have a significant effect on the Nusselt numbers.

The computed Nusselt numbers were also compared with measurements made by Northrop and Owen (1988) for an air-cooled rotating cavity. For $1400 \le C_w \le 7000$ and $6.50 \times 10^5 \le Re_\phi \le 3.29 \times 10^6$, the agreement between the measured and computed Nusselt numbers was mainly good. In the source region, the measured and computed Nusselt numbers increased in magnitude with increasing radius; in the Ekman-type layers outside the source region, the Nusselt numbers decreased with increasing radius. For the case where the temperature of the disk decreased radially, negative Nusselt numbers could occur near the outer edge of the disk.

For C_w = 14,000, the boundary-layer solutions underestimated the increase in heat transfer caused by the impingement of cooling air near the center of the downstream disk. Also, for conditions in which flow rates were high enough for the source region to fill the entire cavity, the computed Nusselt numbers tended to underestimate the measured values. However, in gas turbine engines, where the source region is unlikely to be extensive, the boundary-layer equations should provide solutions of sufficient accuracy for design purposes.

Acknowledgments

We should like to thank the Science and Engineering Research Council, Rolls Royce plc, and Ruston Gas Turbines Ltd. for supporting the research discussed in this paper.

References

Cebeci, T., and Smith, A. M. O., 1974, *Analysis of Turbulent Boundary Layers*, Academic Press, New York.

Chew, J. W., 1982, "Computation of Flow and Heat Transfer in Rotating Cavities," D. Phil. Thesis, University of Sussex, United Kingdom.

Chew, J. W., and Rogers, R. H., 1988, "An Integral Method for the Calculation of Turbulent Forced Convection in a Rotating Cavity With Radial Outflow," *Int. J. Heat Fluid Flow*, Vol. 9, pp. 37–48.

Dorfman, L. A., 1963, *Hydrodynamic Resistance and the Heat Loss of Rotating Solids*, Oliver and Boyd, Edinburgh, United Kingdom.

Koosinlin, M. L., Launder, B. E., and Sharma, B. I., 1974, "Prediction of Momentum, Heat and Mass Transfer in Swirling Turbulent Boundary Layers," ASME *Journal of Heat Transfer*, Vol. 96, pp. 204–209.

Morse, A. P., 1988, "Numerical Prediction of Turbulent Flow in Rotating Cavities," ASME JOURNAL OF TURBOMACHINERY, Vol. 110, pp. 202–212.

Northrop, A., and Owen, J. M., 1988, "Heat Transfer Measurements in Rotating-Disc Systems. Part II: The Rotating Cavity With a Radial Outflow of Cooling Air," *Int. J. Heat Fluid Flow*, Vol. 9, pp. 27–36.

Ong, C. L., 1988, "Computation of Fluid Flow and Heat Transfer in Rotating-Disc Systems," D. Phil. Thesis, University of Sussex, United Kingdom.

Ong, C. L., and Owen, J. M., 1989, "Boundary-Layer Flows in Rotating Cavities," ASME JOURNAL OF TURBOMACHINERY, Vol. 111, pp. 341–348.

Owen, J. M., Pincombe, J. R., and Rogers, R. H., 1985, "Source-Sink Flow Inside a Rotating Cylindrical Cavity," *J. Fluid Mech.*, Vol. 155, pp. 233–265.

Pincombe, J. R., 1983, "Optical Measurements of the Flow Inside a Rotating Cylinder," D. Phil. Thesis, University of Sussex, United Kingdom.

Shirazi, S. A., and Truman, C. R., 1988, "Prediction of Turbulent Source Flow Between Corotating Disks With an Anisotropic Two-Equation Turbulence Model," ASME JOURNAL OF TURBOMACHINERY, Vol. 110, pp. 187–194.

Effect of Rib-Angle Orientation on Local Mass Transfer Distribution in a Three-Pass Rib-Roughened Channel

J. C. Han
Professor.
Mem. ASME

P. Zhang
Graduate Assistant.

Turbine Heat Transfer Laboratory,
Department of Mechanical Engineering,
Texas A&M University,
College Station, TX 77843

In this experimental investigation of the heat transfer characteristics of turbulent air flow in a three-pass square channel, the test section consisted of three straight square channels jointed by two 180 deg turns, modeling the internal cooling passages of gas turbine airfoils. Naphthalene-coated ribs were attached to the top and bottom walls of the naphthalene-coated, three-pass channel. The rib height-to-hydraulic diameter ratio was 0.063; the rib pitch-to-height ratio was 10; the rib angles were 90 and 60 deg. For α = 60 deg, both the crossed ribs (on two opposite walls of the cooling channel) and the parallel ribs (on two opposite walls of the cooling channel) were investigated. The combined effects of the two sharp 180 deg turns and the rib orientations on the distributions of the local mass transfer coefficient in the entire three-pass channel were determined. The rib angle, the rib orientation, and the sharp 180 deg turn significantly affect the local mass transfer distributions. The combined effects of these parameters can increase or decrease the mass transfer coefficients after the sharp 180 deg turns. The angled ribs, in general, provide higher mass transfer coefficients than the transverse ribs; the parallel ribs give higher mass transfer than the crossed ribs.

Introduction

For high thermal efficiency and high power density, the trend in advanced aeroengine design is toward high entry gas temperature (1400°–1500°C), far above the allowable metal temperature. Therefore, highly sophisticated cooling technologies such as film cooling, impingement cooling, and rib/pin augmented cooling are employed for blades and vanes of advanced gas turbine engines. This investigation focuses on the augmented heat transfer in turbine cooling passages with rib turbulators. Since heat is transferred from the pressure and suction surfaces, rib turbulators (turbulence promoters) are cast only on two opposite walls of the cooling passages (i.e., inner walls of the pressure and suction surface) to enhance heat transfer to the cooling air, as shown in Fig. 1. A typical cooling passage can be modeled as a straight or a multipass rectangular channel with two opposite rib-roughened walls. In a straight rib-roughened channel, the effects of the turbulators' configuration (such as rib height, spacing, and angle), the flow channel aspect ratio, and the flow Reynolds number on the distributions of the local heat transfer and pressure drop have been reported (Han, 1984, 1988; Han et al., 1985; Han and Park, 1988).

In a multipass rib-roughened channel, in addition to the rib turbulators and the flow channel aspect ratios, the effects of the sharp 180 deg turns on the distributions of the local heat

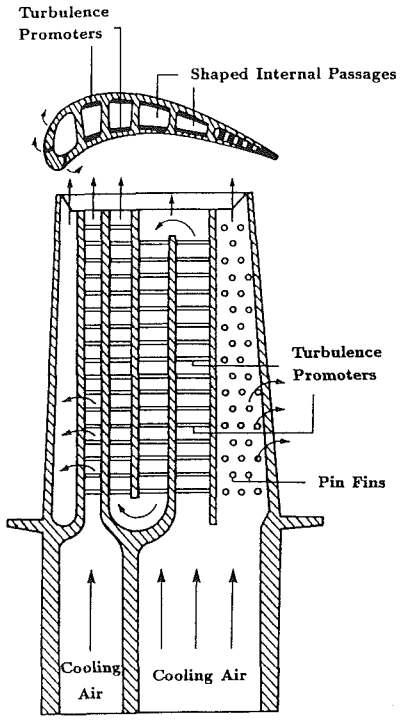

Fig. 1 Cooling concepts of a modern multipass turbine blade

Contributed by the International Gas Turbine Institute and presented at the 34th International Gas Turbine and Aeroengine Congress and Exhibition, Toronto, Ontario, Canada, June 4–8, 1989. Manuscript received at ASME Headquarters March 1989. Paper No. 89-GT-98.

transfer and pressure drop are important to the turbine cooling design. Boyle (1984) studied the effect of the sharp 180 deg turn on the local heat transfer coefficient in a two-pass square channel roughened by the transverse ribs. In two-pass smooth rectangular channels, Metzger and Sahm (1986) and Fan and Metzger (1987) studied the effect of the channel geometry (such as the before-turn and after-turn channel aspect ratios, and the turn clearance) on the regionally averaged heat transfer coefficient. With the naphthalene sublimation technique, the effect of the sharp 180 deg turn on the distributions of the local mass transfer coefficient around the turn region in a two-pass square channel roughened by the transverse ribs and by the angled ribs was presented by Han et al. (1988) and by Chandra et al. (1988).

After these studies of a two-pass square channel with rib turbulators by the naphthalene sublimation technique (Han et al., 1988; Chandra et al., 1988), some basic questions have been raised. The first question is whether the results from the two-pass channel can be applied for the three- or more pass channel. This is important because the cooling passages in the air-cooled turbine blades and vanes may have more than two passages, as shown in Fig. 1. The open literature contains no information on the distributions of the local heat transfer coefficient in such three-pass rectangular channels with rib turbulators. The other question is whether the mass transfer coefficients from the surfaces between the ribs will be affected by the thermal boundary condition of the ribs. In previous mass transfer studies, metallic ribs were turbulence promoters. Metallic ribs on mass transfer surfaces are equivalent to insulated ribs on heat transfer surfaces. It is important to clarify their effects on the surface mass transfer coefficients.

This investigation is a continuation of the work of Han et al. (1988) and Chandra et al. (1988). The differences between this and the previous investigation are as follows. The previous investigations were for a two-pass square channel with one sharp 180 deg turn; this investigation is for a three-pass square channel with two sharp 180 deg turns. The previous investigation focused on the turn region; this focuses on the entire three-pass channel. Metallic ribs were attached on the naphthalene-coated channel walls in the previous study; naphthalene-coated ribs are attached on the naphthalene-coated channel walls for this study. Two issues are emphasized in this study: (1) effects of the complicated interactions between the two sharp 180 deg turns and the rib orientations on the local mass transfer augmentation, and (2) comparison of the local mass transfer augmentation by the crossed ribs (on two opposite walls of the cooling channels) and by the parallel ribs (on two opposite walls of the cooling channels) in the previous studies.

In this experimental investigation of the heat transfer characteristics of turbulent air flow in a three-pass rib-roughened channel by the naphthalene sublimation technique, the test section consisted of three straight square channels jointed by two sharp 180 deg turns, modeling the internal cooling passages of gas turbine airfoils. Naphthalene-coated ribs were attached to the top and bottom walls of the naphthalene-coated, three-pass, horizontal channel. The flow Reynolds number was 30,000; the rib height-to-hydraulic diameter ratio was 0.063; the rib pitch-to-height ratio was 10; the rib angles were 90 and 60 deg. The previous studies (Han et al., 1985; Han and Park, 1988) indicated that 60 deg angled ribs give the highest heat transfer and the highest pressure drop penalty, whereas 45 deg angled ribs provide the optimum thermal performance for the same pumping power consumption. To maximize the highest heat transfer coefficients, 60 deg angled ribs were chosen for this study. For $\alpha = 60$ deg, three different rib orientations were studied: The ribs on two opposite walls were parallel toward the same left-hand-side direction (parallel ribs—left direction); the ribs on two opposite walls were parallel toward the same right-hand-side direction (parallel ribs—right direction); the ribs on two opposite walls were in the crossed direction (one toward the left-hand-side direction and the other toward the right-hand-side direction, crossed ribs). The combined effects of the two sharp 180 deg turns with the three different rib orientations on the distributions of the local mass transfer coefficient in the entire three-pass square channel were determined. The best rib orientation to produce the highest mass transfer coefficient was identified. Additional information on the present investigation may be found in a thesis by Zhang (1988).

Experimental Apparatus and Procedure

Apparatus. The test apparatus, an open air flow loop, consisted of the test section, a calibrated orifice flow meter, a gate valve, and a centrifugal fan. The test apparatus and the instrumentation were in an air-conditioned laboratory. Figure 2 is a schematic of the test section, a three-pass channel with a 1.27 cm (0.5 in.) square cross section. The top, bottom, and two side walls of the channel were made of 1.27 cm (0.5 in.) thick aluminum plates; the two divider walls were made of two 0.159 cm (0.0625 in.) thick aluminum plates bonded back-to-back with double-sided tape. The thickness of each of the two divider walls was 0.25 times the channel width (1.27 cm); the turn clearance of each of the two sharp 180 deg turns was equivalent to the channel width (1.27 cm); and the length of each of the three straight sections of the test channel was 12 times the channel width (1.27 cm). All the dimensions were

Nomenclature

D = channel width; also channel hydraulic diameter
$\overline{D}$ = diffusion coefficient, equation (5)
e = rib height
h_m = local mass transfer coefficient, equation (2)
$\dot{m}''$ = local mass transfer rate per unit area, equation (1)
Nu = Nusselt number
P = rib pitch
Pr = Prandtl number of air
P_W = naphthalene vapor pressure at the wall, equation (4)
Re = Reynolds number based on channel hydraulic diameter
Sc = Schmidt number for naphthalene
Sh = local Sherwood number, equation (5)
Sh_o = Sherwood number of fully developed turbulent tube flow
$\overline{\mathrm{Sh}}$ = average Sherwood number in each pass of the channel
$\overline{\overline{\mathrm{Sh}}}$ = average Sherwood number in the entire three-pass channel
Δt = duration of the test run, equation (1)
T_W = naphthalene wall temperature, equations (3) and (4)
X = axial distance from channel entrance
ΔZ = measured change of elevation at the measurement point
α = rib angle of attack
ν = kinematic viscosity of pure air
ρ_b = bulk naphthalene vapor density, equation (2)
ρ_s = density of solid naphthalene, equation (1)
ρ_w = local naphthalene vapor density at wall, equation (2)

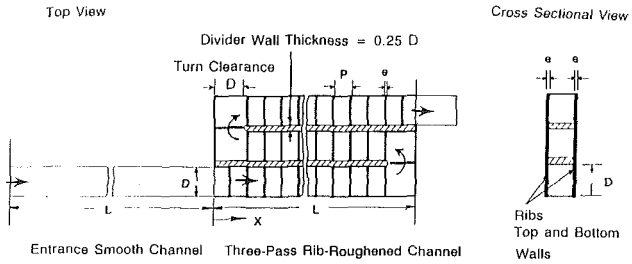

Fig. 2 Sketch of the test section

selected so that the test channel modeled the actual internal cooling passages of turbine airfoils. The test section was designed and constructed for rapid assembly and disassembly. The entire test assembly was secured with machine screws.

All the inside surfaces of the three straight sections of the test channel, and those at the 180 deg turn between them, were coated with naphthalene in a casting process against a highly polished, flat, stainless steel plate. For the roughened channel test, the brass ribs coated with naphthalene, with a 0.079 cm (0.0313 in.) square cross section, were glued on the naphthalene-coated, top and bottom surfaces of the three-pass channel. The naphthalene-coated ribs were also placed in the two-turn clearance regions.

A smooth square channel (with length 12 times the width) was attached to the entrance of the test section. This smooth entrance channel ensured a fully developed flow before entering the test section. The entire test section was oriented horizontally. During test runs, air was drawn through the test section from the naphthalene-free laboratory (by suction). On exiting the fan, the air was ducted to the outside of the building.

Separate experiments were conducted to determine the distributions of the local pressure drop in the similar three-pass square channel fabricated of plexiglass. The results of pressure loss distributions and friction factor correlations in the three-pass square channel and three-pass rectangular channels with rib turbulators are given by Zhang (1988) and Han and Zhang (1989).

Instrumentation. The instrumentation, procedure, and data reduction are similar to those of Han et al. (1988) and Chandra et al. (1988). The distributions of the local mass transferred away from the naphthalene surfaces before and after the test runs were determined by a programmable indexer (which can automatically control the stepping motor), a Starret electrical depth gage (with a resolution of 0.0000254 cm or 0.00001 in.), and a Texas Instrument personal computer (with an A to D board converter). The surfaces of the test section were measured in X–Y directions on a coordinate table. The gaging head was fixed to a stand mounted on the stationary base of the coordinate table and was hung over the naphthalene surface to be measured. To measure the elevation at a point on the naphthalene surface, the platform of the coordinate table was moved by the stepping motor so that the gaging head rested against the surface at the measurement point. The deflection of the tip of the gaging head was converted into an electrical signal (d-c voltage) by the amplifier. The signal was recorded on a Texas Instrument personal computer connected to the amplifier through an A/D converter.

Six 36-gage, copper-constantan thermocouples with a six-channel, digital temperature indicator recorded the temperature of the naphthalene surfaces during the test runs.

Procedure. After all the naphthalene plates (the top, bottom, two side walls, two divider walls, and two end walls) were prepared under a fume hood, they were sealed tightly in plastic bags to prevent natural sublimation of the naphthalene and left in the laboratory for 8–10 hours to attain thermal equilibrium. Before a test run, the surface contours of all the

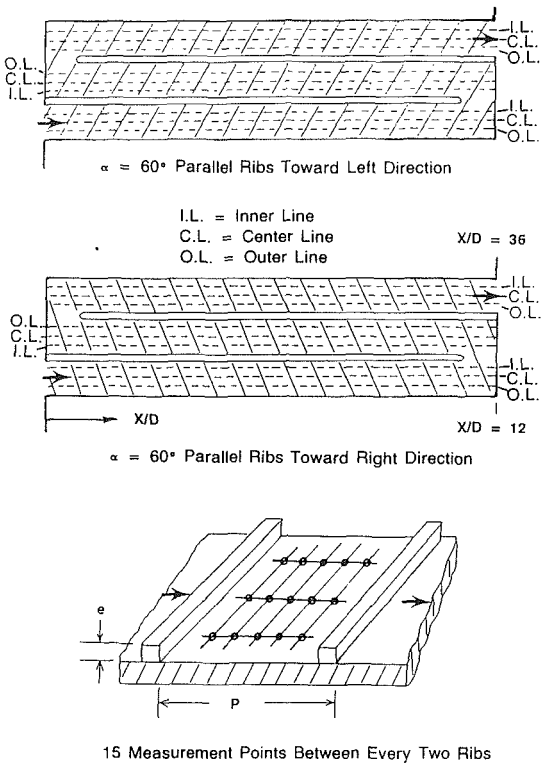

Fig. 3 Measurement points for typical ribbed channels

naphthalene plates placed on the coordinate table were measured and recorded. The measurements at the two solid metal edges of each naphthalene plate, the reference data, were required in order to get an equation for the plane of the plate. With reference to that plane equation, the elevations at various measurement points were calculated. The elevation measurement points for typical ribbed channel experiments are shown in Fig. 3 for $\alpha = 60$ deg parallel ribs toward the left and right direction. There are 15 measurement points between every two ribs (5 in the streamwise and 3 in the spanwise direction).

In a ribbed channel test run, brass ribs were glued to the appropriate naphthalene surfaces in a predetermined configuration. Before the test run, naphthalene in crystal form was heated above its melting point and then coated uniformly on the brass ribs with a fine brush. Separate tests were conducted to examine the uniformity of the naphthalene coating on the ribs. Samples of napthalene-coated ribs were prepared. The uniformity of typical naphthalene-coated ribs was determined by measuring rib height profiles at five discrete locations along the rib axes with a micrometer. The thickness of the coated layer on the ribs was about 0.01 cm. The maximum nonuniformity on the surface of the naphthalene-coated ribs was calculated as 6 percent.

The test section was then assembled and attached to the test rig. Air was drawn through the test section and a calibrated orifice flowmeter at the required Reynolds number for about 35 minutes. During the test run, the temperatures at the six stations on the naphthalene surfaces were recorded. After the test run, the contours of the naphthalene surfaces were measured and recorded again on the same measurement points. From the before-run and after-run surface contour measurements, the depth changes at various points were calculated. Note that these mass transfer measurements were performed on the surfaces between every two ribs, not including measurements on and around naphthalene-coated ribs (see Fig. 3). The coating was partially removed from the parts of the rib surfaces at the end of the test run. Five test runs were performed. The test conditions of the runs are given in Table 1.

Table 1 Test conditions for the present investigation

Case No.	Channel Condition	Rib Orientation	P/e	e/D
1	Smooth	None	0	0
2	α = 90°	Transverse Ribs	10	0.063
3	α = 60°	Parallel Ribs (Left Direction)	10	0.063
4	α = 60°	Parallel Ribs (Right Direction)	10	0.063
5	α = 60°	Crossed Ribs	10	0.063

Data Reduction

Local Sherwood Number. The local mass flux at any measurement point is calculated by the following equation:

$$\dot{m}'' = \rho_s \Delta Z/\Delta t \quad (1)$$

where ΔZ is the measured change of elevation at the measurement point and Δt is the duration of the test run.

The local mass transfer coefficient is defined as

$$h_m = \dot{m}''/(\rho_w - \rho_b) \quad (2)$$

where the bulk naphthalene vapor density is the cumulative mass transferred from the naphthalene surfaces to the airstream divided by the air volumetric flow rate. The local vapor density is determined by the perfect gas law and the vapor pressure-temperature relationship and the measured surface temperature (Sogin, 1958):

$$\rho_W = P_W/(R_V T_W) \quad (3)$$

$$\log_{10} P_W = A - B/T_W \quad (4)$$

where R_V, A, and B are given by Sogin (1958).

The local Sherwood number is defined as

$$\mathrm{Sh} = h_m D/\overline{D} = h_m D/(\nu/\mathrm{Sc}) \quad (5)$$

where the Schmidt number Sc is 2.5 for naphthalene (Sogin, 1958). Based on the heat and mass transfer analogy (Sogin, 1958), the local Sherwood number is converted to the corresponding local Nusselt number as

$$\mathrm{Nu} = (\mathrm{Pr}/\mathrm{Sc})^{0.4}\,\mathrm{Sh} \quad (6)$$

where the Prandtl number is 0.707 for air at room temperature.

The Nusselt number for fully developed turbulent tube flow correlated by McAdams (1954)

$$\mathrm{Nu}_o = 0.023\,\mathrm{Re}^{0.8}\,\mathrm{Pr}^{0.4} \quad (7)$$

was the reference for comparison. By combining equations (5), (6), and (7), the experimentally determined local Sherwood number is normalized by the Sherwood number for fully developed turbulent tube flow as follows:

$$\mathrm{Sh}/\mathrm{Sh}_o = (h_m D/\overline{D})/[0.023\,\mathrm{Re}^{0.8}\,\mathrm{Pr}^{0.4}\,(\mathrm{Sc}/\mathrm{Pr})^{0.4}] \quad (8)$$

Uncertainties in Data Reduction. Separate experiments were conducted to determine the mass losses from the various naphthalene surfaces by natural convection when the surface contours were measured and when the ribs were glued to the appropriate naphthalene surfaces. The total mass losses by natural convection were no more than 4 percent of the total mass transfer during the test run. The mass losses were subtracted from the mass transfer at the various measurement points in the local mass transfer coefficient calculations.

Since the surface contours were measured at discrete points along three axial lines on the naphthalene surfaces as shown in Fig. 3, errors were introduced into the calculations of the bulk naphthalene vapor densities (ρ_b) that were determined from the cumulative mass transferred into the airstream. The values of the bulk vapor density were small, with a maximum of about 10 percent at the end of the third straight section of the test channel, compared to those of the local naphthalene vapor density at the wall (ρ_w). Therefore, the maximum uncertainty in the calculation of ($\rho_w - \rho_b$) was estimated to be 6 percent. The uncertainty in the calculations of the density of solid naphthalene, ρ_s, the elevation measurement, ΔZ, and the duration of the test run, Δt, were estimated to be 1.5, 3, and 3 percent, respectively. The maximum uncertainty of the local Sherwood number was determined to be about 7 percent by the uncertainty estimation method of Kline and McClintock (1953).

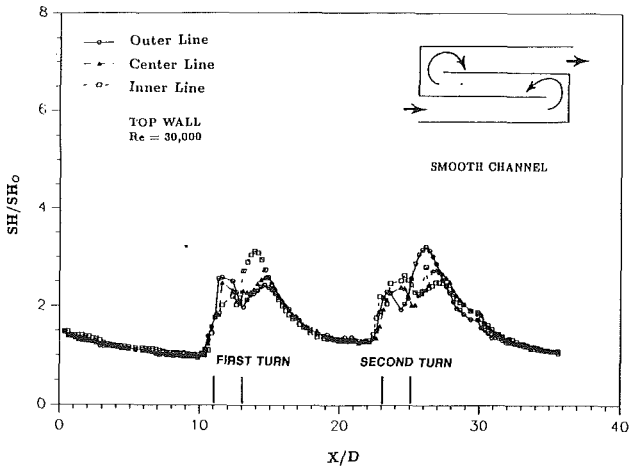

Fig. 4 Local Sherwood number ratio for a smooth channel (case 1)

Experimental Results and Discussion

Results for Smooth Channel. The local mass transfer results are presented as the axial distributions of a dimensionless Sherwood number ratio Sh/Sh$_o$, as given in equation (8). Typical results of the top-wall Sherwood number ratios for the smooth channel are shown in Fig. 4 for Re = 30,000 (case 1). Results of the side-wall and divider-wall Sherwood number ratios for the same smooth channel are from Zhang (1988). In the first pass (X/D = 0–11), the Sherwood number ratios along the inner line, the center line, and the outer line on the top wall decrease monotonically with increasing axial distance until the Sh/Sh$_o$ ratios reach a value of one at $X/D \simeq 10$.

Entering the first turn region (X/D = 11–13), the Sh/Sh$_o$ ratios increase rapidly because of the secondary flow effect of the sharp 180 deg turn. It is conjectured that the lower Sh/Sh$_o$ ratios at X/D = 12.5–13 are due to the flow separation at the tip of the divider wall. The high Sh/Sh$_o$ ratios along the inner line at X/D = 13.5 are due to the flow reattachment and the flow being pushed back toward the first divider wall after the turn; the peaks in the Sh/Sh$_o$ ratios along the outer line at X/D = 14.5 are caused by the flow being pushed back toward the second divider wall. After the first turn, the Sh/Sh$_o$ ratios in the second pass (X/D = 13–23) are higher than those in the first pass. The Sh/Sh$_o$ ratio distributions in the first two passes are similar to those of Han et al. (1988). The distributions of the local Sh/Sh$_o$ ratios in the second turn region (X/D = 23–25) and in the third pass (X/D = 25–36) show the same trend as those in the first turn region and the second pass, respectively. This implies that the mass transfer coefficients in the third pass after the second turn are reproducible from those in the second pass after the first turn.

Results for Ribbed Channel. The distributions of the ribbed-wall (top-wall) Sherwood number ratios along the three axial lines with α = 90 deg (P/e = 10, e/D = 0.063) are shown in Fig. 5 for Re = 30,000 (case 2). The center line Sherwood

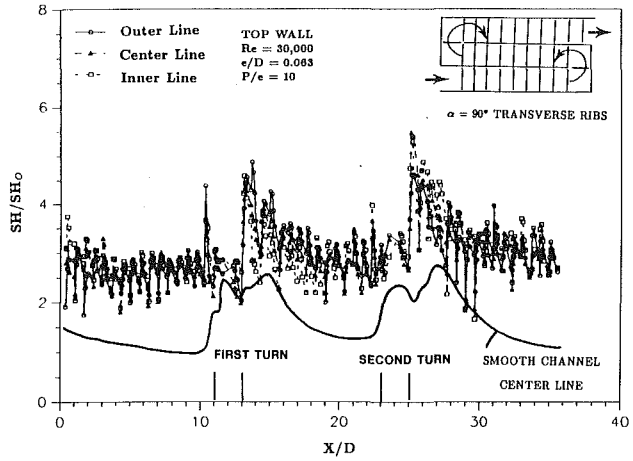

Fig. 5 Local Sherwood number ratio for a ribbed channel with α = 90 deg ribs (case 2)

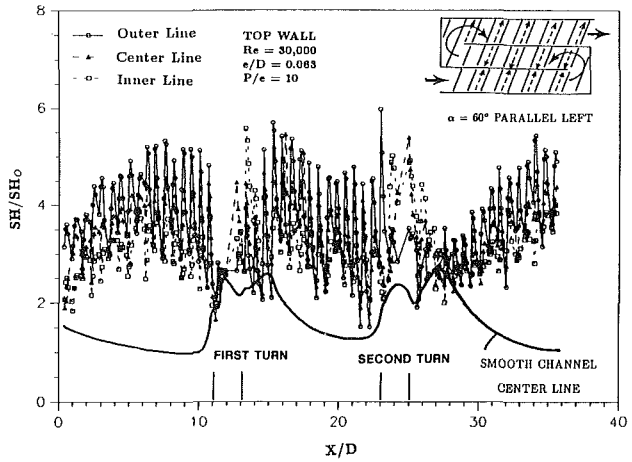

Fig. 6 Local Sherwood number ratio for a ribbed channel with α = 60 deg parallel ribs toward left direction (case 3)

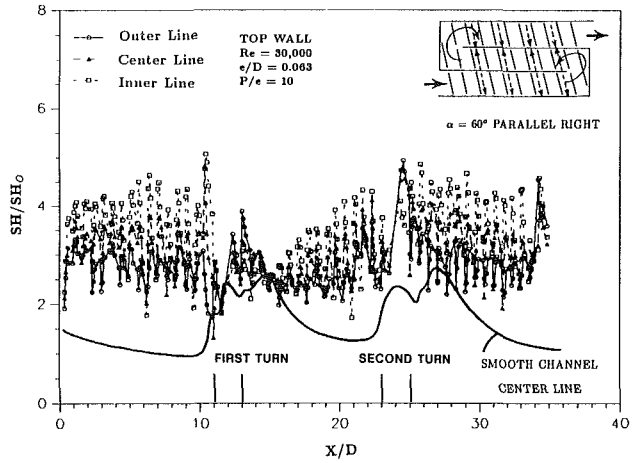

Fig. 7 Local Sherwood number ratio for a ribbed channel with α = 60 deg parallel ribs toward right direction (case 4)

number ratios in the case of the smooth channel for Re = 30,000 are included for comparison. Results of the side-wall and the divider-wall Sherwood number ratios for the same ribbed channel with α = 90 deg are given by Zhang (1988). In the first pass, the axial Sh/Sh$_o$ distributions on the top wall become a periodic pattern with a small spanwise variation. The Sh/Sh$_o$ ratios reach the maximum values at the points of flow reattachment, slightly upstream of the midpoints between adjacent ribs (i.e., $P/e \simeq 4$).

In the second pass, the top-wall Sh/Sh$_o$ distributions are generally higher than those in the first pass of the channel. There is an increase in the Sh/Sh$_o$ in the spanwise direction toward the outer line because of the flow turning effect. Farther downstream of the turn, the peak values between adjacent ribs in the Sh/Sh$_o$ ratios decrease gradually and the spanwise variation becomes smaller. The Sh/Sh$_o$ ratio distributions in the first two passes are similar to those reported by Chandra et al. (1988). The distributions of the local Sh/Sh$_o$ ratios in the third pass show the same trend as those in the second pass of the channel. This implies that the mass transfer coefficients in the third pass after the second turn are reproducible from those in the second pass after the first turn.

Effect of Rib Angle. The distributions of the ribbed-wall Sherwood number ratios along three axial lines with α = 60 deg parallel ribs toward the left-hand direction (P/e = 10, e/D = 0.063) are shown in Fig. 6 for Re = 30,000 (case 3). In the first pass, the magnitude of the variations of the ribbed-wall Sh/Sh$_o$ in the spanwise direction is comparable to those of the axial periodic Sh/Sh$_o$ distributions; the values of Sh/Sh$_o$ along the outer line are always higher than the corresponding values along the inner line. It is conjectured that these spanwise variations of Sh/Sh$_o$ are caused by the secondary flow (broken lines in the upper corner sketch of Fig. 6) along the rib axes (rib orientations) from the outer line toward the inner line. This secondary flow increases its strength from the entrance and produces the maximum Sh/Sh$_o$ at X/D = 7.

In the second pass, the spanwise Sh/Sh$_o$ ratios show the same trend as those in the first pass of the channel. Again, the higher Sh/Sh$_o$ ratios along the outer line are caused by the secondary flow along the rib axes from the outer line toward the inner line after the first 180 deg turn. In the third pass, however, the Sh/Sh$_o$ ratios immediately after the second 180 deg turn are much lower than those in the second pass of the channel. This may be caused by the conflicting interaction of the main flow (solid line in the upper corner sketch of Fig. 6), which is forced toward the second divider wall due to the turn, and the secondary flow (broken lines in the same sketch) along the rib axes toward the side wall. The Sh/Sh$_o$ ratios increase gradually when the flow is redeveloped at the end of the third pass. To eliminate the low Sh/Sh$_o$ ratios after the second 180 deg turn, the ribs in the third pass should be oriented in a different 60 deg orientation from those in the second pass of the channel. If the ribs in the third pass are rearranged in a different 60 deg orientation from those in the second pass, the mass transfer coefficients in the third pass should be reproducible from those in the second pass.

Effect of Rib Orientation. Figure 7 shows the results for α = 60 deg parallel ribs toward the right-hand direction (P/e = 10, e/D = 0.063) and Re = 30,000 (case 4). Both cases 3 and 4 are for α = 60 deg parallel ribs but in a different rib orientation. As shown in Fig. 7, the low Sh/Sh$_o$ ratios after the first 180 deg turn are observed. This may be caused by the conflicting interaction of the main flow, which is forced toward the inner line because of the turn, and the secondary flow along the rib axes toward the outer line (see upper corner sketch in Fig. 7). To prevent the low Sh/Sh$_o$ ratios after the first 180 deg turn, the ribs in the second pass should be oriented in a different 60 deg direction from those in the first pass of the channel. In the first pass, the Sh/Sh$_o$ ratios along the inner line are higher than those along the outer line because of the secondary flow along the rib axes toward the outer line. The results are the same in the third pass in which the secondary flow and the main flow turn toward the outer line, producing higher Sh/Sh$_o$ ratios along the inner line (square symbols in the third pass in Fig. 7).

In a comparison of Figs. 7 and 6, the Sh/Sh$_o$ ratios along the inner line are always higher than the corresponding values

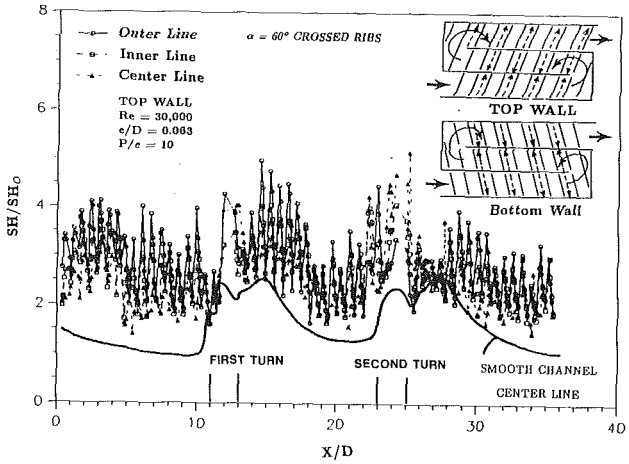

Fig. 8 Local Sherwood number ratio for a ribbed channel with α = 60 deg crossed ribs (case 5)

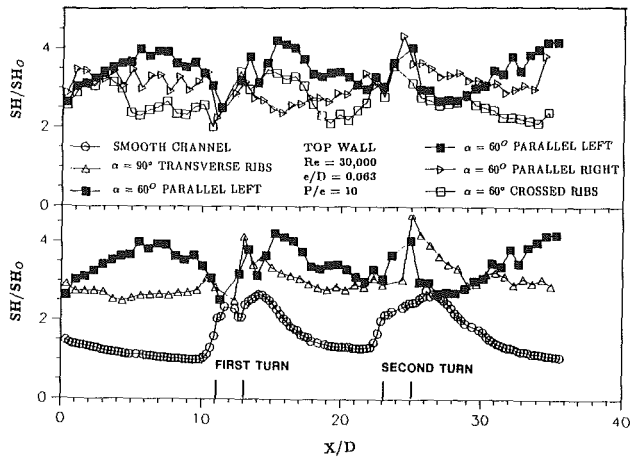

Fig. 9 Rib-pitch averaged Sherwood number ratio for all cases studied

along the outer line for case 4; the reverse is true for case 3 because of the different rib orientation. The rib orientations (and therefore the Sh/Sh$_o$ ratios) in the second pass and the third pass of case 4 are similar to those in the third pass and the second pass of case 3, respectively.

Effect of Crossed Ribs. Figure 8 shows the results for the top wall Sh/Sh$_o$ ratios with α = 60 deg parallel ribs toward the left direction (P/e = 10, e/D = 0.063) and Re = 30,000, but the ribs on the opposite (bottom) wall toward the right direction (crossed ribs, case 5). The top-wall Sh/Sh$_o$ ratios in Fig. 8 (crossed ribs case) are much lower than those in Fig. 6 (parallel ribs case). As shown in Fig. 8, the top-wall Sh/Sh$_o$ ratios are low in regions before the first turn and before and after the second turn. The lower Sh/Sh$_o$ ratios for the crossed rib orientation may be caused by the cancellation of the secondary flow generated by the rib axes from the top and bottom walls (see upper corner sketch in Fig. 8). The results shown in Fig. 8 are repeatable. The lower mass transfer coefficients obtained with crossed ribs as opposed to parallel ribs are similar to those reported by Metzger and Vedula (1987) in a straight triangular cross-sectional channel with a transient heat transfer method. It is conjectured that the flow pattern induced by the cross ribs contains a single cell of secondary flow whereas the parallel ribs generate a pair of counterrotating cells. For cooling design, the parallel ribs (between the top and bottom walls) are recommended instead of the crossed ribs. Details of Sherwood number ratio between ribs in the before-turn region of the first-pass channel (X/D) = 8.09-9.44) are tabulated in Table 2 for cases 2, 3, 4, and 5.

Table 2 Details of Sherwood number ratio between ribs in the before-turn region of the first-pass channel (X/D = 8.09 to 9.44, two rib spacings)

Case 2 α = 90° transverse ribs

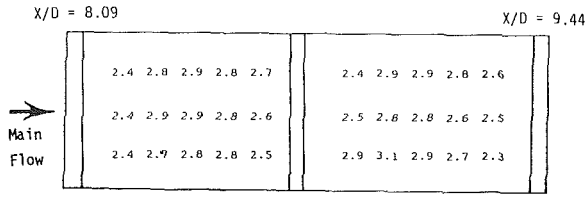

Case 3 α = 60° parallel ribs left direction

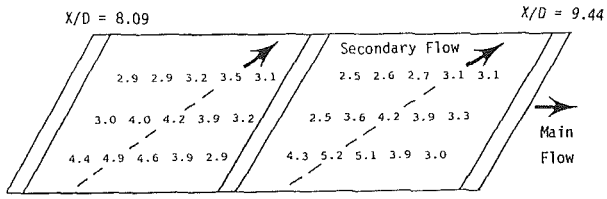

Case 4 α = 60° parallel ribs right direction

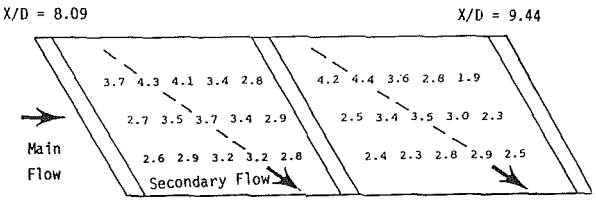

Case 5 α = 60° crossed-ribs

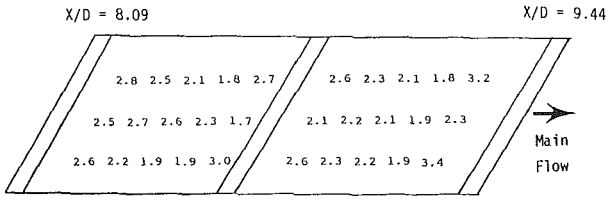

Pitch-Averaged Sherwood Number Ratios. To compare the mass transfer performance for the different rib orientation, the rib-pitch averaged Sherwood number ratios against the X/D ratio are given in Fig. 9 for Re = 30,000 and P/e = 10, e/D = 0.063. Every rib-pitch averaged Sherwood number ratio represents the average value of the 15 local Sh/Sh$_o$ ratios between every two ribs (five in the streamwise and three in the spanwise direction, as shown in Fig. 3). Figure 9 shows that in the first pass and the second pass of the channel, the Sh/Sh$_o$ ratios with α = 60 deg parallel ribs left direction (case 3) are higher than those with α = 60 deg parallel ribs right direction (case 4), with α = 60 deg crossed ribs (case 5), and with α = 90 deg transverse ribs (case 2), respectively. In the third pass of the channel, however, the Sh/Sh$_o$ ratios with α = 60 deg parallel ribs left direction (case 3) can be lower or higher than other cases of rib orientations. The Sh/Sh$_o$ ratios with α = 60 deg parallel ribs left direction (case 3) are always higher than those with α = 60 deg crossed ribs (case 5) in the entire three-pass channel.

Note in the before-turn region of the first pass (X/D = 5-10), that the pitch-averaged Sherwood number ratios for 60 deg parallel ribs left direction (case 3) are higher than those for 60 deg parallel ribs right direction (case 4). The lower Sh/Sh$_o$ ratios for case 4 may be caused by the conflicting inter-

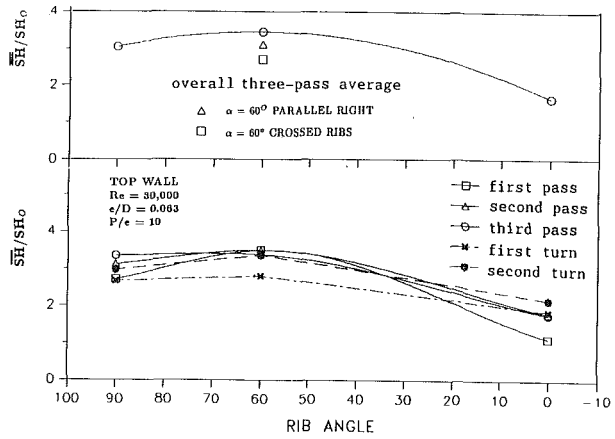

Fig. 10 Average Sherwood number ratio for α = 90, 60, and 0 deg

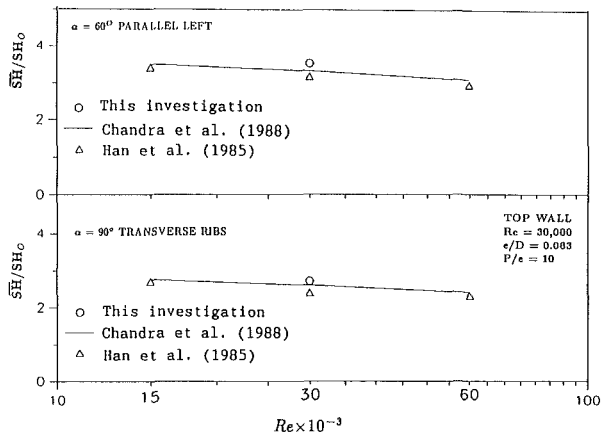

Fig. 11 Comparison between this study and previous investigations

action of the main flow, which is forced toward the inner line when approaching the first turn, and the secondary flow along the rib axes toward the outer line (see upper corner sketch in Fig. 7).

Pass-Averaged Sherwood Number Ratios. The average top-wall Sherwood number ratios, $\overline{Sh}/Sh_o$, in the first pass (X/D = 0–11), the first turn (X/D = 11–13), the second pass (X/D = 13–23), the second turn (X/D = 23–25), and the third pass (X/D = 25–36) of the flow channel versus the rib angle of attack (cases 2 and 3) are shown in Fig. 10 (bottom) for Re = 30,000 and P/e = 10, e/D = 0.063. The results for the smooth channel (case 1, α = 0 deg) are included for comparison. In the first pass, the first turn, the second pass, and the second turn of the channel, the $\overline{Sh}/Sh_o$ ratios increase with decreasing rib angle and then decrease with further decreasing rib angle of attack from 60 deg (see Fig. 10). In the third pass of the channel, however, the $\overline{Sh}/Sh_o$ ratios decrease monotonically with decreasing rib angle. Figure 10 also shows that the $\overline{Sh}/Sh_o$ ratios increase when the flow moves from the first pass to the second pass for α = 90 and 0 deg, respectively, but the $\overline{Sh}/Sh_o$ ratios in the third pass are about the same as those in the second pass; the $\overline{Sh}/Sh_o$ ratios remain constant in each pass of the channel for α = 60 deg; the $\overline{Sh}/Sh_o$ ratios in the second turn are higher than those in the first turn for α = 90, 60, and 0 deg. The average top-wall Sherwood number ratios for all cases studied are tabulated in Table 3.

The entire three-pass overall Sherwood number ratios ($\overline{\overline{Sh}}/Sh_o$) on the top wall of the channel against the rib angle are also shown in Fig. 10 (top) for all cases studied. The 60 deg

Table 3 Average Sherwood number ratio $\overline{Sh}/Sh_o$

Case No.	First Pass	First Turn	Second Pass	Second Turn	Third Pass
1	1.13	1.86	1.81	2.18	1.78
2	2.17	2.67	3.12	2.97	3.35
3	3.50	2.79	3.50	3.37	3.38
4	3:22	2.26	2.80	3.04	3.37
5	2.65	2.25	2.87	3.06	2.56

parallel ribs left direction (case 3) produce the highest overall Sherwood number augmentation of the rib orientations studied. Note that the 60 deg crossed ribs produce a lower overall mass transfer augmentation than the transverse ribs (α = 90 deg).

Comparison With Previous Investigations. In Fig. 11, the average ribbed-wall Sherwood number ratios on the first pass of the channel ($\overline{Sh}/Sh_o$) for α = 90 and 60 deg were compared with the average ribbed-wall mass transfer data (correlation) on the before-turn region (the first pass) reported by Chandra et al. (1988), and with the average heat transfer data (correlation) of Han et al. (1985). Note that the present mass transfer study used the naphthalene-coated ribs as turbulence promoters but the previous study (Chandra et al., 1988) used the metallic ribs. Figure 11 shows that the present mass transfer results in the first pass compare well with the published mass transfer correlations. The present mass transfer results for α = 90 deg and α = 60 deg are 4 and 6 percent higher than the previous mass transfer correlation, respectively, implying that the mass transfer coefficients from the surfaces between adjacent ribs are not affected significantly by either naphthalene-coated or metallic ribs.

The previous heat transfer data from Han et al. (1985) were obtained for flow in a uniformly heated, straight, square channel with two opposite ribbed walls, and with the same values of e/D, P/e, α, and Re as those of the present mass transfer study. In the previous study, heat was transferred from the ribs and from the surface between adjacent ribs, but the area for the average heat transfer coefficient calculations was only the original smooth surface area not including the area from the ribs. Based on the heat and mass transfer analogy, the Nusselt number ratios from Han et al. (1985) are converted to Sherwood number ratios for comparison.

As seen from Fig. 11, the present mass transfer results for α = 90 deg and α = 60 deg are 12 and 10 percent higher than the previous heat transfer data (Han et al., 1985). Note that, in the present mass transfer study, the mass transfer coefficients were determined only from the surfaces between adjacent naphthalene-coated ribs, not from those on and around the naphthalene-coated ribs. In real turbine cooling passages, the total heat transfer rates are from the ribs and from the surfaces between adjacent ribs.

Concluding Remarks

The effects of rib-angle orientation on local mass transfer distributions in a three-pass square channel with a pair of opposite rib-roughened walls have been investigated. The main findings are as follows:

1 In the smooth channel, the second-pass mass transfer coefficients are 60 percent higher than the first-pass because of the sharp 180 deg turning effect. The third-pass mass transfer coefficients, however, are about the same as those in the second pass of the channel.

2 In the ribbed channel, the second-pass mass transfer coefficients with 90 deg ribs are 15 percent higher than those in the first-pass because of the sharp 180 deg turning effect. The third-pass mass transfer coefficients are 7 percent higher than those in the second-pass of the channel. For 60 deg parallel ribs left direction (case 3), average mass transfer coefficients are about the same in each pass of the channel. Results from smooth and ribbed channel tests indicate that the mass transfer coefficients in the third pass are about the same as those in the second pass of the channel.

3 In comparing 60 deg parallel ribs left direction (case 3) to 90 deg transverse ribs, the mass transfer coefficients in the first pass are 30 percent higher because of the rib-induced secondary flow effect. The mass transfer coefficients are still 12 percent higher in the second pass and level off in the third pass, suggesting that the rib-induced secondary flow effect is balanced with the sharp 180 deg turning effect when the flow moves consecutively into the second and third passes of the channel.

4 For angled ribs, the mass transfer coefficients with 60 deg parallel ribs left direction (case 3) are higher than those with 60 deg ribs right direction (case 4) and with 60 deg crossed ribs (case 5). For all cases studied, the 60 deg parallel ribs left direction (case 3) gives the highest mass transfer coefficients in each pass of the channel. To improve mass transfer uniformity for case 3, it is recommended that the 60 deg parallel ribs in the third-pass be oriented toward the "right direction" instead of "left direction."

5 The combined effects of the sharp turn and the rib-angle orientation can increase or decrease the mass transfer augmentation immediately after the sharp turn. The rib-angle orientation is a guide for heat transfer design in turbine cooling passages.

6 The published heat transfer results for straight ribbed channels can be applied to the design of the first pass in multipass ribbed cooling channels in a turbine blade.

7 The average mass transfer coefficients from the surfaces between adjacent ribs with mass transfer active rib surfaces are not significantly different from those of previous studies with metallic ribs.

Acknowledgments

The investigation was supported in part by the NSF through Grant No. CBT-8713833. Very special thanks are due to Dr. S. C. Lau of Texas A&M University for his suggestions and discussions on the measurement and instrumentation.

References

Boyle, R. J., 1984, "Heat Transfer in Serpentine Passages With Turbulence Promoters," ASME Paper No. 84-HT-24.

Chandra, P. R., Han, J. C., and Lau, S. C., 1988, "Effect of Rib Angle on Local Heat/Mass Transfer Distribution in a Two-Pass Rib Roughened Channel," ASME JOURNAL OF TURBOMACHINERY, Vol. 110, pp. 233–241.

Fan, C. S., and Metzger, D. E., 1987, "Effects of Channel Aspect Ratio on Heat Transfer in Rectangular Passage Sharp 180° Turns," ASME Paper No. 87-GT-113.

Han, J. C., 1984, "Heat Transfer and Friction in Channels With Two Opposite Rib-Roughened Walls," ASME *Journal of Heat Transfer*, Vol. 106, pp. 774–781.

Han, J. C., Park, J. S., and Lei, C. K., 1985, "Heat Transfer Enhancement in Channels With Turbulence Promoters," ASME *Journal of Engineering for Gas Turbines and Power*, Vol. 107, pp. 629–635.

Han, J. C., 1988, "Heat Transfer and Friction Characteristics in Rectangular Channels With Rib Turbulators," ASME *Journal of Heat Transfer*, Vol. 110, No. 2, pp. 321–328.

Han, J. C., Chandra, P. R., and Lau, S. C., 1988, "Local Heat/Mass Transfer Distributions Around Sharp 180° Turns in Two-Pass Smooth and Rib-Roughened Channels," ASME *Journal of Heat Transfer*, Vol. 110, No. 1, pp. 91–98.

Han, J. C., and Park, J. S., 1988, "Developing Heat Transfer in Rectangular Channels With Rib Turbulators," *International Journal of Heat and Mass Transfer*, Vol. 31, No. 1, pp. 183–195.

Han, J. C., and Zhang, P., 1989, "Pressure Loss Distribution in Three-Pass Rectangular Channels With Rib Turbulators," ASME JOURNAL OF TURBOMACHINERY, Vol. 111, pp. 515–521.

Kline, S. J., and McClintock, F. A., 1953, "Describing Uncertainties in Single-Sample Experiments," *Mechanical Engineering*, Vol. 75, pp. 3–8.

McAdams, W. H., 1954, *Heat Transmission*, 3rd ed., McGraw-Hill, New York.

Metzger, D. E., and Sahm, M. K., 1986, "Heat Transfer Around Sharp 180° Turns in Smooth Rectangular Channels," ASME *Journal of Heat Transfer*, Vol. 108, pp. 500–506.

Metzger, D. E., and Vedula, R. P., 1987, "Heat Transfer in Triangular Channels With Angled Roughness Ribs on Two Walls," *Experimental Heat Transfer*, Vol. 1, pp. 31–44.

Sogin, H. H., 1958, "Sublimation From Disks to Air Streams Flowing Normal to Their Surfaces," *Trans. ASME*, Vol. 80, pp. 61–69.

Zhang, P., 1988, "Pressure Drop and Heat Transfer Distributions in Three-Pass Rectangular Channels With Rib Turbulators," M.S. Thesis, Texas A&M University.

Assessment of Laminar-Turbulent Transition in Closed Disk Geometries

A. P. Morse
Thermo-Fluid Mechanics Research Centre,
School of Engineering & Applied Sciences,
University of Sussex,
Falmer, Brighton, United Kingdom

Finite-difference solutions are presented for rotationally induced flows in the closed space between two coaxial disks and an outer cylindrical shroud, in which there is no superimposed flow. The solutions are obtained with an elliptic-flow calculation procedure and an anisotropic low turbulence Reynolds number k–ϵ model for the estimation of turbulent fluxes. The transition from laminar to turbulent flow is effected by including in the energy production term a small fraction (0.002) of the "turbulent viscosity" as calculated from a simple mixing length model. This level for the artificial energy input was chosen as that appropriate for transition at a local rotational Reynolds number of 3×10^5 for the flow over a free, rotating disk. The main focus of the paper is the rotor-stator system, for which the influence of rotational Reynolds number (over the range 10^5–10^7) is investigated. Predicted velocity profiles and disk moment coefficients show reasonably good agreement with available experimental data. The computational procedure is then extended to cover the cases of corotating and counterrotating systems, with variable relative disk speed.

1 Introduction

A turbine or compressor disk rotating near a stationary casing can be modeled in terms of the idealized rotor–stator system of Fig. 1, in which the rotor is shown as the right-hand disk. (Also shown in the figure are details of the coordinate system used in this paper and the geometric parameters relevant to the system.) Throughout this work, the outer shroud has been taken as stationary, while the internal flow boundary may be either an axis of symmetry or the surface of a rotating shaft. It may be noted, however, that the effects of the inner and outer flow boundaries are apparently very localized and do not permeate to the flow structure in the bulk of the cavity space (at least for small values of a/b). Although the system is often subjected to a superimposed radial outflow or inflow of cooling air, the present investigation is restricted to closed geometries, for which there is no such superimposed flow and it is assumed that there is neither ingress nor egress of fluid through any clearance spaces that may be present between the disks, the shroud, and the central shaft.

For the rotor–stator system, Daily and Nece (1960) identified four possible flow regimes, viz. laminar or turbulent flow, with merged or separated boundary layers on the disks. The delineation of the flow between these four regimes is dependent on both the rotational Reynolds number, Re_θ ($=\omega b^2/\nu$), where ω is the angular velocity of the rotor, and the gap ratio, G ($=s/b$), with merged boundary layers being typical of a small axial clearance between the disks. Additionally, the transition from laminar to turbulent flow was estimated to occur at a radial location corresponding to a local rotational Reynolds number, Re^* [$=(r/b)^2\mathrm{Re}_\theta$] of approximately 1.5×10^5.

This paper presents results illustrating the effect of Re_θ over the range 10^5–10^7 for a fixed value of $G=0.1$. Streamline contours in the r–z plane obtained for some of these flow conditions are shown in Fig. 1. The values associated with the streamlines denote mass flow rates normalized with the product of the molecular viscosity and the outer cavity radius, and as such are independent of the fluid properties for incompressible flow. In each case, the basic flow structure is the same, centrifugal effects giving rise to a radial outflow of fluid over the rotor and a radial inflow over the stator. The entire flow forms a single vortex, which recirculates about a center close to the shroud. In the central regions of the flow, a weak "axial wind" of flow represents the detachment of fluid from the boundary layer on the stator, prior to its entrainment into the boundary layer on the rotor.

Figures 1(a), 1(b), and 1(c) show the existence of separate boundary layers on the disks, a central flow region being apparent, where the radial velocity component is essentially zero. In Fig. 1(d), the reduced axial spacing ($G=0.04$) has clearly resulted in some interaction between the boundary layers and the central core region of the flow is largely suppressed. Comparison with Fig. 1(b) (for the same value of Re_θ) shows that the lower gap ratio reduces the total entrained flow rate by about 55 percent. At $\mathrm{Re}_\theta = 10^5$ (Fig. 1a), the predicted flow is

Contributed by the International Gas Turbine Institute and presented at the 34th International Gas Turbine and Aeroengine Congress and Exhibition, Toronto, Ontario, Canada, June 4–8, 1989. Manuscript received at ASME Headquarters January 27, 1989. Paper No. 89-GT-179.

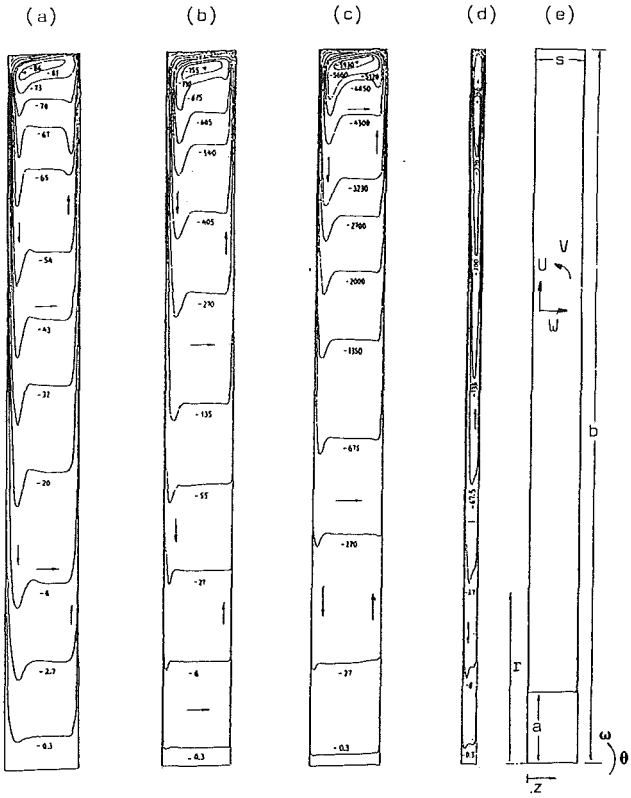

Fig. 1 Predicted streamlines for flow in rotor-stator geometry: (*a*) $Re_\theta = 10^5$, (*b*) $Re_\theta = 10^6$, (*c*) $Re_\theta = 10^7$, all with $a/b = 0$, $G = 0.1$, (*d*) $Re_\theta = 10^6$, $a/b = 0$, $G = 0.04$, (*e*) flow geometry and coordinate system

completely laminar. As the rotational Reynolds number is increased, the transition to turbulent flow occurs at a progressively earlier radius, this corresponding to a location of $r/b \sim 0.14$ at $Re_\theta = 10^7$ (Fig. 1*c*).

Experimental data for flows in closed rotor–stator systems have been obtained by Daily and Nece (1960) and Daily et al. (1964). The data encompass rotational Reynolds numbers up to 4.4×10^6, made feasible by the use of a variety of fluids, including air, water, and oils of differing viscosity. Although pressure differences increase rapidly with rotational speed, the assumption of incompressible flow, used here with air as the working fluid, is valid as the measurements at the highest values of Re_θ were obtained using liquids. Furthermore, the symmetry conditions established in the experiments justify the assumption of closed disk geometries used in this investigation.

Computation of these flows is accomplished here via a finite-difference solution of the governing elliptic equations for steady, axisymmetric, and incompressible flow. In spite of the seemingly complex nature of the strain field in wall-bounded rotating flows, there is evidence that fairly simple turbulence models are capable of predicting such flows with sufficient accuracy for engineering design calculations. For instance, Vaughan and Turner (1987) and Chew and Vaughan (1988) have published predictions for flows in rotor–stator systems, using an isotropic mixing length model, which generally lie within the uncertainty bounds of the experimental measurements. However, one effect of using a mixing length approach is that a very rapid transition to turbulent flow often occurs, which invalidates the model for calculation of regions of the flow space where laminar flow prevails. While it is acknowledged that flows in real-engine geometries will usually be fully turbulent in nature, verification of a computational procedure depends on comparison of calculations with experimental data obtained under conditions where the flow may be subject to the effects of laminar–turbulent transition. Furthermore, mixing length models are largely incapable of predicting the reverse-transition process, where turbulent flow may relaminarize under appropriate circumstances.

In both the above respects, a low turbulence Reynolds number k–ϵ (energy-dissipation) model has a greater potential than the mixing length approach. Using a modified version of the k–ϵ model of Jones and Launder (1972), Morse (1988, 1989) obtained predictions for flows in rotating cavities with a superimposed radial outflow or inflow, which were in good agreement with the available experimental data over a wide range of flow conditions. However, closed disk geometries differ from the rotating cavity in being bounded by four impermeable walls (or three walls and an axis of symmetry). An analogy can be drawn here with a two-dimensional, steady-state conduction problem in which uniform and equal temperatures exist at all the boundaries of the domain. Without a source of heat that is independent of temperature difference, the only possible solution is that of a uniform temperature everywhere. Likewise, in closed disk geometries, the boundary conditions on the turbulent kinetic energy demand that $k = 0$ everywhere and hence only a laminar-flow solution can result, whatever the value of the rotational Reynolds number. This clearly contrasts with experimental evidence, where increasing Re_θ has the effect of promoting a progressively earlier transition.

Nomenclature

a = inner cavity radius
b = outer cavity radius
C_m = moment coefficient = $M/\frac{1}{2}\rho\omega^2 b^5$
C_μ = numerical coefficient in turbulent model
G = gap ratio = s/b
G_k = production rate of turbulent kinetic energy
k = turbulent kinetic energy
M = frictional moment = $2\pi\int_0^b r^2 \tau_{\theta,z} dr$
$\dot{m}$ = mass flow rate
r = radial coordinate
Re_θ = rotational Reynolds number = $\omega b^2/\nu$
Re^* = local rotational Reynolds number = $\omega r^2/\nu$
s = disk spacing
U = time-averaged radial velocity component
$\overline{u_i u_j}$ = Reynolds stress tensor
$\overline{uv}$ = turbulent shear stress in r–θ plane
$\overline{uw}$ = turbulent shear stress in r–z plane
U_τ = friction velocity = $\sqrt{\tau_s/\rho}$
V = time-averaged circumferential velocity component
$\overline{vw}$ = turbulent shear stress in θ–z plane
W = time-averaged axial velocity component
y = generalized wall distance
y^+ = wall-distance Reynolds number = yU_τ/ν
z = axial coordinate
γ = numerical coefficient for artificial energy input
δ_{ij} = Kronecker delta
ϵ = dissipation rate of turbulent kinetic energy
θ = circumferential coordinate
μ = viscosity (without subscript = molecular viscosity)
ν = kinematic viscosity = μ/ρ
ρ = fluid density
τ_s = resultant wall shear stress
$\tau_{\theta,z}$ = shear stress in θ–z plane
ω = angular velocity
Ω^* = ratio of disk speeds

Subscripts

i, j = Cartesian tensor coordinates
T = turbulent

This situation contains echoes of the often-voiced criticism of the low Reynolds number k–ϵ model (Chew, 1984; Ong, 1988) that it fails to predict turbulent flow under conditions for which it is known to prevail experimentally. In the present work, an ad hoc approach is adopted to circumvent such difficulties. An artificial energy input (which has to be independent of k itself) is obtained by including in the energy production term a proportion of the "turbulent viscosity" as calculated from a simple mixing length formulation. The contribution from the mixing length model is kept small and merely provides a background turbulence production rate from which the kinetic energy levels can either decay or intensify, depending on the flow geometry and conditions. The magnitude of the necessary artificial input has been found to show good consistency in predictions of transition in pipe flow, the flat-plate boundary layer, and the flow over a free, rotating disk. It is therefore suggested that a similar approach could be used successfully in other situations where the low Reynolds number k–ϵ model has given problems in generating turbulent flow.

2 Mathematical Solution

The computational procedure used a modified version of the TEACH elliptic solver with a finite-difference mesh of 65 × 115 (axial-radial) nodes for all the predictions shown. In the axial direction, the grid employed a constant geometric expansion/contraction factor of 1.22 and was placed symmetrically with respect to the mid-axial plane, $z = s/2$. In the radial direction, a uniform grid was used for the central regions of the cavity, but with respective contraction factors of 1.10 and 1.19 to cluster nodes near the internal and external flow boundaries. This grid distribution resulted in a closest off-wall node distance from both disks and the shroud, which never exceeded $y^+ = 0.5$ in any of the cases considered. Tests were carried out with different axial mesh expansion factors in order to ensure that this proximity was sufficiently close to ensure grid independence of the calculated disk moment coefficients. Throughout the computations, the clearance between the disks and the outer shroud was fixed at a nominal value of 0.2 mm, with an assumed linear variation of angular velocity across the gap. Fluid properties were taken as those appropriate to air at 1 bar and 20°C, viz, $\rho = 1.19$ kg/m^3 and $\mu = 1.81 \times 10^{-5}$ kg/ms.

2.1 Details of Computational Procedure. The computer code solved discretized transport equations for the axial and radial velocity components W and U, respectively, the angular velocity V/r, and the turbulent quantities k and ϵ. In addition, mass continuity was satisfied and the pressure field updated by the solution of a pressure-correction equation, embodying a block-correction procedure to ensure only small aggregate mass residual throughout the calculation. Details of the governing equations and experiments with the operation of the computer code may be found from Morse (1988, 1989).

As noted by Morse (1989), convergence of the procedure for high rotational Reynolds number presents no special difficulties, but invokes a significant CPU time penalty on account of the larger pressure differences occurring within the cavity. The greatest CPU requirement (on a VAX VMS/8530 computer) for any of the rotor–stator predictions shown here was 3.5 h at $\mathrm{Re}_\theta = 10^7$, while converged solutions could generally be obtained within 1 h for $\mathrm{Re}_\theta \leq 10^6$.

2.2 The Turbulence Model. The low turbulence Reynolds number k–ϵ model used here has been developed from that first used by Jones and Launder (1972) for the prediction of laminarization, and subsequently used (with modified numerical coefficients) by Launder and Sharma (1974) and Launder et al. (1977) for wall-bounded rotating flows. The performance of the model was improved by Morse (1988, 1989) by, first, the inclusion of an additional negative source (sink) term in the ϵ equation and, second, the use of a different correlation to express the effect of wall proximity on the "turbulent viscosity." These modifications were made without compromising the predictive accuracy of the model for nonrotating flows.

It is conventional, in the turbulent viscosity representation, to express the Reynolds stresses via the constitutive relationship

$$\rho\overline{u_i u_j} = 2/3\delta_{ij}\rho k - \mu_T\left(\frac{\partial U_i}{\partial x_j} + \frac{\partial U_j}{\partial x_i}\right) \tag{1}$$

where μ_T is given by

$$\mu_T = c_\mu \rho k^2/\epsilon \tag{2}$$

and is assumed to have the same value for all six Reynolds stresses.

The flow over a free disk provides a well-documented test case for the assessment of turbulence models in flows subject to rotational effects. The results are discussed more fully in Section 2.3, but it is sufficient to note here that use of the isotropic k–ϵ model leads to a consistent underestimate of about 6 percent in the disk moment coefficient. A similar discrepancy is found also in predictions for rotor–stator systems. The reasons for this behavior are not clear, but are thought to stem, in order of probability, from (*i*) the assumption of an isotropic turbulent viscosity for $\rho\overline{uw}$ and $\rho\overline{vw}$, (*ii*) modeling deficiencies in the ϵ equation, and (*iii*) the pronounced wall-jet effect that is characteristic of these flows. In this work, the simple expedient has been adopted that the turbulent viscosity is anisotropic. Since the high Reynolds number forms of the stress transport equations (see, e.g., Launder and Morse, 1979) give no clue as to possible sources of anisotropic effects, it has been assumed for the present purpose that the anisotropy is confined to the near-wall region. Accordingly, the viscosity coefficient, c_μ, which is formulated as

$$C_\mu = 0.09[1 - \exp(-y^+/A^+)]^2 \tag{3}$$

adopts a value of $A^+ = 24.5$ (see Morse, 1989) for the calculation of $\rho\overline{uw}$ and 22.0 for $\rho\overline{uv}$ and $\rho\overline{vw}$. The modification is irrelevant in the case of $\rho\overline{uv}$, as predictions of this shear stress will generally be erroneous in the present flows. In the absence of rotation, the model is unaffected by the proposed change.

2.3 Application to the Flow Over a Free Disk. Computations of this flow were made using the parabolic (marching) procedures of Patankar and Spalding (1970), which is a valid approach as the full elliptic equations are not needed. A finite-difference grid of 120 cross-stream nodes was employed, these being heavily concentrated within the viscous sublayer. Radial step length was set at 0.05 times the local boundary layer thickness, subject to entrainment control.

For values of the rotational Reynolds number up to approximately 7×10^6, the moment coefficient for one side of the disk is known from experiment to follow the equation of Dorfman (1963), viz.

$$C_m = 0.491(\log_{10}\mathrm{Re}_\theta)^{-2.58} \tag{4}$$

Transition from laminar to turbulent flow occurs at a radius corresponding to a local rotational number, $\mathrm{Re}* [= (r/b)^2\mathrm{Re}_\theta]$ in the range 2×10^5–3×10^5, the upper value corresponding to the data of Theodorsen and Regier (1944).

It has been reported (Ong, 1988), and confirmed in the present work, that it is indeed difficult to effect the transition to turbulent flow with the computation started from reasonable levels of the turbulent kinetic energy. Used alone, the k–ϵ solution never departs significantly from the solution for laminar flow. Similarly, predictions for closed disk geometries always decay to laminar flow, because of the boundary conditions on the turbulent kinetic energy. For both cases, a turbulent solution is only possible if allowance is made for some artificial input of turbulent energy. Furthermore, this artificial input has to be independent of k itself. For the purposes of

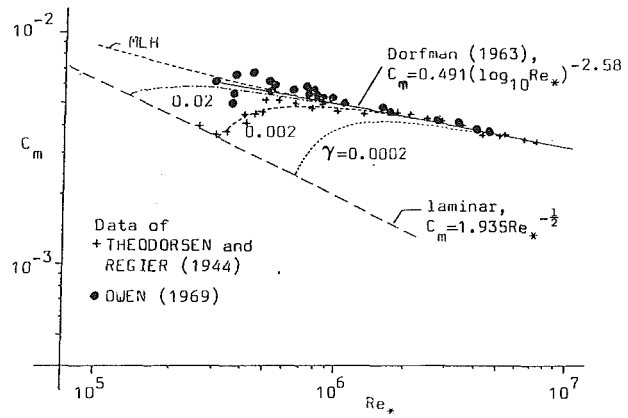

Fig. 2 Predicted variation of moment coefficient for the flow over a free disk

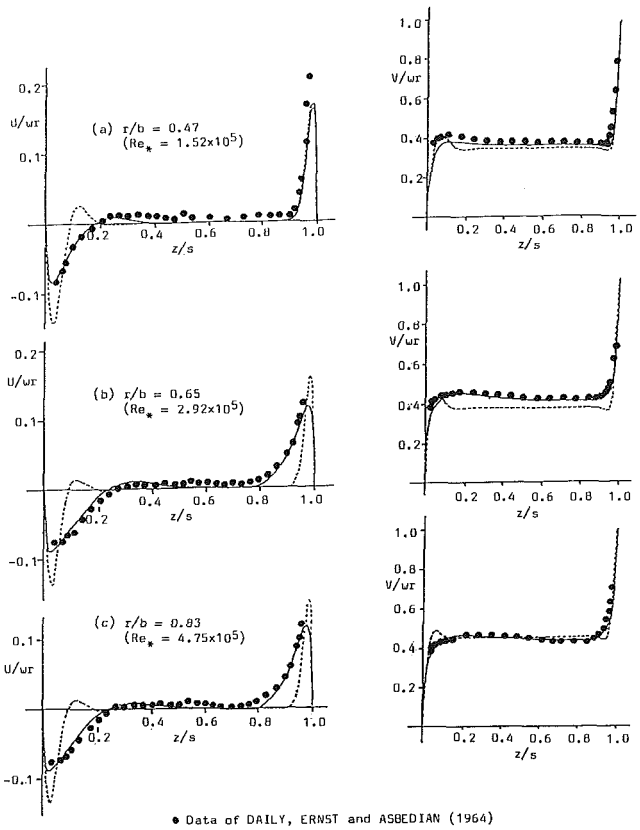

Fig. 3 Rotor-stator: predicted profiles of radial and circumferential velocity components for $Re_\theta = 6.9 \times 10^5$ ($a/b = 0.11$, $G = 0.0685$)

the present work, the necessary effect has been obtained by including in the turbulent energy production term, viz.

$$G_k = \mu_T \frac{\partial U_i}{\partial x_j}\left(\frac{\partial U_i}{\partial x_j}+\frac{\partial U_j}{\partial x_i}\right) \tag{5}$$

(as modified for anisotropic effects), a turbulent viscosity formulated as

$$\mu_T = (1-\gamma)\mu_{T,1} + \gamma\mu_{T,2} \tag{6}$$

where $\mu_{T,1}$ is the turbulent viscosity as calculated from equation (2) and $\mu_{T,2}$ is the value given by a simple mixing length prescription. The parameter γ in equation (7) is admittedly freely adjustable, subject to the vague constraint that it should be small ($\ll 1$). Clearly, use of $\gamma = 0$ will result in quasi-laminar flow, but if γ is too large, the transition to turbulent flow will occur prematurely.

Figure 2 shows predicted moment coefficients for the free disk with the anisotropic k–ϵ model. Irrespective of the value of γ (over the range shown), the moment coefficients agree closely with the Dorfman equation for $Re* > 5 \times 10^6$. A value of $\gamma = 0.002$ seems appropriate for transition at $Re* = 3 \times 10^5$; $\gamma = 0.02$ results in an earlier transition ($Re* \sim 1.2 \times 10^5$), which is perhaps more in keeping with the effect observed by Owen (1969). Clearly, the value needed for γ reflects, to some extent, the influence of external conditions and general flow unsteadiness characteristic of each experiment.

Using the data of Theodorsen and Regier as a baseline, the value of $\gamma = 0.002$ has been used for all the predictions of closed disk geometries shown in this work. While it is recognized that closed disk geometries differ from the free disk in that the core fluid also rotates and that the flow entrained into the boundary layers carries a significant turbulent intensity, such effects can be taken into account by the k–ϵ model, so that the predicted transition location is case dependent. Because γ is numerically small, there is no need for an elaborate mixing length treatment such as that used by Chew and Vaughan (1988).

3 Numerical Results

Validation of the turbulence model and the computational procedure is shown in Section 3.1 for the experimental data of Daily and Nece (1960) and Daily, et al. (1964) for rotor–stator flows. Section 3.2 presents predictions to illustrate the effects of variation in the rotational Reynolds number. Finally, Section 3.3 extends the method to the calculation of flows in corotating and counterrotating disk systems.

3.1 Rotor–Stator Systems. Predicted profiles of the radial circumferential velocities for a rotational Reynolds number of 6.9×10^5 are shown in Fig. 3. Shown also, as a guide to the assessment of transition effects, are the results of a solution assuming purely laminar flow. For this value of Re_θ, the estimated transition location of $Re^* = 1.5 \times 10^5$ (Daily and Nece, 1960) corresponds to a radius of $r/b = 0.47$, close to the first position of measurement. At this location (Fig. 3*a*), the predictions show only the faintest signs of incipient turbulence near the rotor, there being no significant departure of the wall shear stress from the laminar-flow solution until $r/b = 0.58$ ($Re^* = 2.31 \times 10^5$). In contrast, turbulence appears to be well established for the flow over the stator, where the boundary layer is appreciably thicker and the region of reverse (outward) flow much less pronounced than for laminar flow. In the core region, the predicted rotation level is intermediate between the data and the laminar solution, a behavior that is indicative of the delayed occurrence of transition. At $r/b = 0.65$ (Fig. 3*b*), both the measurements and the predictions show the development of fully turbulent flow in each boundary layer, this trend continuing at $r/b = 0.83$ (Fig. 3*c*). At this latter location, there appears to be some underestimate of the circumferential velocities near the rotor, although the core rotation level is predicted accurately. In view of the difficulties inherent in the experimental technique, particularly as regards positional measurement, the overall agreement with the data can be regarded as encouraging.

The calculated moment coefficient for (one side of) the rotor in this flow is 2.59×10^{-3}, which is approximately 4 percent lower than the measured values of 2.70×10^{-3}. Assuming purely laminar flow, the predicted moment coefficient is 1.74×10^{-3}. Hence the anisotropic k–ϵ model accounts for roughly 90 percent of the effect of the transition between the two flow regimes. (The isotropic model predicts a moment coefficient of 2.48×10^{-3}.) The discrepancy is largely due to the delayed occurrence of transition in the calculation; in this respect, use of a higher value of γ in equation (7) would presumably lead to better agreement with the data.

Further insight into the transition process is provided by Fig. 4, which shows the predicted variation of the disk shear

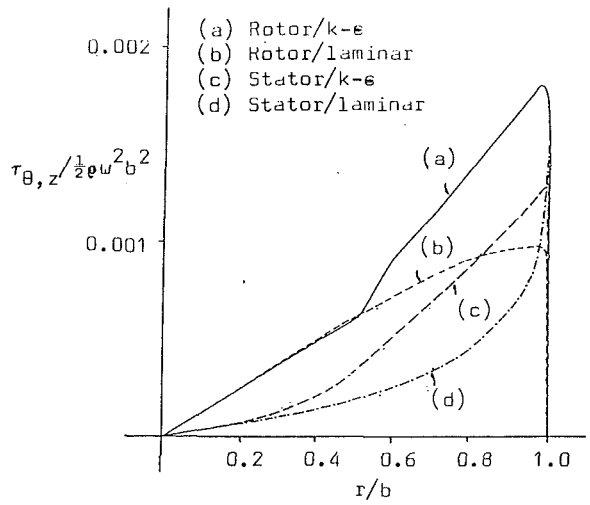

Fig. 4 Rotor-stator: predicted variation of shear stress on disks for $Re_\theta = 7 \times 10^5$ ($a/b = 0$, $G = 0.1$)

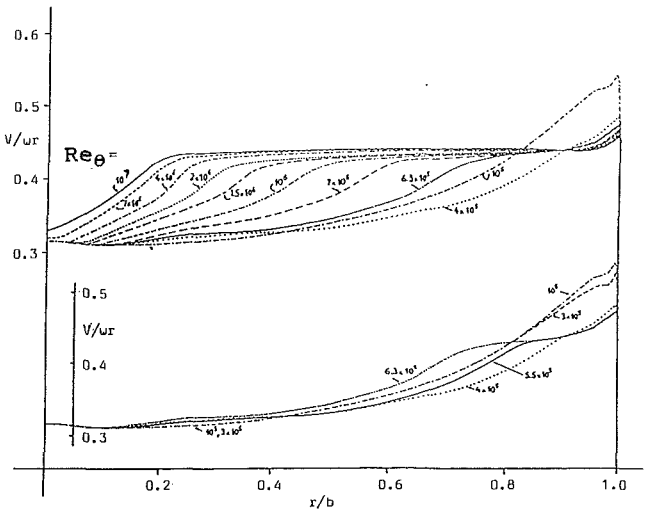

Fig. 6 Predicted variation with rotational Reynolds number of angular velocity at mid-axial plane ($a/b = 0$, $G = 0.1$)

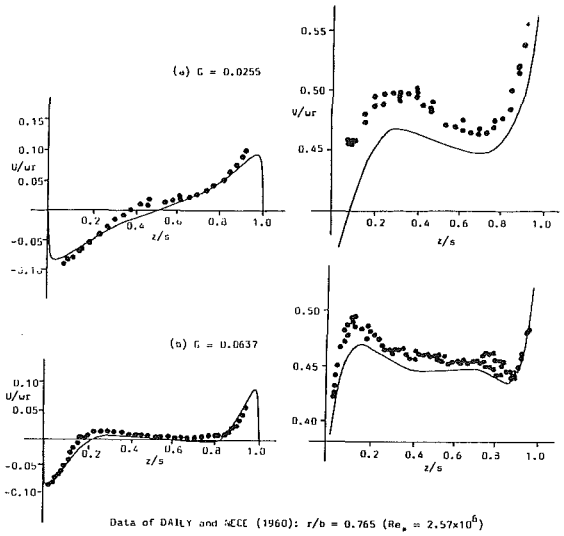

Fig. 5 Rotor-stator: predicted profiles of radial and circumferential velocity components for $Re_\theta = 4.4 \times 10^6$ ($a/b = 0.1$)

stresses in the θ–z plane for conditions similar to those discussed above, but with a gap ratio of 0.1. For the rotor, the shear stress departs abruptly from the laminar-flow solution at $r/b = 0.52$ ($Re^* = 1.9 \times 10^5$). In contrast, the corresponding results for the stator indicate a departure as early as a radial location of $r/b = 0.2$. A plausible explanation for this phenomenon is that the rechanneling of the flow from the rotor to the stator (see Fig. 1) is accompanied by strong amplification of the turbulence in the high-shear region near the outer shroud, whereas, in the subsequent rechanneling from the stator to the rotor, the flow passes through the central core region where strain rates are negligible. Hence, turbulence intensities decay rapidly before the flow is entrained into the rotor boundary layer, and the inner regions of the cavity are characterized by turbulence on the stator at radial locations where the flow over the rotor is essentially laminar.

Figure 5 compares predicted velocity profiles at $r/b = 0.765$ with the experimental data of Daily and Nece (1960) for a rotational Reynolds number of 4.4×10^6 and two values of the gap ratio, $G = 0.0255$ and 0.0637. At the lower axial clearance between the disks, there is clearly some interaction between the boundary layers and the central core does not develop. Due to the higher value of Re_θ, transition is predicted to occur at a lower radius ($r/b = 0.18$, $Re^* = 1.4 \times 10^5$) than before, so that the influence of the region of laminar flow is minimal. There appear to be some systematic differences between the predictions and the data, especially regarding the peak circumferential velocity near the stator, which is typically underestimated by 2–3 percent of the disk speed. There is noticeably better overall agreement with the data for $G = 0.0637$. The calculated moment coefficients for the rotor are 1.67×10^{-3} ($G = 0.0255$) and 1.815×10^{-3} ($G = 0.0637$). The former is 3.7 percent higher than the correlation of Daily and Nece for merged boundary-layer flow, while the latter agrees with the correlation for separate boundary layers to within three significant figures.

3.2 Effect of Rotational Reynolds Number. Predictions illlustrating the effect of the rotational Reynolds number on the angular velocity at the midaxial plane ($z = s/2$) are shown in Fig. 6 for a rotor-stator geometry of gap ratio 0.1. The internal flow boundary comprises an axis of symmetry and the outer shroud is stationary. Streamline contour plots for three of the values of Re_θ have already been introduced as Fig. 1.

At $Re_\theta = 10^5$, transition does not occur, the predicted rotational levels at midaxis are virtually identical to those for laminar flow, and the moment coefficient for the rotor differs from the laminar solution by only 0.3 percent. The first definite signs of turbulent flow over the rotor are observed at $Re_\theta = 4 \times 10^5$, for which transition occurs at $r/b \sim 0.8$ ($Re^* = 2.5 \times 10^5$). The subsequent amplification of the turbulence in the high-shearing region adjacent to the shroud then results in an abrupt decrease in velocity values for $r/b \gtrsim 0.9$. At lower radii, there is also a decrease in the rotational level as the enhanced turbulence near the stator produces a preferential transport of angular momentum away from the central region of the flow. However, for $Re_\theta > 5.5 \times 10^5$, the core rotation level begins to rise steadily and to develop a uniform region, which grows in extent to give a level constant to within ± 0.5 percent over two-thirds of the cavity radius at $Re_\theta = 10^7$. Over the range $7 \times 10^5 \leq Re_\theta \leq 10^7$, the level of the (uniform) core rotation shows a slight but progressive increase from 0.430 to 0.442 of the disk speed. As the computed profile for laminar flow is independent of the rotational Reynolds number, the predictions serve to indicate that nonuniformity of the core rotation is essentially due to the effects of laminar–turbulent transition. For $Re_\theta \leq 4 \times 10^6$, the angular velocity near the axis of symmetry remains constant at 0.315 (± 0.001) of that of the rotor, which is in keeping with the similarity solution of Dijkstra and van Heist (1983).

Predictions with the isotropic turbulence model show the

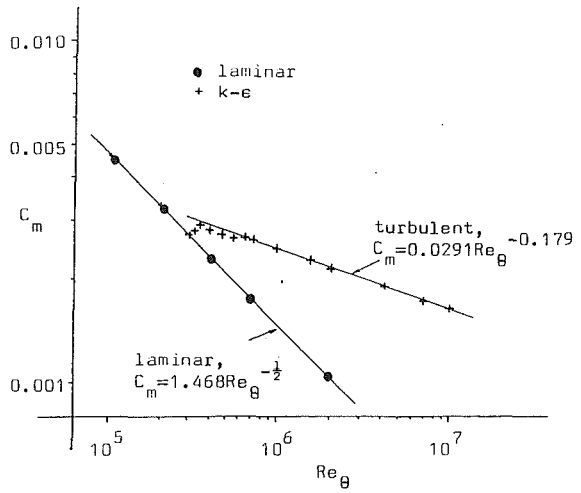

Fig. 7 Rotor-stator: predicted variation with rotational Reynolds number of moment coefficient of the rotor

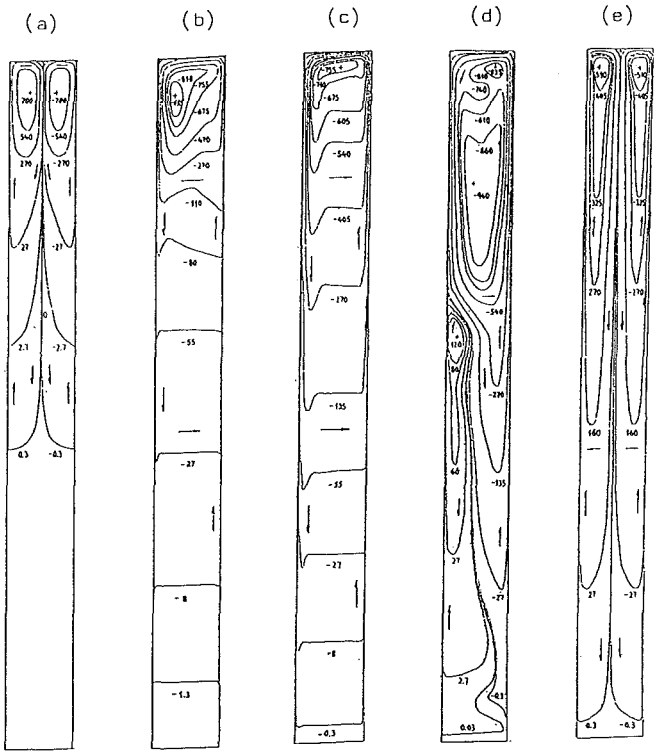

Fig. 8 Predicted streamlines for corotating and counterrotating disk flows; $Re_\theta = 10^6$: (*a*) $\Omega^* = +1$, (*b*) $\Omega^* = +0.5$, (*c*) $\Omega^* = 0$, (*d*) $\Omega^* = -0.5$, (*e*) $\Omega^* = -1$ ($a/b = 0$, $G = 0.1$)

same trends as indicated in Fig. 6, the only difference being that the core rotation level is reduced by about 1 percent of the disk speed.

The predicted variation of the moment coefficient for the rotor is shown in Fig. 7. For laminar flow, the results follow the correlation of Daily and Nece (1960) to an accuracy of four significant figures. There is some erratic behavior for values of Re_θ between 3×10^5 and 4×10^5, which is probably symptomatic of the predicted occurrence of turbulent flow over the stator at radii where the flow over the rotor is laminar. For higher values of Re_θ, the influence of the laminar region becomes of less importance and the predicted moment coefficients (for $Re_\theta \geq 7 \times 10^5$) conform to the correlation

$$C_m = 0.0291\ Re_\theta^{-0.179} \tag{7}$$

to within ± 0.2 percent. This may be compared to the correlation of Daily and Nece (1960), which, for a gap ratio of 0.1, reduces to

$$C_m = 0.0405\ Re_\theta^{-0.2} \tag{8}$$

the difference resulting in an underprediction of 4.0 percent at $Re_\theta = 10^6$, 1.1 percent at $Re_\theta = 4 \times 10^6$, and an overprediction of 0.8 percent at $Re_\theta = 10^7$.

3.3 Corotating and Counterrotating Disk Systems. In addition to the rotational Reynolds number and gap ratio, an influencial parameter for corotating and counterrotating disk systems is the relative disk speed Ω^*. Thus $\Omega^* = 0$ for the rotor–stator system, $+1$ for the case of pure corotation (equal disk speeds), and -1 for the case of pure counterrotation. In the following, the value quoted for Re_θ is based on the fixed rotational speed of the right-hand (or primary) disk, while the speed of the left-hand (secondary) disk is allowed to vary.

Velocity measurements in corotating and counterrotating systems have been reported by Szeri et al. (1983) and Dijkstra and van Heijst (1983), but only for laminar-flow conditions, while Graber et al. (1987) have obtained torque measurements for turbulent conditions.

Figure 8 shows streamline plots for values of Ω^* varying between $+1$ and -1 in stages of 0.5. The rotational Reynolds number is 10^6 and the gap ratio is 0.1. Again, the outer shroud is stationary. Working outward from Fig. 8(*c*), which represents the rotor–stator system, there is no dramatic change in the flow structure for corotation of the disks up to a value of $\Omega^* = +0.5$, the flow direction remaining outward over the primary and inward over the secondary disk. The total mass flow recirculating in the vortex system in fact shows about a 10 percent increase, although relatively less of this amount penetrates to low radii. As Ω^* approaches $+1$, the direction of motion over the secondary disk gradually reverses, beginning at the outer radii and, for pure corrotation, the flow structure evolves into perfect symmetry at about the midaxial plane. The flow direction is then outward over both disks and radially inward in the center of the cavity, so that a core region does not develop. Note that, for $\Omega^* = +1$, only about 0.5 percent of recirculated mass flow reaches the midradial location; if the shroud were rotating at the same speed as the disks, pure solid-body rotation of the flow would result, with no motion at all in the r–z plane. As Ω^* is increased, the predicted point of transition for the flow over the primary disk moves radially outward, from a location $r/b = 0.41$ ($Re^* = 1.7 \times 10^5$) for $\Omega^* = 0$, to $r/b = 0.61$ ($Re^* = 3.75 \times 10^5$) for $\Omega^* = +0.25$ and $r/b = 0.81$ ($Re^* = 6.6 \times 10^5$) for $\Omega^* = +0.5$. Beyond this last value, there is little further outward shift in the transition point.

For counterrotation, only a low value of Ω^* (~ -0.15) is apparently required to result in the formation of a weak vortex representing radial outflow over the secondary disk near the axis of rotation. This vortex cancels the radial inflow at higher radii, producing a stagnation point (a stagnation ring in three dimensions) at the disk surface. This stagnation point moves outward from a location $r/b = 0.20$ at $\Omega^* = -0.25$ to $r/b = 0.67$ at $\Omega^* = -0.5$ (shown in Fig. 8*d*) and $r/b = 0.90$ at $\Omega^* = -0.75$. The stagnation ring is clearly visible in the visualization experiments of Dijkstra and van Heijst; furthermore, the degree of counterrotation needed to produce it and its outward migration as the speed of the secondary disk is increased are broadly in agreement with their findings for laminar flow. For the case of pure counterrotation ($\Omega^* = -1$), the flow structure forms a symmetric pattern, which is qualitatively similar to that for pure corotation. Although the total mass flow recirculated is less than for the corotating case, significantly more of this penetrates to low radii. Predicted transition locations for the flow over the primary disk are $r/b = 0.41$ ($Re^* = 1.7 \times 10^5$) for $\Omega^* = 0$, $r/b = 0.24$ ($Re^* =$

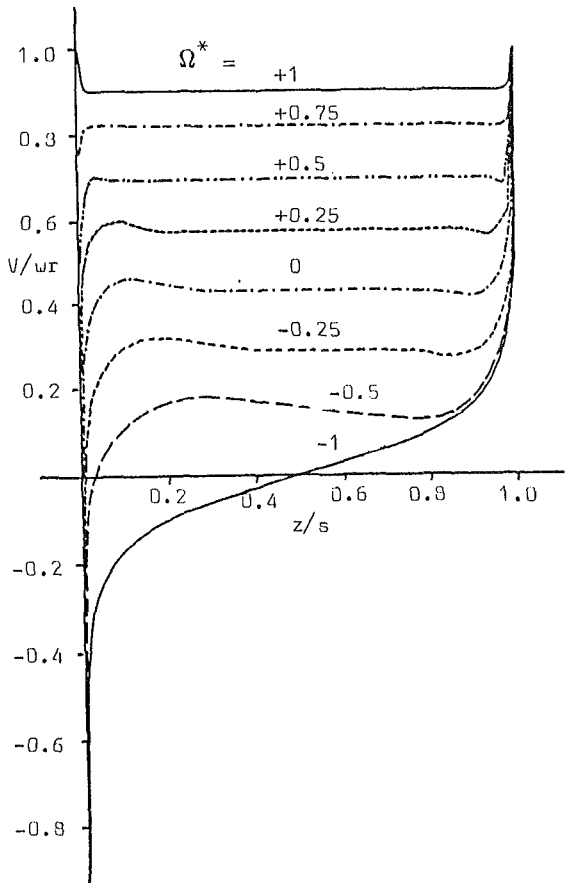

Fig. 9 Predicted variation with relative disk speed of circumferential velocity distribution at $r/b = 0.75$; $Re_\theta = 10^6$ ($a/b = 0$, $G = 0.1$)

6×10^4) for $\Omega^* = -0.25$, and $r/b \sim 0.16$ ($Re^* = 2.6 \times 10^4$) for $\Omega^* \leq -0.5$.

Corresponding predictions of the circumferential velocity distributions at $r/b = 0.75$ and at the midaxial plane are shown in Figs. 9 and 10. For corotating disks, the axial profile (Fig. 9) is always characterized by a central core region rotating at an angular velocity somewhat less than the mean of the disk speeds. At Ω^* approaches $+1$, the central core grows in extent. In contrast, counterrotation reduces the size of the central core, which is no longer in evidence at $\Omega^* = -0.5$. For pure counterrotation, the distribution is symmetric about the midaxial plane (in the converged solution, the frictional torques on the disks are identical to five-figure accuracy). For the radial profiles (Fig. 10), corotation results in an angular velocity distribution that is more uniform than that for the rotor–stator system ($\Omega^* = 0$). Indeed, the rotation level at the midaxial plane is essentially constant for $r/b \leq 0.6$. Counterrotation leads to more erratic behavior, particularly for $\Omega^* \leq -0.5$. Near the axis of symmetry, the direction of rotation reverses between values of Ω^* of -0.25 and -0.5. For pure counterrotation, the angular velocity at midaxis is zero at all radii.

Figure 11 shows the predicted influence of Ω^* on the disk moment coefficients, which, in each case, are evaluated with respect to the (fixed) rotational speed of the primary disk. The results confirm the expectation that the moment coefficient increases the greater the (absolute) difference between the disk speeds: thus C_m is highest for pure counterrotation and lowest for pure corotation. For both these limiting cases, the frictional torques on the disks are identical to five-figure accuracy in the converged solutions. Note that, for corotation, the net torque on the secondary disk reverses in sign at $\Omega^* \sim 0.6$.

Finally, for pure counterrotation, Fig. 12 shows the effect

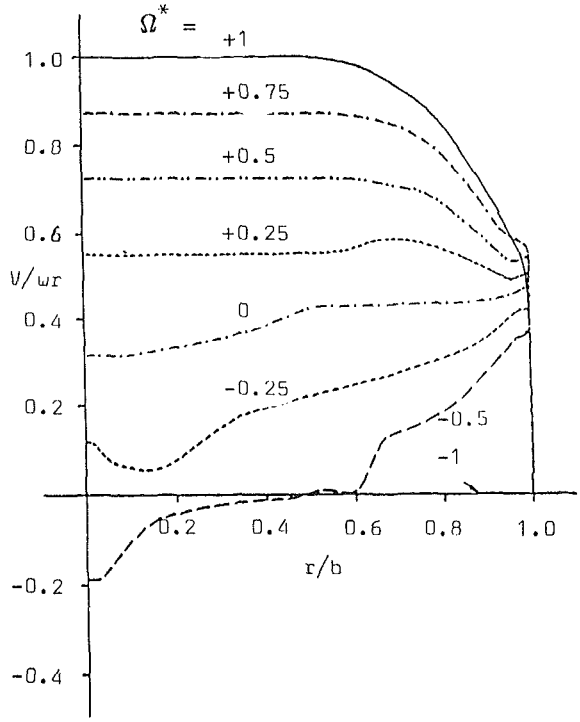

Fig. 10 Predicted variation with relative disk speed of circumferential velocity distribution at midaxial plane; $Re_\theta = 10^6$ ($a/b = 0$, $G = 0.1$)

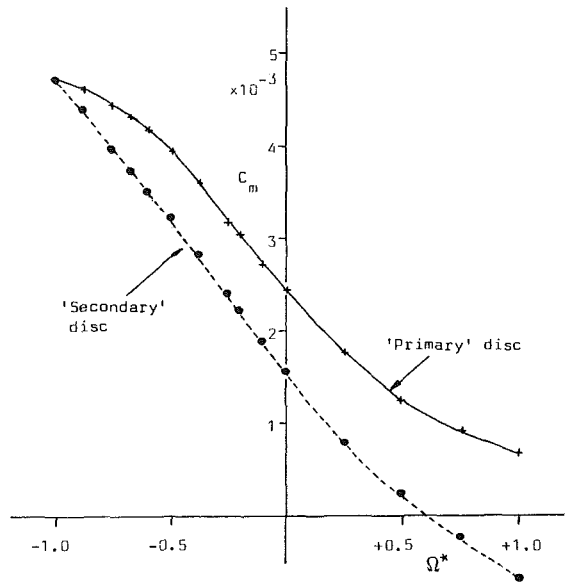

Fig. 11 Predicted variation with relative disk speed of moment coefficients for each disk; $Re_\theta = 10^6$ ($a/b = 0$, $G = 0.1$)

of rotational Reynolds number on the moment coefficients. For $Re_\theta \geq 10^6$, the predicted values correlate (to within $\pm$ 0.2 percent) to

$$C_m = 0.0319\ Re_\theta^{-0.1375} \tag{9}$$

4 Discussion

An anisotropic low-turbulence Reynolds number k–ϵ model has been applied to the prediction of flows in closed disk geometries. The model has been validated by comparison to experimental data obtained for rotor–stator systems and, in its isotropic form (Morse, 1989), for rotating cavity geometries. For the former, there are some systematic differences between the calculated and measured quantities, but erroneous infer-

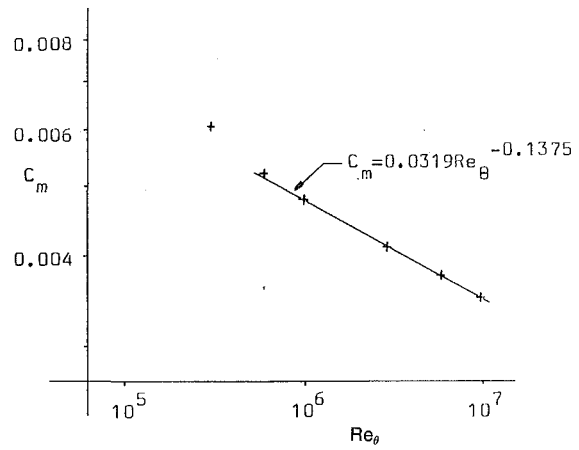

Fig. 12 Counterrotating disks: predicted variation of moment coefficient with rotational Reynolds number (a/b = 0, G = 0.1)

ences should not be drawn about the turbulence model in view of the experimental uncertainties.

The assumption of an anisotropic turbulent viscosity is based on uncertain grounds and has been introduced here largely as a matter of expediency in order to improve calculated disk moment coefficients. It is indeed possible that the discrepancies between the predictions of the isotropic model and the measurements may result from other causes, alluded to in Section 2.2, and these matters are currently receiving attention. It is noteworthy in this respect that inclusion of anisotropic effects is not necessary with the simpler mixing length approach in order to obtain the same accuracy for predicted moment coefficients as obtained here. However, mixing length models often fail in other, more complex flow situations, where the k–ϵ model probably represents the minimum level of sophistication necessary for accurate prediction.

The k–ϵ model, used in isolation, cannot however produce a turbulent-flow solution for closed disk geometries, whatever the value of the rotational Reynolds number. Irrespective of the initial profiles chosen for k and ϵ, the boundary conditions demand that both turbulent quantities will eventually decay to zero, yielding a laminar solution. This decay is slow: For the rotor–stator at $Re_\theta = 10^6$, approximately 6 h CPU time was required for the disk moment coefficient to fall to within 1 percent of that for laminar flow. The present approach to this problem, of including an artificial energy source based on a mixing length prescription, can probably be improved upon, but has led to surprisingly good consistency as to the value of the coefficient γ, which is needed to effect transition in both rotating and nonrotating flows.

The turbulence model and computational procedure have been extended to the cases of corotating and counterrotating systems with variable relative disk speed. Although there is a scarcity of experimental data for comparison, the underlying physics of the problem suggest that the predictions are likely to be of similar accuracy to those shown for the rotor–stator geometries.

5 Conclusions

The paper should prove useful in three respects, viz. (*i*) the validation of the low-turbulence Reynolds number k–ϵ for the prediction of flows in closed rotor–stator geometries, (*ii*) the introduction of a method by which turbulent-flow solutions can be obtained in such geometries, and (*iii*) the extension of the method to give further insight into the nature of the flows in corotating and counterrotating disk systems.

Although the current approach relies on a mixing length prescription to effect transition, the turbulence model can be used to obtain predictions throughout the cavity space, which encompasses regions of laminar, transitional and fully turbulent flow, without further empirical input. The ability to predict these three flow regimes should be a considerable benefit for geometries and flow conditions that bring about a reverse-transition (laminarization) effect.

A logical extension of the present work is the prediction of disk geometries subjected to a superimposed flow, with the inclusion of heat transfer and compressibility effects. All three aspects present no serious problems, but their accurate prediction is dependent on the validity of the turbulence model in the simpler situation of isothermal, incompressible flow considered here. The results of this extension, and a more thorough investigation of corotating and counterrotating disk systems, will be presented in future work.

Acknowledgments

The author is glad to acknowledge the interest shown in this work by Dr. J. M. Owen and Dr. C. M. Vaughan, colleagues at the Thermo-Fluid Mechanics Research Centre, University of Sussex, and the continuing collaboration with Rolls-Royce plc.

References

Chew, J. W., 1984, "Prediction of Flow in Rotating Disk Systems Using the k–ϵ Turbulence Model," ASME Paper No. 84-GT-229.

Chew, J. W., and Baughan, C. M., 1988, "Numerical Predictions for the Flow Induced by an Enclosed Rotating Disk," ASME Paper No. 88-GT-127.

Daily, J. W., and Nece, R. E., 1960, "Chamber Dimension Effects on Induced Flow and Frictional Resistance of Enclosed Rotating Disks," ASME *Journal of Basic Engineering*, Vol. 82, p. 217.

Daily, J. W., Ernst, W. D., and Asbedian, V. V., 1964, "Enclosed Rotating Disks With Superposed Throughflow: Mean Steady and Periodic Unsteady Characteristics of Induced Flow," Hydrodynamics Lab. Rept. 54, Massachusetts Institute of Technology, Cambridge, MA.

Dijkstra, D., and van Heijst, G. J. F., 1983, "The Flow Between Two Finite Rotating Disks Enclosed by a Cylinder," *J. Fluid Mech.*, Vol. 128, p. 123.

Dorfman, L. A., 1963, *Hydrodynamic Resistance and Heat Loss of Rotating Solids*, Oliver and Boyd, Edinburgh, United Kingdom.

Graber, D. J., Daniels, W. A., and Johnson, B. V., 1987, "Disk Pumping Test," UTC, Pratt and Whitney, West Palm Beach, FL.

Jones, W. P., and Launder, B. E., 1972, "The Prediction of Laminarization With a Two-Equation Model of Turbulence," *Int. J. Heat and Mass Transfer*, Vol. 15, p. 301.

Launder, B. E., and Sharma, B. I., 1974, "Application of the Energy-Dissipation Model of Turbulence to the Calculation of Flow Near a Spinning Disk," *Letters in Heat and Mass Transfer*, Vol. 1, p. 131.

Launder, B. E., and Morse, A. P., 1977, "Numerical Prediction of Axisymmetric Free Shear Flows With a Second-Order Reynolds Stress Closure," *Turbulent Shear Flows, I*, Springer Verlag, New York.

Launder, B. E., Pridden, C. H., and Sharma, B. I., 1977, "The Calculation of Turbulent Boundary Layers on Spinning and Curved Surfaces," *J. Fluids Eng.*, Vol. 99, p. 231.

Morse, A. P., 1988, "Numerical Prediction of Turbulent Flow in Rotating Cavities," ASME JOURNAL OF TURBOMACHINERY, Vol. 110, p. 202.

Morse, A. P., 1991, "Application of a Low Reynolds Number k–ϵ Turbulence Model to High-Speed Rotating Cavity Flows," ASME JOURNAL OF TURBOMACHINERY, *this issue*.

Ong, C. L., 1988, "Computation of Fluid Flow and Heat Transfer in Rotating Disk-Systems," D. Phil. Thesis, University of Sussex, United Kingdom.

Owen, J. M., 1969, "Flow Between a Rotating and a Stationary Disk," D. Phil. Thesis, University of Sussex, United Kingdom.

Patankar, S. V., and Spalding, D. B., 1970, *Heat and Mass Transfer in Boundary Layers*, Intertext Books, United Kingdom.

Szeri, A. Z., Schneider, S. J., Labbe, F., and Kaufman, H. N., 1983, "Flow Between Rotating Disks. Part 1: Basic Flow," *J. Fluid Mech.*, Vol. 134, p. 103.

Theodorsen, T., and Reiger, A., 1944, "Experiments on Drag of Revolving Disks Cylinders and Streamline Rods at High Speeds," NACA Rept. 793.

Vaughan, C. M., and Turner, A. B., 1987, "Numerical Predictions of Axisymmetric Flow in a Rotor-Stator System With an External Mainstream Flow," *Proc. 5th Int. Conf. on Num. Methods in Laminar and Turbulent Flow*, Pineridge Press, Swansea, United Kingdom.